

Turbomachine Internal Pressure
and
Blade Response Modelling

By
Christopher Bryan Church

Submitted in Partial Fulfilment of the Requirements for the Degree

MASTER OF MECHANICAL ENGINEERING

Supervisor:
Prof. P.S. Heyns

FACULTY OF ENGINEERING, BUILT ENVIRONMENT AND INFORMATION TECHNOLOGY
DEPARTMENT OF MECHANICAL AND AERONAUTICAL ENGINEERING

UNIVERSITY OF PRETORIA

December 2015

Turbomachine Internal Pressure and Blade Response Modelling

Author: *C.B. Church*

Supervisor: *Prof. P.S. Heyns*

Department: *Department of Mechanical and Aeronautical Engineering*

University: *University of Pretoria*

Year: *2015*

Abstract

Blades are critical components of turbomachines, failure of a single blade may result in catastrophic failure of the entire machine. One study found that blade failure was the third largest cause of power generation unit unavailability. Their condition during operation is therefore of interest to monitor.

Various intrusive and non-intrusive blade vibration measurement (BVM) techniques have been developed for this purpose. Intrusive techniques such as strain gauge approaches and the frequency modulated grid method require expensive and complex alteration of the actual blades and/or casing. Further, they are prone to failure due to operation in harsh working environments. Therefore the use of intrusive techniques has been predominantly limited to design verification, testing and research.

Blade tip timing approaches are currently at the forefront of BVM. The practicality, accuracy and ease of implementation of these approaches have limited their commercial roll out. An alternative non-intrusive source of blade vibration information was found in the internal casing pressure signal (CPS).

As the machine operates the blade movement excites the fluid in the casing, producing a measureable response. Unlike BTT approaches which deal with a scarcity of information, CPS based methods must identify blade vibration from a complex signal which contains multiple other sources of information. The issue of how to model the blades' response and fluid interaction is the topic of this investigation.

An available single stage turbomachine mock setup was modified for internal pressure and direct blade vibration measurements. Pressure measurements were taken in line with a redesigned hub and rotor blade assembly. Strain gauges (SG) were applied to blades in order to capture their response.

The blades' response was modelled as the combination of a forcing function and a multiple degree of freedom transfer function. Repurposed experimental modal analysis frequency response reconstruction techniques were used to model the blades' transfer function. It was found that this technique was able to capture the blades' underlying behaviour to a high degree. The forcing function was modelled in the time domain as a series of Gaussian shaped force distributions. It was found that the model was able to capture many important aspects of the forcing behaviour. Both the forcing function and blade transfer function were explored using constrained optimisation techniques.

The blade-fluid interaction was modelled as a Fourier series. It was shown that the blade behaviour cannot be extracted from a pressure signal using standard frequency analysis techniques. The viability of an inverse problem solution methodology, for the purpose of blade behaviour extraction, was investigated. This was achieved by solving reduced components of the model with SG measurements and observations from pressure measurements. Further the need to isolate the pressure field about individual blades was motivated and a novel time domain windowing technique provided.

Keywords: Turbomachine, blade vibration, casing pressure, signal processing, optimisation.

Acknowledgements

The author would like to acknowledge the personal and professional contributions of individuals without which this project would not have been possible.

Prof. Stephan Heyns was both an academic and personal mentor during the period of this project. His expertise and experience in dynamic analysis, rotor-dynamics of turbomachinery, intelligent systems, systems modelling and signal processing is considered by the author to be unrivalled. As such his time is extremely valuable and extensively sought after by both academics and professionals in industry. Thank you for your open door, even when you didn't have the time to open it. Thank you for always being encouraging.

A fellow colleague and friend, Mr. Dawie Diamond, provided extensive help and support during this research. Although his research was based on blade tip time of arrival technologies, his insight and expertise in intelligent systems and blade behaviour was invaluable. Thanks are also due to him making the experimental setup and data acquisition systems available as well as for the time provided to illustrate to me how these systems work.

An area of expertise of Dr. Nico Wilke is optimisation techniques. Correct formulation of my inverse problems and solution routes were greatly improved by his insight and ability. Thank you for taking the time to review my work and provide constructive and useful criticism.

Investigations would not be possible without the help of highly experienced technical staff. Thank you Mr George Breitenbach and Mr Herman Booysen for making your expertise and time available in the labs.

Finally I would like to thank my friend and fellow masters student Ian Luyt. It has been a challenging ride, thank you.

Contents

Abstract	ii
Acknowledgements	iii
Contents	iv
Nomenclature	vii
Acronyms and Abbreviations	ix
Chapter 1 Introduction	1
1.1. Background	1
1.2. Problem Statement	2
1.3. Literature Review	3
1.3.1. Turbomachine Blade Vibration – Excitation and Response Mechanisms	4
1.3.2. Turbomachine Blade Vibration – Modes, Mode Shapes and Critical Resonances	6
1.3.3. Classical Blade Vibration Measurement Techniques	8
1.3.4. Blade Tip Timing Approach	10
1.3.5. Casing Pressure Signal Methods	13
1.3.6. Blade Effects and System Mode Response	47
1.3.7. Tachometer Geometry Compensation and Shaft Torsional Vibration Estimation	55
1.4. Scope of Research	59
1.5. Document Overview	61
Chapter 2 Theoretical Development	62
2.1. Introduction to Theoretical Development	62
2.2. Literature Discussion	63
2.2.1. Comparison of Casing Pressure Signal Models	63
2.2.2. Discussion on Alternative Casing Pressure Methods	71
2.2.3. Comparison of Casing Pressure Signal Methods with Blade Tip Timing Approaches	73
2.3. Pressure Signal	76
2.4. Blade Vibrational Response Representation	92
2.5. Individual Wave Separation through Novel Time-Domain Windowing	105
2.6. Inverse Problem Formulation	112
Chapter 3 Experimental Setup and Characterisation	129
3.1. Experimental Setup and Characterisation Introduction	129
3.2. Brief Description of the Experimental Test Bench	130
3.3. Experimental Test Bench Design and Components	131
3.4. Turbomachine Blades and Analytical Characterisation	134
	iv

3.4.1.	Blade Design	134
3.4.2.	Analytical Modal Response of Individual Blades	135
3.5.	Instrumentation	137
3.5.1.	General Instrumentation	137
3.5.2.	Blade Mounted Vibration Measurement Sensors	138
3.6.	Experimental Configurations	140
3.6.1.	Blade and Hub Configurations	140
3.6.2.	Excitation Configurations	140
3.7.	Experimental Characterisation of Turbine Blade and System Response	143
3.7.1.	Unconstrained System Response	143
3.7.2.	Blade Response at Installed Position	148
3.7.3.	Run-up Blade Responses	150
3.8.	Experimental Methodology	153
Chapter 4 Investigations and Results		155
4.1.	Introduction to Investigations and Results	155
4.2.	Observations from SG Measurements	156
4.3.	Pressure Signal Observations and Model Assumptions Review	176
Chapter 5 Conclusions and Future Research		195
5.1.	Conclusions	195
5.2.	Future Research	199
Chapter 6 References		202
Chapter 7 Appendices		206
7.1.	Appendix A – Derivations, Blade Models and Algorithms	207
7.1.1.	A1 - Derivation of Bessel Representation of Pressure Signal	207
7.1.2.	A2 – Reformulation of Internal Pressure Signal Equation	208
7.1.3.	A3 – Analytical Blade and Assembly Models	209
7.1.4.	A4 – Shaft Encoder Geometry Compensation Algorithm	214
7.2.	Appendix B – Additional BTT Literature	217
7.2.1.	B1 – General BTT Theory	217
7.2.2.	B2 – Autoregressive Methods	219
7.2.3.	B3 – Circumferential Fourier Fit	224
7.2.4.	B4 – Bayesian Curve Fitting	225
7.3.	Appendix C – Example Application of CPS Method	231
7.4.	Appendix D – FE Analyses	237

7.4.1.	D1 – FE Analysis Configuration	237
7.4.2.	D2 - Analytical Investigation for Strain Gauge Position Choice	239
7.4.3.	D3 – Strain Gauge Positioning for Healthy Blade	240
7.4.4.	D4 – Analytical Campbell Diagrams for Damaged Blades	241
7.5.	Appendix E – Experimental Setup, Characterisation and Methodology	242
7.5.1.	E1 – Instrumentation List	242
7.5.2.	E2 – Sound Pressure Transducer Calibration Report	243
7.5.3.	E3 – Images of Experimental Setup	244
7.5.4.	E4 – Relative Tip Distances	251
7.5.5.	E5 - Unconstrained System Response	252
7.5.6.	E6 – Response Spectra of Individual Blades	263
7.5.7.	E7 – Run-Up Resonance Detection	271
7.5.8.	E8 – Signal Processing Methodology	277
7.6.	Appendix F – Steady Measurement Plan	282
7.7.	Appendix G – SG Response Results	283
7.7.1.	G1 – Waterfall Plots of Full SG Responses	283
7.7.2.	G2 – Waterfall Plots of SG Forcing Function Spectra	289
7.7.3.	G3 – SG Forcing Function Fitting Results	292
7.7.4.	G4 – Multi-Start SG Blade Transfer Function Fitting Results	293
7.7.5.	G5 – Exemplar SG Response and Forcing Function Forms	294
7.8.	Appendix H – Pressure Results	300
7.8.1.	H1 – Average Pressure Waveforms	300
7.8.2.	H2 – Variance Heat Maps for Average Wave Forms	307
7.8.3.	H3– Waterfall Plots of Synchronously Averaged Configuration 1 Pressure Signals	308
7.8.4.	H4 – Selected Pressure Range Plots and Linear Fit Table	309
7.8.5.	H5 – Selected Phase Modulation Due to Forced Response Plots	311

Nomenclature

Symbol	Description	Units
c	Viscous damping coefficient	Ns/m
e	Error between two vector components	
f	Frequency range	Hz
f_{BPF}	Blade passing frequency	Hz
f_f	Excitation frequency	Hz
f_n	Natural frequency	Hz
Δf_{NB}	Narrow band peak spacing	Hz
f_R	Rotor speed	Hz
g	Gaussian distribution	
h	Logistic sigmoid height parameter	
i	Index in set of all natural numbers	
j	Complex number	
k_r	Elemental stiffness matrix/Stiffness coefficient	
k	Travelling wave mode number	
k'	Observed travelling wave mode number	
l	Logistic sigmoid function	
m	Elemental mass matrix/Mass coefficient	kg
n	Noise term (function)	
r	Blade index	
$s_{1,2}$	Logistic sigmoid slope parameters	
t	Time	s
$t_{0,i}$	Blade passing times	s
x	Blade displacement	m
A	Single degree of freedom response amplitude	
A_r	Modal constants	
B	Number of rotor blades in cascade	
C	Blade chord length	m
C'	Effective blade chord length	m
D_i	Fourier coefficient for Doppler model	
D_i'	Positive set Fourier coefficients for Doppler model	
E	Error/Error function	
F	Harmonic blade forcing function	
G	Fourier transform of Gaussian based forcing function	
H	Receptance/Blade transfer function	
$ \hat{H} $	Fundamental frequency peak height	
I	Indicator function	
M	Magnitude tuning factor	
L	Blade length	m
N	Number of modes	
N_{rev}	Number of revolutions	

O_1, O_2	Stationary casing observers	
P	Casing pressure magnitude	Pa
P_i	Stationary pressure distribution Fourier coefficient	
Q_i	Positive set Fourier coefficient	
R	Radius from shaft center to blade tip	m
R^2	Coefficient of determination	
S	Blade-to-blade gap	m
V	Number of stator vanes	
W	Sigmoidal window function	
\bar{W}	Flow quantities relative to blade	
X	Fourier transform of blade tip displacement	
α	Receptance	
χ	Blade vibration phase angle	rad
δ	Dirac delta function	
η	Modal damping ratio	
γ	Blade stagger angle	rad
κ	Scalar penalty parameter	
λ_r	Individual blade vibration phase angle	rad
μ	Gaussian distribution mean blade passing times	s
ν	Phase angle offset/Phase angle tuning parameter	rad
ω	Angular frequency	rad/s
ω'	Observed natural frequencies	rad
ω_a, ω_b	Half power points	rad
ω_f	Excitation frequency	rad/s
ω_n	Natural frequency	rad/s
ω_r	Natural frequency	rad/s
ω_{SPF}	Stator passing frequency	rad/s
ϕ	Single degree of freedom system phase offset	rad
ψ	Blade tip angular displacement	rad
σ	Gaussian distribution standard deviation	s
τ	Scaling factor	
θ	Angle on rotor reference frame	rad
θ_{blade}	Angle blade subtends during excitation	rad
ζ	Viscous damping coefficient	
Γ	Amplitude modulating tuning parameter	
$\Delta_{1,2}$	Sigmoidal window offset parameters	
E	Engine order	
Λ	Doppler model amplitude tuning factor	
Ω	Rotor speed	rad/s
Ψ	Blade angular response in frequency domain	rad
$\Upsilon_{eq,ineq}$	Equality and inequality constraint functions	

Acronyms and Abbreviations

1E	First edgewise mode
1F/1B	First flap/bending mode
2F/2B	Second flap/bending mode
1T	First torsional mode
D1	Damaged blade type 1
D2	Damaged blade type 2
H	Healthy blade
ANOVA	Analysis of variance
AR	Auto-regression curve fitting technique
BMT	Blade mistuning
BPASS	Blade passing time
BPF	Blade passing frequency
BTT	Blade tip timing
BVM	Blade vibration measurement
CAD	Computer aided design
CFD	Computational fluid dynamics
CFF	Circumferential Fourier fit
CPS	Casing pressure signal
DAQ	Data acquisition
DOF	Degree of freedom
EO	Engine order
EOM	Equations of motion
FE	Finite element
FFT	Fast Fourier transform
FM	Frequency modulation
FMG	Frequency modulated grid
FRF	Frequency response function
GA	Genetic algorithm
HP	High pressure
IGV	Inlet guide vane
LM	Lumped mass
LP	Low pressure
MAE	Mean absolute error
MDOF	Multiple degree of freedom
MPSD	Mean percentage standard deviation of blade natural frequencies
MSE	Mean square error
NF	Natural frequency
NSMS	Non-intrusive stress measurement system
OPR	Once per revolution
OT	Order track
PM	Phase modulated
PPR	Pulses per revolution

PSO	Particle swarm algorithm
RPM	Revolutions per minute
RMSE	Root mean square error
RSE	Root square error
SA	Synchronous averaging
SDOF	Single degree of freedom
SE	Square error
SG	Strain gauge
SMD	Spring-mass-damper
SP	Signal processing
SPF	Stator passing frequency
TOA	Time of arrival

Avg.	Average
Config.	Configuration
Det.	Deterministic
Eq.	Equality
Eval.	Evaluations
Freq.	Frequency
Func.	Function
Ineq.	Inequality
Iter.	Iterations
Lin.	Linear
Pres.	Pressure
Sto.	Stochastic
Symm.	Symmetric
Tacho.	Tachometer



Chapter 1 Introduction

1.1. Background

Forced vibration of bladed assemblies in turbomachines may occur in the vicinity of their natural frequencies. This results in magnified structural motion of the blades (Carrington et al., 2001; Kahl, 2002). Structural motion of rotating blades directly affects the fatigue life, performance and integrity of the system as a whole (Heath and Imregun, 1997), therefore the design and validation of methodologies to extract turbomachine blade vibration information during operation is of interest. Accurately determining the vibrational response of a blade can be used to directly report on any change in its health as well as assist in residual life estimation and maintenance planning.

In terms of real world significance turbine failure and maintenance accounts for a large portion of the unavailability of power generation units. Turbine failure was identified as the third largest cause of non-productivity of power generation units behind overhauls and boiler issues (Dewey and Rieger, 1985). The implication of a single blade failing could be the catastrophic failure of the entire turbomachine (Rao and Dutta, 2012). Research shows that blades in the late stages of low pressure (LP) turbines are the most vulnerable to failure (Das et al., 2003; Mukhopadhyay and Chowdhury, 1998; Rao and Dutta, 2014). This phenomenon is attributed to longer blades which result in higher stress levels and a plurality of potential resonance frequencies (Booyesen et al., 2014). It has also been mentioned that final stage LP turbine blades, which experience low and potentially wet steam flow and high back pressure, are potentially susceptible to stall flutter (Rao and Dutta, 2014, 2012).

There are many complex mechanisms by which LP turbine blades fail. Nearly half of all LP turbine blade failures are attributed to stress corrosion cracking, corrosion fatigue and fatigue and as high as 40% of the failure mechanisms are unidentified or not completely understood (Mukhopadhyay and Chowdhury, 1998; Rao and Dutta, 2012). Fatigue damage is accumulated during both steady and transient operation of a turbomachine. Centrifugal stresses are dominant during steady operation, however during run-up or shut down blades may accumulate high cycle fatigue damage as a result of passing through critical speeds which excite blade resonances. This fatigue accumulation is reported to be regardless of low excitation force magnitudes (Booyesen et al., 2015; Rao, 1998).

It was concluded that repeat failure incidents occur as a result of implementation of unproven life-extension methodologies, based on deterministic fatigue life calculations used in tandem with schedule based maintenance regimes (Dewey and Rieger, 1985; Pusey and Pusey, 1990).

Blade residual life is traditionally estimated using deterministic cumulative damage theories. Uncertainty in input parameters, such as loading and material properties, leads to highly conservative parameter choices for life estimations with little confidence (Booyesen et al., 2014). A probabilistic approach to life estimation with cumulative damage theories has been suggested to improve the current practices (Banaszkiewicz, 2015; Booyesen et al., 2014). Blade vibration monitoring can not only provide the much needed accuracy and confidence in input parameters for all residual life calculations, but may also furnish insight into the complex failure mechanisms.

Mechanical engineering as a whole is currently experiencing a paradigm shift from schedule based maintenance to a needs based maintenance regime. In terms of blade vibration monitoring advanced techniques are sought to extend the maintenance schedules safely as well as to provide early warning systems to prevent catastrophic failure.



1.2. Problem Statement

Blade vibration measurement during operation can provide crucial insight into the health and expected residual life of turbomachine blades. Both intrusive and non-contact techniques have been developed for this purpose.

The intrusive techniques suffer many drawbacks, the most significant of which being their cost and complexity to implement, the high possibility of failure during operation and an undesirable influence on the geometry and operation of the turbomachine blades (Zielinski and Ziller, 2000). The use of intrusive techniques has therefore been limited to the design verification stage of blade development and not implemented as a continuous online condition monitoring solution on working turbomachines (Forbes and Randall, 2012).

A robust non-contact and non-intrusive blade vibration measurement technique was thus sought. A possible solution was found in blade tip time of arrival (BTT) techniques. Discrete tip deflections of a blade could be captured during operation and these measured deflections related to the actual blade vibration by means of curve fitting techniques. The BTT techniques are capable of estimating both the frequency of vibration as well as the amplitude of the tip deflection along its oscillatory path.

BTT techniques are limited by the sensors' ability to accurately capture the tip time of arrival (TOA) in a number of operating conditions. Other factors such as the number of sensors required to provide sufficient information for curve fitting processes, the rotor speed, and the general poor performance of many of the curve fitting algorithms when a small amount of noise is present in the measured TOA signal limit the technique. Recent developments incorporating a statistical approach to the BTT curve fitting procedure have yielded encouraging results (Diamond et al., 2014a).

A second non-contact source of blade vibration information was identified. Blade vibration information is inherently present in the fluid flowing through the turbomachine due to excitation from the blades (Forbes and Randall, 2013). It may be possible to extract blade vibration information from the pressure fluctuations of the fluid within the casing by means of signal-processing techniques. Techniques based upon internal pressure or casing vibration measurement are known as casing pressure signal (CPS) methods.

Current CPS techniques require knowledge of the actual blade vibration to within half the rotor frequency of operation during steady operation (Forbes and Randall, 2013) or require measurements to be taken at a minimum of two different rotor operating frequencies (Cox and Anusonti-Inthra, 2014). Analytical models have been proposed for this task, however the most appropriate means to model the fluid-blade interaction and the constituent components of the signal requires work.

In light of the drawbacks and advantages of the current non-intrusive blade vibration measurement techniques, a robust method capable of supplying blade vibration information from non-contact and non-intrusive measurement techniques is desired.

The problem is therefore to investigate aspects related to the modelling and evaluation of a turbomachine internal pressure signal for the purpose of blade vibration measurement. This includes how to construct an internal pressure model with included blade vibration and the evaluation thereof.

The succeeding section contains the literature reviewed for this purpose.



1.3. Literature Review

The principal focus of this dissertation is on blade vibration modelling, specifically in terms of pressure signal analysis based methods. The literature presented in this section was chosen to highlight this choice whilst simultaneously providing brief insight into other related blade vibration measurement and signal processing techniques and concerns.

Depending on the subject matter, additional derivations and explanations have been included in the appendix and are referred to in the text. Different literature sources have used different nomenclature in their derivations. The nomenclature of the source literature is maintained and is defined in the text. The nomenclature of developmental sections remains constant from Chapter 2 onwards.

The following overview may be used as a guide to the literature investigated. Although all topics included are considered as important, certain topics are integral to understanding aspects about the pressure signal and others are supplementary to those topics and may be given less attention. Due to the volume of information considered, the reader is therefore directed towards the crucial literature topics for developing a picture of the internal pressure based problem.

The succeeding section discusses turbomachine blade vibration from an excitation and response point of view. Specifically the difference between asynchronous and synchronous vibration is covered. Thereafter the discussion focuses on the mode shapes and excitation ranges of interest when evaluating blade vibration. These sections provide the basis theory upon which all blade vibration measurement methodologies are based and are thus considered as integral topics.

Classical blade vibration measurement methodologies are then touched on to highlight the importance and need for non-contact non-intrusive methodologies. A classical method, namely the strain gauge approach, forms part of the actual measurement scheme and is thus of importance to briefly discuss.

At the current forefront of non-contact non-intrusive blade vibration measurement is the blade tip timing approach. As the current primary non-interference method, understanding its strengths and weaknesses contribute to the premise for the pressure based methods. This theory does however not contribute significantly to the understanding of the pressure based methods and may be seen in a supplementary light.

The theme which follows investigates and discusses the casing pressure signal based methods. Topics such as analytical representation of a rotating pressure signal and blade vibration identification from pressure signals are reviewed. Two different internal pressure models, from two different literature sources, provide the backbone for the theoretical development in the succeeding chapter (blade mounted pressure analyses methodologies will not be considered as they are inherently intrusive techniques). It is on these pressure based methods and investigations that the remaining chapters of the dissertation are based. These themes are therefore the central focus of the literature review.

Finally a number of factors which may influence experimental observations (such as the tuning of a rotor system, physical coupling between blades and identification of the presence of flutter) are reviewed. The need for zebra-tape based tachometer geometry compensation, for signal processing purposes, is also touched upon. These final literature sections are considered as supplementary.

The chapter ends off by discussing the scope of research as well as provides an overview of the succeeding chapters.

1.3.1. Turbomachine Blade Vibration – Excitation and Response Mechanisms

Many blade excitation mechanisms exist. The excitation mechanisms and corresponding forced responses can be classified into one of two categories: synchronous and asynchronous vibration. Before these mechanisms can be explored it is convenient to define blade vibration in terms of engine order (EO). The EO is the ratio of the excitation frequency ω_f to the frequency of rotation Ω . The relationship is presented in Equation [1.3.1].

$$EO = \frac{\omega_f}{\Omega} \quad [1.3.1]$$

Synchronous excitation phenomena (also known as “engine-ordered”, “integral order” or “harmonic” excitation) are characterised by vibration at frequencies which are integer multiples of the engine rotation speed (Rao and Dutta, 2012). The excitation phenomenon can be due to mechanical effects such as residual unbalance of rotors and non-concentric casings which result in a varying circumferential blade tip clearance. It may also be due to aerodynamic effects such as irregular pressure distributions stemming from engine intake geometry (Zielinski and Ziller, 2000). These mechanisms typically produce vibration at low EOs due to few excitation instances per revolution (Zielinski and Ziller, 2000).

Upstream and downstream stator blades direct fluid flow across rotor blades in order to produce lift. This lift is used to convert axial flow energy into rotational mechanical energy and is the primary purpose of the rotor. This process induces significant pressure fluctuations across the rotor blades and is the principal source of blade excitation (Cookson et al., 2001; Hsu, 2014). The process typically results in a higher engine order excitation when compared to other synchronous phenomena (Zielinski and Ziller, 2000). The associated excitation frequency is a function of the number of upstream stator blades directing flow onto the rotor blades. This frequency is known as the stator passing frequency (SPF) ω_{SPF} or blade passing frequency (BPF) ω_{BPF} . A schematic cross section of a turbomachine with stationary inlet guide vanes (IGVs) and stator rows directing axial flow onto moving rotor blades is presented in Figure 1.3-1. The blade rotation direction is indicated in (a) and fluid flow direction in (b).

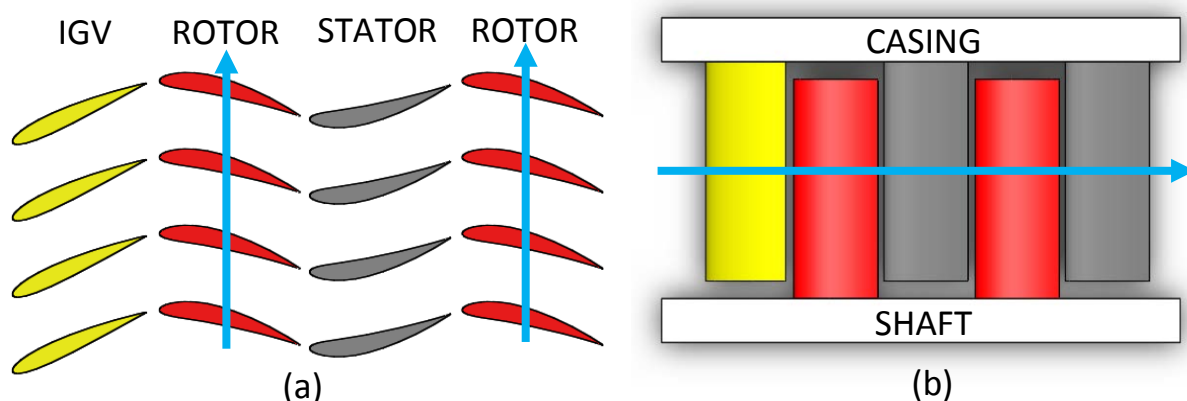


Figure 1.3-1 Schematic turbomachine cross section of blades. (a) Top view with blade direction of rotation indicated. (b) Side view with direction of fluid flow indicated.

The phase of the synchronous response remains constant with respect to a datum arbitrarily fixed to the circumference of rotation (Heath and Imregun, 1996). Thus a single stationary measurement point, capturing a discrete indicator of response (such as tip deflection), will always encounter the



response indicator in the same state (at the same phase angle) along the oscillating cycle given a fixed rotational frequency.

Synchronous excitation is a function of the rotor speed as well as turbomachine geometric configuration. It can thus be viewed as a deterministic source of vibration with clear causality relationships. Due to its deterministic nature designers are generally able to tune a rotor system such that the resonant frequencies of the system do not coincide with synchronous excitation for steady operation (Rao and Dutta, 2012). Similarly, during run-up or shut-down, resonant (or critical) operating speeds are avoided or passed through rapidly to prevent fatigue accumulation and damage.

Asynchronous excitation occurs at frequencies which are not integer multiples of rotational speed and thus results in non-integer EO excitation. Asynchronous phenomena can be viewed as stochastic when compared to the deterministic synchronous vibration as they are not directly a function of rotor speed or geometry. The main causes of asynchronous excitation are attributed to aerodynamic instabilities such as compressor surge, self-exciting flutter, rotating stall and acoustic resonance (Sabbatini et al., 2012a; Zielinski and Ziller, 1997).

Self-exciting flutter is a widely studied asynchronous excitation mechanism due to the fatigue effects it has on turbomachine blades (Rao and Dutta, 2012). It does not require an external excitation frequency as this is generated internally (Rao and Dutta, 2012). If a blade is perturbed from its equilibrium position it will vibrate at one of its natural frequencies until it reaches equilibrium once again (Rao and Dutta, 2012). However, if the flow about the blade is sufficiently affected by the vibrating blade such the dynamic forces acting on the blade sustain the response then a state of self-excitation is achieved (Rao and Dutta, 2012). It has been noted that the relationship between self-excitation and loading conditions is not linear. It has also been noted that self-exciting flutter occurs in lower order modes (Rao and Dutta, 2012).

The response resonant frequency and phase of an asynchronously vibrating blade is arbitrary with respect to the angular velocity and position of the rotor. Therefore a single measurement point on the circumference of rotation is exposed to the full range of possible responses of the measured discrete indicator over a certain number of revolutions (Forbes, 2010). A discrete response indicator, sampled at a single stationary point can thus be utilised with classic sampling and sub-sampling techniques to stitch together the full response cycle of the indicator (Heath and Imregun, 1996). This reconstructed signal can then be related directly to the actual blade vibration.

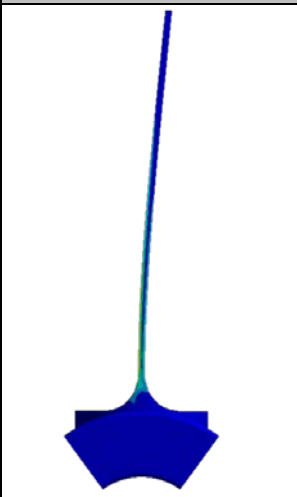
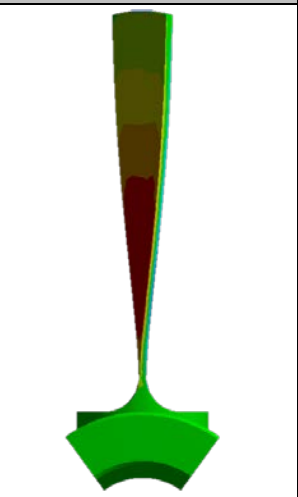

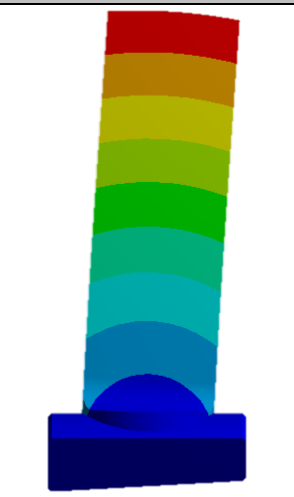
Turbulence and impulse excitation is inherent in the fluid flow and so is an expected source of excitation regardless of the presence of other synchronous or asynchronous phenomena (Forbes and Randall, 2013; Rao and Dutta, 2012). Turbulence within a particular stage may manifest as a result of upstream turbulence, vortex generation at the blade tip, boundary effects and inverted flow (Forbes, 2010, p. 64). Blade and upstream wake interaction may result in both impulse and turbulent excitation due to the 'chopping' of the upstream wake by the moving rotor blades (Forbes, 2010, p. 65).

Therefore a turbomachine blade does not necessarily experience purely synchronous excitation as asynchronous turbulence is inherent, nor does it experience purely asynchronous excitation as synchronous vibration due to machine geometry and operational speeds is intrinsic as well. However the response may be dominated by one or the other. The succeeding section outlines response modes, mode shapes and critical resonances.

1.3.2. Turbomachine Blade Vibration – Modes, Mode Shapes and Critical Resonances

Three basic blade deformation mode shapes exist when exposed to natural vibration conditions, namely flexural (bending), torsional (twisting) and combined (simultaneous bending and twisting) (Cookson et al., 2001). The bending modes can be further subdivided into flap-wise modes (bending about the weak axis) and edgewise modes (bending about the strong axis) (Cookson et al., 2001). Examples of the first four basic flexural and torsional modes for a simplified turbomachine blade geometry are presented in Table 1.3-1.

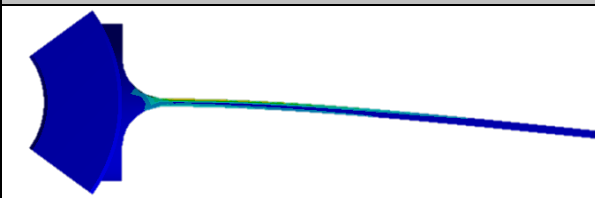
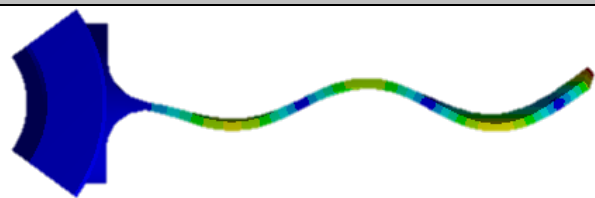
Table 1.3-1 Basic turbomachine blade mode shapes

First Flap (1F)	First Torsional (1T)	Second Flap (2F)	First Edgewise (1E)
			

In general turbomachine blade geometries are more complex than the flat beam approximation presented in Table 1.3-1. The blades may contain twisting, tapering and a complex aerofoil cross sectional shape along the length of the blade (Rao and Dutta, 2012). This complex geometry results in basic mode shapes which are not purely flexural, torsional or edgewise but rather a combination of all with one of the primary mode shapes dominating the response (Kahl, 2002).

When designing blade vibration monitoring systems it is important to consider which blade resonances are of interest and which are not. As excitation frequency increases so does response motion decrease for a given excitation force (Cookson et al., 2001). Moreover as the structural motion of the blade decreases it follows that strain at integral locations on the blade decreases resulting in decreased stresses at those locations. Therefore it is sufficient to concentrate attention upon the lower resonance frequencies and disregard higher order response (Cookson et al., 2001). Consider the first and third flap-wise bending mode shapes of the given geometry presented in Table 1.3-2.

Table 1.3-2 Comparison of first and third bending modes

First Flap (1F)	Third Flap (3F)
	

In the first mode all the blade mass is moving in one direction whereas in the third bending mode near equal portions of the blade are moving in opposite directions. In the first case the resulting energy

from mass motion is additive whereas in the second case the energy due to mass motion roughly balances out (Cookson et al., 2001). Therefore it may be concluded that the root attachment of a blade responding in the first bending mode will experience a higher stress than if it had been responding in the third bending mode given the same excitation force. This trend, of mass motion averaging over the blade, only increases as the complexity of the mode shapes increases (Cookson et al., 2001).

An investigation into the fatigue life of LP turbine blades, using an updated statistical approach, found that the fundamental frequency of vibration (the first flap mode) was the only resonance to have a significant impact on the fatigue life results in the study (Booyesen et al., 2015). These results reinforce the reasoning that only the first few natural modes and corresponding mode shapes of response are of interest (Cookson et al., 2001).

It follows logically to determine at which rotor speeds the first few resonances may be excited. This is best represented on a Campbell diagram. The Campbell diagram illustrates the relationship between the changing natural frequency of a given mode as the rotor speed increases and possible harmonic excitation from synchronous vibration mechanisms.

The speed at which the rotor operates may explicitly appear in the governing equations of motion (EOM) causing the natural frequencies and mode shapes to become a function of speed (Genta, 2005, p. 9). When centripetal forces are accounted for in the EOM it can be shown that they contribute an additive term to the stiffness matrix and are scaled by the square of the rotor speed. This increase in stiffness is termed centrifugal stiffening and leads directly to an increase in the flap-wise blade natural frequencies (Kahl, 2002). The potential engine harmonic excitation is indicated by EO lines which are integer multiples of the rotor speed. An example Campbell diagram, displaying the changing fundamental resonant frequency as a function of shaft speed analytically obtained for the blade geometry represented in Table 1.3-2 and 9, is given in Figure 1.3-2.

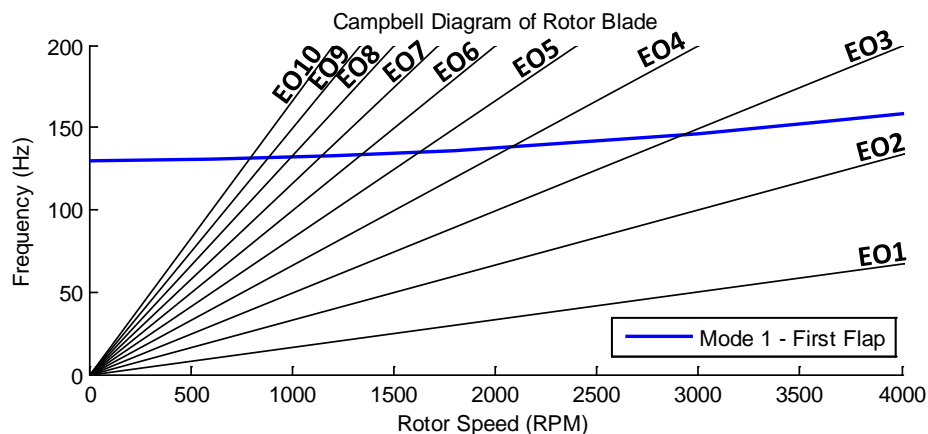


Figure 1.3-2 Example Campbell diagram of first flap mode for arbitrary blade geometry

It is clear from the diagram that a near unlimited number of EO resonances are possible (Cookson et al., 2001). Within the speed range plotted only harmonics at EOs of 3 and above may cause excitation of the blade at its fundamental frequency. However as the engine order increases so does the magnitude of the excitation force diminish given a particular excitation mechanism (Booyesen et al., 2015). Therefore as the EO of the harmonics increase, so do their relative importance decrease.

1.3.3. Classical Blade Vibration Measurement Techniques

Two classical methodologies for capturing blade vibration response are discussed here. The first is known as the frequency modulated grid method and the second the strain gauge (SG) approach (Sabbatini et al., 2012b).

The frequency modulated (FM) grid method requires that permanent magnets be fitted to the tips of rotor blades and receiver wires embedded into the casing about the rotor stage. During operation the vibrating blades induce an alternating current in the receiver wires. The signal produced by this alternating current is modulated by the frequency of response and can therefore be related to the blade frequency of vibration (Sabbatini et al., 2012b; Zielinski and Ziller, 2000).

The method is limited to a few blades on a single stage. It is expensive and complex to implement and requires intrusive alteration of the blades and casing (Zielinski and Ziller, 2000). Figure 1.3-3 illustrates the frequency modulated grid method, the location of the magnet in the blade tip, the blade vibration and the signal measured from the receiver wires embedded into the casing are indicated.

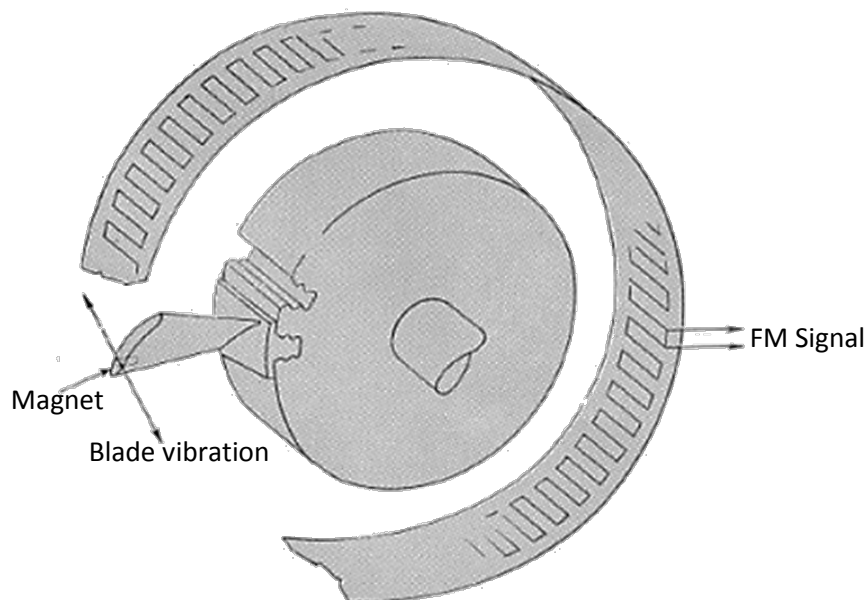


Figure 1.3-3 Frequency modulated grid method (Russhard, 2015)

The SG approach involves vibration capture by means of SGs attached to the surface of the blade. The approach is itself not free from disadvantages. Similar to the frequency modulated grid method it also requires a complex installation procedure and the SGs have an inherent possibility of failure during operation due to exposure to harsh working environments and high operating temperatures. This results in a low expected operating life for the SGs (Robinson and Washburn, 1991; Russhard, 2015). In order to be sensitive to a number of blade response modes, the SG approach may require multiple gauges to be attached across the surfaces of the rotor blade at specially chosen regions.

Further the SG approach requires rotor mounted radio telemetry systems or slip ring systems for data capture (Heath and Imregun, 1997; Russhard, 2015). The mounted strain gauges may interfere with the mechanical behaviour of the vibrating blade to which it is attached, as well as distort the desired fluid-blade interaction (Heath and Imregun, 1997). For these reasons the SG approach is generally

limited to design verification of a limited number of blades and is not practical for online operational condition monitoring (Forbes and Randall, 2013; Russhard, 2015).

Due to the fact that only a few blades are instrumented at specific locations, a very limited picture of the actual strain across an individual blade is obtained. Inter-blade differences and mistuning of the system results in a situation where the behaviour of an individual instrumented blade cannot be directly compared to a neighbouring un-instrumented blade (Russhard, 2015). This limits statistical analyses of the blade and full rotor behaviours (Russhard, 2015).

Although the SG technique suffers from many drawbacks, it is still the most accurate way to capture blade vibration phenomena in real time (Russhard, 2015). It stands as a both a benchmark and means for calibration with which one can compare and fine tune new blade vibration measurement techniques. Unlike the frequency modulated grid method the SG approach does not require that blades and casing be specially designed for instrumentation. SGs can be simply applied to the surface of the rotor blades at chosen regions and reading taken therefrom. For these reasons the SG approach remains the preferred intrusive blade vibration measurement technique (Russhard, 2015). Examples of actual rotor mounted SGs can be seen in Figure 1.3-4.



Figure 1.3-4 Example of rotor mounted strain gauges. (a) Root mounted strain gauges. (b) Blade mounted strain gauges.
(Russhard, 2015)

The early FM method often required calibration with a blade mounted SG system (Russhard, 2015). Once the calibration was complete testing could be performed without reference to the blade mounted SG (Russhard, 2015). The need for calibration with SGs has however lapsed for the reason that numerical blade modelling techniques have matured to the point that they can perform this task adequately well (Russhard, 2015).

Both classical techniques discussed require intrusive intervention in order to capture the blade vibration. The succeeding section outlines one of the first viable non-contact and non-intrusive blade vibration measurement technologies, namely the blade tip timing (BTT) approach.

1.3.4. Blade Tip Timing Approach

BTT techniques are based on the measurement of blade tip times of arrival (TOA) at discrete measurement points on the circumference of the rotor casing. The TOA of a vibrating blade differs from that of a non-vibrating blade as is illustrated in Figure 1.3-5. The theoretical non-vibrating blade's TOA is estimated using a tachometer or similar sensor, whilst the true blade arrival time may be measured using eddy current probes, optical sensors, microwave sensors or any instrumentation sufficiently sensitive to the passing of the blade tip. The sensor choice is of course limited by the operating conditions inside the rotor casing. The TOA difference is used to obtain an instantaneous measurement of the blade tip displacement during motion along its oscillatory path.

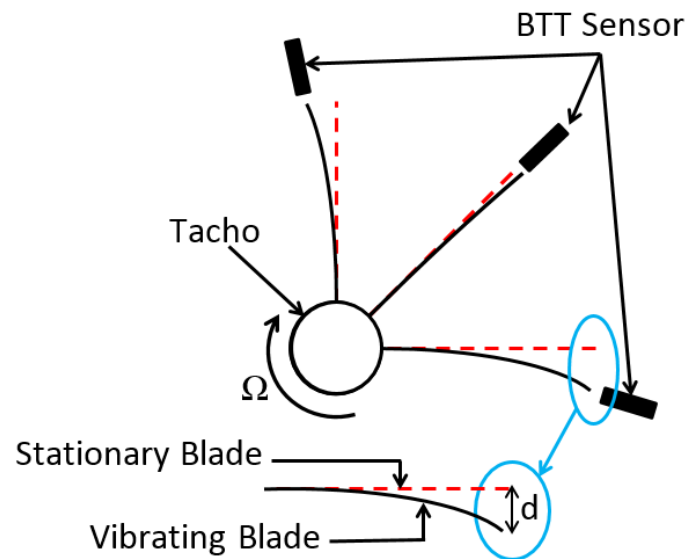


Figure 1.3-5 Principle of BTT

Early synchronous BTT approaches required that data be collected across the entire resonance region of the blades. This is done by sweeping the rotor speed across all natural frequencies of interest (Carrington et al., 2001). This procedure exposes a single measurement point to a full range of excitation amplitudes at varying frequencies. This is similar to the exposure of a sensor to a purely asynchronous response. These methods have been termed indirect approaches and are capable of providing both the response amplitude and frequency of a blade. They are however not suitable for continuous online monitoring of a rotor stage operating at a nominally constant rotational speed.

More recently research has shifted away from the indirect methods to blade vibration measurement at a nominally constant rotational speed under synchronous excitation conditions. As was previously mentioned, if the blade excitation is synchronous then a single BTT measurement point will always capture the same displacement measurement. This issue is overcome by using multiple probes placed about the periphery of the rotor in order to capture multiple points along the blade's actual response cycle. These methods are termed direct approaches. The measured signal is however inherently aliased as the TOAs are subsampled (Diamond et al., 2014a).

The issue of aliasing leads to physical constraints on the positioning of the TOA capture instrumentation and has led to the concept of pulse spacing on resonance (PSR). PSR is the percentage of the response waveform captured by measurement probes during one oscillatory cycle of a blade (Gallego-Garrido et al., 2007b). Consider the example in Figure 1.3-6.

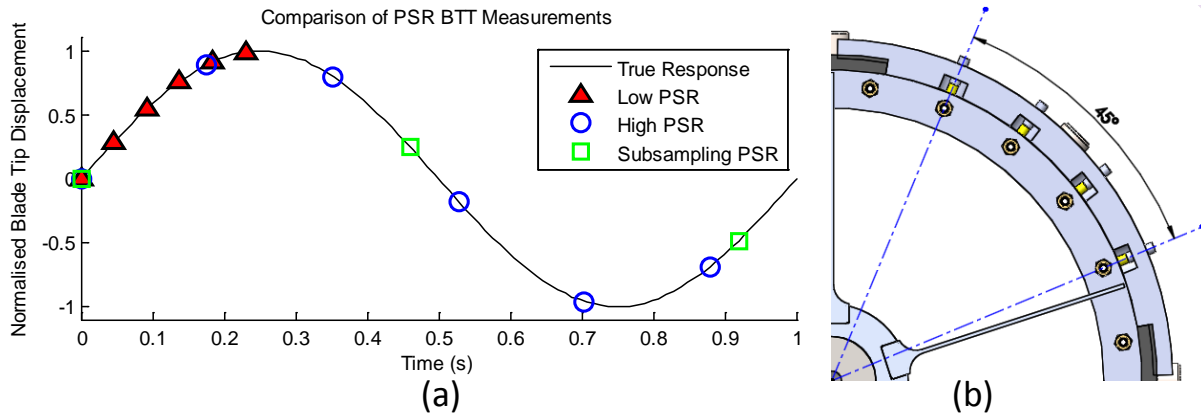


Figure 1.3-6 PSR. (a) Comparison of Pulse Spacing on Resonance for BTT Measurements (adapted from (Gallego-Garrido et al., 2007b)). (b) Rotor cross section with four BTT probes placed equidistant apart between an angle $\gamma = 45^\circ$.

Assuming that the blade responds in a purely sinusoidal single degree of freedom (SDOF) manner, the rotor speed is constant, BTT probes are placed within an angular distance λ between the first and final probe, and a measurement for a single revolution of the rotor is made which captures data across an individual blade response cycle. If the angle λ is too small then only a small fraction of the actual response is captured leading to errors in response estimation (low PSR). If the angle is enlarged sufficiently then measurements are taken over a substantial percentage of the response and a model can be accurately fitted to the data (high PSR). Finally if the angle is too large it will lead to undersampling of the response and thus lead to significant errors (subsampling PSR) (Gallego-Garrido et al., 2007b). The PSR is calculated using Equation [1.3.2] (Gallego-Garrido et al., 2007b).

$$PSR = \frac{EO \cdot \lambda}{2\pi} = \frac{\omega_f \cdot \lambda}{\Omega \cdot 2\pi} \quad [1.3.2]$$

It is important to note that the positioning of the tip timing sensors is optimised to detect blade vibrational response for a specific mode from a specific operating rotor speed. A particular tip timing configuration is therefore limited to detecting the specific response it has been designed for (Murray and Key, 2015). Further, if little tip deflection is present for a particular mode given a particular level of excitation then no useful information will be derived from the technique (Murray and Key, 2015).

The tip displacement data captured during operation is curve fitted to a blade tip vibration model over a chosen number of revolutions to elicit blade vibration parameters (Zielinski and Ziller, 1997). A range of curve fitting techniques have been applied to the direct synchronous BTT problem and their relative performance compared in both simulations and experiments (Carrington et al., 2001; Diamond et al., 2014a, 2014b; Gallego-Garrido et al., 2007a, 2007b).

The most commonly investigated curve fitting approaches use auto-regression (AR). The blade tip response solution is assumed to be a SDOF sinusoid, the forcing frequency is assumed to be the tuned synchronous response at resonance (i.e. $\omega_f = \omega_n$) (Carrington et al., 2001). The tip response solution is given in Equation [1.3.3].

$$x = A_n \cos(\omega_n t + \phi_n) + D \quad [1.3.3]$$

The parameters x , A_n , ϕ_n and D are the response displacement, amplitude, frequency, phase and DC offset respectively.

The fitting equation is derived from a simple form of the EOM which is integrated from acceleration to displacement using a Taylor expansion procedure (Carrington et al., 2001). The initial EOM is presented in Equation [1.3.4].

$$\ddot{x} + \omega_n^2 \cdot x = 0 \quad [1.3.4]$$

The natural frequency and DC offset are solved for by performing a least squares fit over multiple revolutions of the Taylor expanded EOM. The expanded EOM for N revolutions is given in Equation [1.3.5] (Carrington et al., 2001).

$$\begin{bmatrix} x_3 + x_1 \\ x_4 + x_2 \\ \vdots \\ x_N + x_{N-2} \end{bmatrix} = \begin{bmatrix} x_2 & 1 \\ x_3 & 1 \\ \vdots & \vdots \\ x_N & 1 \end{bmatrix} \cdot \begin{bmatrix} -\omega_n^2 \\ D \cdot (2 + \omega_n^2) \end{bmatrix} \quad [1.3.5]$$

Finally the amplitude and phase of response is estimated using two measurement points and solving the assumed form of the response equation simultaneously (Carrington et al., 2001).

$$\begin{aligned} x_1 &= A_n \cdot \cos(\omega_n \cdot t_1 + \phi_n) + D \\ x_2 &= A_n \cdot \cos(\omega_n \cdot t_2 + \phi_n) + D \end{aligned} \quad [1.3.6]$$

The AR technique requires that BTT probes be placed equidistant apart within the probe capture angle λ (Carrington et al., 2001). Improvements have been suggested and include expanding the model to multiple degrees of freedom (MDOF), preventing noise correlation in the least squares solution form and solving over all measured revolutions simultaneously (Carrington et al., 2001; Gallego-Garrido et al., 2007a, 2007b).

Recently an alternative curve fitting technique has been suggested to replace the least squares approach, namely Bayesian curve fitting. The method is similar to the AR class of methods in that a SDOF sinusoidal response solution is assumed for the tip and the unknown amplitude and frequency of response estimated (Diamond et al., 2014b). The assumed tip response is provided in Equation [1.3.7] (Diamond et al., 2014b).

$$x_i(t) = A_1 \cdot \cos(\omega \cdot t_i) + A_2 \cdot \sin(\omega \cdot t_i) + D \quad [1.3.7]$$

The unknown parameters A_1 , A_2 and D are solved for using the standard Bayesian linear regression formulation over a chosen number of revolutions (Diamond et al., 2014a).

Unlike the AR approach the tip response is solved for directly using the assumed solution form and not a Taylor approximation of the estimated governing EOM. The Bayesian method does not require that the probes be placed equidistant apart within the angle λ . It has in fact been found to perform better when they are not (Diamond et al., 2014b). The Bayesian approach was found to perform better than the SDOF AR approach in terms of both response amplitude estimation and natural frequency estimation for a range of simulated noise levels in the particular study (Diamond et al., 2014a).

It is important to note that indirect BTT methods, for blade response capture at changing rotor speeds, were not considered for investigation. Additional information and relevant derivations of various BTT curve fitting techniques are presented in section “7.2 Appendix B – Additional BTT Literature”.

1.3.5. Casing Pressure Signal Methods

The internal pressure signal of a gas turbomachine inherently contains the response signature of the vibrating blades moving through the fluid (Forbes and Randall, 2013). The interaction of this internal pressure profile on the casing of the turbomachine may result in excitation of the casing (Forbes and Randall, 2013).

The casing response and internal pressure signal, measured at the casing wall, are thus two potential sources of blade vibration information which can be measured remotely from the blade itself (Forbes and Randall, 2013; Mathioudakis et al., 1989). Identifying the acoustic characteristics of vibrating blades may thus be used to discern it from other sources of unsteady vibration (Mengle, 1990).

The internal casing pressure undulations, stemming from synchronous excitation, are typically smaller in magnitude when compared to non-integral EO vibration (Murray and Key, 2015). This results in difficulty in measuring blade forced vibration from pressure measurements (Murray and Key, 2015). Furthermore it is believed that the forced response pressure signal of blades, measured by a stationary observer placed at some location on the non-rotating reference frame, are inherently Doppler shifted to stator passing frequencies (SPFs) (Mengle, 1990; Murray and Key, 2015). This may make the identification of the measured blade's response troublesome (Murray and Key, 2015).

The succeeding two sections investigate the constitutive components of the internal pressure signal as well as a means to mathematically represent those components. This forms a basis for blade vibration identification from internal casing pressure and external casing vibration measurements.

1.3.5.1. Model 1: Pressure Model Developed from Rotor Reference Frame

1.3.5.1.1. Pressure Signal Representation

In order to develop an analytical model describing the pressure distribution around an individual rotor cascade a general model is first considered. Figure 1.3-7 illustrates the case of multiple rotor blade and stator rows. The rotor blades are attached to an infinite length shaft and similarly the stators are attached to an infinite length annular duct representing the casing. An acoustic pressure transducer is placed downwind of the stator and rotor rows in order to capture the blade vibration present in the moving fluid. The fluid is moving at a constant velocity of \bar{U} parallel to the casing and shaft.

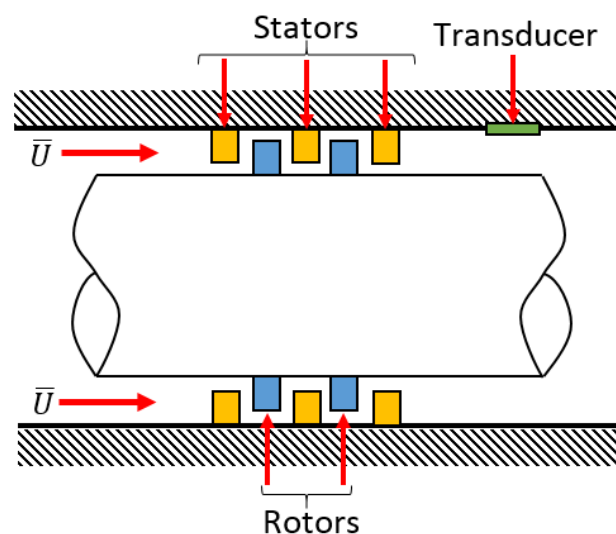


Figure 1.3-7 Stator and rotor schematic attached to infinite length shaft and infinite length annular casing cylinder (adapted from (Mengle, 1990))

Focus is placed on an individual rotor row which contains B rotor blades, each vibrating at an arbitrary frequency, amplitude and phase angle. It is assumed that the net pressure field around the rotor may be obtained by linear superposition of each of the individual blade's contributions to that field (Mengle, 1990). This assumption facilitates the decoupling of each individual blade's behaviour, the situation where only a single blade is vibrating may now be considered. The solution to the individual blade's vibration is obtained by superposition of all possible rotor travelling-wave modes for the specific case (Mengle, 1990).

A rotor travelling-wave mode is defined as the situation where all of the blades are vibrating in the same blade mode, at the same frequency and at the same amplitude. There is however a constant inter-blade phase angle difference (Mengle, 1990). The phase angle difference between the blades, σ , may only take certain discrete values due to cyclic periodicity of the rotor (Mengle, 1990). These discrete values are given by Equation [1.3.8] (Mengle, 1990).

$$\sigma = \frac{k \cdot 2 \cdot \pi}{B} \quad [1.3.8]$$

Where the travelling wave mode number k is limited to the set $\{0, 1, 2, \dots, B - 1\}$.

Finally, in order to obtain the net acoustic response for the general case of arbitrary blade vibration, each unsteady pressure field for each travelling-wave mode is superimposed (Mengle, 1990). The use of superimposed travelling-wave modes facilitates the investigation of flutter conditions (Mengle, 1990). The flutter response frequency is common to all blades regardless of whether the system is tuned or mistuned, the only difference being that in mistuned flutter the inter-blade response phase angle difference is no longer constant (Mengle, 1990).

In order to develop a descriptive model of the pressure distribution due to blade vibration an isolated rotor cascade is considered. The model is initially developed from the rotor frame (as though a stationary observer is present on the moving rotor itself). Consider the two dimensional cascade schematic in Figure 1.3-8 (a) and a rotor schematic with angular coordinates defined on the rotor reference frame in Figure 1.3-8 (b). The y - θ axis in (a) corresponds to the θ axis in (b).

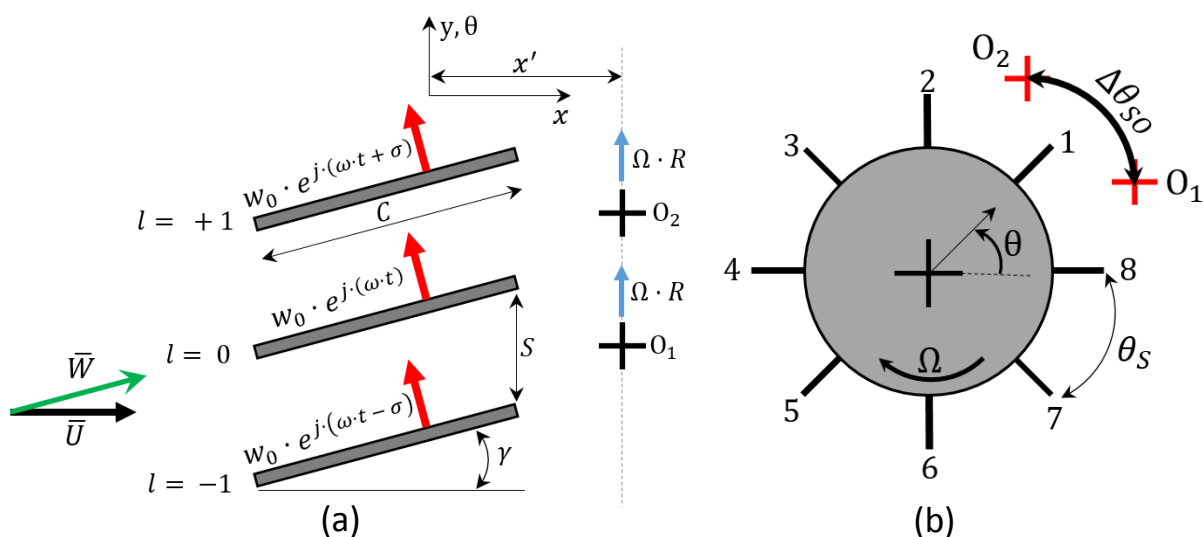


Figure 1.3-8 Rotor and cascade schematic. (a) Two dimensional cascade with one travelling wave mode boundary condition. (b) Angular coordinate system in rotor frame. (adapted from (Mengle, 1990))



It is assumed that the cascade is isolated, the flow from the upstream stators is uniform (or at least not highly sheared) (Mengle, 1990). The axial velocity of the inlet fluid flow is given by \bar{U} , the flow component relative to the blade stagger angle γ is \bar{W} , and the flow normal to the surface of blade l is represented by w_l (Mengle, 1990).

The system comprises of B blades set at a stagger angle of γ and each having a chord length of C (Mengle, 1990). The blade tips are at a radius R from the center of the rotor (Mengle, 1990).

Stationary observers O_1 and O_2 are fixed to the turbomachine's casing at a distance x' downwind of the turbomachine blades. This is measured from an arbitrary position along the chord length of the blades (Mengle, 1990). From the rotor reference frame the stationary observers are seen to be moving at a translational speed of $\Omega \cdot R$ in Figure 1.3-8 (a), or identically an angular speed of Ω in Figure 1.3-8 (b). The blade-to-blade gap S , defined in Figure 1.3-8 (a), is given by:

$$S = \frac{2 \cdot \pi \cdot R}{B} \quad [1.3.9]$$

Similarly the angle between two blades, shown in Figure 1.3-8 (b), can be calculated as:

$$\theta_s = \frac{2 \cdot \pi}{B} \quad [1.3.10]$$

The blades are responding as travelling-wave modes with frequencies ω_l and at phase angles σ_l . The blades' response modes are represented by the previously defined normal fluid velocities $w_l(x)$ indicated in Figure 1.3-8 (a). The blades are assumed to be vibrating sinusoidally and are represented by means of the Euler term. The pressure responses due to blade vibration are assumed to be small with respect to the inlet speed U (Mengle, 1990). Since it is assumed that the blades are responding in a travelling-wave mode the normal velocities about each blade must satisfy Equation [1.3.11] (Mengle, 1990).

$$w_{l+1}(x) \cdot e^{j \cdot (\omega \cdot t)} = w_l \cdot e^{j \cdot (\omega \cdot t)} \cdot e^{j \cdot (\sigma)} \quad [1.3.11]$$

The parameter j is the complex number $\sqrt{-1}$. The linearised unsteady pressure of a neighbouring blade $l + 1$ with reference to blade l , due solely to blade vibration, is given in the rotor reference frame by Equation [1.3.12] (Mengle, 1990).

$$p\left(\theta + \frac{2 \cdot \pi}{B}\right) = p(\theta) \cdot e^{j \cdot (\sigma)} \quad [1.3.12]$$

Equation [1.3.12] may be rearranged such that the pressure in the rotor reference frame, $p(\theta)$, is the subject of the formula. The periodic nature of the unsteady pressure distribution, due to blade vibration, allows describing the phenomenon in the rotor reference frame by means of a Fourier series. After rearrangement and simplification, the unsteady pressure field for a particular mode k , is now described by the Fourier series in Equation [1.3.13] (Mengle, 1990). The rotor reference frame is now explicitly indicated in the equation's variables.

$$p(\theta_{rotor}, t, x) = \sum_{m=-\infty}^{\infty} f_m(x) \cdot e^{j[(k+m \cdot B) \cdot \theta_{rotor} + \omega \cdot t]} \quad [1.3.13]$$

Summation occurs over all integer values of m with the Fourier constants f_m . It is stated that the Fourier coefficients f_m are independent of the angle θ . The axial dependency of the pressure signal (along the pre-defined x-axis) is however contained in the Fourier coefficients (Mengle, 1990). An equivalent form of Equation [1.3.13], with the blade vibration factored out and presented as a separate exponential multiplier is given in Equation [1.3.14].

$$p(\theta_{rotor}, t, x) = \sum_{m=-\infty}^{\infty} f_m(x) \cdot e^{j[(k+m \cdot B) \cdot \theta_{rotor}]} \cdot e^{j[\omega \cdot t]} \quad [1.3.14]$$

According to Mengle the resulting equation shows that about the blades, in the rotor reference frame, there exists $|k + m \cdot B|$ spinning lobes (vortices) about the circumference of the rotor. This is for each value of m (Mengle, 1990). The rate at which the lobes spin is $\omega / (k + m \cdot B)$ (Mengle, 1990). Due to the restriction on the travelling wave mode number k , the direction of the spin is due solely to the value of integer m . The pressure fluctuations due to the vortices are measured by the acoustic pressure transducer.

For any positive value m the lobes spin the same direction as the rotor and conversely a negative m value results in rotation opposite to the direction of the rotor (Mengle, 1990). From the rotor reference frame each lobe is seen as spinning at the blade flutter frequency ω (Mengle, 1990). The significance of the spinning lobes becomes apparent when the system is observed from the casing reference frame.

It is stated that the resulting expression, Equation [1.3.14], was obtained independently using a completely alternative method by Smith (Mengle, 1990; Smith, 1973). The pressures and velocities of a real rotor row blades, in the circumferential direction, were represented by a row of vortices (spinning lobes) occurring about the circumference of the casing (Smith, 1973).

A constant phase angle difference was noted between each vortex (Smith, 1973). This constant phase angle difference has the same significance as the constant inter-blade phase angle difference described by Mengle (Mengle, 1990). The vortex array was characterised using a series representation; the series was integrated over and operated on by Dirac delta functions (Mengle, 1990; Smith, 1973). The relation is provided in Equation [1.3.15] (Smith, 1973).

$$\gamma(y) = \bar{\gamma}(y) \cdot e^{j \cdot \omega \cdot t} = \sum_{r=-\infty}^{\infty} \frac{\Gamma}{s} \cdot e^{j \left[\omega \cdot t + \frac{\phi - 2 \cdot \pi \cdot r}{s} \cdot y \right]} = \sum_{r=-\infty}^{\infty} \frac{\Gamma}{s} \cdot e^{j \cdot [\omega \cdot t + \beta \cdot y]} \quad [1.3.15]$$

The vortices are said to fluctuate at angular frequency ω with amplitude Γ and phase angle between vortices of ϕ (Smith, 1973). The distance between vortices (analogous to blade spacing) is s and the vortex strength per unit length along the circumferential axis y is γ (Smith, 1973). The resultant independently obtained equation is said to be equivalent to the pressure distribution as seen in the rotor reference frame given in Equation [1.3.14] (Mengle, 1990).

It is of interest to describe the unsteady pressure about the rotor in terms of a stationary observer placed on the casing of the rotor. If we consider the case where the system is operating at a constant angular velocity a simple transform of the rotor reference frame, in terms of the stationary observers placed on the casing reference frame, is possible.

The relationship developed between the observer in the rotor reference frame and the stationary observer in the casing reference frame is given by Equation [1.3.16] (Mengle, 1990). θ_{SO} is the angular distance between the stationary observer on the casing and θ_{rotor} at time $t = 0$ (Mengle, 1990).

$$\theta_{casing} = \theta_{SO} + \Omega \cdot t \quad [1.3.16]$$

The resulting pressure observed by a stationary observer on the casing is thus (Mengle, 1990):

$$p(\theta_{casing}, t, x) = \sum_{m=-\infty}^{\infty} f_m(x) \cdot e^{j[k' \cdot \theta_{casing}]} \cdot e^{j[\omega' \cdot t]} \quad [1.3.17]$$

Where $k' = k + m \cdot B$ and $\omega' = \omega + (k + m \cdot B) \cdot \Omega$.

The parameter k' is the observed travelling wave mode number and ω' is the observed blade flutter frequency measured by a stationary observer in the casing reference frame. It is clear from Equation [1.3.17] that each Fourier term of the observed blade vibration is Doppler shifted at an integer multiple of the rotor speed (Mengle, 1990). If the inter-blade phase angle is constant then the integer multiple is related to the number of spinning vortices about the circumference of the rotor.

The Doppler shifting effect is due to the relative angular velocities of the rotor speed and the spin rate of the vortices (Mengle, 1990). If a vortex is spinning in the same direction as the rotor then the observed vortex spin rate will be the rotor speed plus the spin rate in the rotor reference frame (Mengle, 1990). If however the vortex is moving in the opposite direction the observed spin rate of the vortex will be the rotor speed minus the spin rate in the rotor reference frame (Mengle, 1990).

The observed travelling wave mode is in general not symmetric about zero, it is only symmetric for $k = 0$ or a specific combination of k and B . An example of this is provided in Figure 1.3-9.

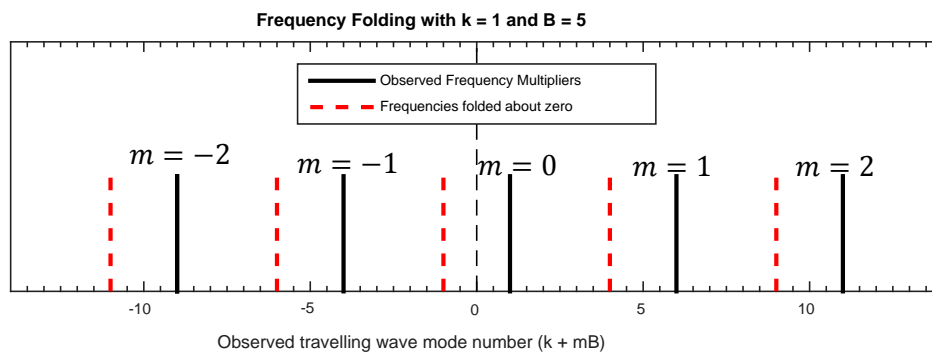


Figure 1.3-9 Frequency folding about zero (adapted from (Mengle, 1990))

The asymmetry of k' results in a folding of the observed blade vibration in the frequency domain about zero; thus the blade vibration is doubly symmetric (Mengle, 1990). This is due to the symmetry of the Fourier transform. The folding effect has consequences for the observed frequency content.

It is stated that when the interblade phase angle is not constant all possible travelling-wave modes participate (Mengle, 1990). An example of a non-constant inter-blade phase angle scenario is mistuned flutter. The consequence of this scenario is that the multipliers can occur at any integer value ($k \in \{0,1,2, \dots, B - 1.\}$ and $-\infty < m < \infty$ where $m \in \mathbb{Z}$). This results in Doppler shifting of observed blade vibration frequencies at all harmonics of rotor speed (Mengle, 1990). This is a special case which results in a symmetric observed travelling wave mode number.



Conversely, if the interblade phase angle between blades is constant then the travelling-wave mode number, k , must be determined in order to identify the blade vibration (Mengle, 1990).

It must also be noted that if an additional stationary observer is present at the same axial distance from the source of vibration (see Figure 1.3-8 (a) and (b)) the observed phase angle difference between the two observers is given by Equation [1.3.18] (Mengle, 1990).

$$\sigma' = (k + m \cdot B) \cdot \Delta\theta_{SO} \quad [1.3.18]$$

The significance of a second observer will be made clear when relating the analytical blade vibration equations to an actual observed pressure response spectrum.

Much of Model 1 is based on a prior investigation by Smith (Smith, 1973). The wave equations and relevant definitions are based on the linearised momentum and continuity equations (Smith, 1973).

1.3.5.1.2. Pressure Measurement Considerations

In the original configuration, presented in Figure 1.3-7, the stationary observer is placed downwind of the rotor row of interest. Potential attenuation of the blade vibration signal along the axial length of the rotor and the associated rate of attenuation are thus of interest. Several conclusions were drawn for each m^{th} Fourier component of the pressure signal and are presented here.

Consider the linearised Euler equation describing the pressure wave in the rotor frame (where x refers to the axial axis and y refers to the circumferential axis as described in Figure 1.3-8 (a)) (Mengle, 1990).

$$p = \bar{p}_m \cdot e^{j(\bar{\alpha} \cdot x + \bar{\beta} \cdot y + \omega \cdot t)} \quad [1.3.19]$$

The expression is obtained by starting with the linearised form of the continuity and mass momentum equations (Smith, 1973). After inter-substitution, rearrangement and simplification a linearised Euler description of pressure waves in the rotor frame is obtained (Smith, 1973).

The definition of the components in Equation [1.3.19] may be found in (Mengle, 1990; Smith, 1973), the conclusions drawn are however of interest (Mengle, 1990). The axial component $\bar{\alpha}$ may be real, imaginary or zero. If the particular m^{th} Fourier α component is real then the associated frequency information propagates axially without diminishing (Mengle, 1990). If it is however complex then the component decays exponentially resulting in difficulty to identify the component downwind or upwind of the rotor (Mengle, 1990). An $\bar{\alpha}$ component of zero indicates acoustic resonance conditions. This results in the acoustic waves propagating solely in the circumferential direction (Mengle, 1990).

There exists a maximum value of $|m|$ above which all frequency components, both axial and circumferential, decay (Mengle, 1990). This means that at a particular point all higher frequency components related to blade vibration will become increasingly difficult to detect (Mengle, 1990).

The circumferential component $\bar{\beta}$ is always real and only ever zero if both $m = 0$ and $\sigma = 0$ (Mengle, 1990). The amplitude of the frequency components, \bar{p}_m , decreases with for an increase in $|m|$ (Mengle, 1990).

In addition to the concerns of signal attenuation is the fact that in practice the rotor row is not isolated. Therefore the interference of nearby rotors and stators must be taken into account. This is because they may affect the acoustic signatures of vibrating blades measured from stationary observers placed



on the casing (Mengle, 1990). This argument is related the original rotor-stator configuration in Figure 1.3-7. Once again the mathematical arguments will not be reported on, only the conclusions drawn.

It was established that a nearby stator stage does not affect the Doppler shift of the original vibrating frequencies of the turbomachine blades. It does however affect the observed modes as well as the corresponding amplitudes of the Fourier components (Mengle, 1990).

The presence of a nearby rotor stage produces an additional Doppler shift of the observed original blade vibration (Mengle, 1990). This could lead to difficulties in identifying individual blade vibration characteristics for an individual stage measured downwind of multiple stages.

Understanding the interference effects of nearby stators and rotor rows on observed spectra may be the key to determining the actual blade vibration. These interference effects may be increasingly significant for blade vibration measurement at an increasing axial distance from the source.

1.3.5.1.3. Acoustic Detection of Rotor Blade Vibration

Given data measured by a stationary observer on the casing wall downwind of a rotor, is it possible to infer the rotor blade vibration characteristics such as the inter-blade response phase angle, and the frequency and amplitude of vibration?

In order to provide a possible solution to this question Mengle limited the investigation to non-integral engine order vibration ($EO \notin \mathbb{Z}$), in specific flutter at a single frequency with multiple possible travelling-wave modes k (Mengle, 1990). The inter-blade phase angle σ is assumed to be constant such that only a single travelling-wave mode exists at any given time. Additionally the rotor is assumed to be isolated and only positive frequency components can be observed (Mengle, 1990).

Given the observed stationary acoustic spectra, the number of rotor blades B and a constant rotor speed of Ω , three unknowns remain, namely the rotor flutter frequency ω , the travelling-wave mode number k and the specific Fourier term number m (Mengle, 1990). Consider the equation for observed blade vibration frequencies given in Equation [1.3.20].

$$\omega' = \omega + (k + m \cdot B) \cdot \Omega \quad [1.3.20]$$

One equation with three unknowns results in an indeterminate system. If an additional stationary observer is placed at the same axial distance as the original stationary observer, then the travelling-wave mode number may be determined (Mengle, 1990). It is chosen that the second observer is placed at a circumferential angular offset equal to the angular distance between two blades for convenience; the phase angle is further limited to the range $\sigma \in [0, 2 \cdot \pi]$ (Mengle, 1990).

This results in the case that the observed phase angle difference is equivalent to the phase angle between two blades' responses (Mengle, 1990). Therefore the travelling-wave mode number can be determined. The process by which the travelling wave number is obtained is expressed in Equations [1.3.21] to [1.3.26].

$$\sigma' = (k + m \cdot B) \cdot \Delta\theta_{SO} \quad [1.3.21]$$

$$\Delta\theta_{SO} = \frac{2 \cdot \pi}{B} \quad [1.3.22]$$



$$\therefore \sigma' = \frac{2 \cdot \pi}{B} \cdot k + m \cdot 2 \cdot \pi \quad [1.3.23]$$

$$\sigma \in [0, 2 \cdot \pi) \quad [1.3.24]$$

$$\therefore \sigma' = \frac{2 \cdot \pi}{B} \cdot k \quad [1.3.25]$$

$$\therefore k = \frac{\sigma' \cdot B}{2 \cdot \pi} \quad [1.3.26]$$

Given k from the above solution two unknowns still remain. We have assumed that the frequencies observed are only positive, thus (Mengle, 1990):

$$\omega_{OBS} \equiv |\omega'| = |\omega + (k + m \cdot B) \cdot \Omega| \quad [1.3.27]$$

Given that m is an integer in the infinite interval and the fact that we are only considering positive frequencies it is possible to divide Equation [1.3.27] into two possible true vibrational frequency sets (Mengle, 1990). The resulting sets are presented in Equation [1.3.28] (Mengle, 1990).

$$\begin{aligned} \omega_{1n} &= (k \cdot \Omega + \omega'_{OBS}) + n \cdot B \cdot \Omega \\ \omega_{2n} &= (k \cdot \Omega - \omega'_{OBS}) + n \cdot B \cdot \Omega \end{aligned} \quad [1.3.28]$$

Where $n \in \mathbb{Z}$, and ω'_{OBS} is the observed flutter frequency (Mengle, 1990).

If one divides the frequency domain into intervals of $B \cdot \Omega$, then in each interval there exists a single value from the set $\{\omega_{1n}\}$ and a single value from the set $\{\omega_{2n}\}$, one of which is the true frequency of blade flutter vibration (Mengle, 1990). Thus for each interval you investigate, two possible frequencies of vibration exist, one of which is the desired value (Mengle, 1990). This is even the case when you know that the true frequency of vibration lies within a specific interval (Mengle, 1990).

The solution for the case of a non-constant phase angle difference between blades is slightly more complicated. This is because there is now an ambiguity in the value for travelling-wave mode k (Mengle, 1990). It is suggested that data be recorded at a slightly different rotor speed Ω which can allow the splitting apart of the different spectra for the different k values. This will only be possible if the frequency of vibration ω , does not change significantly at the altered operating speed (Mengle, 1990).

As was previously noted the blade vibration was assumed to be non-integral engine order flutter. This response is small in comparison to engine ordered information in the pressure signal (Mengle, 1990). It must be stated that the pressure spectrum utilised had been cleared of engine ordered responses (such as the blade passing frequencies and associated harmonics) by means of a deletion process in order to emphasize the actual blade vibration (Mengle, 1990).

Mengle does not mention the process by which the integral engine order responses are removed from the pressure signal, however references are made to an investigation where a pressure spectrum void of blade vibration is subtracted directly from a pressure spectrum which contains blade vibration (Kurkov, 1981; Mengle, 1990). This is done in order to reveal the spectrum comprising solely of blade vibration information (Kurkov, 1981; Mengle, 1990; Murray and Key, 2015). This methodology is a precursor for the succeeding model and associated signal processing approach.

1.3.5.2. Model 2: Pressure Model Developed Directly from Casing Reference Frame

1.3.5.2.1. Pressure Signal Representation

Consider the development of the internal pressure distribution model presented in Figure 1.3-10 (Forbes and Randall, 2013).

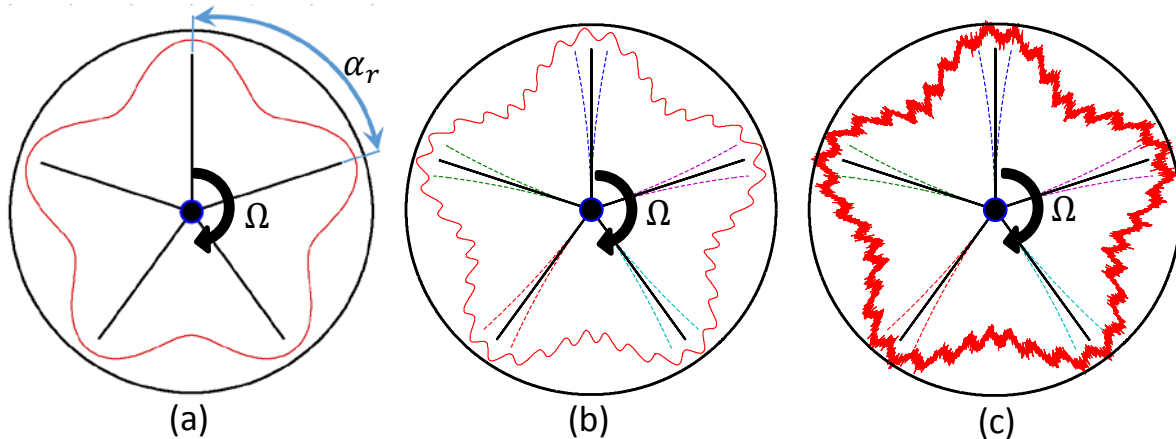


Figure 1.3-10 Schematic of the internal pressure profile. (a) Pressure distribution due to blade rotation. (b) Included blade vibration. (c) Included noise and other vibratory phenomena. (adapted from (Forbes and Randall, 2013))

As the blades rotate a harmonic pressure distribution is formed in the casing (Forbes and Randall, 2013). A simple sinusoid is used to represent the first harmonic in the Figure 1.3-10 (a) (Forbes and Randall, 2013).

At a constant shaft speed of Ω , and without additional sources of vibration, the harmonic pressure distribution will cause a steady state fluctuating pressure profile to be exerted on the inner wall of the casing (Forbes and Randall, 2013). Although the shape of the steady state pressure distribution around each hypothetical non-vibrating blade is dependent on machine geometry, it tends to take the form of a damped impulse (Forbes, 2010, p. 61). An example of a casing wall pressure signal, measured about non-vibrating blades with noise removed, is given in Figure 1.3-11.

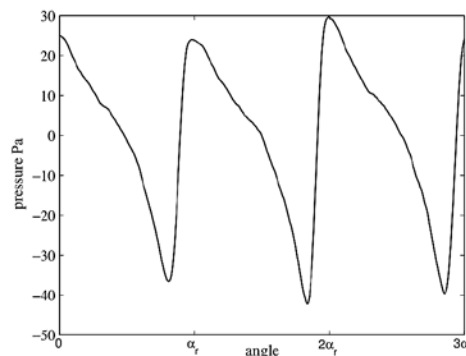


Figure 1.3-11 Casing pressure distribution about non-vibrating blades measured at $\Omega = 1200$ RPM (Forbes, 2010, p. 61)

The damped impulse form is due to a passing blade, ahead of the blade there exists a high pressure region whereas behind the blade there is a low pressure region. As the blade passes the stationary observer a pressure drop is experienced.

The pressure profile shape around the r^{th} non-vibrating blade can be expressed using a Fourier series tuned to produce the periodic shape of interest. A suggested Fourier series form is expressed in Equation [1.3.29] (Forbes and Randall, 2013).



$$P_r(t) = Re\left\{\sum_{i=0}^{\infty} A_i \cdot P \cdot e^{(j \cdot i \cdot [\theta + \Omega(t) + \alpha_r + \gamma_i])}\right\} \quad [1.3.29]$$

The parameters A_i and γ_i are the amplitude and phase of the i^{th} Fourier term, P is the magnitude of the pressure, α_r is the angular distance between the blades (shown in Figure 1.3-10 (a)). The parameter Ω is the angular velocity of the rotor as a function of time and θ is the angular position at which the pressure is measured relative to an arbitrary datum (Forbes and Randall, 2013).

The sources of blade excitation have already been mentioned in Section 1.3.1; the section outlined both synchronous and asynchronous mechanisms. The conclusion was drawn that blade excitation is driven predominantly by upstream stator wake interaction at the stator passing frequency (SPF). The stator passing frequency is a function of rotor speed and number of stators s and is shown in Equation [1.3.30].

$$\omega_{SPF} = s \cdot \Omega = s \cdot 2 \cdot \pi \cdot f_R \quad [1.3.30]$$

It was further noted that noise is inherent in the internal pressure signal and is thus an important additional driving component (Forbes and Randall, 2013). The blade forcing function, modelled with a Fourier periodic series, is provided in Equation [1.3.31] to [1.3.32] (Forbes and Randall, 2013).

$$f(t)_r = F_0 \cdot g(t) \cdot \left\{ \sum_{q=0}^{\infty} C_q \cdot \cos\left(q(\omega_{SPF} \cdot t + \gamma_q + \gamma_r)\right) \right\} \quad [1.3.31]$$

$$\gamma_r = \frac{2 \cdot \pi \cdot s \cdot (r - 1)}{b} - \text{round}\left(\frac{s(r - 1)}{b}\right) \cdot 2 \cdot \pi \quad [1.3.32]$$

The analytical Fourier force relation is capable of taking any periodic shape by selecting the Fourier coefficients C_q , γ_q and phase offset γ_r (Forbes and Randall, 2013). The parameters b and s are the number of rotor blades and upstream stator blades respectively. F_0 is the magnitude of the driving force (Forbes and Randall, 2013). The Gaussian noise component has been included as the term $g(t)$.

Noise in the internal pressure signal is attributed to turbulence or impulses in the flow, propagation of acoustic waves as well as mechanical and rotary vibration resulting from operation of the turbomachine (Forbes and Randall, 2013). Noise is included in the internal pressure distribution model by multiplying the blade forcing function with a zero mean Gaussian random variable $g(t)$, although in practice the frequency content of the noise is expected to be band limited (Forbes and Randall, 2013; Forbes, 2010, p. 65).

It is assumed that the pressure at the casing wall is equivalent to, or at least directly related to, the pressure profile about the blade tip (Forbes, 2010, pp. 68, 172). It is also assumed that the pressure profile around an individual blade follows the blade's motion during vibration about its equilibrium position (Forbes, 2010, p. 69). The blade tip response is therefore of interest. If the blade is excited by a single dominant discrete frequency, such as the SPF, then the response motion of the r^{th} blade tip can be expressed as a single degree of freedom (SDOF) sinusoid (Forbes, 2010, p. 68):

$$x(t)_r = X_k \cdot \sin(k \cdot \Omega(t) + \gamma_k) \quad [1.3.33]$$

If the excitation is synchronous then the parameter k is equivalent to the EO of excitation (Forbes, 2010, p. 68). If the excitation frequency is near to a natural frequency of the blade then the amplitude and phase of response can be resolved using the SDOF forced response solution (Forbes, 2010, p. 68).

The blade is however excited at integer multiples of shaft speed along with a noise component and unless one of the integer multiples lies exactly at the resonant frequency of interest the blade tip response cannot be estimated using a SDOF sine approximation.

Therefore an alternative approach to the sine approximation would be to obtain the full forced blade response spectrum. This is achieved by multiplying the forcing function spectrum with the transfer function of the blade (Forbes and Randall, 2013). Once again a SDOF model approximation is used to obtain the blade's transfer function, the blade representation is provided in Figure 1.3-12.

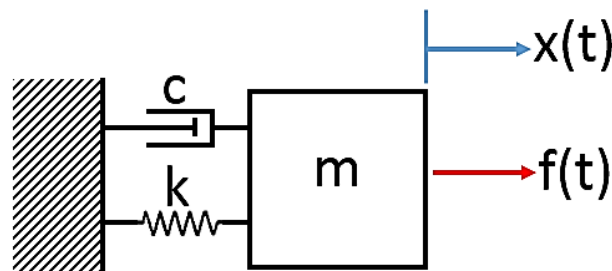


Figure 1.3-12 SDOF blade representation

The coefficients m , k and c refer to the equivalent SDOF mass, stiffness and viscous damping coefficients respectively. The mass is acted on by a forcing function $f(t)$ and has a response displacement of $x(t)$.

It is important to note that in this representation the individual blade is seen as independent of other blades and the assembly. Expressing the blade response as an isolated system independent of the hub assembly is only a valid approximation if the coupling effects between the blades are limited and only a small amount of mistuning is present (Forbes, 2010, p. 138). Had the mistuning and coupling been above a certain threshold a coupled system representation would be required (Forbes, 2010, p. 138).

The section '1.3.6 Blade Effects' briefly explores the effects of coupling and mistuning on a bladed system. Representation of a coupled system, in terms of the governing equations of motion, is given in '7.1.3 A3 – Analytical Blade and Assembly Models' sections '7.1.3.2 Lumped Mass Model' and '7.1.3.3 FE Model'. These sections explore the lumped mass model and the full finite element (FE) model and therefore apply directly to the fully coupled problem.

An alternative multiple degree of freedom (MDOF) representation of a single blade is also presented in the appendix, namely the Euler-Bernoulli beam approximation. The governing equations and brief discussion for this model can be found in section '7.1.3.1.1 Euler-Bernoulli Beam Formulation'.

The governing equations of motion (EOM) corresponding to the model presented in Figure 1.3-12 is provided in Equation [1.3.34].

$$[m]\{\ddot{x}\} + [c]\{\dot{x}\} + [k]\{x\} = \{f(t)\} \quad [1.3.34]$$

The EOM cannot be directly evaluated in the time domain to obtain the response motion. In order to evaluate the system in the time domain to obtain the blade response a time based integration scheme, such as the Runge-Kutta approach, would need to be employed.

An alternative methodology would be to perform the calculations in the frequency domain. The blade response, in the frequency domain, can then be expressed as (Forbes, 2010, p. 153):

$$X(f)_r = H(f)_r \cdot F(f)_r \quad [1.3.35]$$

Where the blade transfer function H is obtained from the EOM and $F(f)_r$ is the Fourier transform of the forcing function. The blade transfer function H , which is the steady state response of a system to unit harmonic excitation force, is provided in Equations [1.3.36] to [1.3.38] (Forbes, 2010, p. 153).

$$H(f)_r = \frac{1/k_r}{(\omega_{nr}^2 - \omega^2) + j \cdot 2 \cdot \zeta \cdot \omega_{nr} \cdot \omega} \quad [1.3.36]$$

$$\omega_{nr}^2 = \frac{k}{m} \quad [1.3.37]$$

$$\zeta = \frac{c}{2 \cdot m \cdot \omega_{nr}} \quad [1.3.38]$$

It was noticed that the original transformation of the blade transfer function to the frequency domain may have been erroneous. A recalculated transfer function is provided in Equation [1.3.39].

$$H(f)_r = \frac{1/k_r}{(\omega_{nr}^2 - \omega^2) + j \cdot 2 \cdot \zeta \cdot \omega / \omega_{nr}} \quad [1.3.39]$$

The Fourier transform of the time based forcing function signal F is given in Equation [1.3.40].

$$F(\omega)_r = F_0 \cdot G(\omega) \cdot \pi \cdot \left[\sum_{q=0}^{\infty} C_q \cdot e^{-\gamma_q \cdot q \cdot j - \gamma_r \cdot q \cdot j} \cdot \delta(\omega + q \cdot \omega_{SPF}) + e^{\gamma_q \cdot q \cdot j + \gamma_r \cdot q \cdot j} \cdot \delta(\omega - q \cdot \omega_{SPF}) \right] \quad [1.3.40]$$

The parameter $G(\omega)$ is the Fourier transform of the Gaussian white noise term and δ is the Dirac delta. A graphical representation of the blade response spectrum derivation (convolution of the forcing spectrum and the blade transfer function) is presented in Figure 1.3-13 (Forbes and Randall, 2013).

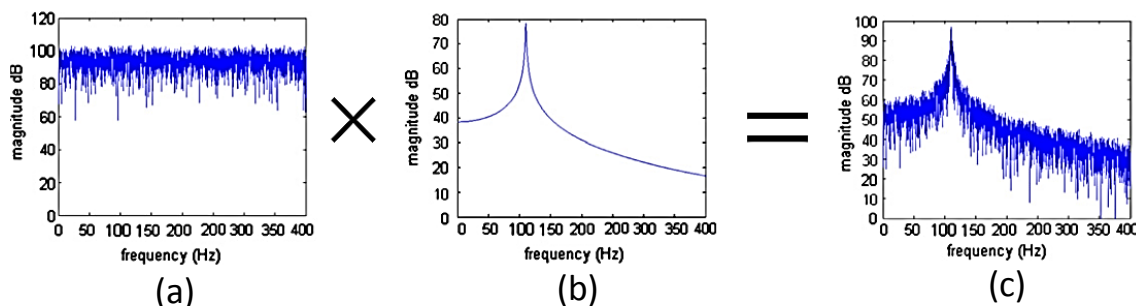


Figure 1.3-13 Derivation of blade response model. (a) Blade force model containing Gaussian noise. (b) SDOF rotor blade transfer function. (c) Rotor blade response spectrum. (Forbes and Randall, 2013)

Assuming that the pressure distribution about a single blade is a function of both the blade motion due to vibration and the rotating internal pressure profile, it follows that the resultant total rotating pressure profile is a combination of these two signals (Forbes, 2010, p. 69). The blade response spectrum (represented as $e^{(j \cdot i \cdot [x(t)_r])}$) combined with the rotating pressure signal is given in Equation [1.3.41] (Forbes and Randall, 2013).

$$P_r(t) = Re \left\{ \sum_{i=0}^{\infty} A_i \cdot P \cdot e^{(j \cdot i \cdot [\theta + \Omega(t) + \alpha_r + \gamma_i])} \cdot e^{(j \cdot i \cdot [x(t)_r])} \right\} \quad [1.3.41]$$

A simplified form of the total pressure signal can be obtained by assuming that the pressure response due to blade motion is a SDOF system (the same as the form indicated in Equation [1.3.33]).

By making use of a Laurent power series expansion of the response exponential ($e^{(j \cdot i \cdot [x(t)_r])}$) whilst employing an integral form of the Bessel function $J_n(x)$; the total internal pressure profile as a function of both blade rotation and vibration is expressed in Equation [1.3.42] (Forbes, 2010, p. 69). The full derivation of the equation is provided in '7.1.1 A1 - Derivation of Bessel Representation of Pressure Signal'.

$$P_r(t) = \sum_{i=0}^{\infty} \sum_{n=-\infty}^{\infty} A_i \cdot P \cdot J_n(i \cdot X_k) \cdot \cos[i \cdot (\theta + \Omega(t) + \alpha_r + \gamma_i) + n \cdot (k \cdot \Omega(t) + \gamma_k)] \quad [1.3.42]$$

It can be seen from the revised form, Equation [1.3.42], that the pressure profile around a particular blade is a phase modulated signal (Forbes, 2010, p. 69). The carrier frequencies are at integer multiples of shaft speed. Due to the SDOF response solution assumption the modulated signal has a dominant response frequency at an integer multiple of shaft speed as well.

Phase modulation of the signal results in sidebands appearing about engine harmonics in the frequency domain and provides a precursor for the actual expected pressure signal spectrum. The topic of phase modulation is explained in more depth in the succeeding section.

The internal pressure signal resulting from the combination of the pressure profile from blade rotation and the forced blade response is illustrated in Figure 1.3-14 (Forbes and Randall, 2013). The spectrum of the internal pressure signal consists of discrete engine harmonics (Figure 1.3-14 (a)). The stochastic portion of the total rotating pressure spectrum consists of sideband peaks which form about integer multiples of the shaft speed (Forbes and Randall, 2013).

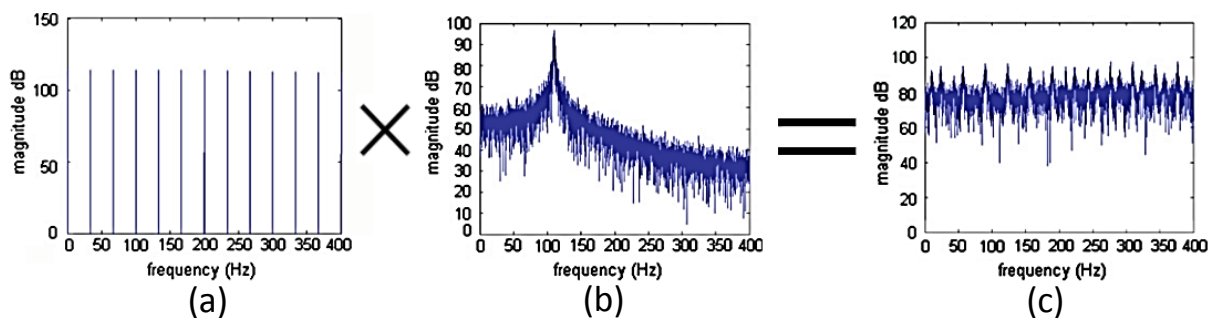


Figure 1.3-14 Derivation of stochastic pressure spectrum. (a) Deterministic pressure signal resulting from assembly rotation. (b) Blade forced response model. (c) Stochastic part of the internal pressure signal. (Forbes and Randall, 2013)



What is not shown in Figure 1.3-14 is that the resultant convolution of the deterministic pressure signal and the blade vibration signal is first signal processed before the stochastic signal is displayed. The signal processing technique is used to separate the engine harmonic signature from the entire pressure spectrum. This is analogous to the deletion of engine ordered responses referred to by Mengle and explained by Kurkov (Kurkov, 1981; Mengle, 1990).

As was already mentioned the appearance of sidebands is attributed to the phase modulation of the response signal. The appearance of sidebands in the stochastic part of the pressure spectrum is significant in that it may contain blade natural frequency information given operation at a particular shaft speed (Forbes, 2010, p. 156). The emphasis of the following subsection is a methodology to reveal these sidebands and relate them to actual blade vibration.

1.3.5.2.2. Blade Vibration Detection Scheme

It was noted that the resulting pressure signal is phase modulated. It should therefore be possible to extract blade response information through phase demodulation of the signal. However before demodulation can be discussed a brief definition of modulation, and then specifically phase modulation, will be given.

Modulation is the process of varying one or more properties of a periodic waveform with a modulating signal (sometimes referred to as the message signal). The periodic waveform signal is termed the carrier signal. Properties such as the carrier signal's amplitude, frequency or phase angle are varied by a modulating signal.

As the name suggests, phase modulation is the process of time varying the carrier signal's phase angle. The modulated signal contains both the carrier signal and the modulating message signal. In terms of blade vibration the carrier signal is the deterministic signal related to the rotation of the system and the message signal is the blade vibration carrying signal.

The presence of blade vibration therefore causes the carrier signal to arrive sooner or later depending on the where the blade vibration is in its oscillatory path. In the frequency domain the modulated signal appears as sidebands flanking the carrier frequencies (specifically at the carrier \pm the modulating frequency). An example of a sine carrier signal being modulated by some periodic modulating signal M to produce a modulated signal S is given in Equation [1.3.42].

$$S(t) = \sin(\omega \cdot t + M(t)) \quad [1.3.43]$$

Demodulation is the process of extracting the modulating signal from a modulated signal. In order to perform conventional phase demodulation certain initial conditions of Bedrosian's theorem must be satisfied (Forbes, 2010, p. 69).

The theorem states that in order to apply conventional phase demodulation, by means of the general solution of the Hilbert transform, the carrier frequency must be higher than the modulating frequency and the respective frequency domains must be non-intersecting (Bedrosian, 1963; Cerejeiras et al., 2009; Forbes, 2010, p. 69).

Additionally in order to avoid aliasing of the modulating signal the carrier frequency must be at least six times greater than the modulating frequency (Forbes, 2010, p. 70). An example of an arbitrary

modulated sinusoid (modulated by another sinusoid) which satisfies Bedrosian's theorem is presented in Figure 1.3-15.

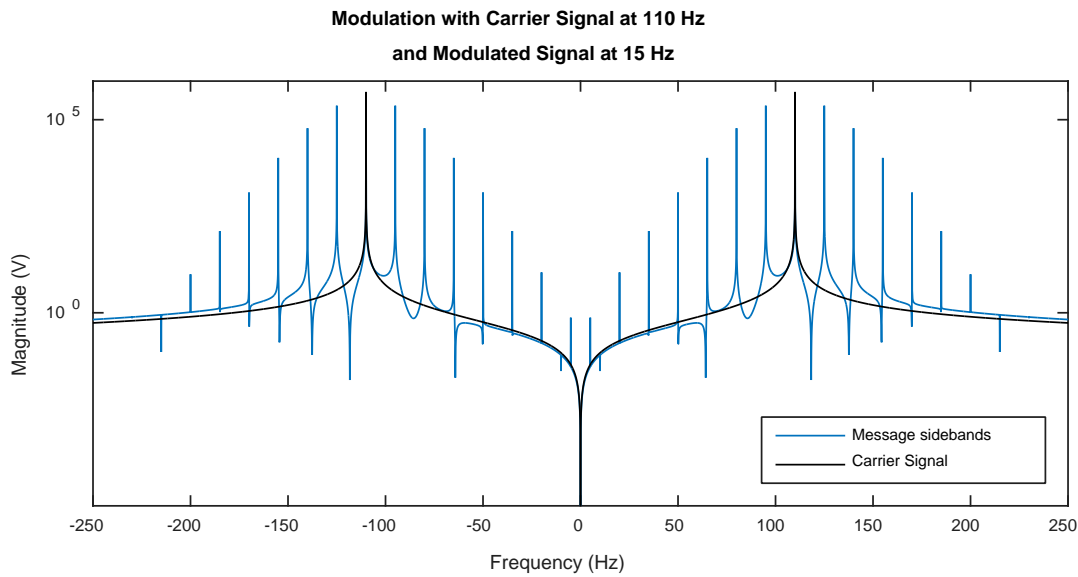


Figure 1.3-15 Arbitrary modulation example with carrier signal at 110 Hz and modulated signal at 15 Hz

It is clear from Figure 1.3-15 that the sidebands which carry the modulated signal are separated and discernible from one another. The sideband frequencies around the carrier signals do not intersect. The conditions of Bedrosian's theorem will however never be satisfied by the blade vibration scenario as multiple carrier frequencies exist at integer multiples of shaft speed along with the dominant blade resonance frequency being one of them (Forbes, 2010, p. 70). An example of an arbitrary modulated sinusoidal which does not satisfy the required conditions, is illustrated in Figure 1.3-16.

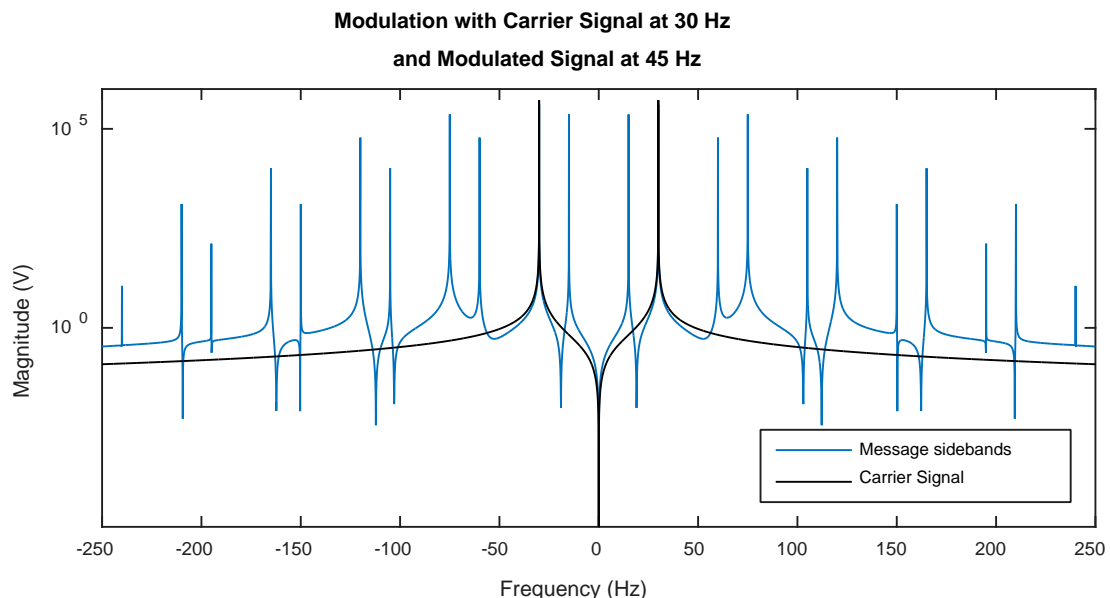


Figure 1.3-16 Arbitrary modulation example with carrier signal at 30 Hz and modulated signal at 45 Hz

It can be seen in Figure 1.3-16 that the sidebands, which contain the modulated message signal, are smeared across one another and a unique solution does not exist.

Finally a modulation example based on a rotor operating at 16 Hz (960 RPM) with a blade vibrating at 128.8 Hz is given in Figure 1.3-17.

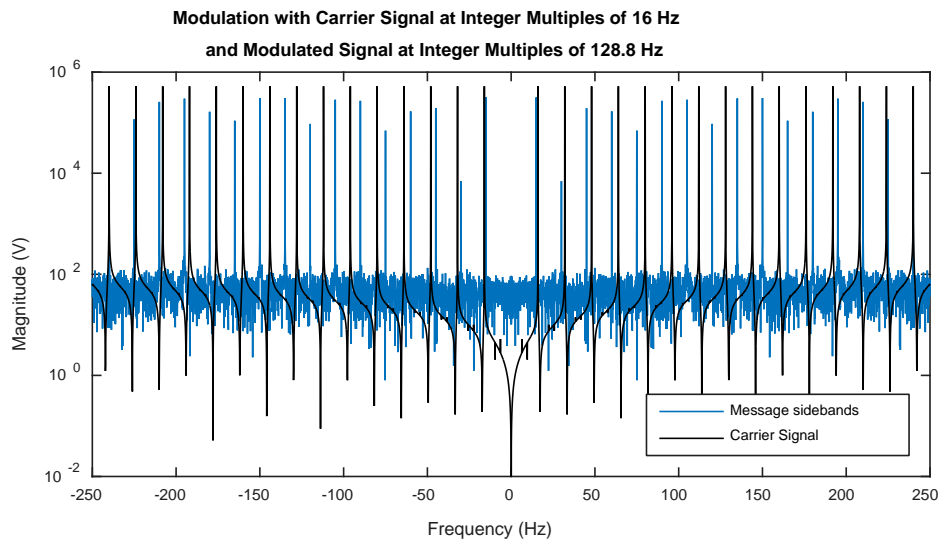


Figure 1.3-17 Modulation example with carrier signal at integer multiples of 16 Hz and modulated signal at integer multiples of 128.8 Hz

A novel demodulation methodology was developed for the problem of identifying blade vibration characteristics. The methodology was tuned for the case where the number of upstream stator blades coincides with the engine order (EO) of excitation for a SDOF system (Forbes, 2010, p. 70). The method was able to infer the response amplitude and phase of a simulated SDOF blade over a range signal to noise (SNR) ratios given the dominant frequency of response (Forbes, 2010, p. 70). The drawback to this approach is that the dominant blade response frequency must be known a priori.

An alternative approach to direct signal demodulation was sought. As was previously mentioned, it was noticed that blade natural frequency information may be present in the stochastic part of the pressure signal. A signal processing method was thus developed to separate the engine harmonic (deterministic) and blade vibration carrying (stochastic) parts of the signal, and then to concentrate any pattern found in the stochastic part. The procedure is outlined in Figure 1.3-18 (Forbes and Randall, 2013). This is the process related to engine harmonic deletion mentioned by Mengle and performed by Kurkov (Kurkov, 1981; Mengle, 1990; Murray and Key, 2015).

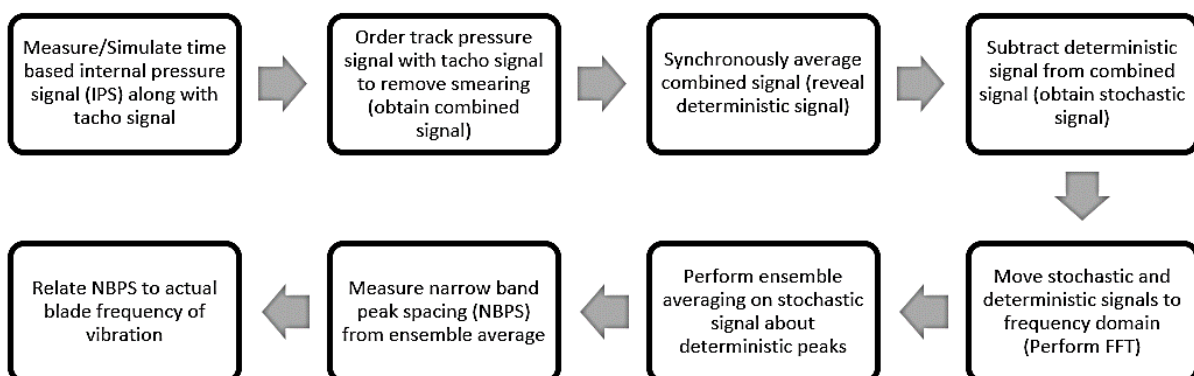


Figure 1.3-18 CPS signal processing procedure (adapted from (Forbes and Randall, 2013))

A brief description of the process is as follows. The internal pressure signal is order tracked (phase resampled) in order to remove smearing in the frequency domain and to provide a resultant signal with a chosen number of linearly spaced measurements per revolution. This signal is then synchronously averaged to determine the average non-vibrating signal over a single revolution. This average is then repeated to form a full time length signal termed the deterministic signal.

The deterministic signal is finally subtracted from the full order tracked signal in order to reveal the stochastic signal. From this point both the deterministic and stochastic signals are moved into the frequency domain by means of a Fourier transform for further analysis. An example of separated deterministic and stochastic signal spectra is presented in Figure 1.3-19. The deterministic portion of the signal is shown in red and the stochastic in blue.

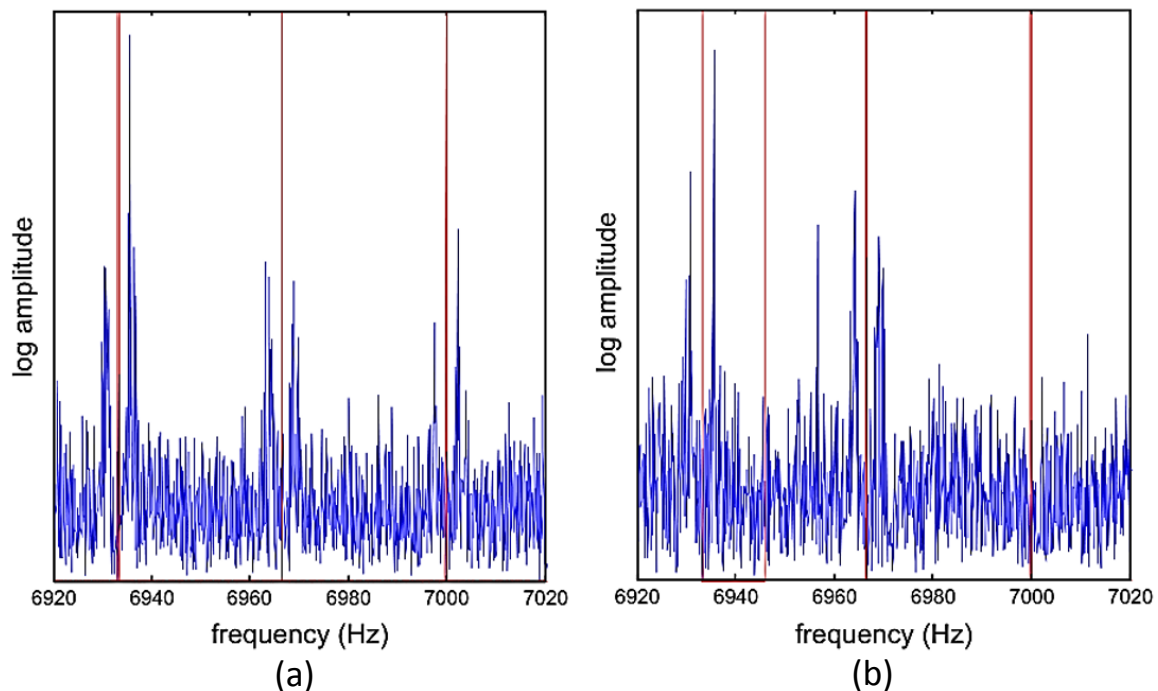


Figure 1.3-19 FRFs of the Stochastic and deterministic portions of the pressure signal for $N = 2000$ RPM. (a) Internal pressure directly measured (IPS). (b) Casing response measured (CPS). (Forbes and Randall, 2013)

It is clear in Figure 1.3-19 that sidebands, in the stochastic portion of the signal, appear about certain engine harmonics. It is also clear from the figure that all deterministic information was successfully removed from the combined pressure signal in order to reveal the stochastic signal.

The spectra in Figure 1.3-19 (a) was evaluated from internal pressure measurements using a sound pressure transducer. More interestingly the spectra in Figure 1.3-19 (b) were obtained by vibration measurements using an accelerometer attached to the outside of the casing (Forbes and Randall, 2013). This is significant in that blade vibration may possibly be monitored without the need for casing alteration to access the internal pressure signature. This results in a truly non-intrusive blade vibration measurement technology (Forbes and Randall, 2013). The casing itself is said to act like a time invariant linear filter on the internal pressure signal (Forbes and Randall, 2013).

After transformation into the frequency domain sideband peaks appear about engine harmonics in the stochastic portion of the signal. An ensemble averaging process was developed in order to obtain

a robust estimate of the form of the narrow band peaks (Forbes and Randall, 2013). The ensemble averaging process is illustrated in Figure 1.3-20.

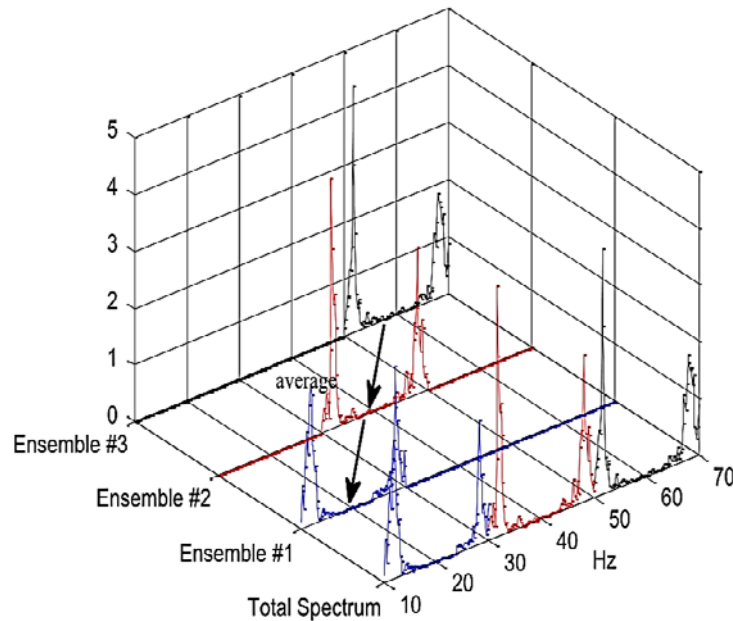


Figure 1.3-20 Ensemble averaging process (Forbes and Randall, 2013)

The stochastic spectrum is divided into ensembles whose width is the same as the rotor speed and centered about engine harmonics. The engine harmonic peaks are determined using the deterministic signal. These ensembles are then summed and the result divided by the total number of ensembles added in order to obtain an average ensemble spectrum (Forbes and Randall, 2013).

The process is analogous to synchronous averaging of rotating signals in the time domain as the process concentrates the sideband peak pattern and removes unwanted noise. An example of analytically derived ensemble averages resulting from operation of the same system (in terms of geometry and material properties) at two separate rotational speeds is provided in Figure 1.3-21.

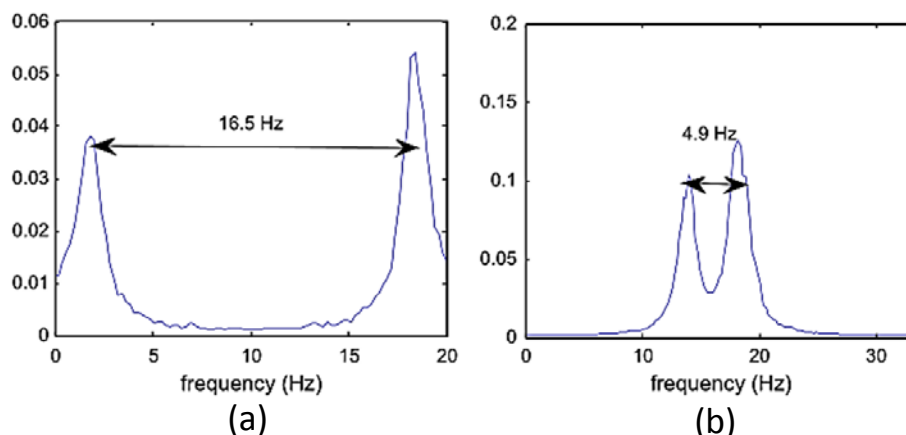


Figure 1.3-21 Ensemble average from analytically derived CPS residual power spectrum. (a) 1200 RPM rotor speed. (b) 2000 RPM rotor speed (Forbes and Randall, 2013)

Experiments were performed in order to confirm that the pressure relation developed accurately describes the periodic pressure signal within the casing. The above analytical ensemble averages are derived using an actual experimental setup's geometry and blade material properties, although the

response amplitudes are arbitrary. Ensemble averages, obtained from experimental measurements, for operation at the same speeds as indicated above, are provided in Figure 1.3-22.

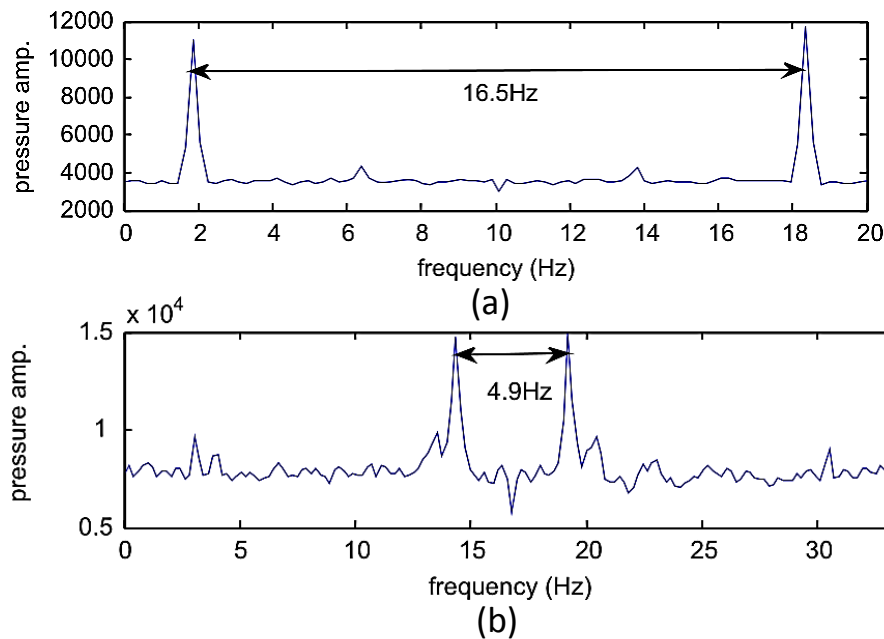


Figure 1.3-22 Ensemble averages from experimentally derived internal pressure measurements. (a) 1200 RPM rotor speed. (b) 2000 RPM rotor speed (Forbes and Randall, 2013)

It can be seen that the experimentally determined ensemble averages produce averaged sideband peaks with a peak to peak distance which is the same as the analytically derived solutions for the same operating speed.

A discussion on the experimental setup used and excitation methodology for the work done by Forbes et al. can be found in section '7.3 Appendix C – Example Application of CPS Method'.

The succeeding section provides a relation between the ensemble average and the blade natural frequency by making use of the modulation and signal processing principles discussed above.

1.3.5.2.3. Analytical Relation between Ensemble Average and Blade Natural Frequency

It was proposed that a method be developed to relate these ensemble averages to the blade's natural frequencies (Forbes and Randall, 2013). As has already been stated the sidebands which contain the blade vibration information occur at multiples of shaft speed plus and minus the blade natural frequency (Forbes, 2010, p. 156). Consider Figure 1.3-23.

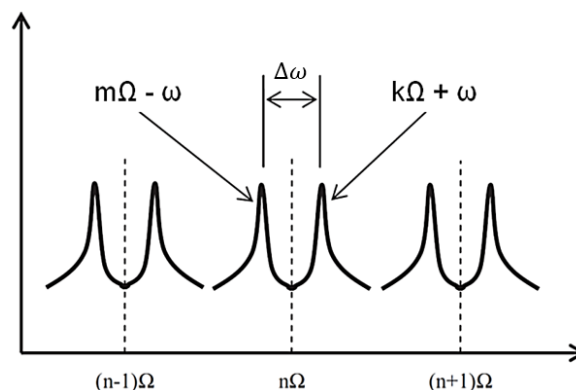


Figure 1.3-23 Sidebands about multiples of shaft speed (Cox and Anusonti-Inthra, 2014; Forbes and Randall, 2013)



Due to the fact that the deterministic carrier signal's frequencies are consistently lower than the blade natural frequencies, and that excitation occurs at all engine harmonics, the frequency domains about the carrier signals intersect. There however exist two peaks related to blade vibration in each range of length Ω .

As has already been noted, this results in a situation where the blade vibration sidebands cannot be uniquely separated to infer the blade's response. There is however a consistent and measureable pattern which emerges from the modulation: this sideband pattern is clearly visible in Figure 1.3-23. It is not clear from which shaft harmonic (m or k in the figure) each individual sideband stems resulting in the aforementioned ambiguity as to which sideband peak is related to which carrier frequency.

It was proposed that the distance between the sidebands, termed the narrow band peak spacing (NBPS), be used in order to estimate the blade natural frequency (Forbes and Randall, 2013). The final step in the ensemble averaging process is therefore to measure the average peak to peak distance between the sidebands in the ensemble average and then relate this measurement back to one of the natural frequencies of the blades. The relation of the NBPS to the actual frequency of vibration and the rotor speed is given in Equations [1.3.44] and [1.3.45] (Forbes and Randall, 2013).

$$\Delta\omega_{NB} = (k \cdot \Omega + \omega_N) - (m \cdot \Omega - \omega_N) \quad [1.3.44]$$

$$\therefore \omega_N = \frac{\Delta\omega_{NB} + (m - k) \cdot \Omega}{2} = \frac{\Delta\omega_{NB} + q \cdot \Omega}{2} \quad [1.3.45]$$

The parameters m and k refer to the rotor speed integer multiplier in Figure 1.3-23. They are both positive integers and $k < m$. The rotor speed Ω is given in hertz.

In order to use the above method the natural frequencies of the blades needs to be known within $\pm 0.5\Omega$ (within half the rotor speed) in order to estimate the positive integer q before natural frequency estimates can be made (Forbes and Randall, 2013). This is because Equation [1.3.45] is linear in the variables ω_N and q and results in an indeterminate system (Cox and Anusonti-Inthra, 2014). The indeterminacy of Equation [1.3.45] is comparable to the analytical solution suggested in Model 1 where for each frequency range investigated two possible solutions for the blade vibration exist (Mengle, 1990).

An example application of Equation [1.3.45] for the purpose of estimating a blade's natural frequency from both analytically derived and experimentally determined NBPS is also presented in section '7.3 Appendix C – Example Application of CPS Method'.

It is suggested that the indeterminacy of Equation [1.3.45] be surmounted by rather employing a system of equations; this is achieved by making use of a slight change in rotor speed (Cox and Anusonti-Inthra, 2014). It is assumed that the stochastic responses of interest, related to the blade natural frequency, do not change significantly with the change in operating speed; this effectively uncouples Equation [1.3.45] (Cox and Anusonti-Inthra, 2014).

Once again a similarity between the work of Mengle and the current approach can be made: Mengle suggested performing measurements at two slightly different operating speeds in order to uncouple the mistuned blade flutter scenario (Mengle, 1990). The concept suggested by Cox et al. is illustrated in Figure 1.3-24 (Cox and Anusonti-Inthra, 2014).

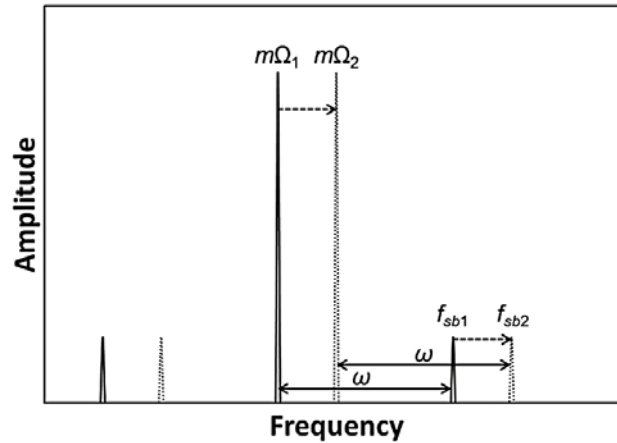


Figure 1.3-24 Adapted Forbes method (Cox and Anusonti-Inthra, 2014)

The rotor blade natural frequency, ω_N , is assumed to be constant over the change in rotor speed; the resulting linear set of equations are given in Equation [1.3.46] (Cox and Anusonti-Inthra, 2014).

$$\begin{aligned} m \cdot \Omega_1 \pm \omega_N &= f_{sb1} \\ m \cdot \Omega_2 \pm \omega_N &= f_{sb2} \end{aligned} \quad [1.3.46]$$

In this system of equations m is a particular multiple of rotor speed. Further f_{sb1} and f_{sb2} are sideband frequencies which occur at the two rotor speeds Ω_1 and Ω_2 respectively.

The natural frequency can then be solved for through substitution of one of the simultaneous equations into the other and rearrangement (Cox and Anusonti-Inthra, 2014).

$$\omega_N = \left| \frac{\Omega_1 \cdot f_{sb2} - \Omega_2 \cdot f_{sb1}}{\Omega_2 - \Omega_1} \right| \quad [1.3.47]$$

An investigation was performed in order to determine the influence of blade response amplitude, signal to noise ratio, sampling time and sampling frequency on the amplitudes of the sidebands and noise in the frequency domain (Cox and Anusonti-Inthra, 2014). A simplified internal pressure signal was developed for investigation and is given in Equation [1.3.48] (Cox and Anusonti-Inthra, 2014).

$$P_n = rand(-1,1) + \frac{(2 \cdot SNR)^{0.5}}{6.6} \cdot \cos(2 \cdot \pi \cdot B \cdot \Omega \cdot t + \epsilon \cdot \cos(2 \cdot \pi \cdot \omega \cdot t)) \quad [1.3.48]$$

In this equation B is the number of rotor blades, t is the time and ϵ is the blade response amplitude.

An analysis of variance (ANOVA) was used to compare the influences of the above mentioned properties. It was found that the blade response pressure amplitude had the greatest effect on sideband height, followed consecutively by the sampling frequency, SNR and sample time (Cox and Anusonti-Inthra, 2014).

The subsequent literature section explores alternative investigations into using the internal casing pressure signal to identify blade faults and blade resonance.

1.3.5.3. Alternative Casing Pressure Methods and Investigations

1.3.5.3.1. Gas Turbomachine Blade Fault Identification from Wall Pressure Measurements

It was proposed that distortions in the unsteady pressure field, about individual blades in a rotating turbomachine, could be used to identify faults associated with the individual blades (Mathioudakis et al., 1991).

At the time of publication it was noted that the current blade fault diagnostic techniques only had the capacity to detect major faults whose magnitudes were of a sufficiently large scale (Mathioudakis et al., 1991). Several blades in a cascade would have to be significantly damaged in order to facilitate a significant variation in either the thermodynamic properties or structural vibration of the turbomachine to produce a measureable fault response (Mathioudakis et al., 1991). The capacity to identify minor faults, such as slight bending or twisting of a few blades or blade fouling, was desired (Mathioudakis et al., 1991).

In order to investigate the effects of minor blade faults on an internal pressure signal a commercial gas turbomachine test setup was modified (Mathioudakis et al., 1991). The gas turbomachine was operated at conditions expected in the field (Mathioudakis et al., 1991). A schematic of the experimental test setup used is presented in Figure 1.3-25.

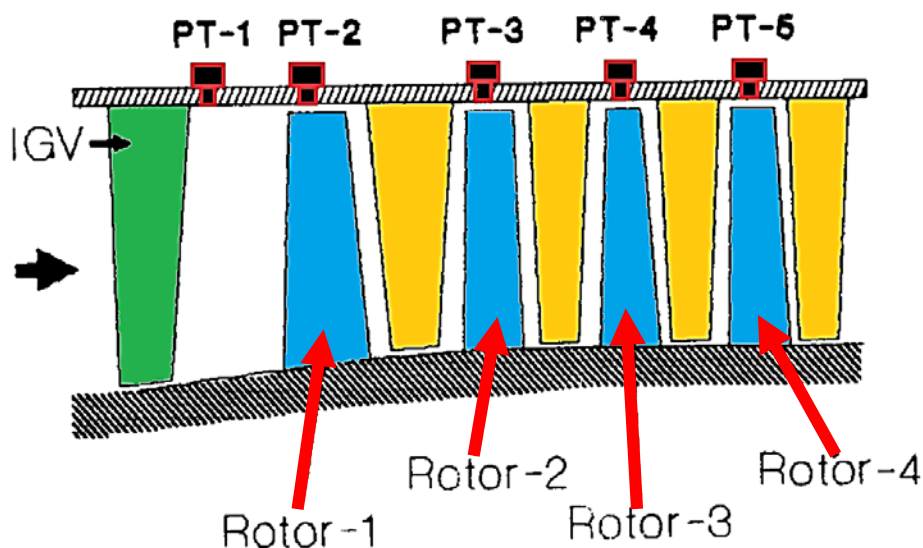


Figure 1.3-25 Gas compressor layout and positioning of fast response pressure transducers (Mathioudakis et al., 1991)

Testing was performed on the compressor end of the gas turbomachine. Five fast response pressure transducers were installed flush to the inner compressor casing wall, as indicated on Figure 1.3-25 (Mathioudakis et al., 1991). The first pressure transducer (PT-1 in the diagram) was positioned just after the row of inlet guide vanes (IGVs). The second, third, fourth and fifth pressure transducers were installed in line with the first, second, third and fourth rotor cascade respectively.

Four separate measurement configurations were used in order to investigate minor blade fault identification from the internal casing pressure measurements. The first measurement configuration provided a datum measurement (void of any artificial blade faults) (Mathioudakis et al., 1991). In the second measurement configuration all of the blades on rotor cascade 2 were artificially fouled by coating them with a textured paint (Mathioudakis et al., 1991). In the third configuration only two blades of rotor cascade 1 were fouled by the same means, these blades were separated by five healthy

unaltered blades (Mathioudakis et al., 1991). In the final configuration the stagger angle of an individual blade of rotor cascade 1 was altered by approximately 8° changing its incidence angle (Mathioudakis et al., 1991).

The comparison of the datum configuration measurement and a measurement from configuration 2 at pressure transducer 3 (in line with rotor cascade 2) is given in Figure 1.3-26.

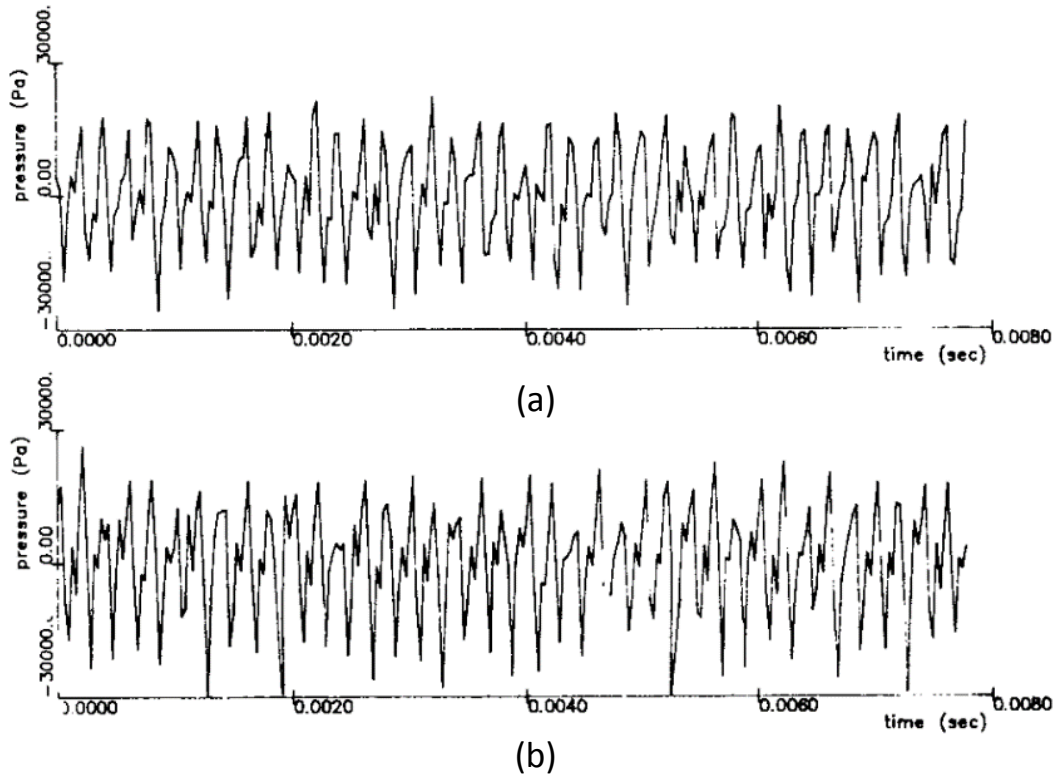


Figure 1.3-26 Comparison of fully fouled rotor (a) and healthy rotor (b) at PT-3 (Mathioudakis et al., 1991)

It was noted that the fouling produced a reduction in the pressure response amplitude as well as altered the form of the pressure peaks (Mathioudakis et al., 1991). The effects of minor faults on rotor cascade 1 (configurations 3 and 4) measured by pressure transducer 2 are presented in Figure 1.3-27.

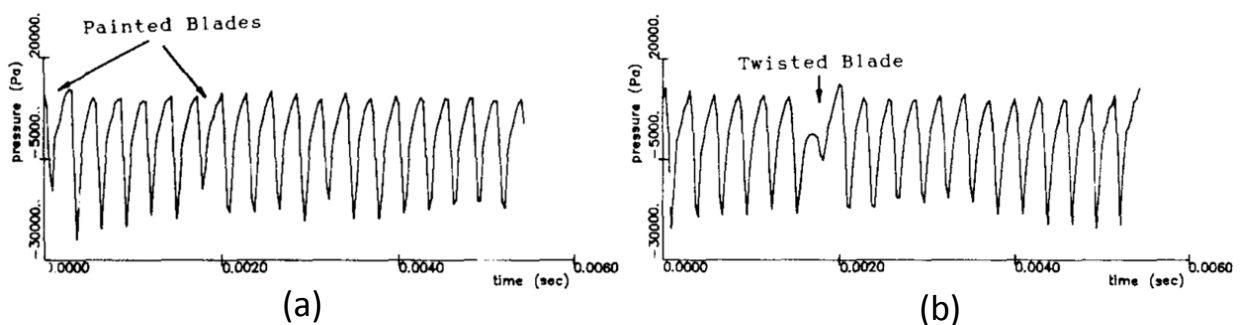


Figure 1.3-27 Effect of minor faults. (a) Fouling of two blades. (b) Twisting of a single blade. (Mathioudakis et al., 1991)

The fouling of the two blades in rotor cascade 1 produced a slight but noticeable difference in the appearance of the pressure peaks (Mathioudakis et al., 1991). The twisting of an individual blade by 8° produced a significant signature in the pressure signal (Mathioudakis et al., 1991).

Power spectra were evaluated for all four measurement configurations at pressure transducer 2. The power spectra for all experimental configurations taken by PT-2 are presented in Figure 1.3-28. Multiples of the blade passing frequency (BPF) and shaft harmonics are indicated in the final figure (d).

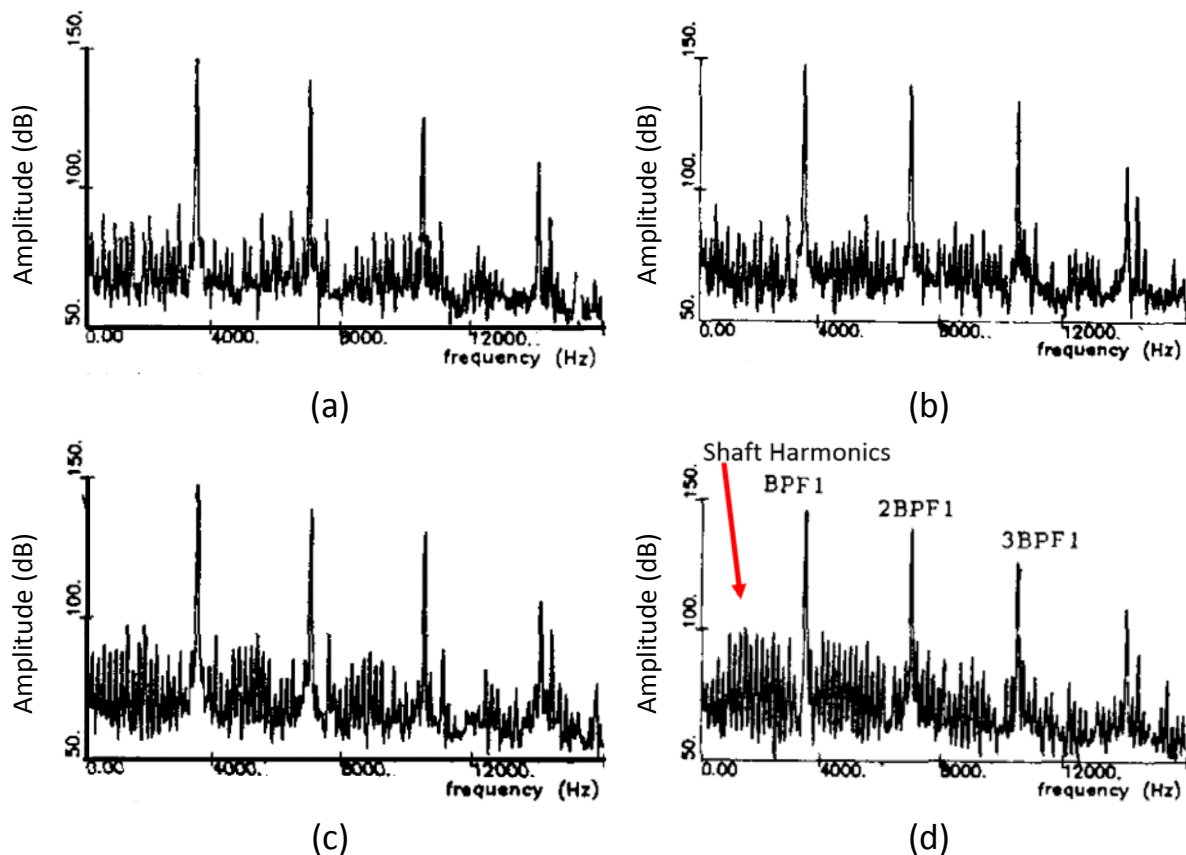


Figure 1.3-28 Power spectra measured at PT 2. (a) Configuration 1. (b) Configuration 2. (c) Configuration 3. (d) Configuration 4. (Mathioudakis et al., 1991)

It is noted that almost no variation is perceived between the spectra for configuration 1 and 2 (when measured by pressure transducer 2) (Mathioudakis et al., 1991). There is however a visible variation between configurations 3 and 4 in the regions between 0 Hz and the first BPF in the shaft harmonics; these variations correspond to the introduction of minor faults (Mathioudakis et al., 1991).

Power spectra were evaluated for the remaining configurations at all measurement points. The main observations noted are as follows (Mathioudakis et al., 1991):

- A visible difference is noted between the spectra measured at pressure transducer 3 between configurations 1 and 2 corresponding the surface preparation across the entire cascade of rotor 2.
- No visible difference in the power spectrum is noted for measurements taken at fast response pressure transducer 3 for measurement configurations 3 and 4.
- When comparing the spectra measured at all locations, for measurement configuration 4, the only noticeable change in the spectra occurred for measurements taken by transducer PT-2

It was concluded that minor blade faults, corresponding to individual blades, could be identified from internal casing pressure measurements (Mathioudakis et al., 1991). The minor fault information is identifiable in both the power spectra and time domain measurements (Mathioudakis et al., 1991).



Further, the minor fault signature decays to the extent that it cannot be observed either up- or downwind from the fault location when measured at the casing wall in line with preceding or succeeding rotor cascades respectively (Mathioudakis et al., 1991). This final conclusion is similar to that expressed by Mengle; namely that certain blade frequency response components will decay and will not be noticeable in a measurement plane removed from the source (Mengle, 1990).

1.3.5.3.2. Blade Natural Frequency Estimation from Run-up and Run-down Measurements

An investigation was performed in order to determine if the deterministic casing vibrational response and internal wall pressure signal could be used to identify blade natural frequencies from run-up and run-down measurements (Ratz et al., 2013).

An analytical model was developed to simulate the internal casing pressure (Ratz et al., 2013). This model is built on the work done by Forbes et al. (Forbes and Randall, 2013). The internal pressure within the casing about blade r is represented by Equation [1.3.49] (Ratz et al., 2013).

$$P_r = Re \left\{ \sum_{i=0}^{\infty} A_i \cdot P \cdot e^{j \cdot i \cdot [\theta + \Omega \cdot t + \tilde{\alpha}_r + \gamma_i + x(t)_r]} \right\} \quad [1.3.49]$$

The Fourier coefficients A_i and γ_i define the frequency response amplitudes and phase angles of the pressure wave associated with rotation of the system without blade vibration (Forbes and Randall, 2013; Ratz et al., 2013). The value θ is the measurement angle define by some arbitrary datum, Ω is the shaft speed, $x(t)_r$ is the vibration of blade r and $\tilde{\alpha}_r$ is the phase offset of each rotor blade (Ratz et al., 2013).

The phase offset $\tilde{\alpha}_r$ is designed to accommodate small deviations in the angular location of the rotor blades, the phase offset is given by Equation [1.3.59] where b is a random variable between 0 and 1 and α_r is the angle between two adjacent blades (Ratz et al., 2013).

$$\tilde{\alpha}_r = [1 + b \cdot 0.001] \cdot \alpha_r \quad [1.3.50]$$

The vibration of blade r is defined by the sinusoid in Equation [1.3.51] (Ratz et al., 2013).

$$x(t)_r = B \cdot \sin(\omega_{SPF} \cdot t + \gamma_r) \quad [1.3.51]$$

The blades are modelled as lumped single degree of freedom (SDOF) spring and mass systems (Ratz et al., 2013). Excitation occurs at the stator passing frequency ω_{SPF} (number of blades multiplied by the shaft speed i.e. $\omega_{SPF} = B_{blades} \cdot \Omega$) with an inter-blade phase angle offset of γ_r . The solution to the SDOF system assumption yields a blade response amplitude B defined in Equation [1.3.52].

$$B = \frac{F_0/k_r}{\sqrt{\left[1 - \left(\frac{\omega_{SPF}}{\omega_{nr}}\right)^2\right]^2 + \left[2 \cdot \zeta \cdot \left(\frac{\omega_{SPF}}{\omega_{nr}}\right)\right]^2}} \quad [1.3.52]$$

The variables F_0 , k_r , ω_{nr} and ζ are the force on each blade, the stiffness of blade r , the natural frequency of blade r and the non-dimensional damping of all blades respectively (Ratz et al., 2013).

The experimental setup is the same as used by Forbes et al. mentioned in section '1.3.5.2 Model 2: Pressure Model Developed Directly from Casing Reference Frame' and fully described and illustrated

in section '7.3 Appendix C – Example Application of CPS Method' (Forbes and Randall, 2013; Ratz et al., 2013).

A brief description of the experimental setup and methodology is as follows: the rotor consists of 19 flat blades attached to a hub; the blades' dimensions are 100mm in length by 50 mm in width by 1.2mm in thickness (Ratz et al., 2013). The natural frequencies for all blades were measured using a stationary test bench. These measurements were then averaged over to determine mean blade resonant values. The mean blade natural frequencies were determined to be 117.4 Hz (first bending mode), 515.9 Hz (first torsional mode) and 726 Hz (second bending mode) (Forbes and Randall, 2013; Ratz et al., 2013).

Six high pressure air jets were used to approximate upstream stators for the purpose of blade excitation (Ratz et al., 2013). Measurements were taken during run-down conditions with the shaft speed being slowed linearly from 1400 RPM to 1000 RPM (approximately from 23.3 Hz to 16.6 Hz) at a speed rate change of approximately -60 RPM/s (-1 Hz/s) (Ratz et al., 2013). It was assumed that the change in blade natural frequencies, due to centrifugal stiffening, is negligible for the chosen operational speed range (Forbes and Randall, 2013). A sound pressure transducer was installed into the casing wall, in line with the row of blades, in order to obtain the internal pressure response (Ratz et al., 2013). At a similar location on the outside of the casing an accelerometer was installed to measure the casing vibrational response (Ratz et al., 2013).

The time domain measurements were divided into 32 parts; these parts were assumed to have a near constant rotational speed over the measurement interval (Ratz et al., 2013). The intervals were then order tracked with a once per revolution tachometer signal (Ratz et al., 2013). Finally the order tracked signal was synchronously averaged to reveal the deterministic signal (Forbes and Randall, 2013; Ratz et al., 2013). A plot containing the Fourier transform of the experimentally obtained deterministic signals, from the 32 time parts, with respect to the quasi-constant operational speed is given in Figure 1.3-29.

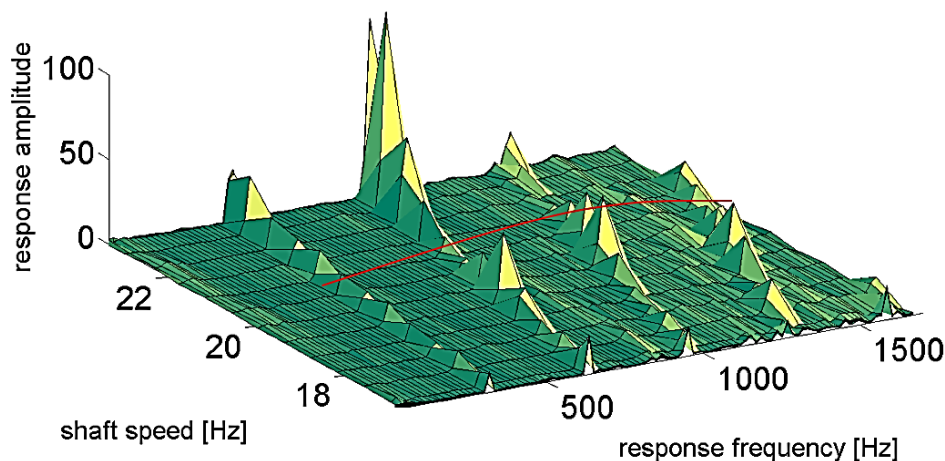


Figure 1.3-29 Experimentally obtained deterministic radial pressure signal for run-down measurement from 23.3 Hz to 16.6 Hz (Ratz et al., 2013)

The four rows of curves represent the first four harmonics of the stator passing frequency ω_{SPF} (Ratz et al., 2013). It can be seen that the harmonics peak as the system passes through a resonance. The first harmonic frequency can be obtained by multiplying the number of blades with the operational

speed in hertz; the first harmonic therefore varies between 315 Hz to 424 Hz for operation between 16.6 Hz and 23.3 Hz. Similarly the remaining harmonic peak rows can be obtained by multiplying the operational speed with the number of blades and harmonic number of interest, the frequency ranges traversed by the first four harmonics, as indicated in Figure 1.3-29, is given in Table 1.3-3.

Table 1.3-3 Harmonics and frequency ranges for operation from 16.6 Hz to 23.3 Hz

Harmonic	Frequency Range (Hz)
1 st	315 to 424
2 nd	630.8 to 885.4
3 rd	946.2 to 1328.1
4 th	1261.6 to 1770.8

The measurement range is expected to traverse the 1st engine order (EO) of the fundamental resonance at a shaft speed of approximately 19.6 Hz (fundamental frequency of 117.4 Hz excited by 6 air pulses per revolution will be excited at $117.4 / (6 \cdot 1) \approx 19.6 \text{ Hz}$) (Ratz et al., 2013). The response at 19.6 Hz is indicated in Figure 1.3-29 by a red curve running perpendicular to the forced harmonic curves. The expected EO resonances, within the operational range of interest, for the first three modes are given in Table 1.3-4.

Table 1.3-4 EO Resonances for Run-Down Experiment

Mode	Natural Frequency of Mode (Hz)	EO	Expected resonance operational speed (Hz)
First Bending	117.4	1	19.6
First torsional	515.9	4	21.5
First torsional	515.9	5	17.2
Second Bending	726	5	24.2
Second Bending	726	6	20.2

The harmonic curves were summed across a chosen frequency range to produce an average response versus shaft speed plot (Ratz et al., 2013). This was done for both an analytically derived and experimentally derived pressure response. The result is given in Figure 1.3-30.

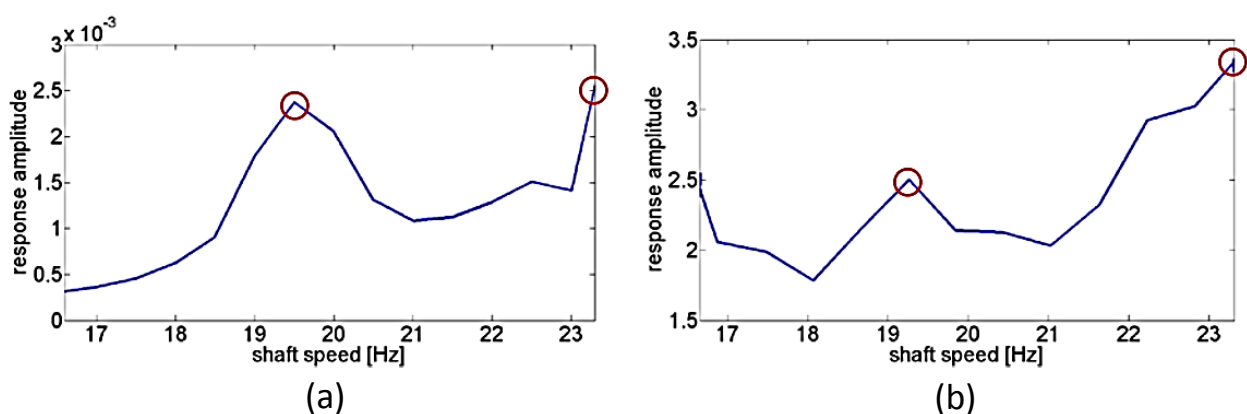


Figure 1.3-30 Radial pressure response versus shaft speed as sum of harmonic curves. (a) Analytical. (b) Experimental.
(Ratz et al., 2013)

Two peaks are highlighted in the figure, namely excitation of the first and second bending mode respectively (Ratz et al., 2013). A clear peak at approximately 19.6 Hz corresponds to excitation of the blades first natural frequency at EO 1 (Ratz et al., 2013). A second peak emerges as the rotational speed approaches 24.2 Hz. This corresponds to the 5th EO excitation of the second bending mode (Ratz

et al., 2013). It is noted that the difference in magnitude between the analytical and experimental model is due a lack of calibration of the analytical model with respect to the experimental results (Ratz et al., 2013). No peak corresponding to torsional vibration is mentioned or observed.

Similar to the investigation by Forbes et al., an individual blade of the 19 blade setup was replaced with a blade of reduced thickness (Forbes and Randall, 2013; Ratz et al., 2013). The first and second bending modes of the 'damaged' blade were measured to occur at 69 Hz and 432 Hz respectively (Ratz et al., 2013).

In order to excite the damaged blade at its fundamental frequency at an EO of 1 the operational speed is estimated to be 11.5 Hz. Similarly to excite the second bending mode at an EO of 5 the operational speed is estimated to be 14.4 Hz. The results of an analytical investigation to determine the pressure response versus shaft speed for the case of 1 damaged blade (by summing the harmonic frequency response across a single operating speed) is presented in Figure 1.3-31.

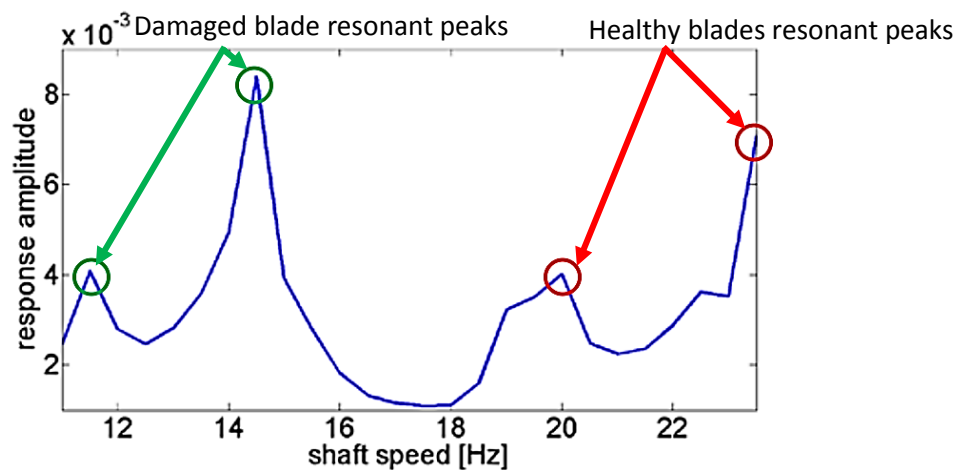


Figure 1.3-31 Analytical internal pressure response amplitude versus operating speed for operation with 18 healthy and 1 damaged blade (Ratz et al., 2013)

It can be seen that peaks corresponding to excitation of both the damaged blade and healthy blades, at their first and second bending modes, appear clearly in the figure (Ratz et al., 2013).

The procedure performed on the internal pressure measurements was repeated for external acceleration measurements taken on the outer casing. It was found that the casing vibration signal contained the same information as the internal pressure signal. It was however difficult to discern excitation of the fundamental frequency for excitation at EO 1 when summing the response amplitudes across the frequency range of interest (Ratz et al., 2013). When viewing the response amplitude versus shaft speed at the third harmonic ($3 \cdot \omega_{SPF}$) the expected resonant response peak of the fundamental frequency (excited at EO 1) at 19.6 Hz was clearly discernible (Ratz et al., 2013).

The investigation showed that the deterministic response amplitude of both the internal pressure signal and the casing vibration is related to excitation of the turbomachine blades. Further a fault was simulated and shown to appear clearly in the response deterministic amplitude.

1.3.5.3.3. Turbomachine Blade Vibration Identification from Downwind Measurements

An investigation was performed in order to detect engine ordered response of rotor blades in an axial compressor using fast response pressure transducers (Murray and Key, 2015). The transducers were installed into stator vanes downwind of the rotor cascade of interest (Murray and Key, 2015).

It was noted that this publication was the first of its kind in open literature, namely the identification of engine ordered resonant response from a pressure signal measured at a stationary observation point in a real compressor (Murray and Key, 2015). A cross section of the experimental compressor used in the investigation is presented in Figure 1.3-32.

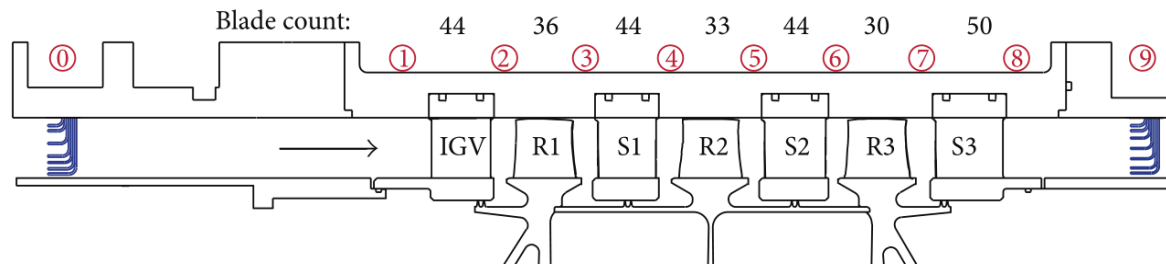


Figure 1.3-32 Cross section of 3 stage Purdue University research compressor (Murray and Key, 2015)

The compressor consists of three rotor stages. Ahead of the first rotor cascade are a set of inlet guide vanes which direct fluid flow onto the first set of rotor blades. The inlet guide vane cascade has 44 blades (Murray and Key, 2015). The three rotor rows R1, R2 and R3 have 36, 33 and 30 blades each respectively (Murray and Key, 2015). The stator vane cascades S1, S2 and S3 have 44, 44 and 50 blades each respectively (Murray and Key, 2015).

Identification of torsional vibration of the second rotor row to engine ordered excitation was of interest to investigate. It was reported that the first torsional mode occurs at 2700 Hz (Murray and Key, 2015). The 44th EO excitation point, in terms of rotor speed, for this mode occurs in the vicinity of 3700 RPM (Murray and Key, 2015). Due to mistuning in the system the band in which the blade response occurs was found to be from 2700 Hz to 2735 Hz (Murray and Key, 2015). The mode response was confirmed to exist at this location using a blade tip timing system (Murray and Key, 2015).

Two stator vanes were modified in order to accommodate the fast response pressure transducers (Murray and Key, 2015). A schematic of the installation locations on two stators in stator row S2 is provided in Figure 1.3-33. Pressure transducers were installed at both half the blade span and at 80% of the span on the suction side of one vane and the pressure side of another (Murray and Key, 2015).

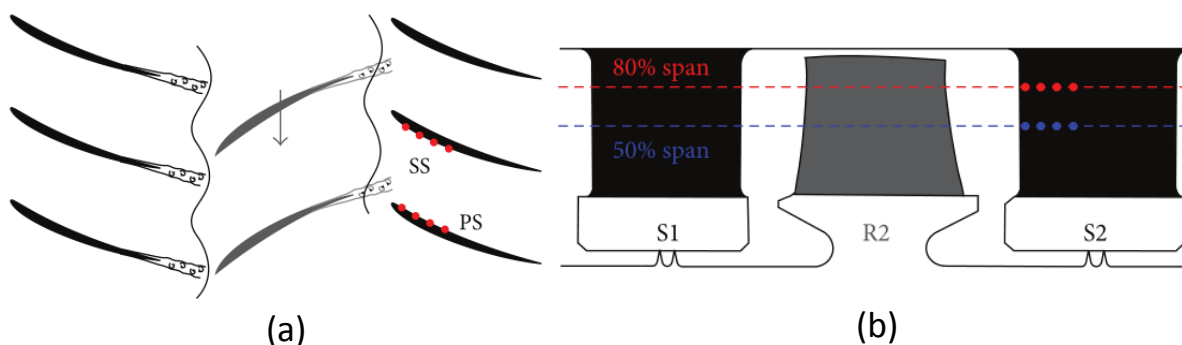


Figure 1.3-33 Stator vane pressure transducer installation. (a) Top view of sensor locations. (b) Side view of sensor locations. (Murray and Key, 2015)



It was noted that the fast response pressure transducers had a frequency response in the range of 100 to 150 kHz. It was further noted that when tests were performed using pressure transducer with a lower frequency response that blade vibration identification was not possible (Murray and Key, 2015).

The expression for observed frequencies, developed by Mengle, was implemented in the study (Mengle, 1990; Murray and Key, 2015). The form used in this investigation is provided in Equation [1.3.53] (Mengle, 1990; Murray and Key, 2015).

$$\omega' = \omega + (ND + m \cdot B)\Omega \quad [1.3.53]$$

In the expression ω' refers to the observed blade response frequency due to Doppler shifting whereas ω is the actual response frequency (Murray and Key, 2015). ND refers to the number of nodal diameters given a particular system response mode shape (travelling wave mode number in the work by Mengle) and is limited to $ND \in \{0, 1, 2, \dots, B - 1\}$. The parameter B is the number of rotor blades in the row, m is the wave number ($m \in \mathbb{Z}$) and Ω is the rotor speed (Mengle, 1990; Murray and Key, 2015).

It was stated that the nodal diameter could be estimated using the blade tip timing data or the difference in the number of upwind stator vanes to rotor blades (Murray and Key, 2015). The investigation was only interested in engine ordered response (Murray and Key, 2015). The latter formulation is shown in Equation [1.3.53] (Murray and Key, 2015).

$$ND = N_{stators} - B \quad [1.3.54]$$

Therefore, for rotor row R2 and upwind stator row S1 the nodal diameter is 11. The wave number m was restricted to the range of -2 to 2 in the investigation; the significant modes were said to lie in this region (Murray and Key, 2015).

According to the work of Mengle the Doppler shifting effect forces the engine ordered blade response to occur at integer multiples of the blade passing frequency (BPF) (Mengle, 1990; Murray and Key, 2015). The rotor row of interest has 33 blades; therefore responses are Doppler shifted to every '33rd per revolution' (33rd/rev) frequency harmonic in the spectrum measured by a stationary observer (Murray and Key, 2015). It was stated that obtaining these responses was the challenge in the investigation (Murray and Key, 2015).

A one dimensional analytical analysis was performed in order to estimate the travelling pressure waves both up- and downstream of rotor cascade 2. The analysis was performed using an algorithm termed LINSUB (linear subsonic) which was developed to obtain the unsteady parameters from turbomachine geometries by using a two-dimensional geometric approximation; the algorithm work for a system operating within the subsonic region (Murray and Key, 2015; Whitehead, 1987). It was estimated that the upstream moving pressure wave component would be in the range of 292.3 Pa and the downstream moving pressure wave would have a magnitude of 584.7 Pa (Murray and Key, 2015).

The upward and downward propagation of pressure waves means that engine ordered response from the upstream and downstream rotor rows may be contained within the pressure signal measured at the instrumented stator vane in row S2. The upstream rotor row has 36 blades and the downstream row has 30 blades. Therefore responses at 36th/rev and 30th/rev frequencies (as well as at integer multiples of these values) may be observed as well (Murray and Key, 2015).



A signal processing technique was developed in order to reveal the engine ordered response spectra. Measurements were taken for a rotor accelerating, for this reason individual revolutions of the rotor were separated from one another (Murray and Key, 2015). The data from each revolution could then be Fourier transformed to obtain its response spectrum. The average speed over each revolution was captured in order to be used in a waterfall plot of the response.

It was stated that the act of separating each individual rotation was equivalent to applying a rectangular window to that measurement (Murray and Key, 2015). Rectangular windows created undesirable effects in the frequency domain due to the abrupt separation of the signals which may lead to discontinuities in the frequency domain (Murray and Key, 2015).

For this reason each individual rotation's data was passed through a Kaiser window before performing a fast Fourier transform (FFT) on the measurement (Murray and Key, 2015). The Kaiser window was chosen because it facilitates a high degree of precision between frequency components which are very closely related in terms of frequency value yet have completely different magnitudes (Murray and Key, 2015).

The frequency axis for each measurement was normalised by dividing it by the blade pass frequency (BPF) (Murray and Key, 2015). This was done in order to make the Doppler shifts immediately apparent in the spectra (Murray and Key, 2015).

Finally the spectrum obtained from the first revolution was subtracted from all of the response spectra of all subsequent revolutions (Murray and Key, 2015). This was done to make the small fluctuations related to resonant blade vibration obvious (Murray and Key, 2015). The response spectra from all revolutions could then be assembled into a waterfall plot for analysis (Murray and Key, 2015).

Measurements were taken for an accelerating rotor with a sweep rate of approximately 2.2 RPM/s (Murray and Key, 2015). The sweep rate had to be specially chosen in order to capture the response (Murray and Key, 2015). The signal processed results for operation at both nominal and high loading compressor conditions are provided in Figure 1.3-34 (Murray and Key, 2015).

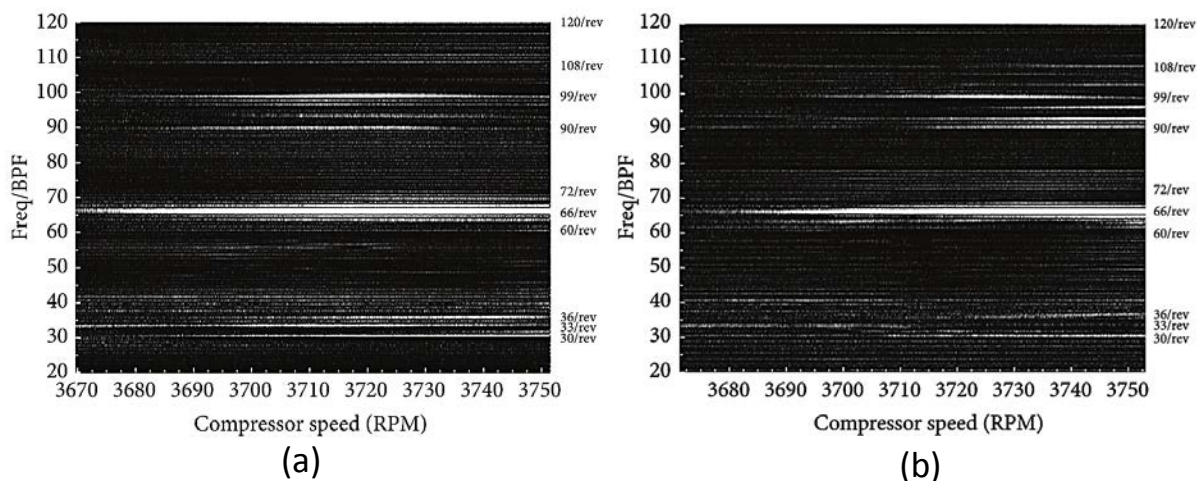


Figure 1.3-34 Waterfall plot of pressure spectra. (a) Nominal loading. (b) High loading. (Murray and Key, 2015)

It can be seen in the figures that blade response information has been successfully isolated for all three rotor rows (Murray and Key, 2015). It is noted that the first harmonic for rotor blade set R2, 33rd/rev response, is however near non-existent in both the high loading condition and nominal loading condition plots (Murray and Key, 2015). The 66th/rev and 99th/rev harmonics for rotor row R2

are however clearly visible (Murray and Key, 2015). It was indicated that the spectra obtained for the pressure measurements for rotor row R2 were in general congruent with the blade tip timing approach findings (Murray and Key, 2015).

It is important to note that the response behaviour of the upwind and downwind rotor rows were apparent in the waterfall plots. The 36th/rev and 30th/rev first harmonics, for blade rows R1 and R3 respectively, are clearly visible as well as many of their integer harmonics (Murray and Key, 2015).

A slice of the 99th/rev pressure spectrum's magnitude was provided and can be seen in Figure 1.3-35.

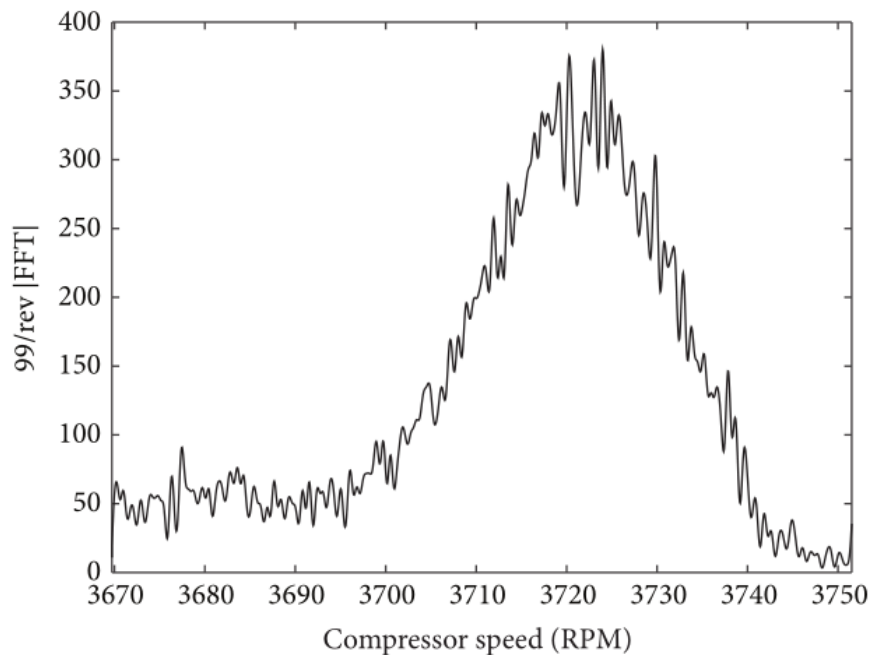


Figure 1.3-35 Magnitude of the 99th/rev pressure response (Murray and Key, 2015)

It can be seen that the pressure response rises as the resonance is approached and then declines once it has been passed (Murray and Key, 2015).

It was concluded that the spectral analysis with the signal processing methodology developed was able to identify the Doppler shifted blade response as blades pass through resonances (Murray and Key, 2015). This was performed using stationary stator vane mounted fast response pressure transducers (Murray and Key, 2015). The results were compared with simultaneously measured blade tip timing results and were found to be congruent (Murray and Key, 2015). Therefore a novel method for blade engine ordered vibration identification from downwind pressure measurements for an accelerating or decelerating rotor has been developed (Murray and Key, 2015).

1.3.5.3.4. Turbomachine Blade Vibration Identification from Casing BPF Measurements

Turbomachine casing vibration has been shown to contain blade vibration information (Forbes and Randall, 2013; Rao and Dutta, 2012). Frequency components which are related to blade vibration are known as blade passing frequencies (BPF). As has already been stated the BPF is the product of the number of blades in a given stage and the rotor operating frequency (Rao and Dutta, 2012).

In steam turbomachines the BPF is generated by flow off of the rotor blades which impinges upon the inner casing wall (Rao and Dutta, 2012). This causes excitation of the casing which can be measured externally by means of externally attached accelerometers (Forbes and Randall, 2013; Rao and Dutta, 2012). The ease with which the casing vibration can be monitored when compared to other non-intrusive methods is significant as no sealing arrangements or other casing alterations are required on the turbomachine (Rao and Dutta, 2012).

During the observation of BPFs on steam turbomachines it was noticed that changes in the BPF may be related to unexpected off resonance vibration of rotor blades (Rao and Dutta, 2012).

The casing vibration of a LP turbine in a 500 MWe thermal power plant was monitored in order to ascertain the condition of the blades (Rao and Dutta, 2012). The final three stages of the turbine under investigation had rotor rows with 48, 58 and 68 blades respectively (Rao and Dutta, 2012). The blades in these stages were free standing (Rao and Dutta, 2012). The turbine was operated at 3000 RPM (50 Hz) resulting in expected BPFs for the final three blade rows to be 2400 Hz, 2900 Hz and 3400 Hz respectively (Rao and Dutta, 2012).

When investigating the BPF for the stage with 48 blades it was noticed that in the region about the specific BPF of 2400 Hz sidebands appeared at 20 Hz intervals above and below the BPF (Rao and Dutta, 2012). It was stated that these sidebands occurring at 20 Hz intervals were completely unexpected as they have no integer valued (engine ordered) relation to the rotor speed (Rao and Dutta, 2012). Modulation at 50 Hz due to slight rotor imbalance is however normally expected in the spectrum (Rao and Dutta, 2012). The time-frequency plot of the casing vibration spectra with sidebands is shown in Figure 1.3-36 (a).

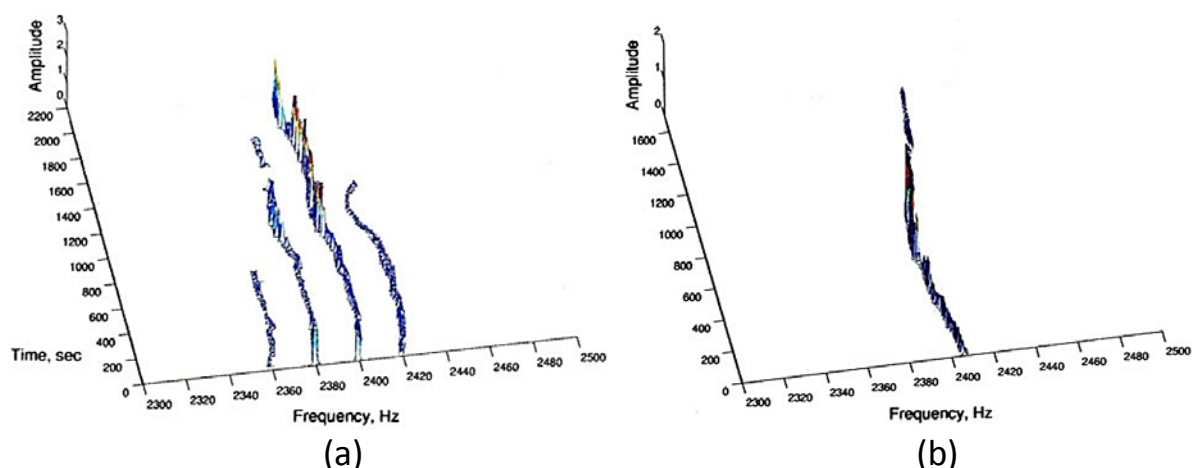


Figure 1.3-36 BPF trend for LP turbine. (a) Before damaged blade replacement. (b) After replacement of damaged blades. (Rao and Dutta, 2012)

During a maintenance outage the blades from the turbine were inspected for faults. Non-destructive testing lead to the identification of 14 blades with root cracks and 2 blades with cracks along the leading edge (Rao and Dutta, 2012). All of the flaws were significant as they could be identified visually

(Rao and Dutta, 2012). After maintenance and replacement of the damaged blades the casing vibration was monitored once again. The spectrum after maintenance can be seen in Figure 1.3-36 (b). It is clear from the figure that after the damaged blades were replaced the modulating sidebands at 20 Hz no longer appeared about the BPF (Rao and Dutta, 2012).

A premise to experimentally investigate the changes in the BPF in order to verify that it does indeed indicate changes in blade condition was thus found. A mock rotor setup consisting of a single bladed fan with three blades was constructed (Rao and Dutta, 2012). The fan was excited using a single air jet directed towards the blades (Rao and Dutta, 2012). A microphone was installed in line with the fan blades plane in the casing in order to obtain internal casing pressure readings (Rao and Dutta, 2012).

The system was operated at 11.75 Hz resulting in a BPF of 35.25 Hz (Rao and Dutta, 2012). The air jet was installed such that it could be vibrated sinusoidally at a chosen frequency (Rao and Dutta, 2012). Frequency spectra about the BPF obtained for the experimental setup are provided in Figure 1.3-37.

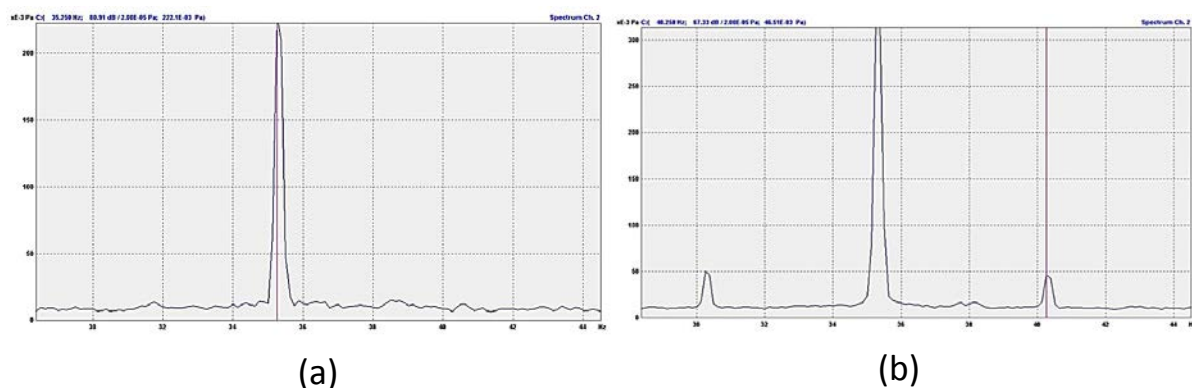


Figure 1.3-37 Experimentally obtained BPF trend. (a) Without Sidebands. (b) With sidebands. (Rao and Dutta, 2012)

Without air pulsation no sidebands about the BPF were detected. With air jet pulsation set at 5 Hz, sidebands about the BPF become immediately apparent at $BPF \pm 5$ Hz (Rao and Dutta, 2012). Modulation of the BPF by low frequency air excitation was therefore confirmed (Rao and Dutta, 2012).

It was then postulated that the 20 Hz sidebands, found in the casing vibration measurement of the 500 MWe steam turbine, was therefore directly related to the damaged blades' behaviour (Rao and Dutta, 2012).

The changes in the BPF were shown to be directly associated with changes in the blade's behaviour in an experimental setting (Rao and Dutta, 2012). A novel non-intrusive method to monitor off EO blade vibration was thus developed. Blade behaviour measurement is achieved by monitoring the BPF amplitudes and surrounding spectrum (Rao and Dutta, 2012).

If the BPF is monitored through the casing vibration no complex and expensive cabling or sealing arrangements are necessary making the method more desirable and reliable for implementation at power plants (Rao and Dutta, 2012).



1.3.6. Blade Effects and System Mode Response

In the prior sections turbomachine blades were discussed from a predominantly isolated point of view. Specifically blades were seen as individual entities attached to a rigid support which respond in isolated and discrete modes.

In practice turbomachine blades form part of an assembly system and do not respond in isolation of one another (Forbes, 2010, p. 17). They are coupled through attachment to the rotor shaft. This is generally achieved by an attachment hub with some or other attachment mechanism (such as fir tree root attachment) (Forbes, 2010, p. 17). Attachment of multiple blades to a rotor leads to physical coupling and associated response effects between the blades.

The effect of coupling is often disregarded due to a high ratio of individual blade mass to rotor hub mass, as well as a high stiffness of the attachment geometry itself; this situation is termed light coupling (Forbes, 2010). When the ratio between the blade and hub mass is large enough as well as the stiffness of the attachment rotor high enough, the blades' behaviour can be evaluated as uncoupled from one another (as was the assumption on most literature up until this point).

The geometric, material, wear and attachment condition variance between blades lead to mistuning of the system (Campobasso and Giles, 2000; Castanier and Pierre, 2006; Forbes, 2010; Kaszynski et al., 2013). When all of the blades' geometric, material and coupling properties are equivalent then the system is referred to as tuned. A perfectly tuned rotor is however an idealisation as minor random deviations in the blade and disk assembly always exist (Castanier and Pierre, 2006).

Mistuning can either increase or decrease the forced vibration response. An increase in forced response of one or more blades may lead to dangerous mechanical failures and so must be taken into account during the design phase (Campobasso and Giles, 2000; Castanier and Pierre, 2006).

Outside of the design phase blade mistuning must be considered when investigating an experimentally obtained system response as it may explain unexpected response behaviours.

Several definitions of mistuning have been proposed. The first is to define it as the difference between the nominal natural frequency of the bladed system with the natural frequency of an isolated blade responding free from the system (Forbes, 2010, p. 20). In this way the individual mistuning of a blade can be described. Another manner in which it is defined is as the percentage standard deviation of the change in blade natural frequencies experienced by isolated blades from the nominal natural frequency of all of the blades in the system (Forbes, 2010, p. 21). This provides a global characterisation of mistuning in a system (Forbes, 2010, p. 21).

For the case of a tuned lightly coupled system mode shapes are dominated by individual blade modes (where all of the blades respond simultaneously in the same mode) (Forbes, 2010, p. 17). There may however be a relative phase angle difference between the response of the individual blades given a particular mode (Forbes, 2010, p. 17; Mengle, 1990). The mistuned mode shapes are also dominated by individual blade modes, they however appear in a slightly more complex form (Forbes, 2010, p. 17).

This section presents findings from three separate studies into blade mistuning, coupling and their inter-relationship. The first study provides an introduction to mistuning and localised mode shapes from a lumped mass modelling perspective. This is done for both a lightly coupled and an uncoupled system (Forbes, 2010). The second study investigates the mistuning of an actual rotor geometry and

presents an analytically derived frequency domain indicator of mistuning (Kaszynski et al., 2013). The final investigation involves an depth review of mistuning, coupling, mode localisation, and expected excitation mode patterns (Castanier and Pierre, 2006).

1.3.6.1. Analytical Modelling of Blade Mistuning and Lumped Mass Model Mode Shapes

Due to geometric symmetry rotors are often modelled as cyclic symmetric systems. A single blade and attachment hub cross section can be modelled and a cyclic symmetry boundary condition applied to the relevant surfaces (Campobasso and Giles, 2000; Castanier and Pierre, 2006). The cyclic symmetry assumption allows drastic simplification of the physical model (Castanier and Pierre, 2006).

Mistuning causes the cyclic symmetry assumption of the turbomachine structure to no longer hold. In terms of full dynamic finite element (FE) modelling and analysis mistuning presents some unique problems to which interesting evaluation methodologies have been developed (Castanier and Pierre, 2006).

A convenient means to analytically investigate minor differences between blades and their attachment geometries is by representing the assembly as a simplified lumped mass parameter model (Carrington et al., 2001). Individual blades are attached to the shaft via an elastic spring and damper. Similarly adjacent blades are coupled to one another by means of springs and dampers. Consider the four blade lumped mass model illustrated in Figure 1.3-38.

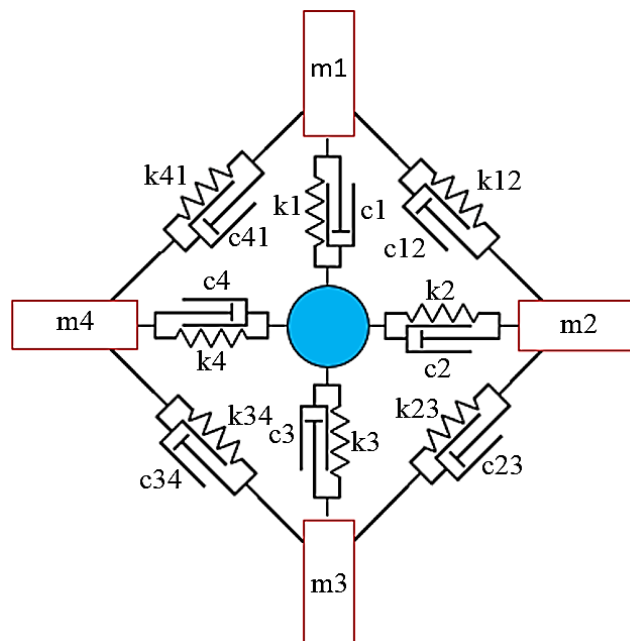


Figure 1.3-38 Lumped mass parameter model

The normalised governing equations of motion (EOM), derived for a general lumped mass rotor model as well as a discussion of the model, is provided in section '7.1.3 A3 – Analytical Blade and Assembly Models' subsection '7.1.3.2 Lumped Mass Model'. These equations were used to investigate the mode shapes of coupled and uncoupled tuned and mistuned systems consisting of 10 blades.

The normalised mode shapes of a perfectly tuned uncoupled system can be shown to be the identity matrix (Forbes, 2010, p. 26). This is because all of the masses respond regardless of one another. Due to their identical mass, stiffness and damping their response amplitudes are identical.

The tuned coupled situation is slightly more interesting. A lightly coupled system was achieved by keeping the ratio of the blade stiffness to the coupling stiffness, R , equivalent to 0.1 (Forbes, 2010, p. 29,32). The blade stiffness refers to the stiffness between the blade and the shaft, whereas the coupling stiffness refers to the inter-blade stiffness. The coupling ratio is provided in Equation [1.3.55] (Forbes, 2010, p. 29). A perfectly uncoupled system would have a coupling value of $R = 0$.

$$R = \frac{k_{coupling}}{k_{blade}} \quad [1.3.55]$$

The first four normalised mode shapes for a tuned coupled 10 bladed lumped mass model is given in Figure 1.3-39 (Forbes, 2010, p. 32).

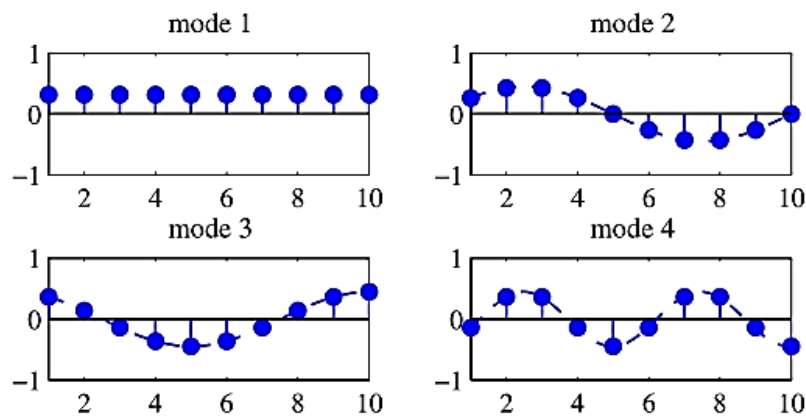


Figure 1.3-39 Mode shapes for tuned coupled system with $R = 0.1$. (Forbes, 2010, p. 32)

The masses of the tuned systems are seen to displace together in discernible patterns. The behaviour of one mass has an effect on an adjacent mass due to the coupling. It is reported that the spatial distribution of the mode shapes for the tuned coupled system are harmonic (Forbes, 2010, p. 30).

Mistuning was introduced into the above system by randomly altering the individual blades' mass and stiffness values such that their isolated fundamental frequencies were within 5% of the nominal fundamental frequency (Forbes, 2010, p. 27,33). The first four mode shapes of a mistuned uncoupled and a mistuned coupled system is given in Figure 1.3-40 (Forbes, 2010). The coupled system's coupling ratio was maintained at $R = 0.1$ (Forbes, 2010, p. 35). It is important to note that the unique mistuning of the coupled and uncoupled systems is not the same (mistuning was applied randomly to both systems) (Forbes, 2010).

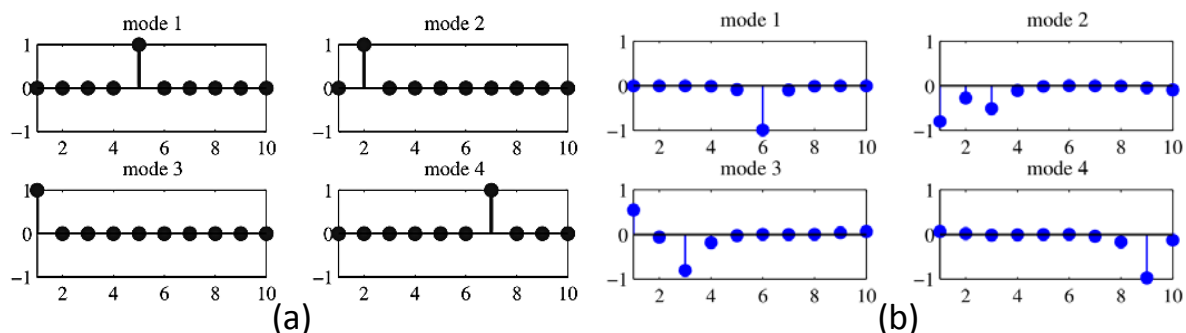


Figure 1.3-40 Mode shapes for mistuned lumped mass models. (a) Uncoupled system. (b) Coupled system with $R = 0.1$. (Forbes, 2010, p. 27,35)

The response of a mistuned system is significantly different to that of a tuned system. The masses of the fully uncoupled mistuned system are seen to operate in complete isolation of one another. The response of the coupled mistuned system is similar to that of the uncoupled system, however adjacent masses are inherently affected due to the physical coupling. The same effect was noted for the tuned coupled system where adjacent masses have an effect on one another.

It is reported that the response amplitude of the mistuned system is seen to increase significantly given the same excitation when compared to the tuned system. It is suggested that the difference arises due to the individual mass responding to the entire input excitation whereas in the tuned system the response is shared across all masses (Forbes, 2010).

1.3.6.2. Experimental Investigation into Integrally Bladed Rotor Mistuning

The effects of blade mistuning on an actual integrally bladed rotor (IBR) was investigated by Kaszynski et al. (Kaszynski et al., 2013). The investigation involved automated optical 3D geometry measurement, finite element modelling and analysis processes (Kaszynski et al., 2013).

The first process involved scanning the IBR geometry with an automated dual camera optical measurement system (Kaszynski et al., 2013). The accuracy of similar measurement systems was reported to be within $2.5 \mu\text{m}$ (Kaszynski et al., 2013). The optical measurement system provides a point cloud of the geometry's outer surface. This requires significant post processing to generate a computer aided design (CAD) object (Kaszynski et al., 2013).

In this particular investigation five separate optical scans were captured which provided five separate CAD geometries of the same IBR (Kaszynski et al., 2013). The optical technique and a low resolution point cloud obtained for a scan of the IBR is provided in Figure 1.3-41.

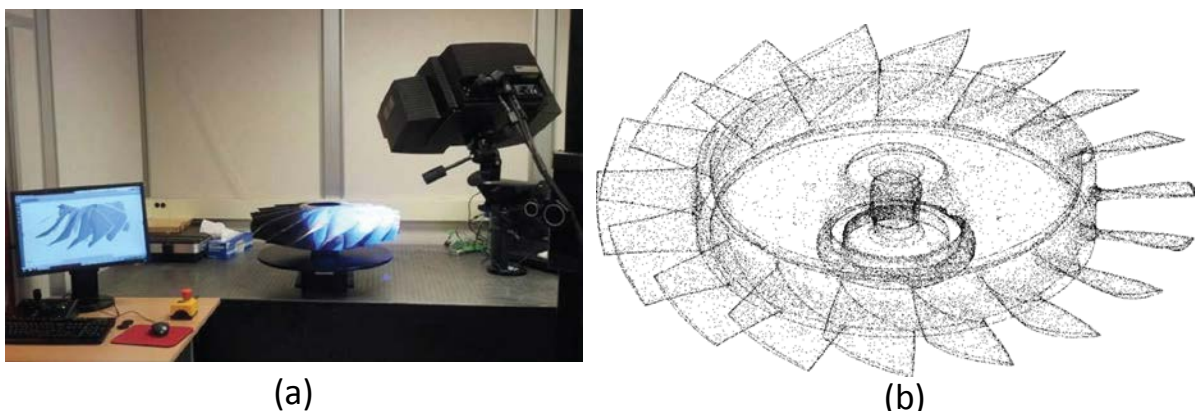


Figure 1.3-41 Integrally bladed rotor. (a) Optical measurement system. (b) Low resolution point cloud. (Kaszynski et al., 2013)

Once the CAD objects had been generated they were then aligned and meshed so that finite element (FE) analyses could be performed (Kaszynski et al., 2013). It is important to note that the meshing itself can artificially introduce geometric differences into the model (Kaszynski et al., 2013). These artificial differences may lead to mistuning which is not related to the actual geometric variances of the physical system (Kaszynski et al., 2013).

Once the meshing was complete a FE frequency analysis was performed on the various geometries. The nominal blade and hub geometry was determined by averaging across the aligned geometries to find the average IBR shape. Thereafter averaging was performed across all blade and hub cross

sections of the average IBR (Kaszynski et al., 2013). This was done in order to find the average blade and hub cross section geometry (Kaszynski et al., 2013). Finally, this average blade and hub cross section was used in a cyclic symmetric FE model to obtain the mean tuned system response (Kaszynski et al., 2013).

The frequency response, in the region of the first bending and first torsional mode of the system, is presented in Figure 1.3-42. The frequency response obtained from all five scans; their average response and the cyclic symmetric tuned system's response are plotted together.

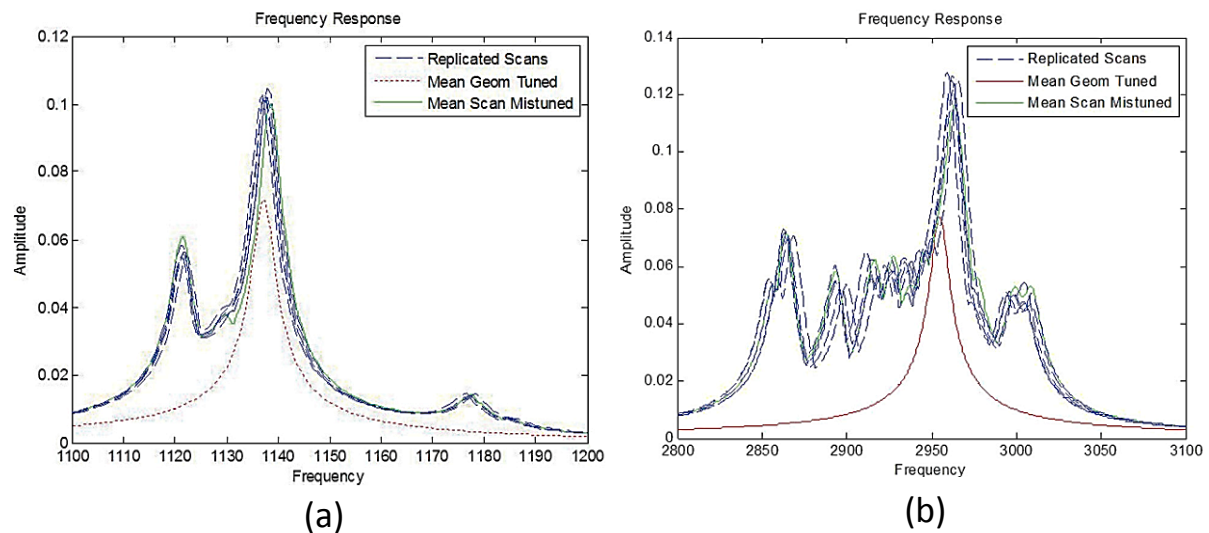


Figure 1.3-42 Blade mistuning of IBR. (a) First Bending Mode. (b) First torsional mode. (Kaszynski et al., 2013)

It can be seen that multiple mistuned peaks appear near to the mean tuned peak response. There is also a slight shifting of the peak locations with respect to the mean tuned peak frequency location (Kaszynski et al., 2013).

Multiple closely packed peaks near the mean tuned peak are expected as each blade geometry will differ only slightly from the norm of the system. The response amplitude of the mistuned system is also seen to increase significantly (Kaszynski et al., 2013).

It is interesting to note that around the frequency response of the first bending mode two additional resonance peaks appear somewhat removed from the mean tuned peak, one large peak to the left of the mean tuned peak and a smaller one further to the right. Thus additional modes and mode shapes may appear due to even slight mistuning.

The level of coupling between the blades was not mentioned in this investigation although the individual blade to hub mass ratio is assumed to be large. The entire IBR geometry is comprised of the same material. These observations may indicate that the system investigated is indeed lightly coupled.

The investigation provided insight into the appearance of a slightly mistuned system in the frequency domain. Mistuning affects the resonant response amplitude and its associated position on the frequency axis. It also appears to bring about additional modes and mode shapes not present in a perfectly tuned system.

1.3.6.3. Survey of Mistuned Bladed Disk Vibration and System Response Modes

The cyclic symmetric geometry of a bladed rotor introduces interesting system response mode shapes and blade effects. The individual blade modes, sometimes referred to as cantilevered blade modes, were important to investigate as they relate closely to the individual blade motion in the larger blade-dominated system mode shapes (Castanier and Pierre, 2006). This is also true for the situation of forced vibration response (Castanier and Pierre, 2006). Disk-dominated mode shapes refer to modes where the motion is mostly governed by the response of the attachment geometry as opposed to the blades (Castanier and Pierre, 2006).

In FE investigations of cyclic symmetric structures it is commonplace to subdivide the geometry into the smallest geometric component, or sector, that can be used to reconstruct the full geometry (Castanier and Pierre, 2006). For a bladed disk the smallest sector comprises of a single blade and the associated segment of the attachment rotor (referred to as the disk) (Castanier and Pierre, 2006). For the ideal case of identical sectors the cyclic symmetric boundary conditions can be applied to the individual sector, thus facilitating a less expensive model to solve (Castanier and Pierre, 2006).

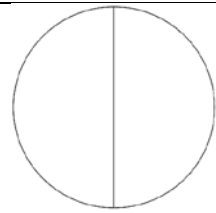
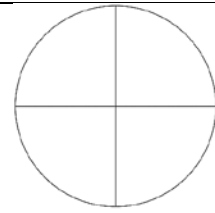
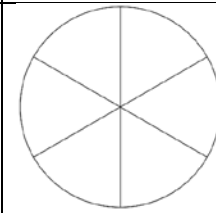
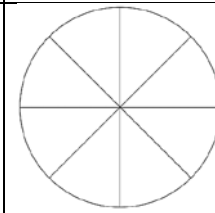
An interesting characteristic of cyclically symmetric systems is that their response mode shapes are identical in each individual sector, except for a constant phase difference between sectors (Castanier and Pierre, 2006). Here, a sector refers to a section of the cyclic geometry responding at the same phase angle. This constant phase angle difference is known as the inter-blade phase angle for rotors (Castanier and Pierre, 2006). The interblade phase angle ϕ_h for a system with N blades and responding with h nodal diameters is provided in Equation [1.3.56] (Castanier and Pierre, 2006).

$$\phi_h = \frac{h \cdot 2 \cdot \pi}{N} \quad [1.3.56]$$

The inter-blade phase angle difference for a tuned system was referred to in the work by Mengle and the relation derived found to be equivalent (where the travelling wave mode number is equivalent to the number of system nodal diameters; this is referred to as the harmonic index) (Mengle, 1990).

In terms of system mode shapes, this inter-blade phase angle causes nodal lines to form across the geometry (Castanier and Pierre, 2006). The number of nodal lines that form, termed nodal diameters, gives the system mode shapes (Castanier and Pierre, 2006). Nodal diameters and associated system mode shapes for cyclically symmetric systems are illustrated in Table 1.3-5.

Table 1.3-5 Nodal diameters and associated system mode shapes

Nodal diameters:	1	2	3	4
System mode shapes:				

The ideal cyclically symmetric case cannot however be found in practice due to reasons previously discussed. This leads to the situation previously referred to as mistuning. When the cyclic symmetry of a system breaks down, or in other words small random differences in the structure manifest themselves, they can have a significant impact on the dynamic response of the system as a whole (Castanier and Pierre, 2006).

For one, pure nodal diameter modes no longer exist for a mistuned system. Instead the mode shape is characterised by multiple harmonic content which can be excited by all EOs (Castanier and Pierre, 2006). As discussed in the development of Model 1, mistuning means that the blade flutter response is excited at all engine harmonics causing Doppler shifting at all engine harmonics (Mengle, 1990). Another phenomenon that occurs due to mistuning is known as mode localisation; these effects will be discussed shortly (Castanier and Pierre, 2006).

Mistuning is often introduced into analytical models by making small changes to the stiffness coefficients associated with individual blades (Castanier and Pierre, 2006). This was the case in terms of the lumped mass model investigated by Forbes where small random adjustments were introduced into the numerical model (Forbes, 2010).

A FE model of an integrally bladed rotor was constructed to investigate the effects of mistuning and coupling effects (Castanier and Pierre, 2006). The geometry was based upon an industrial gas turbine rotor with 29 blades (Castanier and Pierre, 2006). The results for a tuned system's dynamic response and a mistuned system's dynamic response is provided in Figure 1.3-43.

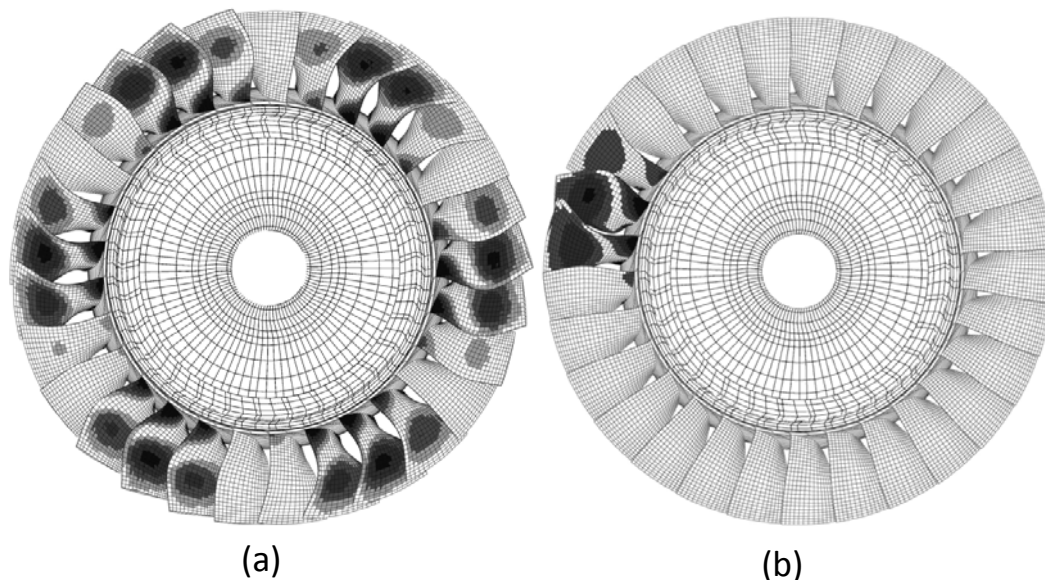


Figure 1.3-43 FE Model of an industrial bladed disk. (a) Tuned. (b) Mistuned. (Castanier and Pierre, 2006)

The particular mode shape displayed for the tuned system, Figure 1.3-43 (a), consist of three nodal diameters (Castanier and Pierre, 2006). It is stated that for engine ordered response of a rotor due to excitation from disturbances in the flow field (upstream stator wake interaction) a travelling wave mode is generated (Castanier and Pierre, 2006). This is the same travelling wave mode referred to by Mengle (Mengle, 1990). The equation for the observed travelling wave mode number, given here as an absolute value, is provided in Equation [1.3.58].

$$k' = |k + m \cdot B| \quad [1.3.57]$$

Therefore the engine orders which would excite this 3 nodal diameter mode shape would be 3 ($m = 0$), 26 ($m = -1$), 32 ($m = 1$) and so on (Castanier and Pierre, 2006). Thus for engine ordered response the system mode shape must be excited at an EO equivalent to the harmonic index of the particular system mode shape (Castanier and Pierre, 2006). Given the excitation conditions the expected system mode shapes can be obtained.



When evaluating the mistuned system's response, Figure 1.3-43 (b), it is clear that pure modal diameters no longer exist and the mode shape is confined to a small region on the geometry (mode localisation) (Castanier and Pierre, 2006).

Perfectly cyclic symmetric structures form part of a larger group of structures known as periodic structures (Castanier and Pierre, 2006). Periodic structures are made up of a set of identical substructures that are connected to one another by some or other dynamic relation (Castanier and Pierre, 2006). That dynamic relation between individual subsystems is known as coupling (Castanier and Pierre, 2006).

If ever differences between the individual substructures exist, even when the differences are particularly small, the dynamic response of the system as a whole can change significantly (Castanier and Pierre, 2006). These differences in the substructure are called disorder (Castanier and Pierre, 2006). In terms of bladed disk structures disorder is the same as mistuning and coupling refers to structural and aerodynamic coupling between adjacent blades (Castanier and Pierre, 2006).

Bladed disks are a unique case of periodic structures for a couple of reasons (Castanier and Pierre, 2006). Firstly, each near identical substructure receives engine ordered excitation (Castanier and Pierre, 2006). And secondly the systems are cyclic (Castanier and Pierre, 2006). Thus, it has already been shown that had the system been perfectly tuned the only response modes to be excited would be where the EO matches the harmonic index of the mode (Castanier and Pierre, 2006).

However for a mistuned system, engine ordered excitation would result in multiple mode excitation (Castanier and Pierre, 2006). The particular modes that will be excited most intensely will have harmonic content which is equivalent to the engine order of excitation (Castanier and Pierre, 2006).

One particularly destructive facet of disorder is the mode localisation phenomenon alluded to earlier (Castanier and Pierre, 2006). Mode localisation is the phenomenon whereby the dynamic response of an entire system becomes restricted to a small region of that system (Castanier and Pierre, 2006).

Mode localisation was observed in the lumped mass model investigation by Forbes where for an uncoupled and lightly coupled system the dynamic response become confined to an individual mass or region surrounding an individual mass (Forbes, 2010). It was found that as disorder increases, or coupling decreases, the mode localisation phenomenon increases (both of these driving influences were noted in the lumped mass study by Forbes) (Castanier and Pierre, 2006; Forbes, 2010).

Mode localisation leads to a forced response increase. This is due to the confinement of the energy entering the system to a small region (Castanier and Pierre, 2006). In the FE study of the gas turbine bladed rotor it was found that with some EO responses the magnitude of the mistuned system's response was up to one and a half times bigger than that for the tuned system (Castanier and Pierre, 2006). This value is in terms of the maximum response amplitude found over the frequency range of interest (Castanier and Pierre, 2006). This increase in response magnitude, with respect to the perfectly tuned system, is therefore significant (Castanier and Pierre, 2006).

There is however a point at which an increase in random mistuning across the entire system results in a decreasing amplification of the maximum response (Castanier and Pierre, 2006). This point was found to be at approximately a standard deviation of random mistuning of 0.01 for the rotor geometry investigated (using the global mistuning estimation parameter) (Castanier and Pierre, 2006).



1.3.7. Tachometer Geometry Compensation and Shaft Torsional Vibration Estimation

Accurate measurement of angular velocity and displacement of rotating equipment is important from an analysis and diagnostics point of view (Resor et al., 2005). Applications such as torsional vibration estimation and non-vibrating blade tip passing time estimation rely on tachometer signals originating from geometrically uniform multiple pulse per revolution (PPR) encoders (Resor et al., 2005). Geometrical uniformity refers to equal pulse width originating from a number of equally spaced (in terms of angle) references about the circumference of the rotating object (assuming measurement at a constant angular velocity). The tachometer signal can be used to estimate the shaft position, velocity and angular vibration over the measurement period.

In terms of the pressure based methods, accurate shaft position and velocity measurements are used in the order tracking and synchronous averaging signal processing techniques to deliver the deterministic and stochastic pressure signals (Forbes and Randall, 2013). These techniques assume that the tachometer signal originates from a geometrically symmetric reference.

Encoder based systems operate by means of a device, or reference object, attached to the rotating body from which geometrically uniform passing times can be sampled (Resor et al., 2005). Angular encoding devices and reference objects include keyways, splines, gear-teeth, optical rotary encoders and zebra-tape based systems (Resor et al., 2005).

Transducers, such as eddy current proximity probes and fibre-optic reflective light intensity sensors, are capable of supplying multiple PPR signals from mechanical attachments such as gears, keyways and splines. Fibre-optic reflective light intensity sensors are suited to adhesive zebra-tape applications. Optical rotary encoders use a grating disk based system through which light is passed; a light sensor then detects a multiple PPR signal for each grating through which the light passes (Resor et al., 2005).

The transducers supply a voltage change corresponding to the passing encoding reference; for example the transducer may supply a high or low voltage depending on the proximity of gear teeth (as is the case of an eddy current proximity sensor) or a high and low voltage corresponding to reflection or no reflection from the black and white segments of a zebra-tape (Resor et al., 2005).

The most desirable encoder system is the high precision optical encoder; manufacturing processes are capable of delivering high density grating segments which are practically geometrically identical (Resor et al., 2005). Optical encoders are also capable of supplying direction of rotation. Although favoured, it may not be possible or feasible to implement optical encoder systems. Such cases include the retrofitting of equipment and/or when shaft access or size may be an issue (Resor et al., 2005).

In such cases pre-existing rotating references may be used (such as gear teeth or splines) to generate the tachometer signal. Significant geometric variation is however inherent in such signals due to manufacturing, installation and measurement transducer positioning. An example of which is gear tooth spacing variation as well as surface finish variation (Resor et al., 2005). Rotating references are also limited to a set number of PPR (i.e. number of features (gear teeth) are equal to PPR) which may not supply the desired measurement angular resolution.

An appealing alternative to pre-existing rotating references is the striped zebra-tape method. An adhesive tape, with a printed striped zebra pattern, is applied to an open section of the rotating shaft. It is preferred due to its simplicity and control over the tape pattern (Resor et al., 2005). Although

preferred to pre-existing rotating references, zebra-tape has a much higher geometric variation between segments when compared to high precision optical encoder devices (Resor et al., 2005).

Variation in the zebra tape is attributed to uneven printing and errors resulting from installation (Resor et al., 2005). During installation the zebra tape may become slightly misoriented with the shaft leading to a situation where stripes are not exactly parallel with the axis of rotation. Furthermore the ends of the zebra tape may not match perfectly leading to either slightly wider or shorter segment at the butt joint (Janssens et al., 2010; Resor et al., 2005).

Variation of the encoder geometry and fluctuations in the angular velocity of the rotating system leads to non-uniform time interval sampling of the encoder signal (Resor et al., 2005). An example of a uniform and non-uniform zebra tape is presented in Figure 1.3-44. The non-uniform example shows exaggerated effects of misprinting every fifth blade stripe as well as an enlarged butt joint.

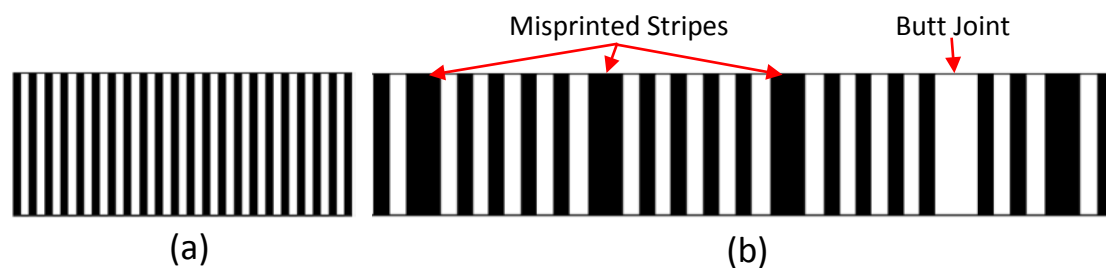


Figure 1.3-44 Zebra tape examples. (a) Geometrically uniform. (b) Zebra tape with exaggerated errors. (Resor et al., 2005)

Non-uniform time sampling leads to potentially significant errors and unwanted bias when used in conjunction with uniform time interval algorithms such as the discrete Fourier transform, shaft torsional vibration estimation, synchronous averaging or order tracking (Resor et al., 2005).

The impact of encoder geometry variation on shaft torsional vibration is highlighted. Consider Figure 1.3-45 which contains a reference signal and an encoder signal from a torsionally excited shaft.

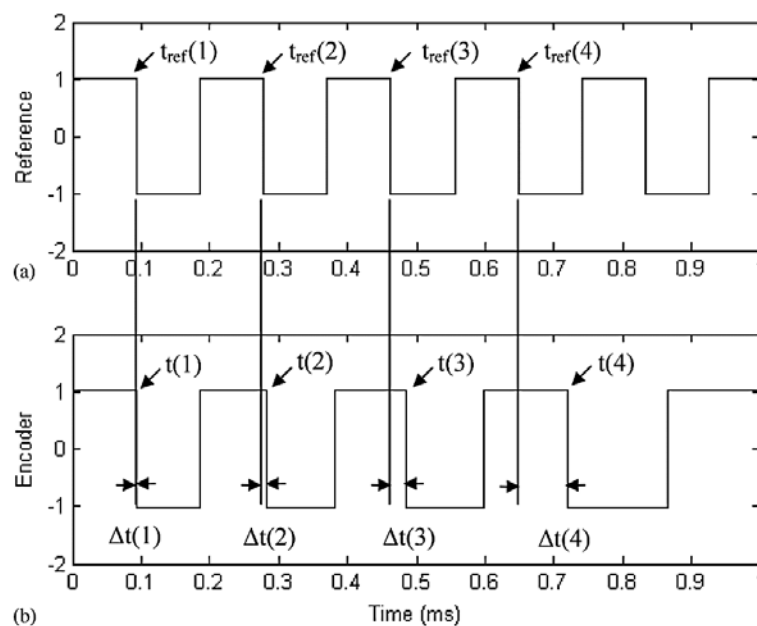


Figure 1.3-45 Method to obtain shaft torsional vibration from reference signal. (a) Reference signal. (b) Encoder signal. (Resor et al., 2005)



Passing times are captured corresponding to negative slope zero crossings (the times at which the encoder signal drops from a 'high' to a 'low' voltage). Assuming that the encoder geometry (zebra tape/optical encoder grating/gear teeth) on the rotating system is uniform, a reference vector containing zero crossing times for a non-vibrating system can be computed (Resor et al., 2005). The variables 'N' and ' f_{shaft} ' in Equation [1.3.58] refer to the number of PPR (corresponding to the number of geometric reference features) and the shaft speed in hertz respectively.

$$t_{ref}(n) = \frac{n}{N \cdot f_{shaft}} \text{ (s)} \quad [1.3.58]$$

The true zero crossing times less the reference zero crossing times can then be computed. The time difference vector is then used to compute an angular vibration array, $\theta(n)$, corresponding angular displacements at the true zero crossing times (Resor et al., 2005).

$$\Delta t(n) = t_{encoder}(n) - t_{ref}(n) \text{ (s)} \quad [1.3.59]$$

$$\theta(n) = \Delta t(n) \cdot f_{shaft} \cdot 360 \text{ (deg)} \quad [1.3.60]$$

Or: $\theta(n) = \Delta t(n) \cdot f_{shaft} \cdot 2 \cdot \pi \text{ (rad)}$

Assuming that the torsional vibration time interval is much smaller than the time interval associated with rotation of the shaft it is possible to compute a constant sampling time interval value (related to the angular displacement intervals) (Resor et al., 2005).

$$\Delta t_{sample} = f_{shaft} \cdot N \quad [1.3.61]$$

Finally by combining the constant time interval with the angular variation array the angular vibration as a function of time can be determined (Resor et al., 2005).

$$\theta(t(n)) = \theta(n) \quad [1.3.62]$$

$$t(n) = \Delta t_{sample} \cdot n \quad [1.3.63]$$

Resor et al. noted potential issues with the above model. Firstly the reference signal assumes a perfectly uniform encoder geometry and constant rotational speed (Resor et al., 2005). Neither assumption holds in practice which leads to non-uniform sampling times (Resor et al., 2005).

Sources of geometric asymmetries have already been noted: non-constant shaft speed arises from fluctuations in the operation of the drive motor as well as by torsional oscillations in the shaft resulting in non-uniform time and angular sampling intervals (Resor et al., 2005).

The model also assumes an infinitesimal time interval from which exact zero passing times are extracted (Resor et al., 2005). The accuracy of capturing the zero passing times is related to the sampling rate, zero passing threshold and the transducer's performance across the entire geometric surface, none of which are perfect (Resor et al., 2005). Finally non-torsional vibration (lateral vibration of the shaft) may also contaminate the zero crossing times measurement (Resor et al., 2005). An algorithm capable of compensating for encoder geometry variation for operation at a nominally constant shaft speed was thus sought.



Various solution routes were suggested. One suggestion involves recording the response of the system at a constant speed without torsional excitation in order to determine noise, this can then be removed from the signal at a later stage (Resor et al., 2005; Vance, 1988). A second author suggested that identification and correction for the errors is possible due to their unchanging nature, no method was however provided (Resor et al., 2005; Williams, 1996).

A method was suggested to determine the geometric ratio for each segment of the passing reference geometry (such as the segment sizes of a zebra tape) during operation at a constant speed without torsional vibration for a single revolution. This is then used to generate a calibration file for later use (Resor et al., 2005; Wang et al., 1992). Methods of this nature are however not suited to systems where a near perfectly constant running speed is not possible, nor where shaft torsional vibration is unavoidable (due to rotating masses or loads) (Resor et al., 2005). Even with a calibration file if the system is changed significantly by adding loads then the calibration file may no longer be valid.

A robust in situ calibration technique, based on synchronous averaging of the zero crossing times, was developed (Resor et al., 2005). Synchronous averaging of the tachometer signal over many revolutions is used to provide the average segment geometric ratios for an individual revolution of the shaft. This alleviates the issue of minor rotational speed fluctuations during data capture; this relaxes the requirement for a near constant shaft speed to a nominally constant shaft speed scenario.

A corrected time difference vector is then computed using the averaged shaft segment ratios. This corrected time difference vector can then be used to correct the tachometer signal or compute the shaft torsional vibration directly (Resor et al., 2005).

$$\theta(n) = \Delta t_{corrected}(n) \cdot f_{shaft} \cdot 360 \text{ (deg)} \quad [1.3.64]$$

$$t_{encoder \text{ corrected}}(n) = t_{encoder} - \Delta t_{corrected} \quad [1.3.65]$$

The geometric compensation algorithm developed by Resor et al. is presented in ‘7.1.4 A4 – Shaft Encoder Geometry Compensation Algorithm’.

More recently an algorithm was developed to detect and correct for zebra tape butt joints (Janssens et al., 2010). A function was developed to determine the angular error associated with an imperfect butt joint across an individual revolution and then correct the tachometer signal by using a spline interpolation method coupled with a finite impulse response bandpass filter (Janssens et al., 2010). The method was reported to perform well for both steady state and run-up measurements (Janssens et al., 2010). The method is however restricted solely to correcting the error associated with a single butt joint and is thus not appropriate when multiple error sources are present.

The consequences of not correcting for a geometrically non-uniform encoder/zebra tape have been highlighted. An in situ tachometer compensation technique for measurements taken at a nominally constant shaft speed has been suggested as well as an improved means for obtaining shaft torsional vibration from a non-uniform tachometer source. A robust method capable of correcting stationary geometry variations from a reference geometry, originating from multiple sources, in situ for non-steady state operation is still however desired.



1.4. Scope of Research

The purpose of this study is to investigate internal pressure signal modelling and solution route techniques for the purpose of turbomachine blade behaviour identification. This study is done with relation to other current and applicable non-intrusive blade vibration measurement methodologies.

Intrusive is defined as a method which requires direct blade and/or rotor shaft alteration in the vicinity of the rotor cascade. Alteration of the casing in order to facilitate measurements is not considered as intrusive. Various assumptions and theoretical and physical limitations apply to the investigation.

Focus is placed on pressure and direct blade behaviour measurements taken at a nominally constant rotor speeds. This is done in order to approximate steady state operating conditions. Run-up tests may be used to determine critical resonance speeds by means of strain gauges attached to the surface of blades, they may however also be used for additional analyses.

Of the casing pressure signal literature reviewed, obtaining blade vibration characteristics from nominally constant rotor operation has been experimentally attempted by Forbes et al. and by a reference in the work of Mengle (Forbes and Randall, 2013; Mengle, 1990). Mathioudakis investigated minor blade faults, not specifically vibration, at nominally constant speeds (Mathioudakis et al., 1991). Ratz et al. used run-down tests (Ratz et al., 2013). The work by Rao and Dutta as well as Murray and Key used run-up tests (Murray and Key, 2015; Rao and Dutta, 2012). Obtaining blade vibration characteristics at a nominally constant shaft speed is specifically advantageous from a condition monitoring point of view as the majority of turbomachine operation is at nominally constant speeds.

Derivations and investigations are confined to axial flow turbomachines, the effects of nearby rotor rows or additional downwind stator rows on the pressure signal are not considered. Pressure measurements are confined to the plane in which the rotor operates, therefore blade vibration measurement up- and/or downwind of the rotor is not included in the investigation. Only a single isolated rotor cascade is considered with one set of upwind stators. Blades passing through upstream stator wakes is considered as the primary forced excitation source. Fluid-structure interaction studies, whether by FE and CFD coupling or from basis analytical equations, are outside the scope of research.

Amendments to the internal pressure models suggested by Mengle, Forbes et al. and Ratz et al. are proposed using insight obtained from all of the investigations reviewed in literature (Forbes and Randall, 2013; Mengle, 1990; Ratz et al., 2013). The applicability of these reformulated models and their constituent components are investigated using numerical and experimental investigations.

An available test bench was modified in order to facilitate direct internal casing pressure measurements by means of an acoustic pressure transducer. Casing vibration measurements obtained on the outer casing surface, used to infer blade vibration characteristics, are not investigated.

Testing is restricted to the current operational limits of the experimental setup (with a maximum rotational speed of 1470 RPM). Excitation was created by means of the available upwind air jets approximating upwind stator vanes. The existing experimental test bench has a total of 24 available air nozzles with which to create the excitation. However only a limited number of these could be operated simultaneously due to the available pressure source. The number of air nozzles used as well as their usage configuration are considered.



A rotor blade and hub assembly was designed and manufactured to operate with the available test bench. The hub design allowed multiple blade stagger angles. Investigations were however limited to a single blade stagger angle. Consideration of fundamental frequency excitation was included in the blade design. Replacement of individual blades on the hub is possible.

Alternative excitation configurations were achieved by choosing the number of active air jets and their configurations. Multiple rotor and hub configurations were explored by means of altering one or more of the blades' geometries on the rotor assembly. Alteration of a blade's geometry was limited to a region sufficiently removed from its tip. This was done in order to maintain similarity between the tip and casing conditions regardless of the root condition of the blade.

This is in contrast to the work done by Mathioudakis et al. which specifically altered the surface condition and blade angle which effectively changed the physical conditions at the blade tip (Mathioudakis et al., 1991). Similarly, in the work by Forbes et al. and Ratz et al. a 'damaged' blade of reduced thickness was used, this directly altered the blade tip conditions and associated pressure signature about the tip (Forbes and Randall, 2013; Ratz et al., 2013). None of the literature reviewed specifically considered blade alteration at a location sufficiently removed from the casing wall.

One blade in one experimental configuration was fully instrumented by means of strain gauges in order to determine a blade's actual response during steady operation.

All the casing pressure based literature reviewed only considered single degree of freedom (SDOF) blade models. In terms of Model 1 a SDOF sinusoid was considered and in terms of Model 2 a single spring-mass-damper system was considered. A SDOF model may be sufficient to describe the blade vibration effect on the internal pressure signal, it is however limited to a single resonant frequency. A MDOF model, based upon experimental modal analysis FRF reconstruction techniques, is used here in a novel way to generate the blade forced response model for inclusion in the internal pressure signal models. Use of this model is evaluated using strain gauge measurements.

The measurement techniques described, in the pressure based models and investigations, do not make much provision for individual blade behaviour identification and isolation. In contrast the BTT approach is capable of monitoring the condition of individual blades. It becomes increasingly difficult to isolate the pressure waves associated with individual blade behaviour when measuring the casing vibration (as it provides the cumulative response of all of the blades), or when measuring at an axial location removed from the rotor row of interest (due to the mixing of flow off of blades). An investigation into the advantages of measuring the pressure signal in the rotor plane and the use of novel windowing techniques to isolate individual pressure waves about blades are investigated.

The reformulated internal pressure models, for in plane steady state pressure measurement, are expressed as inverse problems in order to obtain blade vibration characteristics. Such an inverse problem approach to blade vibration identification from pressure and SG signals was not found in literature and is considered novel. An optimisation strategy is suggested. It is evaluated for the resolution of reduced inverse problems. Analyses are performed in order to determine the viability of using such an approach to obtain blade vibration information from experimentally obtained signals.

An improved means to model blade vibration in an internal pressure signal, in order to infer blade vibration characteristics, is the primary deliverable of this investigation.



1.5. Document Overview

The literature reviewed provides an in depth investigation into many aspects related to a turbomachine's internal pressure signal and the associated blade vibration within. Due to the volume of literature considered, integral and supplementary topics were separated from one another at the beginning of the section. This was done in order to direct the reader towards the crucial themes whilst still providing a wide synopsis of relevant topics. The following document overview sketches the same picture by directing the reader towards the primary topics under investigation whilst highlighting which topics may be considered as supplementary.

Theoretical development of the pressure signal method is explored in Chapter 2. The chapter begins by critically discussing relevant aspects of the literature reviewed. This is followed by the development of alternative pressure signal models and an associated multiple degree of freedom blade vibration model. A signal processing based method for the purpose of separating individual pressure waves associated with the behaviour of individual blades is presented. Finally the chapter suggests an optimisation based method for the identification of blade physical characteristics. This is done by presenting the internal pressure signal and associated models in an inverse problem format. The essential topics within this section are the blade vibration and internal pressure signal models developed. Only the blade vibration model components of the full inverse problem are solved for using the inverse methodology (reduced inverse problems referred to earlier).

Chapter 3 outlines the experimental setup and instrumentation used in experimental investigations. The system's frequency response is characterised both numerically and experimentally. One of the goals of the characterisation is to determine the mistuning in the system, both from the global assembly perspective as well as each individual blade's relative mistuning. Run-up tests are used to determine the critical operating speeds at which blades resonate in their fundamental modes. These critical speeds are briefly compared with selected analytically obtained critical speeds. Chapter 3 is not crucial to understanding the topics at hand, it does however provide a roadmap for experimental repeatability.

Investigations into the experimentally obtained signals is the topic of Chapter 4. The chapter begins by comparing the blade vibration models, developed in Chapter 2, with direct on blade response measurements obtained from strain gauges. There-after the internal pressure signal is explored. The results and discussion of results are both included in this section.

Conclusions drawn and suggestions for future research opportunities are presented in Chapter 5. The future research section inherently provides a scope conformity check and ensures that the scope and work performed is in alignment.

Chapters 6 and 7 provide the research references and appendix respectively. The appendix constitutes a large percentage of the document as a whole (approximately a third). It contains all non-integral derivations, additional literature, photographs of the experimental setup and additional results from the various investigations. Many aspects required in order to repeat this investigation are provided in this section, it is therefore mostly supplementary to the document and can be seen in a supportive yet non-integral role.

Chapter 2 Theoretical Development

2.1. Introduction to Theoretical Development

Obtaining turbomachine blade vibration indicators from an internal pressure signal, measured by a stationary observer on the inner casing wall, presents various challenges. Challenges include how to accurately describe the internal pressure phenomena, how to depict the blades' forced response, how to separate out the pressure signal contributions stemming from individual blades and finally a means to synthesize this information into a format which may allow extraction of blade vibration information.

Many aspects of the internal pressure signal, which contains blade vibration, were addressed in the literature review. The first section of the theoretical development will compare the various models, in light of all of the information gathered. These models include both the internal pressure signal models as well as the physical blade forced response models. The literature discussion provides a platform for the development of adjusted internal pressure and blade vibration models.

In light of all of the literature discussion two adjusted internal pressure models are developed in the next section. These two models originate from the two separate models introduced in the literature review, namely Model 1 and Model 2. The development explores what similarities and differences are expected to be seen in the frequency domain given the two models and their adjustments.

The following section advances the blade forced response model provided by Forbes et al. (Forbes and Randall, 2013). Instead of basing the blade response transfer function on a SDOF spring-mass-damper system, an alternative MDOF transfer function based on experimental modal analysis frequency response function (FRF) reconstruction techniques is suggested (repurposing of a pre-existing technique). Further, a means to model the upwind stator forcing function is developed.

It is believed that the pressure distribution which occurs about individual blades may contain information about the behaviour of those individual blades. The question has to be asked how to separate the individual waves. The development of a separation methodology based on windowing techniques follows the section on blade forced response. The separation technique will be used to isolate individual waves about blades from experimental measurements. Signal processing techniques discussed in literature will then be applied to the separated signals to identify whether or not they are able to identify unique information about the individual blades behaviour.

The final section in the chapter presents the synthesized ideas of the previous sections in an inverse problem format. The inverse problem is designed to compare the combined internal pressure models and the blade forced response model with actual blade vibration containing pressure signals. It is suggested blade vibration models first be compared to actual on blade vibration measurements using a reduced version of the inverse problem format. Depending on the internal pressure model included in the problem statement, separation of the pressure waves about individual blades using the above mentioned windowing technique becomes important. It is proposed that the inverse problem be solved using standard optimisation techniques which minimise the error between the measured signal and the analytically generated signal by changing the internal pressure model parameters.

The ability to resolve the casual factors of the observed internal pressure signal, specifically those attributed to blade vibration, provides an indication as to the usefulness of pressure based methods for the purpose of blade vibration information extraction. This is in terms of both signal processing and direct data analysis thereof, as well as for the inverse problem formulation.

2.2. Literature Discussion

Many aspects of turbomachine blade vibration, from an internal pressure measurement perspective, we addressed in the literature review. The inter-play of these ideas and their consequences are explored in this section.

2.2.1. Comparison of Casing Pressure Signal Models

In Chapter 1 two internal pressure models were introduced. Model 1 was based upon the work of Mengle and Model 2 on the work of Forbes et al. (Forbes and Randall, 2013; Mengle, 1990). It is not clear in the development of Model 2 if the authors were aware of Model 1. A contribution of this work is to compare their relative behaviour and discuss the models' applicability.

In principle Model 1 is based upon the propagation of travelling waves originating from vibrating turbomachine blades and what is expected to be observed down- or up-wind of the source of vibration. This was done specifically for internal pressure observation from a stationary point on the casing. Due to the fact the vibration source is moving with relation to the observation point, Model 1 investigates how this will cause Doppler shifting of the observed blade vibration frequency components in the pressure signature.

Model 2 relies on the effect that blade vibration has on the otherwise stationary pressure distribution which forms about the blades during steady state observation (stationary from the rotor reference frame perspective). It was proposed that as the blades vibrate they cause the internal pressure distribution, which forms about the blades, to arrive either earlier or later when compared to a non-vibrating blade situation. It is suggested that this phenomenon causes phase modulation of the otherwise stationary pressure signal.

Both models use a Fourier series representation of the internal pressure signal, and both models predict that the blade vibration will appear about certain rotor harmonics. Significant differences between the models exist and will now be explored in this subsection.

Model 1 commences by defining the pressure of a fluid moving through an individual cascade of a turbomachine by means of wave equations which describe blade vibration induced vortices. The pressure distribution measured at the casing is therefore affected by oscillation of all of the turbomachine blades reacting as a system. Provision for both tuned and mistuned response has been included in the development of the model.

Pressure signal measurement down- and upwind of the rotor plane is considered as well as the effects of nearby stator and rotor rows. The resulting periodic expression devised for the pressure signal, measured at some axial distance x downwind from the source of vibration by a stationary observer on the casing, is given by the Fourier series in Equation [2.2.1] (Mengle, 1990).

$$p(\theta_{casing}, t, x) = \sum_{m=-\infty}^{\infty} f_m(x) \cdot e^{j[(k+m \cdot B) \cdot (\theta + \Omega \cdot t)]} \cdot e^{j[\omega \cdot t]} \quad [2.2.1]$$

It is stated that any unsteady linearised flow quantity in a turbomachine (in this case pressure fluctuations due to blade vibration) can be written using the rotor reference frame formulation of Equation [2.2.1] (Mengle, 1990). This formulation can then be transformed to the casing reference frame by means of a simple linear angular velocity relation provided that the rotor speed remains nominally constant over the time interval of investigation (Mengle, 1990).

It is further stated that the Fourier coefficients of Model 1 are independent of rotor frame measurement position θ (Mengle, 1990). Specifically, they are tuned according to the pressure fluctuations arising solely from bladed hub assembly vibration. This effectively means that the circumferential pressure distribution, due purely to rotation of the assembly, is not taken directly into account in the formulation of Model 1.

Model 2 begins by taking the steady state pressure distribution, due solely to rotation of the cascade in the rotor plane, into account. The effect of individual blade vibration on this stationary pressure distribution is then added at a later stage. The proposed internal pressure distribution, which includes blade vibration, derived in the formulation of Model 2 and represented as a Fourier series is repeated in Equation [2.2.2] (Forbes and Randall, 2013).

$$P_r(t) = Re \left\{ \sum_{i=0}^{\infty} A_i \cdot P \cdot e^{(j \cdot i \cdot [\theta + \Omega(t) + \alpha_r + \gamma_i])} \cdot e^{(j \cdot i \cdot [x(t)_r])} \right\} \quad [2.2.2]$$

It is important to note that pressure field measurement in the rotor plane may not be as feasible or simple to implement when compared to measuring the response down- or upwind of the vibration source for an actual turbomachine. Being able to describe the pressure phenomena related to blade vibration at a location removed from the source plane is advantageous in terms of implementation practicality. This method is however limited by what can be observed down- or upwind of the vibration source.

Model 2 does not develop the pressure effect due to blade vibration in terms of propagating pressure waves and their associated fluid dynamics (with respect to induced vortices). Instead the displacement of a blade tip $x(t)$ is considered to alter the phase angle at which the otherwise stationary pressure waves arrive at the acoustic transducer. This method facilitates construction and implementation of a physical blade vibration model based on the geometry and material properties of a turbomachine bladed assembly (assuming that the physical assembly's properties are known within a certain tolerance). The effects of nearby stator and rotor rows were not explored in the development of Model 2, neither were axial attenuation effects on the frequency components mentioned. This is because in rotor plane measurements were taken.

An improved solution route for both Model 1 and Model 2 would be to take the physical forced response behaviour of the turbomachine blade assembly into account and then relate that to the fluid behaviour and expected wave propagation effects through that fluid. This may require a fluid-structure interaction study starting from the governing momentum and continuity equations.

An alternative to a direct analytical study of the underlying physics would be a combined FE and CFD fluid-structure investigation. Although this fluid-structure interaction study may be difficult or costly to implement in practice, it may provide a better numerical approximation of the actual conditions within the casing.

When comparing the form of the Fourier series in Models 1 and 2 several distinct differences become immediately clear. The first difference is noticed in the summing process. Model 1 sums across all integers from negative infinity to positive infinity whereas Model 2 only considers positive integers from zero to infinity. Therefore Model 2 assumes that the frequency content is symmetric about zero and the Fourier coefficients are inherently adjusted accordingly (by ensuring that the amplitudes are

doubled to take the neglected negative part of the spectrum into account). This assumption allows consideration of only the positive Fourier coefficients. This is similar to the assumption made in the development of Model 1 in that only positive frequencies can actually be observed.

The second significant difference in the models is that Model 2 only considers the real parts of each individual term in the series. In practice only fluctuating pressure magnitudes can be observed by a single stationary observer on the casing. So when comparing a numerically obtained pressure signal to a measured pressure signal only the real components of the series will be of value to compare.

All of these model differences must be compared and evaluated when considering the development of a similar expression for the pressure signal.

The pressure relations derived in Model 1 and Model 2, rewritten into the trigonometric format, are presented in Equations [2.2.3] and [2.2.4] respectively. The conversion and rearrangement process is outlined in section '7.1.2 A2 – Reformulation of Internal Pressure Signal Equation'.

$$p(\theta, t, x) = \sum_{m=-\infty}^{\infty} f_m(x) \cdot \left[\begin{array}{l} \cos((k + m \cdot B) \cdot (\theta + \Omega \cdot t) + \omega \cdot t) + \\ j \cdot \sin((k + m \cdot B) \cdot (\theta + \Omega \cdot t) + \omega \cdot t) \end{array} \right] \quad [2.2.3]$$

$$P_r(t) = \sum_{i=0}^{\infty} A_i \cdot P \cdot \cos(i \cdot [\theta + \Omega(t) + \alpha_r + \gamma_i] + i \cdot [x(t)_r]) \quad [2.2.4]$$

As was stated, Model 1 refers to the effect of Doppler shifting of the flutter response frequency due to travelling wave modes, and Model 2 refers to phase modulation of the internal pressure signal due to individual blade vibration. Both explanations attempt to describe the appearance of repeated non-integer engine order frequencies in the measured pressure spectrum. From inspection of both models it can be concluded that the observed sideband frequencies, related to non-engine order blade vibration, are connected to some integer multiple of rotor speed.

When comparing the internal pressure relations, in a trigonometric format, it is seen that only certain engine harmonic multiples in Model 1 will be Doppler shifted. The specific engine harmonics are controlled by the travelling wave number k (the harmonic index) and the number of blades B in the relation $(k + m \cdot B)$.

Model 1 is therefore designed to describe the entire system's modal response in terms of the number of nodal diameters active at any given time. This is important to note as cyclically symmetric structures are part of the periodic structures family and so respond in specific and discernible patterns.

As has already been stated, if flutter ensues and mistuning is significantly present in the system then the wave number k can take any integer value within its set. This results in the case of Doppler frequency shifting about all engine harmonics (as $(k + m \cdot B)$ can take any integer value) (Mengle, 1990).

The Doppler shifted solution for the casing observed flutter frequency ω , deduced in the formulation of Model 1, is presented in Equation [2.2.5] for the case of a constant phase angle σ (Mengle, 1990).

$$\omega'_{model\ 1} = \omega + (k + m \cdot B) \cdot \Omega \quad [2.2.5]$$

Similarly Equation [2.2.6] presents the case of a non-constant phase angle σ (Mengle, 1990).

$$\omega'_{model\ 1} = m \cdot \Omega + \omega \quad [2.2.6]$$

In both the above relations the travelling mode number k must be part of the set $k \in \{1, 2, \dots, B - 1\}$ and the index $m \in \mathbb{Z}$.

The effect of mistuning investigated in the development of Model 1 is congruent with the later discussion on the effects of mistuning. Both discussions concluded that because of mistuning there will be multiple sources of harmonic content in the response signature. The discussion on mistuning emphasized that the presence of the various system mode shapes depends on the level of mistuning as well as the excitation frequency.

In order to analyse Model 1 from a phase modulation point of view it is useful to rearrange the trigonometric formulation one final time. The rearranged formula is presented in Equation [2.2.7].

$$p(\theta, t, x) = \sum_{m=-\infty}^{\infty} f_m(x) \cdot \left[\cos(t \cdot ((k + m \cdot B) \cdot \Omega + \omega) + (k + m \cdot B) \cdot \theta) + j \cdot \sin(t \cdot ((k + m \cdot B) \cdot \Omega + \omega) + (k + m \cdot B) \cdot \theta) \right] \quad [2.2.7]$$

It can be seen that according to the equation no phase modulation actually occurs. This is because only a single component in the periodic expressions is dependent on time. Each frequency component is simply phase shifted by a fixed amount. The would-be carrier frequencies are simply functions of the rotor frequency and blade vibration frequency.

Therefore no modulation sidebands related to blade vibration are expected about engine harmonics if this model is assumed. A simple plot of the scenario defined by Equation [2.2.7] is provided in Figure 2.2-1. The model is plotted for arbitrarily chosen rotor speed and blade flutter frequencies. Only the real components have been plotted, the wave number k is assumed as 1 (one nodal diameter) and the number of blades has been chosen as 5. The Fourier coefficients have also been assumed as unity.

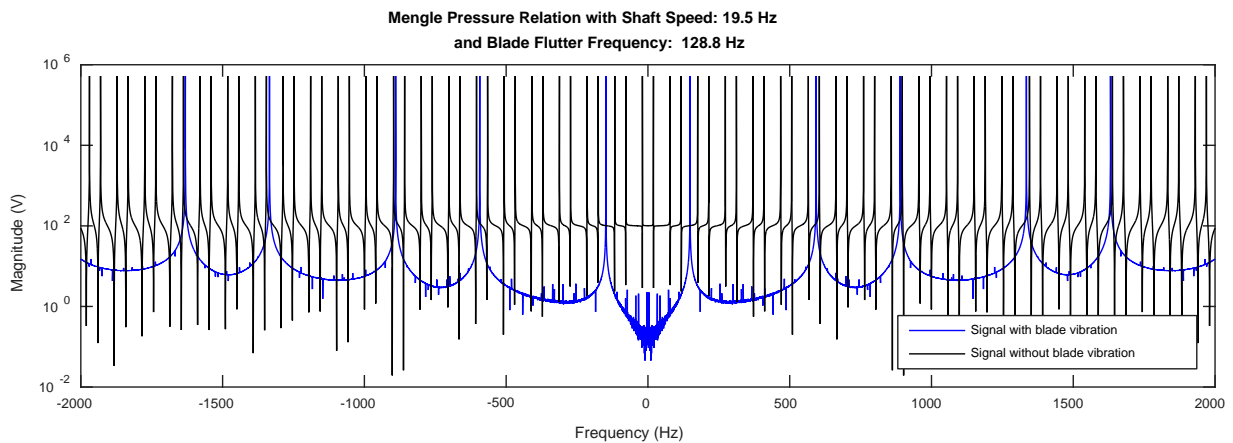


Figure 2.2-1 Pressure distribution from Mengle relation for arbitrary rotor speed and blade flutter frequency

It is clear from the example that the relation predicts a frequency shift for each Fourier term due to blade vibration as opposed to phase modulation.

The effect of Doppler frequency shifting is more apparent when only considering positive frequency components (as suggested by Mengle) and allowing $(k + m \cdot B)$ to take any integer value (assuming a mistuned system). This situation is presented in Figure 2.2-2.

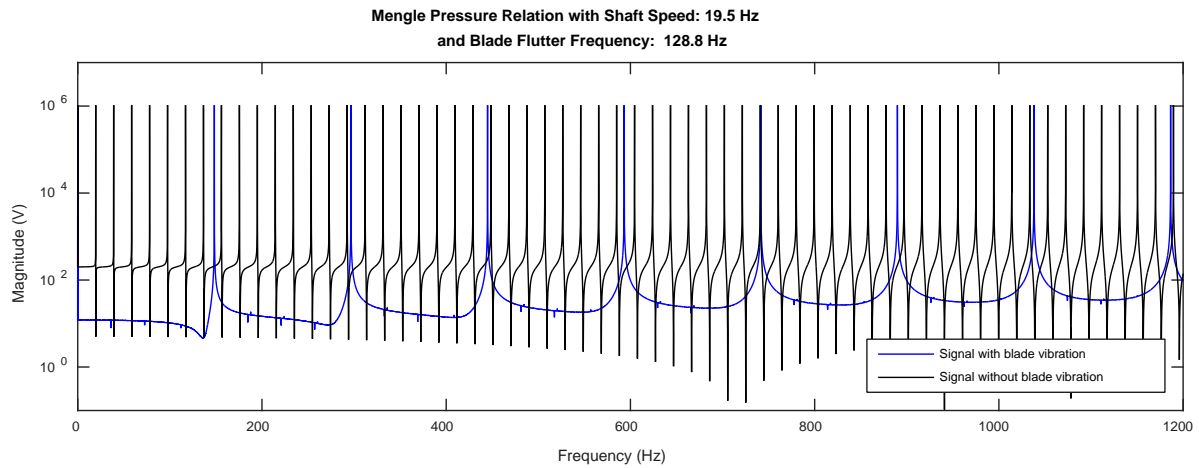


Figure 2.2-2 Alternative pressure distribution from Mengle relation for arbitrary rotor speed and blade flutter frequency

One final note on the Doppler shifting effect mentioned in the development of Model 1. Consider the observed travelling wave mode number k' in Equation [2.2.8] (Mengle, 1990).

$$k' = k + m \cdot B \quad [2.2.8]$$

Observed travelling wave mode numbers k' are in general not symmetric about 0. They are only symmetric about zero when k is either 0 or when k assumes all possible values (for the case of mistuning). Due to the symmetry of the Fourier transform, the asymmetry of the travelling wave mode results in frequency content which is termed doubly symmetric. This is due to a folding of frequency content about zero hertz (Mengle, 1990). This may have repercussions on Fourier pressure signal reconstructions using the expression derived in Model 1.

According to Model 2 each engine harmonic is phase modulated by the blade tip vibration. This tip vibration is multiplied by the integer related to the specific harmonic (Forbes and Randall, 2013). Therefore, as the number of Fourier terms increases, so do the phase modulation amplitudes for each term linearly increase.

Model 2 has not specifically made provision for the individual blades to oscillate at specific phase angles with respect to one another. This is important for the case for tuned vibration where the phase angle between sectors assumes a specific value due to the presence of travelling wave modes (discrete number of nodal diameters depending on the excitation conditions).

However no system is ever perfectly tuned, and because of this a contribution of each system mode is expected to be present simultaneously (Castanier and Pierre, 2006). As was stated, the contribution of each mode, and the effect of mode localisation, depends on the excitation frequency and the level of mistuning (Castanier and Pierre, 2006). Therefore when viewing Model 2 from Model 1's perspective, it can be seen that during its development mistuning has been intrinsically included without directly realising it. The contribution of each travelling wave mode is constant when assuming this model.

In terms of Model 2 the effect of mistuning may however not be of concern when evaluating the pressure distribution about an individual blade. This is because the pressure distribution is investigated about the individual blade regardless of the combined system's response.

An arbitrary example of phase modulation based on the pressure relation derived in Model 2 can be seen in Figure 2.2-3. Once again all Fourier terms are assumed as unity for the example and rotor speed and blade natural frequency are arbitrarily chosen.

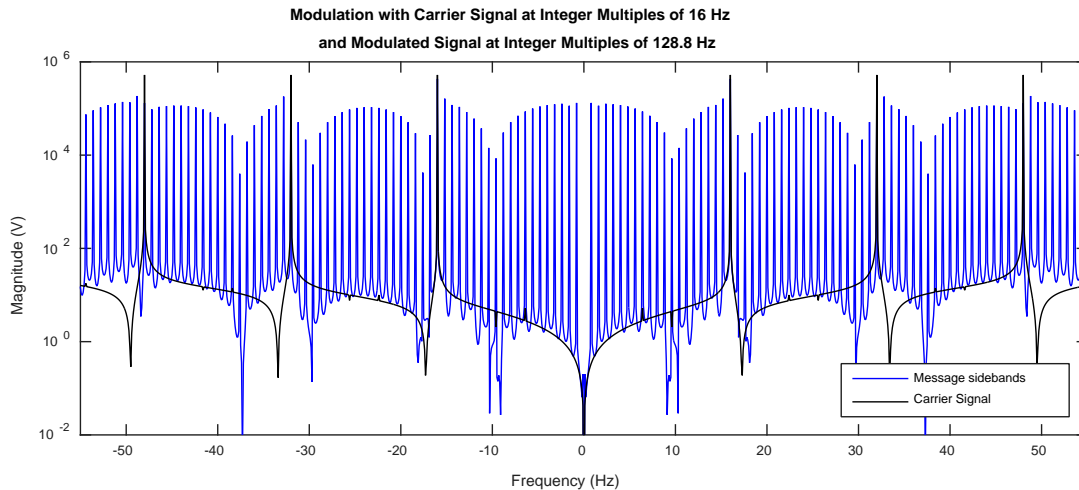


Figure 2.2-3 Model 2 arbitrary example of phase modulation in pressure relation

The frequency of the modulating term in the expression remains constant at the blade response frequency. This results in sidebands occurring at fixed distances from the carrier frequencies. The sideband amplitudes are however no longer constant.

It is clear from the figure that ambiguity exists as to which sideband belongs to which carrier term. This is due to the carrier frequencies occurring at lower frequencies to the message signal (resulting in intersecting of frequency ranges), and multiple carrier and sideband sets occurring in close proximity to one another. The sideband spacing predicted by Model 2 is provided in Equation [2.2.9].

$$\omega'_{model\ 2} = m \cdot \Omega \pm n \cdot \omega \quad [2.2.9]$$

In the equation both parameters n and m are positive integers. The parameter n has been included to emphasize that phase modulation causes multiple sideband peaks per carrier peak.

Unlike Model 1, Model 2 captures the presence of all engine harmonics in the pressure signal. All harmonics will be observed, however the harmonics about which phase modulation occurs may be governed by the harmonic index describing the number of nodal diameters present in the system's response.

Within the signal processing (SP) procedures, mentioned in the development of both models, a method is described to remove the pressure signal void of blade vibration from the full pressure signal. This is done in order to obtain a signal comprised predominantly of blade vibration information (or simply to emphasize blade vibration). Both models suggest a time domain based method which requires aligning of the pressure signals to perform the operation. In neither models' development is a frequency domain method mentioned to perform this task. Removing the deterministic signal from the full signal in the frequency domain may overcome certain issues and difficulties associated with

time domain operations as the magnitude components of the deterministic peaks will lie directly at the required frequencies. The phase information of the deterministic peaks are irrelevant as the process requires the time domain information to already be aligned (in phase). Murray and Key successfully performed this operation in the frequency domain (Murray and Key, 2015).

Both models indicate that blade vibration information is present in the pressure signal once it has been denuded of engine harmonics and other deterministic phenomena (provided that the system is not operating at a blade resonance). A difference in the deterministic peak magnitudes, due to blade vibration approaching and passing through resonance, may however be present. This phenomenon is not explored in the development of either model. It is therefore clear that only non-integer engine order blade response or flutter may be investigated using the stochastic signals isolated in the direct use of these models (along with noise and other vibration not associated with the rotor geometry and speed of operation).

Sufficient broad spectrum energy must be entering the system in order to excite the various natural frequencies and associated mode shapes outside of resonance conditions to an observable state. Forbes et al. noted that the noise entering the system is however band limited, although no explanation is provided for this (Forbes and Randall, 2013). The main source of excitation energy is however due to impingement of the rotor blades by upstream stator wakes. The closer a deterministic peak lies to a natural frequency greater the amount of energy will be entering that particular mode. As a result resonance of that particular mode will ensue.

Even though blade response amplitudes are magnified at resonance, the above mentioned SP techniques are not able to separate the blade natural frequency information from the deterministic portion of the signal. Once again it is seen that the ensemble averaging procedure described by Forbes et al., when performed on the stochastic part of the pressure signal, is expected to only be suitable for non-engine order (EO) vibration situations only (Forbes and Randall, 2013). The same restriction applies to non-EO flutter identification by means of Mengle's suggested approach (Mengle, 1990).

The premise behind the ensemble averaging procedure developed by Forbes et al. is similar to a conclusion drawn by Mengle. Namely that within a certain frequency range only a single stochastic peak will actually be related to the blades' response frequency given a particular carrier frequency (or Doppler shift). The frequency range suggested in Model 1 is the blade passing frequency $B \cdot \Omega$ (assuming that the interblade phase angle is constant and only positive frequencies are observable). This is because it is assumed that only a single travelling-wave mode is present for the system investigated.

Had the interblade phase angle been non-constant multiple modes would be present in the pressure signal simultaneously and an alternative method would have to be applied in order to determine the participation of each mode before blade vibration can be estimated (Mengle, 1990).

According to Model 2, within each frequency range (the size of the rotational speed Ω) two peaks will occur due to the modulation effect (carrier plus and minus vibrational frequency repeated for each carrier frequency). If it is observed that sideband peaks do not appear about each engine harmonic then it may be prudent to treat the blade vibration situation in a similar manner to Model 1 where only a single travelling-wave mode is present in the pressure signal. This would require an adjustment of the appropriate analytical pressure relation.

In terms of measurement sensor requirements, Mengle's method requires two stationary observers to be placed on the casing at the same axial distance from the rotor. It is also noted that the angular distance between the two observers must be specially chosen (Mengle, 1990). This is done in order to relieve the indeterminacy of the observed frequency equation. The solution derived in Model 1 for blade vibration identification is repeated in Equation [2.2.10].

$$\begin{aligned}\{\omega_{1n}\} &= (k \cdot \Omega + \omega'_{OBS}) + n \cdot B \cdot \Omega \\ \{\omega_{2n}\} &= (k \cdot \Omega - \omega'_{OBS}) + n \cdot B \cdot \Omega\end{aligned}\quad [2.2.10]$$

The parameter n in the simultaneous equations is a positive integer.

A similar indeterminacy problem exists when using the solution presented in Model 2. Either the actual frequency of vibration must be known within plus and minus half the rotor frequency, or measurements must be taken at at least two different operating speeds (Cox and Anusonti-Inthra, 2014; Forbes and Randall, 2013).

The possible advantage of using two observers to obtain the rotor response frequency was however not explored in the development of Model 2. It would be a significant advantage if only a single observer is required to perform this operation or no additional information is required to resolve the blade frequency of vibration. The solution derived by Forbes, for measurement at a single operating frequency, is presented in Equation [2.2.11]. The solution determined by Cox et al. is given in Equation [2.2.12].

$$\omega_N = \frac{\Delta\omega_{NB} + q \cdot \Omega}{2} \quad [2.2.11]$$

$$\omega_N = \left| \frac{\Omega_1 \cdot f_{sb2} - \Omega_2 \cdot f_{sb1}}{\Omega_2 - \Omega_1} \right| \quad [2.2.12]$$

The pressure relation used by Cox et al. for the evaluation of Equation [2.2.12] is simplified when compared to both Mengle and Forbes' relations (given in Equations [2.2.1] and [2.2.2]). The pressure relation explored by Cox et al. is repeated in Equation [2.2.13] (Cox and Anusonti-Inthra, 2014).

$$P_n = rand(-1,1) + \frac{(2 \cdot SNR)^{0.5}}{6.6} \cdot \cos(2 \cdot \pi \cdot b \cdot \Omega \cdot t + \epsilon \cdot \cos(2 \cdot \pi \cdot \omega \cdot t)) \quad [2.2.13]$$

It is clear from Equation [2.2.13] that only a single carrier frequency is considered with a single modulating signal operating at a single unchanging frequency. In terms of Mengle's work the blade flutter frequency is Doppler shifted at multiple integer products of engine harmonics (Mengle, 1990). With respect to the work of Forbes carrier frequencies are estimated to occur at all engine harmonics along with the blade vibration signal being multiplied by integers corresponding to each Fourier term (Forbes and Randall, 2013).

Both cases result in ambiguity of which sideband is related to which carrier frequency. The issues associated with sideband ambiguity are however not present with the simplified model as the spectrum obtained from the equation results in a single carrier frequency with associated sidebands that can easily be observed in the frequency domain. This is thus a highly unrealistic model to use when investigating the proposed improvement in the solution.

The unsteady pressure relation derived in Model 1, observed in the rotor reference frame, is noted to have been derived independently using a completely alternative methodology (Mengle, 1990; Smith, 1973). A rotor cascade is represented as a row of vortices using a series expression (Smith, 1973). The resultant relation is provided in Equation [2.2.14] (Smith, 1973).

$$\gamma(y) = \bar{\gamma}(y) \cdot e^{j\omega \cdot t} = \sum_{r=-\infty}^{\infty} \frac{\Gamma}{s} \cdot e^{j\left[\omega \cdot t + \frac{\phi - 2 \cdot \pi \cdot r}{s} \cdot y\right]} = \sum_{r=-\infty}^{\infty} \frac{\Gamma}{s} \cdot e^{j \cdot [\omega \cdot t + \beta \cdot y]} \quad [2.2.14]$$

Equation [2.2.14] is said to be equivalent to the unsteady pressure measured on the rotor reference frame provided in the development of Model 1 (Mengle, 1990). This finding strengthens the argument that blade frequency content will only be observed at every $k + m \cdot B$ frequency component in the casing reference frame unless significant mistuning is present (Castanier and Pierre, 2006; Mengle, 1990).

Further the Doppler shifting argument provided in the development of Model 1 was used to successfully identify frequency components in the experimental investigation by Murray and Key (Murray and Key, 2015). The frequency content findings may need to be implemented in an updated model in order to better capture the casing pressure signal.

Model 2 was investigated from more than just a theoretical point of view. Model 2 was directly used to generate an internal pressure signal based on the geometry and operating conditions of an actual experimental setup. Measurements were taken from the experimental setup and were shown, after signal processing, to provide the same narrow band peak spacing estimator as the analytically generated internal pressure signal. This adds confidence to the accuracy and ability of the model.

Further, some of the experimental measurements, taken in the investigation of Model 2, were made available. After following the same signal processing procedure outlined by Forbes et al. similar results to the basis material were obtained (Forbes and Randall, 2013). These results can be viewed in section '7.3 Appendix C – Example Application of CPS Method'.

After evaluation of the models it is clear that Model 1 is concerned with the travelling waves emanating from a whole moving cascade as well as the Doppler shifting effect on the observed blade flutter frequencies. It is tailored for measurement downwind of the rotating source by a stationary observer. These travelling wave modes are believed to manifest as vortices about the blades. The model was constructed taking the fact that the system is cyclically symmetric into account.

Model 2 concentrates on the modulating effect individual blade vibration has on the otherwise stationary pressure distribution that is generated about the rotor. Model 1 is concerned with measuring the Doppler effects outside of the rotor plane, whereas Model 2 concentrates on in plane measurements. The stationary casing measurement location, in plane or downwind, has been shown to affect the observable phenomena. Model 2 does not account for the cyclic symmetry of the system.

2.2.2. Discussion on Alternative Casing Pressure Methods

Various additional casing pressure and vibration investigations were reviewed as part of the literature. This section explores their contribution to the understanding of the internal pressure signal and the effects of these contributions to a more appropriate internal pressure model.

As was stated, the effect of blade vibration on the internal pressure distribution for operation at speeds traversing resonances, may cause the deterministic pressure peak heights to change. This was the conclusion of the study done by Ratz et al. (Ratz et al., 2013).

The study showed that as the rotor moves through resonance conditions some of the deterministic peak amplitudes (occurring at certain integer multiples of blade passing frequencies) spike (Ratz et al., 2013). This is significant in that the overall pressure amplitude is affected by blade vibration as the system moves through resonances. Therefore the internal pressure signal (in terms of Model 2) may not only be phase modulated but somewhat amplitude modulated by the level of blade vibration as well, even for operation at nominally constant rotor speeds.

The scope suggested that only internal pressure measurements would be considered for investigation. In none of the models and methods thus far had any of the experimentally obtained internal pressure measurements been used to isolate pressure waves about individual blades specifically for the purpose of blade vibration analysis. Outer casing vibration does not provide the localised internal effects about individual blades. Therefore if the behaviour of an individual blade does not affect the global casing response significantly then identifying individual anomalies associated with the behaviour of that blade would be difficult using external casing measurements.

In the study by Mathioudakis et al. it was shown that the surface condition and angle of individual blades caused a unique signature within the pressure distribution (Mathioudakis et al., 1991). Therefore by investigating the individual pressure waves about individual blade tips it may be possible to provide an indicator of their individual condition and response behaviour.

A further finding in the study by Mathioudakis was that the fault signatures could only be observed when measured in the rotor plane which contained the artificial damage (Mathioudakis et al., 1991). The unique fault signatures decayed to the point of being unobservable both one stage up- and downwind of the source. A similar conclusion was drawn by Mengle in that certain frequency components may decay exponentially along the axial length of the machine. This leads to a situation where specific frequency components related to blade vibration cannot be observed in a plane removed from the source. It is for this reason that in plane measurements, although possibly less practical than measurement downwind, is of sole consideration in this investigation.

The investigation by Mathioudakis et al. was however significantly different to the other studies considered in that blade vibration identification was not directly investigated or of interest. Only the effect of introducing local minor damage effects to the blades was studied (Mathioudakis et al., 1991).

The investigation by Murray and Key was able to isolate torsional blade vibration emanating from different rotor rows. This was achieved by making use of stationary observers installed within stator vanes attached to the casing of an experimental compressor (Murray and Key, 2015).

It was once again noticed that as the system moves through a resonance that the pressure amplitudes peak. This reinforces the belief that not only the phase angle, but the amplitude of the pressure distribution is directly related to the blades behaviour.

It was found that the fast response sound pressure transducer had to have a particularly high frequency response in order to capture the vibration behaviour (Murray and Key, 2015). Thus the blade frequency content of interest, sampling frequency and associated measurement equipment must be simultaneously considered for appropriate measurement and acquisition device choice.

A novel signal processing methodology was implemented in order to investigate the signal (Murray and Key, 2015). Data from individual revolutions were separated. Due to the disruptive nature of the separation process a Kaiser window was passed over each revolution's measurement (Murray and Key, 2015). In order to make the blade response phenomena visible in the spectra the spectrum from the first revolution was subtracted from all following revolutions spectra. This is similar to the engine harmonic deletion process discussed by Mengle, Kurkov and Forbes et al., it is however performed in the frequency domain as opposed to the time domain (Forbes and Randall, 2013; Kurkov, 1981; Mengle, 1990). The measurements for individual revolutions could then be assembled into a full waterfall plot which clearly emphasized trends within the data.

It is important to note that measurements were taken for an accelerating rotor moving through known resonance regions and not at constant steady state conditions. Further the vane mounted pressure sensors do not necessarily detect the same information as a casing mounted sensor as they are directly within the flow path.

The final casing pressure signal study reviewed tracked the changes of the BPF and surrounding spectrum for the case of low frequency non-engine order blade flutter (Rao and Dutta, 2012). For the specific geometry and operation conditions the carrier frequencies were much higher than the blade vibration frequencies making the sideband peaks associated with the modulation effect apparent.

The investigation showed that casing vibration measurements could be used to diagnose undesirable blade behaviour from an actual steam turbine. As soon as damaged blades were replaced on the steam turbine rotor that the sideband peaks no longer appeared about the BPFs.

The phenomenon was recreated using an experimental setup, the modulation of the pressure signal could be externally controlled and easily identified in the pressure spectrum. Of all of the methods investigated this one would be the most convenient and lightweight on resources to implement.

2.2.3. Comparison of Casing Pressure Signal Methods with Blade Tip Timing Approaches

Blade tip timing (BTT) approaches and casing pressure signal (CPS) methods both attempt to capture blade vibration information, they are however completely different in their approaches. Due to the current interest in BTT technologies it is important to provide a relative standing between the two techniques. This topic is addressed here.

In both direct and indirect BTT it is only possible to capture a limited number of points of the blade's actual response cycle. The number of points that you capture, per revolution, is exactly related to the number of BTT sensors installed on your turbomachine. This situation leads to a highly aliased signal which requires advanced curve fitting techniques in order to determine the blade's response amplitude and frequency of vibration (Diamond et al., 2014a).

Further, most methods require that your data acquisition setup must be designed and optimised for operation at a particular speed in order to capture a particular response mode. Recall that this is done in order to achieve a high pulse spacing on resonance (PSR) to capture the mode of interest. The amplitude of the individual blade vibration must also be large enough such that the available sensors and data acquisition systems are able to measure a discernible change in time of arrival (TOA). This is done in order to infer the amplitude, frequency and phase of response. According to literature, this generally means that the rotor must be operated at or through resonances in order to pick up blade

vibration information. Operation at or through critical speeds for any approach, both BTT based and CPS based, is however highly undesirable (due to blade fatigue accumulation among others).

Another considerable issue with BTT is that current implementations rely on highly accurate measurement of the shaft position. This measurement is ideally performed near to the blades' roots such that an accurate estimate of the theoretical non-vibrating blades' positions can be made.

When considering implementation on long shafts, with multiple rotor and stator cascades stacked consecutively, access to an available portion of the shaft near to the rotor row of interest may be difficult or impossible to obtain. Measuring the shaft angular position at an axial location far removed from the rotor row of interest may lead to undesirable shaft torsional vibration effects in the tachometer signal. These effects may be completely unrelated to the actual blade vibration or conditions at the root locations.

Casing pressure signal (CPS) methods on the other hand are based on measuring a continuous pressure signal. Unlike direct BTT, the pressure signal can be captured at a range of nominally constant shaft speeds because there is no longer a pulse spacing on resonance requirement. The pressure signal may not be inherently aliased, as is the case for BTT, but it contains a large amount of information completely unrelated to the blades' behaviour.

The pressure signal contains blade vibration information about the rotor row of interest (for all blades simultaneously), as well as a pressure signature related to the rotation of the shaft and periodic effects from both up- and downwind rotor and stator rows. The signal will also contain noise stemming from various other fluid and mechanical sources. Where BTT attempts to infer blade behaviour from a scarcity of information, CPS endeavours to uncover it from an excessive amount of unrelated or heavily mixed information. Further BTT approaches use a direct measurement of individual blades' behaviour to infer vibration characteristics. CPS must on the other hand infer blade behaviour through the behaviour of another medium (namely the fluid moving through the turbomachine).

It is of interest to develop a CPS method capable of separating the behaviour of individual blades. BTT approaches directly capture information related to the behaviour of individual blades. This is particularly important when considering the response of a mistuned system as the amplitudes of response for the individual blades may differ significantly. This effect may not be captured or obvious when evaluating a global pressure signal which contains the simultaneous behaviour of all of the blades in the cascade of interest (along with all of the other sources of pressure information). This is further compounded if the pressure field is measured downwind or upwind of the rotor row of interest through succeeding stator and rotor stages.

The majority of CPS methods reviewed requires that the blade vibration be non-engine ordered. Model 1 was specifically designed for the case of self-excited flutter occurring at a frequency which is not an integer relation of the shaft speed. Similarly Model 2 was used for the case of turbomachine operation at a rotor speed which is not an integer multiple of the natural frequency of the blade being investigated. BTT, as has been stated, requires operation at or near to resonances in order to pick up tip displacements associated with blade vibration.

Similar to the BTT approach, the signal processing techniques involved in the CPS methods require accurate measurement of the shaft position. So the same concerns regarding tachometer sensor position apply for CPS methods that were outlined for BTT methods. Both BTT and CPS techniques

which rely on zebra tape encoder systems require some form of geometry compensation to be applied to the measured tachometer signal. As has already been stated, bias and errors may result in the use of uncorrected tachometer signals because the signal processing algorithms inherently assume linearly spaced time domain sampling which may not be the case for the measured signal.

In the formulation of both BTT approaches and CPS methods single degree of freedom (SDOF) blade response models are generally assumed. In terms of BTT the response model normally takes the form of a simple sinusoid where the unknown values are solved for by means of auto-regression or other similar curve fitting techniques.

Attempts have been made to implement multiple degree of freedom models for use in the BTT approach (see '7.2 Appendix B – Additional BTT Literature'). Due to the freedom that MDOF systems provide, improvements in blade vibration estimation was noticed.

This however is not the case for the CPS methods. In terms of Mengle's work the blades are assumed to be responding sinusoidally at an individual flutter frequency. Similarly in the work done by Forbes at al. a SDOF sinusoidal blade tip solution response is based on a single spring-mass-damper system (Forbes and Randall, 2013; Mengle, 1990). The advantages of a multiple degree of freedom (MDOF) implementation have yet to be seen. Alternatively a FE model based or Euler-Bernoulli beam approach may be able to capture the system's response more accurately.

BTT has the advantage that an estimate can be made on both the frequency and physical deflection amplitude of vibration. In terms of CPS, attempts have been made to infer the frequency of vibration or one of the first few natural frequencies of the turbomachine blades. An amplitude value obtained via a CPS based method will however be in terms of pressure changes. This may not necessarily be linearly related to actual blade deflection amplitude. It may however be possible to relate blade deflection amplitude to the associated pressure response amplitude, although no attempts to do this were noticed in the literature reviewed.

Although it is not the topic of this study, external casing vibration has been shown to contain blade vibration information. In terms of practicality and ease of implementation this sort of methodology would be far preferred to both BTT and internal pressure signal CPS methods. This is because neither casing nor blade and attachment mechanism alteration is required. Although the likelihood of identifying the behaviour of individual blades from a method of this description may be low as direct access to phenomena related to individual blades is not available.

An advantage of implementing a CPS method based on direct internal pressure measurements is that the signal may contain information related to the performance and other operating aspects of the turbomachine. Thus a CPS based method may be used to monitor multiple aspects of an operating machine whereas BTT will only be able to capture blade behaviour information.

Both CPS and BTT have associated advantages and disadvantages. CPS methods may be able to supplement current BTT approaches to provide a more comprehensive indicator of the blades condition and behaviour (as well as give an estimation of the global conditions within the casing environment). The passing pressure waves, associated with the individual blades, may also be able to provide an additional tip time of arrival estimation if used in conjunction with a BTT approach.

2.3. Pressure Signal

The development of an accurate internal casing pressure model may not only provide insight into the form of the signal characteristics, it may also provide pointers for blade vibration identification from said signal. This section focuses on the development of internal pressure relations based upon the work of both Mengle and Forbes et al. (Forbes and Randall, 2013; Mengle, 1990). Observations from the alternative pressure investigations reviewed in the literature study have also been incorporated.

Consider the schematic of an axial flow turbomachine which contains a single set of stator vanes and a single set of rotor blades in Figure 2.3-1. It is important to note that the nomenclature from this point forward remains constant and can be referred to at the beginning of the dissertation.

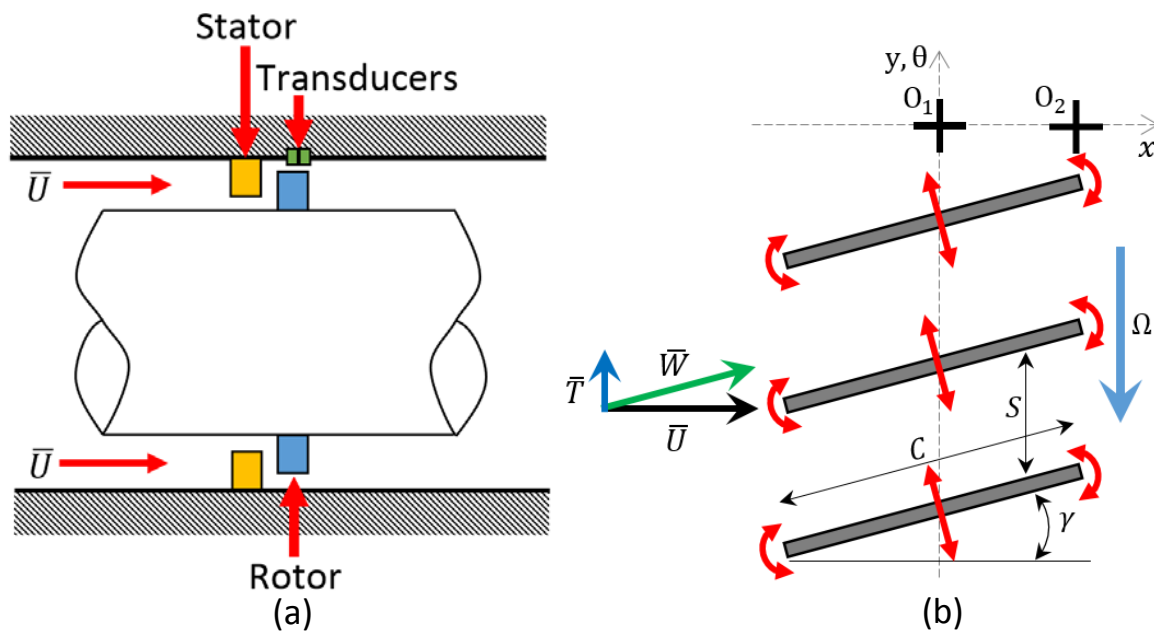


Figure 2.3-1 Axial turbomachine schematics. (a) Rotor and stator on infinitely long shaft. (b) Two dimensional flow across rotor.

In the figure \bar{U} and \bar{W} refer to the flow which is parallel to the casing and shaft, as well as the flow relative to the stagger angle γ respectively. \bar{T} is the flow in the circumferential direction. The chord length at the blade tip is C and the blade-to-blade gap is S . The rotor is operating at a shaft speed of Ω .

Two stationary observers have been placed on the casing wall, namely O_1 and O_2 . O_1 is in line with the centre of the rotating blades and O_2 is in line with the outer edge of the blades' tips downwind of the first observer. A set of V upwind stators are assumed to be stationary non-vibrating elements. This is fixed such that they do not contribute oscillatory information to the pressure signal (they only direct flow onto the downwind rotor blades). A total of B blades are on the rotor row of interest.

The range of motion that the blade tips may exhibit during flap modes, first torsional mode and combinatorial flap and torsional modes is illustrated Figure 2.3-1 (b). Edgewise motion has been neglected in the schematic as it was found that only the first few response modes are of interest.

It is assumed that the casing pressure signal, measured flush with the casing wall by the stationary observers, is directly related to the blade tip behaviour. If we start our analysis by neglecting waves propagating from the vibrating blades as vortices (Model 1), and maintain that only phase modulation

of the rotating pressure profile due to blade tip vibration can be observed then the two observers are expected to register completely different signals depending on the blade mode shape excited.

If a flap mode is excited then the two observers are expected to register a highly similar signal. If however a purely first torsional mode is excited then O_2 may capture the torsional response behaviour whereas observer 1 will not (assuming that the torsional mode occurs about an axis which runs lengthwise along the blade at its center). Further, if a combinatorial mode ensues then O_2 may capture all of the response behaviour whereas O_1 will only be sensitive to the bending component of the mode. Combinatorial modes are also however outside of the response range of interest.

If we now consider the effect of wave vortices propagating from the blade tip, differences in the measured signal may still be expected due to axial attenuation of certain of the vibrating frequency components emanating from the blades. Once again O_1 may only register flap mode response whereas O_2 will be exposed to all response modes. If the torsional mode frequency information does not attenuate axially then both O_1 and O_2 should be able to pick up both types of responses.

Consider the development of an internal pressure profile due solely to system rotation in Figure 2.3-2. The pressure profile due solely to system rotation is called the stationary pressure distribution or stationary wave because when observed from the rotor frame of reference the profile about the rotor should be unchanging with respect to time. This is of course based on the provision that no blade vibration or other effects are present in the signal. The development of this model is constructed upon the work by Forbes et al. and Ratz et al. (Forbes and Randall, 2013; Ratz et al., 2013).

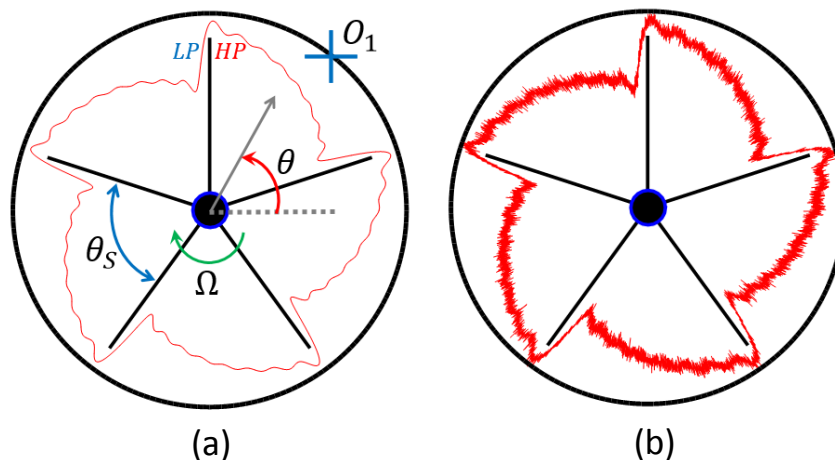


Figure 2.3-2 In plane pressure model without blade vibration. (a) Without noise. (b) With Noise.

In the first figure it can be seen that the angular distance between blades is θ_s , the rotor is moving in a clockwise direction at Ω and an angular reference frame, measured in the rotor frame of reference from an arbitrary datum, is θ . The pressure ahead of the blades are shown as high pressure (HP) regions whereas pressures behind the blades are shown as low pressure regions (LP). This is assuming that the system is operating as a compressor (as will be the convention for the dissertation).

There is a single stationary pressure observer on the casing indicated as O_1 . The stationary casing observer is in the same plane as the blade and hub assembly (at the same position as O_1 in Figure 2.3-1). Figure 2.3-2 (b) simply shows the inclusion of Gaussian noise in the pressure profile.

The stationary pressure distribution about blade r , as seen from the rotor reference frame, can be represented by the Fourier series in Equation [2.3.1].

$$P_r(t) = \sum_{i=-\infty}^{\infty} P_i \cdot e^{(j \cdot i \cdot [\omega_0 \cdot \theta])} \quad [2.3.1]$$

The Fourier coefficients P_i and the basis angular frequency ω_0 are tuned to the stationary pressure distribution using a Fourier transformation. It must be noted that the Fourier formulation assumes linearity. The Fourier coefficients contain information about both the amplitude and phase angle of the distribution. The series can be fitted to any stationary distribution about the rotor.

Due to the fact that the sound pressure transducer can only identify real pressure magnitudes, and that in the frequency domain information is symmetric about zero hertz, it is only necessary to use the real and positive part of the frequency spectrum to reconstruct the pressure signal. Further the function has a period of $2 \cdot \pi$ which results in the basis angular frequency ω_0 being equal to unity. Therefore the deterministic pressure relation can be updated to Equation [2.3.2].

$$P_r(\theta) = Re \left\{ \sum_{i=0}^{\infty} Q_i \cdot e^{(j \cdot i \cdot [\theta])} \right\} \quad [2.3.2]$$

The Fourier coefficient Q_0 is equivalent to P_0 and $Q_n = 2 \cdot P_n$ for $n \in \mathbb{N}_{>0}$.

If we assume that the rotor speed remains nominally constant and want to describe the above relation from the casing reference frame then a linear transformation is required. The same stationary observer transformation used by Mengle may be used here (Mengle, 1990). This is done in order to convert from measurement in the rotor frame to the casing frame. The resulting relation is highly similar to that found by Forbes et al. and is provided in Equation [2.3.3] (Forbes and Randall, 2013).

$$P_r(t) = Re \left\{ \sum_{i=0}^{\infty} Q_i \cdot e^{(j \cdot i \cdot [\theta + \Omega \cdot t])} \right\} \quad [2.3.3]$$

It is now appropriate to add the effect of blade tip vibration to the signal. As has already been stated, the blade tip behaviour is assumed to affect when exactly the stationary pressure wave, about each blade, arrives at the casing observer. The stationary wave arrives sooner or later depending on the arrival of the tip at the casing observation point. A single stationary blade and associated pressure distribution schematic is provided in Figure 2.3-3. Once again the direction of blade rotation, rotation speed and HP/LP blade sides have been indicated in the diagram.

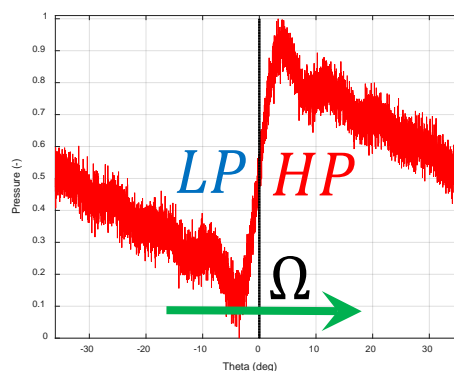


Figure 2.3-3 Stationary pressure distribution about non-vibrating blade

The early and late arrival of the stationary wave, due to blade vibration, are illustrated in Figure 2.3-4 (a) and (b) respectively. The first blade flap mode has been included for descriptive purposes. It can be seen that the arrival time of the stationary wave is simply time shifted according the angular position of the blade tips.

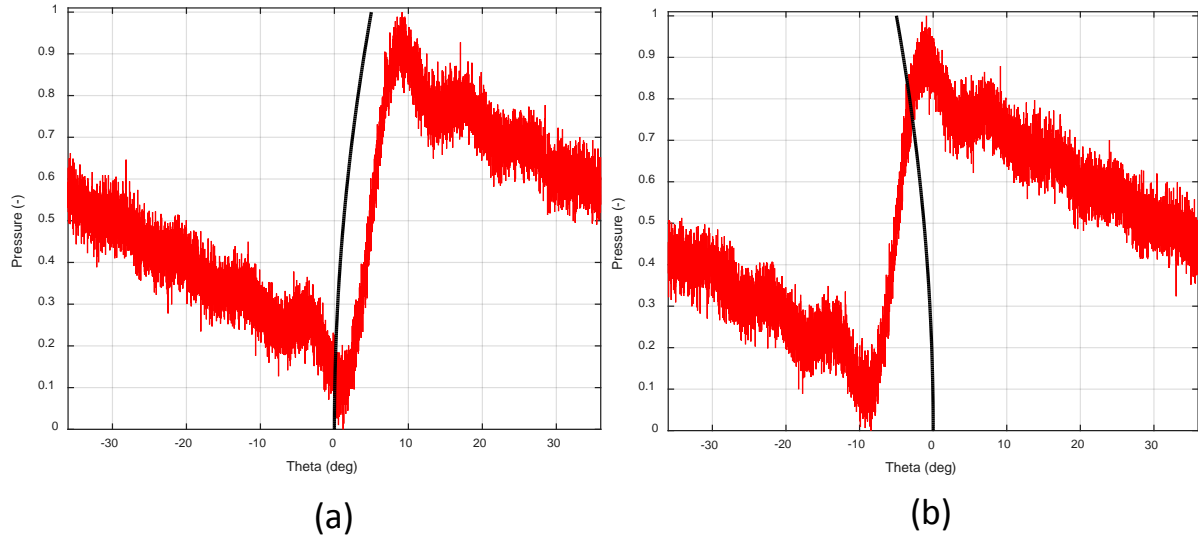


Figure 2.3-4 Pressure distribution about vibrating blades. (a) Blade bending in direction of rotation. (b) Blade bending in opposite direction of rotation.

The arrival time of the stationary pressure wave is related to the blade tip's displacement. The arrival time difference occurs in terms of angular displacement of the blade tip, therefore the translational tip displacement must be rewritten in terms of an angular displacement. The angular tip displacement about blade r , $\psi(t)_r$, in terms of the translational displacement, $x(t)_r$ and the blade length L is indicated in Equation [2.3.4]. The angle subtended is assumed to be small.

$$\psi(t)_r = \sin(x(t)_r/L) \approx x(t)_r/L \quad [2.3.4]$$

The pressure profile, in the casing reference frame, which now includes blade vibration is therefore given by Equation [2.3.5]. The pressure distribution is about blade r .

$$P_r(t) = Re \left\{ \sum_{i=0}^{\infty} Q_i \cdot e^{(j \cdot i \cdot [\theta + \Omega \cdot t + \psi(t)_r])} \right\} \quad [2.3.5]$$

The system however contains B blades. And the stationary pressure distribution measured captures the passing of all blades. Therefore in order to differentiate between individual blades, by isolating the nominal angle at which the individual blade tip occurs about the rotor circumference, an additional parameter must be included in the formulation. When measured from an arbitrary angular position θ in the rotor reference frame the individual blades occur at a distance $r \cdot \theta_s$ apart from one another where the parameter r is an integer between 0 and the number of blades B . The resulting internal pressure spectrum is provided in Equation [2.3.6].

$$P_r(t) = Re \left\{ \sum_{i=0}^{\infty} Q_i \cdot e^{(j \cdot i \cdot [\theta + \Omega \cdot t + \psi(t)_r + r \cdot \theta_s + \lambda_r])} \right\} \quad [2.3.6]$$

Due to the cyclic symmetric nature of the rotor geometry the individual blades may be oscillating at specific phase angle differences with respect to one another. A phase angle parameter for each blade, namely λ_r , is included to capture this phase angle difference between the blades.

The values that the phase angle parameter may take are of course controlled by the level of mistuning in the system, the excitation conditions and the rotor geometry. If the system is responding in a single travelling wave mode then the nodal diameters must be estimated in order to determine the phase angle for each separate sector and associated blades. By including the parameter as an open value it can be tuned to the actual response phase angle of each individual blade without having to evaluate the effect of mistuning on the whole system. Thus individual blades can be evaluated separately.

It was noted in the study by Ratz et al. that as the blades pass through resonance the deterministic peaks' amplitudes reach a maximum value as well (Ratz et al., 2013). Therefore the pressure amplitude, and not only the phase angle, may also be a function of the blades tips' behaviour. Thus, in order to account for this amplitude modulating effect the above relation can be multiplied by the blades tips' behaviour. Consideration must be made as to whether the amplitude modulation is due to the angular displacement of the blades, their angular velocity or some combination of both.

When the blades pass through resonance both the amplitude of response and frequency of response increase. The blade tip must traverse a larger distance at a higher frequency, this means that the blade tip speed relative to its root position is increasing as it approaches resonance.

It was found in the study by Ratz et al. that the deterministic pressure amplitude decreases again after resonance has been passed (Ratz et al., 2013). This result was echoed in the work done by Murray and Key (Murray and Key, 2015). The frequency of the response is still increasing once the rotor has moved just past resonance, the tip displacement is however decreasing once resonance has been passed because a smaller angular distance is traversed by the blade tip. Therefore the tip speed, in terms of tip angular displacement, is also decreasing. The pressure amplitudes are therefore believed to be related to the tip speed $\dot{\psi}(t)_r$ rather than the tip angular displacement $\psi(t)_r$.

If the effect is considered from the casing reference frame point of view, then it can be argued that as the blade tip moves towards the observer (in the direction of the rotor spin) the observed velocity is higher than when it moves opposite to rotor spin. Therefore this velocity oscillation at nominally constant rotor speed may cause amplitude modulation of the measured pressure signal. A suggested amplitude modulation effect of the tip speed is included in Equation [2.3.7].

$$P_r(t) = (1 + \Gamma \cdot \dot{\psi}(t)_r) \cdot Re \left\{ \sum_{i=0}^{\infty} Q_i \cdot e^{(j \cdot i \cdot [\theta + \Omega \cdot t + \gamma_r + \psi(t)_r + r \cdot \theta_s])} \right\} \quad [2.3.7]$$

A tuning parameter Γ has been included in the formulation. If Γ is equal to zero then there is no amplitude modulation effect. As Γ increases the effect of amplitude modulation increases. Thus by tuning the parameter the effect of amplitude modulation can be controlled in the formulation.

In order to obtain the angular velocity of the blade tip the angular displacement must be differentiated with respect to time. It is irrelevant if this operation is performed in either the time domain or the frequency domain and so can be performed where it is most convenient. Care must just be taken to ensure that no artificial effects are introduced into the signal due to the differentiation operation.

The effects of amplitude modulation, and appropriate demodulation concerns, are the same as for phase modulation. An amplitude modulated sinusoidal frequency, with a higher carrier frequency than modulating frequency, shown in the Fourier domain is illustrated in Figure 2.3-5. The frequencies have been chosen arbitrarily, the only concern was that the carrier frequency be significantly greater than the modulating frequency.

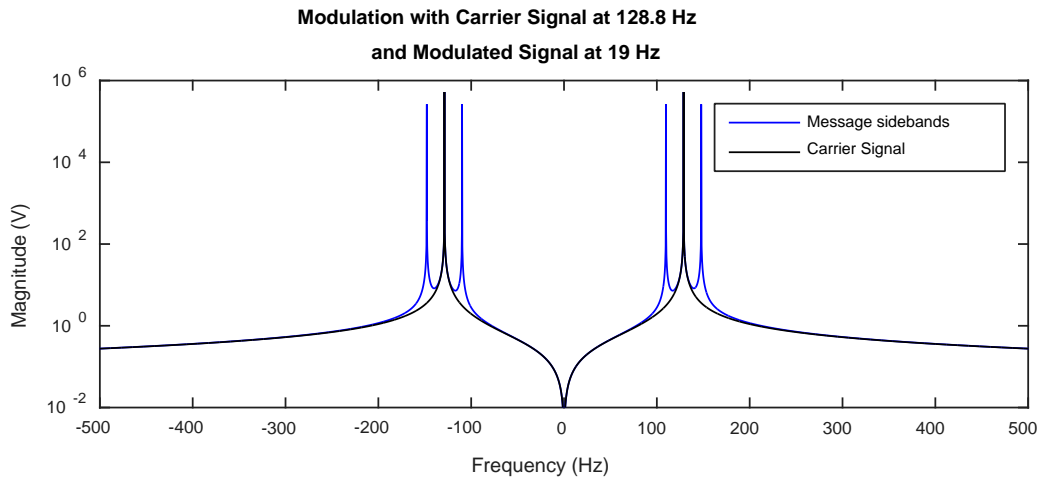


Figure 2.3-5 Amplitude modulation with higher carrier frequency than modulating frequency

It is clear from the figure that because the carrier frequency is much higher than the modulating frequency there is no overlapping of modulating (or message) frequency content. Therefore standard demodulation techniques based upon Bedrosian’s theorem may be applied in order to recover the message signal from the overall signal in this example.

Another significant difference between phase and amplitude modulation for these particular models can be seen. Only one pair of sidebands appear about the carrier peaks. This is in contrast to the multitude of sidebands which occur due to phase modulation. The consequence of this difference can only be investigated when investigating an actual pressure signal.

The case for lower carrier frequency to modulating frequency is now illustrated. The moment the modulating frequency is higher than the carrier frequency there is overlapping of the frequency content, as was the case for phase modulation. This has been illustrated in Figure 2.3-6.

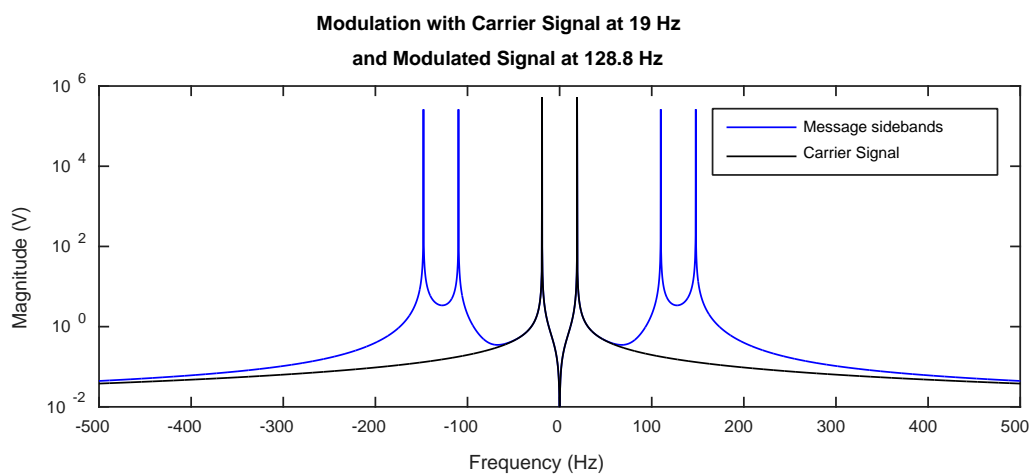


Figure 2.3-6 Amplitude modulation with lower carrier frequency than modulating frequency

It can be seen in the figure that two sidebands per carrier exist. It is easy enough to determine which peak relates to which carrier in the simple example as only a single pair of sidebands exist per carrier frequency. However as soon as multiple carrier frequencies exist the differentiation between sideband peaks and which carrier frequency they are related is expected to become more difficult. This is further compounded when multiple modulating (message) frequencies are present in the signal.

An example of amplitude modulation of the form expressed in Equation [2.3.7] for multiple carrier (stationary pressure) signals is provided in Figure 2.3-7. The Fourier coefficients are assumed to be unity, and the message signal (blade vibration) is assumed as a SDOF sinusoid with an amplitude of 0.1 (i.e. the modulating term in the expression is chosen as $(1 + 0.1 \cdot \sin(2 \cdot \pi \cdot 128.8 \cdot t))$).

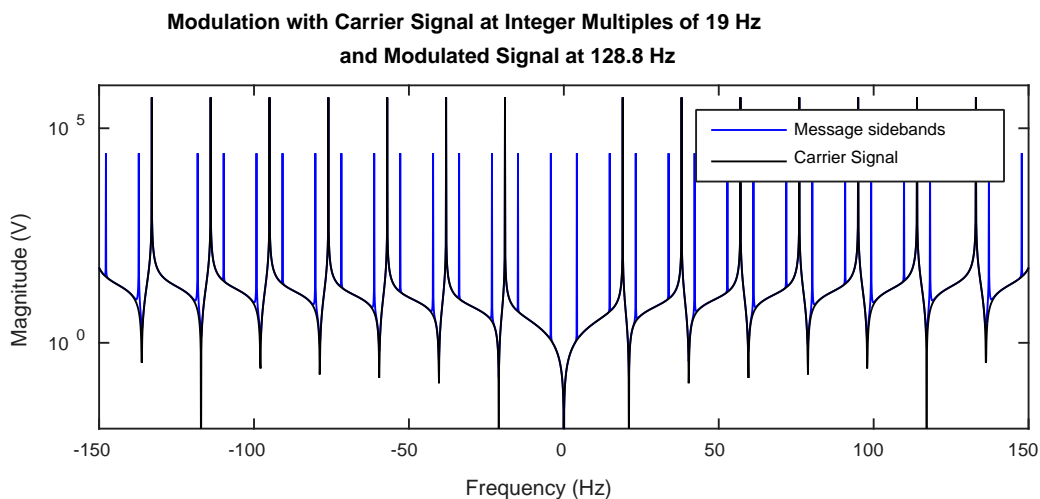


Figure 2.3-7 Amplitude modulation with multiple carrier frequencies lower than a single modulating frequency

In the final illustration both phase and amplitude modulation are mixed. The magnitude of the amplitude modulating term is maintained at 0.1 and the phase modulation amplitude is unity. The frequency of both modulation mechanisms is set at 128.8 Hz and the carriers are integer multiples of 19Hz. The Fourier coefficients are assumed as unity as well. The resulting frequency domain representation of the signal is supplied in Figure 2.3-8.

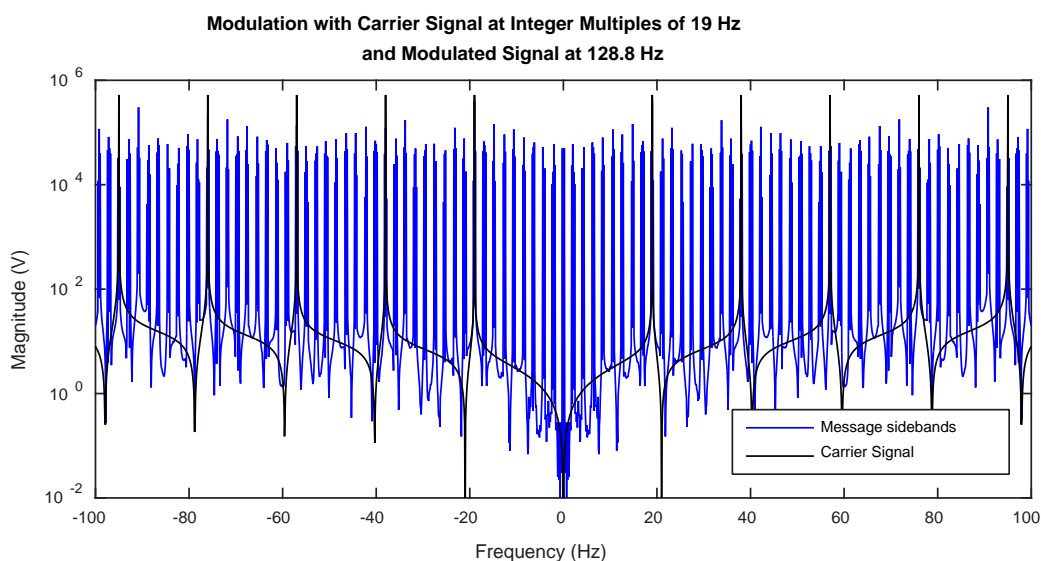


Figure 2.3-8 A mixture of phase and amplitude modulation with multiple carrier frequencies

There is now complete ambiguity as to which sideband peak is related to which modulation mechanism and carrier frequency as they now lie on top of one another at all $n \cdot \Omega \pm \omega$.

Equation [2.3.7] is reformulated into the trigonometric equivalent in Equation [2.3.8]. The reformulation process is the same as mentioned before and is presented in section '7.1.2 A2 – Reformulation of Internal Pressure Signal Equation'.

$$P_r(t) = (1 + \Gamma \cdot \dot{\psi}(t)_r) \cdot \sum_{i=0}^{\infty} Q_i \cdot \cos(i \cdot [\theta + \Omega \cdot t + \psi(t)_r + r \cdot \theta_s + \lambda_r]) \quad [2.3.8]$$

A stationary observer can only detect the pressure at an individual point about the circumference of the casing. We therefore require only a point measurement with respect to time and not the entire distribution with respect to all points about the circumference θ .

If we assume that observations are being recorded at θ equal to zero radians we see that the expression becomes independent of measurement angle θ . This can be done as the observation point is arbitrary with respect to the rotor reference frame and that the phase angle of response is variable. The θ independence was first noted in the development of Model 1 (Mengle, 1990). The trigonometric form of the equation, independent of θ is given in Equation [2.3.9].

$$P_r(t) = (1 + \Gamma \cdot \dot{\psi}(t)_r) \cdot \sum_{i=0}^{\infty} Q_i \cdot \cos(i \cdot [\Omega \cdot t + \psi(t)_r + r \cdot \theta_s + \lambda_r]) \quad [2.3.9]$$

A stationary casing observer views the spinning internal pressure distribution from an arbitrary position. If the rotor is operating at Ω then the stationary observer can be seen as moving about the pressure distribution, as seen from the rotor reference frame, at $-\Omega$.

A method is required to compare the relation given in Equation [2.3.9] to actual pressure measurements. This is done in order to see how well it describes the underlying casing pressure behaviour. Fortunately a few of the parameters in the expression are known or can be estimated a priori.

The rotor is known to be operating at a nominally constant speed, therefore the rotor speed can be continuously measured and an average value used. The expression was developed to describe the distribution about an individual waveform. So if it is possible to separate the passing waves, associated with individual blades, and then perform further signal processing on these waves the behaviour of individual blades may be able to be extracted. The splitting of pressure waves about individual passing blades is the topic of a following section.

The Fourier coefficients, for the stationary wave, can be obtained by synchronously averaging the separated signal to determine the average waveform per revolution. Assuming that the blade vibration is asynchronous (aspects of the blade vibration occur at speeds which are not integer multiples of the rotor speed) then the synchronous averaging process should average out the phase and amplitude modulation effects directly related to the blades' vibration. The synchronous averaging process is performed using a tachometer signal which was measured simultaneously.

The tachometer signal used to perform the synchronous averaging can then be used to reconstruct the deterministic full time length pressure signal. This signal should now be free of blade vibration

effects which are not at integer multiples of the rotor speed. A Fourier transform can then be applied to this signal in order to obtain the stationary pressure distribution's Fourier coefficients.

The phase angle offset at which the measurements are taken is not known, therefore a constant phase angle offset parameter can be used to tune the simulated signal to match a measured signal. The unknown phase angle is introduced into the equation and is represented by ν . The resulting expression is provided in Equation [2.3.10].

$$P_r(t) = (1 + \Gamma \cdot \dot{\psi}(t)_r) \cdot \sum_{i=0}^{\infty} Q_i \cdot \cos(i \cdot [\Omega \cdot t + \psi(t)_r + \nu]) \quad [2.3.10]$$

The phase angle ν is however limited to $\nu \in [-\pi, \pi]$ radians as the period of the stationary pressure distribution is $2 \cdot \pi$.

The remaining unaccounted for information is the blade angular displacement and velocity with respect to time as well as the tuning parameter Γ . Once the angular displacement is known with respect to time the angular velocity follows trivially. The amplitude modulation tuning parameter must be adjusted according to the measurements and cannot be directly inferred.

The phase angle at which the blade vibrates relative to the system's response has not yet been discussed. Although this topic will be covered during the development of the blade forced response model a brief comment will be made. Had the system been tuned and multiple distributions about all blades considered then the global behaviour of the system could be introduced by linking the blades' individual phase angles according to the system mode shapes described in nodal diameters. The blade tip angular displacement is a function of the blade material and geometric properties as well as the excitation force. This is the subject of the succeeding section.

The effect of pressure measurements at blade EO resonances will now be explored. If we assume that the blade vibrates as a SDOF sinusoid (the most common assumption for both BTT and CPS methods) then we can represent the angular displacement and velocity as Equations [2.3.11] and [2.3.12] respectively.

$$\psi(t)_r = A \cdot \sin(\omega \cdot t + \phi) \quad [2.3.11]$$

$$\dot{\psi}(t)_r = \omega \cdot A \cdot \cos(\omega \cdot t + \phi) \quad [2.3.12]$$

These terms are substituted into Equation [2.3.10] to yield Equation [2.3.13].

$$P_r(t) = (1 + \Gamma \cdot \omega \cdot A \cdot \cos(\omega \cdot t + \phi)) \cdot \sum_{i=0}^{\infty} P_i \cdot \cos(i \cdot [\Omega \cdot t + A \cdot \sin(\omega \cdot t + \phi) + \nu]) \quad [2.3.13]$$

Modulation will result in observed sidebands at locations indicated in Equation [2.3.14].

$$\omega' = i \cdot \Omega \pm \omega \quad [2.3.14]$$

The multipliers i are part of the set $i \in \mathbb{Z}$.

Finally, if the system is being excited at an integer EO E of the rotor speed then the observed sidebands will coincide with the rotor harmonics, the observed sidebands for this case is given in Equations [2.3.15] and [2.3.16].

$$\omega' = i \cdot \Omega \pm E \cdot \Omega = \Omega(i \pm E) \quad [2.3.15]$$

Due to the fact that $i \in \mathbb{Z}$ and $E \in \mathbb{N}_{>0}$, the observed vibration frequencies reduce to:

$$\therefore \omega' = i \cdot \Omega \quad [2.3.16]$$

Therefore the frequency locations of the sidebands will be indistinguishable from the engine harmonics for the case of resonant response. The engine harmonics' amplitudes will however peak at resonance, as was found by Ratz et al. (Ratz et al., 2013).

Therefore, so long as the system is being operated just off the desired resonance of a blade being investigated then information regarding its behaviour will be present in the stochastic part of the pressure signal. This is of course subject to sufficient broad spectrum energy entering the system in order to excite modes off of engine harmonics.

By performing the signal processing (SP) procedure suggested by Forbes et al. on pressure measurements approaching EO vibration, the narrow band side peaks will appear with increasing magnitudes as the EO is approached (Forbes and Randall, 2013). This increase in sideband peak amplitude is attributed to the response level (angular displacement and velocity) increasing. Further the sideband peaks should disappear at the EO excitation point as the SP techniques remove all engine ordered response. Once the EO excitation point has been passed the narrow band side peaks are expected to reappear once again and then decrease in magnitude.

The significance of this effect is that the narrow band side peaks may be used to identify resonance points from a pressure signal. It may thus be used to monitor the system's behaviour. If individual blade's pressure distributions can be separated out of the entire pressure signal and the SP procedure applied to these signals it may be possible to obtain an indicator of the individual blade's behaviour.

Up until this point only the modulating effects of individual blade vibration on the stationary pressure distribution about that blade have been discussed. As was said, this was based on the original work in the development of Model 2.

The global pressure response due to system modes forming and the Doppler shifting of frequency content due to that system response has not been handled thus far (Model 1). We start by considering the observed blade frequencies due to blade vibrational effects on the internal spinning lobes; the expression is expanded in Equations [2.3.17] to [2.3.20] (Mengle, 1990).

$$\omega' = \omega + k' \cdot \Omega \quad [2.3.17]$$

$$k' = k + m \cdot B \quad [2.3.18]$$

$$\therefore \omega' = \omega + (k + m \cdot B) \cdot \Omega \quad [2.3.19]$$

$$\therefore \omega' = \omega + k \cdot \Omega + m \cdot B \cdot \Omega \quad [2.3.20]$$

In the equations the parameter m is an integer, the travelling wave mode number k lies within the set $k \in \{0, 1, 2, \dots, B - 1\}$ and B is the number of blades on the rotor of interest.

We can split the observed frequencies into three sections. Namely where the parameter m is less than zero, equal to zero and greater than 0. This results in two sections for the observed frequencies, namely frequencies less than zero for m less than zero, and observed frequencies greater than zero for m equal to and greater than zero.

The observed wave numbers k' are in general not symmetric about zero. The Fourier transform of a real time domain signal is however symmetric about zero hertz. Therefore the observed frequencies must also be symmetric in the frequency domain. This is referred to as frequency folding.

In order to find the symmetric observed frequencies, due to negative observed travelling wave numbers, the symmetry of the observed wave numbers must be explored. For every negative wave number there now exists a positive value of the magnitude (and similarly for every positive value there exists a negative value). The observed wave numbers for positive and negative m values are presented in Equations [2.3.21] and [2.3.22] respectively.

$$k^{+'} = k + m_{\geq 0} \cdot B \quad [2.3.21]$$

$$k^{-'} = |m_{< 0}| \cdot B - k \quad [2.3.22]$$

The observed blade response frequencies due to positive m values are given by Equation [2.3.23].

$$\omega^{+'} = m_{\geq 0} \cdot B \cdot \Omega + k \cdot \Omega + \omega \quad [2.3.23]$$

The observed frequencies due to negative m values are a little trickier to handle. Before we apply folding to reveal them it may be useful to review the observed frequencies due to negative m values in an expanded form, this is given in Equation [2.3.24].

$$\omega^{-'} = m_{< 0} \cdot B \cdot \Omega + k \cdot \Omega + \omega \quad [2.3.24]$$

The observed frequencies must be symmetric in the frequency domain, therefore the observed frequencies due to negative m values in the positive half of the frequency spectrum can be given by Equation [2.3.25].

$$\omega^{-'} = |m_{< 0}| \cdot B \cdot \Omega - k \cdot \Omega - \omega \quad [2.3.25]$$

It is now possible to combine Equations [2.3.23] and [2.3.25] to obtain an expression for all observed blade response frequencies regardless of the value of m . The result is provided in Equation [2.3.26].

$$\omega' = |m| \cdot B \cdot \Omega \pm (k \cdot \Omega + \omega) \quad [2.3.26]$$

Once again the parameter m in Equation [2.3.26] may take any integer value.

Symmetry is now achieved in the frequency domain due to the doubly symmetric nature of the system stemming from the folding of the observed travelling mode wave numbers k' .

It can be now seen that two observed frequency peaks, per value of m , exist in each frequency range of length $B \cdot \Omega$ and that both are related to blade vibration. Mengle had already alluded to the

problem that two peaks will exist per blade passing frequency range when only the positive half of the frequency spectrum was considered (Mengle, 1990).

In the formulation the absolute value of the original observed flutter frequencies was taken and results in the same solution as was found in Equation [2.3.26]. Therefore the same difficulties in identifying the blade flutter frequencies still exists.

The originally suggested solution involved determining the observed travelling wave number by using a second stationary observer placed on the casing. The second stationary observer had to be placed at an angular offset equal to the angular distance between two blades (at the arbitrary axial distance x downwind of the rotor row of interest). An alternative to this solution route is rather sought.

It would be interesting to apply the ensemble averaging process on full time domain measured signals using a frequency range of blade passing frequency (BPF) rather than rotor frequency Ω . This is done in order to see if two peaks related to vortex generation and system tuned response appear separate from the other stochastic information. This was suggested by the work of Mengle (Mengle, 1990).

The problem now arises as to how to express the observed frequency content in the time domain. Even though there exists a symmetry in the frequency domain, considering only positive m values and adjusting the provided expression simply leads to a cancelling of specific terms in the pressure relation developed by Mengle (this can easily be deduced when reviewing the components $+\omega, -\omega, +k \cdot \Omega$ and $-k \cdot \Omega$) (Mengle, 1990).

The trigonometric form of Model 1 was shown to not modulate the signal but rather simply shift frequency components by a certain amount given the travelling wave mode number k , the rotor speed Ω and the number of blades B . If we express the global pressure spectrum, with shifted blade vibration frequencies, in the same form as the trigonometric representation of Model 1 we obtain Equation [2.3.27].

$$P(t) = \sum_{m=-\infty}^{\infty} D_m \cdot [\cos(t \cdot (m \cdot B \cdot \Omega + k \cdot \Omega + \omega)) + j \cdot \sin(t \cdot (m \cdot B \cdot \Omega + k \cdot \Omega + \omega))] \quad [2.3.27]$$

In this formulation the only observed frequencies will be those that are Doppler shifted to BPF (Mengle, 1990; Murray and Key, 2015). In practice the pressure spectrum contains all blade passing harmonics. The assertion that all blade passing harmonics are contained in the pressure signal is supported by the experimental work done by Forbes et al. (Forbes and Randall, 2013). From experimental measurements and signal processing all blade passing harmonics are clearly seen.

According to Model 1 Doppler shifting of the blade vibration signal is however expected to only occur about certain engine harmonics. Therefore the above suggested model is incomplete from a physical point of view as it does not describe the full pressure spectrum within the casing.

It was shown that the Doppler shifts occur in symmetric pairs about certain engine harmonics due to the folding phenomenon (Mengle, 1990). It may therefore be useful to rather employ an expression similar to that derived originally by Forbes et al. in order to describe the full pressure signal (Forbes and Randall, 2013). The expression must be constructed to contain both all engine harmonics and symmetric Doppler shifted terms about certain chosen harmonics simultaneously.

The symmetry of the Doppler shifts allows modelling the phenomenon as a modulation effect. Specifically, as though it modulates the global pressure signal captured by the stationary observer on the casing.

At this point it is unknown whether or not the best representation of the phenomenon would be phase or amplitude modulation and thus an investigation must be performed to determine which would best suit the application. Initially a phase modulation form of the signal is proposed to be investigated, this is provided in Equations [2.3.28] and [2.3.29].

$$P_r(t) = Re \left\{ \sum_{i=0}^{\infty} D'_i \cdot e^{(j \cdot i \cdot [\Omega \cdot t + \nu] + j \cdot [I(i) \cdot \Lambda \cdot \sin(k \cdot \Omega \cdot t + \omega \cdot t + \chi)])} \right\} \quad [2.3.28]$$

$$I(i) = \begin{cases} 1, & \text{If } i \equiv \{1 \cdot B, 2 \cdot B, \dots, n \cdot B\} \\ 0, & \text{Otherwise} \end{cases} \quad [2.3.29]$$

The parameter k lies within the set $k \in \{0, 1, 2, \dots, B - 1\}$, $D'_0 = D_0$ and $D'_i = 2 \cdot D_i$ for $i \in \mathbb{Z}^+$.

In the formulation an indicator function $I(i)$ is used to specify about which specific engine harmonic sidebands should appear. The indicator values are chosen depending on the rotor geometry. The rotor geometry of interest is the number of blades on the rotor. The expression is constructed such that the frequency content is mirrored about BPFs (as was found in the Equation [2.3.26]). Thus a symmetric pair of sidebands have been artificially forced about the BPFs. Further, the expression now retains the presence of all engine harmonics in the full pressure signal.

An additional tuning parameter Λ has been included in the formulation in order to allow scaling of the vibration response. The phase angle at which the blade vibration occurs relative to the full system's response is contained within the blade phase angle parameter χ . This parameter is equivalent to the blade phase angle parameter in the forced response expression derived from experimental modal analysis techniques. The full pressure system has an offset phase angle ν . Finally the Fourier coefficients D'_i are equivalent to those developed for the model based on the stationary pressure wave (see Equation [2.3.10]).

An advantage of Equation [2.3.28] is that the sidebands due to phase modulation of the stationary pressure wave can be easily included by adding the blade vibration in terms of angular displacement (as well as the amplitude modulation due to blade tip angular velocity). A major disadvantage of the expression is that it is no longer directly based on the physics describing vortex generation and global system mode response in terms of nodal diameters. It is based solely on observations from the expected observed blade vibration frequencies. Therefore there is no guarantee that it will produce the same true effect in either the frequency or time domain.

It is important to illustrate that the relation does indeed place blade vibration frequency components at the expected locations. The frequency content of a simplistic three bladed system will now be illustrated using the above developed relation.

It is assumed that the system is tuned, therefore only one travelling wave mode is present. The blade vibration frequency is chosen as 19 Hz and the rotor speed as 125 Hz such that it can be seen where the frequency content is shifted to (in order to adhere to the conditions of Bedrosian's theorem). The case for the travelling wave mode number k equal to zero is shown in Figure 2.3-9.

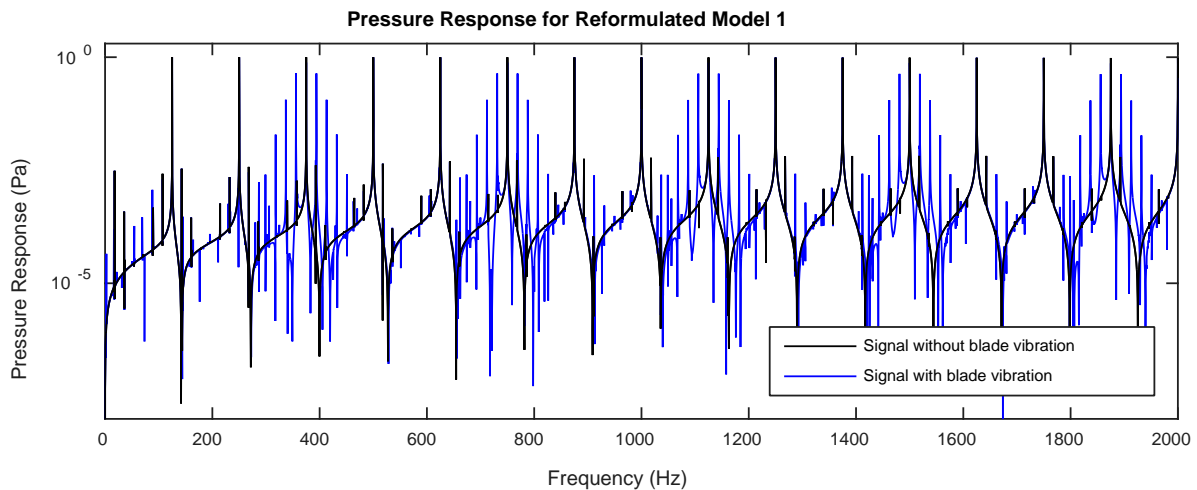


Figure 2.3-9 Pressure response for reformulated Model 1 with $k = 0$

According to Equation [2.3.26] the blade vibration sidebands must occur about the BPFs at a distance of ω for the case of k equal to zero. It is clear in the figure that this is indeed what happens as sidebands at 19 Hz appear about every third BPF. The case for k equal to 1 is shown in Figure 2.3-10.

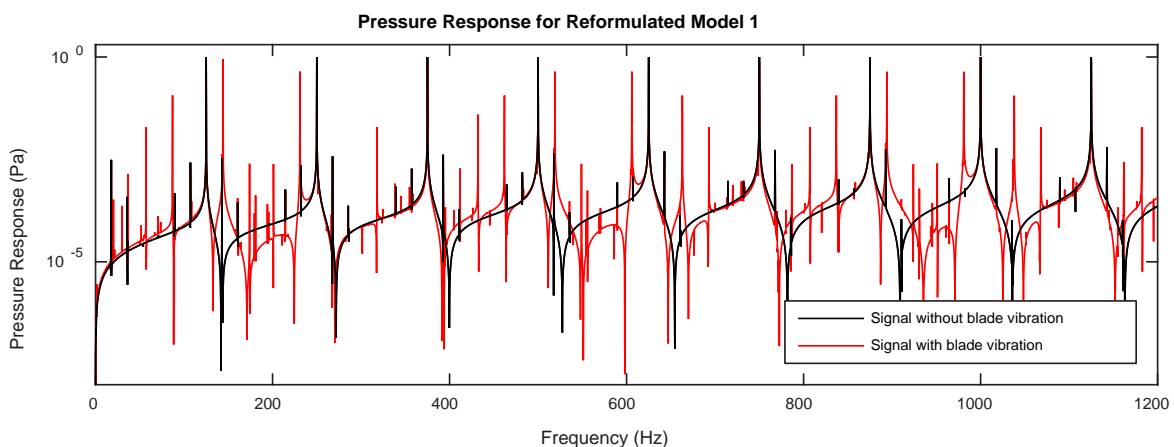


Figure 2.3-10 Pressure response for reformulated Model 1 with $k = 1$

For this specific case ($k = 1$) the sidebands are expected to occur at a distance of $1 \cdot \Omega + \omega$ about the BPFs. It can be seen in the figure that this is indeed the case with sidebands occurring at a distance of 144 Hz about the BPFs.

The case of mistuning must now be included in the model. It is known that no system is perfect, therefore a small amount of mistuning will always be present. A combination of all travelling wave modes is expected to occur simultaneously for the mistuned case.

The strength of each individual mode's presence in the full pressure signal depends on the excitation conditions and level of mistuning. Using the same simple system which contains three blades, and plotting the responses for all possible k -values separately you obtain Figure 2.3-11.

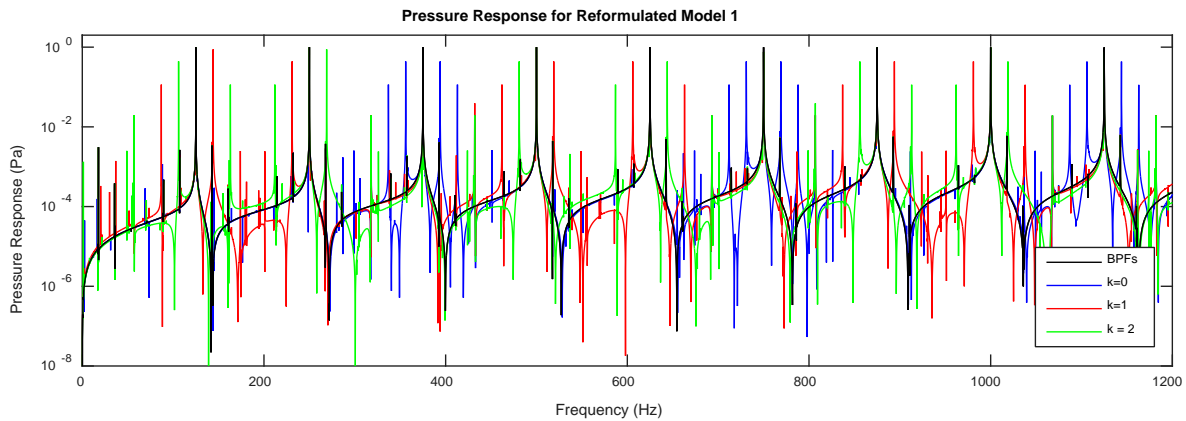


Figure 2.3-11 Pressure response for reformulated Model 1 with all possible k values plotted separately

As expected, when all possible k values are plotted simultaneously then the Doppler shifting effect is seen to occur about all engine harmonics.

An expression which captures all possible k -values simultaneously has been proposed in Equation [2.3.30]. All possible modes are included using a sum. Each component of the sum has an associated tuning parameter Λ_k , depending on the strength of its contribution the parameter can be scaled accordingly.

$$P_r(t) = Re \left\{ \sum_{i=0}^{\infty} D'_i \cdot e^{(j \cdot i \cdot [\Omega \cdot t + \nu] + j \cdot [\sum_{k=0}^{B-1} [I(i) \cdot \Lambda_k \cdot \sin(k \cdot \Omega \cdot t + \omega \cdot t + \chi)])]} \right\} \quad [2.3.30]$$

Using Equation [2.3.30] to generate a signal with all possible k -values occurring simultaneously (all with a scaling factor Λ at unity) is presented in Figure 2.3-12.

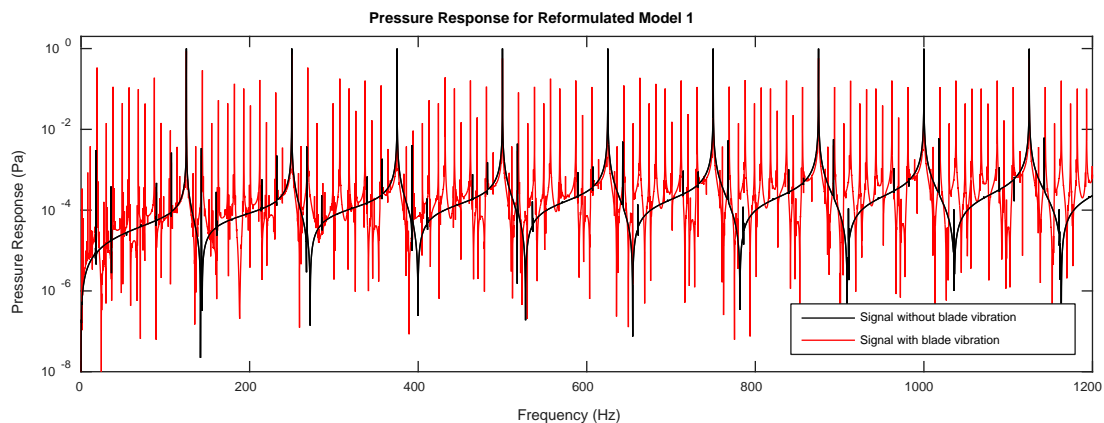


Figure 2.3-12 Pressure response for reformulated Model 1 with all possible k values

Once again sidebands appear about each engine harmonic when all k - values are simultaneously present. The ability to tune each of the system modes present separately has been included in the parameter Λ_k . Therefore the relation is able to be adjusted according to the excitation conditions, the level of mistuning and the system's geometry.

The case for amplitude modulation must now be explored. It was seen that phase modulation of the signal causes multiple sidebands to pair about each BPF. According to the expected observed frequencies, provided in Equation [2.3.26], only a single pair of sidebands should be present about

each engine harmonic. Amplitude modulation of the signal is expected to only cause a single pair of sidebands per carrier frequency. The replacement of the phase modulation with amplitude modulation is illustrated in Equation [2.3.31].

$$P_r(t) = Re \left\{ \sum_{i=0}^{\infty} \left[\sum_{k=0}^{B-1} [I(i) \cdot \Lambda_k \cdot \sin(k \cdot \Omega \cdot t + \omega \cdot t + \chi)] \right] \cdot D'_i \cdot e^{(j \cdot i \cdot [\Omega \cdot t + \nu])} \right\} \quad [2.3.31]$$

The effect of the adjustment is shown in Figure 2.3-13. The same system was plotted (three blades on a rotor operating at 125 Hz with the blades vibrating at 19 Hz), for all possible values of k each occurring at the same magnitude.

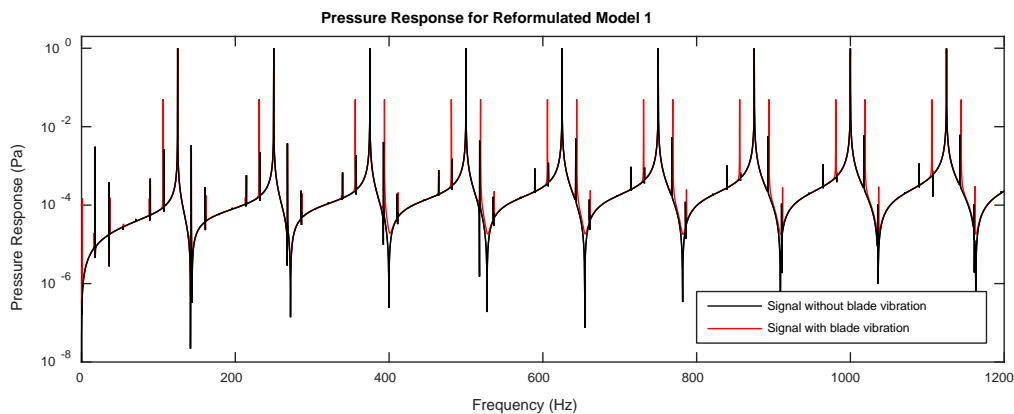


Figure 2.3-13 Pressure response for reformulated Model 1 with all possible k values using amplitude modulation

It can be seen now that only a single pair of sidebands appear about each engine harmonic. Therefore the amplitude modulation representation of the phenomenon may be more appropriate than the phase modulation representation. As was previously mentioned, this is because it places only a single pair of symmetric sidebands per travelling wave mode number k as opposed to multiple sidebands per travelling wave mode number k .

As a final check the expression was used to plot the frequency response for a tuned system with a single k -value of zero. It is therefore expected that the sidebands occur about every third engine harmonic (at the BPF).

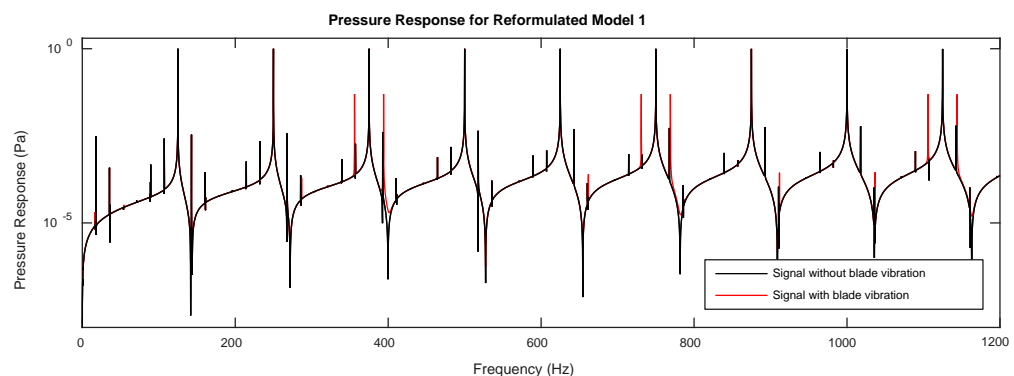


Figure 2.3-14 Pressure response for reformulated Model 1 with $k=0$ using amplitude modulation

It can be seen that the final form of the expression, Equation [2.3.31], best describes the pressure distributions behaviour when reviewing it from a Model 1 perspective.

2.4. Blade Vibrational Response Representation

Being able to represent a blade's behaviour accurately is an integral part of the pressure signal representation. Most research has suggested that simply fitting a SDOF sinusoid to the blade response is sufficient. A more advanced technique was proposed by Forbes et al. whereby the blade is represented by a single spring-mass-damper (SMD) system (Forbes and Randall, 2013). The SMD is based upon the geometric and material properties of a single blade. The response of this representation to a forcing function is then used to create the blade's forced response.

Multiple alternative representation techniques have been considered for the purpose. They include the use of a full dynamic FE model to represent the blade geometric and material properties along with a time based integration scheme to obtain the systems response to a harmonic input. Alternatively the blades are represented as simplified Euler-Bernoulli beams, the same time domain integration procedure would be required to obtain the system's response in this case.

We have assumed that the pressure profile about the casing inner wall, in line with the rotor and hub assembly, is influenced solely by the blade tip's behaviour. It is therefore believed that a full FE or Euler-Bernoulli approach, which requires time domain integration, may be too costly or complex to employ as a response representation for use in an inverse problem scenario.

A lumped mass model approach would also not be appropriate as we are only interested in individual blade tips local effect on the pressure distribution, the physical coupling of blades is therefore believed to be inconsequential for this purpose because it can be modelled as separate to the whole system.

The question must be asked what can be gained by modelling a blade as a multiple degree of freedom (MDOF) system as opposed to the first two systems suggested (SDOF sinusoid or SMD system).

Firstly under forced response the blades are not being excited strictly by a sinusoidal or harmonic force acting at a single frequency. The excitation, impingement of the blades by upstream stator wakes, is more closely matched to an impulse excitation which occurs at the blade passing frequency (BPF). Thus, it is believed that in addition to being excited at all engine harmonics, broad spectrum energy is entering the system via various excitation mechanisms.

Further the blade and hub assemblies are never perfectly tuned and so will be influenced by all of the rotor harmonics to differing degrees. It can be seen that a SDOF sinusoidal model will not be able to capture the response to multiple excitation frequencies simultaneously.

The SDOF SMD system, suggested by Forbes et al., captures the response more closely to reality when compared to the SDOF sinusoidal model. This is because it is based directly on the blades geometry and material properties (Forbes and Randall, 2013). It is capable of representing the response to a range of input frequencies as well as broad spectrum energy entering the system through additional sources of noise.

However a SDOF SMD system only facilitates estimation of a single natural frequency, therefore the frequency response function (FRF) for the blade will have a single peak at the fundamental frequency and then taper off. The true FRF will have additional peaks related to the remaining natural frequencies across the full excitation region. This is important because we assumed that excitation occurs over a large frequency range at multiples of the shaft speed (due to impingement of upstream stator wakes) as well as due to broad spectrum noise.

Excitation at rotor harmonics will inherently lie near to the additional natural frequencies. Their interaction with the system supplies unique information to the individual blade's response. They will therefore have a unique effect on the pressure spectrum. Further, the relative response magnitudes at all engine harmonics follow the form of the blade's FRF and so by inclusion of additional natural frequencies the response magnitudes of each engine harmonic will be more closely related to the true response nature. The inclusion of this unique blade behaviour information may be able to be used to separate it from the complex pressure distribution.

Reconstruction of full FRFs, by adding individual SDOF FRFs, has been widely used in experimental modal analysis. Methods such as the Ewins-Gleeson, peak-picking and circle fitting algorithms, among others, have been proposed for this purpose (Ewins and Gleeson, 1982; Ewins, 1995; Kennedy and Pancu, 1947).

An approach based on adding a certain number of individual SDOF FRFs to represent a chosen number of modes is therefore suggested. The number of SDOF systems included depends on which modes are expected to have a significant influence on the blade response. In the literature reviewed it was found that only the first few modes and associated mode shapes play a significant role with respect to blade vibration, therefore a natural limit to the number SDOF FRFs added to the model exists.

We start our derivation by stating that the time domain tip response is the inverse Fourier transform of the frequency response, this is given in Equation [2.4.1].

$$x(t)_r = \mathcal{F}^{-1}(X(j \cdot \omega)) \quad [2.4.1]$$

The blade response in the frequency domain is simply the convolution of the blade's transfer function H and the forcing function F . This is indicated in Equation [2.4.2].

$$\{X(j \cdot \omega)\} = [H(j \cdot \omega)] \cdot \{F(j \cdot \omega)\} \quad [2.4.2]$$

The blade transfer function and forcing function will be tackled separately. We start with the blade displacement transfer function, represented as the sum of individual SDOF FRFs, in Equation [2.4.3].

$$H(j \cdot \omega) = \sum_{r=1}^N \frac{A_r}{\omega_r^2 - \omega^2 + j \cdot \eta_r \cdot \omega_r^2} \quad [2.4.3]$$

The formulation assumes a system with structural damping. Each individual mode has a modal damping ratio of η_r . The natural frequency of each mode is ω_r and the modal constants A_r scale the amplitude of each mode in the sum.

The modal damping ratio can either be assumed given the material and geometric properties of the rotor and hub assembly structure, or determined from experimental observations. If experimental modal test data is available then the half power point method described by Ewins may be used to estimate the damping (Ewins, 1995). Modal damping estimation from the half power points is shown in Equation [2.4.4].

$$\eta_r = \frac{\omega_a^2 - \omega_b^2}{2 \cdot \omega_r^2} \quad [2.4.4]$$

The method used to obtain the half power points, ω_b and ω_a , for modal damping constant estimation is shown in Figure 2.4-1.

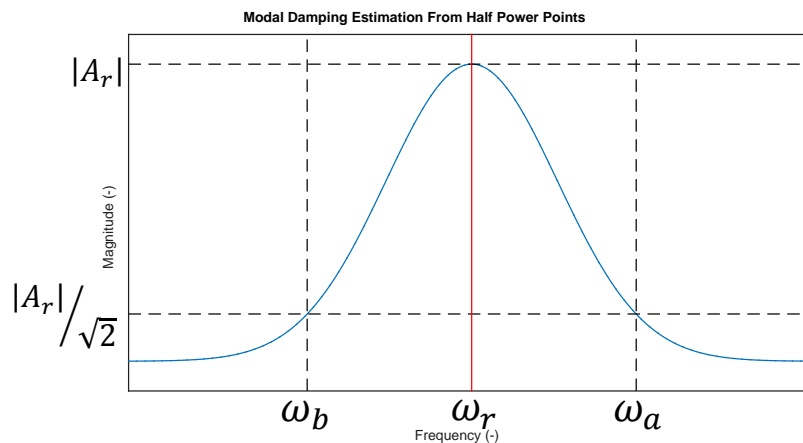


Figure 2.4-1 Modal damping estimation using half power points

As was previously stated, if the modal damping cannot be obtained experimentally then a value must be chosen and tuned according to the material and geometric properties of the blades. The damping however does not change where the resonance peaks lie, and so long as the system is assumed to be lightly damped it is not expected to have a significant impact on the form of the frequency response function (FRF).

An example FRF constructed by using the above proposed methodology is presented in Figure 2.4-2. Three natural frequencies were chosen for demonstration at 128.8 Hz, 710 Hz and 790 Hz. Modal damping for all modes was assumed as 0.01, and the modal constants from modes 1 to 3 were arbitrarily chosen as 1, 0.5 and 0.5.

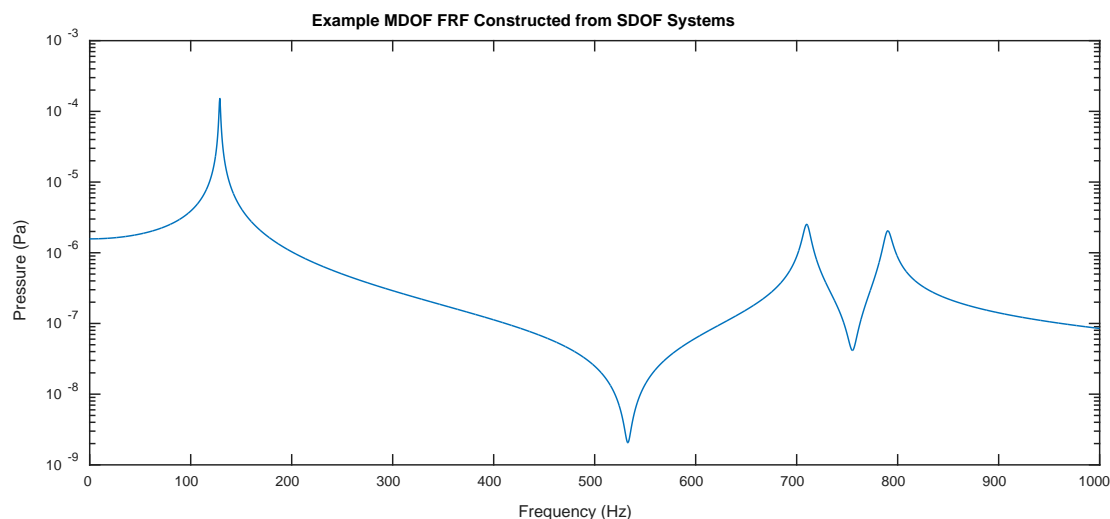


Figure 2.4-2 Example MDOF FRF constructed from individual FRFs

An artefact of the construction methodology is the generation of anti-resonances in between each SDOF system added. Anti-resonances occur in the FRF because the SDOF systems are added at the same phase angle, and at each resonance (and anti-resonance) there is a 180° phase shift. These anti-resonances cause undesirable discontinuities in the FRF which may not be attributed to actual physical behaviour. Therefore, in order to ensure that they do not form each individual receptance must be

added at 180° phase difference to the prior SDOF receptance. This adjustment phase shift to prevent the occurrence of anti-resonances has been included in Equation [2.4.5].

$$H(j \cdot \omega) = \left(\sum_{r=1}^N \left(\frac{A_r}{\omega_r^2 - \omega^2 + j \cdot \eta_r \cdot \omega_r^2} \right) \cdot e^{j \cdot \pi \cdot \text{mod}(r,2)} \right) \cdot e^{j \cdot \chi} \quad [2.4.5]$$

The function $\text{mod}(r, 2)$ is a remainder function and returns a 1 if r is even or 0 if r is odd. The blade response phase angle χ has also been included in the formulation so that it can be adjusted accordingly, the phase angle is limited to the range $\chi \in [-\pi, \pi]$.

An anti-resonance free example, using the above mentioned method, is given in Figure 2.4-3.

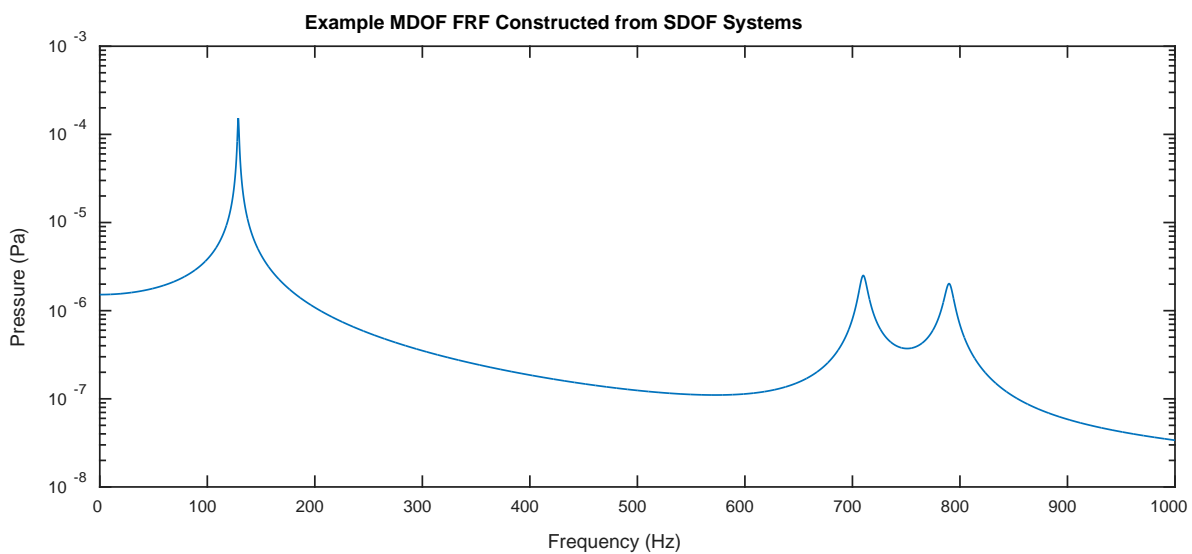


Figure 2.4-3 Example MDOF FRF constructed without anti-resonances

A problem still exists with the above system. Even if the three resonance peak amplitudes are correctly scaled with respect to their relative heights on the FRF, their absolute magnitude with respect to unit input force is still unknown.

When obtaining a receptance from an analytical study the modal constants are obtained from the system mode shapes (or via the eigenvectors obtained when solving the eigen-problem with the mass, stiffness and damping matrices for the numerically derived case).

In terms of experimental modal analysis, the receptance peak heights (modal constants) can be obtained directly from the experimentally obtained FRF. If the input force is known (as is the case when the system is excited with a modal hammer) the response in terms of force can be obtained. This information is however unknown for the system developed thus far.

In this case a scaling factor can be estimated from a SDOF spring-mass-damper (SMD) approximation or FE analysis of a blade. This scaling factor can then be used to adjust the global FRF's heights appropriately. The SDOF transfer function for a SMD system is repeated in Equation [2.4.6].

$$H(j \cdot \omega)_r = \frac{1/k_r}{(\omega_r^2 - \omega^2) + j \cdot \eta_r \cdot \omega/\omega_r} \quad [2.4.6]$$

The scaling factor is represented by τ in the final form of the system FRF.

$$H(j \cdot \omega) = \tau \cdot \left(\sum_{r=1}^N \left(\frac{A_r}{\omega_r^2 - \omega^2 + j \cdot \eta_r \cdot \omega_r^2} \right) \cdot e^{j \cdot \pi \cdot \text{mod}(r,2)} \right) \cdot e^{j \cdot \chi} \quad [2.4.7]$$

$$\tau = \frac{|\hat{H}_1|}{A_1} \quad [2.4.8]$$

The parameter $|\hat{H}_1|$ is the fundamental peak height obtained from a SDOF blade approximation.

The next concern is how to represent the blade forcing function. It is important to note that the blade transfer function describes the blade's physical response with respect to a unit harmonic input force. Therefore the forcing function model used must be harmonic in nature.

Forbes et al. described the input force using a Fourier series (Forbes and Randall, 2013). The Fourier series is inherently a sum of harmonic terms and so is a good choice to describe the input force from a formulation point of view.

In the work of Forbes et al. it was stated that the Fourier coefficients can be chosen such that any excitation shape can be obtained, however no indication as to the shape that was used to model the input force simulated for Model 2 was provided (Forbes and Randall, 2013). An appropriate input forcing shape model is therefore sought.

As the blades pass through an upstream wake the force applied by the upstream wake is expected to increase (due to a larger amount of the flow being present on the blade's surface). The force is expected to peak when all of the flow from the upstream stator is being directed onto the blade. Once the blade starts to move beyond the stream the force applied by that individual stream is once again expected to decrease. A method to describe this phenomenon is required.

It is proposed that the periodic input force be modelled as a sum of individual univariate Gaussian distributions in the time domain. Each time a blade passes an upstream stator wake a Gaussian shaped force distribution is applied to a blade (with respect to time). This will provide the expected force increase, peak and decrease. A Fourier transform can then be applied to the time domain forcing function signal in order to convert it to a harmonic form. The univariate Gaussian distribution with mean μ and standard deviation σ is given in Equation [2.4.6].

$$g(t|\mu, \sigma) = \left(\frac{1}{\sigma\sqrt{2 \cdot \pi}} \right) \cdot e^{-\frac{(t-\mu)^2}{2 \cdot (\sigma)^2}} \quad [2.4.9]$$

The forcing pulse signal is therefore the sum of the individual Gaussians. The periodic force with respect to time is provided in Equation [2.4.10]. For simplicity the force applied by each upstream stator is assumed to be equivalent. This assumption is addressed further on.

$$g(t|\mu_i, \sigma) = \sum_{i=1}^n \left(\frac{1}{\sigma\sqrt{2 \cdot \pi}} \right) \cdot e^{-\frac{(t-\mu_i)^2}{2 \cdot (\sigma)^2}} \quad [2.4.10]$$

It is proposed that the standard deviation of the Gaussian is to be a function of the rotor speed and the angle through which the blade passes the upstream stator wake. Thus as the rotor speed increases the amount of time that the force is applied to the blade, per upstream stator, decreases as is expected. If the maximum height of the Gaussian sum is limited to unity then as the speed approaches infinity the individual input forces approach unit impulse excitation.

The use of a Gaussian has an added advantage. For very closely packed blades, as is the case on a real rotor, two adjacent blades may be experiencing flow from the same upstream stator at particular time. Only the magnitude of the force applied to each blade by the stream would be different. The force depends on the position of the blades as they move past the stator. The leading blade will start to experience flow from the upcoming stator before the lagging blade does. Representing the force acting on the blades as Gaussians facilitates simple mixing of the forces acting simultaneously on an individual blade.

For steady operation and blades experiencing flow from multiple upstream stators simultaneously the force on the blades should never drop to zero (as a force is being constantly applied to the blade). Had the system been modelled as a set of impulses the forces acting on the blade would however always return to zero, and as per the argument this is not expected in practice.

If the blades are very closely packed then the angle through which each blade will be excited by each upstream stator can be estimated as the circumference divided by the number of blades. This relation is given in Equation [2.4.11].

$$\theta_{blade} = \frac{2 \cdot \pi}{B} \text{ rad} \quad [2.4.11]$$

If the blades are not closely packed (for example when using an experimental hub and blade assembly with a large angular spacing between blades) the angle must be estimated using a different approach.

An estimate can be obtained by using the radius from the center of the shaft to the tip, R , and the effective tip chord length C' . The effective chord length is a function of the chord length and the stagger angle γ . The alternative relation is given in Equation [2.4.12].

$$\theta_{blade} = 2 \cdot \sin^{-1} \left(\frac{C'}{2 \cdot R} \right) = 2 \cdot \sin^{-1} \left(\frac{C \cdot \sin(\gamma)}{2 \cdot R} \right) \text{ rad} \quad [2.4.12]$$

Finally the standard deviation can be calculated using the above derived angle and the rotor speed Ω . It is chosen that the standard deviation be half the amount of time that it takes the blade to pass through the wake. This is done so that approximately 95% of the force is applied over the duration that it takes a blade to move through the angle θ_{blade} (all of the force is applied within two standard deviations).

$$\sigma = \frac{\theta_{blade}}{2 \cdot \Omega} \quad [2.4.13]$$

The last step in the formulation of a time based forcing function is to specify the mean values for each of the normal distributions. This is simply the set of the blade passing times, which is a direct function of the blade passing frequency.

The blade passing frequency (BPF) can be calculated by multiplying the number of upstream stators V by the rotor speed in Hertz. Thus an excitation time point for each upstream stator has been established. The relation for the time points at which the blades pass the upstream stator vanes is provided in Equation [2.4.14].

$$\mu_i = i \cdot f_{BPF} = i \cdot V \cdot f_R \quad [2.4.14]$$

The parameter i is simply a counter restricted to the positive set of integers.

Equation [2.4.9] has been used to create an exemplar periodic force model based on Gaussian distributions. The blade forcing function has a blade passing frequency of 16 Hz and the standard deviation of the Gaussians is 0.00625 seconds. The example is illustrated in Figure 2.4-4.

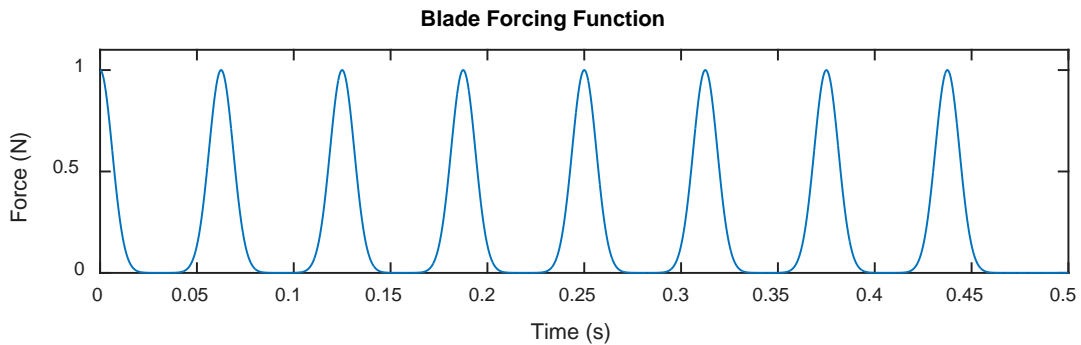


Figure 2.4-4 Blade forcing function

Thus far the model has assumed a noise free environment in the casing. This is however not the case in practice. Similar to the model developed by Forbes at al., a Gaussian noise term is simply added to the time based forcing function (Forbes and Randall, 2013). The noise is given by $n(t)$ in Equation [2.4.15].

$$g(t|\mu_i, \sigma) = n(t) \cdot \sum_{i=1}^n \left(\frac{1}{\sigma\sqrt{2 \cdot \pi}} \right) \cdot e^{-\frac{(t-\mu_i)^2}{2 \cdot (\sigma)^2}} \quad [2.4.15]$$

For the same arbitrary forcing example above the effect of noise with a signal-to-noise ratio of 35 on the forcing function has been illustrated in Figure 2.4-5.

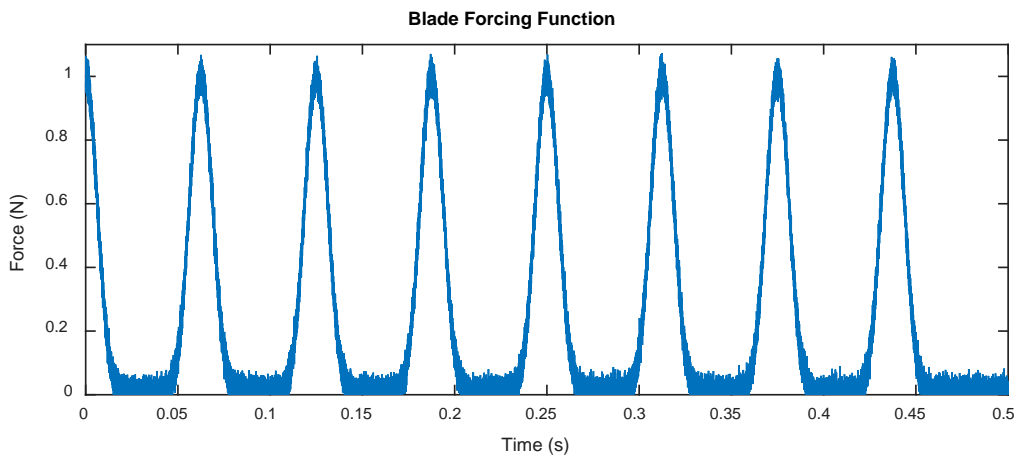


Figure 2.4-5 Blade forcing function with Gaussian noise

A final example of a forcing function, where the force applied by each upstream stator wake is equivalent, is shown in Figure 2.4-6. It can be seen that the forcing function never drops to zero, a constant minimum force is always being applied to the blades along with the force peaks due to passing stator vanes. It is the author's opinion that this would be a valid case in practice when at no point in time is the single blade not experiencing flow from the upstream stators.

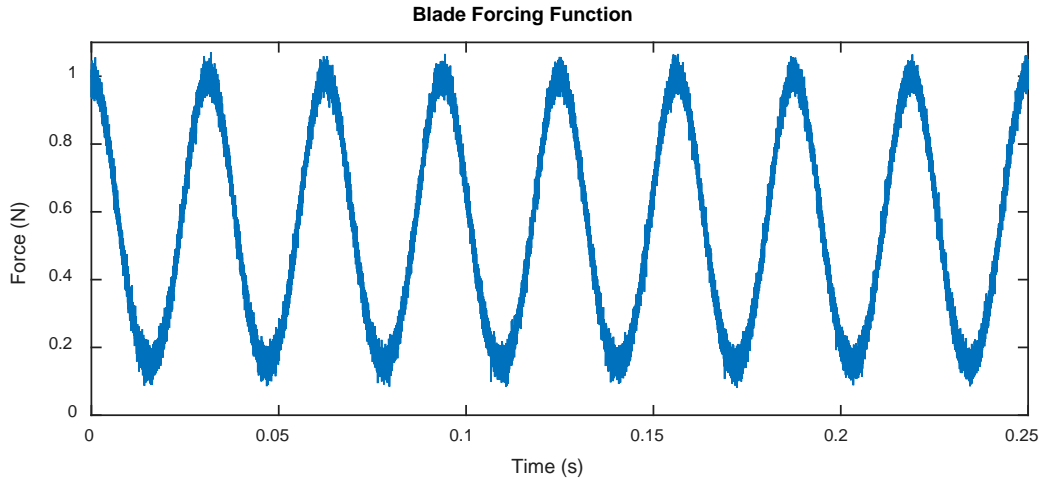


Figure 2.4-6 Blade forcing function with mixing Gaussians

The Fourier transform can now be applied to the time domain signal in order for it to be convolved with the blade transfer function. This is shown in Equation [2.4.16].

$$F(j \cdot \omega) = \mathcal{F} \left(n(t) \cdot \sum_{i=1}^n \left(\frac{1}{\sigma\sqrt{2 \cdot \pi}} \right) \cdot e^{-\frac{(t-\mu_i)^2}{2 \cdot (\sigma)^2}} \right) = \mathcal{F}(g(t|\mu_i, \sigma)) \quad [2.4.16]$$

An example of a force response spectrum for a system operating at 16 Hz, along with the addition of white noise, using the above mentioned formulation is provided in Figure 2.4-7.

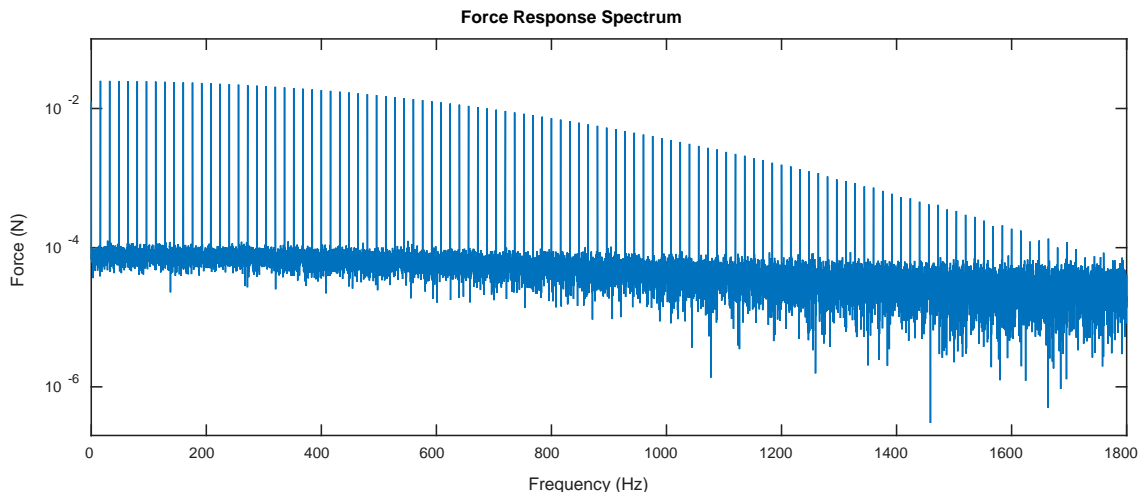


Figure 2.4-7 Force response spectrum for forcing function operating at 16 Hz

It can be seen in the figure that excitation occurs at multiple engine harmonics. It is also interesting to note that the formulation captures a decreasing harmonic force value with a near constant noise floor. The noise added was Gaussian and so the constant noise floor level is expected. The amount of energy

associated with the higher frequency engine harmonic excitation is expected to fall (this has been noted in the literature reviewed). The characteristics of the forcing function are therefore as expected when comparing it to the model derived by Forbes (Forbes and Randall, 2013; Forbes, 2010, p. 152).

The maximum force applied at any point, given in the time domain Gaussian formulation, was 1N. Further the transfer function of the blade is written in terms of expected response to unit harmonic force. Therefore the convolution of the two halves results in a relation which must still be multiplied with an estimation of the true force magnitude in order to obtain the tip response.

A constant phase angle offset χ was included in the blade transfer function formulation. This term can be factored out so that the phase angle of the blade response to the forcing function can be varied with respect to the stationary pressure distribution about the individual blades. These adjustments are included in Equation [2.4.17]. The magnitude tuning parameter is included as M .

$$\{X(j \cdot \omega)\} = M \cdot [H(j \cdot \omega)] \cdot \{F(j \cdot \omega)\} \cdot e^{j \cdot \chi} \quad [2.4.17]$$

Finally, we are interested in the angle that the blades subtend and not the displacement, therefore all that is required is to divide the above relation by the blade length (assuming small angle theory).

$$\{\Psi(j \cdot \omega)\} = \frac{M}{L} \cdot [H(j \cdot \omega)] \cdot \{F(j \cdot \omega)\} \cdot e^{j \cdot \chi} \quad [2.4.18]$$

The parameter Ψ is the blades angular displacement in the frequency domain. An example of a blade tip frequency response spectrum, using the same blade transfer function as before for response to a forcing function of the form described above (operating at 16 Hz), is shown in Figure 2.4-8.

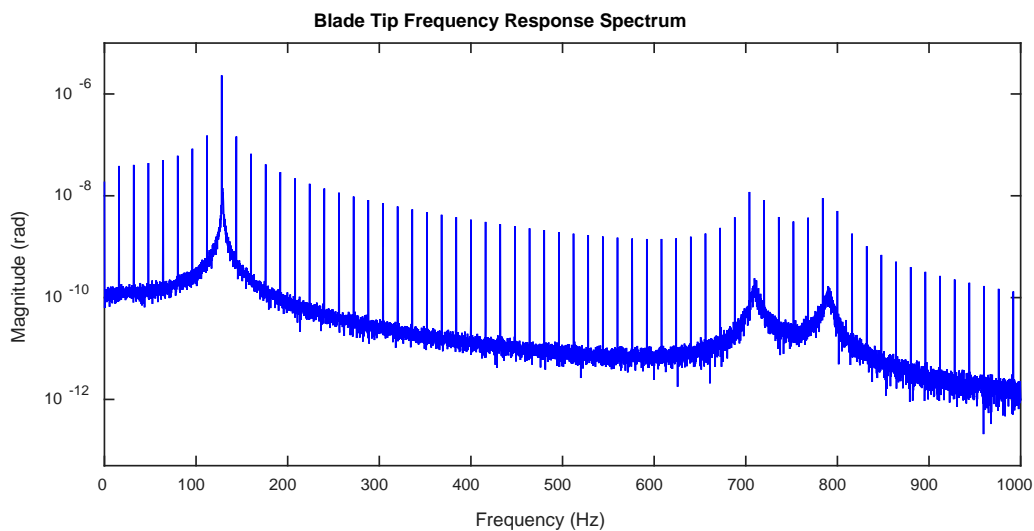


Figure 2.4-8 Blade tip frequency response spectrum to Gaussian based input force

It can be seen in the figure how the blade transfer function and forcing function interacts across the frequency domain of interest. Further, the addition of Gaussian noise to the system has made the original form of the blade transfer function apparent.

It is important to consider the case where the upstream stator wakes do not apply the same force, as may be the case in practice. The assumption that the upstream stators apply the same force (for the sake of simplicity) was previously mentioned. Comparison of this model with actual on blade

measurements will then allow verification of this model’s predicted forcing behaviour in both the time and frequency domains. Differences in the forces applied by the streams are attributed to manufacturing tolerances and unique geometric and operating conditions within the turbomachine.

Consider the hypothetical case of a rotor with two upstream stators. The second stator is assumed to provide exactly half the force of the first. Once again Gaussian noise has been included in the signal illustrated in Figure 2.4-9.

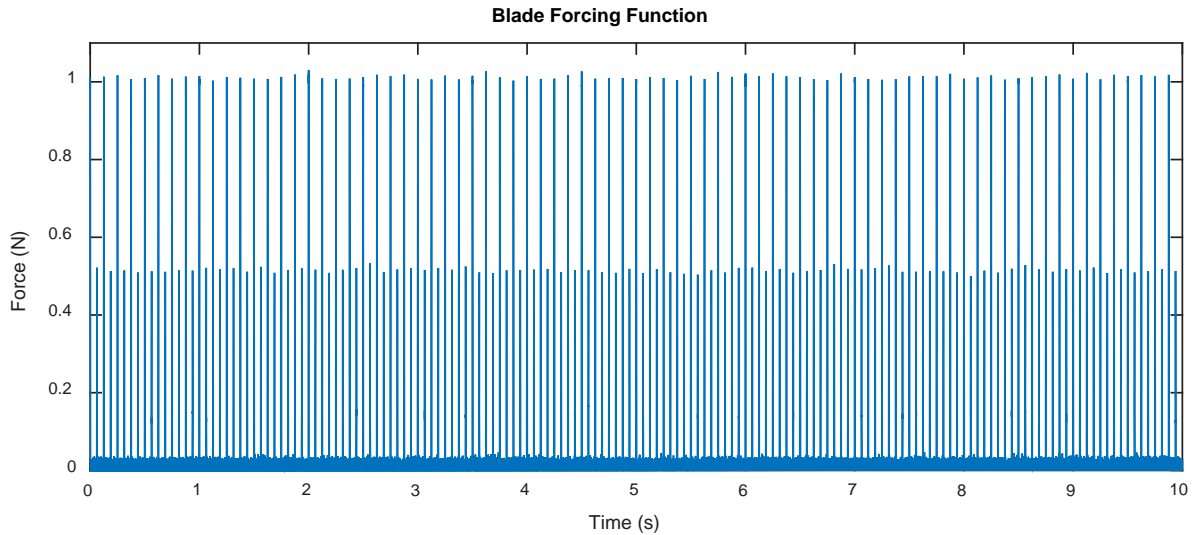


Figure 2.4-9 Time domain blade forcing function with two upstream stators with difference force values

In the frequency domain it can be seen that every second rotor harmonic occurs at a reduced magnitude when compared to the ideal case where all forcing wakes apply the same force. This is illustrated in Figure 2.4-10.

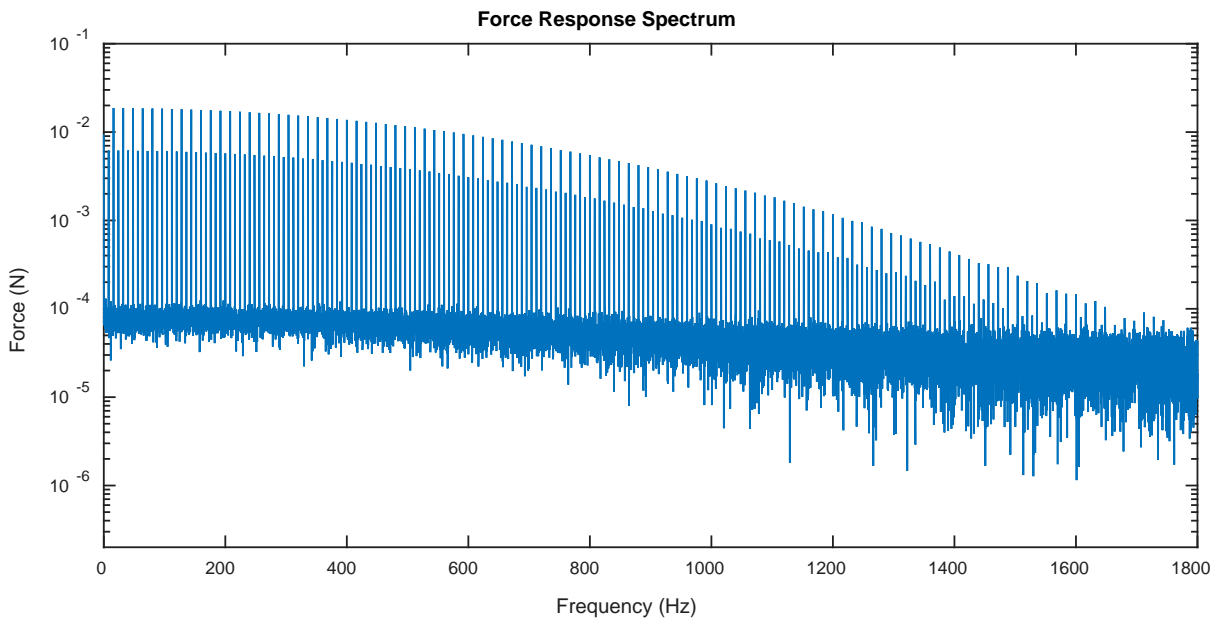


Figure 2.4-10 Frequency domain blade forcing function with two upstream stators with difference force values

A further layer of complexity can be added by increasing the number of upstream stators to 4 and randomly assigning a force value for each for investigation. A section of the time domain forcing

function for the case of stators 1 to for supplying force values of 1 N, 0.53 N, 0.81 N and 0.68 N respectively is shown in Figure 2.4-11. Once again Gaussian noise has been included in the model.

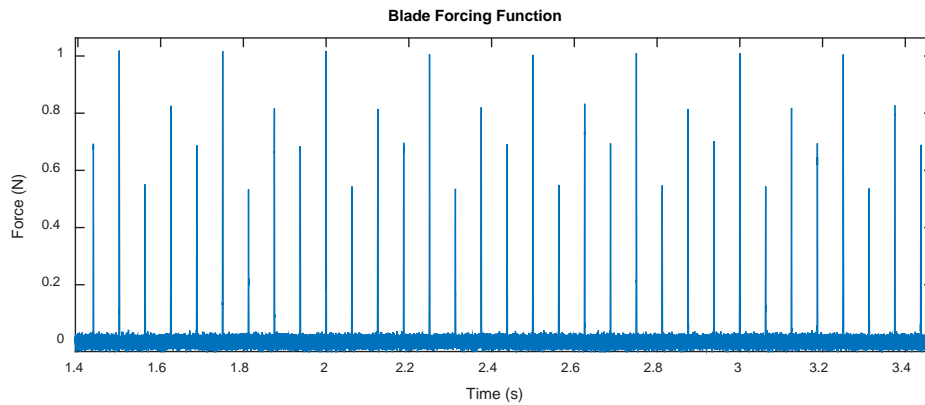


Figure 2.4-11 Time domain blade forcing function with four upstream stators with difference force values

The frequency representation of the same forcing function is shown in Figure 2.4-12.

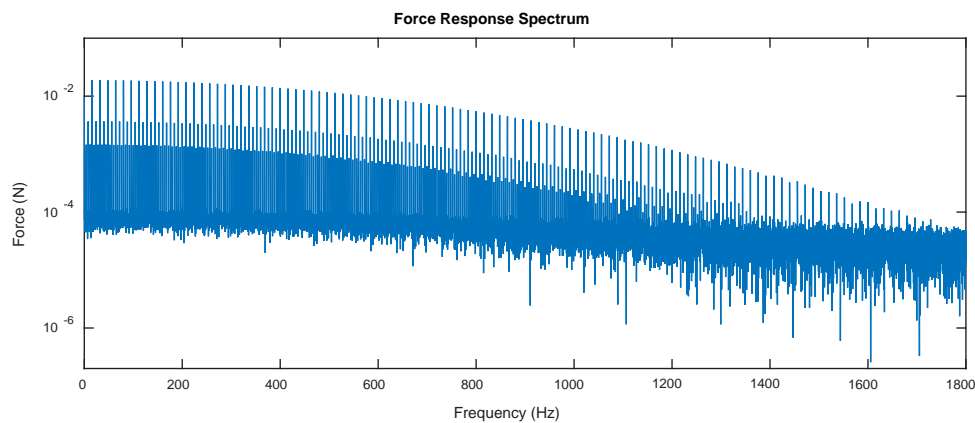


Figure 2.4-12 Frequency domain blade forcing function with four upstream stators with difference force values

A closer look at the frequency response is provided in Figure 2.4-13.

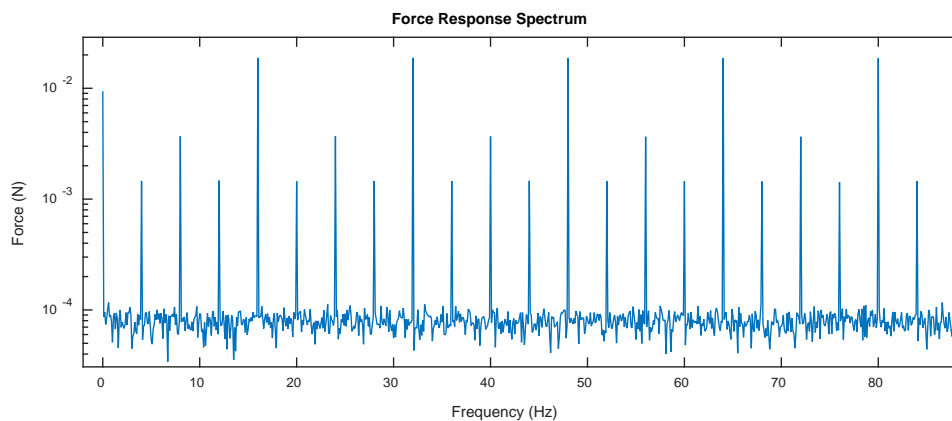


Figure 2.4-13 Zoomed in frequency domain blade forcing function with four upstream stators with difference force values

It can be seen that the order in which the force peaks change remains constant in the frequency domain. Thus the force from each individual upstream stator and the order in which the force changes can be identified.

Finally geometric differences in the construction of the stator row results in a case where each upstream wake impinges on the blade slightly sooner or later depending on the assembly's geometry. An exaggerated time domain representation of this scenario is given in Figure 2.4-14.

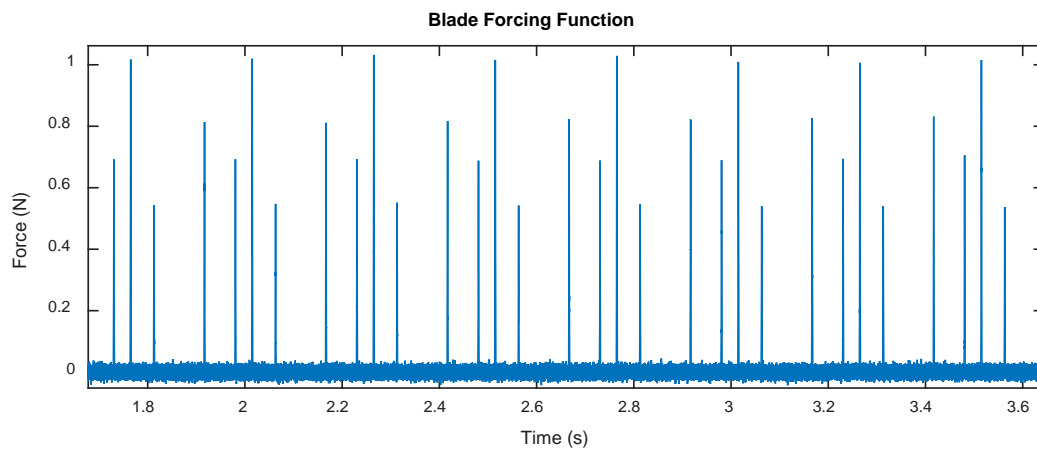


Figure 2.4-14 Time domain blade forcing function with four upstream stators with difference force values for an asymmetric rotor

The equivalent frequency domain representation of the forcing function is supplied in Figure 2.4-15.

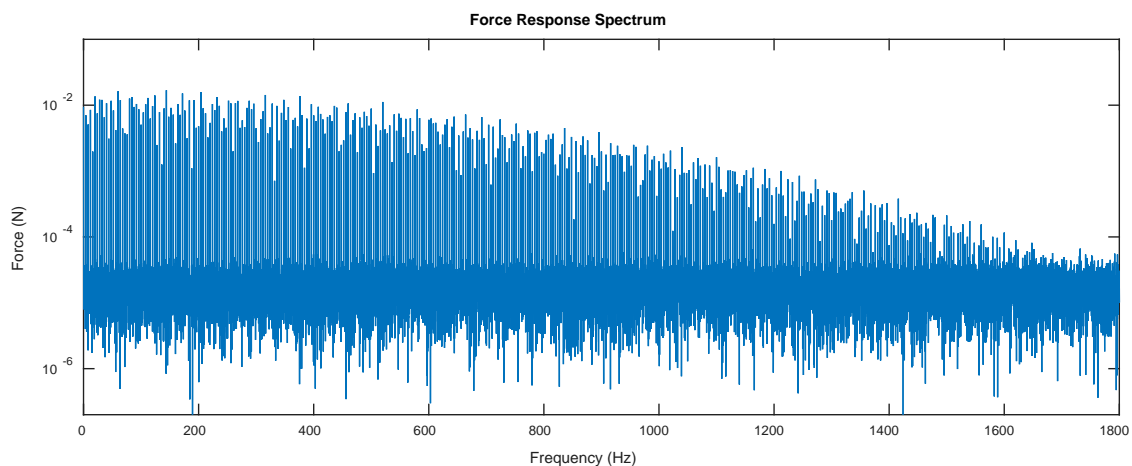


Figure 2.4-15 Frequency domain blade forcing function with four upstream stators with difference force values for an asymmetric rotor

Once again a closer look at the frequency domain reveals the effects of the asymmetry.

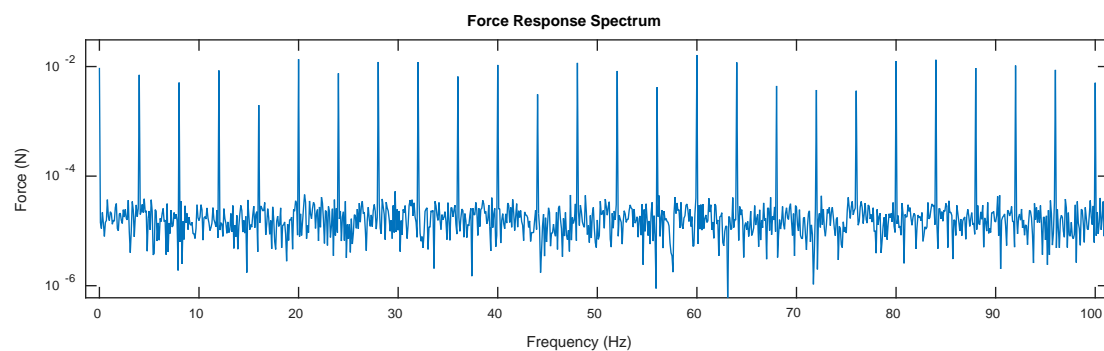


Figure 2.4-16 Zoomed in frequency domain blade forcing function with four upstream stators with difference force values for an asymmetric rotor

The order in which the blade is impinged upon by the upstream stators is no longer easily identifiable from the FRF by simple visual inspection. The trend has been destroyed by the exaggerated differences. The above FRF convolved with the previously employed blade transfer function is shown in Figure 2.4-17.

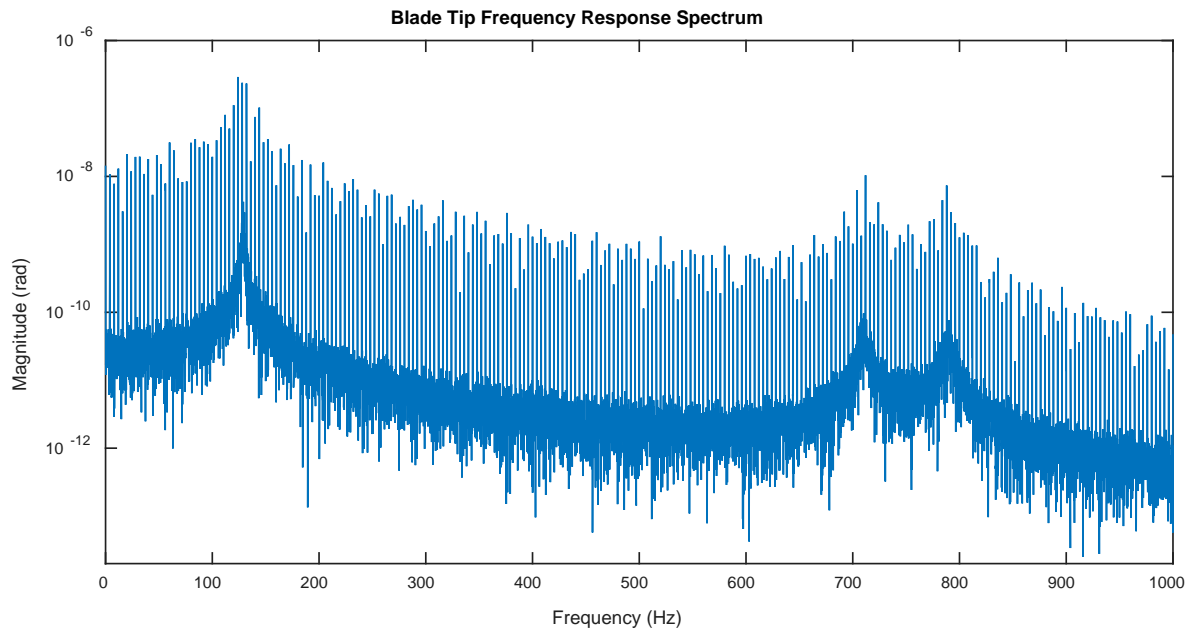


Figure 2.4-17 Combined blade tip response for excitation at different forcing values in a stemming from an asymmetric upstream stator row

Although the forcing function is highly erratic, the form of the response FRF clearly follows the blade transfer function.

As was previously stated, within a real turbomachine stator rows are not expected to be perfectly symmetric. Further, each stator stream is expected to apply a slightly different nominal force due to geometric differences in the upstream stator row. Small fluctuations in the nominal force are attributed to noise in the stream. By allowing modification of each stator wake may provide a better model fit when comparing it to actual forcing conditions within the rotor.

The representation discussed above is just a model of the physical blade response based upon observations and insight from literature reviewed. Only experimental investigations which directly measured the blade's response to the upstream stator wakes will be able to confirm or refute the applicability of this model. They will be able to answer questions such as: is the model flexible enough to be fitted to actual data? How sensitive is the model to slight variances in initial condition guesses? An experimental investigation which explores the validity of this model is provided in section '4.2 Observations from SG Measurements'. The investigation also focuses on the same aspects, however for the blade transfer function model.

It is believed that by using the tuning parameters carefully the above system, in terms of both the MDOF blade transfer function and the proposed blade forcing function, can be successfully modified to represent an accurate response of blade to upstream stator wakes. However, as has been stated, only numerical and experimental investigations will be able to tell.

2.5. Individual Wave Separation through Novel Time-Domain Windowing

The individual waves, associated with the passing of single blades, may contain discernible blade behaviour information from one another in the time and frequency domains. This was shown in the work of Mathioudakis and predicted by the works of Mengle and Castanier et al. (Castanier and Pierre, 2006; Mathioudakis et al., 1991; Mengle, 1990).

Specifically Mathioudakis showed that changing an individual blade's stagger angle or surface condition directly alters the form of the passing wave (Mathioudakis et al., 1991). Phenomena related to this may be observed through visual inspection of the passing wave forms or associated response spectra (Mathioudakis et al., 1991).

According to the work of Mengle, depending on the level of mistuning and excitation conditions each blade, or symmetric section of blades, could be responding at different phase angles even if they are responding at the exact same frequency (Mengle, 1990). When taken in the light of the work by Forbes et al. this phase angle difference may affect when each individual stationary pressure distribution, about a blade, arrives at a stationary observer on the casing (Forbes and Randall, 2013). This effect is however much more subtle than those expressed by the work of Mathioudakis (Mathioudakis et al., 1991).

With respect to the work of Castanier et al. mistuning may cause mode localisation which directly affects the response amplitude of each blade (Castanier and Pierre, 2006). A mistuned blade may be responding at a completely different amplitude when compared to the mean response amplitude of all of the blades. Thus by separating the pressure distribution about each blade each response amplitude may be individually observed, which would not be possible without a wave separation methodology.

Thus the individual pressure distributions about individual blades may provide insight into the blades' response phase angles, amplitudes of response and geometric tip conditions. A means to separate the wave forms about individual blades is sought for two reasons. Firstly in order to investigate the wave forms about individual blades to obtain individual blade behaviour information, and secondly for the purpose of modelling a response spectrum.

In signal processing a window refers to an interval about which the signal is forced to zero. A function is generally used to shape the transition from the window boundary to the interior of the window. Windowing has applications in statistical analysis of large datasets, spectral analysis and filter design to name a few. It can help emphasize or clarify otherwise hidden components of a signal. They may be used when only a short length of signal exists which is not perfectly periodic causing errors when transforming it to the frequency domain.

Depending on the choice of window it may influence the signal's frequency content, amplitude content or both. Windowing may also cause or reduce a phenomenon known as spectral leakage. Spectral leakage is the phenomenon whereby energy associated with specific frequency content is artificially spread across a wider frequency band resulting in errors in the observed spectrum.

Therefore a window must be carefully selected depending on the intended application. For our purpose windowing will be used to isolate specific periodic time-domain information. It is intended to have a minimal impact on the amplitude and frequency content of the signal whilst simultaneously minimising spectral leakage.

A rectangular window is the simplest form of window. Outside of the window domain all of the sample points are simply replaced by zero values whereas within the window domain the signal is multiplied by unity (remains unchanged). An example of an arbitrary rectangular window is presented in Figure 2.5-1.

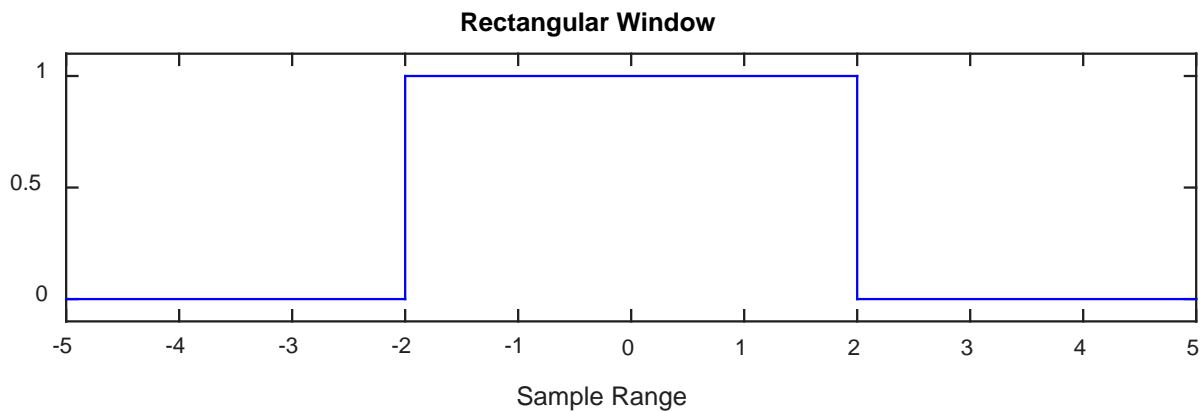


Figure 2.5-1 Example of a rectangular window

As discussed in the work of Murray and Key, a rectangular window may introduce undesirable effects in the frequency spectrum due to the abrupt change at the boundaries (Murray and Key, 2015). It is for this reason that smooth transition windows have been designed.

A rectangular window however does not attenuate the amplitude content of a signal, this is a desirable facet of the window. We therefore desire a window with a controllable and continuous smooth transition from the boundary to an interior with a ‘flat top’ of unity magnitude.

Combination windows which provide the ‘flat top’ associated with the rectangular window and a smooth controllable boundary have been designed. Depending on their design they may provide a best compromise situation between amplitude attenuation and spectral leakage whilst still providing an acceptable frequency resolution for certain applications.

Generally windows are symmetric about their center. They often have a single tuning parameter which provides control over the symmetric window shape by changing the boundary slopes. Further, they are frequently defined using piecewise functions which can make direct implementation tedious.

Once a time domain window has been generated the component wise product of the window and the signal in the time domain will result in the windowed signal. The process may also be used in the frequency domain by the convolution of the window spectrum and original signal’s spectrum. The time domain implementation is illustrated in Equation [2.5.1].

$$\bar{f}(t)_i = W(t)_i \cdot f(t)_i \tag{2.5.1}$$

Each component of the original signal $f(t)$ is operated on individually by the window $W(t)$. The parameter i is just the index of the vectors.

Unlike window functions in general, it is desired that the solution chosen facilitates independent control over the left and right window slope gradients. This will enable isolation not only of individual pressure blade waves, but portions of individual pressure blade waves as well. It is also desired that a continuous function which describes the entire window be chosen for implementation simplicity.

A class of functions exist known as sigmoid functions. They are able to generate an ‘S’ function shape where the slope, height and abscissa midpoint of the curve are all controllable. The logistic function, presented in Equation [2.5.2], is one such sigmoidal curve (Bishop, 2009, p. 197).

$$l(t) = \frac{h}{1 + e^{-s(t-t_0)}} \quad [2.5.2]$$

The parameters h , s and t_0 control the height, gradient and midpoint of the logistic function respectively. The larger the value of parameter s the steeper the sigmoidal curve. The sigmoid has an initial function value of zero. An example plot of the logistic sigmoid centered at zero and with a slope parameter of 2 is given in Figure 2.5-2.

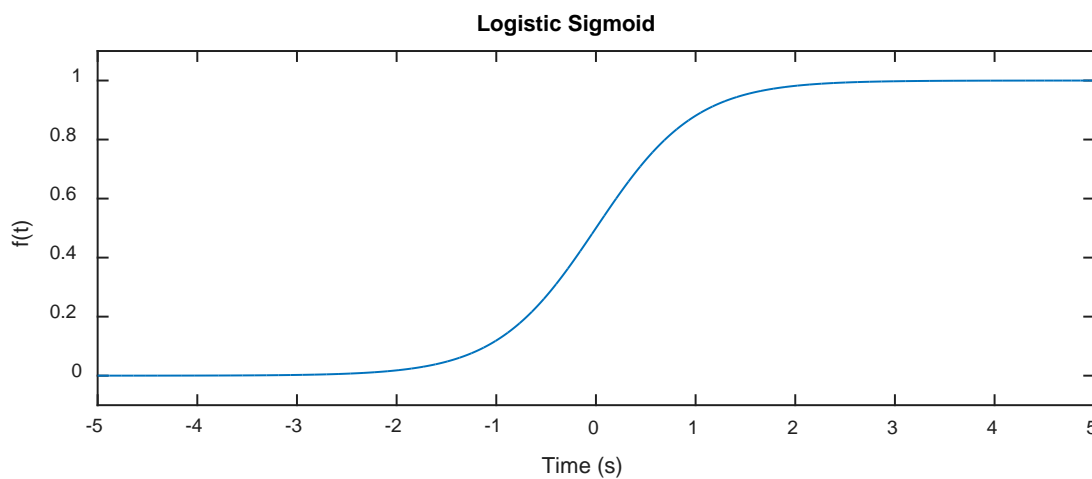


Figure 2.5-2 Logistic sigmoid

It is proposed that sigmoidal functions can be used to construct a window like signal to isolate passing blade waves and components of passing blade wakes. We are only interested in windows which tend towards an amplitude of unity, therefore the height parameter is simply set to one. A single sigmoid only provides half of the window, therefore a second sigmoid will have to be employed to obtain the right hand side of the window. As was stated, independent control of the window sides is desired, therefore two slope parameters will need to be used.

The center of the two sigmoid functions cannot be at the same location to prevent interference with one another. Therefore in order to define the width of the window an offset will have to be included in the formulation for both halves. If the offset value is equivalent then the sigmoid will be symmetric about its chosen center location. If the offset values are however not equivalent, but the slope parameters are equivalent, then the sigmoidal window will still be symmetric, however no longer about the chosen center time point.

Simply adding two sigmoid functions together will result in the curve no longer starting at zero and peaking at one. All function values will be shifted by the positive height value. This can be simply subtracted from the window signal once it has been constructed. The updated sigmoidal window function is given in Equation [2.5.3].

$$W(t) = \frac{1}{1 + e^{-s_1(t-t_0+\Delta_1)}} + \frac{1}{1 + e^{s_2(t-t_0-\Delta_2)}} - 1 \quad [2.5.3]$$

In the equation $s_{1,2}$ and $\Delta_{1,2}$ control the slope and sigmoid offsets on the left and right hand sides respectively. In this form of the equation if the slope parameters are not chosen carefully the window may not peak at one and severe amplitude attenuation of the signal will result due to the windowing.

An alternative method to normalise the window between 0 and 1 was thus sought. It is therefore chosen to rather subtract the minimum window value from the window signal and then divide all points by its maximum signal value. This effectively forces all values outside of the window boundaries to zero and a peak value of one. This procedure is provided in Equations [2.5.4] and [2.5.5].

$$W_{sigmoid}(t) = \frac{1}{1 + e^{-s_1(t-t_0+\Delta_1)}} + \frac{1}{1 + e^{s_2(t-t_0-\Delta_2)}} \quad [2.5.4]$$

$$W_{norm}(t) = \frac{W_{sigmoid}(t) - \min(W_{sigmoid}(t))}{\max(W_{sigmoid}(t)) - \min(W_{sigmoid}(t))} \quad [2.5.5]$$

An example of a symmetric sigmoidal window, with the center of the individual sigmoids positioned at plus and minus 4 seconds about the center which is at zero seconds is provided in Figure 2.5-3. Both slope parameters have been chosen as 2.

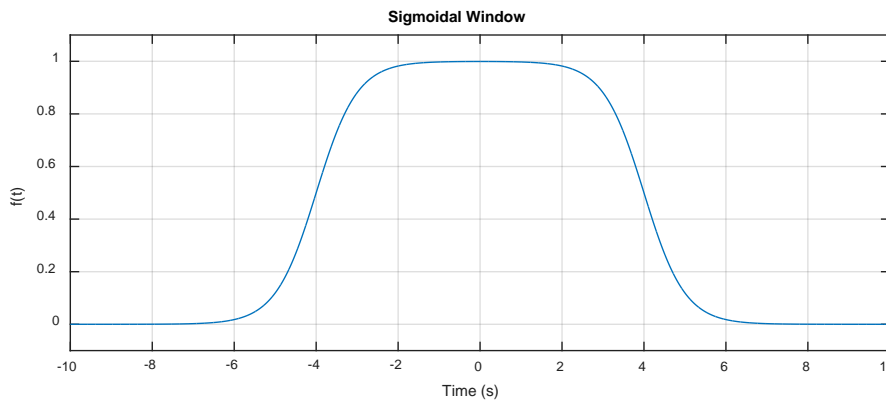


Figure 2.5-3 Sigmoidal window

The shape that the window assumes as the slope parameters approach their limits will now be illustrated. As the slope parameters $s_{1,2}$ approach their upper limit of ∞ the window approaches a rectangular window form. This is shown for a window with $s_{1,2} = 1E4$ and $\Delta_{1,2} = 1$ s in Figure 2.5-4.

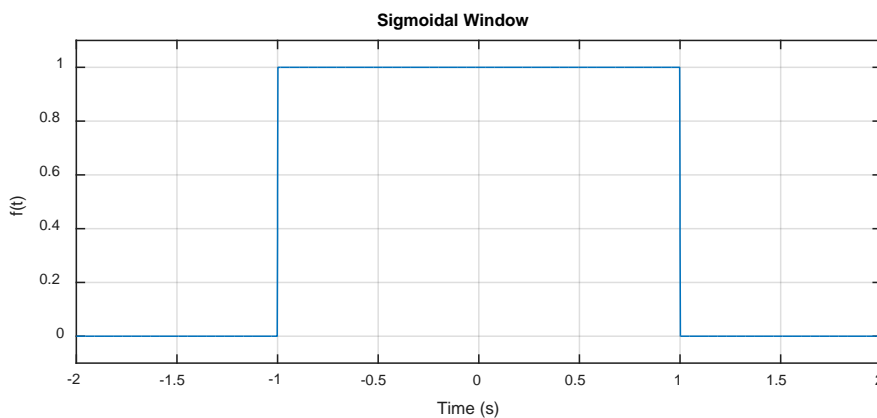


Figure 2.5-4 Sigmoidal window as slope parameters approach ∞

The lower slope limit is zero. A sigmoidal window with slope parameters $s_{1,2} = 0.33$ and offset of $\Delta_{1,2} = 1s$ is plotted alongside a normalized Gaussian distribution with a standard deviation of 5 seconds in Figure 2.5-5.

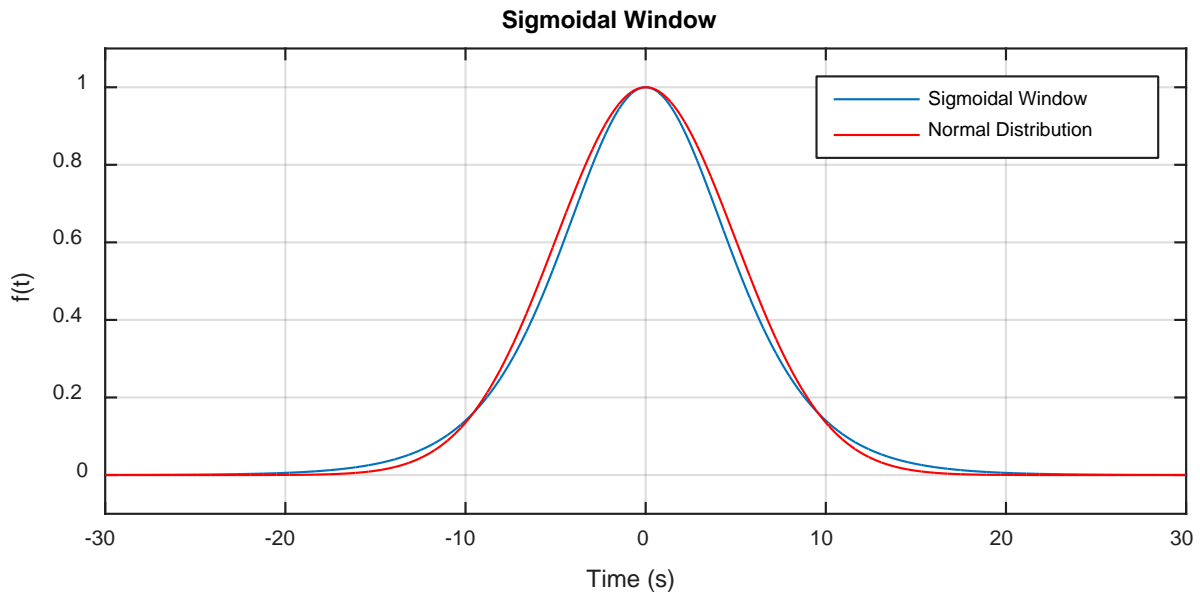


Figure 2.5-5 Sigmoidal window as slope parameters approach zero

It can be seen that as the slope parameters approach zero a bell shaped curve similar to the normal distribution is achieved. It is important to note that normal distributions have been successfully used as windowing functions.

The individual blade pressure waves pass the stationary casing observer once every revolution. Therefore, depending on the number of revolutions, there will be a number of pressure waves associated with each individual blade. If the wave passing times can be determined then a window like function can be constructed to capture all of the passing waves associated with the behaviour of an individual blade. This signal can then be used for spectral and/or other analysis purposes.

Therefore the final step in the window generation process is to add all of the individual windows for all of the blade passing times of interest. The final form of the windowing function is presented in Equations [2.5.6] and [2.5.7]. The individual blade passing times are given as $t_{0,i}$ in the expression and the number of revolutions by N_{rev} .

$$W_{sigmoid}(t, t_{0,i}, s_{1,2}, \Delta_{1,2}) = \sum_{i=1}^{N_{rev}} \left(\frac{1}{1 + e^{-s_1(t-t_{0,i}+\Delta_1)}} + \frac{1}{1 + e^{s_2(t-t_{0,i}-\Delta_2)}} \right) \quad [2.5.6]$$

$$W_{norm}(t) = \frac{W_{sigmoid}(t) - \min(W_{sigmoid}(t))}{\max(W_{sigmoid}(t)) - \min(W_{sigmoid}(t))} \quad [2.5.7]$$

The offset values $\Delta_{1,2}$ must be chosen in order to capture the maximum amount of information associated with the passing of an individual blade pressure wave. Consider the pressure distribution representation in Figure 2.5-6 for an arbitrary 5 bladed system rotating at Ω .

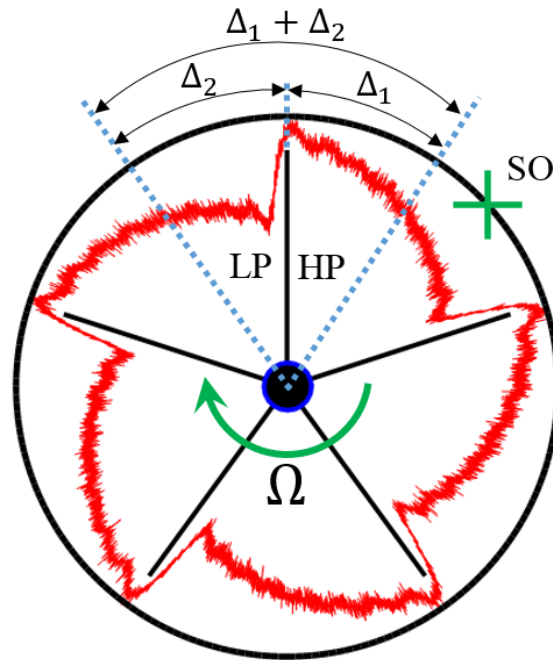


Figure 2.5-6 Individual pressure wave isolation

The stationary observer (SO) will always encounter the HP side of a passing wave first (once again assuming that the turbomachine is operating as a compressor). The HP side will therefore appear as the left hand side of the individual pressure wave in a time domain plot. Similarly the LP side of the wave will appear on the right hand side of the wave. Therefore offset Δ_1 is associated with the HP side and offset Δ_2 is associated with the LP side of the passing pressure waves.

If the entire passing wave for an individual blade is to be isolated then the maximum offset values can be chosen such that the interval about the wave is the same size as the time difference between the passing wave and the next passing wave. This interval has been represented as $\Delta_1 + \Delta_2$ in the figure. The offsets that achieve this are provided in Equations [2.5.8] and [2.5.9].

$$\Delta_1 = \left| \frac{t_{0,i} - t_{0,i-1}}{2} \right| \quad [2.5.8]$$

$$\Delta_2 = \left| \frac{t_{0,i} - t_{0,i+1}}{2} \right| \quad [2.5.9]$$

It may be of interest to determine if the HP wave sides contain different blade vibration information when compared to the LP sides. If the left (HP) side of a passing wave is of interest then the windows can be constructed such that the right boundary slope passes through the middle of the pressure wave, the offset values for left wave side isolation is given in Equation [2.5.10]. Similarly if the right (LP) side of the wave is of interest to isolate then the offset values provided in Equation [2.5.11] can be used.

$$\Delta_1 = \left| \frac{t_{0,i} - t_{0,i-1}}{2} \right|, \quad \Delta_2 = 0 \quad [2.5.10]$$

$$\Delta_1 = 0, \quad \Delta_2 = \left| \frac{t_{0,i} - t_{0,i+1}}{2} \right| \quad [2.5.11]$$

Due to the formulation of the window function, the slope of the window's side that passes through the center of the pressure waves (for separation of the left and right sides of the pressure wave) can be individually steepened. This is done to better separate the left and right halves of the pressure wave. Further, the transition at the outer boundary can remain gradual.

The opinion that individual pressure distributions which form about individual blade tips contain information about that blade's behaviour is supported by the works of both Forbes et al. and Mathioudakis (Forbes and Randall, 2013; Mathioudakis et al., 1991). Whether or not enough unique information exists within this distribution's behaviour of over time in order to estimate blade forced response is however still unknown. Only by experimental investigation can this assertion be validated, although enough evidence exists in order to warrant such a study. Experimental investigations for this purpose can be seen in section '4.3 Pressure Signal'.

A means to isolate waves associated with the passing of individual blades has been suggested. The function proposed generates a window like form about the individual waves of interest. Both slopes on the left and right hand side of the windows are individually controllable. Depending on the choice of slope and offset values a 'flat top' can be achieved for the window which will prevent amplitude attenuation of the pressure wave signal whilst simultaneously providing a smooth transition from the window boundary to the interior.

2.6. Inverse Problem Formulation

Both models and signal processing techniques were developed to describe and isolate the inner casing wall pressure signal associated with turbomachine blade vibration. The purpose of this section is to combine one of the suggested internal pressure models with the blade forced response vibration model and present it in the form of an inverse problem. The goal of solving the entire inverse problem would be to resolve information about the blades' actual behaviour from internal pressure measurements. It is important to note that even though the inverse problem is outlined for a pressure signal, the constituent blade vibration components (blade transfer function and forced response model) may first be fitted in a reduced inverse problem format to actual on blade response measurements. A basic schematic of the inverse problem proposed is presented in Figure 2.6-1.

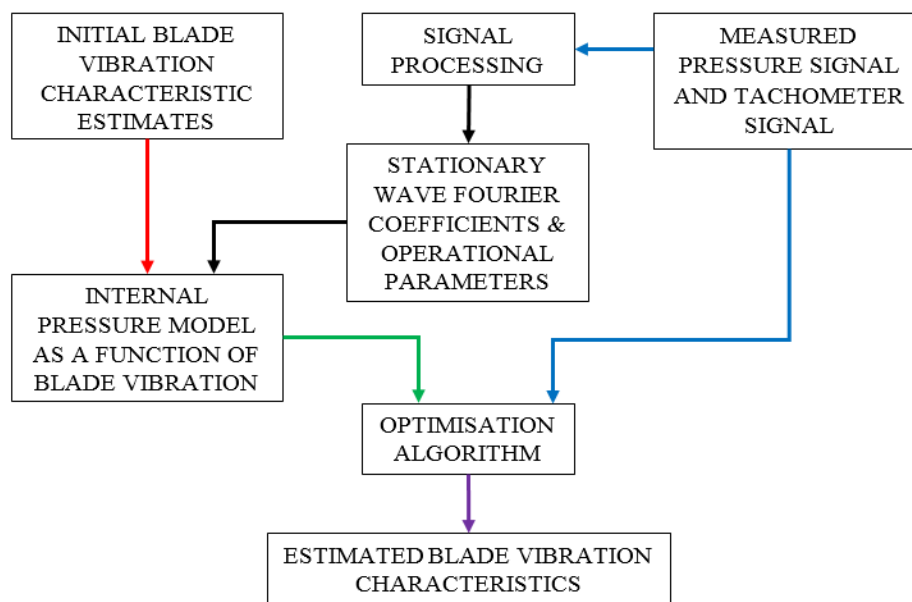


Figure 2.6-1 Schematic of inverse problem

Measured pressure and tachometer signals are used to obtain all unknown parameters associated with the internal pressure model, save those related directly to blade vibration. The full internal pressure model, with unknown blade vibration, is compared with the measured pressure signal using an optimisation based approach.

As was stated, this is done in order to estimate the unknown blade vibration characteristics. The signals are compared by minimising the error difference between the measured and partially artificially generated pressure signals by changing the unknown blade vibration characteristics. The unknown blade vibration characteristics, and the internal pressure model's associated tuning parameters, are the design variables solved for during the resolution of the inverse problem.

Before the inverse problem is formally defined it may be useful to briefly discuss issues associated with the pressure models developed in literature and the suggested reformulated expressions derived from those models.

Model 1 was developed to describe the system's combined blade and hub assembly global pressure response. Depending on the level of mistuning in the assembly and the excitation conditions, certain travelling wave mode components are expected to be present in the global pressure signal. The blade vibration was represented as a SDOF sinusoid with an individual associated flutter frequency ω . This

flutter frequency is Doppler shifted by a certain amount depending on the system mode/modes present (in terms of nodal diameters), the number of rotor blades B and the rotor speed.

The model was shown to be an incomplete representation of the internal pressure signal as it does not account for the presence of all rotor harmonics within that signal. The original representation was reformulated to include both Doppler shifted blade vibration effects and all engine harmonics associated with the passing of all blades.

The blade vibration information, due to Doppler shifting, was represented as modulation of the otherwise stationary pressure signal. The suggested representation of the blade vibration as a modulation effect is based upon the symmetry of the Doppler shifting phenomenon in the frequency domain.

Multiple additional parameters were included to allow freedom for fine tuning of the reformulated model to an actual pressure signal. The specific goal of solving an inverse problem, based on the expression derived from Model 1, would be to obtain the individual flutter frequency ω . The additional tuning parameters are also design variables which must be solved for simultaneously in order to obtain the flutter frequency.

Unlike Model 1, Model 2 was originally developed considering the effect of individual blade vibration on the surrounding pressure wave. The reformulated Model 2 expression provides the pressure response about an individual blade with consideration for both amplitude and phase modulating effects. The model was designed for forced response conditions as opposed to self-excited flutter.

Once again tuning parameters were included to allow fine tuning of the model with respect to an actual measured pressure signal. The model was designed to facilitate any blade tip forced response model. Whether that model is a SDOF sinusoid, a dynamic FE model or constructed using experimental modal analysis techniques is irrelevant in terms of the full pressure model's formulation. All that is required from the model is a time domain tip forced response signal. This investigation will however only consider the blade tip response modelled using the repurposed experimental modal analysis technique described in a prior section.

The reformulated version of Model 1 is only suitable for solving the global blade and hub assembly's response as opposed to an individual blade response. This is because it was designed taking the cumulative system's effect on the pressure signal into account. Model 2 can however be formulated using the pressure wave about an individual blade or about all B blades in the assembly simultaneously.

In terms of the reformulated Model 2 the most important design variables are those associated with the blade transfer function. This is assuming that the experimental modal analysis blade vibration representation is used as opposed to a SDOF representation. The specific design variables contained within the transfer function are the modal damping, modal constants and blade natural frequencies. Once again the remaining tuning parameters are there to provide the model with freedom to better fit the measured pressure signal, although they may also indicate certain physical effects and phenomena within the measured signal.

The success of the original models' and associated signal processing (SP) techniques abilities to unearth useful information was hindered by the ambiguity of the off engine harmonic frequency content captured in the pressure signal. As was previously stated, this off engine harmonic frequency

content (stochastic content) is said to contain the desired blade vibration information (specifically for off EO operation).

The question has to be asked if there is enough unique information in the stochastic part of the pressure signal to factor out the blades' vibrational response given either of the two reformulated models. And if so how to proceed with extraction of that unique information. Hence the formulation of an inverse problem.

As has already been stated, certain components of the pressure models are known or can be extracted prior to attempting the inverse problem. These components are common to both reformulated models and have been alluded to in the SP schematic of Figure 2.6-1. The identification and extraction of these components are described in the initial portion of establishing the inverse problem.

Various options are available for setting up the inverse problem. The first requirement is to decide which reformulated model to explore and then consider the implications of that choice.

The reformulated expression based on Model 2 is initially chosen for investigation. A repercussion of choosing Model 2 is that either the full pressure signal is evaluated with all blades, and thus models for all blades must be included, or individual waves about blades can be investigated.

The model will however not be able to provide information about the Doppler shifting of frequency content. This is if the Doppler shifting phenomenon is indeed present in measurements taken in line with the rotor (as opposed to measurements taken downwind of the rotor row of interest as investigated by Mengle and Murray and Key (Mengle, 1990; Murray and Key, 2015)).

Given the underlying assumption that the casing pressure signal is directly related to a blade tip's local behaviour, and that the effect of adjacent blade tips is assumed to have a negligible impact on the pressure signal directly about the individual blade tip of interest, it is possible to investigate the effect that an individual blade has on an individual pressure distribution about that blade. This is the premise for isolating the pressure waves about the individual blades, even though the blades are structurally coupled through the hub and attachment mechanism.

Therefore, instead of solving for all blades simultaneously (each with a set of its own design variables), a smaller inverse problem may be tackled. The consideration of individual waves about blades will become apparent further on in the development of the model.

The associated pressure relation equivalent to Equation [2.3.10], provided in the Fourier Euler format, is shown in Equations [2.6.1] and [2.6.2].

$$P_r(t, \mathbf{x}) = (1 + \Gamma \cdot \dot{\psi}(t, \mathbf{y})_r) \cdot Re \left\{ \sum_{i=0}^{\infty} Q_i \cdot e^{(j \cdot i \cdot [\Omega \cdot t + \psi(t, \mathbf{y})_r + \nu])} \right\} \quad [2.6.1]$$

$$\mathbf{x} \supseteq (\Gamma, \mathbf{y}) \quad [2.6.2]$$

The full set of design variables which must be obtained is referred to as \mathbf{x} . A subset of the design variables \mathbf{x} is the set \mathbf{y} shown in Equation [2.6.1]. The subset \mathbf{y} refers to all of the design variables associated with the blade vibration forced response expressions (angular displacement and velocity).

As was stated, it is useful to first separate the pressure information that can be obtained trivially (outside of the optimisation problem), from that which cannot. The only variables in Equation [2.6.1] that can be determined from a measured pressure signal and tachometer signal without significant signal processing are the time t and the nominal rotor speed Ω .

A signal void of blade vibration is required for the estimation of the Fourier coefficients Q_i . Either this signal must be measured experimentally, or an alternative method to derive a blade vibration free signal is required.

Direct experimental measurement of a signal without blade vibration is difficult to achieve in practice. This is because it may not be possible to simply 'switch off' the excitation on an actual turbomachine. Even if the upwind stator excitation can be removed there is still slight excitation due to gravitational effects (assuming that the turbomachine's drive shaft is parallel with the ground).

It may be possible to operate the turbomachine, with upwind stator excitation, sufficiently far away from any resonance that a near blade vibration free signal can be measured. It is suggested that a better solution would be a means to estimate a blade vibration free signal directly from the measured pressure signal of interest itself. The reason given is that a blade vibration free signal derived from the original signal will have the most appropriate waveform given the operating speed and excitation conditions. Further, the signal's phase will be very closely aligned with the original signal's phase as it is derived directly there from.

It has been shown that the deterministic pressure signal, obtained directly from the measured pressure signal with blade vibration, may be used to estimate a vibration free signal (specifically for off EO resonance) (Forbes and Randall, 2013; Forbes, 2010). Therefore the Fourier coefficients Q_i may be extracted from the stationary pressure distribution once the signal has been post processed to obtain the deterministic signal.

As has already been stated, the deterministic pressure signal P_D is obtained through a synchronous averaging and reconstruction process using the measured pressure signal P_M and the tachometer signal. The synchronous averaging procedure uses the tachometer signal to find the average pressure waveform over a single revolution. This is termed the synchronously averaged pressure signal P_{SA} .

The synchronous averaging process averages out the non-engine order pressure information (such as the modulation effects due to blade vibration and Gaussian noise). The average signal over a single revolution is then repeated over the full time length, with aid from the tachometer signal, to produce a deterministic pressure signal P_D .

As was stated the reconstruction process, using the synchronously averaged pressure signal P_{SA} , will deliver a deterministic signal which is fairly well synchronised with the original measured pressure signal. An expression for the deterministic pressure signal P_D (the signal without blade vibration) is provided in Equation [2.6.3].

$$P_D(t) = Re \left\{ \sum_{i=0}^{\infty} Q_i \cdot e^{(j \cdot i \cdot [\Omega \cdot t + \nu])} \right\} \quad [2.6.3]$$

The first design variable which cannot be calculated directly or inferred from the signal processing step is the stationary wave's phase angle ν . The phase angle is common to both the deterministic and

fully combined pressure signals. An option now exists to either solve for this phase angle along with other design variables in the full signal representation, or to obtain it separately if possible.

The question must be asked what can be gained by taking either route. By solving for the value separately it means that the remaining optimisation problem has one fewer design variable to solve for, thus making the remaining problem smaller to solve. It however requires an additional optimisation process, so it can be argued that nothing is therefore gained by splitting it into a step of its own.

Recall that the individual blade phase angle χ must also be aligned with respect to time. Therefore the individual blade phase angle χ is dependent on the whole pressure distribution's phase angle ν . So by determining ν first and holding it constant in the remaining problem, any negative interaction between these two design variables can be avoided. Negative interaction refers to the effect of changing ν which misaligns the blade vibration phase χ resulting in a longer solve time.

So, in order to make the remaining optimisation process smaller and to prevent a relative slip between the two phase angles it is chosen to first obtain ν separately and then to solve for the remaining design variables in a second step.

Once the phase angle value for ν has been obtained it can be used to shift the deterministic pressure signal to better line up with the measured pressure signal.

A generic error function E is proposed to evaluate the differences between the measured signal and the deterministic signal. The generic error function can take many forms such as the mean square error (MSE), the root mean square error (RMSE) or an appropriate p-norm formulation. A discussion on error function choice and the associated ramifications of that choice is provided further on in this section. The generic error function is shown in Equation [2.6.4].

$$E_{DM} = E(P_M, P_D) \quad [2.6.4]$$

The only unknown in this initial optimisation process is the phase angle ν . Further, the only constraints required are those on the phase angle ν . The proposed constraints can be seen in Equation [2.6.5].

$$\frac{-\pi}{B} \leq \nu \leq \frac{\pi}{B} \quad [2.6.5]$$

The reconstruction process is expected to align the deterministic pressure waves with the original measured pressure signal with a fair amount of precision. This is because the deterministic signal is derived directly from the measured pressure signal and associated tachometer signal. Therefore only a slight phase adjustment of the deterministic pressure wave may be necessary to optimise its alignment in the time domain.

Had the stationary (or deterministic) pressure signal been obtained from an alternative source (such as measurement at a different rotor speed), then the phase alignment step would become more important as it cannot be assumed that the two signals will inherently line up (in terms of phase angle). It would also have to be ensured that the waves associated with specific blades in the additional signal line up with those in the measured signal (i.e. the wave about blade 1 from signal 1 is aligned with the wave about blade 1 in signal 2).

In order to prevent the entire signal from being shifted too far forwards or backwards the shift is limited to within the maximum angle that the blade subtends. Once the phase angle ν has been obtained the first optimisation process is complete.

When evaluating the full pressure relation given in Equation [2.6.1] it can be seen than a variable which scales the velocity based amplitude modulation is thus far unaccounted for. The scaling factor Γ is the first identified design variable for estimation by the second optimisation process. Since the magnitude of amplitude modulation is completely unknown bounds and limits about zero may have to be best tuned to obtain this design variable.

A diversion from the optimisation process must now be taken in order to obtain the individual measured pressure and deterministic signals about individual blades from the full measured signal. This step was referred to earlier when choosing to only investigate the pressure waves about individual blades instead of for all blades simultaneously.

The unshifted deterministic and measured pressure signals are passed through a splitting algorithm which applies the windowing process discussed in the previous section. The algorithm requires estimation of the individual wave passing times. These times can either be obtained from the deterministic pressure signal itself, or by blade passing time measurements obtained through the use of proximity, or similar, sensors installed near the stationary sound pressure observer.

A total of B deterministic and B measured pressure signals will be obtained from the splitting process (as there are B rotor blades on the rotor row of interest). From the B deterministic and B measured pressure signals a pair of signals associated with a single blade are chosen for further analysis. The previously obtained phase shift ν can now be applied to the split deterministic signal of interest to best line it up with the split measured pressure signal associated with the same blade.

Thus far we have obtained or confirmed the pressure relation values of the variables t , Q_i , Ω and ν . The only outstanding variables are those associated with the blade vibration displacement and velocity terms. This is given by the subset of design variables \mathbf{y} . In order to separate the known and unknown blade vibration related variables the effect of blade vibration on the deterministic signal will be considered.

The blade tip angular vibration in the time domain is obtained through an inverse Fourier transform of its frequency domain representation. This is because the blade vibration model is constructed in the frequency domain. The blade vibration, in terms of velocity, is obtained by differentiating the displacement with respect to time. As was stated, the differentiation may be performed in either the time or frequency domains. These operations are shown in Equations [2.6.6] and [2.6.7].

$$\psi(t, \mathbf{y})_r = \mathcal{F}^{-1}(\Psi(j \cdot \omega, \mathbf{y})) \quad [2.6.6]$$

$$\dot{\psi}(t, \mathbf{y})_r = \frac{d}{dt}(\psi(t, \mathbf{y})_r) \quad [2.6.7]$$

As was previously stated, the blade vibration in the frequency domain is the convolution of the blade transfer function and the forcing function. The frequency representation of the blade vibration is repeated in Equations [2.6.8] and [2.6.9].

$$\{\Psi(j \cdot \omega, \mathbf{y})\} = \frac{M}{L} \cdot [H(j \cdot \omega, \mathbf{z})] \cdot \{\mathcal{F}(g(t))\} \cdot e^{j \cdot \chi} \quad [2.6.8]$$

$$\mathbf{y} \supseteq \{M, \chi, \mathbf{z}\} \quad [2.6.9]$$

The forcing function can be estimated from the known blade and upstream stator geometry, rotor speed and time vector t using the Gaussian based modelling process outlined in a previous section.

The length of the blade L is assumed to be known. Two further design variables are seen in the equation. The first is the forcing function scaling factor M and the second is the blade response phase angle χ . Reasonable limits must be set for the force scaling factor. Estimates as to what the minimum and maximum force limits are expected to be must thus be obtained. The blade vibration response phase angle cannot shift more than $2 \cdot \pi$ (as the system period is $2 \cdot \pi$), its limits are therefore set to $-\pi \leq \chi \leq \pi$.

The blade transfer function design variables are all that remains to be estimated. The set of design variables strictly associated with the blade transfer function are contained in the vector \mathbf{z} . The vector contains the modal constants A_r , the modal damping ratios η_r and the blade natural frequencies ω_r . A suitable frequency response range ω for the blades must be chosen for reconstruction of the time domain response representation. The blade transfer function is given in Equation [2.6.10].

$$H(j \cdot \omega) = \left(\sum_{r=1}^N \left(\frac{A_r}{\omega_r^2 - \omega^2 + j \cdot \eta_r \cdot \omega_r^2} \right) \cdot e^{j \cdot \pi \cdot \text{mod}(r,2)} \right) \quad [2.6.10]$$

If only the first three modes are to be investigated (N=3) then a total of 9 variables' values must be estimated.

Stationary bench tests can be used to obtain estimates of the modal damping constants η_r . If access to bench test results are not available then reasonable estimates for the modal damping constants, based on the material and geometric properties of the blades, will have to be made. These values can then be set as design variables with critically chosen boundary limits.

The blade transfer function is the blade's unit response to a unit harmonic input force. Therefore work may be necessary to estimate the modal constants A_r . A FE or stationary bench test may provide insight into the parameters choice. Limits and inequality relationships may need to be set in order to constrain these values appropriately if they are set as design variables and not simply included as numerical estimates.

The remaining outstanding design variables are the individual blade's natural frequencies. Estimates based on the blade's geometry and material properties will provide the best starting point for an optimisation process to pin-point their values. If this is not possible, coarser design variable boundary limits may be set. For example limits based on the knowledge that the fundamental frequency is lower than the second natural frequency, and so on, may be used.

It is also important to consider whether or not centrifugal stiffening will have a significant effect on the blade's operational natural frequencies. This phenomenon may affect the initial parameter guesses given the operating speed. According to the literature reviewed, centrifugal stiffening is expected to only influence the bending mode values. The degree to which it influences the values can only be estimated through numerical or experimental processes. For this particular investigation both

FE based and experimental investigations were used and will be commented on in the relevant sections.

Finally, an error function has to be chosen to compare the measured pressure signal against the full analytically derived pressure signal. This error function is once again the objective function of the second optimisation process to be minimised over.

Once again a generic error function E between the analytically generated pressure signal P_A and the measured pressure signal P_M is chosen, this been provided in Equation [2.6.11]. Alternative error functions may be explored and minimised over in order to investigate different facets of the problem, as was stated these functions are discussed further on. The generic error function between the measured and analytically derived signals is provided in Equation [2.6.11]

$$E_{MA} = E(P_M, P_A) \quad [2.6.11]$$

The optimisation processes, for both optimisation problems, will now be provided in the standard optimisation format. Equations [2.6.12] to [2.6.15] outline the first optimisation process, namely the estimation of the phase angle ν .

Minimise the following cost function:

$$ArgMin: f(\nu) = E(P_M, P_D(\nu)) \quad [2.6.12]$$

Where:

$$P_D(\nu) = Re \left\{ \sum_{i=0}^{\infty} Q_i \cdot e^{(j \cdot i \cdot [\Omega \cdot t + \nu])} \right\} \quad [2.6.13]$$

The cost function is subject to the following inequality constraints

$$Y_{ineq} (Y_{ineq}(\mathbf{x}) \leq 0):$$

$$\nu - \frac{\pi}{B} \leq 0 \quad [2.6.14]$$

$$-\nu - \frac{\pi}{B} \leq 0 \quad [2.6.15]$$

The first optimisation process only has a single design variable and two inequality constraints associated with that individual design variable. Analytical gradient and Hessian arrays may be resolved if the problem proves difficult to solve (these terms will be explained further on). A standard gradient based approach is recommended for this problem.

Similarly Equations [2.6.16] to [2.6.38] provides the standard format for determining the remaining outstanding design variables. Various proposed numerical values for the constraints have been included in the formulation.

Minimise the following cost function:

$$ArgMin: f(\mathbf{x}) = E(P_M, P_A(\mathbf{x})) \quad [2.6.16]$$

The independent variables are defined as:

$$\mathbf{x} \ni \{\Gamma, \mathbf{y}\} \quad [2.6.17]$$

The pressure model associated with the independent variables is given by:

$$P_A(\mathbf{x}) = (1 + \Gamma \cdot \dot{\psi}(t, \mathbf{y})_r) \cdot \text{Re} \left\{ \sum_{i=0}^{\infty} Q_i \cdot e^{(j \cdot i \cdot [\Omega \cdot t + \psi(t, \mathbf{y})_r + v])} \right\} \quad [2.6.18]$$

$$\psi(t, \mathbf{y})_r = \mathcal{F}^{-1}(\Psi(j \cdot \omega, \mathbf{y})) \quad [2.6.19]$$

A subset of the independent variables contains the following parameters:

$$\mathbf{y} \ni \{M, \chi, \mathbf{z}\} \quad [2.6.20]$$

These parameters are used in the following equations:

$$\{\Psi(j \cdot \omega, \mathbf{y})\} = \frac{M}{L} \cdot [H(j \cdot \omega, \mathbf{z})] \cdot [F(j \cdot \omega)] \cdot e^{j \cdot \chi} \quad [2.6.21]$$

$$F(j \cdot \omega) = \mathcal{F}(g(t|\mu_i, \sigma)) \quad [2.6.22]$$

$$g(t|\mu_i, \sigma) = n(t) \cdot \sum_{i=1}^n \left(\frac{1}{\sigma \sqrt{2 \cdot \pi}} \right) \cdot e^{-\frac{(t-\mu_i)^2}{2 \cdot (\sigma)^2}} \quad [2.6.23]$$

The final subset of the design variables are:

$$\mathbf{z} \ni \{\mathbf{A}_r, \boldsymbol{\omega}_r, \boldsymbol{\eta}_r\} \quad [2.6.24]$$

The remaining component of the cost function is the blade transfer function:

$$H(j \cdot \omega, \mathbf{z}) = \left(\sum_{r=1}^N \left(\frac{A_r}{\boldsymbol{\omega}_r^2 - \omega^2 + j \cdot \boldsymbol{\eta}_r \cdot \boldsymbol{\omega}_r^2} \right) \cdot e^{j \cdot \pi \cdot \text{mod}(r, 2)} \right) \quad [2.6.25]$$

$$\mathbf{x} \ni \{\Gamma, M, \chi, \boldsymbol{\omega}_r, \boldsymbol{\eta}_r\} \text{ for } r \in \{1, 2, 3\} \quad [2.6.26]$$

The cost function is subject to the following inequality constraints

$$Y_{ineq} (Y_{ineq}(\mathbf{x}) \leq 0):$$

$$\Gamma - 0.5 \leq 0 \quad [2.6.27]$$

$$-\Gamma + 0.5 \leq 0 \quad [2.6.28]$$

$$M - 2.0 \leq 0 \quad [2.6.29]$$

$$-M + 0.1 \leq 0 \quad [2.6.30]$$

$$\chi - \pi \leq 0 \quad [2.6.31]$$

$$-\chi - \pi \leq 0 \quad [2.6.32]$$

$$\omega_r - f_{r,high} \cdot 2 \cdot \pi \leq 0, \quad \text{for } r \in \{1, 2, 3\} \quad [2.6.33]$$

$$-\omega_r + f_{r,low} \cdot 2 \cdot \pi \leq 0, \quad for\ r \in \{1,2,3\} \quad [2.6.34]$$

$$\eta_r - 0.025 \leq 0\ for\ r \in \{1,2,3\} \quad [2.6.35]$$

$$-\eta_r + 0.005 \leq 0\ for\ r \in \{1,2,3\} \quad [2.6.36]$$

$$A_r - A_{upper} \leq 0\ for\ r \in \{1,2,3\} \quad [2.6.37]$$

$$-A_r + A_{lower} \leq 0\ for\ r \in \{1,2,3\} \quad [2.6.38]$$

The second optimisation problem is far larger than the first, in terms of both design variables and inequality constraints. There are nearly two inequality constraints for every design variable. Further, analytically evaluating the gradient and Hessian for this problem is not possible.

The gradient vector, simply referred to as the gradient, is a vector which contains the partial derivatives of the objective function with respect to the design variables (Arora, 2011). In terms of gradient based optimisation, the gradient provides the direction towards a local minimum given the current design variables' values and the cost function (in this case the cost function is the generic error function) (Arora, 2011).

The Hessian matrix is obtained through differentiation of the gradient vector with respect to all of the design variables (Arora, 2011). It is therefore simply the second-order partial derivative matrix of the cost function with respect to all of the design variables (Arora, 2011). Similar to the gradient which provides information as to the direction in which minimisation must occur, the Hessian provides information regarding whether or not a local maximum, minimum or inflection point has been found.

Difficulty, in terms of analytical evaluation of the Hessian and gradient, is attributed to the fact that blade vibration is transformed to the time domain through an inverse Fourier transform. In order to obtain the analytical gradient and Hessian differentiation of the objective function with respect to all of the design variables is required. Further, the blade vibration in terms of velocity is the derivative of the displacement (which requires an inverse Fourier transformation as well).

It may simply not be possible to supply the analytical gradient and Hessian to a gradient based optimisation algorithm. In terms of gradient based approaches, the gradient and Hessian terms will then have to be numerically estimated at each step in the optimisation process in order to provide the algorithm with a minimisation direction and optimal solution estimate. Numerical estimation of the gradient and Hessian, as opposed to analytical evaluation, can be quite an expensive operation depending on the number of design variables and constraints contained in the problem.

Another issue with the formulation is the orders of magnitude of the various design variables and inequality constraints. The orders of magnitude of the different design variables vary greatly. For example the damping coefficients have an order of magnitude of -2 whereas the natural frequencies have an order of magnitude of 2 or 3 (when in Hertz).

The orders of magnitude of the design variables in the constraint and cost functions plays an important role in the rate of convergence for gradient based approaches. This is because they affect the condition number of the Hessian (Arora, 2011). The greater the order of magnitude difference

between the design variables, the worse the condition number of the Hessian becomes, this results in a system which is ill-conditioned.

Simply rescaling the design variables in the cost and constraints functions, such that they are within the same order of magnitude, may improve the convergence rate of a gradient based approach significantly by improving the Hessian's condition number (Arora, 2011).

The inequality constraints in this particular problem can be easily scaled between -1 and 1 by simply dividing each inequality through by the numerical value associated with that inequality. If a system is highly ill-conditioned then the initial design variables guesses have a major impact on the solution derived. Poorly chosen initial guesses may result in large solution errors. The effect of rescaling the inequality constraints and cost function design variables can only be obtained through numerical investigation of the problem, thus until this particular problem has been numerically or experimentally investigated the direct consequences of rescaling the inequality constraints is unknown.

The question has to be asked if the problem is well-posed or ill-posed. In order for a problem to be well-posed three conditions have to be met. Namely that the solution exists, that the solution is unique (at least within the interval of investigation) and that the solution to the problem changes continuously with respect to the initial conditions and boundary conditions (Hadamard, 1902).

Many useful inverse problems are however ill-posed. Techniques have been developed to aid in solving ill-posed problems such as regularisation of the cost function (regularisation refers to including penalty terms in the objective function). Regularisation of the cost function will be discussed once the error functions have been outlined.

It can be postulated that due to the ambiguity of the blade vibration frequency components, the error surface being optimised over will be highly modal. A highly modal problem results in a case where multiple solutions exist for the same problem. Multiple solutions automatically cause the problem to be ill-posed (as the solution is non-unique).

In cases where a high degree of modality exists, starting estimates for the design variables are extremely important. One initial design variable set $x_{initial,1}$ may easily converge to the desired solution whereas a second slightly different set $x_{initial,2}$ may converge to an undesirable local minimum. Multiple starts with randomised initial guesses may then be required to obtain the sensitivity of the system to the initial guesses or to estimate the best possible solution given the problem.

The postulate regarding the modality of the problem remains just that, until numerical results have been critically evaluated. However for the purpose of the discussion it is assumed that the problem is ill-posed in order to develop a robust solution methodology.

A useful tool for understanding the modality of the problem as well as how well or ill-posed the problem is, is to investigate the virtual problem. The virtual problem allows one to generate a 'measured' signal artificially where all of the design variables are pre-chosen and thus known. Multi-start optimisations, which use randomly generated initial design variable guesses, are then used to explore facets of the model. A further discussion on the virtual problem is provided further on.

The discussion will now focus on the error function choice. The error e between two corresponding components of a measured and analytically derived pressure vector is given in Equation [2.6.39]

$$e_i = P_{M,i} - P_{A,i} \quad [2.6.39]$$

The parameter i is once again simply the vector index. The time stamp for both vectors at index i is equivalent (as both pressure arrays are functions of time in this formulation). The various error functions considered are provided in Equations [2.6.40] to [2.6.46].

$$E_{LIN} = \sum_{i=1}^N |e_i| \quad [2.6.40]$$

$$E_{MAE} = \frac{1}{N} \cdot \sum_{i=1}^N |e_i| \quad [2.6.41]$$

$$E_{SE} = \sum_{i=1}^N |e_i|^2 \quad [2.6.42]$$

$$E_{MSE} = \frac{1}{N} \cdot \sum_{i=1}^N |e_i|^2 \quad [2.6.43]$$

$$E_{RSE} = \sqrt{\sum_{i=1}^N |e_i|^2} \quad [2.6.44]$$

$$E_{RMSE} = \sqrt{\frac{1}{N} \cdot \sum_{i=1}^N |e_i|^2} \quad [2.6.45]$$

$$E_{p-norm} = \left(\sum_{i=1}^N |e_i|^p \right)^{\frac{1}{p}} \quad [2.6.46]$$

In order, the errors are the absolute linear error (LIN), the mean absolute error (MAE), the square error (SE), the mean square error (MSE), the root square error (RSE), the root mean square error (RMSE) and the generic p-norm expressed as an error function.

The MAE, MSE and the RMSE are simply the LIN, SE and RSE which have been normalised with respect to the number of items being compared. The normalisation is useful for comparing relative errors derived from different data sets of different lengths. Their behaviours are however similar to their non-normalised counterparts and so will not be discussed as isolated error functions further.

As the power of the errors increase so do their sensitivity to outliers increase. Sensitivity here refers to how the error function weights the individual component errors e_i . A high sensitivity to outliers means that large component errors have a higher weighting than small errors. An outlier will only have a linear effect in the LIN error, it will however have a quadratic effect in the SE or RSE. Depending on the p-value chosen for the p-norm error, the sensitivity to outliers increases as the p-value increases.

A high sensitivity to outliers' means that the objective function may over-fit the error data instead of providing a more general solution. In terms of the noisy measured pressure data, a high sensitivity to outliers may not be appropriate as fitting to the general trend is the objective.

The p-norm error is equivalent to the absolute linear error for a p-value of 1, similarly the p-norm error is equivalent to the square error for a p-value of 2. As the value for p approaches infinity, the objective function and optimisation process approaches the mini-max optimisation problem. The mini-max problem aims to minimise the maximum error between any two components of the error set e_i . It is therefore tuned to optimising over the greatest outlier value in the problem.

A comparison of the various error functions' behaviours, for increasing and decreasing component error values e_i , is shown in Figure 2.6-2. The p-value for the p_∞ -norm was chosen arbitrarily high at p equal to 150 for evaluation purposes.

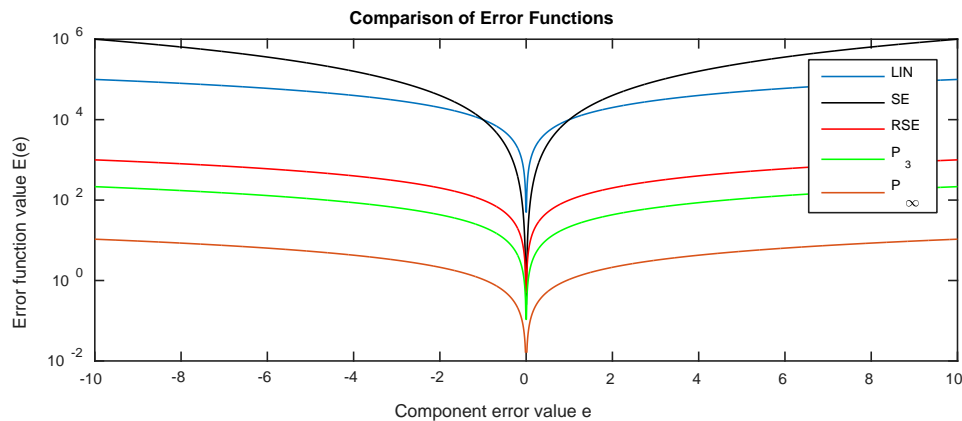


Figure 2.6-2 Comparison of error functions with logarithmic error function values

The only error function presented which does not have a near p-norm equivalent is the MSE. It can be seen that any outlier value evaluated using the MSE will have a significant effect on the actual overall error function value. For all other error terms which have a p-norm equivalent it can be seen that as the p-value increases the summed error magnitudes decrease and the error function flattens out.

In terms of gradient based approaches, a smooth convex error surface with a measurable gradient is preferred. This is because the error surface gradient directly affects the rate of convergence of an optimisation algorithm. Further a smooth convex shaped bottom allows a prediction to be made as to whether or not the actual minimum has been found (i.e. in the Hessian information).

A decision needs to be made in order to choose the most appropriate error function for the problem at hand. As was previously stated, we are not interested in fitting the model to the extreme outliers, therefore it is proposed that a high p-value error function or the mini-max problem would not be appropriate as they are designed to specifically minimise over the largest outlier values.

An error value normalised to the number of terms added is an advantage as errors from different investigations may then be directly compared. The quadratic errors provide a continuous convex error surface which facilitates an exit point for a gradient based optimisation approach. The error function therefore initially chosen to compare the measured and analytically derived pressure signals is the RMSE. If it is found that the error function does not perform well, an alternative may be chosen from the provided set.

Returning to the assumption that the inverse problem is inherently ill-posed, it was stated that regularisation of the cost function may be useful. Regularisation of the cost function works by applying a penalty factor to the objective function being minimised over. The penalty factor is a function of the

problem's constraints. As the constraints are violated a penalty is added to the cost function driving up the error value.

Therefore, instead of supplying the equality and inequality constraints to a constraints based optimisation algorithm, the constraints are rather included directly in the penalty term (PT). The generic form of the cost function with included penalty term is shown in Equation [2.6.47] (Arora, 2011).

$$f(\mathbf{x}, \kappa) = E(P_M, P_A(\mathbf{x})) + PT(Y_{eq}(\mathbf{x}), Y_{ineq}(\mathbf{x}), \kappa) \quad [2.6.47]$$

As was stated the penalty term is a function of the equality constraints Y_{eq} , the inequality constraints Y_{ineq} and a positive scalar penalty factor κ (Arora, 2011). Depending on the choice for the penalty factor, the cost function will be penalised more or less harshly (Arora, 2011). A common penalty term is the quadratic penalty term and is shown in Equation [2.6.48] (Arora, 2011).

$$PT(Y_{eq}(\mathbf{x}), Y_{ineq}(\mathbf{x}), \kappa) = \kappa \cdot \left\{ \sum_{i=1}^p [Y_{eq,i}(\mathbf{x})]^2 + \sum_{i=1}^m [\max(0, Y_{ineq,i}(\mathbf{x}))]^2 \right\} \quad [2.6.48]$$

The investigation of interest only contains inequality constraints, therefore the penalty term reduces to Equation [2.6.49].

$$PT(Y_{ineq}(\mathbf{x}), \kappa) = \kappa \cdot \left\{ \sum_{i=1}^m [\max(0, Y_{ineq,i}(\mathbf{x}))]^2 \right\} \quad [2.6.49]$$

It can be seen that the quadratic penalty function only penalises the cost function when the constraint is violated. Multiple options for penalty functions exist such as the set of barrier functions (Arora, 2011). The barrier functions would be an appropriate choice for this problem as they are only applicable when inequality constraints exist, as is the case for this problem (Arora, 2011).

Barrier functions, such as the inverse barrier function or the log barrier function, create a barrier about the feasible region defined by the inequality constraints (Arora, 2011). As the constraints approach their limits, the barriers approaches infinity. This means that an initial guess must be chosen within the feasible set of design variables or else the optimisation will end prematurely (Arora, 2011). An advantage of the quadratic penalty function is that initial guesses may be chosen outside of the feasible set (Arora, 2011). Many nonlinear constrained optimisation algorithms have intelligent pre-integrated penalty functions and so the cost function does not need to be manually regularised.

An optimisation strategy to solve the proposed inverse problem must now be formulated. Multiple options exist, however a strategy based on the problem at hand is desired. It is known that the larger of the two optimisation problems analytical gradient and Hessian information is unavailable. It is assumed that the problem is ill-posed due to the highly modal nature of the analytical pressure signal relation. Strategies such as gradient based approaches, stochastic approaches (approaches which do not use gradient information to find local minima), and combinatorial gradient and stochastic approaches may be considered.

Stochastic approaches have been found to sometimes work well under highly modal conditions where no analytical gradient information is available. A stochastic approach such as the particle swarm (PSO) algorithm, or the genetic algorithm (GA), with multiple randomly generated particles (or individuals)

may be able to cover a larger portion of the error surface when compared to a strictly gradient based approach.

Stochastic approaches may however take a long time to converge to the local minimum once a favourable area on the error surface has been identified. Therefore a stochastic based approach may be used to determine reasonable initial guesses for a gradient based approach and then the process terminated after a limited number of iterations.

A gradient based approach, even without analytical gradient and Hessian information, may converge quickly once a good starting point near a local minimum has been estimated. Due to the lack of analytical gradient and Hessian information and the assumed highly modal nature of the problem a combinatorial based approach has therefore been proposed. It also provides a measure of the relative performance of the two different approaches without having to perform additional studies.

This investigation is however not a comparison of different optimisation algorithms, therefore the specific choice of the gradient-based and/or stochastic algorithms to be combined is somewhat arbitrary. An informed trial and error approach in the numerical investigation will provide better insight into this issue and the choices made. A PSO and interior-point gradient based algorithm combination is initially suggested. The full solution process proposed, including signal processing and optimisation, for this specific inverse problem is provided in Figure 2.6-3.

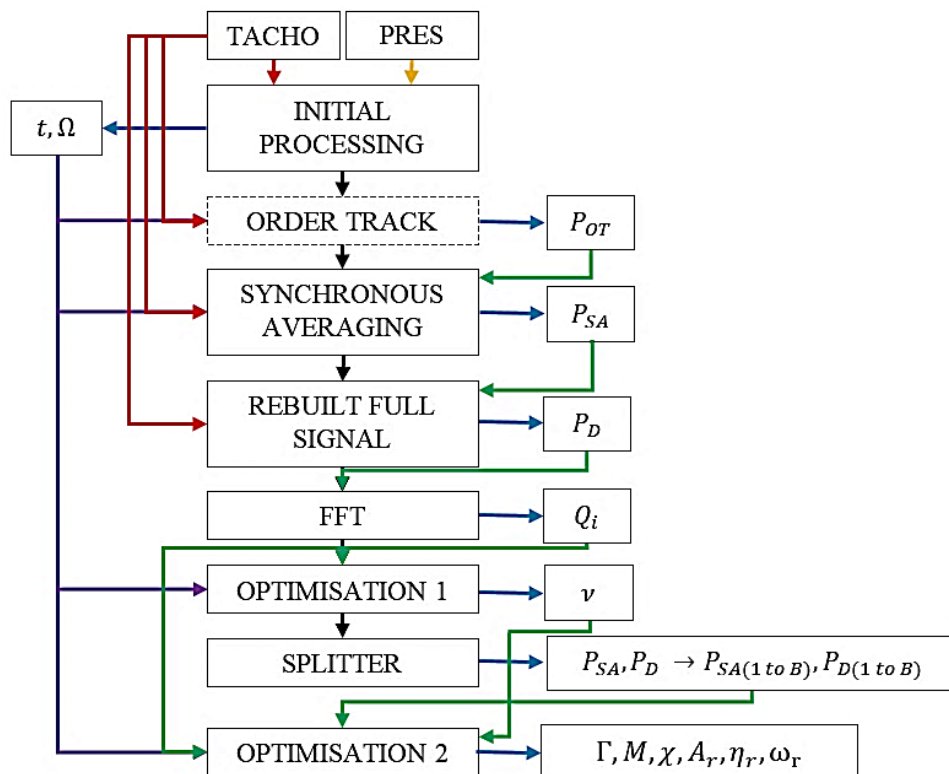


Figure 2.6-3 Optimisation and signal processing flow chart

In the above schematic an additional signal processing technique has been included. Namely the order tracking process. Order tracking was suggested as a part of the signal processing in work of Forbes et al. (Forbes and Randall, 2013). As was previously stated, it is a phase resampling technique which supplies a signal which contains specific number of linearly resampled points (a specific number of points per revolution).

Order tracking removes smearing of frequency domain components due to slight rotor speed fluctuations when used on measurements taken at a nominal rotor speed. It may however denude the signal of unique components which is the reason for including it from an evaluative point of view. Until an experimental comparison between an order tracked signal and synchronously averaged signal is performed, the repercussions or benefits of including the process will remain unknown. This investigation is performed as part of the signal processing investigation in Chapter 4.

If the optimisation process is unable to converge to one or more of the design variables associated with the blade natural responses then there may perhaps not be enough unique information in the pressure signal to describe that particular mode. For example if insufficiently broad spectrum energy is entering the blade or a rotor harmonic peak supplying energy to that particular mode is too far removed from the resonance of interest. Another concern would be if the given experimental setup and instrumentation choices allow capture of the missed modes. Depending on the position and orientation of the sound pressure transducer bending modes may be visible and torsional blade modes may not. Stationary bench tests may provide insight here.

As was previously stated, an alternative to using the split measured signal and deterministic signal about an individual blade would be to use the full measured pressure signal and then multiple individual blade representations simultaneously (obtained through the same splitting procedure). In this way the travelling wave modes and associated nodal diameters can be included in the design of the problem by forcing a constant phase angle difference between the blades (or sections of blades given the number of modal diameters). The global behaviour and blade coupling can therefore be included in the inverse problem.

The global version problem will however scale up the number of design variables and constraints significantly. This is because each individual blade already has quite a large number of design variables associated with it. Even if the modal constants, modal damping ratios, force and velocity scaling parameters are assumed to be equivalent for all blades, a larger number of independent variables are still expected (namely the natural frequencies for each of the blades included in the investigation).

An advantage of the global approach would be that information about all blades' behaviours will be used simultaneously to determine the combined blade and hub assembly's response. Further, given that no system is perfect, a certain level of mistuning will always be present. Mistuning will cause mode localisation. This means that at least one of the blades (or sector contains blades) will be responding at a higher amplitude than the others and thus may provide more tangible information than the other blades. In the original process each blade may have to be evaluated separately in order to resolve the inverse problem.

A second alternative to using the individual waves about blades to obtain a global pressure response indicator would be to use the relation based upon the work of Mengle (reformulated Model 1) (Mengle, 1990).

In this way the travelling wave mode number (or number of nodal diameters) may be directly incorporated into the optimisation problem without having to individually include all blades simultaneously. The Fourier coefficients and system phase angle ν may be obtained in the same way as previously described. Therefore only the cost function of the second optimisation process and the associated constraints will be affected. Consider Equation [2.6.50].

$$P_r(t) = Re \left\{ \sum_{i=0}^{\infty} \left[1 + \sum_{k=0}^{B-1} [I(i) \cdot \Lambda_k \cdot \sin(k \cdot \Omega \cdot t + \omega \cdot t + \chi)] \right] \cdot D'_i \cdot e^{(j \cdot i \cdot [\Omega \cdot t + \nu])} \right\} \quad [2.6.50]$$

The number of design variables which requires solving for is significantly reduced in this model when compared to the reformulated pressure Model 2. The design variables associated with this model are the response scaling factors Λ_k , the blade vibration phase angle χ and the overall phase angle of the analytical signal with respect to the measured signal ν which is obtained in an initial optimisation step. A major disadvantage of the model in its current form is that the blade response is modelled as a SDOF sinusoid and so would not be appropriate for evaluation of blade forced response with multiple forcing frequencies.

The use of a numerical investigation in order to determine how well- or ill-posed the inverse problem is has already been mentioned. Prior to using either of these models on an actual pressure signal it is suggested that an ideal virtual problem be solved to determine if the technique is feasible.

As was stated, a virtual problem allows one to set up a 'measured' pressure signal with known design variables. The problem can initially be solved for without adding additional noise to the signal. This is done in order to determine if it is first possible to resolve the blade vibration characteristics from the models in the first place. This allows direct evaluation of the proposed solution strategy (in terms of algorithm choice and combination) and indicates if one's chosen error function is appropriate given the data. The ideal virtual problem will indicate the modality and smoothness of the error surface regardless of noise.

If it is possible to resolve the blade vibration characteristics given the model and an ideal noise free signal then the next step would be to investigate an increasingly noisy signal. The interaction between the blade vibration amplitude and the signal to noise ratio (SNR) can then be established. Minimum SNR thresholds can then be established for a particular blade vibration amplitude. The virtual problem route makes sense of the inverse problem.

It must be noted that these models and methods have been generated for the case of non-engine ordered blade vibration and they are not expected to provide significant insight into the case of resonant vibration.

Further, as was stated in the scope and beginning of this section, the initial aim would be to fit components of the pressure model to signals which definitely contain the blade vibration phenomena of interest. For example fitting the blade vibration models to actual direct blade vibration signals (such as on blade SG signals). Only once the constituent internal pressure model components have been proven to adequately describe the phenomena would it be prudent to attempt the full inverse problem. Such a rigorous combined stochastic and gradient based approach may not be necessary to solve the reduced inverse problems. It is important to note that solving the full inverse problem is outside the scope of this project.

An alternative method for obtaining blade vibration characteristics from a pressure signal has been suggested. The performance of the methodology depends heavily on the presence of blade vibration information within the signal and the ability to differentiate unique components of the signal. The following chapter outlines the experimental setup and experimental methodology employed to obtain casing pressure signals.

Chapter 3 Experimental Setup and Characterisation

3.1. Experimental Setup and Characterisation Introduction

An experimental test setup was designed and built for the purpose of investigating blade vibration measurement techniques such as BTT and CPS based methods. Various design considerations and modifications were outlined in the scope of the project and were incorporated into the design.

The critical components of the experimental setup, with respect to CPS techniques, are the hub and blades as well as the sound pressure transducer and associated mounting arrangements. The blade and hub assembly designs required analytical characterisation and investigation prior to manufacture. This was done in order to determine the expected blade and assembly response during operation. This also provided insight into the required instrumentation and instrumentation positioning.

After manufacture these components were experimentally characterised in order to ensure that they responded as expected according to the FE investigation. A second significant motivation for the modal characterisation of the hub and blade assembly exists. In order to analyse the internal pressure signatures, from both a signal processing and inverse problem perspective, it is important to know what each individual blade's expected behaviour is as well as the behaviour of the system as a whole.

The following two sections explore the experimental test bench design and main mechanical components. This is followed by the individual blade design and analytical analysis. Three different blade designs were considered, each was designed to have a different fundamental frequency. This is achieved by altering the basis 'healthy' blade geometry at a location far remove from the blade's tip.

A dynamic finite element (FE) investigation was used to obtain the expected blade natural frequencies at both stationary and across a range of operating conditions. The experimental test bench's operational limits were incorporated into the investigation. The FE analysis provided analytical Campbell diagrams with associated EO resonance locations (critical speeds).

A general instrumentation list and schematic is then provided. The instrumentation used places limits on what can be observed, given the instrumentation's sensitivity and the data acquisition system's maximum sampling rate. A blade instrumentation plan, based on the FE investigation, is also included.

Various experimental configurations are suggested. Four blade and hub assembly configurations are suggested (by making use of the three different blade designs), as well as three different excitation configurations (given the experimental setup's design).

Experimental modal analyses are performed on the various blade and hub assemblies in order to obtain both the system and individual blades response spectra to various excitation sources. The unconstrained hub and blade assemblies' response spectra and operational mode shapes were obtained using a scanning laser vibrometry system. Thereafter the individual blades' behaviours, in the installed position in the experimental setup, were obtained using a modal hammer approach. Run-up tests were performed to obtain the critical operating speeds given the various hub and assembly configurations as well as excitation configurations. The data was obtained using strain gauges attached to the surfaces of individual blades. The run-up tests, coupled with the individual blade modal response test results, provided the expected engine order excitation locations.

Finally a brief overview of the steady state data capture methodology and associated concerns are discussed.

3.2. Brief Description of the Experimental Test Bench

The test bench was designed such that upstream stator excitation could be simulated using a combination of air nozzles attached to a high pressure air source. A CAD rendering of the complete experimental setup is presented in Figure 3.2-1.

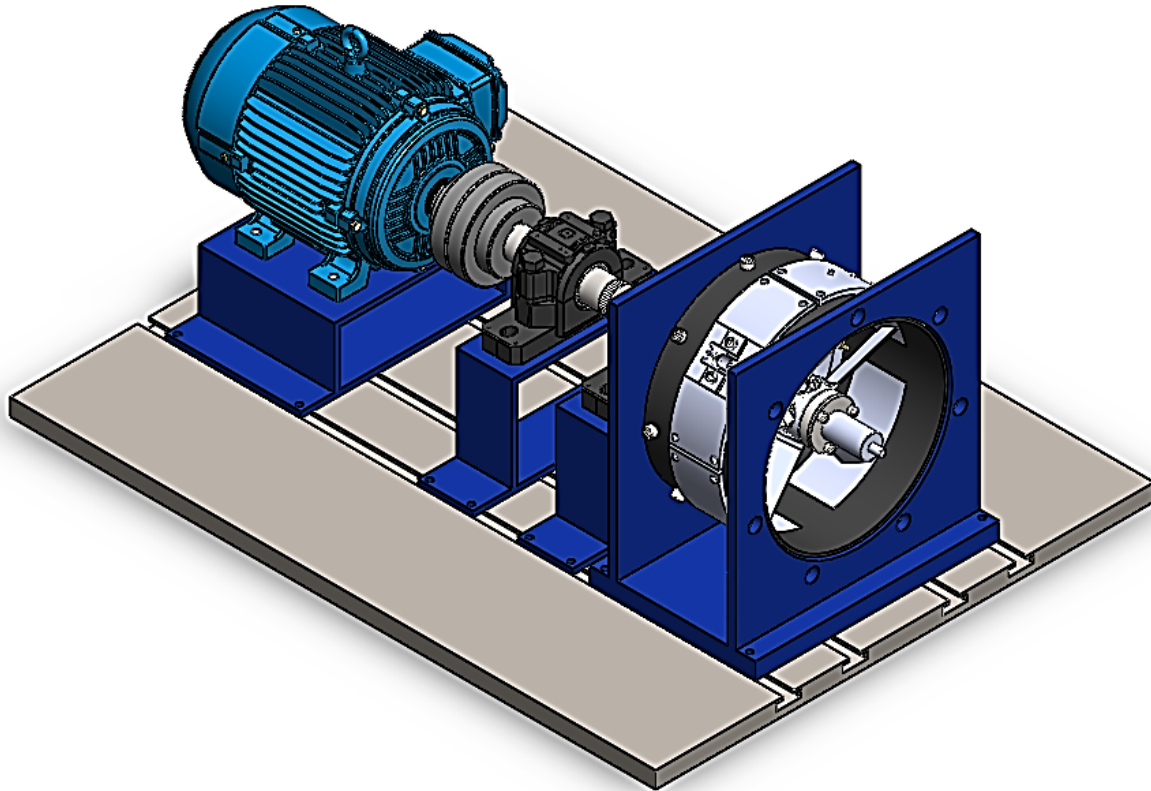


Figure 3.2-1 Experimental test bench

The shaft, onto which the mock turbomachine hub and blades assembly is attached, is connected to an electric motor via an inline flexible shaft coupling. The flexible shaft coupling arrangement was chosen in order to minimise noise stemming from the operation of the motor and aid in system alignment. The shaft is aligned by means of two floating plunger block bearings which can be fixed into place after the alignment process.

The electric motor is capable of providing a range of rotational speeds from approximately 0 RPM to 1470 RPM by means of a motor controller. The shaft direction of rotation can be controlled manually by changing the attachment of the motor's poles to a power source.

The casing around the hub and blade assembly was designed such that instrumentation pallets could be removed and replaced as required. Alteration of these pallets allows multiple sensor configurations for a range of BTT and CPS tests. Once pallet was modified for CPS measurements.

The end of the drive shaft was fitted with a slip ring mount. This mount has the dual purpose of locking the blade and hub assembly onto the tapered end of the shaft as well as allows attachment to a slip ring system for data acquisition of blade mounted sensors such as strain gauges.

A schematic of the test bench and associated mechanical components is provided in the following section.

3.3. Experimental Test Bench Design and Components

Figure 3.3-1 contains a schematic of the experimental test bench and its main components.

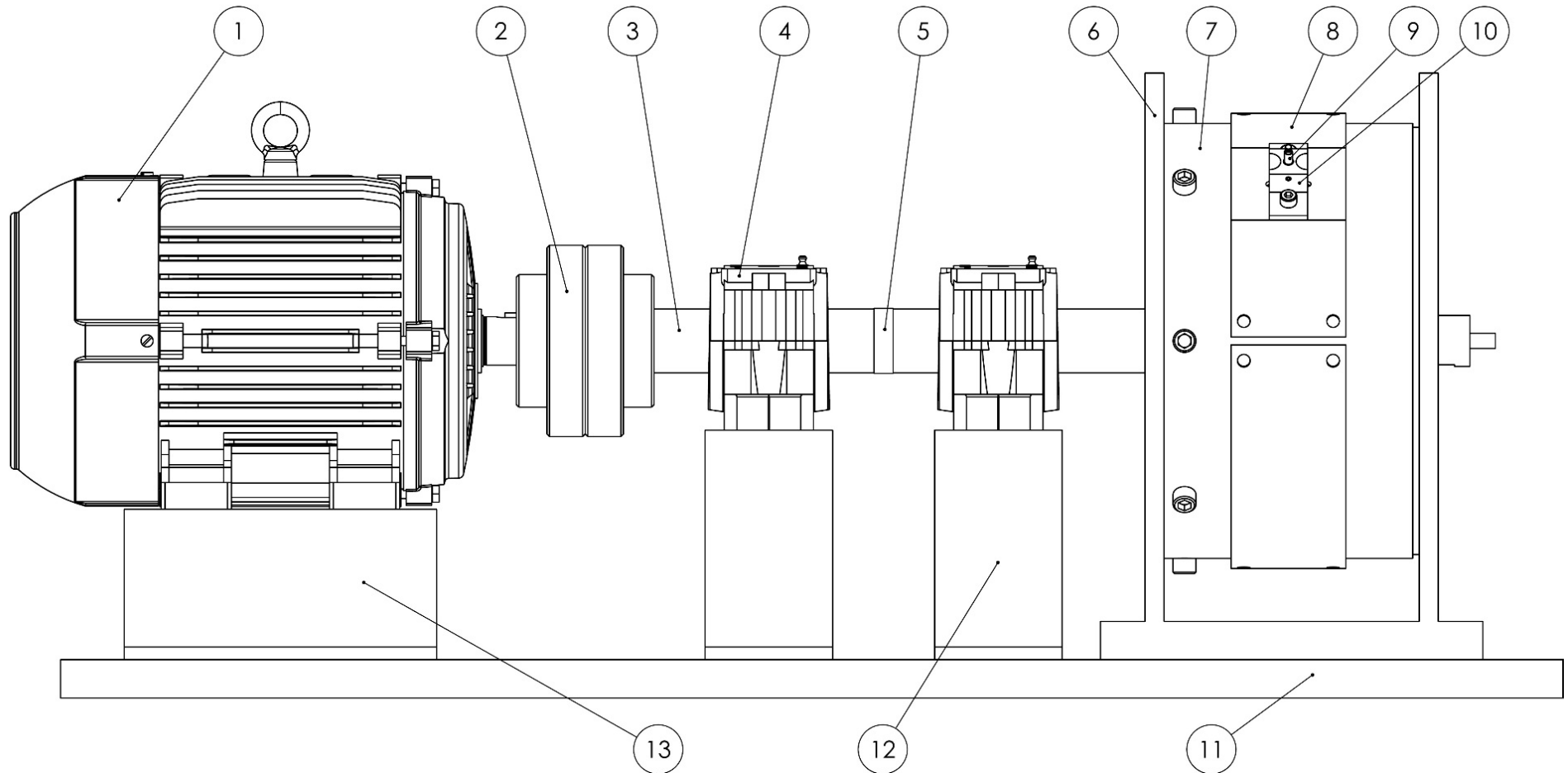


Figure 3.3-1 Schematic of experimental test bench

The component list associated with Figure 3.3-1 is provided in Table 3.3-1.

Table 3.3-1 Experimental test bench component list

#	Component	#	Component
1	Electric motor (5.5 kW at 1470 RPM)	8	Sensor mounting plate
2	Flexible shaft coupling	9	Microphone
3	Shaft with tapered end	10	Microphone mounting block
4	Plumber block and bearing	11	Bench
5	Zebra tape	12	Bearing mount
6	Drum housing	13	Motor mount
7	Drum		

The drum housing and associated components are presented in Figure 3.3-2. The tapered end of the shaft to which the hub assembly mounts is clear in this section view.

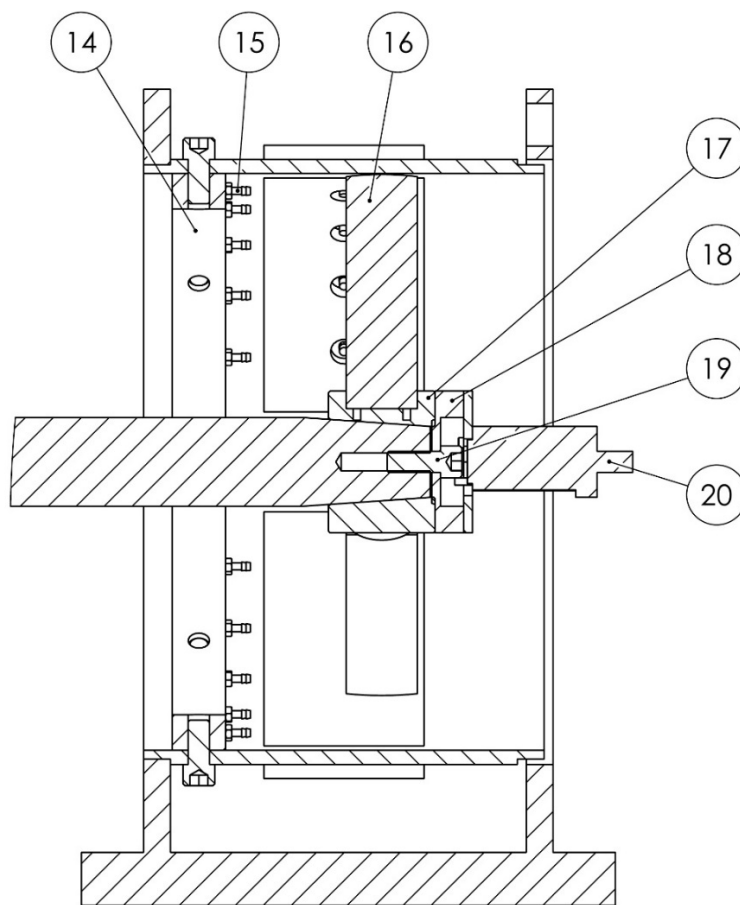


Figure 3.3-2 Cross section of drum housing

The components indicated on the drum housing figure are provided in Table 3.3-2.

Table 3.3-2 Drum housing components

#	Component	#	Component
14	Air jet ring	18	Slip ring coupling
15	Air jet	19	Slip ring coupling attachment bolt
16	Turbine blade	20	Slip ring
17	Turbine blade attachment hub		

The sensor mounting plate and attachments for CPS measurements are illustrated in Figure 3.3-3. The sensor mounting plate was designed such that the centre of a blade tip would pass the sound pressure transducer during operation. The design includes provision for two eddy current proximity probes to be placed on either side of the sound pressure transducer parallel to the drive shaft. The eddy current proximity probes serve two purposes, firstly they provide average blade passing times and secondly they may be used to differentiate between individual blades passing the sound pressure transducer.

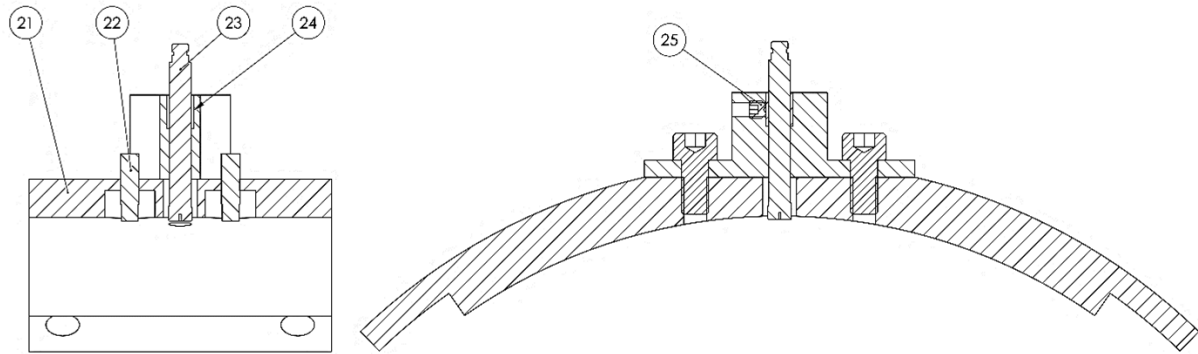


Figure 3.3-3 Cross section of sensor mounting plate and attachments

The components associated with Figure 3.3-3 are presented in Table 3.3-3.

Table 3.3-3 Sensor mounting plate components

#	Component	#	Component
21	Sensor mounting plate	24	Split bush
22	Eddy current probe	25	Microphone set screw
23	Microphone		

The blade attachment hub was designed to support convenient changing of individual blades as well as allow multiple blade stagger angle orientations. The attachment hub design is presented in Figure 3.3-4.

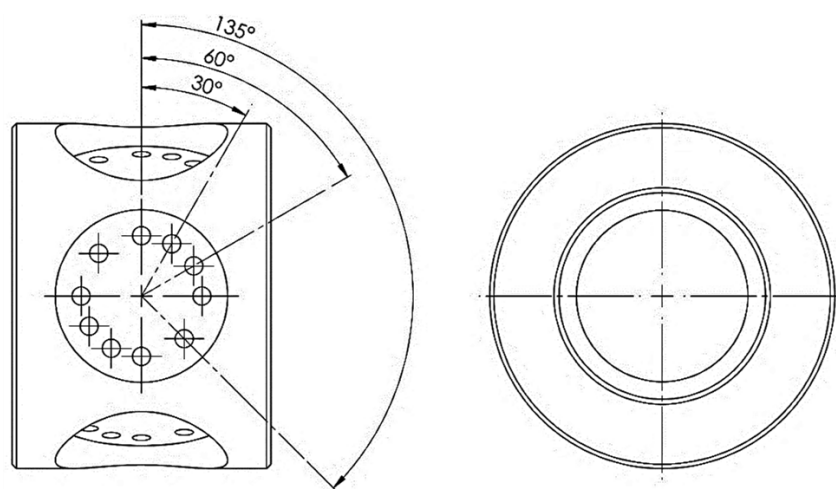


Figure 3.3-4 Blade attachment hub

The possible blade stagger angle orientations are 0°, 30°, 45°, 60° and 90°. Due to the reversibility of the motor velocity, the 45° stagger angle is specified among the other blade stagger angles.

3.4. Turbomachine Blades and Analytical Characterisation

3.4.1. Blade Design

Three separate blade designs were considered for manufacture. The designs were chosen such that three distinctly different fundamental blade frequencies exist with minimal geometrical differences along the length of the blade, and near identical blade geometries at the tip. Before manufacture the blade natural frequencies were estimated using the finite element (FE) package ANSYS™ (“ANSYS® Academic Research, Release 16.1,” 2015). The full FE investigation is provided in section ‘7.4.1 D1 – FE Analysis Configuration’. Significant results from this investigation are discussed in the succeeding section. The blade designs along with significant dimensions are provided in Figure 3.4-1.

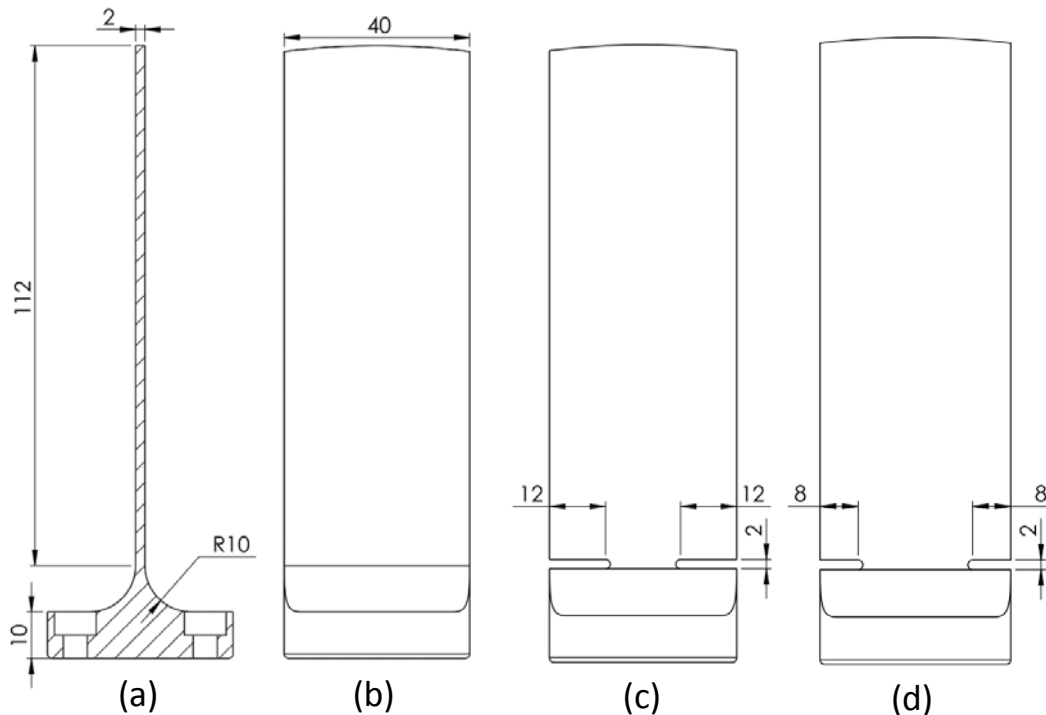


Figure 3.4-1 Blade designs. (a) Blade cross section. (b) Healthy Blade. (c) Damaged blade 1. (d) Damaged blade 2.

The ‘healthy’ blade was designed to have a fundamental frequency of approximately 125 Hz, ‘damaged blade type 1’ was designed to have a fundamental frequency of approximately 20 Hz lower than the healthy blade, and finally ‘damaged blade type 2’ was designed to have its fundamental frequency between the healthy blade and ‘damaged blade type 1’ at approximately 115 Hz.

The material chosen for the preliminary FE investigation was a generic aluminium alloy. The blade’s actual material of manufacture was 6082-T6 round bar. A hot wire cutting process was used to produce the blades. It is noted that the manufacturing process may have altered the heat treatment condition of the raw material. This is not considered to be of concern as each of the blade’s dynamic responses are individually characterised by means of experimental modal testing.

The blade length, excluding the attachment radius, was chosen as 112 mm. All of the blades had a thickness of 2mm and a constant chord length of 40mm. The blades are attached to the hub by means of two machine screws. Damage was achieved on the two alternate blades by cutting 2mm wide slots at the radius end on the blades to a depth of either 12mm or 8mm depending on the blade type.

The succeeding section outlines the FE modal results of the finalised designs corresponding to the blade geometries provided in Figure 3.4-1.

3.4.2. Analytical Modal Response of Individual Blades

As was stated, a finite element (FE) modal analysis was performed using ANSYS™ to ascertain the natural frequencies and mode shapes of the different blade geometries in their installed positions (“ANSYS® Academic Research, Release 16.1,” 2015).

The general analysis choices are provided in ‘7.4.1 D1 – FE Analysis Configuration’ section ‘7.4.1.1 Fifth Model’ along with mode shape visualisations. The blades were modelled attached to the hub in a symmetric fifth configuration as the hub could accommodate 5 blades at any time. The cyclic symmetry boundary condition was applied to the symmetric models.

Table 3.4-1 presents the first 5 theoretical natural frequencies and mode shapes for the various blade types (at stationary conditions). Due to the simple blade geometry, void of tapering and twisting, all modes are of a pure form, i.e. first bending is purely a bending mode and so on.

Table 3.4-1 Analytical stationary blade natural frequencies

Mode	Blade Type 1: Healthy		Blade Type 2: Damaged 1		Blade Type 2: Damaged 2	
	Freq. (Hz)	Mode Shape	Freq. (Hz)	Mode Shape	Freq. (Hz)	Mode Shape
1	127.08	First bending	105.22	First bending	116.40	First bending
2	733.55	First torsional	620.08	First torsional	676.96	First torsional
3	791.15	Second bending	707.18	Second bending	744.43	Second bending
4	2110.80	First edgewise	870.23	First edgewise	1393.80	First edgewise
5	2214.70	Third bending	1976.7	Second torsional	2107.70	Second bending

The effects of rotation on mode natural frequencies were investigated in the same study. The change in natural frequencies versus a change in rotational speed for the first three modes of a healthy blade is presented in Campbell diagram Figure 3.4-2. The first 100 EO lines are provided in the same plot.

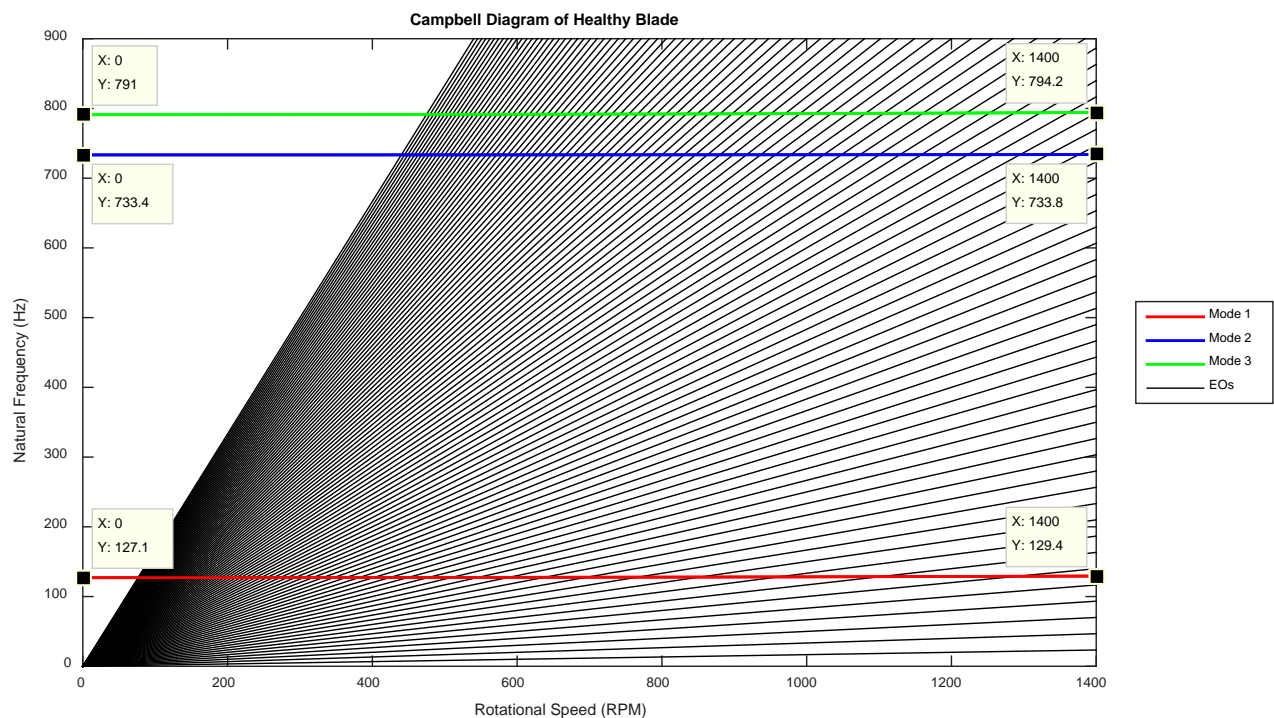


Figure 3.4-2 Campbell diagram of healthy blade



The Campbell diagram was generated using 11 pre-stress analyses in order to determine the natural frequencies across the range of 0 RPM to 1400 RPM. The pre-stress analyses were performed by setting a rotational speed boundary condition about the center of rotation. Once the pre-stress was applied a FE modal analysis could be performed in order to obtain the natural frequencies of the system given the particular rotor speed.

It was seen that a negligible increase in natural frequency occurred due to centrifugal stiffening for all three modes and for all three different blade geometries over the operational range. It is also noted that as the shaft speed increases the spacing between critical resonance speeds increases.

With respect to the healthy blade Campbell diagram, it can be seen that the smallest change occurred for the first torsional mode. This is in line with the expected behaviour as centrifugal stiffening was only expected to significantly influence the flap modes. The change in natural frequency 1, 2 and 3 over the speed range was 2.3 Hz, 0.4 Hz and 3.2 Hz respectively. The natural frequencies (NF) for all blade types at 0 RPM and 1400 RPM for the first three natural frequencies are given in Table 3.4-2.

Table 3.4-2 Natural frequencies for all blade types at 0 RPM and 1400 RPM

Blade	1 st NF at 0 RPM (Hz)	1 st NF at 1400 RPM (Hz)	2 nd NF at 0 RPM (Hz)	2 nd NF at 1400 RPM (Hz)	3 rd NF at 0 RPM (Hz)	3 rd NF at 1400 RPM (Hz)
Healthy	127.1	129.4	733.4	733.8	791	794.2
Damaged Blade 1	105.7	108.3	622.6	622.9	708.8	712.2
Damaged Blade 2	116.6	119	678	678.4	745.5	748.8

The change in natural frequencies over the speed range of interest are given in Table 1.3-3.

Table 3.4-3 Change in natural frequencies for all blades over speed range of interest

Blade	Change in 1 st NF (Hz)	Change in 2 nd NF (Hz)	Change in 3 rd NF (Hz)
Healthy	2.3	0.4	3.2
Damaged Blade 1	2.6	0.3	3.4
Damaged Blade 2	2.4	0.4	3.3

The Campbell diagrams for the two remaining blade geometries are provided in section ‘7.4.4 D4 – Analytical Campbell Diagrams for Damaged Blades’. The same conclusions were drawn, the change in natural frequencies for all first three modes, due to rotational speed effects are negligible over the considered shaft speed operating range.

The FE Campbell diagram results were stored such that changes in natural frequencies, due to operational speed, could be easily queried at a later stage for comparison with experimental results for rotor operation at any specific speed within the range investigated (namely 0 RPM to 1400 RPM).

A total of 8 blades were manufactured. Five were of the healthy type, two were of damaged type 1 and one was of damaged type two. The actual blade and hub assembly manufactured can be seen in section ‘7.5.3 E3 – Images of Experimental Setup’ subsection ‘7.5.3.3 Blade and Hub Assembly Components’.

3.5. Instrumentation

3.5.1. General Instrumentation

This section provides a general overview of the instrumentation setup used during run-up and steady state testing. The experimental setup's instrumentation schematic is provided in Figure 3.5-1.

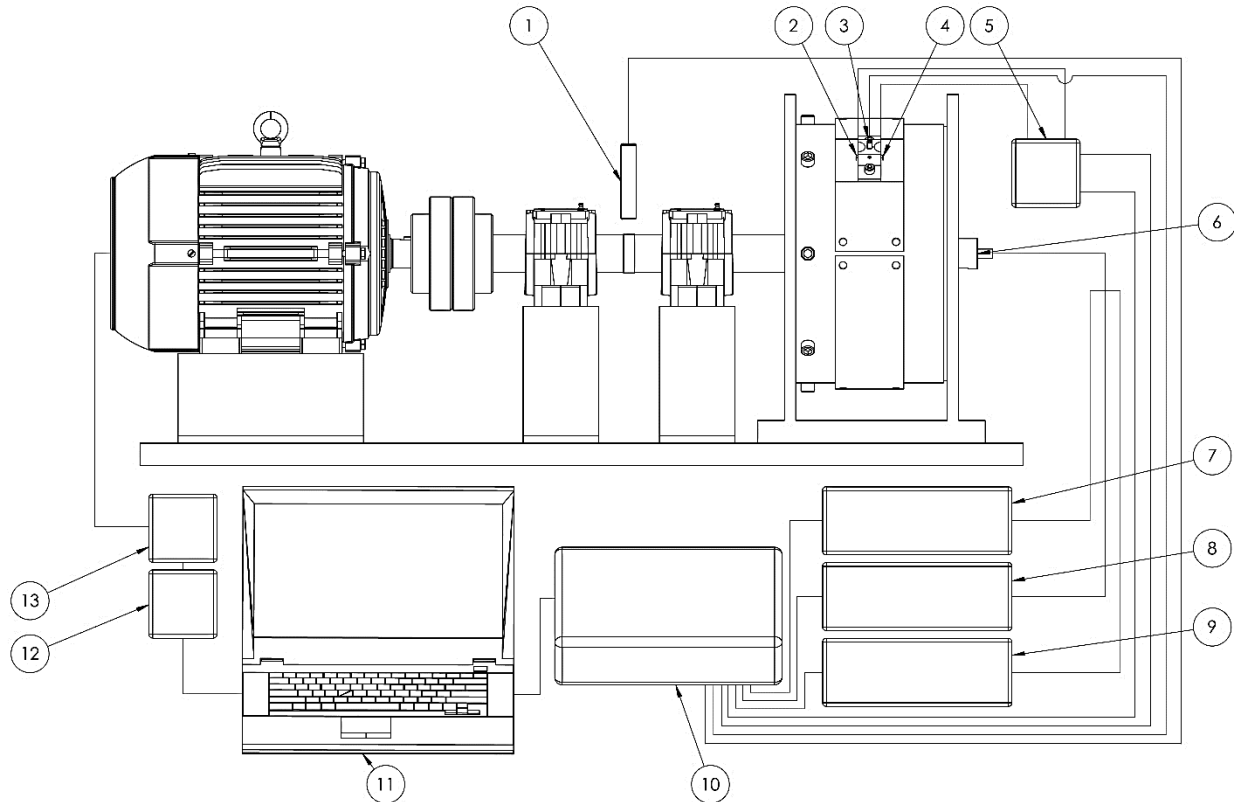


Figure 3.5-1 Experimental setup instrumentation schematic

The corresponding instrumentation list is provided in Table 3.5-1.

Table 3.5-1 Experimental setup instrumentation guide

Item Number	Item
1	Optical tachometer sensor
2	Eddy current proximity probe 1
3	Sound pressure transducer
4	Eddy current proximity probe 2
5	Eddy current proximity probe amplifier
6	Slip ring system
7	Analog strain gauge amplifier 1
8	Analog strain gauge amplifier 2
9	Analog strain gauge amplifier 3
10	Data acquisition system
11	Laptop
12	Signal generator
13	Motor speed controller

An OROS™ OR35 data acquisition system was used for all data capture purposes. The system has 8 available input channels, and a maximum sampling rate of 102.4 kHz. The system is limited to five input channels when sampling at the maximum sampling frequency. The system is capable of interfacing with AC voltage, DC voltage and powered ICP® measurement devices. The available NVGate® software allows interfacing with the device. The program has built in modal analyses algorithms which were used in the individual blade modal testing (see section ‘3.7.2 Blade Response at Installed Position’). All measurements were taken at the maximum sampling rate of 102.4 kHz.

All of the measurement instrumentation was externally powered with the exception of the sound pressure transducer as this device was a powered ICP® instrument. The sound pressure transducer was a pre-polarised ¼” free-field microphone with a maximum dynamic range of 165 dB (maximum sound pressure level without clipping the measured response). The calibrated instrument has a flat frequency response at 0dB from 20 Hz to 10 kHz and a near flat response from 10 kHz to 100 kHz (calibration was performed at 251.2 Hz). The instrument has a lower limiting frequency in the range of 0.25 Hz to 3 Hz with associated noise in the range of 3 dB. The calibration report for the specific microphone used is given in section ‘7.5.2 E2 – Sound Pressure Transducer Calibration Report’.

The blade mounted strain gauges were powered by analogue strain gauge amplifiers which interfaced with the data acquisition system via a DC voltage coupling. The amplifiers required calibration in order to match the DC voltage output with the displayed micro-strain value on the SG amplifier.

The assembly was arranged such that the sound pressure transducer lay in a plane centered with the blade and hub assembly such that the center of the blade tips pass by the sensor. As was previously mentioned, the microphone was flanked by two eddy current proximity probes which facilitated blade passing time estimation and differentiation of individual blades.

A full instrumentation list along with associated calibration values, make and model numbers can be found in section ‘7.5.1 E1 – Instrumentation List’. Images of the instrumentation can be seen in section ‘7.5.3.5 Instrumentation and Sensors’.

3.5.2. Blade Mounted Vibration Measurement Sensors

Strain gauges (SG) were used to directly measure the response of various blades during operation and modal analyses. The instrumentation positions for all blade geometries are indicated in Figure 3.5-2.

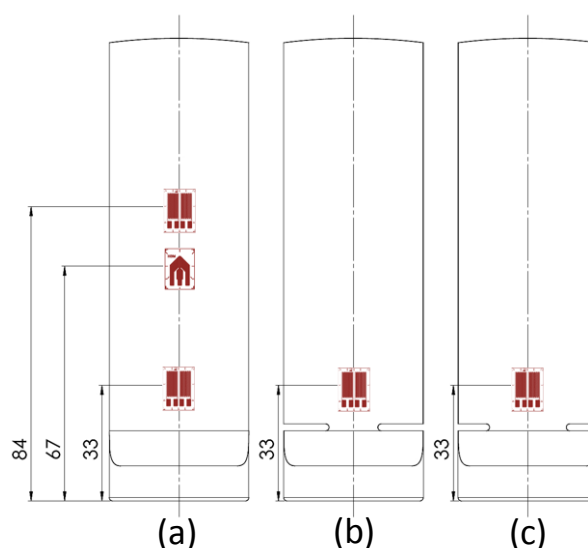


Figure 3.5-2 Strain gauge positioning. (a) Healthy blade. (b) Damaged blade type 1. (c) Damaged blade type 2.



All SG configurations were of the full bridge type. Therefore the application positions are mirrored on both sides of the blades. The full bridge configuration was chosen in order to maximise sensitivity to response deflection whilst simultaneously negating the effects of temperature change on the strain measurements.

Only one of each blade geometry type was instrumented. The unaltered healthy blade was instrumented with three full bridges. Two of the bridges were designed to capture bending modes and the remaining bridge was chosen to measure torsion.

The SG position choice was chosen such that the gauges would be sufficiently far away from geometric stress raisers (such as the blade attachment radius and damage slots) whilst still being near to positions of maximum strain depending on the mode of interest. The bridge closest to the blade attachment point (set at 33mm from the bottom end of the blade) was positioned to capture the first flap mode. The second torsional bridge, positioned 67mm from the bottom of the blade, was positioned to capture the first torsional mode. And finally the second bending bridge was positioned at a distance of 84mm from the blade bottom to capture the second flap mode. The FE analysis behind the position choices are presented in section '7.4.3 D3 – Strain Gauge Positioning for Healthy Blade'.

The two damaged blades were only instrumented with a single full bridge each. These bridges were positioned in order to capture natural mode 1, the first flap mode.

After data acquisition it was noticed that the measured voltage of one of the gauges on the healthy blade wandered. This could have been due to multiple causes. Causes such as incomplete cohesion of the gauge to the blade surface due to an adhesive fault, or a bubble captured under the gauge during application for example. The particular faulty gauge was the one nearest to the bottom of the blade (positioned at 33mm from the bottom in order to capture the first flap mode).

It was seen that the frequency content captured by the gauge was the same as that captured by the second bending gauge on the blade. This was confirmed by comparison with the data obtained by the second bending gauge on the same blade.

After later inspection it was found that only one half of the full bridge (attached to one side of the blade) was affected. Therefore only the voltage magnitudes captured would be influenced by the damaged gauge.

A near linear wandering pattern was observed, therefore it was chosen to linearly detrend the data captured by this SG and consider only the frequency content and relative voltage amplitudes. This was done as opposed to converting all of the SG measurements from a direct voltage reading to a micro-strain value. The DC offset of the remaining SG measurements was determined during post processing and subtracted from the signals such that they oscillate about a zero mean.

3.6. Experimental Configurations

Multiple geometric and excitation configurations were explored for data acquisition. This section outlines the experimental configurations considered.

3.6.1. Blade and Hub Configurations

As was previously stated, a total of 5 healthy blades, 2 damaged blades type 1 and 1 damaged blade type 2 were manufactured. This allowed multiple setup configurations. A front view of the hub and blade assembly is presented in Figure 3.6-1.

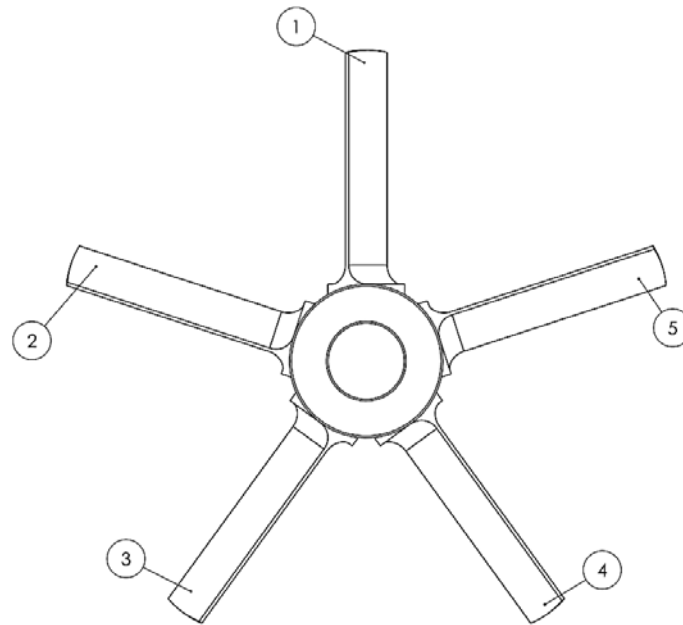


Figure 3.6-1 Blade and hub numbering convention (front view, clockwise rotation)

It was chosen that the stagger angle of the blades, as defined in the theoretical development chapter, be arbitrarily set to 30° for all configurations. All measurements are taken for clockwise rotation of the system. The blades are numbered counter clockwise in the figure. The numbering coincides with the order in which the stationary observer on the casing will be passed by the blades. Signal processing will ensure that in all measurements the blade order will always begin with the passing of blade 1.

Four separate configurations were considered. The configurations build on top of one another, in each new configuration a single healthy blade is replaced with a damaged blade. The four blade and hub assembly configurations are:

1. All blades are of the healthy type
2. Blade 5 is replaced with damaged blade type 1
3. Blade 2 is replaced with damaged blade type 2
4. Blade 3 is replaced with damaged blade type 1

The dynamic behaviour of all of the configurations, and individual blades, were experimentally determined using modal tests. These tests are outlined in section '3.7 Experimental Characterisation of Turbine Blade and System Response'.

3.6.2. Excitation Configurations

A toroidal ring containing 24 high pressure air jet attachment nozzles was installed upwind of the rotor hub and blade assembly. These nozzles direct high pressure air onto the turbomachine blades in order

to approximate upwind stator vane excitation conditions. Previous experimental work on the test bench found that with the available high pressure air source a maximum of four jets could be used simultaneously in order to produce a significant excitation condition. Four separate excitation configurations were considered: no air excitation, one jet excitation, two jet excitation and four jet excitation. A side view of the casing and attachment legend are provided in Figure 3.6-2.

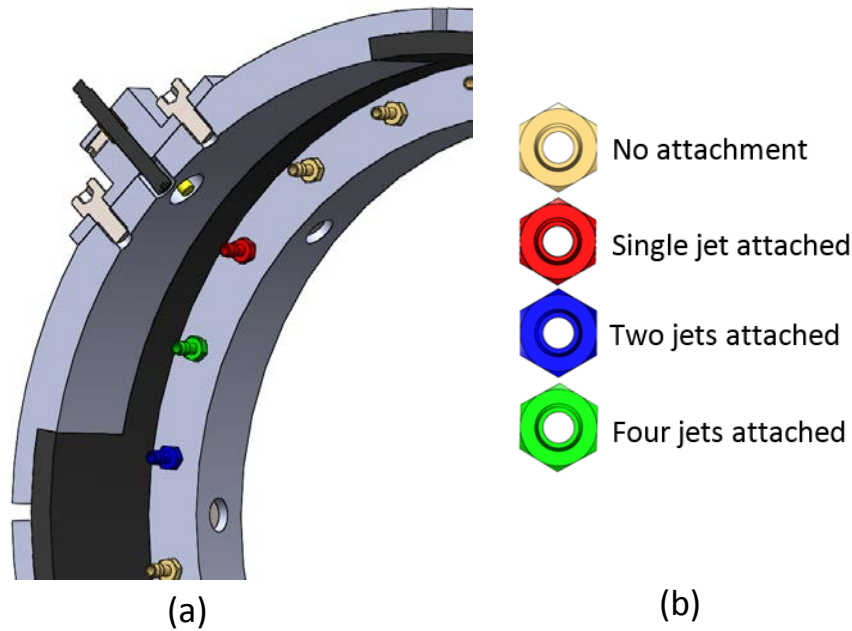


Figure 3.6-2 Excitation nozzles from side view of casing section. (a) Side view of casing section. (b) Jet attachment legend.

A front view of the casing with the different excitation configurations is given in Figure 3.6-3. The position of the sound pressure transducer can be seen in the top left quadrant of the figure.

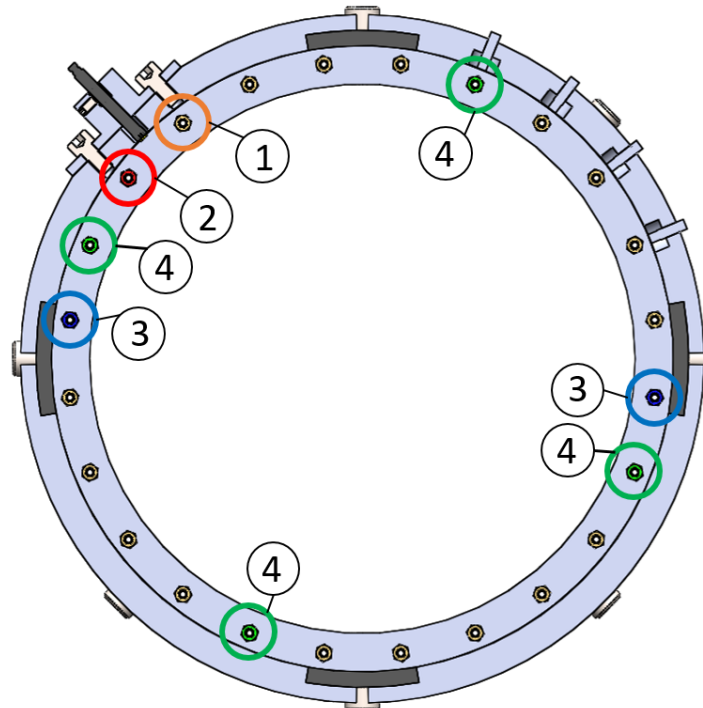


Figure 3.6-3 Front view of excitation nozzles. (1) No attachment. (2) 1 jet configuration. (3) 2 jet configuration. (4) 4 jet configuration.



All configurations, save the single jet configuration, ensure that symmetric excitation conditions exist during operation. In practice the upstream stator configurations would be symmetric about the shaft and hence the consideration.

It was found that running the motor below 200 RPM was not feasible due to hardware related issues. For safety concerns the motor was not operated at its maximum speed. The maximum measurement speed was generally limited to the vicinity of 1400 RPM. This reduced the operational range to 200 RPM – 1400 RPM.

When no air excitation was applied it was noticed that a small excitation condition still existed. This periodic excitation is attributed to gravitational effects. During each rotation a single blade experiences a range of alternating forces related to moving through a maximum and minimum pull due to gravity. These excitation forces were however significantly smaller than that the air excitation. They are therefore assumed to be negligible during operation with air excitation.

The excitation frequency ranges, for the three air excitation configurations, are given in Table 3.6-1.

Table 3.6-1 Frequency excitation ranges for air excitation configurations

Excitation Configuration	Excitation frequency at 200 RPM (3.33 Hz) (Hz)	Excitation frequency at 1400 RPM (23.33) (Hz)
1 jet	3.33	23.33
2 jets	6.66	46.66
4 jets	13.33	93.33

Although the excitation ranges do not directly coincide with any of the blades' fundamental frequencies, multiple engine order excitation possibilities for all natural frequencies of interest exist.

Three even number analytical engine order (EO) excitation conditions and associated critical speeds were chosen for comparison with experimentally obtained critical speeds. The analytically estimated critical speeds of the three different blade geometries for excitation of their fundamental modes by a single excitation jet is given in Table 3.6-2.

Table 3.6-2 Analytical critical speeds for chosen EO excitation of blade fundamental frequencies

Excitation	Healthy Blade	Damaged Blade 1	Damaged Blade 2
Fundamental Frequency (Hz)	127.08	105.22	116.40
EO 6 (RPM) [Hz]	1270.8 [21.18]	1052.40 [17.54]	1164.00 [19.4]
EO 8 (RPM) [Hz]	953.40 [15.89]	789.00 [13.15]	873.00 [14.55]
EO 12 (RPM) [Hz]	635.4 [10.59]	525.60 [8.76]	582.00 [9.70]

The various blade designs and excitation configurations provide multiple different excitation and response scenarios.

3.7. Experimental Characterisation of Turbine Blade and System Response

Experimental modal analyses were performed in order to validate the analytically expected natural frequencies and mode shapes, as well as to provide an indication of the expected response during operation. Both the system response to uniform hydrostatic excitation and the individual blade response to impact excitation were investigated and are presented in the two succeeding sections.

3.7.1. Unconstrained System Response

The unconstrained system response was determined using a scanning laser vibrometer. The test setup can be viewed in section '7.5.3 E3 – Images of Experimental Setup' subsection '7.5.3.6 Scanning Laser Vibrometer'.

Excitation was achieved by hanging the blade and hub assembly by elastic chords in front of a speaker. The speaker was attached to an amplifier which received a signal generated by the laser vibrometer. A chirp excitation was used to excite the assembly. Multiple points across the entire assembly were chosen for scanning. An average of 15 excitation and response measurements were taken for each measurement point chosen. The average response spectrum, containing the first three blade natural frequencies, obtained for blade and hub assembly configuration 1 is presented in Figure 3.7-1.

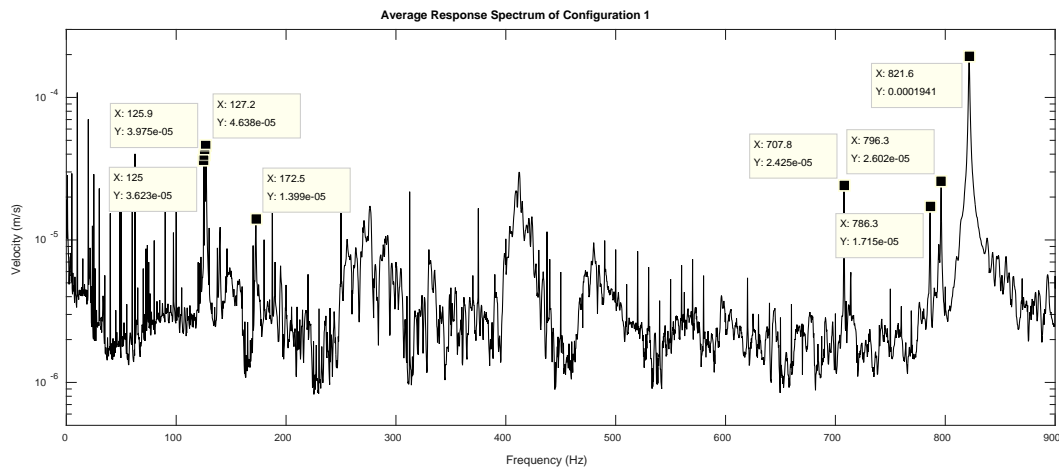


Figure 3.7-1 Average response spectrum of unconstrained assembly in configuration 1

Figure 3.7-2 is a closer look at the response spectrum in the vicinity of blade mode 1 (the blades' mode 1 was calculated in the FE analysis to be in the region of 127 Hz). It can be seen that multiple individual peaks exist in the vicinity of mode 1. Unexpected additional peaks appear near 140 Hz and 172.5 Hz.

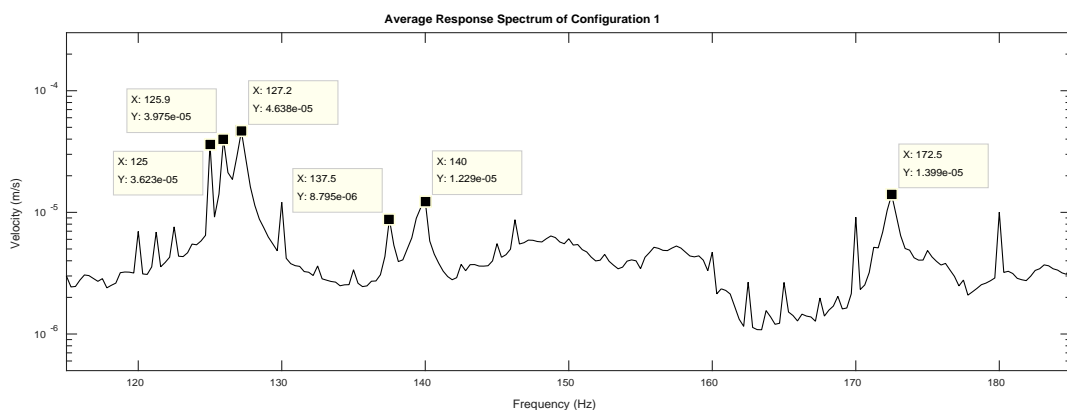


Figure 3.7-2 Average response spectrum of unconstrained config. 1 in vicinity of mode 1

The three separate peaks in the vicinity of mode 1 are related to slight differences in the fundamental frequencies of all of the individual healthy blades. Depending on the specific resonance frequency peak chosen, in the region of 127 Hz, one or more blades exhibit mode 1 bending.

The differences between the excitation frequencies can be seen to cause the blades to oscillate at different phase angles and have different maximum response magnitudes (for the specific blade-dominated system mode shape investigated). Two operational mode shapes obtained for configuration 1 and at slightly different response frequencies in the vicinity of 127 Hz have been provided in Figure 3.7-3. The individual blades are numbered from 1 to 5 starting with 1 at the 12 o'clock position, with blades 2 to 5 following clockwise (the positioning of the blades remains constant for all operational mode shape figures presented in this section as well as those to follow).

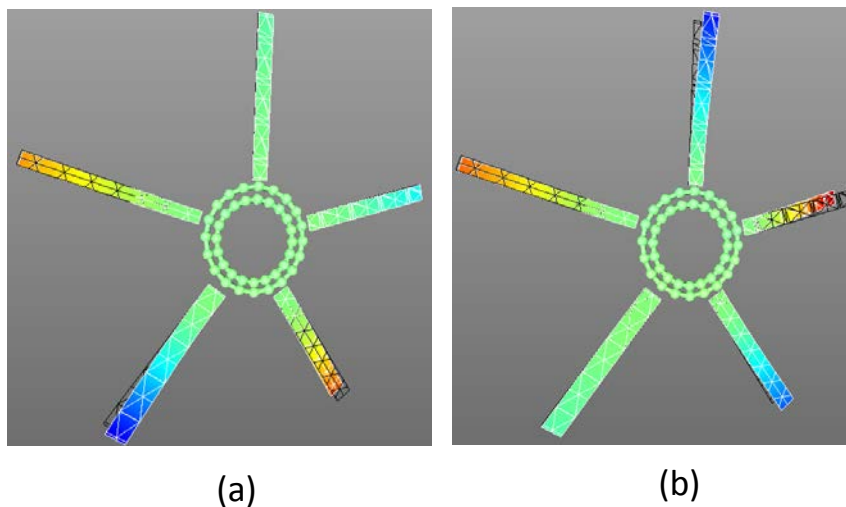


Figure 3.7-3 Operational mode shapes for configuration 1. (a) Response at 125.94 Hz. (b) Response at 127.19 Hz.

The blades which respond at the same phase angle are seen to have closer fundamental frequencies when compared to the other blades, this is confirmed in the succeeding section. For the case of excitation at 127.19 Hz blades 1 and 3 respond at a 180° phase angle difference to blades 2 and 5.

It is interesting to note that at approximately 170 Hz all five blades oscillate in their first bending mode at the same phase angle. A similar occurrence is seen for the second bending mode for excitation at 822 Hz (higher than the expected mode 2 frequency). These mode shapes are shown in Figure 3.7-4.

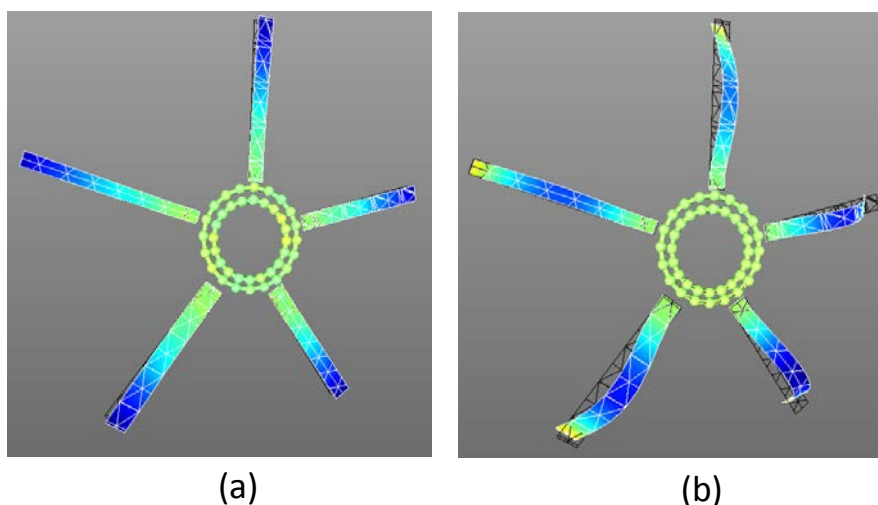


Figure 3.7-4 Operational mode shapes for configuration 1. (a) Mode 1 bending at 172 Hz. (b) Mode 2 bending at 822 Hz.

Thus unexpected system modes were uncovered, no such modes was noticed in the cyclic symmetric FE modal analysis and investigation. As expected the blade dominated torsional modes occur in the vicinity of 710 Hz.

In configuration 2 blade 5 was replaced with a blade of reduced fundamental frequency (damaged blade type 1). The individual blade's fundamental frequency was expected to be approximately 20 Hz lower than that of the healthy blades. The operational mode shapes for excitation of configuration 2 near the blade dominated mode 1 can be seen in Figure 3.7-5.

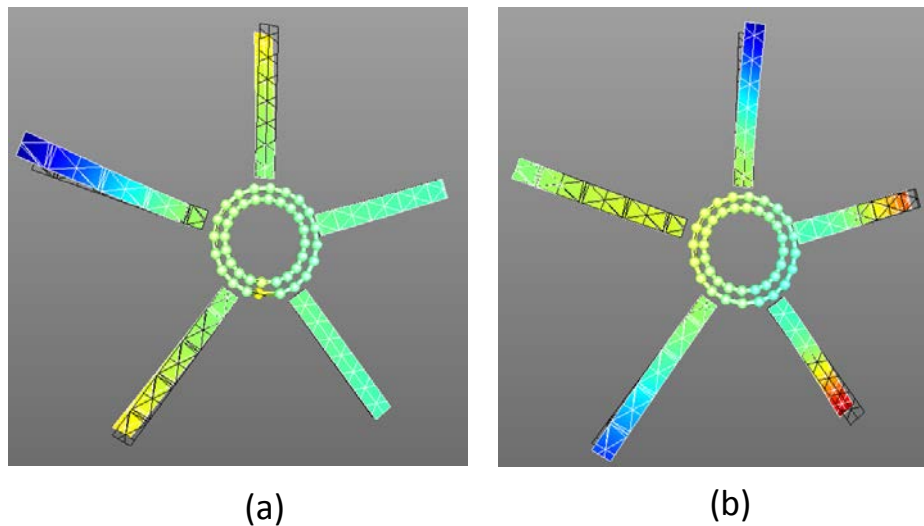


Figure 3.7-5 Operational mode shapes for configuration 2. (a) Mode 1 bending at 110 Hz. (b) Mode 1 bending at 134 Hz.

As expected the fundamental mode of blade 5 is seen to be excited at a much lower frequency than the other blades. Further, there is sympathetic excitation of the adjacent blades due to the physical coupling of the system. Due to the increase in mistuning mode localisation has now occurred.

Once again additional unexpected modes which cause all blades to oscillate at the same phase angle appear. Due to the replacement of an individual blade the frequencies at which these modes occur is seen to reduce. These operational mode shapes for these cases are provided in Figure 3.7-6.

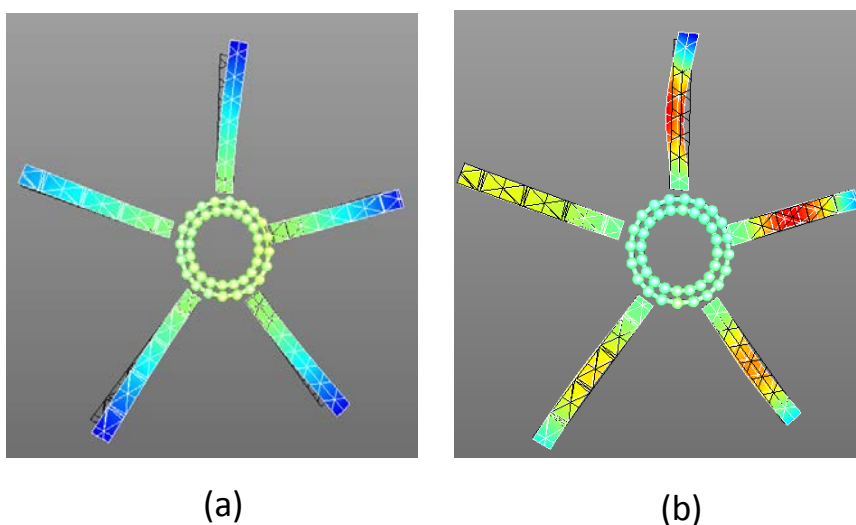


Figure 3.7-6 Operational mode shapes for configuration 2. (a) Mode 1 bending at 169 Hz. (b) Mode 2 bending at 813 Hz.

The response amplitude of the changed blades, blade 5, is much lower than that of the other 4 blades for these particular modes.

In configuration 3 blade 2 was replaced with a blade of reduced fundamental frequency, where the reduction was in the order of 10 Hz (damaged blade type 2). The system response in the vicinity of excitation frequency of blades 5 and 2 can be seen in Figure 3.7-7 (a) and (b) respectively.

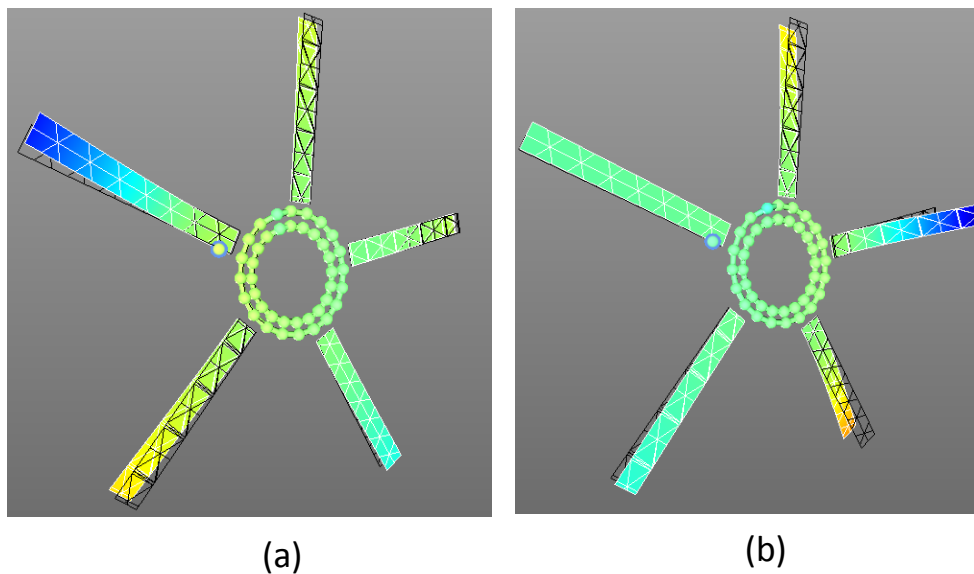


Figure 3.7-7 Operational mode shapes for configuration 3. (a) Mode 1 bending at 109 Hz. (b) Mode 1 bending at 118 Hz.

Once again sympathetic excitation of the adjacent blades and mode localisation is noticed. When the system was excited at approximately 140 Hz blades 1, 3 and 4 can be seen to respond at the greatest magnitudes with blade 1 responding at 180° phase difference to blades 3 and 4. This is illustrated in Figure 3.7-8 (a).

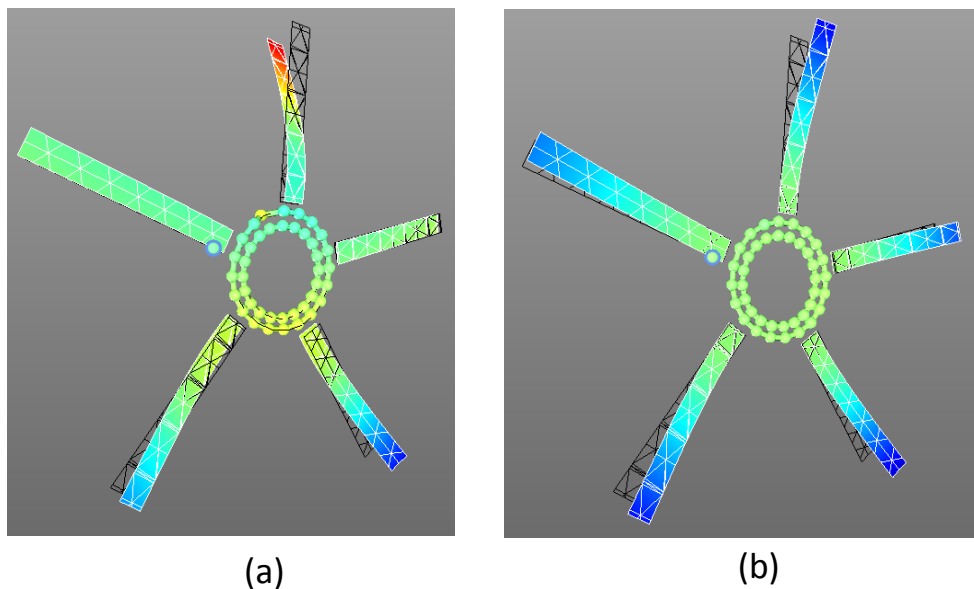


Figure 3.7-8 Operational mode shapes for configuration 3. (a) Mode 1 bending at 139 Hz. (b) Mode 1 bending at 165 Hz.

Once again modes exist where all the blades oscillate in phase with one another. Once again these particular modes occur at reduced frequencies when compared to the previous two configurations. This is illustrated in Figure 3.7-8 (b) (as the average blade natural frequencies decrease with the replacement of healthy blades with damaged ones).



In terms of configuration 4 blade 3 is replaced with a blade of similar fundamental frequency to blade 5 (damaged blade type 1). The operational mode shapes won't be presented in this section, however it is again seen that blades of similar geometry respond at the same excitation frequency. Mode localisation is still present as well as sympathetic excitation due to movement of adjacent blades when the blades of different geometry are excited.

The mistuning of the system was shown to cause unexpected modes and mode shapes. For the case where all of the blades were most similar, namely configuration 1, it was seen that at slightly different excitation frequencies, in the vicinity of the expected blade fundamental mode, slightly different system modes were achieved. Multiple peaks occur in the vicinity of the mean tuned peak value (mean mode frequencies across all blades) on the system's response FRF. This was expected according to the literature reviewed. It was further seen that the individual blade response amplitudes differed significantly between blades under the same excitation and with similar fundamental frequencies.

The operational mode shapes obtained provides insight into the expected system response during operation. Given the data acquisition system it was not possible to instrument and measure the response of all of the blades simultaneously. Several conclusions can be drawn from this investigation which can be used when investigating the experimentally obtained internal pressure signals.

When configuration 1 is excited in the vicinity of the blade mode 1 (for the healthy blade) all of the blades are expected to respond at different phase angles depending on the system mode and nodal diameters. When any of the other configurations are excited in the vicinity of the damaged blades' natural frequencies only slight participation of the adjacent blades is expected. This is because the damaged blades have natural frequencies which are far removed from the healthy blades.

During the analysis an additional mode may be found where all of the blades respond in the same blade mode shape and at the same phase angle regardless of the configuration.

It is important to note that both the forcing function and boundary conditions for the unconstrained system differ significantly from the installed (on shaft) position. The system's behaviour in the unconstrained position only provides an indication of what is to be expected when installed on the rotor.

In the installed operating position the blades are expected to be impinged upon by the high pressure air nozzles (and by a modal hammer during the individual blade modal response investigation). These are completely different excitation mechanisms when compared to the uniform hydrostatic pressure applied to the one side of the assembly by the speaker during the unconstrained excitation.

Further, in the installed position, the hub is forced onto the tapered end of the shaft. Thus the hub attachment is seen to be significantly stiffer in the installed position when compared to the unconstrained configuration.

The blades are a fair approximation of Euler-Bernoulli beams, and as such are highly sensitive to the boundary conditions. Therefore it is expected that the blade natural frequencies and associated mode shapes in the installed position may differ slightly from those found in the unconstrained condition.

The remaining average response spectra and operational mode shapes for all configurations can be found in section '7.5.5 E5 - Unconstrained System Response'.

3.7.2. Blade Response at Installed Position

A modal test was performed with the hub and blade assembly installed on the experimental setup. This was done in order to determine the response spectra of the individual blades at stationary installed conditions. Measurements were taken by both the installed strain gauges (SG) on the various blades and the sound pressure transducer (microphone) during these investigations.

Excitation was achieved by a nylon tipped modal hammer. Various excitation locations across the length of the blades were investigated. Trial and error was used to determine a suitable excitation point on each of the blades. In general this point was found to be approximately one third of the length of the blade measured from the radius on the blade. The blades were oriented in the experimental setup such that the centre of their tips coincided with the sound pressure transducer installed in the casing. One modal SG response set for excitation of blade 1 on configuration 1 is provided in Figure 3.7-9, the microphone's response for the same measurement is provided in Figure 3.7-10.

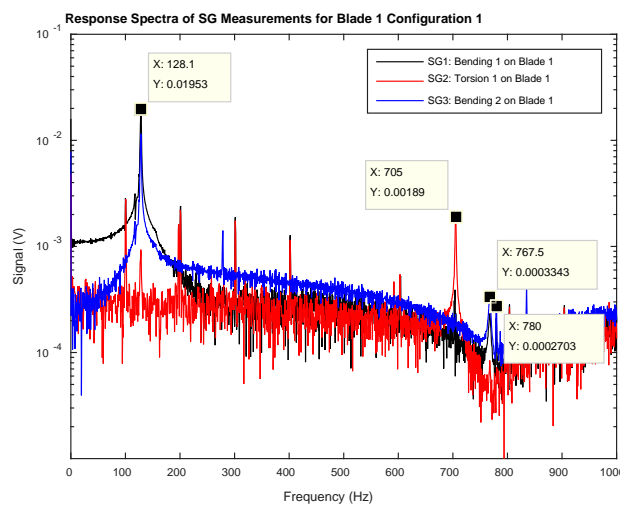


Figure 3.7-9 Response spectra for blade 1 in configuration 1 measured by 3 SGs

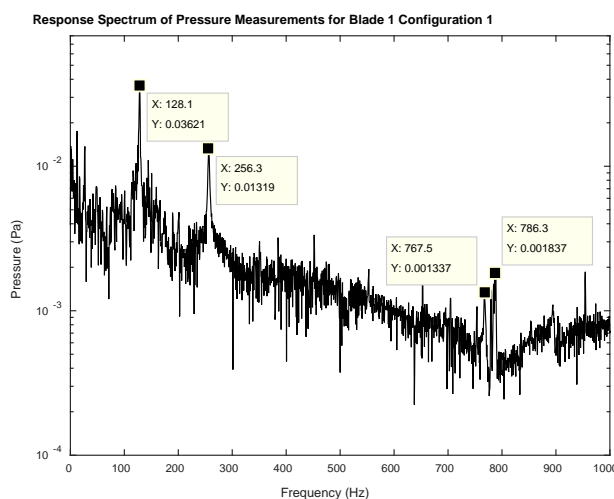


Figure 3.7-10 Response spectra for blade 1 in configuration 1 measured by sound pressure transducer

The microphone was in general less sensitive to the torsional modes in comparison with the torsional SG measurements and all flapwise mode measurements (both SG and microphone based). The first harmonic of the fundamental frequency was always present in the microphone's results, and often the second flapwise bending mode produced a greater response amplitude than the first.



Table 3.7-1 provides the results for all of the blades and for all of the assembly configurations. The symbols ‘H’, ‘D1’ and ‘D2’ refer to blade types healthy, damaged 1 and damaged 2 respectively. The individual blade mistuning (BMT), percentage difference of natural frequency to nominal natural frequency, has also been indicated in the table.

Table 3.7-1 Individual blade fundamental responses for different experimental configurations at stationary conditions

Blade	Configuration 1 blade fundamental frequency (Hz)		Configuration 2 blade fundamental frequency (Hz)		Configuration 3 blade fundamental frequency (Hz)		Configuration 4 blade fundamental frequency (Hz)	
	NF (Hz)	BMT (%)	NF (Hz)	BMT (%)	NF (Hz)	BMT (%)	NF (Hz)	BMT (%)
1	128.1 ^{#*}	1.570	128.1 ^{#*}	5.641	128.1 ^{#*}	7.865	128.1 ^{#*}	13.103
2	125.0 [*]	0.888	125.0 [*]	3.084	112.5 ^{#*}	5.271	111.9 [#]	1.201
3	126.3 [*]	0.143	126.3 [*]	4.156	126.3 [*]	6.349	100.0 ^{#*}	11.708
4	125.6 [*]	0.412	125.0 [*]	3.084	125.0 [*]	5.254	124.4 [*]	9.836
5	125.6 ^{#*}	0.412	101.9 ^{#*}	15.966	101.9 ^{#*}	14.197	101.9 [#]	10.030
Mean	126.12	0.685	121.26	6.386	118.76	7.787	113.26	9.175
σ	1.072194		9.746507		10.06451		11.41098	
$\% \Delta \sigma$	0.005034		0.048806		0.033437		0.041616	

#SG measurement. *Microphone measurement. Measured with SG on blade. σ = Standard Deviation.

Depending on the configuration certain blades had SGs installed (as mentioned in a prior section). All SG measurements and sound pressure transducer measurements were compared to produce the table. Depending on whether the value was obtained by both a SG on the blade and the microphone or by a SG on another blade and the microphone an indicator has been specified.

The analytically obtained fundamental frequencies for the healthy, damaged blade type 1 and damaged blade type 2 were found to be approximately 127 Hz, 105 Hz and 116 Hz respectively. It can be seen that all of the natural frequencies, for modes 1 to 3, are within ± 5 Hz of the analytically obtained natural frequencies. These differences are attributed to manufacturing tolerances. Therefore it is expected that the critical resonance speeds, as predicted in section ‘3.6.2 Excitation Configurations’, remain fairly close to the actual critical resonance speeds. These speeds will be confirmed in the succeeding section which investigates the run-up resonance responses.

With respect to configuration 1, the slight differences in the individual blade natural frequencies were seen to causing mistuning effects in the previous section. It was seen that, given a particular excitation frequency blades 2 and 4 oscillated in phase whilst blades 1 and three were 180.

A global measure of the system’s mistuning has been included in the table. Namely the mean percentage standard deviation change ($\% \Delta \sigma$) of the blades natural frequency with respect to the configurations nominal (mean) natural frequency. The global mistuning for configuration 1 was found to be significantly smaller than the remaining three configurations. Configuration 2 was found to have the largest level of mistuning, followed by configuration 4 and 3 respectively.

The response spectra obtained for stationary measurements, both SG and sound pressure transducer based, under modal hammer excitation for all of the individual blades and geometric configurations can be seen in ‘7.5.6 E6 – Response Spectra of Individual Blades’.

3.7.3. Run-up Blade Responses

A run-up investigation was performed in order to obtain experimental critical resonance speeds for steady state measurement speed choice. Investigations were performed on the first three experimental configurations as each investigation provided additional response information with an additional SG measurement (SGs applied to the damaged blades which replaced healthy blades). The expected resonance speeds for configuration 4 were inferred from this information.

Due to hardware limitations not all SGs on all blades could be measured simultaneously. Table 3.7-2 contains the instrumentation scheme for the investigation. The parameters B1, B2 and T1 refer to strain gauges optimised to measure the first flap, second flap and first torsional modes respectively. As was previously mentioned it was found that SG optimised to capture B2 on blade 1 provided the same information as SG B1 on the same blade. This result is confirmed here.

Table 3.7-2 Ramp-up instrumentation

Blade	Ramp-Up 1 – Configuration 1	Ramp-Up 2 – Configuration 2	Ramp-Up 3 – Configuration 3
1	B1, B2, T1	B1	B1
2	Not instrumented	Not instrumented	B1
3	Not instrumented	Not instrumented	Not instrumented
4	Not instrumented	Not instrumented	Not instrumented
5	Not instrumented	B1	B1

Due to the fact that the SGs only supply point information for one blade, on a hub and assembly configuration, it is only possible to deduce that blades, of a similar design, would have similar responses under the same excitation conditions. No information would be available to determine the relative phase angle in between individual blades using the SG measurements to determine the system’s full response.

Measurements were taken for all four excitation configurations as well: namely no air excitation, 1 jet, 2 jet and 4 jet excitation. The run-up SG responses for configuration 1 with 1 air jet being used to excite the system is given in Figure 3.7-11.

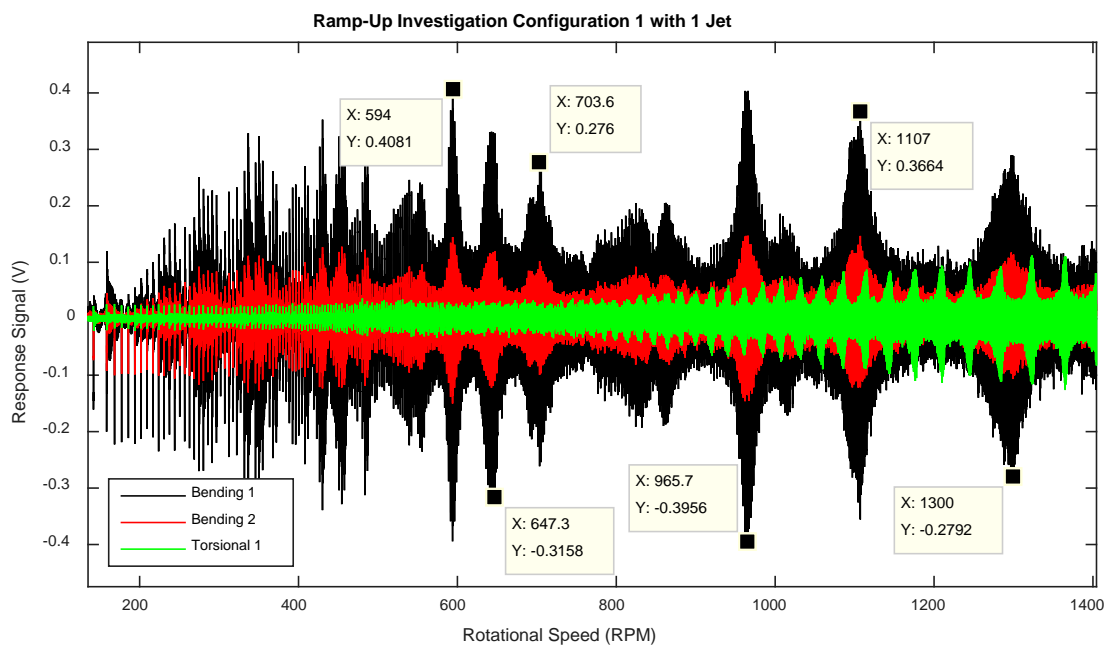


Figure 3.7-11 Run-up investigation of configuration 1 with 1 jet

It can be seen that the greatest amplitudes occur at 594 RPM and 965.7 RPM (EO 13 and 8 respectively). As the number of jets increased from 1 to 2 and then finally to 4 it was found that the response amplitudes decreased significantly.

The greatest response amplitude found during the evaluation of configuration 1 was 0.39 V at approximately 966 RPM. The largest response amplitude for the 2 jet configuration was found to be 0.29 V (at 967 RPM), and finally 0.24 V (at 967 RPM) for the 4 jet configuration. This trend, of decreasing response amplitude, was found across all run-up measurements. Therefore, as the number of active jets increased the relative applied force, per blade, decreased.

All of the run-up responses for configurations 1 through 4 under 0, 1, 2 and 4 jet excitation can be seen in '7.5.7 E7 – Run-Up Resonance Detection'. An example of a run-up test, performed for configuration 3 under 1 jet excitation, is provided in Figure 3.7-12.

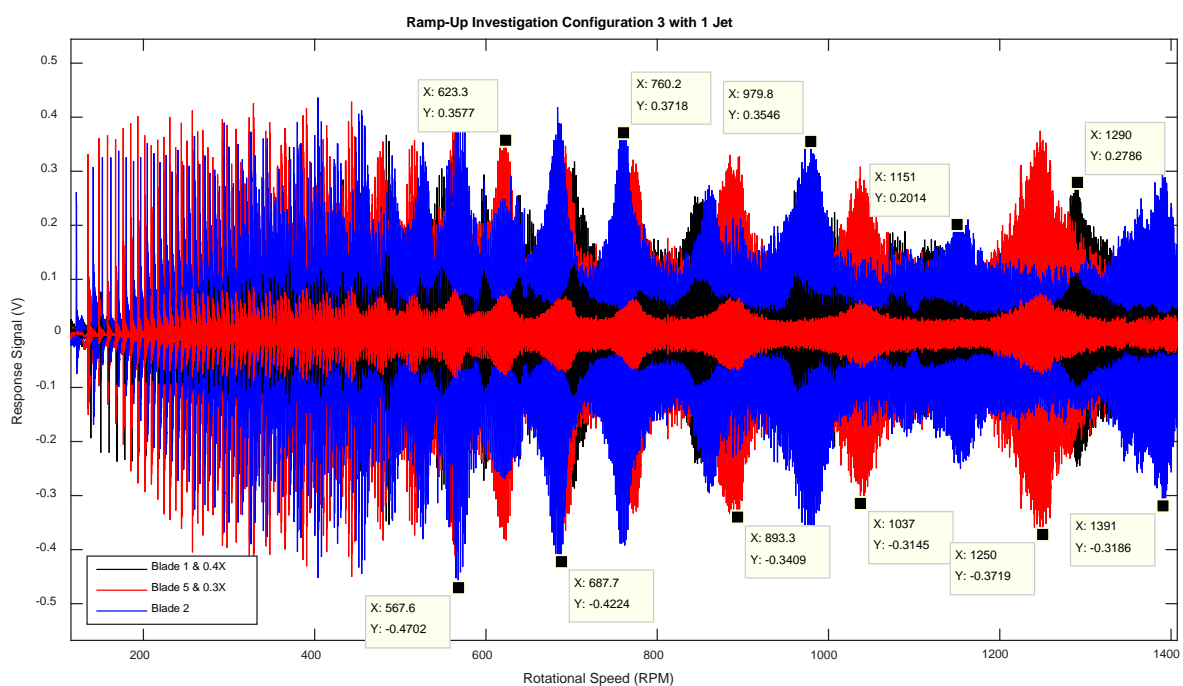


Figure 3.7-12 Run-up configuration 3 with 1 jet

The responses from three separate blades were recorded and compared in this run-up investigation. In order to better present the data, the run-up information for blade 1 and 5 was re-plotted on top of the full signals at reduced amplitudes so that the resonance locations could be clearly seen in the figure.

It can be seen from the figure that the critical speeds, for individual blades of different fundamental frequencies, are still individually excited at their own blade natural frequencies. Even though the blades are structurally coupled through the hub and attachment shaft. Blades 1, 2 and 5 all lie adjacent of one another, and so sympathetic excitation of the surrounding blades was expected due to the physical coupling. The coupling effect was seen in the unconstrained system response characterisation investigation. Further, it can be seen that many of the individual blade resonances are close to one another. Therefore by choosing to excite the system at one blade's resonance, a measurement of another blades response will often be in the vicinity of its individual resonance.



The observed fundamental EO responses at experimentally determined operational speeds for the three different blade geometries and single jet excitation is provided in Table 3.7-3.

Table 3.7-3 Observed operational speed and fundamental EO response relationships for 1 jet excitation

Healthy blade (B1 & B2)		Damaged blade type 1 (B1)		Damaged blade type 2 (B1)	
Speed (RPM) [Hz]	EO	Speed (RPM) [Hz]	EO	Speed (RPM) [Hz]	EO
594.0 [9.90]	13	514.5 [8.56]	12	567.6 [9.46]	12
647.3 [10.78]	12	565.6 [9.43]	11	623.3 [10.39]	11
703.6 [11.73]	11	623.3 [10.39]	10	687.7 [11.46]	10
824.6 [13.74]	10	691.0 [11.52]	9	760.2 [12.67]	9
862.4 [14.73]	9	782.1 [13.04]	8	860.8 [14.35]	8
965.7 [16.10]	8	888.1 [14.80]	7	979.8 [16.33]	7
1107 [18.45]	7	1040 [17.33]	6	1151 [19.18]	6
1300 [21.67]	6	1251 [20.85]	5	1290 [21.50]	5

The table was generated using observations from multiple single jet excitation run-up measurements. It is important to note that the resonance speeds are approximated for all blades of the same type because only 1 blade of each type was instrumented. Further, the overall system behaviour is expected to change with the swapping of a blade for a configurational change, and as such the critical speeds are only approximations. The experimentally obtained critical resonance speeds, for EOs 12, 8 and 6 are all within 30 RPM (0.5 Hz) of the chosen analytically obtained values for all blade geometries.

The observed fundamental EO and critical speeds for operation with 2 and 4 jets are available in Table 3.7-4 and Table 3.7-5 respectively.

Table 3.7-4 Observed operational speed and fundamental EO response relationships for 2 jet excitation

Healthy blade (B1 & B2)		Damaged blade type 1 (B1)		Damaged blade type 2 (B1)	
Speed (RPM) [Hz]	EO	Speed (RPM) [Hz]	EO	Speed (RPM) [Hz]	EO
419.7 [7.00]	9	375.7 [6.26]	8	428.4 [7.14]	8
477.3 [7.96]	8	433.3 [7.22]	7	489.7 [8.16]	7
550.7 [9.18]	7	512.9 [8.55]	6	569.5 [9.49]	6
645.4 [10.76]	6	621.2 [10.35]	5	683.6 [11.39]	5
779.5 [12.99]	5	776.8 [12.95]	4	855.7 [14.26]	4
964.7 [16.08]	4	1046 [17.43]	3	1147 [19.11]	3
1294 [21.57]	3				

Table 3.7-5 Observed operational speed and fundamental EO response relationships for 4 jet excitation

Healthy blade (B1 & B2)		Damaged blade type 1 (B1)		Damaged blade type 2 (B1)	
Speed (RPM) [Hz]	EO	Speed (RPM) [Hz]	EO	Speed (RPM) [Hz]	EO
479.8 [8.00]	4	252.7 [4.21]	6	286.9 [4.78]	6
647 [10.78]	3	307.1 [5.12]	5	344.5 [5.74]	5
967 [16.12]	2	387.4 [6.46]	4	430.9 [7.18]	4
		514.6 [8.58]	3	572.1 [9.54]	3
		777.8 [12.96]	2	848.4 [14.14]	2

As was previously stated, these run-up resonance locations, obtained from the responses of individual blades, were used to generate a steady measurement plan.



3.8. Experimental Methodology

The purpose of this section is to briefly outline the methodology and related choices used to obtain steady state internal pressure measurements. This section is further used to outline the associated concerns with the signal processing performed on those measurements.

The experimental characterisation of the blade and hub assembly provided the resonance locations (in terms of operating speed) for the various experimental and excitation configurations. Direct on blade measurements confirmed the analytical predictions for the blades' resonance response behaviour (namely the locations of the critical speeds).

This information is used in tandem with the instrumentation and data acquisition system's characteristics in order to outline the data capture limitations from a signal processing point of view. It further provides insight into the measurement plan used to obtain a library of different measurement scenarios in terms of the various assembly and excitation configurations at and about resonant conditions.

A range of nominally constant speed measurements were to be taken. This was done for all hub assembly and excitation configurations. It was chosen that each steady state record be 10 seconds in length.

All measurements were taken at the maximum sampling rate of the data acquisition system, namely at 102.4 kHz. This provided the finest time resolution possible given the available equipment. The sampling rate and sample length provided a frequency resolution of approximately 0.1 Hz with a maximum effective bandwidth of approximately 51.2 kHz (taking the Nyquist-Shannon sampling theorem into account).

Taking the sound pressure transducer's lower and upper limiting frequencies into account for a relatively flat sensor response (3 Hz to 100 kHz), frequency content in the range of approximately 3 Hz to 51.2 kHz could be successfully captured using this measurement scheme. Given the instrumentation and sampling frequency, this content is expected to be without significant sensor noise nor sampling related aliasing.

Taking the measurement scheme limitations into account, the slowest rotor speed which could be considered for once per revolution frequency content capture was 180 RPM (3 Hz). Given the sampling rate, no maximum operating speed existed for once per revolution frequency content capture.

The first 3 blade natural frequencies, for all blade geometries, were all well within the flat 0 dB response region of the sound pressure transducer (namely 3Hz to 10 kHz) for direct measurement (i.e. not Doppler shifted). The calibration report for the sound pressure transducer, which contains its response curve, has been provided in section '7.5.2 E2 – Sound Pressure Transducer Calibration Report'.

Only the fundamental blade response modes were found to be significantly present during the run-up resonance investigations. Measurement speed choice was based solely on these observed resonances.

For hub and blade assembly configuration 1 measurements were taken at resonance, resonance ± 5 RPM (0.083 Hz), resonance ± 10 RPM (0.167 Hz) and resonance ± 20 RPM (0.333 Hz). This was done for EO resonances 13, 12 and 8 with 1 jet excitation, EOs 6 and 4 with 2 jet excitation and finally EOs 3 and 2 with 4 jet excitation. EO 8 with 1 jet excitation was found to have the largest response



amplitude when compared to all other EOs observed for all excitation conditions. The data obtained using hub and assembly configuration 1 was the primary data set for analysis. All other data obtained is considered as supplementary for the purpose of further investigations.

For the remaining assembly configurations, which contained ‘damaged’ blades of reduced fundamental frequencies, measurements were taken at various critical and non-critical speeds for all excitation configurations. The speed locations were chosen across the operational range of the experimental setup.

Due to the proximity of the resonances of the different blade types, measuring at the resonance of one blade type was often found to be within a close proximity to the resonance of another (see the measurement plan mentioned below as well as the run-up resonance plots for configurations 2 to 4). Measurements were also taken in between resonance peaks. Thus a multitude of on and just off resonance measurements were obtained using this measurement scheme.

As was stated, all of the measurements taken provided a library of different excitation and response conditions from which example or batch cases could be investigated. The steady measurement plan is provided in section ‘7.6 Appendix F – Steady Measurement Plan’. The run-up resonance investigation used for this purpose can be found in section ‘7.5.7 E7 – Run-Up Resonance Detection’.

A signal processing methodology, which outlines the steps taken in order to separate the waves about individual blades and into the deterministic and stochastic parts, has been provided in section ‘7.5.8 E8 – Signal Processing Methodology’. It is important to note that the signal processing methodology was developed to provide a wide range of interim and result signals which could be evaluated, all signals will not however be used for evaluation and analysis.

Chapter 4 Investigations and Results

4.1. Introduction to Investigations and Results

The pressure signal within a turbomachine casing is complex. It contains multiple constituents stemming from various sources. Some of the components and associated sources are well understood and others less so.

Analytical models have been developed to describe the internal turbomachine casing conditions. Construction of the analytical models covers many broad topics. Topics such as how to model the blades' response, how to describe the upstream stator forcing behaviour as well as how to incorporate the blade vibration signature into the internal pressure signal have been theoretically explored. The performance and flexibility of the constituent and combined models must now be ascertained.

It is from these analytical models that hope is placed in order to obtain an indicator of blade response behaviour from steady state turbomachine internal pressure measurements. The blade vibration signature within the pressure signal as a whole is slight. Investigations must be performed in order to determine whether or not any useful blade vibration characteristics may be extracted from such a signal given the models, signal processing and optimisation techniques developed and discussed.

An existing experimental setup was modified for the purpose of this investigation. Multiple blade and hub as well as excitation configurations were considered. This was done in order to provide a library of response data at nominally constant rotor speeds. The library was developed taking multiple run-up SG response measurements into account. It is from this data collection that case examples can be further investigated. The blade and hub assemblies were characterised at stationary conditions using proven experimental modal analysis techniques to ensure that their response behaviour at stationary conditions is well understood before investigating their interaction with the internal pressure signal.

The purpose of this chapter is to bring together all of the theory developed in Chapter 2 by comparing and incorporating it with experimental measurements. Questions such as: how well does the blade response model fit the actual blade response behaviour, and what can be learned from internal pressure signals observations needs to be answered.

The proceeding section explores aspects of the steady state SG measurements recorded. This is done in order to provide a better picture of the forced response behaviour during operation. The effect of centrifugal stiffening on the blades' fundamental frequencies is initially examined. The investigation into centrifugal stiffening will indicate the applicability of the system and individual blade characterisation done at stationary conditions. Excessive change in the fundamental frequencies during operation may indicate that the stationary characterisation observations are no longer applicable for later steady state behaviour inference.

Once the topic of centrifugal stiffening has been covered, the measured SG responses are used to explore crucial aspects of the blade forced response model. This model consists of the blade transfer function model and the blade forcing function model. Reduced forms of the inverse problem are used to solve for blade vibration characteristics from SG measurements.

The second section explores what can be learned through inspection of the internal pressure signal using the signal processing techniques discussed. Finally the observations from the signal processing results and SG measurements are incorporated into the inverse problem with the pressure models.

4.2. Observations from SG Measurements

The behaviour of two chosen blades' was monitored during steady state data acquisition (first bending SG on blade 1 for configuration 1 and the SG on blade 5 for configuration 2). The SG data is used to confirm that minimal blade centrifugal stiffening is present, investigate the true form of the forcing and response behaviour (given the experimental setup) as well as to provide blade transfer function parameter estimates. The waterfall plot of blade 1's response during 1 jet excitation is shown in Figure 4.2-1.

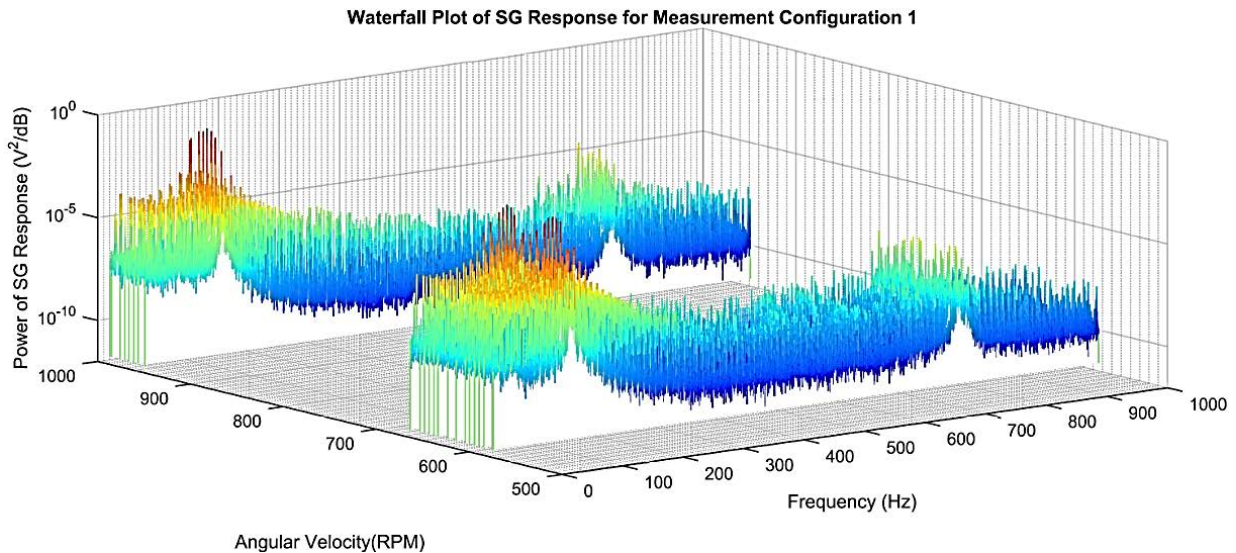


Figure 4.2-1 Waterfall plot of SG responses measured on blade 1 configuration 1 under 1 jet excitation conditions

For configuration 1 under 1 jet excitation it was chosen that measurements be taken at and about fundamental EO resonances 13, 12 and 8 (which occur at approximately 594 RPM, 643 RPM and 966 RPM respectively). It can be seen on the above waterfall plot that three clear fundamental resonance peaks are noticed in the vicinity of the stated critical speeds, corresponding to the three chosen EO resonances. An alternate power-frequency view of the same waterfall plot is provided in Figure 4.2-2.

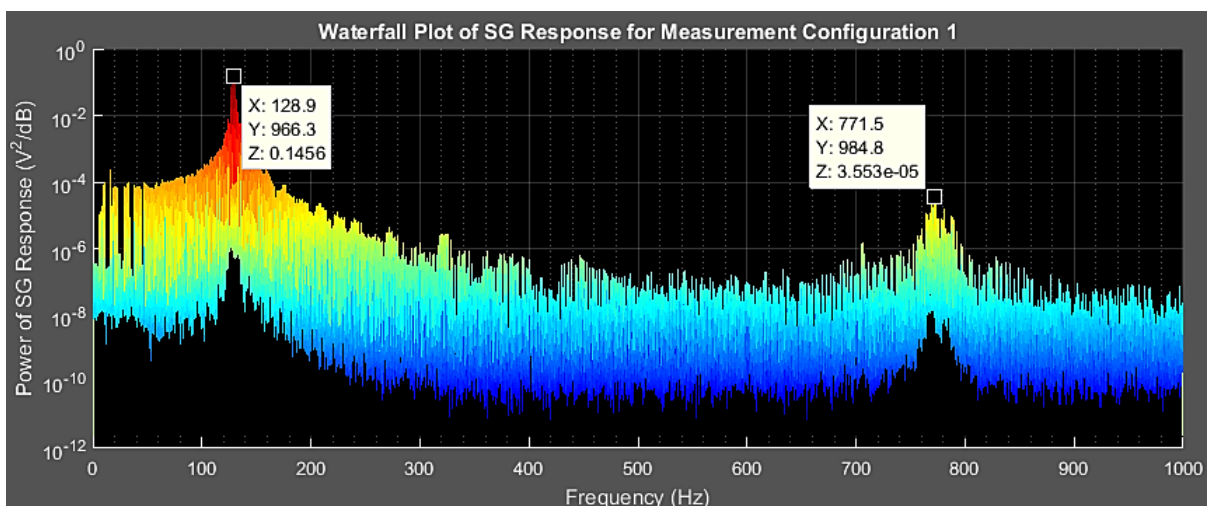


Figure 4.2-2 Frequency-Power view of SG waterfall plot for configuration 1 under 1 jet excitation

Under closer qualitative investigation it can be seen that the first two flapwise bending natural frequencies do not shift significantly (shifting is attributed to the centrifugal stiffening phenomenon).

These findings are aligned with the numerical FE investigation's results. The first and second bending mode peaks are seen to remain near stationary in Figure 4.2-3 (top view of the initial waterfall plot).

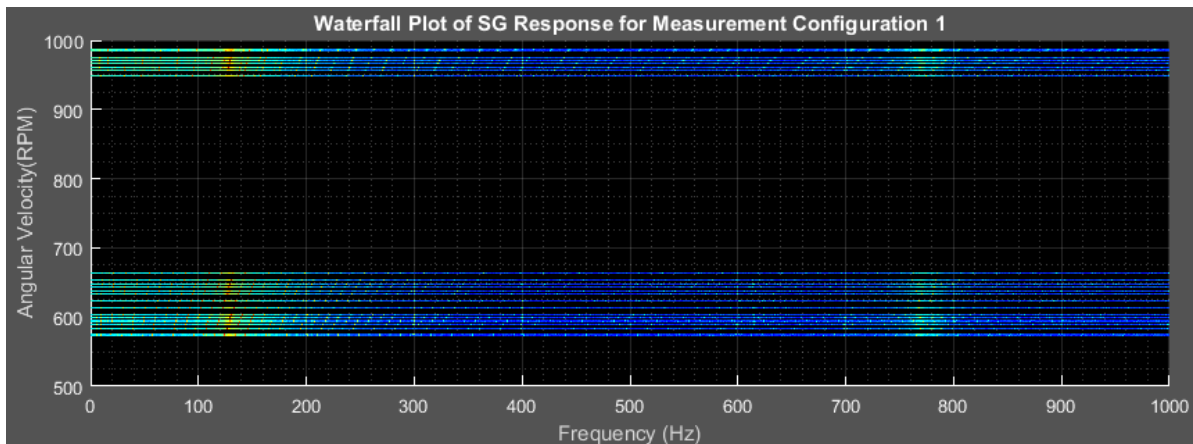


Figure 4.2-3 Frequency-Angular Velocity view of SG waterfall plot for configuration 1 under 1 jet excitation

Qualitative observations from the SG measurements suggest that centrifugal stiffening is negligible for both blades 1 and 5 in assembly configurations 1 and 2 respectively. Recall that the FE analysis predicted a maximum shift of the healthy blade's fundamental frequency of approximately 2.3 Hz and similarly a maximum shift of 2.6 Hz for the fundamental frequency of damaged blade type 1 (operating at 1400 RPM). The waterfall plots of all of the SG data upon which these initial qualitative observations have been produced can be found in section '7.7.1 G1 – Waterfall Plots of Full SG Responses'. A more concrete approach is however required before inferences can be made about the actual impact of centrifugal stiffening on the blade fundamental frequencies across the measurement range.

The SG responses across all hub and assembly configuration 1 blade 1 measurements were averaged in order to obtain a robust estimate of the blade transfer function form during steady operation (the blade forcing behaviour is averaged out in this process as the only constant across the measurements is the blade geometry). The averaged response was then further filtered and smoothed. This was done in order to minimise the noise and remaining forcing components present in the signal. The averaged and filtered SG response for hub and assembly configuration 1 can be seen in Figure 4.2-4.

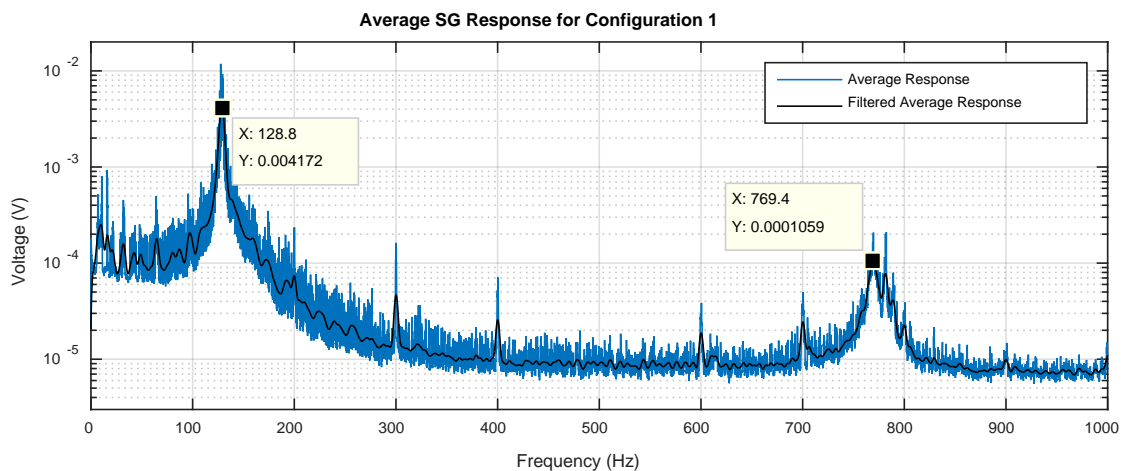


Figure 4.2-4 Average SG response measured on blade 1 for all configuration 1 steady state measurements

The fundamental frequency of blade 1 in configuration 1, picked from the filtered and smoothed response curve, was found to be approximately 128.8 Hz. A total of 144 independent steady state measurements were used to construct the average response. The average rotor speed for all configuration 1 measurements was approximately 772.0 RPM (with a standard deviation of approximately 162.4 RPM). The FE model predicts an increase of approximately 0.68 Hz for operation at 772 RPM for the healthy type blade. Recalling that the stationary fundamental frequency for blade 1 was found to be 128.1 Hz, the increase of 0.7 Hz is within 3% of the expected value.

It is important to note that the averaging process flattens out the response leading to an average response spectrum with resonance peaks which have artificially higher damping than had no averaging been performed. Consider the exaggerated example presented in Figure 4.2-5. A total of 5 separate blade responses, within increasing fundamental frequencies simulating exaggerated centrifugal stiffening, are plotted along with the averaged response.

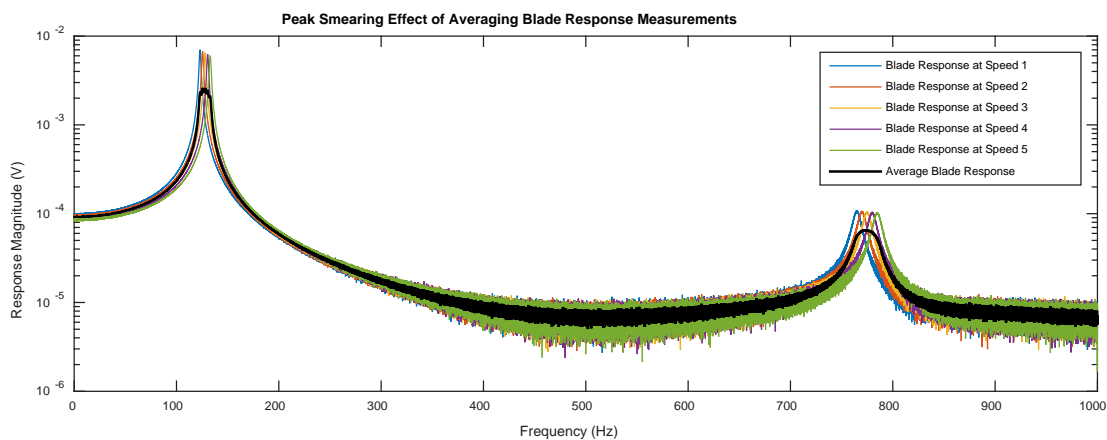


Figure 4.2-5 Blade averaging peak smearing effect

So long as the centrifugal stiffening remains small, with respect to the resonance peak locations, the flattening effect is expected to have a minimal impact on the resulting average spectrum.

Similar to the process performed on the blade 1 configuration 1 measurements, the averaged and filtered response for blade 5 in configuration 2 is provided in Figure 4.2-6. A total of 158 independent experimental measurements were used to construct the average response plot. The collection of measurements used have a mean rotor speed of 805.8 RPM and a standard deviation of 227.0 RPM.

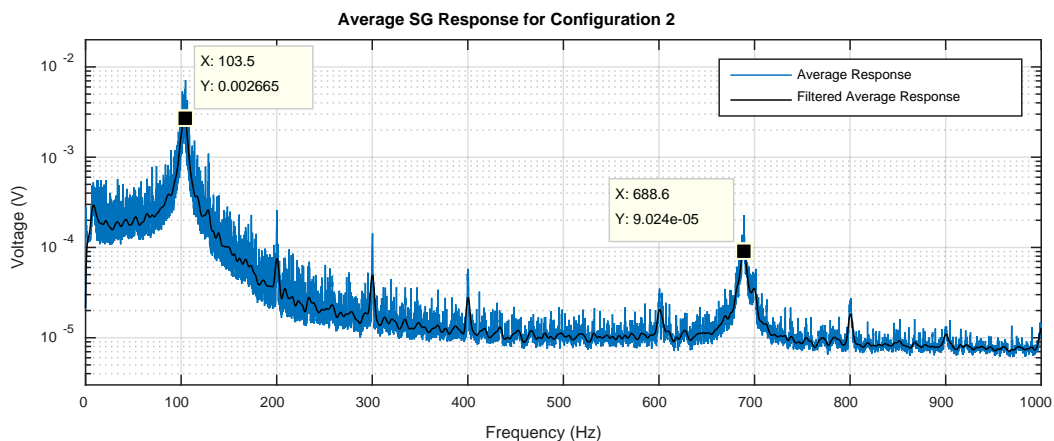


Figure 4.2-6 Average SG response measured on blade 5 for all configuration 2 steady state measurements

The fundamental frequency obtained from the above plot for configuration 2 blade 5 is 103.5 Hz. The stationary fundamental frequency was measured to be 101.9 Hz during the modal analysis. This results in a frequency increase of approximately 1.6 Hz. The FE analysis predicts an increase of approximately 0.85 Hz for damaged blade type 1 operating at approximately 806 RPM. The increase in fundamental frequency is therefore nearly double that predicted by the FE model, the shift is however still small in comparison to the value of the stationary fundamental frequency itself (101.9 Hz).

A later investigation, which fits the analytical blade transfer function to the averaged and filtered curve, predicts an increase in fundamental frequency to within 20% of the expected value, taken with respect to the FE investigation's results. The result obtained is much closer to the FE analysis's results.

The increase in fundamental frequencies, for both blades 1 and 5 in configuration 1 and 2, were found to be small in comparison to their stationary fundamental frequencies (well within 5% for both blades). The stationary characterisation results of the remaining blades is therefore still expected to be applicable, this is attributed to the similarity of the various blade geometries. The shift in the blade fundamental frequencies, due to centrifugal stiffening, is expected to be approximately within the maximum bounds obtained for the FE systems. Namely within 2.3 Hz for all healthy blades, 2.6 Hz for all damaged blades type 1 and 2.3 Hz for all damaged blades type 2 for operation up to 1400 RPM.

The averaged and filtered responses were used in order to obtain an approximation of the forcing function form. Recall that the blade response X is a function of the blade transfer function H and the forcing function F . This relation is repeated in Equation [4.2.1].

$$\{X(j \cdot \omega)\} = [H(j \cdot \omega)] \cdot \{F(j \cdot \omega)\} \quad [4.2.1]$$

Therefore in order to obtain an estimate of the forcing function's behaviour, the average blade transfer function estimate is factored out from the full response, as is indicated in Equation [4.2.2].

$$\{F(j \cdot \omega)\} = \frac{\{X(j \cdot \omega)\}}{[H(j \cdot \omega)]} \quad [4.2.2]$$

Consider the captured SG response for assembly configuration 1 under 1 jet excitation operating at 574 RPM (9.6 Hz, approximately 20 RPM lower than fundamental EO 13) shown in Figure 4.2-7.

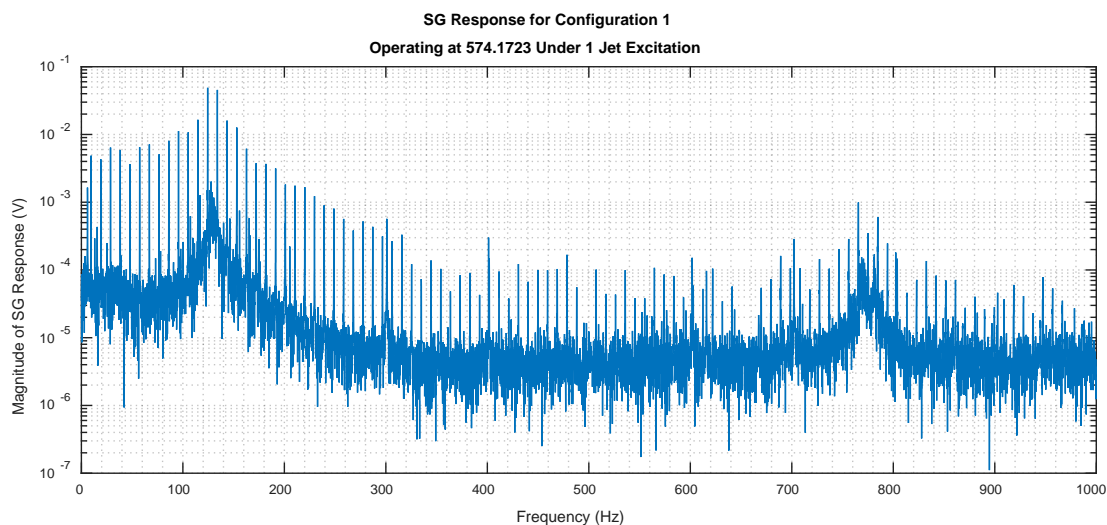


Figure 4.2-7 SG response for configuration 1 under 1 jet excitation operating at 574 RPM

It can be seen that the blade's forced response is very similar to what was expected during the development of the blade forced response model. Namely that the blade is excited across a large frequency range by both Gaussian white noise and rotor harmonics. This trend was noticed during the evaluation of all SG measurements for both configuration 1 and 2 measurements. Dividing the individual blade response through by the average SG response, obtained from the averaging process, yields an approximate form of the forcing function, the resulting spectrum is given in Figure 4.2-8.

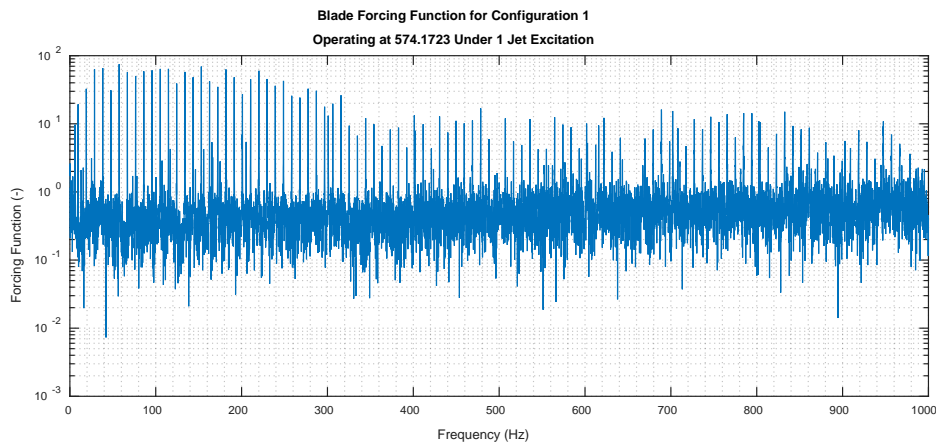


Figure 4.2-8 Extracted blade forcing function for configuration 1 under 1 jet excitation operating at 574 RPM

Additional examples of individual SG response and extracted forcing function plots for configurations 1 and 2 under all excitation schemes is provided in section '7.7.5 G5 – Exemplar SG Response and Forcing Function Forms'. Examples presented are chosen at and about various resonance conditions.

The relationship between the force applied by the upstream stators and the measured response (in volts) is unknown, therefore only relative magnitudes are considered for investigation. Upon inspection of the forcing behaviour, it is once again seen that the blade is excited at integer multiples of the rotor speed, as was the behaviour of the theoretical forcing model. Further the forcing magnitude is seen to decrease and then remain fairly constant after a specific point. There is also a fairly large amount of wide spectrum noise in the forcing function. This behaviour was noted for both configurations 1 and 2 under 1 jet excitation conditions. The waterfall plot for the extracted forcing function form, across all configuration 1 measurements with 1 jet excitation, is given in Figure 4.2-9.

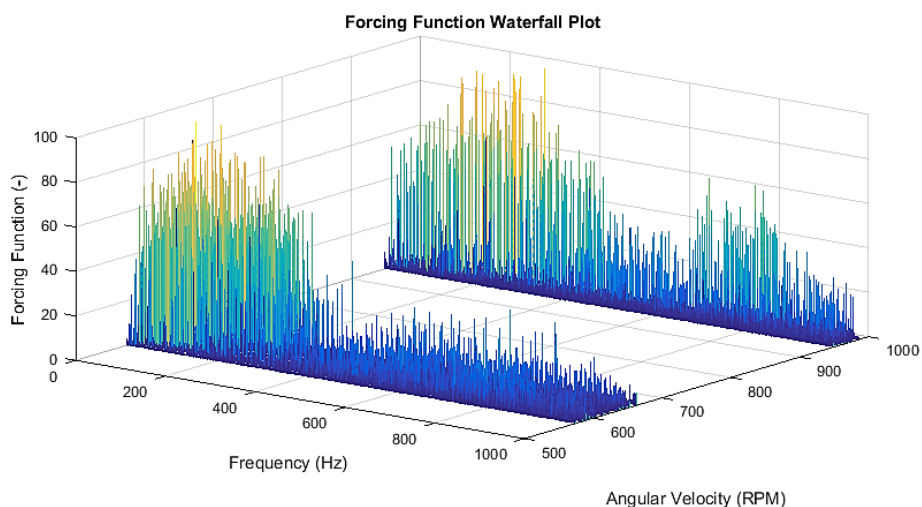


Figure 4.2-9 Waterfall plot of extracted blade forcing function for configuration 1 under 1 jet excitation

Similar to the spectra obtained for the theoretical forcing function, it can be seen that the excitation rotor harmonics taper off after a particular point. The remaining waterfall plots determined for the forcing function form from configurations 1 and 2, under 1, 2 and 4 jet excitation can be seen in section '7.7.2 G2 – Waterfall Plots of SG Forcing Function Spectra'.

During the investigation of the proposed forcing function model, it was indicated that if the force applied by the various upstream stator vanes differed then it may be possible to identify excitation from the different streams. A comparison is quantitatively accomplished by visually inspecting the rotor harmonics adjacent to one another. Consider the forcing function form obtained for blade and hub assembly 1 under 2 jet excitation whilst operating at 627 RPM (10.44 Hz) given in Figure 4.2-10.

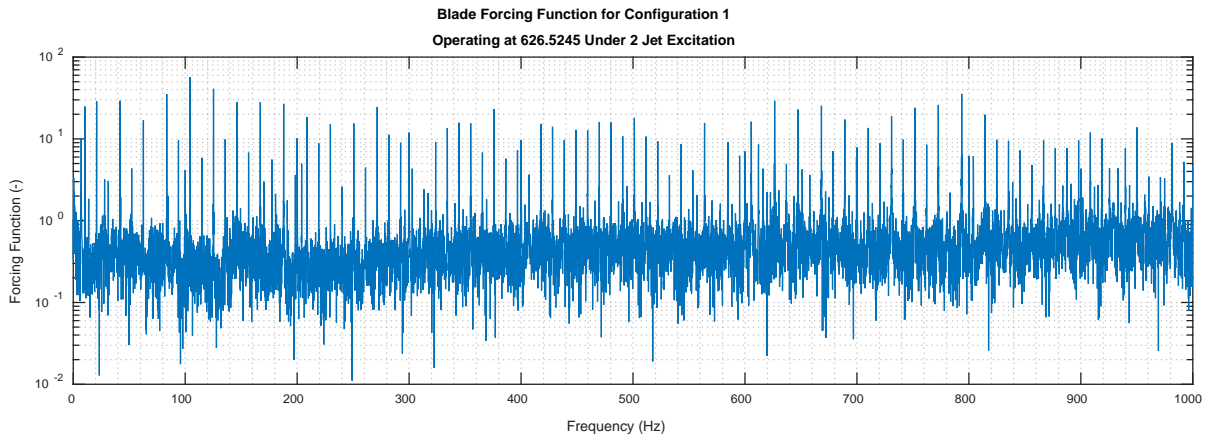


Figure 4.2-10 *Extracted blade forcing function for configuration 1 under 2 jet excitation operating at 627 RPM*

Taking a closer look at the above plot from approximately 600 to 800 Hz, shown in Figure 4.2-11, it is clear that every second rotor harmonic, within the range of interest shown, generally occurs at a reduced magnitude in the frequency range of interest.

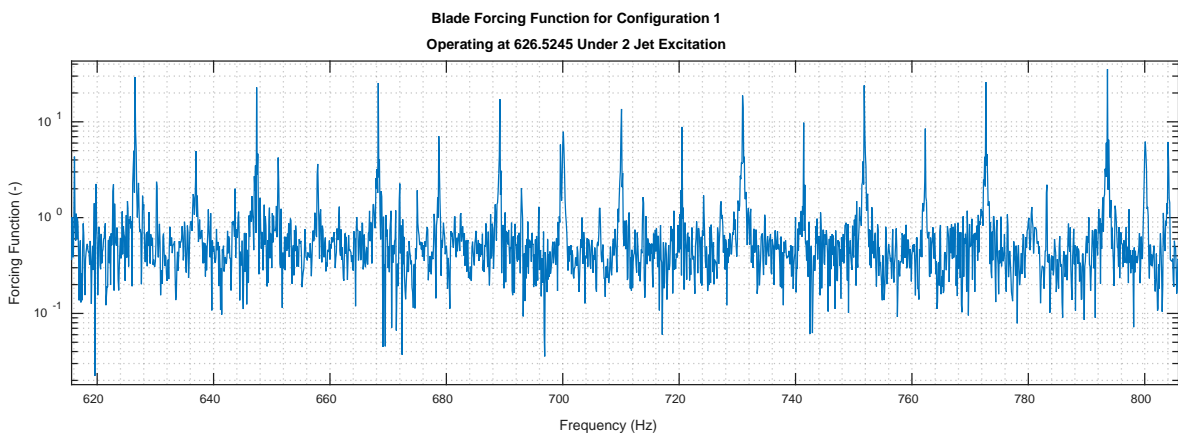


Figure 4.2-11 *Zoomed in view of blade forcing function for configuration 1 under 2 jet excitation operating at 627 RPM*

When compared to the Gaussian based forcing model spectra, this implies that the forces applied by the two upstream nozzles do indeed differ by a set amount. Upon qualitative inspection of the whole spectrum it is clear that the trend is however not quite as prominent as that found during the development of the ideal situation. Namely that every second frequency harmonic peak is always at a distinctly different amplitude across the full response spectrum and that there is a clear decrease in the rotor harmonics' peak amplitudes after a specific point.

This result is however expected as the experimental setup and excitation system is not ideal. Pressure losses in the air supply to the various nozzles, due to the presence of multiple non-ideal connectors and manufacturing tolerances, lead to a situation where each nozzle is not capable of supplying the exact same forcing pressure stream at the exact same angle of attack. This causes an asymmetry in the forcing phenomenon about the circumference of the experimental setup which is noticeable in the SG measurements in both the time and frequency domains.

In the final qualitative example of the forcing function evaluation, consider the blade forcing form obtained for configuration 1 under 4 jet excitation. Depending on the cyclic symmetry of the excitation system a pattern of four repeating harmonic peaks is expected in the forcing spectrum. The example chosen is for operation at 988 RPM (16.46 Hz, approximately 20 RPM above fundamental resonance EO 2 for 4 jet excitation) and is shown in Figure 4.2-12.

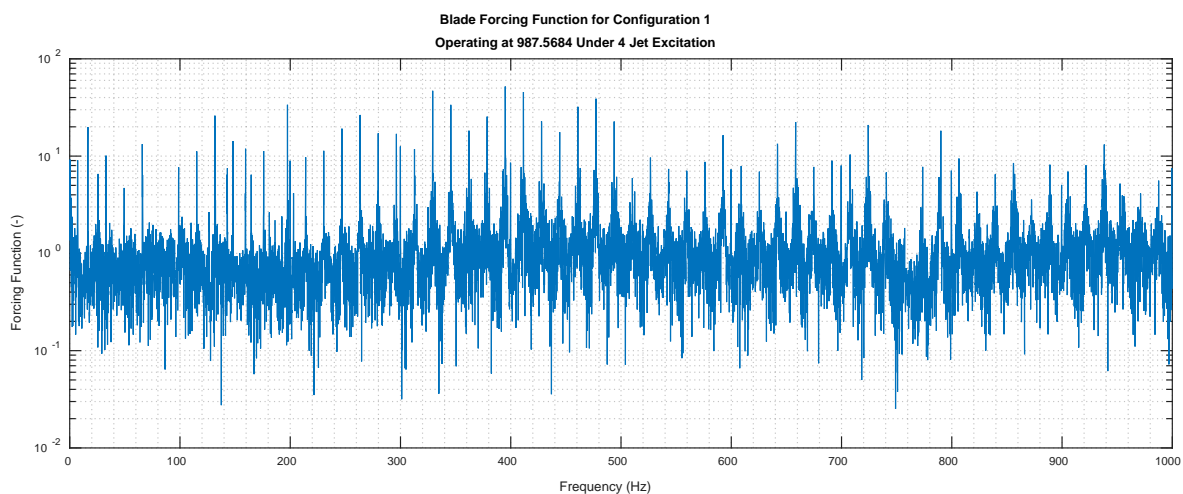


Figure 4.2-12 Extracted blade forcing function for configuration 1 under 4 jet excitation operating at 988 RPM

A closer look at a section of the spectrum shows that a distinct harmonic forcing pattern is indeed present, and that pattern repeats for every 4 harmonics. However, once again under qualitative visual inspection of the spectrum, the prominence of the trend is diminished when compared to the ideal geometrically symmetric noise-free situation, as explored during the theoretical development of the forcing function model. This case is shown in Figure 4.2-13.

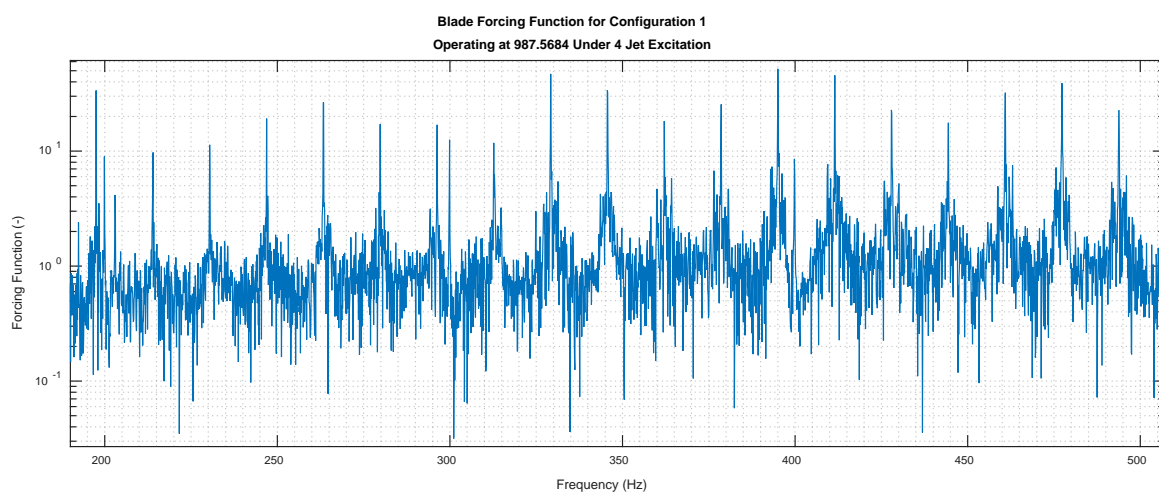


Figure 4.2-13 Zoomed in view of blade forcing function for configuration 1 under 4 jet excitation operating at 988 RPM

The relative peak height of every set of four peaks remains fairly constant in the chosen range. Specifically it can be seen that the first peak of every set of four generally remains the highest in the chosen interval of investigation.

The visual based observations however do not provide an indication as to whether or not the proposed time domain forcing function model, based upon the sum of individual Gaussian peaks representing the periodic force applied to the blades, will be able to be tuned to the actual behaviour.

The forcing function model was fitted to the steady state SG measurements taken for both configurations in order to understand its ability to describe the underlying behaviour. Recall that the model was based upon the number of upstream stators, the blade and hub geometry and the rotor angular velocity. A nonlinear constrained optimisation technique was used to fit this model to the experimental results (first reduced inverse problem). The design variables were chosen as follows:

- The individual relative stream peak magnitudes, the total number depending on the number of jets in the system (as each upstream jet may apply a slightly different nominal force value). They are scaled relative to one another by limiting their numerical values to between 0 and 1.
- The width of the Gaussian pressure peaks, added to produce the forcing function, are defined by a single standard deviation value. Recall that it is expected that as the system's rotational speed increases the amount of time that the force is applied to the blade decreases. The percentage angle, per revolution, that the stator stream applies a force to the blade is used to define the standard deviation of the individual Gaussians added. This percentage value is the second design variable.
- A scalar force multiplier is the third design variable. It is used in order to align the overall magnitude of the model with the measurement's magnitude. The multiplier is chosen to be in the form of two design variables a and b such that the overall multiplier is given by: $a \cdot 10^b$
- The fourth design variable is the signal to noise (SNR) ratio of the forcing function
- The fifth and final design variable is system's angular velocity in RPM

The system's angular velocity and number of jets determine the number of Gaussian shaped pulses per revolution, as per the theoretical development. The only constraints in the problem pertain to the design variables' upper and lower limits, namely the lower bounds (LB) and upper bounds (UB). The measured system's angular velocity, RPM_M , was used in order to provide bounds for the angular velocity design variable. The limits chosen have been presented in Table 4.2-1.

Table 4.2-1 Boundary conditions for design variables of blade forcing function fitting problem

Limit	Relative jet height	Gaussian std. dev. %	Scalar force multiplier 'a'	Scalar force multiplier 'b'	SNR	Angular velocity (RPM)
LB	0.01	1e-15	1e-7	0	5	$RPM_M - 0.1 \cdot RPM_M$
UB	1	1	10	5	1000	$RPM_M + 0.1 \cdot RPM_M$

As was stated, it is chosen that the relative upstream jet heights are scaled between approximately 0 and 1. The Gaussian standard deviation percentage per revolution, which defines the force pulse widths, was also defined between nearly 0 and 1 (where a value of 1 corresponds to a full 360° of constant applied force per revolution, and a near zero value implies an impulse excitation).

The combination of the design variables a and b allow scaling of the forcing function to be between 0 and 1e6. The signal to noise (SNR) ratio bounds allows a wide range additive noise to the signal. The

only design variable assumed to be known with some confidence is the system rotational speed (as it was measured). It was therefore chosen to allow this design variable to only shift by a maximum of $\pm 10\%$ from the measured value. The large width of the remaining design variable bounds was chosen due to insufficient knowledge about their true nature.

The chosen initial design variable guesses, for all initial forcing function form optimisations, are presented in Table 4.2-2. As was previously stated, the initial guess for the angular velocity value was obtained from the measured rotor’s angular velocity. The initial pulse width was chosen such that it approximates a near impulse excitation (approximately 0.004° in the stationary reference frame). The physical significance of the forcing pulse width is explored further on.

Table 4.2-2 Initial conditions for blade forcing function fitting problem

Item	Relative jet height	Gaussian std. dev. %	Scalar force multiplier a	Scalar force multiplier b	SNR	Angular velocity (RPM)
Guess	0.9	1e-5	1	1	500	RPM_M

The initial design variable guesses were held constant for all excitation and geometric configuration measurements. This was done in order for the optimisation results to be directly comparable to one another. A total of 285 optimisation problems were solved across all of the excitation and geometric configurations. A detailed table which compares all of the results has been provided in section ‘7.7.3 G3 – SG Forcing Function Fitting Results’.

The mean square error (MSE) between the absolute of the experimentally derived forcing function vector and the absolute of the numerically generated forcing function vector was minimised over during the optimisations. All optimisations employed the gradient based ‘interior-point’ algorithm. Once each optimisation problem had been solved the coefficient of determination, R^2 , was calculated from the result to provide a goodness of fit measurement for the model.

The MSE values obtained are only comparable between datasets of the same forcing excitation conditions (i.e. a 1 jet excitation MSE can only be compared to another 1 jet excitation MSE). This is because the forcing magnitude between the excitation conditions differed. As the number of jets increased, so did the nominal excitation magnitude of each pulse decrease. Therefore forcing magnitudes between sets differed, and it is on these magnitudes that the MSEs were calculated. The R^2 value is however directly comparable between sets as it is inherently scaled between 0 and 1. A summary of the results outlined in the appendix can be seen in Table 4.2-3.

Table 4.2-3 Summary of SG Based forcing function fitting results

Data Set	Number of Items	Mean R^2	Std. Dev. R^2	Min R^2	Max R^2	Mean iterations	Mean Function Count
Complete	285	0.3694	0.2574	0	0.7974	49.6877	500.4386
Config. 1 Jets 1	62	0.6352	0.0479	0.5220	0.7974	21.3226	180.6935
Config. 1 Jets 2	31	0.3048	0.1456	0	0.4967	44.8065	451.9355
Config. 1 Jets 4	42	0.0447	0.0771	0	0.2605	98.7381	1063.20
Config. 2 Jets 1	71	0.5901	0.0902	0.2413	0.6985	22.7746	189.1127
Config. 2 Jets 2	36	0.2522	0.0807	0.0941	0.4374	35.3333	339.0278
Config. 2 Jets 4	43	0.0833	0.1183	0	0.3519	102.6512	1095.90

A couple of trends in the data are noticed. Firstly as the number of jets (and design variables) increases so does the model's predictive ability (as defined by the R^2 value) decrease significantly. So does the expense of the problem increase (as defined by the number of iterations and cost function evaluations). Further, the nature of certain higher jet excitation configurations could not be captured at all resulting in R^2 values of 0.

The best single fit was found for a configuration 1 measurement under 1 jet excitation (R^2 of 0.7974). Within the same dataset the worst correlation between the experimentally and numerically derived results achieved a coefficient of determination of 0.5220. The mean R^2 value for the dataset is over 60%, the highest of all the all datasets. The best fit model is presented in Figure 4.2-14.

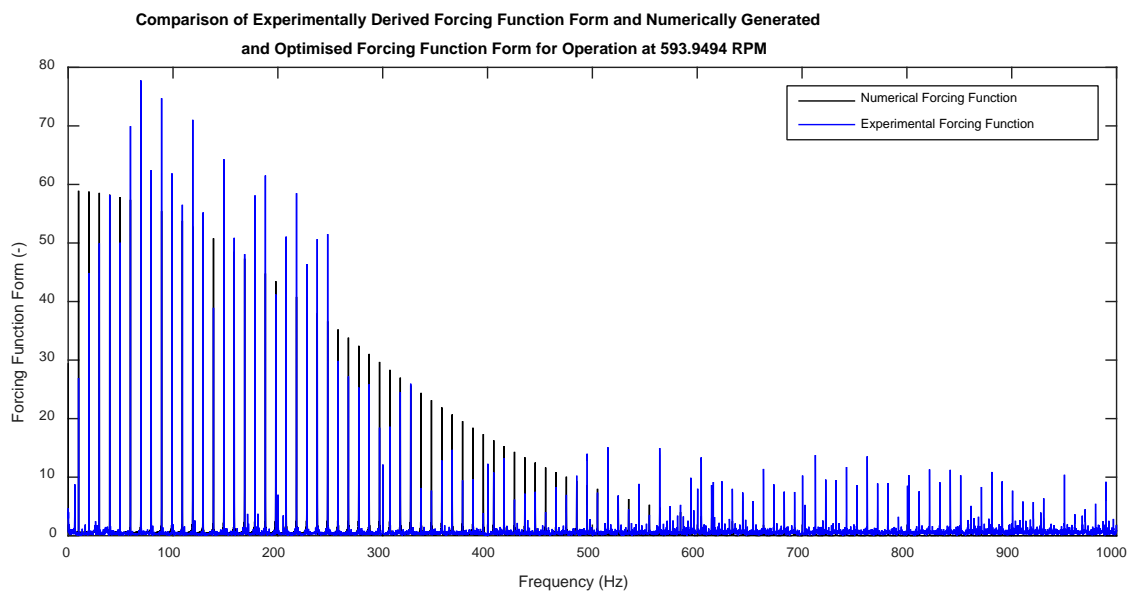


Figure 4.2-14 Best forcing function form fit with $R^2 = 0.7974$ (config. 1 with 1 jet operating at 594 RPM)

Similarly the worst fit for the same dataset (configuration 1 under 1 jet excitation operating at 961 RPM) is provided in Figure 4.2-15.

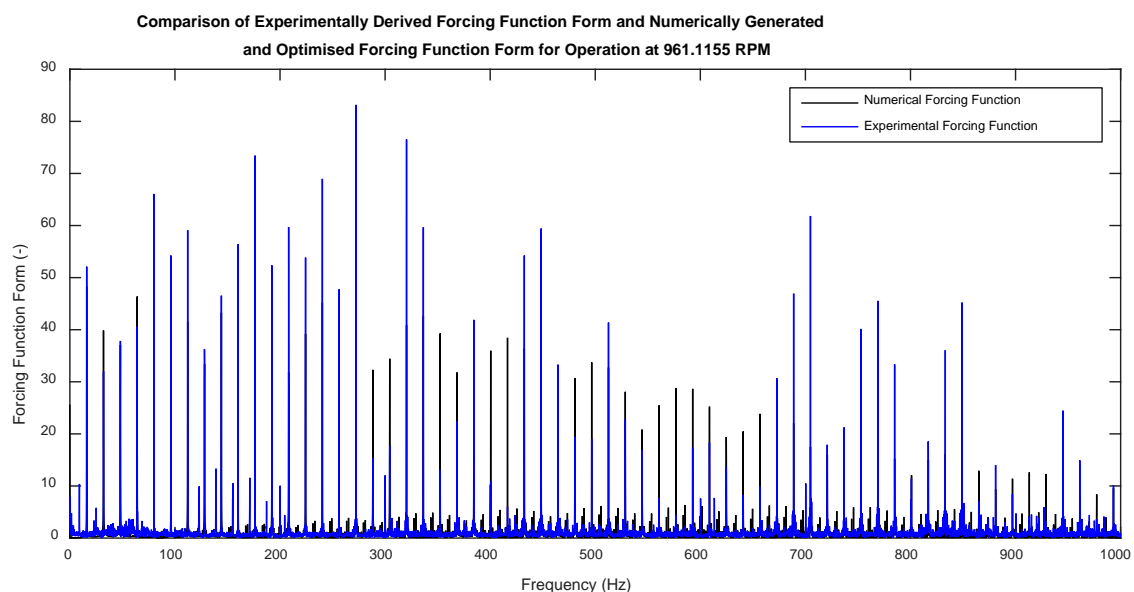


Figure 4.2-15 Worst forcing function form fit in config. 1 with 1 jet excitation with $R^2 = 0.5220$ (operating at 961 RPM)

It can be seen in both examples that the optimisation technique is able to place the harmonic excitation peaks at the desired frequency locations. It is proposed that the erratic nature of the excitation's forcing magnitude behaviour limits the ability of the forcing function model to capture the response fully.

The best coefficient of determination, obtained for the higher jet excitation scenarios (both 2 and 4 jet), was found for a configuration 1 measurement where the assembly was under 2 jet excitation ($R^2 \approx 0.5$). The specific case had an angular velocity of 655 RPM. This result is given in Figure 4.2-16.

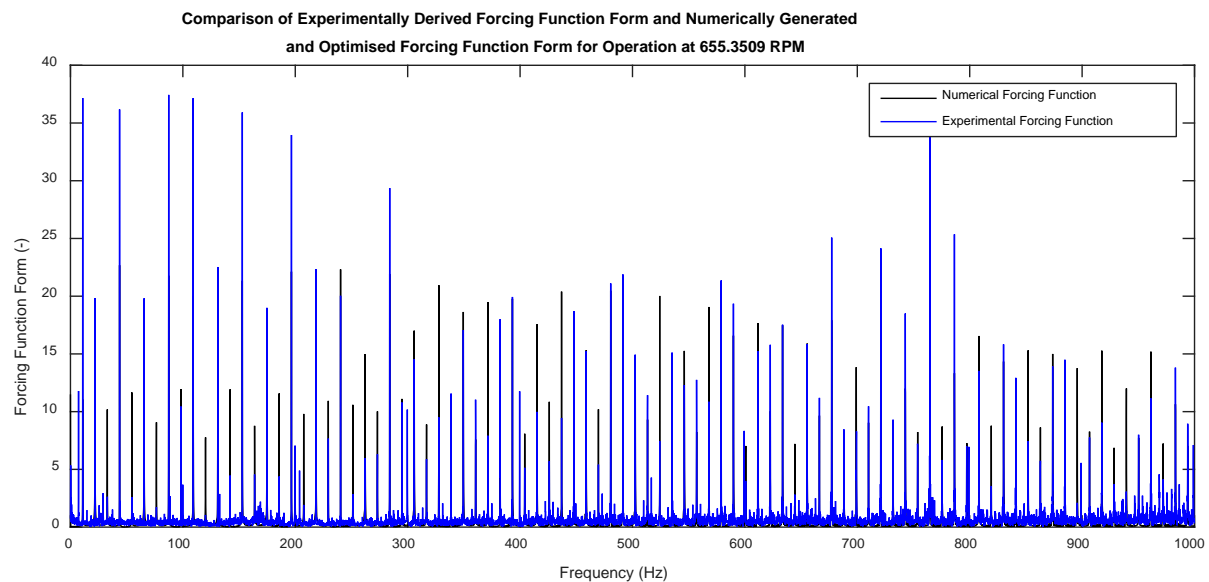


Figure 4.2-16 Best higher jet forcing function form fit with $R^2 = 0.4967$ (operating at 655 RPM in config. 1 with 2 jets)

It can be seen that the numerical model places an excitation peak pattern corresponding to one jet having a much higher nominal forcing value than another. Specifically the algorithm obtained the two relative peaks heights to be 0.6446 and 0.2007. Therefore it is estimated that the one forcing peak has a nominal magnitude which is more than 3 times larger than the other, as was expected from the prior discussion on the non-deal nature of the excitation. Further it is clear from the experimental results that this trend is partially present in the true forcing behaviour across the spectrum investigated.

In general the forcing function model performed poorly when it was fitted to excitation conditions containing multiple jets. This is when it is compared to the single jet measurement optimisations. The mean R^2 for all single jet measurements was found to be 0.6111, whereas the 2 and 4 jet cases achieved average R^2 values of 0.2765 and 0.0642 respectively. The blade forcing conditions within the casing become increasingly complex as the number of jets increase.

Focus is now placed on the best forcing function results set, namely configuration 1 under 1 jet excitation. The physical significance of the forcing function's angle, as defined by the individual Gaussians' standard deviation, will be investigated using this dataset. Further optimisation analyses of the forcing behaviour is also limited to this dataset.

Recall that it was suggested that the angle through which the blades pass a forcing stream is related to the actual forcing behaviour. Further, it was suggested that this angle could be estimated from the geometry of the system and incorporated into the forcing function's model. The upstream nozzles were placed at a radius of 154mm in the experimental setup. The blades each had a width of 40mm

and they were all installed at a stagger angle of 30° . This results in an effective forcing angle of approximately 7.5° (as defined in the theoretical development). This is illustrated in Figure 4.2-17.

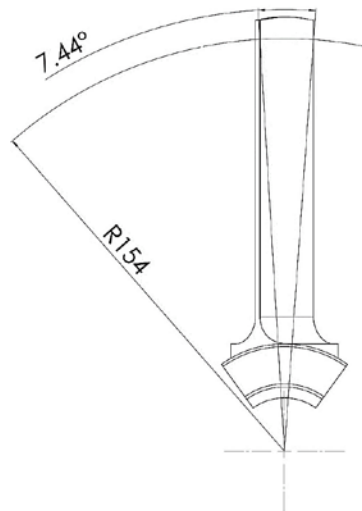


Figure 4.2-17 Blade forcing location and angle through which force subtends

It is expected that the majority of the force is applied to the individual blades within this angle. The design variable associated with this is the percentage standard deviation multiplier. The multiplier provides the percentage standard deviation per revolution that the force is applied to an individual blade in the model.

Recall that approximately 68% of a normal distribution lies within 1 standard deviation, 95% within 2 standard deviations and 98% within 3 standard deviations. Therefore, by converting the design variable solution from a percentage of the angle per revolution into degrees it is possible to obtain the forcing angle as predicted by the model. The forcing angle converted to degrees for 98% of the force application (within 3 standard deviations) is given in Figure 4.2-18.

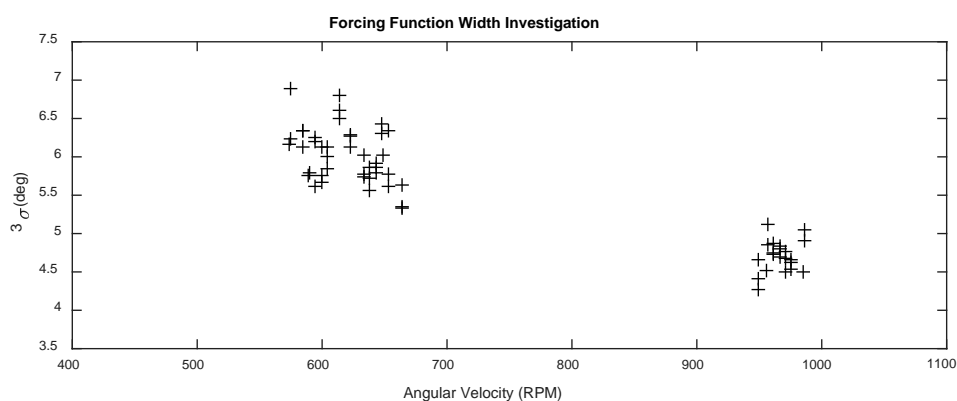


Figure 4.2-18 Forcing function width investigation for configuration 1 under 1 jet excitation

It is first noticed that the predicted angle, for the third standard deviation where at least 98% of the force has been applied, is consistently less than the physical angle across the blade (7.44°). Further the predicted angle never drops below half of the effective blade excitation width in degrees over the interval of interest.

The question has to be asked if this indeed makes physical sense. Firstly, at no point is a near ideal impulse excitation estimated. Recall that the initial guess provides an effective angle (in terms of the

third standard deviation) of 0.01° . The algorithm was therefore able to increase this value to within the physical realm.

Further, at no point does the algorithm estimate the forcing angle to be greater than the actual effective blade angle of 7.5° . It is also interesting to note that as the system's angular velocity increases so does the effective angle decrease. There is however not enough information across the measurement region to suggest whether or not the relation is linear or otherwise diminishing. The results of this analysis do however provide information to make clearer boundary condition choices for this particular design variable and provide confidence in the model's physical significance.

For the case of 1 jet excitation the individual peak height parameter becomes redundant (due to the presence of the scaling multiplier defined by a and b). This parameter can therefore be left out for future analyses containing only single jet excitation conditions.

The values for the scalar multiplier parameter a were found to be between 1.84 and 2.68. The parameter b was found to converge to approximately 2.99 for all items in the configuration 1 set with 1 jet excitation. Recall that an initial guess of 1 was made for both of these in the previous study.

The SNR design variable did not change significantly during all optimisations. For configuration 1 under 1 jet excitation the design variable stayed within the vicinity of the starting guess (500) with a mean value of 502 and a standard deviation of 0.31. The value was not driven to zero indicating that noise is indeed an important component of the signal.

The final design variable which will be commented on in some detail is the system's angular velocity in RPM. For configuration 1 under 1 jet excitation the maximum difference between the initial guess angular velocity value and the tuned angular velocity value was found to be 0.0624 RPM. The smallest difference was found very close to 0. The mean difference was 0.0020 RPM with a standard deviation of 0.0096 RPM. These figures indicate that the upper and lower bounds initially suggested can be tightened significantly. Previously bounds of 10% were used about the angular velocity initial guess. This meant that for the slowest experimental measurement in the data set bounds of approximately 60 RPM were used. If this limit is now set to 0.1% then the tuned values are still well within the bounds.

The performance and flexibility of the forcing function model is tested for a final time using a multi-start optimisation approach. The best and worst case scenarios from configuration 1 with 1 jet excitation are used to see if the model's predictive capability can be improved. This also gives an indication as to the system's sensitivity to initial conditions. The new adjusted upper and lower bounds, chosen for the problem by taking the prior analysis into account, are given in Table 4.2-4

Table 4.2-4 Boundary conditions for design variables of multi-start blade forcing function fitting problem

Limit	Gaussian std. dev. %	Scalar force multiplier 'a'	Scalar force multiplier 'b'	SNR	Angular velocity (RPM)
LB	0.00185	0.5	2	5	$RPM_M - 0.001 \cdot RPM_M$
UB	0.00925	5	4	1000	$RPM_M + 0.001 \cdot RPM_M$

The forcing pulse width is effectively limited to between 2° and 10° (originally between 0° and 360°) for 98% of the force application angle in order to take the blade geometry into account.

Initial guesses are obtained by generating a Latin hypercube with 1000 samples for the now 5 design variables. Unlike before where the initial guess remained constant and the measurement derived

forcing function changed; now the forcing function signals from best and worst case scenarios for a set are held constant and the initial guesses are changed.

The Latin hypercube method allows an initial guess sampling scheme which is random yet still simultaneously uniformly distributed over each design variable, provided that a large enough sample set is chosen. The results from the investigation are provided in Table 4.2-5 and Table 4.2-6.

Table 4.2-5 Results of multi-start forcing function investigation for best case from configuration 1 with 1 jet excitation

Value	Gaussian std. dev. % [deg]	Scalar force multi. <i>a</i>	Scalar force multi. <i>b</i>	SNR (x500)	Angular velocity (RPM)	MSE	R^2	Iter.	Func. Evals.
Mean	0.005 [5.4]	1.5695	2.9675	0.9219	593.95	4.6009	0.6476	28.3	252.7
Std. Dev.	0.0020 [2.16]	0.6875	0.2718	0.3369	0.11	24.9787	0.2517	13.5	120.7
Min	0.0019 [2.052]	0.500	2.0000	0.01	593.36	1.6582	0	2	48
Max	0.0092 [9.936]	4.1329	3.9999	1.9470	594.52	611.313	0.8046	132	998

Table 4.2-6 Results of multi-start forcing function investigation for worst case from configuration 1 with 1 jet excitation

Value	Gaussian std. dev. % [deg]	Scalar force multi. <i>a</i>	Scalar force multi. <i>b</i>	SNR (x500)	Angular velocity (RPM)	MSE	R^2	Iter.	Func. Evals.
Mean	0.0041 [4.428]	1.6146	2.9729	0.9139	961.10	6.0181	0.4189	27.4	243.1
Std. Dev.	0.0020 [2.16]	0.8899	0.2436	0.3321	960.15	5.1531	0.2407	13.4	123.7
Min	0.0019 [2.052]	0.500	2.0000	0.0100	960.15	3.2126	0	2	38
Max	0.00920 [9.936]	4.9873	4.0000	1.9427	962.07	105.75	0.6602	95	944

The mean coefficient of determination for the best case scenario is found to be within 10% of 0.7974 (value obtained in the prior optimisation). The best fit achieved an R^2 value of 0.8046, which is less than a 1% improvement on the previously obtained value for the best case scenario. This indicates that the initial guess for the best case scenario in the first optimisation was close to the ideal. The minimum R^2 value obtained for the best case scenario was found to be zero, thus a very poor initial guess will not be able to converge to a useful result. The standard deviation of the R^2 value, 0.2517, indicates that the system is quite sensitive to initial guesses.

When taking the prior optimisation results into account, from the configuration 1 set under 1 jet excitation, it can be said that so long as a good initial guess is provided then the forcing function model has a good chance at fitting the frequency peak locations. However the goodness of the fit is sensitive to the forcing function's frequency peak magnitudes which may be highly erratic.

The worst case scenario optimisation was able to achieve a best fit of R^2 equal to 0.6602. This is an improvement of approximately 25% on the initial value of 0.5220. This indicates that there was room

for improvement in both the result and associated initial guesses. The mean R^2 value was however found to be approximately 20% less than that obtained in the original optimisation. This once again echoes the sensitivity of the model to the initial guesses.

The results indicate that there is room for improvement on the optimisation's results by simply choosing better starting points for the optimisation algorithm. This is most apparent when comparing the mean R^2 values with the maximum R^2 values for both the best and worst case scenarios. Further, poor choices of initial guesses will lead to a poor fit of the model. The model is however reasonably flexible when it comes to fitting single jet excitation conditions.

The focus of the discussion is now shifted to fitting the blade transfer function model to the experimentally obtained SG results. This fitting procedure is the second reduced inverse problem considered (second component of the pressure model independently solved for using SG measurements). The filtered and smoothed average blade response spectra are once again used for this purpose. The goal of the analysis is to obtain estimates of the blade transfer function's parameters and to better understand the model's flexibility and ability to fit the true response behaviour. Recall that the MDOF blade transfer function can be modelled as the sum of individual SDOF system FRFs. This relation is repeated in Equation [4.2.3].

$$H(j \cdot \omega) = \left(\sum_{r=1}^N \left(\frac{A_r}{\omega_r^2 - \omega^2 + j \cdot \eta_r \cdot \omega_r^2} \right) \cdot e^{j \cdot \pi \cdot \text{mod}(r,2)} \right) \quad [4.2.3]$$

The initial conditions of the design variables, namely the modal constants A_r , the blade natural frequencies ω_r and the modal damping η_r , are initially estimated using an automated form of the peak-picking algorithm, as described in the theoretical development. There after the model is tuned to the experimentally derived results using a non-linear constrained optimisation algorithm in order to obtain optimised parameter estimates.

The mean square error (MSE) was chosen as the error function for this purpose. The difference between the \log_{10} filtered and smoothed response and the \log_{10} of the absolute transfer function (found using Equation [4.2.3]) defines the individual error vector e_i between each point in the numerical model and the smoothed and filtered spectrum.

By minimising over the \log_{10} individual error values the error weighting between small and large errors shift significantly (recall the discussion on error functions). Specifically small errors are weighted closer to larger errors than would have been the case if just the absolute errors were employed.

Wide bounds are set about the design variables for this initial investigation as little knowledge pertaining to the true values is known. These bounds are defined in Table 4.2-7.

Table 4.2-7 Boundary conditions for design variables of blade transfer function fitting problem

Limit	Ar_1 (V)	Ar_2 (V)	Ar_3 (V)	$f_{nr,1}$ (Hz)	$f_{nr,2}$ (Hz)	$f_{nr,3}$ (Hz)	$\eta_{nr,1}$	$\eta_{nr,2}$	$\eta_{nr,3}$
LB	0.1	0.1	0.1	90	650	785	5e-4	5e-4	0
UB	300	300	300	135	780	1350	0.0350	0.0350	0.9999

The SGs applied to blade 1 in configuration 1 and blade 5 in configuration 2, for the purpose of steady state measurement evaluation, were only sensitive to flapwise bending modes. They were insensitive to any torsional modes that were identified during the stationary characterisation. As per the scope, interest in only the first few modes is considered. For the purpose of this evaluation the modes are

therefore limited to the first two flapwise bending modes, as found in the characterisation and steady state evaluation. For all blades the first two bending modes lie within 0 Hz and 1000 Hz.

It is important to note that an additional SDOF system was included in the evaluation (defined by $Ar_{3,}$ $f_{nr,3}$ and $\eta_{nr,3}$). This was done in order to better tune the higher frequency portion response spectrum to the measurement derived spectrum. Specifically, the mode was added after the second flapwise bending mode in order to account for the remaining higher order modes excluded from the model, this is similar to adjusting the response model's mass line (an experimental modal analysis technique).

The resulting model found for blade 1 in configuration 1 from the filtered and smoothed response spectrum is provided in Figure 4.2-19.

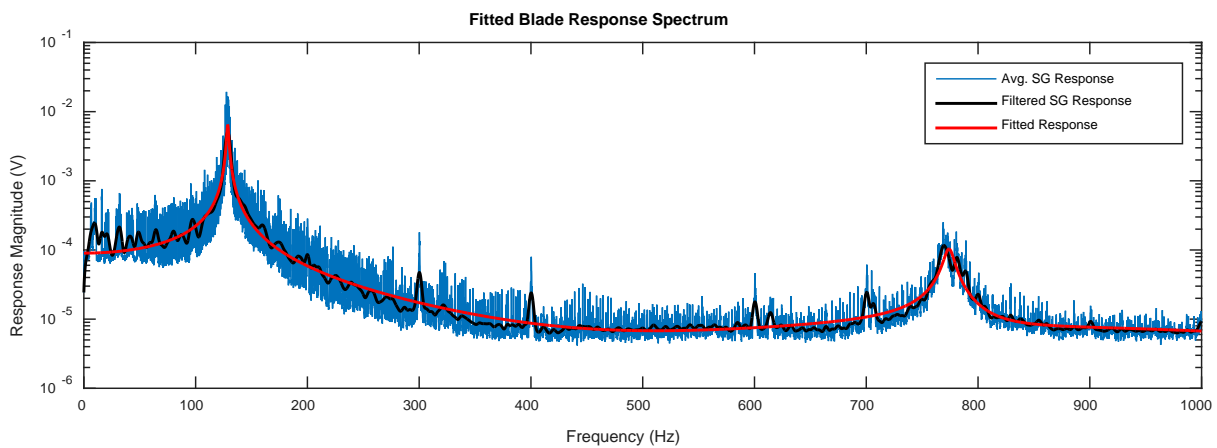


Figure 4.2-19 Estimate of blade transfer function using filtered and smooth blade response spectrum for blade 1 in configuration 1

Similarly, the model resulting from optimising over the filtered and smoothed response spectrum obtained for blade 5 in configuration 2 is provided in Figure 4.2-20.

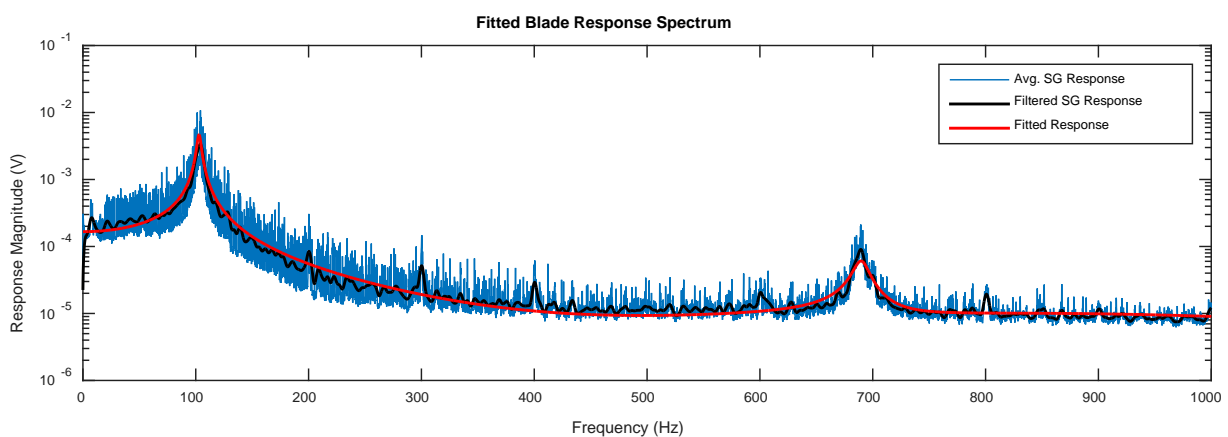


Figure 4.2-20 Estimate of blade transfer function using filtered and smooth blade response spectrum for blade 5 in configuration 2

The initial optimisation choices and results for the above two curves is presented in Table 4.2-8. Additionally the maximum number of iterations was set to 2000, the maximum number of function evaluations was set to 3000 and the function value stopping criterion was chosen as $1e-9$. All optimisation runs were found to cease when the default minimum step size of was reached (as opposed to stopping once the minimum function value was achieved).

Table 4.2-8 Results of optimisation to fit blade transfer function model to averaged and smoothed response spectra

Item	Blade 1 Configuration 1	Blade 5 Configuration 2
Algorithm	Interior point	Interior point
$Ar_{initial}$	[102.3393, 26.5445, 39.8168]	[74.6994, 16.7175, 25.0762]
$f_{nr,initial}$ (Hz)	[128.8000, 769.6000, 923.5200]	[104.1000, 689.5000, 827.4000]
$\eta_{nr,initial}$	[0.0155, 0.0049, 0.0000]	[0.0259, 0.0049, 0.0000]
Iterations	176	133
Function evaluations	1810	1349
$MSE(\log_{10} x - \log_{10} y)$	9.7786e-03	8.322499e-03
$MSE(x - y)$	5.1166e-09	6.5154e-09
R^2	0.9527	0.9426
Ar	[57.0444, 30.2125, 171.5708]	[67.8708, 25.5915, 251.5964]
f_{nr} (Hz)	[128.7176, 774.1028, 798.1213]	[102.8947, 689.8195, 785.0000]
η_{nr}	[0.0136, 0.0114, 0.7865]	[0.0350, 0.0193, 0.9999]

Both optimisation runs required more than a 1000 function evaluations and more than 100 iterations in order to solve the problems to within the desired tolerances. The individual function evaluations were however relatively inexpensive to perform when compared to the forcing function optimisation investigations resulting in a shorter run time.

It can be seen that the additional SDOF system added, for both optimisation investigations, resulted in an artificial mode close to the second bending mode with an extremely high modal damping factor. As was mentioned, this accounted for the remaining higher order modes which were disregarded from the MDOF model.

Both models have a coefficient of determination greater than 90%, indicating a high goodness-of fit between the models of the smoothed and filtered spectra. This means that both models are able to account for nearly all of the variability in the data, given the good starting point obtained from the automated peak-picking procedure.

It is interesting to note that the fundamental frequency determined for blade 5 (in configuration 2) in the curve fitting process, namely 102.89Hz, aligns more closely with the expected centrifugal stiffening value of 0.85 Hz for operation at 805 RPM (expected value from the FE analysis). This result was referred to in the earlier discussion on centrifugal stiffening. The fitted curve suggests that the increase in the fundamental frequency, due to centrifugal stiffening, is approximately 0.99 Hz, closer than the previously estimated value of 1.6 Hz.

Further the fundamental frequency estimated for blade 1 in configuration 1 only shifted by approximately -0.1 Hz (when compared to the value derived from the fitted and smoothed curve). This results in an approximated increase in fundamental frequency of 0.62 Hz which is still within 10% of the FE analysis predicted value of 0.68 Hz.

The question has to be asked if the optimised design variable results make physical sense. Consider the results for blade 1 in configuration 1. The natural frequencies obtained are within a close tolerance when compared to the experimentally obtained values (obtained during both the stationary characterisation and the operating averaged, filtered and smoothed results to which the model is fitted). Specifically, the values for both bending mode natural frequencies are within 1% of the

stationary characterisation’s results. The magnitudes of the modal constant values are somewhat arbitrary as they were measured in volts without a clear link between input force magnitude and response displacement magnitude. Finally the modal damping constants for the two real bending modes for blade 1 show that the system is indeed lightly damped (the modal damping values are in the vicinity of 0.01 and 0.02), as was the expectation for the structure.

The final damping values, obtained for the dummy modes, are many times higher than that of the first two for both result sets. This final dummy mode had to take into account all of the remaining modes’ contributions into the system in order to align the mass line of the frequency response.

As was previously stated, this analysis was performed with initial guesses derived from proven experimental modal analysis techniques. The sensitivity of the optimisation problem to poor initial condition choice was however not captured in the analysis. Therefore a second multi-start analysis was set up in order to investigate the model’s predictive ability from a range of initial conditions. This provides an indication as to the robustness of the blade transfer function model. The result also indicates what the best expected fit could be given the model and experimentally derived frequency response.

A Latin hypercube was generated for the problem with 1000 initial guess entries. The ranges for the design variable guesses were taken across the original lower and upper problem bounds. The full results set of fitting the blade transfer model to the experimentally obtained response spectrum of both blade 1 in configuration 1 and blade 5 in configuration 2 can be seen in section ‘7.7.4 G4 – Multi-Start SG Blade Transfer Function Fitting Results’. A summary of the most important results is provided in Table 4.2-9 and Table 4.2-10.

Table 4.2-9 Summary of results of multi-start SG blade transfer function optimisation problem for blade 1 in config. 1

Item	Mean	Std. Dev.	Max	Min
MSE	6.2649e-09	1.1608e-08	1.2352e-07	2.9361e-09
R^2	0.9440	0.0934	0.9735	0
Iter.	163.2440	18.6413	296	73
Func. Evals.	1674.30	196.4343	3009	748

Table 4.2-10 Summary of results of multi-start SG blade transfer function optimisation problem for blade 5 in config. 2

Item	Mean	Std. Dev.	Max	Min
MSE	1.1459e-08	2.4136e-08	1.8766e-07	5.3583e-09
R^2	0.9238	0.1050	0.9429	0
Iter.	144.2900	13.8475	238	71
Func. Evals.	1471.20	143.7380	2424	724

When reviewing the multi-start results for blade 1 in configuration 1 it can be seen that the best run obtained an R^2 value of 0.9735 (recall that the initial investigation obtained an R^2 value of 0.9527). A mean R^2 value of 0.9440 with a standard deviation of 0.0934 indicates that the model is usually able to converge to a reasonable result, even if the initial guesses are far off. The minimum R^2 value of zero indicates that if the starting points are chosen extremely far away from the optimised solution then the algorithm may fail. So long as a reasonable guess is made then it is expected that the model will perform well. The results for blade 5 in configuration 2 echo those of blade 1 in configuration 1.

The discussion will now focus on the implications of the SG investigations' findings on the reformulated pressure models developed in Chapter 2. Consider the reformulated internal pressure model based on the work by Mengle, namely reformulated Model 1, presented in Equation [4.2.4] (Mengle, 1990). Recall that the blade vibration was represented as a SDOF sinusoid in this model and not as a combination of the blade transfer function and forcing function.

$$P_r(t) = Re \left\{ \sum_{i=0}^{\infty} \left[1 + \sum_{k=0}^{B-1} [I(i) \cdot \Lambda_k \cdot (k \cdot \Omega + \omega) \cdot \cos((k \cdot \Omega + \omega) \cdot t + \chi)] \right] \cdot D_i' \right. \\ \left. \cdot e^{(j \cdot i \cdot [\Omega \cdot t + \nu] + j \cdot [\sum_{k=0}^{B-1} [I(i) \cdot \Lambda_k \cdot \sin((k \cdot \Omega + \omega) \cdot t + \chi)])} \right\} \quad [4.2.4]$$

The Doppler shifting effect of the blade vibration signal has been represented as both amplitude and phase modulation in the above equation (in the development the two effects were handled separately). The amplitude modulation has been represented as the tip velocity by simply taking the time derivative of the tip displacement as it stands in the exponential of the function.

Recall that in the work of Mengle that the model was initially based on flutter response at an individual wave number (and individual response frequency ω), and that if a significant amount of mistuning was present then the excitation occurs at all wave numbers k (Mengle, 1990).

Through qualitative visual inspection of the SG results it was seen that all blade forcing phenomena had both a Gaussian noise component and a rotor harmonics component (see section '7.7.5 G5 – Exemplar SG Response and Forcing Function Forms'). At no point was the system responding at a single dominant frequency (as would be the case under self-excited flutter). Further, all geometric hub and assembly configurations were mistuned somewhat. In the stationary characterisation it was found that configuration 1 was the least mistuned and configuration 2 was the most mistuned from the overall system's mistuning point of view.

The combination of these findings have a direct impact on the application of the reformulated Model 1. Due to Doppler shifting at all possible wave numbers k , the blade response which is represented as the combination of the indicator function I , scaling function Λ_k and SDOF sinusoid can be simply replaced with a SDOF sinusoid responding at the individual frequency ω . This new representation is however at the expense of being able to scale each of the wave number contributions individually. The resulting expression is shown in Equation [4.2.5]. The ability to scale the blade response amplitude has been maintained by inclusion of the scaling factor Λ .

$$P_r(t) = Re \left\{ \sum_{i=0}^{\infty} [1 + \Lambda \cdot \omega \cdot \cos(\omega \cdot t + \chi)] \cdot D_i' \cdot e^{(j \cdot i \cdot [\Omega \cdot t + \nu] + j \cdot i \cdot [\Lambda \cdot \sin(\omega \cdot t + \chi)])} \right\} \quad [4.2.5]$$

The SDOF blade response can now be replaced with the combined blade transfer function and forcing function response model which was shown to fit the true blade behaviour (as the response occurs at harmonics of shaft speed with a Gaussian noise component). This is shown in Equation [4.2.6].

$$P_r(t) = Re \left\{ \sum_{i=0}^{\infty} [1 + \Lambda \cdot \psi(t)_r] \cdot D_i' \cdot e^{(j \cdot i \cdot [\Omega \cdot t + \nu] + j \cdot i \cdot [\Lambda \cdot \psi(t)_r])} \right\} \quad [4.2.6]$$

Taking into consideration that the blade response model inherently allowed response magnitude scaling and rearrangement of the formulation results in Equation [4.2.7].

$$P_r(t) = Re \left\{ \sum_{i=0}^{\infty} [1 + \Lambda \cdot \psi(t)_r] \cdot D_i' \cdot e^{(j \cdot i \cdot [\Omega \cdot t + \nu + \psi(t)_r])} \right\} \quad [4.2.7]$$

Equation [4.2.7] is equivalent to reformulated Model 2 (see Equation [2.3.10]). Therefore at the expense of being able to scale each wave number contribution separately, the blade response model can be based upon the true geometric, material and forcing behaviour of the system.

In summary, the SG investigations indicated that significant shifting of the fundamental frequency peaks, due to centrifugal stiffening, is not expected across the measurement range for all blade geometries considered. This was predicted during the initial FE investigation into the various blade geometries.

The blade forcing function model was fitted to the experimentally obtained forcing forms to differing degrees of success. The multi-start optimisation approach applied to the forcing function inverse problem indicates that if work is done to obtain better starting points, a great improvement on the fit can be achieved (when compared to the mean fit across a wide range of initial guesses). The success of the optimisation is however extremely sensitive to the initial guess. The blade forcing model performed poorly when more than 1 jet was exciting the system which suggests that work should be made to better understand the forcing phenomena form.

The results from analysing the Gaussian standard deviation pulse width estimator indicate that the forcing function form, in the time domain, makes physical sense as the forcing angle was never greater than the actual angle in which the force is applied (when converting the percentage multiplier to an angle within which 98% of the force will be applied). Nor did the angle approach impulse excitation.

The blade transfer function model was successfully fitted to experimentally derived blade transfer function forms. The coefficients of determination for these inverse problems indicated that the model is capable of being fitted to different frequency response forms to a high degree, somewhat regardless of poor initial guess choices (as the initial optimisation and multi-start optimisation obtained mean R^2 values of above 0.9 with relatively small standard deviations). This indicates that the model has a high degree of flexibility and robustness. In order to obtain the fit an additional artificial mode had to be incorporated in order to line up the mass line of the systems which accounts for the excluded modes.

Further, the damping factors obtained indicate that the system is lightly damped, as was expected for the hub and blade assembly design. The multi-start optimisation approach was not able to improve on the fits to a significant degree, although it may be difficult to improve on system's whose mean R^2 values are already above 0.9.

It is still unknown whether or not errors incurred from poorer forcing function fit will diminish or propagate when exploring the inverse pressure problem. However tighter bounds for all design variables have been established which may aid in the solving of the problem.

Finally pressure model choice for further investigations was motivated, through manipulation of reformulated Model 1 an equivalent to reformulated Model 2 is found. The proceeding section explores the experimentally obtained pressure signals from a signal processing point of view.

4.3. Pressure Signal Observations and Model Assumptions Review

The main objective of the following study is to explore the possibilities and issues associated with identifying blade behaviour indicators directly from experimentally obtained steady state internal pressure casing signals. Aspects of the internal pressure signals will be evaluated in light of the proposed reformulated pressure models, and their implications on those models discussed. The experimentally obtained signals are analysed using signal processing techniques and observation.

It is however first useful to briefly analyse the assumptions made during the development of the original pressure models and their associated significances. This is done in order to ascertain the pressure models' applicability with respect to the specific internal pressure conditions and blade response for the experimental setup. Certain assumptions are common to both models, and will be handled simultaneously. The principal assumptions made during the development and evaluation of the original Model 1, for an isolated rotor cascade in a turbomachine, are as follows (Mengle, 1990):

1. The net casing pressure field can be obtained through linear superposition of each individual blade's pressure signal contribution.
2. The cascade is isolated and the flow from upstream stators is uniform (or at the very least the flow is not excessively sheared).
3. The inter-blade response phase angle is constant (thus only a single travelling wave mode k exists).
4. The blade response is non-integral EO flutter occurring at a single frequency.

The principal assumptions made during the development and evaluation of the original Model 2 are as follows (Forbes and Randall, 2013; Forbes, 2010):

1. Physical blade coupling, which may be explored using the hub-to-blade mass ratio, is light. The blades' response behaviour can therefore, for all intents and purposes, be treated as uncoupled and individual blade behaviour may be evaluated and modelled separately.
2. Pressure at the casing wall is directly related to the pressure profile about blade tip, and that pressure profile follows the blade motion during steady state operating conditions.
3. Changes in natural frequencies, due to centrifugal stiffening, is negligible across the operational range of interest.

The first assumption for Model 1 and the combination of the first two assumptions for Model 2 can be seen as equivalent. Namely that the effect of individual blade vibration on the pressure signal is independent and thus the pressure effects of each individual blade tip may be evaluated separately. This is the premise for separating the pressure distributions about each blade tip and evaluating those signals separately (for instance using the suggested sigmoidal time domain windowing technique provided in the theoretical development). The physical blade coupling component, assumption 1 of Model 2, can however be commented on independent of the pressure models.

According the work by Forbes, the physical coupling between blades and their subsequent response independence, can be evaluated to some degree by considering the individual blade-to-hub mass ratios (so long as the hub and blades are made of the same material, which is the case) (Forbes, 2010).

The system is seen as lightly coupled when the hub-to-blade mass ratio is small (Forbes, 2010). In this case the hub-to-blade mass ratio for the healthy blade design is approximately 1:0.03 (i.e. the mass of one healthy blade is approximately 3% of the hub mass). The hub-to-blade ratio decreases for all blade

designs of reduced fundamental frequency (as does the associated physical coupling effects). Although no indication as to what the minimum required mass ratio must be was found, it is proposed that the maximum ratio of 1:0.03 is small enough. This result is supported by the run-up resonance investigations for assembly configurations 2 and 3 where SGs were applied to adjacent blades. Consider the run-up resonance investigation for configuration 2 with 1 jet excitation in Figure 4.3-1.

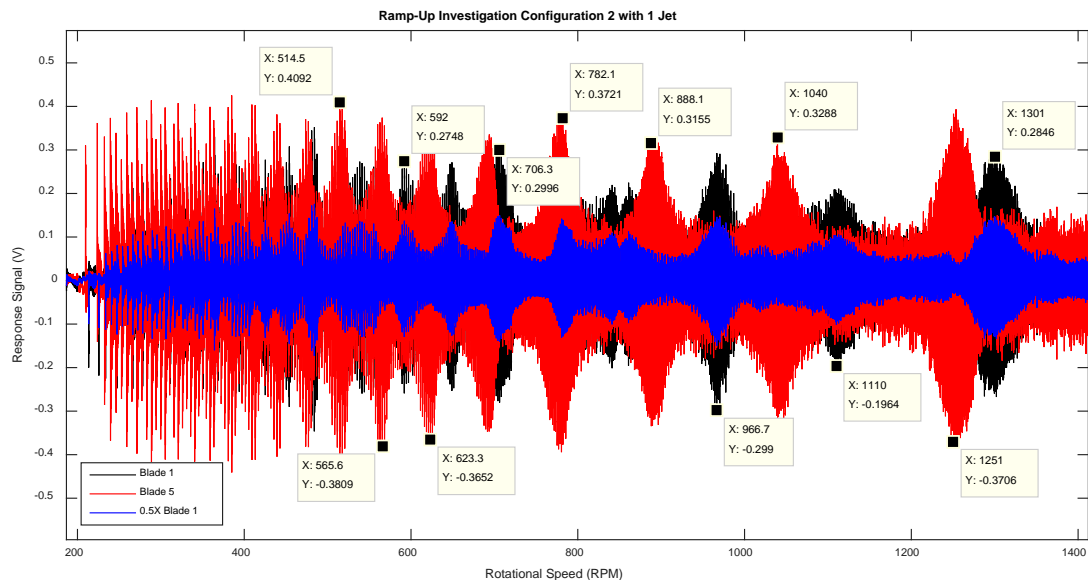


Figure 4.3-1 Ramp-up configuration 2 with 1 jet

Recall that blade 1 is of the healthy design and blade 5 is damaged blade type 1 (blade 5 has a significantly reduced fundamental frequency). Further blades 1 and 5 are adjacent to one another. It can be seen that the individual blades, with different root geometries, respond independently as they move through their own critical speeds. Further, their resonance behaviour does not appear to generate visually observable sympathetic vibration from the adjacent blades during the run-up (as would be the case for significant inter-blade coupling). Their response however never drops to zero. All run-up resonance investigations can be seen in section '7.5.7 E7 – Run-Up Resonance Detection'.

It is important to stress that the suggestions made on physical coupling do not conclusively prove that the pressure fields about the blade tips are independent of one another. It only indicates that the blades may be sufficiently uncoupled that their physical response behaviour can be evaluated and modelled separately. The independence of the pressure response about individual blade tips must still be ascertained.

The second assumption of Model 1, namely that the cascade is isolated with uniform upstream flow, inherently holds. This is because the experimental setup only consisted of a single open air rotor excited by upstream stator nozzles. The air stream supplied by the nozzles was nominally constant as the source was a high pressure compressed vessel. The nozzles were also installed in a stationary position. Therefore no significant periodic fluctuations in the upstream air supply are expected over the measurements (recall that 10 second steady state measurements were taken). Neither are back-pressure effects present as no downwind blading or geometries are present near to the outlet.

The upstream flow generated solely by the blades' rotation is also uniform as the rotor is open to the atmosphere on both sides. Recall that this assumption was made because additional stators and rotors affect what can be captured from the pressure signal both up- and down-wind of the rotor row of

interest. Further, the pressure signal is captured in line with the rotor plane, and so the effects of axial attenuation or additional Doppler shifting of certain signal frequency components is not of concern.

The third assumption of Model 1, namely that the interblade-phase angle is constant resulting in a single travelling wave number k , does not strictly hold. Recall that for this assumption to hold the system had to be perfectly tuned. This was found to not be the case during the characterisation of all configurations. This assumption was made so that the theoretical pressure response could be simplified for evaluation purposes (as one wave mode may be dominant given the geometry and excitation). When the assumption does not hold k may assume all possible B values. Recall that this results in blade response Doppler shifting about all harmonics of rotor speed (Mengle, 1990).

The fourth and final assumption made during the development of the original Model 1 was that the blade response is non-integral EO flutter. The need for non-EO response was so that the engine harmonics, in the pressure signal, could be separated from the blade vibration components in the frequency domain. In this investigation measurements were taken both at EO resonances and about engine ordered resonances. With respect to the original Model 2, the formulation was inherently designed for off EO harmonic forced response evaluation.

The second component of the assumption was that the blade response mechanism be flutter at a single frequency. During the evaluation of the SG response signals it was seen that the blades did not respond at an individual frequency as they were excited at multiple rotor speed harmonics. The magnitude of each harmonic was however governed by the number of active jets and the system's cyclic symmetry. Therefore the blade response cannot be accurately modelled as a single sinusoid.

In the previous section it was shown that the reformulated Model 1 could be represented as the reformulated Model 2 by sacrificing the ability to scale each travelling wave mode component individually. In this way the sinusoidal blade response could be replaced by the blade response model presented in the theoretical development. It must also be noted that in the reformulation the Doppler shifting was expressed as modulation of the otherwise stationary pressure distribution about the blades. This is the same mechanism identified by Forbes et al. (Forbes and Randall, 2013). Although Model 1 was designed for flutter at an individual frequency, it was successfully used for blade forced response evaluation for a rotor moving through an EO resonance (Murray and Key, 2015).

Assumption 3 for Model 2 is the final principal assumption considered. It was assumed that centrifugal stiffening is negligible across the operational testing range. This assumption was made so that the system modal characterisation, performed at stationary conditions, would hold when evaluating the response at speed (Forbes and Randall, 2013). In this investigation centrifugal stiffening was not assumed as negligible for all blades as it was evaluated both experimentally and with FE analyses.

Recall that the maximum fundamental frequency shift was predicted to be within approximately 3 Hz for system operation up to 1400 RPM. The actual centrifugal stiffening for the healthy blade and damaged blade type 1 was found to be very closely aligned with the FE model's predictions. Taking these findings into account it is assumed that centrifugal stiffening is also negligible for the blades which were not instrumented and tested at speed. This is because their geometry, material properties and stationary characterisation results were similar to those blades which were tested at speed.

Taking the assumptions review and SG findings into account, the reformulated pressure Model 2 will be the basis for modelling and assessing the internal pressure conditions from this point forward.

The next step is to investigate the impact of intentionally changing the environment within the casing. Conditions such as the blade excitation scheme, blade root geometry and rotor speed can be independently controlled. Although the hub design facilitated investigating different blade stagger angles, all blades were held at a constant stagger angle of 30°. The surface condition of all of the blade tips remained unchanged. Understanding their impact on the internal pressure signal will prevent attributing pressure signal features to inappropriate mechanisms such as blade vibration effects.

The average pressure waveform about the casing is chosen for this investigation. It was shown in the previous section that averaging across all of the SG measurements averaged out the forcing behaviour. Similarly, by averaging the pressure measurements it is expected that the majority of the blade forced vibration effects on the pressure signal are averaged out. The differences between the average signals, for a particular configuration and excitation scheme, can then be confidently compared and their impact attributed. Consider the average pressure waveform about hub and blade assembly configuration 1, taking all single jet pressure measurements into account. This is provided in Figure 4.3-2.

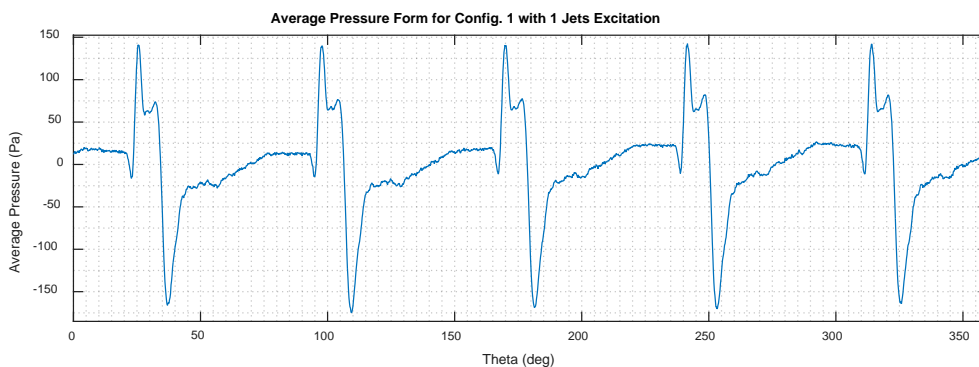


Figure 4.3-2 Average pressure waveform for configuration 1 under 1 jet excitation

As the blade approaches the stationary observer a rise in pressure is noted. As the blade passes the stationary observer a pressure drop is seen. These phenomena are congruent with the system acting as a compressor. The form of the single jet pressure distribution about the blades is however quite different from the damped impulse distribution described in the work by Forbes (Forbes, 2010). However, as the number of excitation jets increases, the pressure waveform starts to approach the form described by Forbes (Forbes, 2010). An example case is shown in Figure 4.3-3 for configuration 1 under four jet excitation. It is important to note that all of the pressure distributions considered are ordered such that the first wave is associated with the passing of blade 1, and so forth.

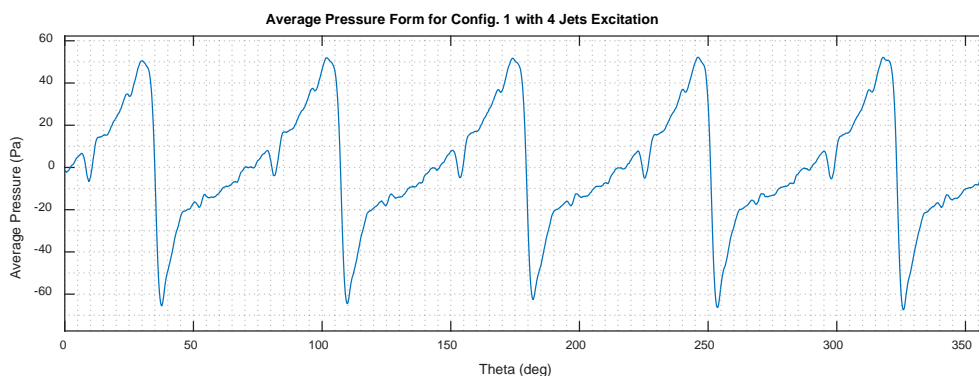


Figure 4.3-3 Average pressure waveform for configuration 1 under 4 jet excitation

The number of active pressure jets has a direct impact on the pressure distribution form about the individual blades. Further, it was noticed that as the number of jets increased, the maximum pressure range for the distributions decreased.

This finding is in line with what was noticed when investigating the SG signals. Namely that as the number of jets increased the maximum forcing range seen by the SGs decreased. Recall that this effect was attributed to losses in the pressure feed pipes. As the number of jets increase so does the number of pipe connectors and branches in the pressure system increase, and so does the nominal force applied to the blades decrease. All average pressure waveforms can be seen in section '7.8.1 H1 – Average Pressure Waveforms'.

It was therefore confirmed for this experimental setup that the fluid forcing behaviour has a direct impact on the average form of the pressure distribution measured at the casing wall. The next condition investigated is the effect of changing the blade root geometry on the average pressure waveform.

Recall that in order to obtain blades of differing fundamental frequencies, slots were cut into the blade roots. These slots are expected to have a significant impact on the local pressure distribution about the slot region. The impact of changing the root condition on the casing pressure distribution, measured near to the blade tips, must be surveyed.

Consider the normalised average pressure waveforms about blades 1 and 5 for 1 jet excitation for all four configurations presented in Figure 4.3-4. The signals were once again averaged over and there after normalised between 0 and 1. This was done such that a direct comparison between pressure distributions from different measurement sets could be made. Recall that blade 5 was replaced in configuration 2 and that blade 1 remained unchanged though all configurations.

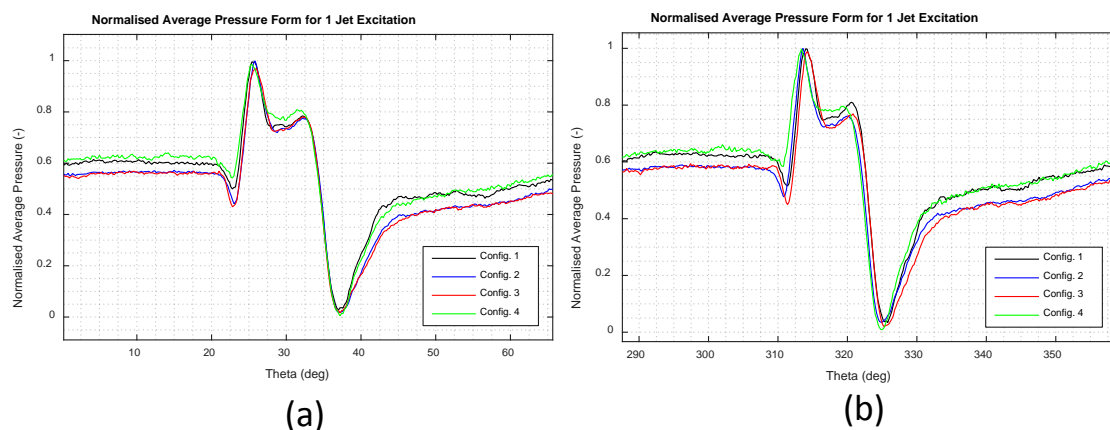


Figure 4.3-4 Average pressure waveform under 1 jet excitation for all configurations. (a) Blade 1. (b) Blade 5.

Through visual observation it can be seen that the number of pressure signal features (major peaks and troughs) about the individual blades remains fairly constant. There is no significant change in the pressure wave forms or number of prominent features once blade 5 is replaced (recall that replacement occurs in configuration 2). The variance between all of the configurations' averaged and normalised pressure waveforms appears to remain the same regardless of the root conditions. It is important to note that the most important regions in the signals to inspect are those closest to the main pressure rise and drop. This is because these features are directly aligned to the passing of individual blades. Further, during the development of the original Model 2 these pressure waveforms were assumed to follow the blade tip behaviour (this assumption must still be investigated).

The average pressure distribution for configuration 4 appears to follow that of configuration 1, similarly the pressure distribution for configuration 2 remains in line with that of configuration 3. This tendency is noted to remain constant across all blade tip pressure fields. Further, this trend was noticed for all average wave forms about all blades, the individual plots can be seen in section ‘7.8.1 H1 – Average Pressure Waveforms’ subsection ‘7.8.1.5 Comparison of Average Pressure Distributions’. It is therefore believed that this pattern cannot be attributed to a change in blade root conditions.

A means to quantify the difference between the normalised average pressure distribution forms about individual blades is desired. This is done in order to quantify the above visual observations. The variance in the difference between average normalised wave forms about individual blades is chosen for this purpose (i.e. quantifies the impact of changing a blade root condition between configurations). Consider Table 4.3-1 which compares average normalised pressure distributions about blades from the four different configurations. Blades changed between configurations are shown in **bold**.

Table 4.3-1 Variance heat map in normalised average pressure wave form about blades given 1 Jet excitation

Config.	Blade 1	Blade 2	Blade 3	Blade 4	Blade 5
Config. 1/Config. 2	0.000601	0.000734	0.001022	0.001308	0.000872
Config. 1/Config. 3	0.000724	0.000517	0.001155	0.000912	0.000453
Config. 1/Config. 4	0.000469	0.000602	0.000861	0.000659	0.002598
Config. 2/Config. 3	8.65E-05	0.000378	0.000168	0.000217	0.001657
Config. 2/Config. 4	0.000803	0.001374	0.00049	0.000551	0.000886
Config. 3/Config. 4	0.000814	0.000699	0.000467	0.000523	0.004033

Recall that blade 5 was changed in the swap to configuration 2, blade 2 was changed in the swap to configuration 3 and finally blade 3 was changed in the swap to configuration 4. It can be seen that the maximum variance in the difference between configuration wave forms for individual blades is erratically spread across the heat map. This is regardless of whether a blade was changed between configurations or not. Had the blade root conditions changed the mean casing pressure distribution significantly then the maximum variances would have been expected to follow the blade replacement regime. This would thus produce an observable pattern. It can be seen that this is not the case.

Consider two examples from the above heat map. The maximum variance between configuration 1 and 2 was found for blade 4, which remained unchanged between configurations. Similarly the maximum variance between configuration 2 and configuration 3 was for blade 5, which was also left unchanged between configurations. Similar trends were noticed for 2 and 4 jet excitation, the relevant variance heat maps for all excitation schemes can be seen in section ‘7.8.2 H2 – Variance Heat Maps for Average Wave Forms’. Further, no correlation is observed between the three different variance heat maps. The only condition which is changed between heat maps is the excitation scheme. Had the same variance trends (such as hot spot maxima and minima locations) been noticed between the different heat maps then that may have indicated that root conditions effects play a role.

These findings do not conclusively rule out root geometry effects on the average casing pressure form. They do however suggest that a change in blade geometry sufficiently far from the blade tip, such as the root slots in this case, has a negligible impact on the average pressure distribution measured at the casing. They further indicate that even large changes in fundamental blade behaviour has a negligible impact on average pressure waveforms. It is noted that no investigation into quantifying ‘sufficiently far’ was made.

The next internal condition to be considered is the rotor speed. It is at this point that blade vibration cannot be completely uncoupled from the internal pressure signal and the analytical pressure model must be considered. The reformulated Model 2, upon which all further investigations are based, is provided in the Euler format in Equation [4.3.1]. The change in rotor speed and excitation conditions will be used to investigate the phase and amplitude modulation effects as described by the model. Note that in the model, amplitude modulation has been specified to occur about unity (maximum Γ is one). Similarly phase modulation of the pressure signal components occurs about zero degrees.

$$P_r(t) = Re \left\{ (1 + \Gamma \cdot \dot{\psi}(t)_r) \cdot \sum_{i=0}^{\infty} Q_i \cdot e^{(j \cdot i \cdot [\Omega \cdot t + \psi(t)_r + \nu])} \right\} \quad [4.3.1]$$

As has been stated, the internal pressure measurements were taken at and about EO resonances. This was achieved by changing the rotor speed. Therefore a better understanding of the blade forced response behaviour will be presented before returning to the effect of rotor speed on the internal pressure signal.

For pressure measurements taken off of EO resonance speeds, the modulation effects attributed to the fundamental peak are expected to be averaged out over many revolutions. This is because the blade fundamental behaviour is not in phase with the rotor speed. Therefore a stationary casing observer will measure the pressure signal with the blade fundamental response peak having an effect at a different phase angle during each subsequent revolution.

For engine ordered operation the effects of fundamental blade vibration are in phase with the rotor speed. A single stationary casing pressure observer will therefore always observe the blade's fundamental vibration effects on the pressure signal at the same blade response phase angle for each revolution (a common issue noted for synchronous blade vibration identification via BTT methods).

The blade response will however always have engine ordered frequency components. This is because the blade is being excited at multiple engine harmonics when under forced excitation conditions. These engine ordered components will inherently be scaled by the blade transfer function. Further, the closer a harmonic peak lies to a resonance, the greater that peak's magnitude will be. The effects of these conditions may be illustrated with on blade SG response measurements at and off of resonance. Consider Figure 4.3-5 which contains excitation at and about a fundamental resonance.

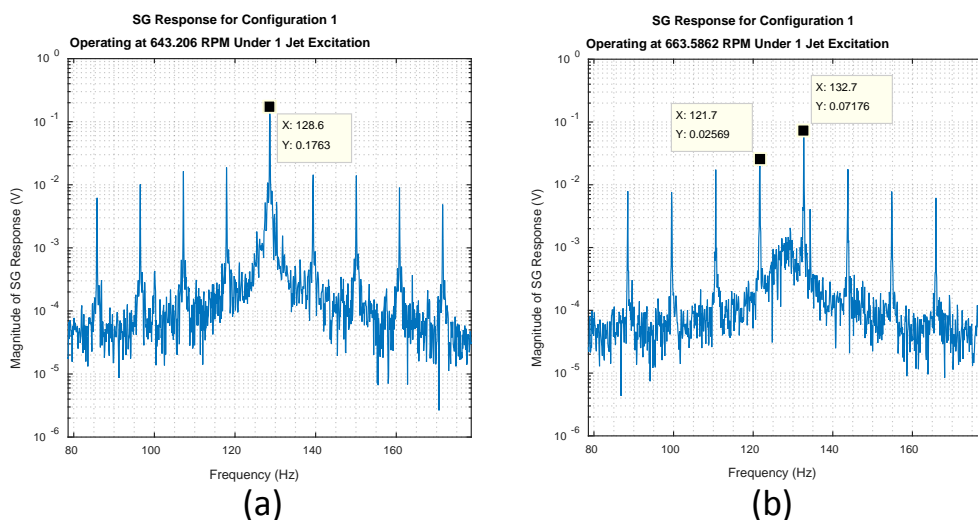


Figure 4.3-5 SG response about EO 12 for config. 1 under 1 jet excitation. (a) At resonance. (b) 20 RPM above resonance.

It can be seen in Figure 4.3-5 (a) that an engine harmonic lies at the fundamental peak, whereas in Figure 4.3-5 (b) the fundamental peak is flanked by two nearby engine harmonics. The excitation peaks are inherently in phase with the stationary pressure distribution about the blades. It can be seen that the response peaks are scaled relative to one another according to the blade transfer function. Both examples are from single jet excitation conditions, both measurements are within 20 RPM of one another. The harmonic peak located at resonance has a significantly larger amplitude when compared to both flanking peaks for the off-resonance excitation (approximately twice the response amplitude height). This is for near identical speed and forced excitation conditions.

In terms of any blade forced response containing signal, there will always be blade frequency response components in phase with the rotor speed. And these components are scaled by the blade transfer function. Further, the closer a harmonic peak lies to a resonance peak the greater that specific peak response amplitude will be magnified. These findings are significant in that they can help to identify when forced blade vibration is present in a pressure signal by evaluating the phase and amplitude of pressure features within that signal.

If we briefly consider a signal processing methodology which removes engine harmonic behaviour (such as the ensemble averaging method described by Forbes et al., or the integral engine order denuding process described by Mengle), then the fundamental response peak information will be removed if a signal corresponding to Figure 4.3-5 (a) is used (Forbes and Randall, 2013; Mengle, 1990). However, remnants of the fundamental peak might still be present if the process is applied to a signal corresponding to Figure 4.3-5 (b). This is the entire premise for the ensemble averaging methodology. If the entire response is considered and the harmonics are not removed then the response is still scaled by the blade transfer function regardless of the excitation conditions.

Now that a clearer picture of the response behaviour has been provided, the effects of changing the rotor speed on the average pressure signal will be investigated. Figure 4.3-6 contains a waterfall plot of the average pressure distributions for all configuration 1 measurements under 1 jet excitation.

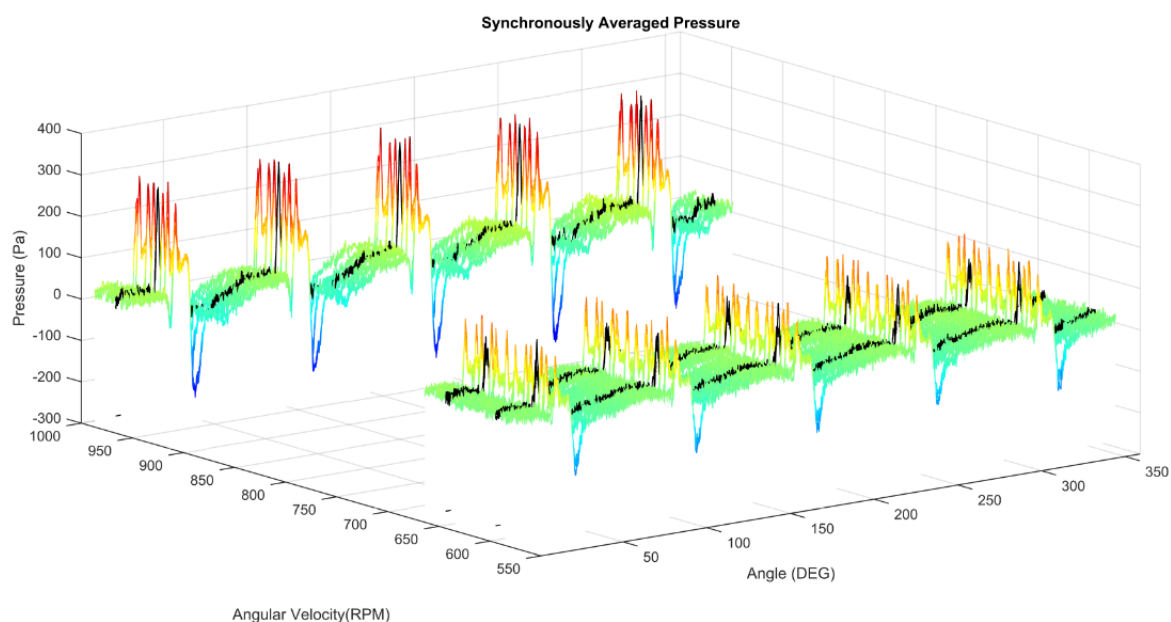


Figure 4.3-6 Waterfall plot of synchronously averaged pressure wave forms for configuration 1 under 1 jet excitation

Recall that steady state measurements for configuration 1 under 1 jet excitation were taken about blade 1's fundamental EOs 8, 12 and 13 (found at approximately 966 RPM, 643 RPM and 594 RPM respectively). Upon review of all corresponding SG measurements, it can be seen that blade 1 is always responding to the forced excitation (blade vibration behaviour is present in all measurements). Measurements at the three predicted critical speed locations have been plotted in black on the figure.

The first effect noticed is that the average pressure range for one revolution, averaged over multiple revolutions, increases with the rotor speed. The range is defined as the absolute difference between the maximum and minimum pressures (corresponding to the pressure peak ahead of the blade tip and trough behind the blade tip respectively). This effect was noticed for all average pressure distribution waterfall plots. Additional waterfall plots can be seen in section '7.8.3 H3– Waterfall Plots of Synchronously Averaged Configuration 1 Pressure'.

An investigation was performed in order to better understand the rotor speed and pressure response range relationship. This was done in order to understand if pressure fluctuations could be attributed to blade vibration from direct observation of the signal or not (as this effect was included in the reformulation of Model 2). The alternative situations would be that pressure fluctuations are solely a function of rotor operation, geometry and upstream excitation conditions (and thus are not associated specifically with blade vibration); or the pressure fluctuations are too erratic or small to make a confident call as to their effect.

It was found that a linear fit best suited the maximum pressure range and angular velocity relationship. The best linear fit example is provided in Figure 4.3-7 (a least squares approach was employed). A goodness of fit of R^2 equal to 0.99 was achieved for this dataset (the mean R^2 value achieved across all configurations and excitation schemes was found to be 0.94). Selected investigation result plots and a results table is provided in section '7.8.4 H4 – Selected Pressure Range Plots and Linear Fit Table'.

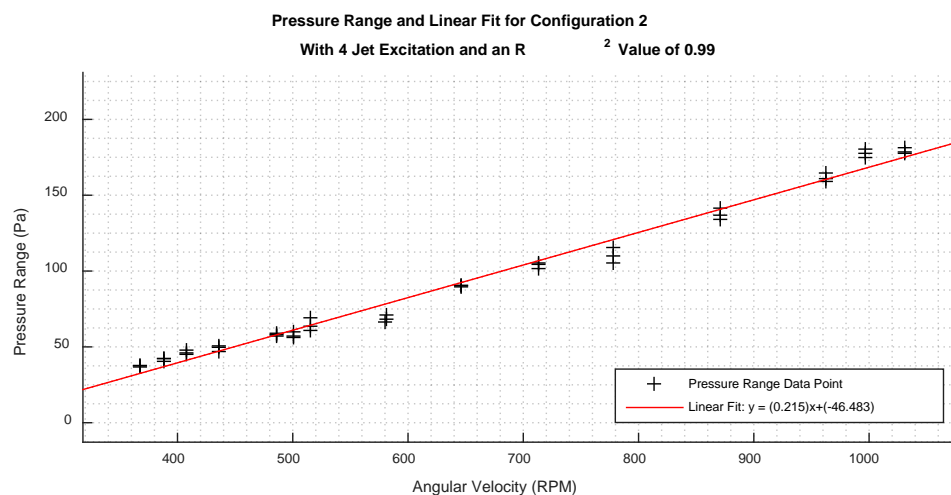


Figure 4.3-7 Pressure range and linear fit for configuration 2 under 1 jet excitation

According to the reformulated Model 2, if blade vibration does indeed cause the pressure field magnitude about the blade tip to fluctuate, then as rotor operation approaches a critical speed so does the pressure response fluctuation amplitude increase. This is because the amplitude modulation is a direct function of the blade transfer function. The amplitude increase should then be about the expected pressure value given the specific operating speed. Further, the theoretical vibration-free pressure range magnitude can now be estimated.

In terms of investigating the average pressure distribution about the casing, non-EO pressure fluctuations associated with blade vibration will be averaged out as they are out of phase with the rotor operation. The engine ordered blade vibration induced pressure components will still however be preserved in the average signal. This is because they are in phase with operation of the system. It is important to once again stress that their magnitude will be scaled by the blade transfer function.

There is however a catch. The pressure observer is not placed on the rotating blade tip. It therefore does not see the full response amplitude range change as the blade moves through its vibration path. The single stationary observer was placed on the casing wall. The instantaneous fluctuation amplitude captured by the stationary observer therefore depends on the angular position of the observer relative to the phase of the blade response. The blade response phase angle is a function of the forcing phase angle. This issue was alluded to earlier as a common issue associated with synchronous BTT.

Therefore, as the rotor approaches a critical speed the potential to capture a larger amplitude fluctuation exists. However, as was stated, the point along the path of the blade's response (and associated pressure magnitude fluctuation) captured is wholly dependent on the relative phase angle between the observer and the blade response. Therefore the full potential may not be realised.

The same issues exists when investigating the phase modulation aspect of the blade vibration model. Consider the case of an assembly with and without a vibrating blade presented in Figure 4.3-8.

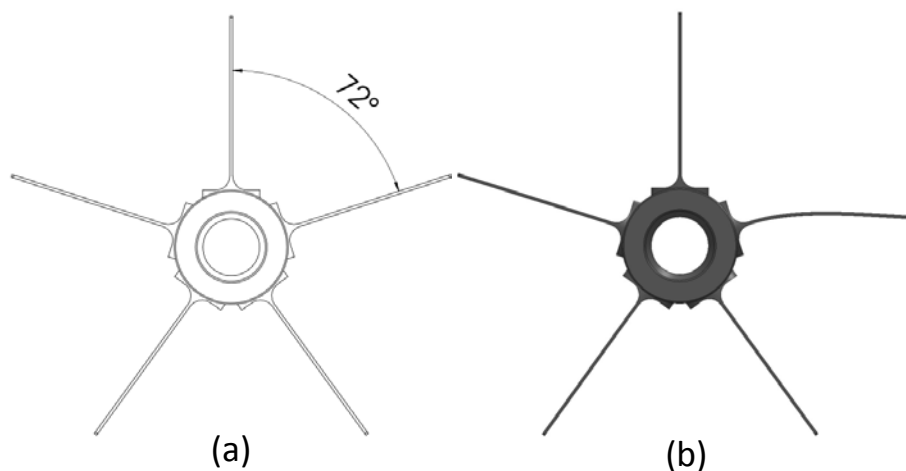


Figure 4.3-8 Angular distance between blades. (a) Undeformed shape. (b) Deformed shape.

If the blades are not vibrating (or their vibration does not have an effect on the pressure signal) then the arrival time of the pressure features, associated with the passing of the blade, should remain constant. If however one or more blades are vibrating then the pressure wave features' arrival times, measured at the stationary casing observer, should be affected. Once again pressure features refer to a pressure peak, or trough, which would rotate in steady state about the casing had no blade vibration been present (i.e. the rotating angular position is only affected by the blade tip behaviour).

Once again, as the rotor approaches a critical speed then the absolute magnitude between the expected arrival time, for a signal which contains no blade vibration, and the actual arrival time should increase. This is because the pressure features' arrival times are dependent on the blade's phase angles (i.e. it was assumed that the pressure fields follow the blade tips during steady operation). However, this phenomenon is once again being measured from the casing wall and the actual magnitude observed depends on the relative phase angle between the observation point and the individual blade's vibration phase. Thus as the system approaches resonance, the potential to observe

a larger phase shift of pressure signal features is present. Once again that potential is not necessarily realised by the stationary observer.

It was therefore found that when looking at individual response indicators in the pressure signal, such as the pressure distribution's peaks and troughs (or maximum amplitude ranges about blades), the same issues associated with BTT methods are found. Specifically, only a single point measurement of a feature, along the blade response path, is observed during synchronous rotor operation. This situation therefore requires multiple sensors and fitting algorithms to overcome the aliasing of these observations.

Further, the pulse spacing on resonance condition (PSR) must also be considered for optimal sensor positioning given a particular mode of interest and operating speed (recall that the PSR was a measure of how much of an individual response oscillation is captured due to sensor position, rotor speed and excitation over one revolution of the rotor, see section '1.3.4 Blade Tip Timing Approach'). According to this case a single stationary pressure observer, used to obtain pressure feature arrival times or local pressure fluctuations, does not gain anything over the established BTT approaches.

One advantage of using pressure signals over blade passing times however exists. The pressure signal form about a moving blade contains multiple features (such as peaks and troughs and their associated magnitudes). In a BTT signal only individual peaks associated with the passing of a blade are present. Therefore the locations and amplitudes of these multiple features in the pressure signal might be useful when used in an advanced fitting procedure for the purpose of obtaining blade vibration information.

It is however still of interest to determine if it is possible to identify blade vibration components, in terms of phase and amplitude modulation effects, in the measured pressure signals via simple signal processing and visual observation techniques. This will provide confidence in the proposed reformulated model as well as aid in evaluating the assumption that the pressure waves do indeed follow the individual tip behaviour during steady operation (and are thus linearly separable).

Consider the effects of both amplitude and phase modulation on pressure signal features presented in Figure 4.3-9 (a).

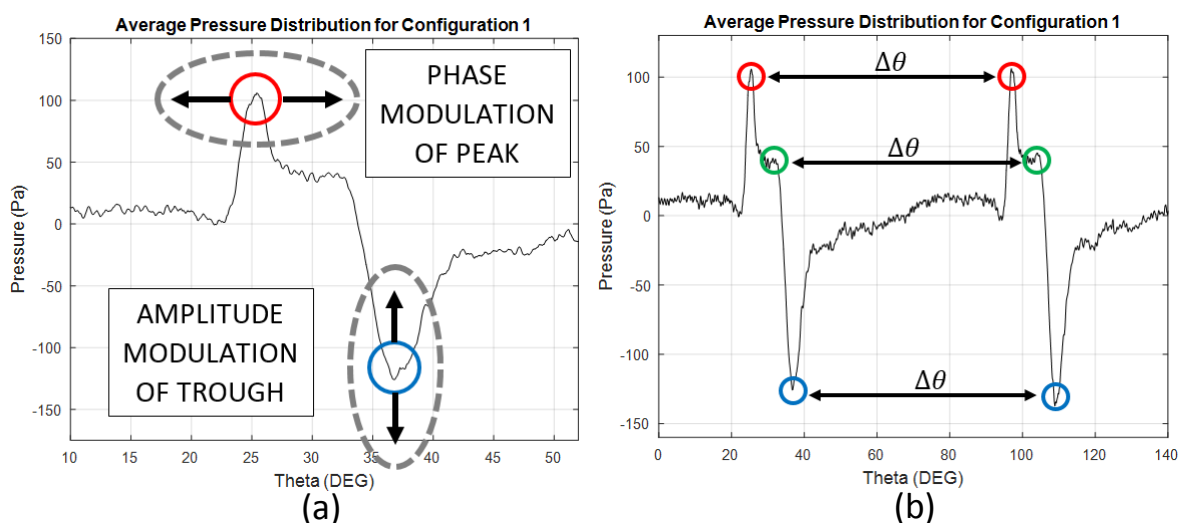


Figure 4.3-9 (a) Modulation effects on pressure signal features. (b) Change in feature angular displacement due to phase modulation.

It can be seen in the figure that amplitude modulation is expected to cause the pressure signal features' amplitudes to fluctuate about their mean values. It can also be seen that phase modulation is expected to cause those specific pressure features to arrive sooner or later than anticipated (depending on the blade vibration). The case of phase modulation will be explored first.

A means to determine if the pressure signal features are following the tip is desired (being phase modulated). Consider Figure 4.3-9 (b). If blade vibration is not present then the angular displacement between two features is expected to remain constant, even between measurements taken at different operating speeds. This is because this angle depends only on the rotor's geometry. If two adjacent blades are however vibrating, then the change in this angle is expected to follow the blade vibration.

It is important to once again stress that the stationary observer is however placed on the casing. And so the measured change in angle, due to forced EO vibration, will be constant in every subsequent rotation. If however the blades are vibrating and a rotor operating condition, such as angular velocity, is changed then a change in the angle between two blades may be expected. This can therefore be used to identify whether forced blade vibration is present in the pressure signal or not.

The effect of stochastic vibration must also be considered. Off-EO vibration will cause this angle to fluctuate slightly between rotations. If however the average pressure signal across multiple revolutions is used then this stochastic component is expected to be averaged out.

The operating speed and data acquisition sampling rate however place limits on what minimum magnitude of response is observable. Consider a rotor operating at a constant speed of 24 Hz (1440 RPM) and recall that the data acquisition sampling rate was chosen at 102.4 kHz (see sections '3.5.1 General Instrumentation' and '3.8 Experimental Methodology'). This results in approximately 4267 samples per revolution or 11.85 samples per degree that the rotor turns. Therefore, between two data points the rotor has moved an angular distance of approximately 0.084°. The radius from the center of the rotor to the blade tips was designed to be 162 mm. Thus the arc length subtended by the blade tip, between the two measurement points, is approximately 2.2 mm.

The change in the magnitude of the measured tip displacement, due to blade vibration, must therefore be larger than the minimum observable phenomenon in order to be considered as blade actual vibration. Which in this case is an arc length of 2.2 mm or angular displacement of 0.084°.

The change in angle between blades 1 and 2, across all configuration 1 measurements (under 1 jet excitation) is provided in Figure 4.3-10. The maximum blade pressure peak was the feature used.

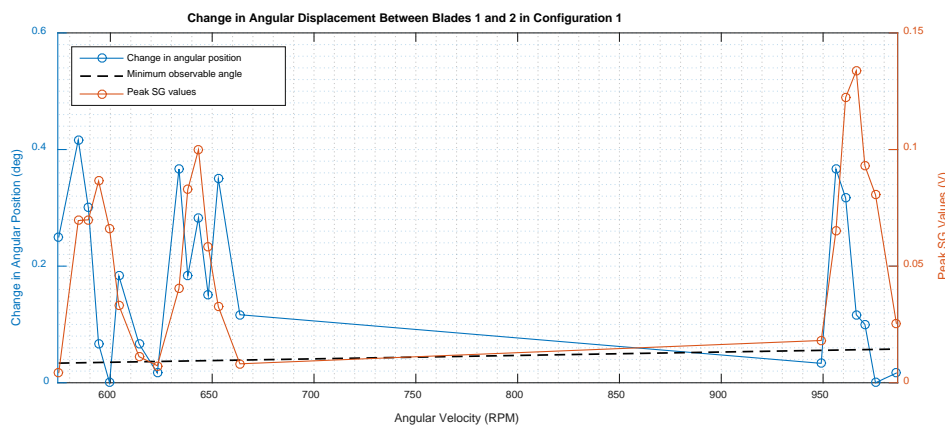


Figure 4.3-10 Change in angular displacement between blades 1 and 2 in configuration 1 with 1 jet excitation

The change in angular position between the blade pressure peaks has been plotted along with the fundamental peak heights obtained from the SG measurements. The SG measurements were recorded simultaneously. The predicted minimum observable angle has also been plotted as a function of the rotor speed and sampling rate. Recall that the configuration 1 experiments obtained under 1 jet excitation conditions were about three resonance locations. Three resonance peaks are clearly seen in the SG results as well as in the change in angle results.

Firstly it can be seen that the forced blade vibration components are large enough to be considered (the change in angles are above the minimum threshold). It can also be seen that as the SG measurements peak, so does the angular displacement change follow that trend in general. However, as expected, the full amplitude potential is not achieved. As has been stated, this is because the stationary observer is on the casing and only a potential for that observer to be exposed to a maximum phase angle change exists.

This is a crucial finding as it indicates (for this particular measurement) that the pressure phase response, about the blade tip, is a function of the blade transfer function. Thus the assumption that the pressure field follows the blade tip motion might be validated for this case. It is important to note that the phase modulation effect was first predicted in the work of Forbes which strengthens this argument (Forbes and Randall, 2013). Additional phase modulation due to forced response plots has been provided in section '7.8.5 H5 – Selected Phase Modulation Due to Forced Response Plots'.

The congruency, between the change in blade angle due to the forced response and the fundamental peak height, was evaluated by using a correlation analysis between the two curves. The correlation coefficient is scaled between zero and one. A value of 1 indicates perfect correlation, and value of zero no correlation. The results of the correlation analysis are presented in Table 4.3-2.

Table 4.3-2 Correlation between SG peak trend and change in blade peak pressure angle

Jets	Configuration 1					Configuration 2				
	B1/B2	B2/B3	B3/B4	B4/B5	B5/B1	B1/B2	B2/B3	B3/B4	B4/B5	B5/B1
1	0.1763	0.0365	0.2055	0.2554	0.345	0.0842	0.017	0.0278	0.0198	0.1134
2	0.2941	0.4739	0.4409	0.1418	0.1195	0.1439	0.0598	0.0018	0.3933	0.4867
4	0.068	0.0503	0.0603	0.2204	0.2049	0.445	0.5241	0.366	0.0034	0.6575

The absolute correlation value itself is not of great importance, the relative value between the blade-to-blade angle measurements, given a particular excitation scheme and configuration, however is. This is because the pressure distribution about a particular blade is expected to follow the SG trend for that blade. This is however taking into consideration that the casing observer is stationary, mistuning is present and there is a large amount of noise in the system.

In configuration 1 the SG measurements used were obtained from blade 1. Therefore, the highest correlation is expected for measurements which take the pressure distribution about blade 1 into account. The remainder of the blades in configuration 1 did however have similar fundamental frequencies to blade 1, and so similar correlation values are not unexpected.

In the stationary characterisation blade 3 was found to have the closest fundamental frequency to blade 1. Further, its mistuning was second only to blade 1. Therefore mode localisation effects are expected to affect these two blades most significantly. Recall that mode localisation may cause this by producing the larger response amplitudes on the most highly mistuned blades and smaller response

amplitudes on the remaining blades. The 2 jet excitation scheme, for configuration 1, performed the poorest with neither of the blade 1 pressure data sets (B1/B2 and B5/B1) having the highest correlation with the SG results.

When reviewing the results for configuration 2 the expected trend is more prominent. Measurements were taken at and off of expected critical speeds of both blade 1 and blade 5. The SG was applied to blade 5, and all of the highest correlations were found for angular fluctuations which include a blade 5 pressure feature. Particularly for the 2 jet data set, both blade 5 containing results obtained the highest correlation with the SG measurements.

It is important to note that due to the unexpected maxima in the correlation analysis this investigation only gives an indication that the pressure field about the tip follows the tip behaviour. It does not conclusively prove it. The sample size is also too small to perform a significant statistical evaluation of the information. Therefore at the bare minimum these findings indicate that the pressure features, about the blades, move relative to one another. Further, this effect might be attributed to blade vibration. This is still however an important finding.

The next step is to investigate whether or not the features' magnitudes are subject to amplitude modulation. The pressure range measure, used previously, cannot be applied here as it requires more than one feature to calculate. The feature points will most likely be at different blade vibration phase angles. This causes the results to be somewhat senseless when compared to blade behaviour information, although the pressure range would be expected to peak at resonance.

The pressure range investigation does however provide a starting point to investigate individual features. The pressure distributions about blades were found to fluctuate about nearly zero. The range increased linearly. It is therefore expected that the pressure peaks increase linearly. Similarly the pressure troughs are expected to decrease linearly. It may therefore be possible to fit a straight line through the data in order to remove this linear trend from the data.

Once the data is about zero then the absolute of the values can be taken in order to compare their magnitudes. Once again the peak amplitudes might follow the fundamental peak behaviour obtained from the SG measurements. This would indicate that amplitude modulation is a function of blade behaviour and is therefore a prudent component to include in the pressure model. The converse is also a possible outcome, namely that simply not enough information is available to say that the features magnitudes are amplitude modulated.

The results of the correlation between the change in peak magnitudes and the SG trend is presented in Table 4.3-3.

Table 4.3-3 Correlation between SG peak trend and change in blade peak pressure angle

Jets	Configuration 1					Configuration 2				
	B1	B2	B3	B4	B5	B1	B2	B3	B4	B5
1	0.1415	0.0408	0.1857	0.2153	0.0059	0.3042	0.3110	0.1454	0.4307	0.3301
2	0.3524	0.4704	0.6930	0.2083	0.0094	0.1873	0.5094	0.2578	0.3036	0.4559
4	0.4103	0.5995	0.4422	0.0218	0.0456	0.3124	0.2622	0.2664	0.2813	0.3900

If the amplitude modulation effects did indeed play a role, then the configuration 1 measurements should show the greatest correlation with blade 1 (B1). Similarly the configuration 2 measurements should show the greatest correlation with blade 5 (B5). It is however clear from the correlation analysis

that this is not the case. It appears that the blade vibration is not correlated with the amplitude fluctuations at all.

As was stated, this could be due to a number of reasons. Firstly the pressure fluctuations, potentially caused by the blade vibration, may simply be smaller in magnitude than the noise inside the casing. Further, the number of revolutions used in the averaging procedure may not have been able to completely remove that noise from the signal. This is a highly likely reason as the casing environment is extremely noisy to start with.

The second reason could be that the blade vibration has no effect on the pressure magnitude fluctuations. This was a suggested effect, however it was not supported by findings in literature or by these experimental results. This is still a significant result though as it simplifies the reformulated models by allowing the exclusion of the amplitude modulation effect. This reduces the number of design variables and calculations required to solve for during the evaluation of the full inverse problem. Recall that the blade angular velocity would need to be calculated from the blade angular displacement through differentiation of the signal. The need to simplify the model will shortly be shown to be an issue of great importance.

In terms of using a single pressure feature for the purpose of blade vibration identification from a steady state signal, it was found that similar issues associated with synchronous BTT methods exist. This method is however not completely at a loss though. This is because the angles between features can be measured over time. Changes in these angles, over long operational durations, may indicate that individual blade's integrity is changing. This method may therefore still be used as an online condition monitoring solution to identify if individual blades are vibrating and their integrity changing.

The resulting simplified reformulated Model 2 is provided in Equation [4.3.2].

$$P_r(t) = Re \left\{ \sum_{i=0}^{\infty} Q_i \cdot e^{(j \cdot i \cdot [\Omega \cdot t + \psi(t)_r + v])} \right\} \quad [4.3.2]$$

The resulting model is equivalent to that developed by Forbes, save the updated blade forced response model $\psi(t)_r$ (Forbes and Randall, 2013; Forbes, 2010). Now that the assumptions related to the model, pressure effects and blade vibration model effects have been investigated it is important to review certain aspects related to evaluating this model. As has been stated, the goal of which would be to obtain blade vibration information from an internal pressure signal.

It was seen that the average number of function evaluations required to solve for the blade transfer function parameters, from SG measurements, in the multi-start investigation was approximately 1670 (blade 1 in configuration 1). Further, the multi-start investigation required approximately 250 function evaluations to obtain a result for the best case scenario forcing function fit.

Fitting the blade transfer function had many more design variables than fitting the forcing function, hence the larger number of function evaluations. The complete internal pressure model however has more design variables than both these reduced problems combined. Further, the pressure signal is expected to have a significantly reduced blade vibration component when compared to the direct on-blade SG measurements. Therefore the number of required function evaluations for the full inverse problem is expected to increase significantly as they do not scale linearly with the number of design variables as well as due to the reduced prominence of the blade vibration effect in the signal itself.

Further, in order to capture blade phase modulation the required sampling rate was shown to be extremely high. And in order to have a high enough frequency resolution a significantly long enough signal had to be captured (a 10 second length signal provides a frequency resolution of 0.1 Hz). In this case a sampling rate of 102.4 kHz was used and the record length was 10 seconds.

Therefore in order to near perfectly reconstruct the pressure signal, using Fourier coefficients obtained from the deterministic signal, the minimum number of sums required would be in the order of 51.2×10^3 (the frequency bandwidth). This is in order to fully describe the phenomenon without down-sampling the data.

In order to evaluate the model, each sum must handle a vector which contains approximately 1×10^6 data points (sampling rate multiplied by the sample length). Thus a single function evaluation would be extremely expensive to perform using the full signals obtained. This coupled with the expected number of function evaluations required causes a traditional optimisation approach to be infeasible for this problem (at the specified resolution).

Methods have however been developed to handle optimisation problems which are extremely expensive to solve. One solution is to generate a cheaper surrogate model from a number of measurements, and then use the surrogate model in the optimisation process. A second solution methodology would be to solve the problem at a reduced resolution (resample at a lower sampling rate and decrease the signal length) and increase the data's resolution as the optimisation converges to a result. A final proposed solution would be to investigate which Fourier components are of a significant magnitude and evaluate the sum with only these components before considering the full dataset.

The final proposed solution will be briefly discussed. The complex Fourier coefficients are simply the full set of frequency information for a particular signal (it includes both phase and magnitude information). The absolute of the Fourier coefficients for an individual pressure measurement, sigmoidally windowed about blade 1, is provided in Figure 4.3-11.

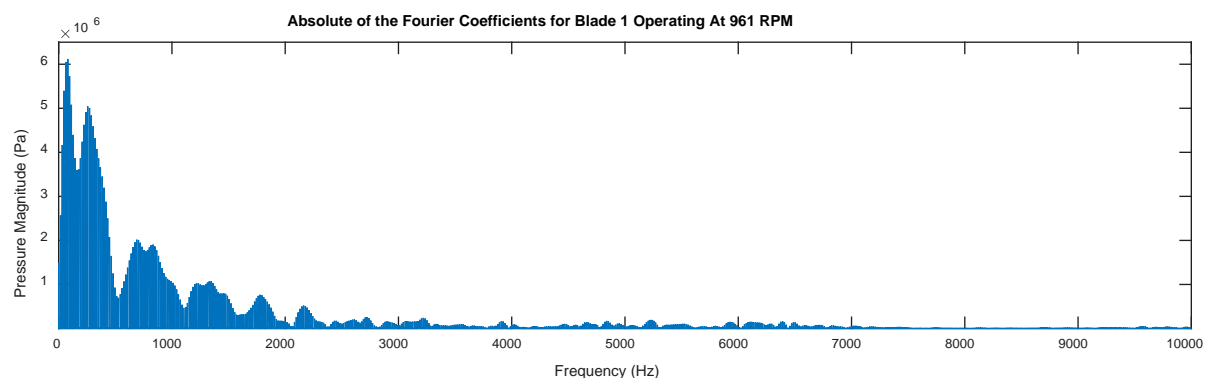


Figure 4.3-11 Absolute of the Fourier coefficients for blade 1 in configuration 1 under 1 jet excitation at 961 RPM

It is clear from the figure that the magnitude of the frequency information decreases with an increase in frequency. The majority of the important information lies within a small band of the full frequency spectrum (full band is 51.2 kHz). Further, the blade vibration is expected to modulate all frequency components related to features about the blade under investigation. Therefore, it may be possible to simply reduce the number of working Fourier coefficients in the model sum in order to provide a

significantly cheaper function to evaluate. The desired bandwidth can be continuously altered during the full optimisation run, and the final iterations can use the full spectrum.

The final concern regarding evaluating the above model, using a full pressure signal, is that the individual blades are most likely not responding at the same phase angle. Further, due to the blade mistuning, the inter-blade phase angle is not expected to be constant. Another effect of the blade mistuning is that the response amplitudes of the individual blades are also expected to differ. This results in different pressure feature phase shift magnitudes for each of the blades.

Taking all of these concerns into consideration a means to separate pressure features related to individual blade behaviour was desired. This is supported by the assumptions made in the development of both models, namely that the overall pressure response can be obtained by linear superposition of the individual blade contributions. These assumptions were evaluated earlier in this section. The blades were found to be lightly coupled. Further, the pressure investigation has suggested that the pressure waves about the individual blades are somewhat independent.

When compared to the evaluation of individual pressure features about blades, this bulk methodology should capture all of the features associated with an individual blade over an entire record length. Bulk feature evaluation of individual blades is the driving force behind the proposed inverse solution methodology (i.e. fitting the model to all pressure features associated with one blade). Using bulk feature measurements and fitting, noise associated with using a single feature is mitigated.

A windowing technique, based on combining sigmoid functions, was provided for this purpose in the theoretical development section (and as was stated used to evaluate frequency components of pressure waveforms about individual blades). A brief discussion of this windowing technique is the final component of the pressure signal investigation.

The windowing technique was designed such that it could capture the majority of the features associated to individual blades. This was to be done without attenuating the signal features associated with those individual blades. Consider Figure 4.3-12.

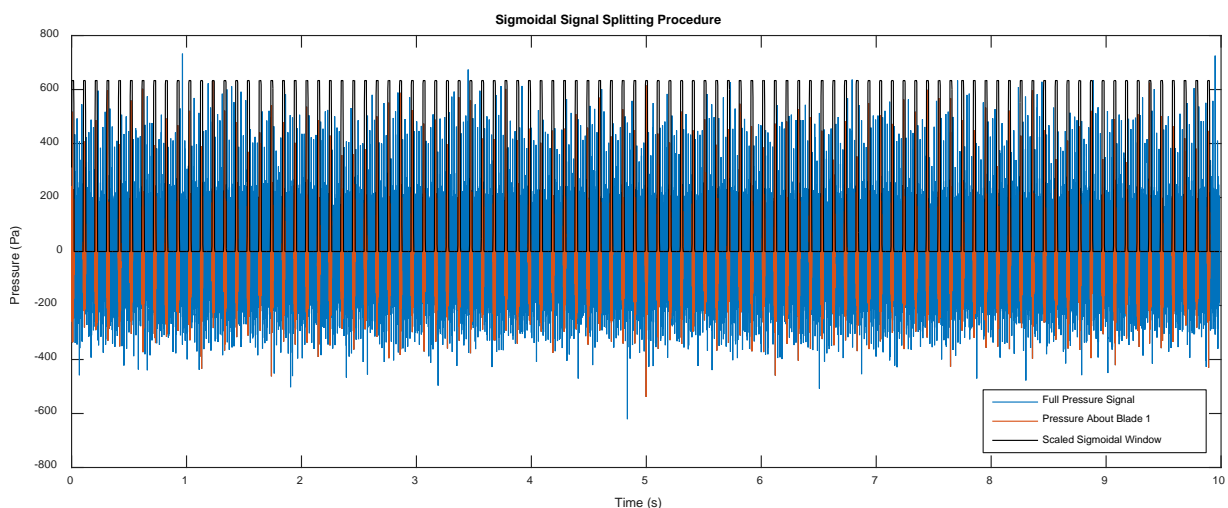


Figure 4.3-12 Sigmoidal windowing technique for a full signal

The sigmoidal windows are placed about the desired blade pressure signal features by using blade passing times (in this instance blade 1). The blade passing times were obtained from eddy current

proximity probes installed into the casing about the sound pressure transducer. They could have however been estimated using prominent signal features (specifically the peak and trough from a passing blade). A closer look at the same windowing technique, however on the deterministic portion of the same signal, is provided in Figure 4.3-13.

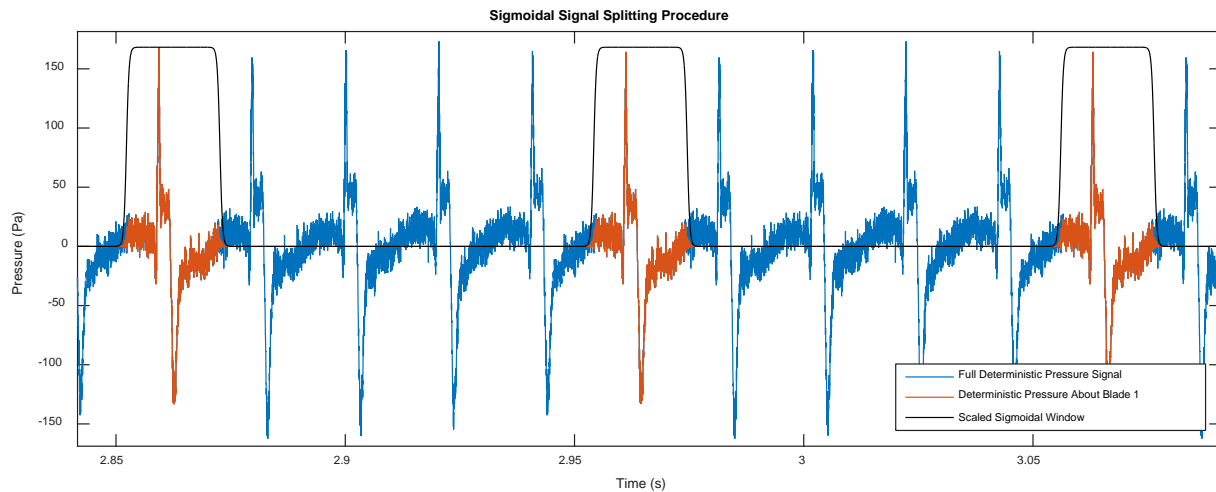


Figure 4.3-13 Sigmoidal windowing about blade 1 deterministic pressure signal in configuration 1 under 1 jet excitation

It can be seen from the figure that the windowing technique does not attenuate the signal features close to the pressure features near to the blade tip. Further, it provides a smooth transition between the blades. Recall that this was the desired behaviour of the window.

In summary, the principal underlying pressure model assumptions were evaluated. Each assumption was individually considered. Taking the assumptions evaluation and SG findings into account it was decided that reformulated pressure Model 2 would be used to analytically represent the signal. It must be stressed that this is at the expense of being able to sort and characterise the individual wave mode contributions individually.

The hub-to-blade mass ratio, in conjunction with the run-up resonance investigations, indicate that all of the configurations are indeed lightly coupled. Thus the physical blade tip behaviours may be considered in isolation of one another for evaluation and modelling purposes.

It was found that as the number of excitation jets increases, so does the pressure waveform approach the damped exponential form described by Forbes (Forbes, 2010). Altering the blade root condition was not found to have an effect on the average pressure distribution features about blades when captured at the casing wall.

It was shown that regardless of whether the system is being operated at or off of an engine ordered resonance, there will always be blade response frequency components which are in phase with the rotor operation. Further the blade response, including rotor harmonics about the resonance peaks, will be scaled by the blade's transfer function.

Indications were found to suggest that the pressure features about individual blades were indeed phase modulated. In simpler terms it suggests that they do indeed follow the blade tip motion. The pressure features were however not found to be amplitude modulated, and this resulted in the final pressure model taking the same form as provided by Forbes (Forbes and Randall, 2013).

Individual pressure feature evaluation, for the purpose of blade vibration identification, was found to suffer the same issues as those experienced by synchronous BTT approaches. Namely that multiple measurements need to be taken about the circumference of the rotor in order to obtain data across the full response of the blade. These measurements would then need to be fitted using advanced curve fitting techniques.

A brief look into the implications of using the full signals in the optimisation was made. It was found that it would be extremely expensive to evaluate, when considering the full signals. Alternative approaches were provided, one of which was discussed. A significant advantage of using the inverse problem formulation along with pressure signals captured about blades is that the behaviour of individual blades can be monitored. All other CPS based methods reviewed took the blade assembly's response into account.

Finally an example use of the windowing technique was provided. The need for the windowing technique was discussed, it was found that the blades do not necessarily move in phase with one another and neither are their response magnitudes expected to be the same. Therefore, features associated with individual blades would have to be evaluated separately. Hence further justification for the windowing technique.

The succeeding section contains the final conclusions of this investigation along with recommended avenues of future research.

Chapter 5 Conclusions and Future Research

5.1. Conclusions

The need for a means to non-intrusively monitor the behaviour of turbomachine blades during steady state operation was outlined during the introduction of this study. It was stated that the failure of even a single blade during operation could result in the catastrophic failure of an entire turbomachine.

The internal casing pressure signal was identified as a possible alternative source of blade behaviour information which can be captured non-intrusively. The signal itself comprises multiple constituents which must be assembled in such a way as to describe the true nature of the pressure phenomena within the casing. The purpose of this investigation was to study aspects of analytically modelling the internal casing pressure signal along with its elemental components. Focus was placed on modelling the blade behaviour itself within that signal. Blade response modelling inherently crosses all blade vibration measurement approaches. Therefore robust and inexpensive blade models are of great interest to develop and explore.

Two separate internal pressure models were uncovered during the literature review. Both analytical expressions describe the internal pressure signal from a single stationary casing measurement location. Both achieved this by using Fourier series representations (Forbes and Randall, 2013; Forbes, 2010; Mengle, 1990; Ratz et al., 2013). Both models were used in independent studies to investigate internal pressure signals. Further, both studies had some degree of success in uncovering blade resonance locations, using these models, during transient turbomachine operation (Murray and Key, 2015; Ratz et al., 2013). These models were the basis for the reformulated internal pressure models.

This investigation concentrated on pressure and SG measurements taken at nominally constant rotor operation. This was done for the purpose of evaluating and modelling blade vibration behaviour. Although this is not entirely novel, the majority of literature surveyed concentrated on transient rotor operation. An advantage of evaluating steady state system operation is that condition indicators can be obtained during long uninterrupted runs. They may therefore serve as early warning systems. This is as opposed to relying on transient measurements to provide condition indicators.

Before steady state operating measurements were taken, the hub and blade assemblies and associated components were thoroughly characterised. Both system characterisation and individual blade response characterisations were performed. The various configurations' responses were confirmed to be near to those estimated during FE analysis investigations. During the run-up resonance investigations, the instrumented blades were shown to respond at their estimated critical speeds. The results from the various characterisations performed complemented one another. These characterisations were found to be extremely useful when investigating the system's response during steady operation.

Results from the SG investigations and assumptions review facilitated alterations to the reformulated analytical internal pressure Model 1. This produced the same expression as the reformulated Model 2. The implications of making the required changes were discussed. Taking the success of other independent studies into account, along with this finding, a higher degree of confidence is gained in the models themselves. Specifically with regards to their predicted internal casing pressure behaviour as a function of blade tip behaviour. Both the models' behaviour and applicability were investigated extensively in the theoretical development and experimental investigations.

Common to all blade vibration measurement methodologies, both intrusive and non-intrusive, is the blade vibration and associated blade vibration model. As has been stated, in terms of this investigation it is an integral component of the pressure signal under investigation. Therefore care was taken in the choice of model for the purpose of representing its presence in the pressure signal. Multiple blade response representations were suggested in literature. Models considered included simple sinusoids, combinations of sinusoids (to obtain MDOF systems), lumped mass representations, Euler-Bernoulli beam representations and both partial and full FE representations. Brief reviews of these methods were provided in the appendix (see section '7.1.3 A3 – Analytical Blade and Assembly Models').

It was concluded that the sinusoidal models were too simplistic to capture the desired blade behaviour sufficiently. The lumped mass approach, although useful for evaluating a full systems response economically, was still incapable of providing the desired individual blade response resolution. Although capable of providing the desired tip response resolution the Euler-Bernoulli beam, partial and full FE models were on the other hand considered too expensive to evaluate in an inverse problem formulation. This is because they would have a significant effect on the number of design variables, for a model which is already expensive to evaluate.

It was found that the repurposed experimental modal analysis methodology, used to reconstruct a system's frequency response, was not only able to fit the measured SG data to a high degree, it also provided physical indicators of the system itself. The ability to resolve physical indicators accurately provides confidence in the model and allows blade condition inference from the results. Fitting the repurposed model to SG measurements is an example of one of the reduced inverse problems which was successfully solved.

When the fitting results were compared to the expected response parameters they made physical sense (such as a direct comparison of the modal damping). This provides assurance in the model's applicability to the problem. The technique allows easier modelling of the system's response to a chosen number of degrees of freedom, when compared to the other MDOF methods considered.

The method also facilitates modelling the forcing behaviour separately (both stochastic and forced). This allows similar physical checks on the forcing function fitting results. The repurposed technique is therefore not only useful for CPS based methods, it is useful for other techniques which hope to model the blade's response in an inexpensive MDOF manner whilst still providing links to the true physical nature of the system. It is believed that the repurposed technique has been used in a novel way in this investigation.

Following from the above discussion, it can be said that another useful component of the blade response model is the forcing function model. In this investigation a time-domain based signal construction methodology was suggested, implemented and experimentally evaluated. The model was evaluated by using blade SG response measurements in an inverse problem format. Specifically, the stream forcing behaviour was modelled as a series of Gaussian shaped force pulses applied to a region of a blade. Similar to the fitting of the blade transfer function, this model was fitted to experimental measurement using standard gradient based optimisation techniques.

Once again the forcing model was useful in the sense that certain of the design variables, once found after fitting the model to experimentally derived results, could be compared to the physical make-up of the experimental setup, geometry and operating conditions. This allows a sanity check between the expected behaviour and the fitted behaviour.

The model was less capable of being fitted to higher jet excitation conditions, however qualitative comparisons between the theoretical forcing model behaviour and the experimentally derived forcing behaviour showed some degree of correspondence in forcing form in the frequency domain. It is believed that the model is a useful step towards accurately describing all upstream flow based forcing behaviour. This forcing model is considered as entirely novel for modelling the forces applied to turbomachine blades, although work must be done to improve its performance.

It is therefore believed that an improved means to model blade response (both stochastic and forced) has been provided. The full SG response spectra showed that the blades were indeed excited by both noise and engine ordered harmonics. Therefore a single sinusoid would not be an appropriate model to capture the full complex behaviour of a blade in a turbomachine. Recall that an improved means to model blade behaviour was a primary deliverable of this investigation.

It must be stressed again that models which allow direct comparison with expected physical behaviour are believed to be of more use than those which cannot. This is because they allow extraction of physical quantities. These physical quantities can be used to report on the condition of a system whilst simultaneously providing the sanity check as mentioned earlier.

An investigation into an actual internal pressure signal was made. The investigation started by reviewing the assumptions related to the models developed. The applicability of all assumptions, and their implications was discussed.

During the investigation indications were found to corroborate the belief that blade vibration causes the phase of pressure signal features to shift. An investigation into the possibility of amplitude modulation of pressure signals returned inconclusive results. These findings had a significant impact on the reformulated Model 2. It was specifically found that the model reduces to that expressed in the work of Forbes (Forbes and Randall, 2013).

This has both positive and negative repercussions for the use of the model in an inverse problem setting. In terms of negative repercussions, it means that there are fewer unique features in the pressure signal related to the blade vibration than were expected. This has an impact on the ability of fitting the model to resolve blade vibration information from an internal pressure signal, which already masks its signature. On the other hand, it means that the internal pressure model itself is less expensive to evaluate which is useful as the model is already costly.

In the pressure investigations section the need and usefulness of the sigmoid based windowing technique was touched upon. The blades do not necessarily vibrate at the same phase angle and with the same amplitude. Therefore, in terms of the inverse problem formulation, it is prudent to solve for the blade vibration in a blade by blade fashion. The sigmoidal windowing technique is believed to separate pressure features related to the blade behaviour without attenuating them whilst simultaneously allowing a smooth transition between pressure fields surrounding blades. The window is especially capable of being stretched to fit the response shape of interest as to not attenuate important pressure features.

A full inverse problem formulation, in order to obtain blade response characteristics, was theoretically developed. As was stated, components of the inverse problem methodology were successfully used to fit the SG data to components of the suggested analytical pressure models. An inverse problem

methodology to blade vibration resolution in a pressure signal was not encountered in literature, and is therefore considered novel. A discussion on its feasibility and practicality is provided further on.

Unlike other CPS methodologies encountered, the full inverse formulation for pressure distributions about individual blades has the potential to uncover the behaviour of individual blades. All other CPS methodologies reviewed evaluated the cumulative effect of blade vibration. This was done either by monitoring the casing vibration or by direct measurement of the full pressure field within the casing. The ability to pinpoint individual problem blades is an extremely useful facet of this formulation.

It was however found that evaluating the objective function of the full inverse problem is extremely expensive to perform and so an alternative or modified solution route to that which was provided is desired. Suggestions in the relevant sections and in the section to come have been made.

Feasibility and practical implementation of the above discussed ideas are possibly the most important concerns to address from an engineering perspective. The forced blade response model will first be considered separately from its presence in the pressure signal.

As was stated, all blade vibration measurement methodologies, intrusive and otherwise, require a blade response model. When the SDOF sinusoid is fitted to blade response measurements the amplitude, frequency of response and phase angle are solved for. In terms of the blade response model presented in this work, similar variables must be obtained. For each degree of freedom considered, a natural frequency, modal damping value and modal amplitude must be resolved. On top of that the forcing function's design variables must be obtained, and then finally the combined forced response amplitude and phase angle. Both models can be used in fitting procedures to obtain an indication of blade vibration, however the model presented in this work provides direct estimation of both the physical condition of the blade and the forces acting on the blade.

The model suggested in this work may be more expensive to implement, however the potential gains in terms of understanding how the blade is behaving and its conditions are extremely useful. It is both a feasible and practical alternative when the source of blade vibration information is measured directly. Such is the case for BTT approaches. Within the current BTT curve fitting algorithms the blade response model can be substituted with the model developed in this investigation. Further, the number of degrees of freedom can be individually chosen in a case to case manner.

The next question regarding feasibility and practicality pertains to using the internal pressure model in an inverse problem formulation. Namely for the purpose of obtaining blade vibration information. In order for the method to be feasible the blade vibration must cause a measurable pressure effect. If indeed the fluid in the casing is being excited sufficiently by the blade vibration then the inverse problem approach would have to be far less expensive than the one presented here. Specifically for the purpose of online condition monitoring. Further, the internal pressure sensors must be both fast enough to capture the response whilst simultaneously robust enough to survive the internal casing environment. For these reasons, the use of an internal pressure signal for steady state blade vibration measurement is still uncertain and further research is required.

Modelling and evaluating a turbomachine's internal casing pressure signal requires consideration of multiple facets. If used in conjunction with other non-intrusive methodologies it may prove to be a highly useful and robust blade vibration measurement solution. The succeeding section suggests further avenues of investigation surrounding the topics explored in this investigation.

5.2. Future Research

The modelling of a turbomachine's internal casing pressure signal is a challenging task. One solution route would be to initially determine an appropriate representation of the pressure signal, without blade vibration, and then thereafter consider what effect blade vibration would have on the signal. This was the route followed in the theoretical development of this investigation (and by Forbes et al.), it is however by no means the only appropriate solution methodology for modelling an internal pressure signal (Forbes and Randall, 2013).

For example the inverse operation, namely determining a pressure signal which comprises solely of blade vibration, and then including the effects of system rotation and flow, may be an alternative route. This was the solution route followed by Mengle, namely that the signal construction started in the rotating reference frame considering the effects of blade vibration on the fluid and was then moved into the stationary casing reference frame via a linear transform (Mengle, 1990).

Further investigations can be performed to determine the equivalency of these two signal construction routes and associated models. In this work the reformulated model based on the work of Mengle, namely Model 1, required representing the Doppler shifting as a modulating effect in order to achieve an appropriate representation of the phenomenon in the frequency domain. And then only after simplification of that signal were the two analytical models found to be somewhat equivalent.

In this investigation a Fourier series of the blade vibration free pressure signal was considered, and there-after blade vibration added on top of that signal. The Fourier series representation was found to be an expensive model to evaluate. This is attributed to the required number of individual sums in the series to produce the full time length signal. Alternative surrogate pressure models may however prove to be more appropriate, flexible or economical to evaluate. In terms of the literature reviewed, no alternatives to the Fourier series representation were found. If multiple pressure measurements are used then a radial basis function, or similar, representation may be built to provide an appropriate alternative.

The internal pressure models were developed assuming quasi steady state rotor conditions (rotors operating at a nominally constant speed over the measurement duration). An appropriate means to represent a transient (run-up or run-down) pressure signal with blade vibration was not investigated. Transient conditions may prove to be a useful source of blade vibration information as the blade's behaviour changes as the system moves through critical speeds. A means to model transient pressure conditions was not found during the literature reviewed. In the literature reviewed it was found that transient based pressure measurements were useful for blade vibration identification (Murray and Key, 2015; Ratz et al., 2013).

Pressure measurements were only obtained in line with the rotor row of interest, further investigations as to what blade vibration information is available up- and down-wind of the vibration source during steady state measurement conditions may also prove useful. Effects such as axial attenuation of the blade vibration signal, in terms of modulating effects, may be obtained in an investigation of this description. Further, in practice rotor rows do not act in isolation and so the effect of nearby stators and rotors to the response of blades in the rotor row of interest must be investigated to gain a holistic signal representation. Questions such as: what is the effect of measuring one stage up or down from the rotor row of interest can be further investigated.

The blade forcing function model, namely a time domain based set of Gaussian shaped forcing stream pulses, was flexible enough to be tuned to the single jet excitation condition with reasonable results (in terms of the SG investigations). No other forcing function models, in either the time or frequency domain, were found in the literature. In the work of Forbes et al. it was briefly mentioned that representing the forcing function as a Fourier series allowed the forcing shape to take any form, an indication as to how that forcing shape was developed was not provided (Forbes and Randall, 2013; Forbes, 2010). The Gaussian time domain based representation was a first step towards modelling the forces acting on the turbomachine blades.

The optimal shape of the pressure forcing pulses was not investigated, and a more appropriate time domain forcing shape may be required to fit the higher jet excitation conditions. For example a dual sigmoid based shape, such as that proposed for the time domain windowing technique, may provide a more flexible force shape distribution. This is because a larger number of tuning variables are available to adjust the forcing pulse shape. It is believed that a more appropriate forcing shape could be better tuned to the actual conditions. Further, in this investigation it was assumed that the forcing shape from each upstream nozzle was equivalent, the repercussions of this assumption were however not investigated.

One such means to investigate a more appropriate forcing shape would be to remove the blade transfer function from a direct blade response measurement, such that only the forcing component remains, and then to fit different time domain based forcing shapes to that signal (as was performed for the one forcing shape proposed in this investigation).

The MDOF blade transfer function model, based on experimental modal analysis frequency response reconstruction techniques, proved effective for fitting the actual blade transfer function form. It is however more expensive to evaluate than either a single sinusoid or the combination of summing two sinusoids to create a MDOF solution form. It is however believed to be much less expensive to evaluate than a FE based physical model. The model proved useful for the purposes of this investigation, however an in depth comparison of this model with other blade behaviour models may prove useful not only for internal pressure based models, but BTT based methodologies as well.

Recall that BTT based models generally use a simplistic sinusoid, or in certain formulations a pair of sinusoids, to describe the blade response behaviour. It was however shown that during forced excitation the blade responds at multiple frequencies, indicating that an appropriate MDOF model may better tune to the actual behaviour. This is why it is believed that a direct comparison of blade response models and their ability to be tuned to measurements would be useful.

Further, a noteworthy advantage of using the experimental modal analysis frequency response reconstruction technique described in this investigation is that the tuning parameters can be evaluated with respect to actual physical systems. This is done in order to ascertain if they do indeed make physical sense. This is not possible when using simple sinusoids to describe the blade response.

A single stationary observer was employed to obtain pressure measurements in this investigation. The advantages of rather using multiple stationary pressure observers to obtain a glimpse of the pressure distribution within the casing were not investigated. An investigation into what can be gained by using multiple casing pressure observers, in terms of both pressure modelling and signal processing, is therefore suggested. In this investigation stationary observers were placed in line with the center of the rotor row of interest, a multiple sensor investigation may provide insight into the actual optimal

sensor positioning. The repercussions of slight changes in the sensor position were not investigated in this study.

The scope of this investigation was limited to analytical blade and pressure models. A numerical fluid-structure interaction study was outside the scope of this investigation. A comparison between a fluid-structure interaction study and the analytical model predictions would be useful to investigate how well the analytical models actually describe the fluid-blade interaction. This can be further supplemented by obtaining a pressure field measurement in the casing as opposed to a point measurement.

The final recommended avenue of investigation, and potentially the most significant, is to attempt the full inverse problem. First by making use of a virtual problem to understand the dynamics and issues associated with solving the problem (how well- or ill-posed the problem is), and then on a full pressure signal with known blade behaviour characteristics.

It was shown in the investigation that the objective function of the traditional error minimisation formulation is extremely expensive to evaluate. This is due to the required sampling rate and measurement length. Certain factors need to be accounted for when attempting the full problem:

- The number of function evaluations required to solve the problem. It was shown that a large number (in the order of 200) was required to solve either of the reduced inverse problems based upon SG measurements.
- Understanding that the number of design variables is much greater in the full inverse problem (the sum of design variables from both reduced blade vibration problems is still smaller than that of the full model). The number of iterations does not necessarily scale linearly with the number of design variables. This may result in many more iterations to solve the problem.
- The pressure signal will contain a weaker blade vibration component than the SG signals as it is not a direct measure of the blade behaviour.

Therefore, it may simply not be feasible to attempt the full problem using traditional means. An alternative would be to build a cheaper surrogate model based upon the proposed model and perform the majority of the optimisation iterations on that model. Another alternative would be to find a way to evaluate the sum in the full model in a more efficient manner. This is because the sum in the formulation is the bottleneck in evaluating the error required for minimisation. Or finally abandon traditional optimisation methodologies entirely and find a method better suited to expensive function evaluations (such as modelling the changes in pressure with radial basis functions).

This study has shown that there are still many investigative avenues available with respect to internal casing pressure signal based methods. A combination of additional studies may therefore yield an effective alternative to the current intrusive and non-intrusive blade vibration measurement schemes. Further, a clearer understanding of the internal conditions would be useful in the development of all non-intrusive blade vibration measurement schemes by providing greater understanding of the true internal turbomachine conditions.

Casing pressure signal based methods are still highly under-researched when compared to the amount of literature available on methods such as the BTT approaches. An inclusive approach which combines the information gathered from multiple non-intrusive methodologies would provide the greatest confidence in an online condition monitoring solution for turbomachinery blading.



Chapter 6 References

- ANSYS® Academic Research, Release 16.1, 2015.
- Arora, J., 2011. Introduction to Optimum Design, Third Edition.
- Banaszkiewicz, M., 2015. Multilevel approach to lifetime assessment of steam turbines. *Int. J. Fatigue* 73, 39–47. doi:10.1016/j.ijfatigue.2014.10.009
- Bathe, K.J., 1996. Proportional damping, in: *Finite Element Procedures in Engineering Analysis*. Prentice Hall.
- Bedrosian, E.A., 1963. A product theorem for Hilbert transforms, in: *IEEE*. pp. 868–869.
- Bishop, C.M., 2009. *Pattern Recognition and Machine Learning*, 1st ed. Springer, New York.
- Booyesen, C., Heyns, P.S., Hindley, M.P., Scheepers, R., 2015. Fatigue life assessment of a low pressure steam turbine blade during transient resonant conditions using a probabilistic approach. *Int. J. Fatigue* 73, 17–26. doi:10.1016/j.ijfatigue.2014.11.007
- Booyesen, C., Heyns, S., Scheepers, R., 2014. Fatigue life estimation of a low pressure steam turbine blade during resonant conditions applying probabilistic concepts 1–23.
- Campobasso, M., Giles, M., 2000. Flutter and forced response of mistuned turbomachinery. *Oxford Univ. Comput. Lab. Numer. Anal. Gr.* 1–35.
- Carrington, I.B., Wright, J.R., Cooper, J.E., Dimitriadis, G., 2001. A comparison of blade tip timing data analysis methods. *Proc. Inst. Mech. Eng. Part G J. Aerosp. Eng.* 215, 301–312. doi:10.1243/0954410011533293
- Castanier, M.P., Pierre, C., 2006. Modeling and analysis of mistuned bladed disk vibration: current status and emerging directions. *J. Propuls. Power* 22, 384–396. doi:10.2514/1.16345
- Cerejeiras, P., Chen, Q., Kähler, U., 2009. A necessary and sufficient condition for a Bedrosian identity. *Math. Methods Appl. Sci.*
- Cookson, R.A., Armstrong, K., Howard, M., Pilidis, P., Ramsden, K., 2001. Mechanical integrity of gas turbines. Cranfield, England. doi:SME/PPA/RAC/0937
- Cox, J., Anusonti-Inthra, P., 2014. Turbine engine rotor blade fault diagnostics through casing pressure and vibration sensors. *J. Phys. Conf. Ser. XXII Int. Conf. Spectr. Line Shapes* 548, 1–3. doi:10.1088/1742-6596/548/1/012066
- Das, G., Ghosh Chowdhury, S., Kumar Ray, A., Kumar Das, S., Kumar Bhattacharya, D., 2003. Turbine blade failure in a thermal power plant. *Eng. Fail. Anal.* 10, 85–91. doi:10.1016/S1350-6307(02)00022-5
- Dewey, R.P., Rieger, N.F., 1985. *Survey of steam turbine blade failures CS-3891*. New York.
- Diamond, D.H., Heyns, P.S., Oberholster, A.J., 2014a. A novel technique for estimating synchronous turbomachinery blade vibration from blade tip timing data 1–12.
- Diamond, D.H., Heyns, P.S., Oberholster, A.J., 2014b. A comparison between three blade tip timing algorithms for estimating synchronous turbomachine blade vibration, in: *WCEAM Research Papers, World Congress on Engineering Asset Management*. Springer International Publishing, pp. 215–225. doi:10.1007/978-3-319-15536-4_18
- Ewins, D.J., 1995. *Modal Testing: Theory and Practice*. Research Studies Press Ltd, Taunton.
- Ewins, D.J., Gleeson, P.T., 1982. A method for modal identification of lightly damped structures. *J. Sound Vib.* 84, 57–79.



- Forbes, G.L., 2010. Non-contact gas turbine blade vibration monitoring using internal pressure and casing response measurements. University of New South Wales.
- Forbes, G.L., Randall, R.B., 2012. Estimation of turbine blade natural frequencies from casing pressure and vibration measurements 1–18.
- Forbes, G.L., Randall, R.B., 2013. Estimation of turbine blade natural frequencies from casing pressure and vibration measurements. *Mech. Syst. Signal Process.* 36, 549–561. doi:10.1016/j.ymssp.2012.11.006
- Gallego-Garrido, J., Dimitriadis, G., Carrington, I.B., Wright, J.R., 2007a. A class of methods for the analysis of blade tip timing data from bladed assemblies undergoing simultaneous resonances—Part II: Experimental validation. *Int. J. Rotating Mach.* 2007, 1–10. doi:10.1155/2007/73624
- Gallego-Garrido, J., Dimitriadis, G., Wright, J.R., 2007b. A class of methods for the analysis of blade tip timing data from bladed assemblies undergoing simultaneous resonances—Part I: Theoretical development. *Int. J. Rotating Mach.* 2007, 1–11. doi:10.1155/2007/27247
- Genta, G., 2005. *Dynamics of rotating systems*. Springer, New York. doi:10.1007/0-387-28687-X
- Grant, K., 2004. Experimental testing of tip-timing methods used for blade vibration measurement in the aero-engine. Cranfield University.
- Hadamard, J., 1902. Sur les problèmes aux dérivées partielles et leur signification physique. *Princet. Univ. Bull.* 49–52.
- Heath, S., 2000. A new technique for identifying synchronous resonances using tip-timing. ... *Eng. Gas Turbines ...* 122, 219–225.
- Heath, S., Imregun, M., 1996. An improved single-parameter tip-timing method for turbomachinery blade vibration measurements using optical laser probes. *Int. J. Mech. Sci.* 38, 1047–1058. doi:0020-7403(95)00116-6
- Heath, S., Imregun, M., 1997. A review of analysis techniques for blade tip-timing measurements, in: *International Gas Turbine and Aero Engine Congress and Exhibition*. p. 97–GT–213.
- Heyns, P.S., 2009. *Mechanical Vibration Measurement and Analysis*. University of Pretoria, Pretoria.
- Hsu, C., 2014. A study on fluid self-excited flutter and forced response of turbomachinery rotor blade. *Math. Probl. Eng.* 2014. doi:10.1155/2014/437158
- Janssens, K., Vlierberghe, P. Van, Claes, W., Peeters, B., Martens, T., Hondt, P.D., 2010. Zebra tape butt joint detection and correction algorithm for rotating shafts with torsional vibrations. *Isma* 2869–2882.
- Joung, K., Kang, S., Paeng, K., Park, N., Choi, H., You, Y., von Flotow, A., 2006. Analysis of vibration of the turbine blades using non-intrusive stress measurement system, in: *Proceedings of the ASME Power Conference*. ASME, Georgia, pp. 391–397.
- Kahl, G., 2002. Aeroelastic effects of mistuning and coupling in turbomachinery bladings. *École Polytech. Fédérale Lausanne* 2629.
- Kaszynski, A. a., Beck, J. a., Brown, J.M., 2013. Uncertainties of an automated optical 3D geometry measurement, modeling, and analysis process for mistuned integrally bladed rotor reverse engineering. *J. Eng. Gas Turbines Power* 135, 102504. doi:10.1115/1.4025000
- Kennedy, C.C., Pancu, C.D.P., 1947. Use of vectors in vibration measurement and analysis. *J. Aeronaut. Sci.* 14.
- Kurkov, A.P., 1981. Flutter spectral measurements using stationary pressure transducers. *J. Eng. Power*



- 103, 461. doi:10.1115/1.3230743
- Mathioudakis, K., Loukis, E., Papailiou, K.D., 1989. Casing vibration and gas turbine operating conditions. ASME.
- Mathioudakis, K., Papathanasiou, A., Loukis, E., Papailiou, K., 1991. Fast response wall pressure measurement as a means of gas turbine blade fault identification. *J. Eng. Gas Turbines Power* 113, 269. doi:10.1115/1.2906558
- Mengle, V.G., 1990. Acoustic spectra and detection of vibrating rotor blades, including row-to-row interference. *Aiaa*. doi:doi:10.2514/6.1990-3987
- Milton, K., 2011. Chapter 6: Taylor and Laurent expansions - Analytic continuation. Oklahoma.
- Mukhopadhyay, N., Chowdhury, S., 1998. An investigation of the failure of low pressure steam turbine blades. *Eng. Fail. ...* 5, 181–193.
- Murray, W.L., Key, N.L., 2015. Detection of rotor forced response vibrations using stationary pressure transducers in a multistage axial compressor. *Int. J. Rotating Mach.* 2015. doi:198534
- Pusey, H.C., Pusey, S.C., 1990. Current practices and trends in mechanical failure prevention, in: *Proceedings of the 44th Meeting of the Mechanical Failures Prevention Group*. Vibration Institute.
- Rao, A.R., Dutta, B.K., 2012. In situ detection of turbine blade vibration and prevention. *J. Fail. Anal. Prev.* 12, 567–574. doi:10.1007/s11668-012-9597-6
- Rao, A.R., Dutta, B.K., 2014. Blade vibration triggered by low load and high back pressure. *Eng. Fail. Anal.* 46, 40–48. doi:10.1016/j.engfailanal.2014.07.023
- Rao, J.S., 1998. Application of fracture mechanics in the failure analysis of a last stage steam turbine blade. *Mech. Mach. Theory* 33, 599–609.
- Ratz, J., Forbes, G., Randall, R.B., 2013. Gas turbine blade natural frequency measurement using external casing vibration, in: *MFPT 2013 and ISA's 59th International Instrumentation Symposium May 13-17 2013*.
- Reddy, J.N., 2010. *Principles of Continuum Mechanics*, First. ed. Cambridge University Press.
- Resor, B.R., Trethewey, M.W., Maynard, K.P., 2005. Compensation for encoder geometry and shaft speed variation in time interval torsional vibration measurement. *J. Sound Vib.* 286, 897–920. doi:10.1016/j.jsv.2004.10.044
- Robinson, W.W., Washburn, R.S., 1991. A real time non- interference stress measurement system (NSMS) for determining aero engine blade stress, in: *In Proceedings of the 37th Symposium of the Instrumentation Society of America*. pp. 91–103.
- Russhard, P., 2015. The rise and fall of the rotor blade strain gauge, *Vibration Engineering and technology of Machinery (VETOMAC X)*, Mechanisms and Machine Science. Springer International Publishing, Manchester. doi:10.1007/978-3-319-09918-7
- Sabbatini, D., Peeters, B., Martens, T., Janssens, K., 2012a. Data acquisition and processing for tip timing and operational modal analysis of turbomachinery blades 52, 52–60. doi:10.1063/1.4730542
- Sabbatini, D., Peeters, B., Martens, T., Janssens, K., 2012b. Data acquisition and processing for tip timing and operational modal analysis of turbomachinery blades, in: *10th International Conference on Vibration Measurements by Laser and Noncontact Techniques*. pp. 52–60. doi:10.1063/1.4730542



- Smith, S.N., 1973. Discrete frequency sound generation in axial flow turbomachines, Aeronautical Research Council Reports and Memoranda. Cambridge.
- Vance, J.M., 1988. Rotordynamics of Turbomachinery. John Wiley & Sons, Inc., New York.
- Wang, P., Davies, P., Starkey, J.M., Routson, R.L., 1992. Torsional mode shape measurements on a rotating shaft, in: 10th International Modal Analysis Conference. pp. 676–682.
- Whitehead, D.S., 1987. Unsteady two-dimensional linearized subsonic flow in cascades. AGARD Man. Aeroelasticity Axial-Flow Turbomachines 1, 3.24–3.30.
- Williams, J., 1996. Improved methods for digital measurement of torsional vibration. SAE.
- Zielinski, M., Ziller, G., 1997. Optical blade vibration measurement at MTU, in: AGARD Conference Proceedings 598 on Advanced Non-Intrusive Instrumentation for Propulsion Engines.
- Zielinski, M., Ziller, G., 2000. Noncontact vibration measurements on compressor rotor blades. Meas. Sci. Technol. 11, 847–856.



Chapter 7 Appendices

Appendix A – Derivations, Blade Models and Algorithms

Appendix B – Additional BTT Literature

Appendix C – Example Application of CPS Method

Appendix D – FE Analyses

Appendix E – Experimental Setup

Appendix F – Steady Measurement Plan

Appendix G – SG Response

Appendix H – Pressure Results

7.1. Appendix A – Derivations, Blade Models and Algorithms

7.1.1. A1 - Derivation of Bessel Representation of Pressure Signal

Let the pressure around blade 'r' be represented by the Fourier series in Equation [8.1.1] (Forbes, 2010, p. 69):

$$P_r(t) = Re \left\{ \sum_{i=0}^{\infty} A_i \cdot P \cdot e^{(j \cdot i \cdot [\theta + \Omega(t) + \alpha_r + \gamma_i + x(t)_r])} \right\} \quad [7.1.1]$$

An equivalent form of Equation [7.1.1] with the blade vibration isolated is given in Equation [7.1.2]:

$$P_r(t) = Re \left\{ \sum_{i=0}^{\infty} A_i \cdot P \cdot e^{(j \cdot i \cdot [\theta + \Omega(t) + \alpha_r + \gamma_i])} \cdot e^{(j \cdot i \cdot [x(t)_r])} \right\} \quad [7.1.2]$$

It is assumed that the blade responds at an individual discrete frequency (Forbes, 2010, p. 68). The form of the blade vibration can thus be chosen as Equation [7.1.3] (Forbes, 2010, p. 68):

$$x(t)_r = X_k \cdot \sin(k \cdot \Omega(t) + \gamma_k) \quad [7.1.3]$$

The sine term in Equation [7.1.3] can be converted into an Euler equivalent; this is given in Equation [7.1.4]:

$$x(t)_r = X_k \cdot \frac{e^{j \cdot (k \cdot \Omega(t) + \gamma_k)} - e^{-j \cdot (k \cdot \Omega(t) + \gamma_k)}}{2 \cdot j} \quad [7.1.4]$$

Substitution of Equation [7.1.4] into the blade vibration portion of Equation [7.1.2] yields Equation [7.1.5].

$$e^{(j \cdot i \cdot [x(t)_r])} = e^{j \cdot i \cdot \left(X_k \cdot \frac{e^{j \cdot (k \cdot \Omega(t) + \gamma_k)} - e^{-j \cdot (k \cdot \Omega(t) + \gamma_k)}}{2 \cdot j} \right)} = e^{i \cdot \left(X_k \cdot \frac{e^{j \cdot (k \cdot \Omega(t) + \gamma_k)} - e^{-j \cdot (k \cdot \Omega(t) + \gamma_k)}}{2} \right)} \quad [7.1.5]$$

Noticing that the blade vibration portion of the Fourier series in Equation [7.1.2] has a Laurent series expansion equivalent in terms of Bessel functions it is possible to reformulate the blade vibration representation (Forbes, 2010, p. 69; Milton, 2011). The result of the reformulation is provided in Equation [7.1.8].

$$e^{\frac{x}{2} \cdot \left(z - \frac{1}{z} \right)} = \sum_{n=-\infty}^{\infty} z^n \cdot J_n(x) \quad [7.1.6]$$

$$\text{Where } z = e^{(k \cdot \Omega(t) + \gamma_k)} \text{ and } x = i \cdot X_k \quad [7.1.7]$$

$$\therefore e^{(j \cdot i \cdot [x(t)_r])} = \sum_{n=-\infty}^{\infty} J_n(X_k \cdot i) \cdot e^{n \cdot j \cdot (k \cdot \Omega(t) + \gamma_k)} \quad [7.1.8]$$

Therefore the pressure distribution around blade 'r' with the blade vibration represented using a Bessel function equivalent is given in Equation [7.1.9].

$$P_r(t) = Re \left\{ \sum_{i=0}^{\infty} A_i \cdot P \cdot e^{(j \cdot i \cdot [\theta + \Omega(t) + \alpha_r + \gamma_i])} \cdot \sum_{-\infty}^{\infty} J_n(X_k \cdot i) \cdot e^{n \cdot j \cdot (k \cdot \Omega(t) + \gamma_k)} \right\} \quad [7.1.9]$$

The final form of the pressure distribution around blade 'r' is achieved by converting from the Euler representation to a trigonometric form, multiplying out all of the terms, taking the real of the result and rearranging. The final form is provided in Equation [7.1.10].

$$P_r(t) = \sum_{i=0}^{\infty} \sum_{n=-\infty}^{\infty} A_i \cdot P \cdot J_n(i \cdot X_k) \cdot \cos[i \cdot (\theta + \Omega(t) + \alpha_r + \gamma_i) + n \cdot (k \cdot \Omega(t) + \gamma_k)] \quad [7.1.10]$$

7.1.2. A2 – Reformulation of Internal Pressure Signal Equation

A reformulation of the pressure equation derived by Forbes and Randall into a more familiar form is possible through simple trigonometric manipulation. The original equation presented by Forbes and Randall in Equation [1.3.41] is presented below (Forbes and Randall, 2013):

$$P_r(t) = Re \left\{ \sum_{i=0}^{\infty} A_i \cdot P \cdot e^{(j \cdot i \cdot [\theta + \Omega(t) + \alpha_r + \gamma_i])} \cdot e^{(j \cdot i \cdot [x(t)_r])} \right\} \quad [7.1.11]$$

It was noticed that specifying the blade vibration in terms of translation is erroneous as phase modulation must be specified in terms of a change in phase angle. It is therefore chosen that the blade vibration be specified in terms of angular displacement of the blade tip and not pure translational displacement. The blade tip vibration, in terms of angular displacement, is given below:

$$P_r(t) = Re \left\{ \sum_{i=0}^{\infty} A_i \cdot P \cdot e^{(j \cdot i \cdot [\theta + \Omega(t) + \alpha_r + \gamma_i])} \cdot e^{(j \cdot i \cdot [\psi(t)_r])} \right\} \quad [7.1.12]$$

The symbol gamma, ψ , is chosen to represent the blade vibration. The angular displacement of the blade tip can however be written in terms of the tip's translational displacement:

$$\psi(t)_r = x(t)_r / L \quad [7.1.13]$$

Where L is the length of the blade.

The first step in the reformulation is a substitution of the exponential multipliers:

$$Let X = i \cdot [\theta + \Omega(t) + \alpha_r + \gamma_i] \text{ and } Y = i \cdot [\psi(t)_r] \quad [7.1.14]$$

Through substitution of X and Y and by converting from Euler's representation of the Fourier series to the equivalent trigonometric form we obtain:

$$P_r(t) = Re \left\{ \sum_{i=0}^{\infty} A_i \cdot P \cdot [\cos(X) + j \cdot \sin(X)] \cdot [\cos(Y) + j \cdot \sin(Y)] \right\} \quad [7.1.15]$$

Expanding the above relation reveals:



$$P_r(t) = Re \left\{ \sum_{i=0}^{\infty} A_i \cdot P \cdot [\cos(X) \cdot \cos(Y) + j \cdot (\cos(X) \cdot \sin(Y) + \sin(X) \cdot \cos(Y)) - \sin(X) \cdot \sin(Y)] \right\} \quad [7.1.16]$$

If only the real part of the equation is considered we are left with:

$$P_r(t) = \sum_{i=0}^{\infty} A_i \cdot P \cdot [\cos(X) \cdot \cos(Y) - \sin(X) \cdot \sin(Y)] \quad [7.1.17]$$

Recalling the following trigonometric relation:

$$\cos(X + Y) = \cos(X) \cdot \cos(Y) - \sin(X) \cdot \sin(Y) \quad [7.1.18]$$

We obtain:

$$P_r(t) = \sum_{i=0}^{\infty} A_i \cdot P \cdot \cos(X + Y) \quad [7.1.19]$$

Re-substitution the exponential multipliers reveals:

$$P_r(t) = \sum_{i=0}^{\infty} A_i \cdot P \cdot \cos(i \cdot [\theta + \Omega(t) + \alpha_r + \gamma_i] + i \cdot [\psi(t)_r]) \quad [7.1.20]$$

The terms can finally be grouped:

$$P_r(t) = \sum_{i=0}^{\infty} A_i \cdot P \cdot \cos(i \cdot [\theta + \Omega(t) + \alpha_r + \gamma_i + \psi(t)_r]) \quad [7.1.21]$$

It is clear from the result that all Fourier terms of the pressure signal around a blade are phase modulated by the vibration of the blade.

7.1.3. A3 – Analytical Blade and Assembly Models

Numerical models provide a means to explore the relationship between excitation phenomena and the physical response of a blade or assembly. These models are based upon the underlying equations of motion (EOM) and are constructed and investigated using dynamic FE methods. The basis EOM, with viscous damping, is presented in Equation [7.1.22].

$$[M]\{\ddot{x}\} + [C]\{\dot{x}\} + [K]\{x\} = \{f(t)\} \quad [7.1.22]$$

Various effects may be explored using numerical models such as the influence of physical flaws in the blades, synchronous and asynchronous excitation as well as inter-blade effects resulting from coupling. The numerical models may also form the basis for response identification algorithms.

Three physical blade models are considered for this purpose; namely the Euler-Bernoulli beam model, the lumped mass model and the FE model.

7.1.3.1. Euler-Bernoulli Beam Model

The simplest of the models considered is the Euler-Bernoulli (EB) beam approximation of a single turbine blade. A ten degree of freedom (DOF) Euler-Bernoulli beam model, with 2DOF permitted at each node, is illustrated in Figure 7.1-1. The first two DOF are fixed at the shaft attachment point.

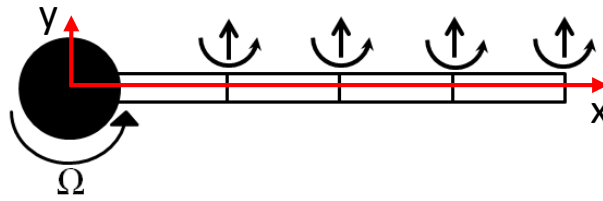


Figure 7.1-1 2DOF Euler-Bernoulli beam model

The model's ability to capture complex mode shapes accurately is governed by the chosen number of DOF per node as well as the number of elements; a single element consists of two nodes attached to one another at a prescribed distance apart. Three translational and three rotational DOF are possible at each node; the translational DOF are aligned with Cartesian axes positioned at each node and rotational DOF about those Cartesian axes.

The blade vibration as a function of time can be obtained once the global mass, stiffness and damping matrices have been composed from the elemental mass and stiffness matrices. The stator passing excitation may be modelled as a periodic impulse excitation acting on an individual or group of translational DOF; the time response of the entire blade is obtained through time based integration of the EOM; one such approach is the Runge-Kutta integration scheme.

The process described thus far will provide an individual blade's response relative to a stationary attachment point. Various rotating scenarios can be modelled by fixing the stationary attachment point of the blade to a point representing the surface of the shaft and then rotating the surface point about the centre of the shaft along with the vibrating beam; this is most easily achieved by transforming the blade's time based displacement, which is in a Cartesian coordinate system, to a cylindrical coordinate system.

Rotating scenarios of interest may include rotation at a constant angular velocity, acceleration or deceleration of the rotor as well as the effects of torsional vibration of the attachment shaft. It is important to note that these effects must be included when formulating the stator passing excitation; torsional vibration will provide excitation at the blade attachment point and so special consideration must be paid in order to model this accurately.

Multiple blades can be modelled by first simulating their individual time responses using a Runge-Kutta integration approach and then attaching them to the rotating shaft at prescribed angular displacements. In this way blade differences can be introduced and the time response of the full rotor obtained.

The inter-blade coupling effects of the entire assembly cannot be modelled with this approach. Inter-blade coupling effects refers to the response of the entire assembly as an interconnected structure where the vibration of one component may affect the response of another. In a weakly coupled



system the behaviour of one blade can be seen to produce negligible influence on another blade attached to the same structure.

There are a few limiting assumptions associated with the use of an Euler-Bernoulli based approach, these assumptions are (Reddy, 2010):

- Sections which are plane before deformation remain plane after deformation
- Plane sections which rotate about the axis of bending remain perpendicular to the centroidal axis (axis running along the centroid of the beam)
- Plane sections retain their geometric dimensions during deformation (no Poisson effect)

One major result of these assumptions is that the only non-zero strain is along the longitudinal axis of the beam (Reddy, 2010). Errors may also be incurred when twisting of the blade is present; such is the case when the torsional modes of the EB beam are excited.

The EB approach provides a simple means to model the vibration response of a turbine blade in a weakly coupled system; it is however incapable of modelling inter-blade effects nor the effect of complex blade geometries on the actual response. The lumped mass approach is better suited to investigations where coupling is present and is discussed in the succeeding section.

7.1.3.1.1. Euler-Bernoulli Beam Formulation

An Euler-Bernoulli beam element consists of two nodes attached to one another with prescribed mass and stiffness properties associated to the DOF at each node. A total of 6 DOF are possible at each node; namely three translational and three rotational frequencies aligned by local Cartesian coordinate axes placed at each node.

It may suffice to investigate vibration in an individual plane by restricting the number of DOF per node to the DOF associated with the in plane motion; such is the case if bending about the weak axis is of interest. A scenario capable of capturing the first two bending modes is given in Figure 7.1-1 where vertical translation and in plane rotation are considered; in plane axial translation along the x-axis has been neglected. A significant decrease in computation time can be achieved by limiting the number of DOF per node when the model is used in a dynamic investigation; however cognisance of lost modes and mode shapes and their influence must be considered when applying these simplifications.

The consistent elemental mass and stiffness matrix for the 2DOF per node Euler-Bernoulli beam model is presented below.

$$k = \left(\frac{EI}{L^3}\right) \cdot \begin{bmatrix} 12 & 6L & -12 & 6L \\ & 4L^2 & -6L & 2L^2 \\ \text{symm.} & & 12 & -6L \\ & & & 4L^2 \end{bmatrix} \quad [7.1.23]$$

$$m = \left(\frac{\rho AL}{420}\right) \cdot \begin{bmatrix} 156 & 22L & 54 & -13L \\ & 4L^2 & 13L & -3L^2 \\ \text{symm.} & & 156 & -22L \\ & & & 4L^2 \end{bmatrix} \quad [7.1.24]$$

The individual mass and stiffness matrices are combined in a simple FE process to produce a global mass and stiffness matrix. It is important to note that the only boundary condition is the attachment of the beam to the rotor; this is accomplished by partitioning the global mass and stiffness matrices

to not include the DOF at the attachment point. The Euler-Bernoulli approach allows an individual blade to be discretised to any desired resolution and thus any desired total number of DOFs.

From the global mass and stiffness matrix appropriate damping matrices can be formulated. One such formulation is Rayleigh damping (Bathe, 1996).

$$[C] = \alpha[M] + \beta[K] \quad [7.1.25]$$

If the damping of two modes is known then the constants α and β can be determined directly by solving a set of simultaneous equations (Heyns, 2009).

$$\phi_i^T [C] \phi_j = 2 \cdot \omega_i \cdot \xi_i \cdot \delta_i \quad [7.1.26]$$

$$\therefore \phi_i^T [\alpha[M] + \beta[K]] \phi_j = 2 \cdot \omega_i \cdot \xi_i \cdot \delta_i \quad [7.1.27]$$

$$\phi_i^T [M] \phi_j = 1 \text{ and } \phi_i^T [K] \phi_j = \omega_i^2 \quad [7.1.28]$$

$$\therefore \alpha + \beta \cdot \omega_i^2 = 2 \cdot \omega_i \cdot \xi_i \quad [7.1.29]$$

For the case where more than two modes' damping is known (or assumed) a least squares or similar curve fitting approach can be used. Once α and β have been determined it is possible to find the damping ratios associated with all of the modes (Bathe, 1996).

$$\xi_i = \frac{\alpha + \beta \cdot \omega_i^2}{2 \cdot \omega_i} \quad [7.1.30]$$

The major advantage of using Rayleigh damping is that the individual mode damping parameters for the first two modes can be obtained by means of a simple modal test and then used to obtain the parameters α and β .

Depending on the material characteristics it may be necessary to use hysteretic damping; hysteretic damping can however not be evaluated in the time domain and thus a viscous damping approximation of hysteretic damping can be used (Heyns, 2009).

7.1.3.2. Lumped Mass Model

An illustration of a lumped mass (LM) approach, consisting of four blades attached to a common shaft, is provided in Figure 7.1-2. Each blade is represented by a single mass; adjacent blades are coupled to one another with individual damping and stiffness ratios and all masses are coupled to ground (the common shaft) similarly with individual damping and stiffness ratios (Carrington et al., 2001; Gallego-Garrido et al., 2007b).

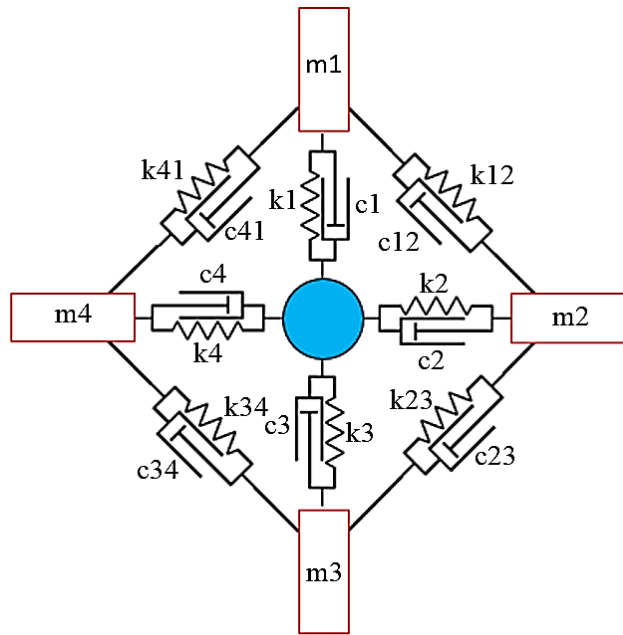


Figure 7.1-2 Lumped mass model

The normalised mass, stiffness and damping matrices associated with this configuration are presented in “7.1.3.2.1 Lumped Mass Model Matrices”.

The response of the system can be obtained using the same formulation of the basis equations of motion (EOM) given in Equation [7.1.22]. The response of the system to synchronous excitation at a particular EO can be determined through Runge-Kutta integration of the EOM; a suggested sinusoidal forcing function is presented in Equation [7.1.31] (Carrington et al., 2001).

$$f_i(t) = F_{0i} \cdot \sin(EO \cdot \Omega \cdot t + (2\pi \cdot EO \cdot i)/B) \quad [7.1.31]$$

The index ‘i’ refers to the *i*th blade, F_{0i} is the amplitude of the force applied to the *i*th blade, Ω is the angular speed of the rotor, B is the total number of blades (Carrington et al., 2001).

The LM approach can successfully investigate coupling effects under a variety of different physical configurations. The simplicity of the model allows fast computation of these configurations. The disadvantage to this approach is found in the reduction of the blade geometry and physical properties to individual mass, stiffness and damping systems which cannot capture higher order mode shapes or the effect of complex blade geometries.

7.1.3.2.1. Lumped Mass Model Matrices

The normalised global mass, stiffness and damping matrices proposed by Carrington et al. for the configuration given in section “7.1.3.2 Lumped Mass Model” are presented below (Carrington et al., 2001).

$$\mathbf{M} = \frac{1}{m_1} \cdot \begin{bmatrix} 1 & 0 & \dots & 0 \\ 0 & m_2 & \dots & 0 \\ \vdots & \vdots & \ddots & \vdots \\ 0 & 0 & 0 & m_B \end{bmatrix} \quad [7.1.32]$$



$$\mathbf{K} = \frac{\omega_{n1}^2}{k_1} \cdot \begin{bmatrix} k_1 + k_{12} + K_{B1} & -k_{12} & 0 & \dots & \dots & -k_{1B} \\ -k_{12} & k_2 + K_{12} + k_{23} & -k_{23} & 0 & \dots & 0 \\ 0 & -k_{23} & k_3 + k_{23} + k_{3B} & -k_{3B} & \dots & 0 \\ \vdots & \vdots & \vdots & \vdots & \vdots & \vdots \\ -k_{1B} & 0 & \dots & \dots & -k_{3B} & k_B + k_{3B} + k_{B1} \end{bmatrix} \quad [7.1.33]$$

\mathbf{C}

$$= \frac{2 \cdot \zeta^1 \cdot \omega_{n1}}{c_1} \cdot \begin{bmatrix} c_1 + c_{12} + c_{B1} & -c_{12} & 0 & \dots & \dots & -c_{1B} \\ -c_{12} & c_2 + c_{12} + c_{23} & -c_{23} & 0 & \dots & 0 \\ 0 & -c_{23} & c_3 + c_{23} + c_{3B} & -c_{3B} & \dots & 0 \\ \vdots & \vdots & \vdots & \vdots & \vdots & \vdots \\ -c_{1B} & 0 & \dots & \dots & -c_{3B} & c_b + c_{3B} + c_{B1} \end{bmatrix} \quad [7.1.34]$$

The parameter B is the blade index.

7.1.3.3. FE Model

The FE element approach suffers none of the drawbacks associated with the EB or LM approaches. Complex blade geometries, blade materials and geometric differences, and assembly configurations can easily be modelled and their response to a variety of excitation phenomena found. The influence of rotary effects such as centrifugal stiffening can be included in the investigation to provide a simulation more closely correlated to the actual physical problem.

Computer aided designs (CAD) of the actual rotor assembly can be directly imported into many of the available packages; model updating can be performed once physical experiments of the actual system have been executed.

The fluid-structure interaction can be modelled through additional computational fluid dynamics (CFD) investigations; this will add a more realistic dimension to the boundary conditions of the problem.

Unlike the EB or LM approaches a full dynamic time based FE or CFD approach is relatively expensive to run. The increased accuracy in the simulated response may be negligible when inter-blade coupling is weak and the blade geometry uncomplicated. As was previously found higher order resonances resulting in complex mode shapes are not of interest and so an EB approach may more than suffice.

7.1.4. A4 – Shaft Encoder Geometry Compensation Algorithm

An algorithm which compensates for encoder geometry variations, developed by Resor et al., is presented in this section (Resor et al., 2005). The algorithm is applicable for measurements taken at nominally constant shaft speeds.

Encoder geometry variations lead to a non-uniform time sampling scenario which may contribute significant errors and bias when measurements are used within algorithms which assume a uniform time sampling situation (such as the discrete Fourier transform) (Resor et al., 2005).

Determine the discrete zero crossing time interval from the sampling rate (Resor et al., 2005).

$$\Delta t_{clock} = \frac{1}{f_{clock}} \quad [7.1.35]$$

Generate a zero crossing time vector for each n^{th} crossing (Resor et al., 2005).



$$t(n) = n \cdot \Delta t_{clock} = \frac{n}{f_{clock}} \quad [7.1.36]$$

Calculate the time required for each revolution 'j' (Resor et al., 2005).

$$T_j = t((j + 1) \cdot N) - t(j \cdot N) \quad [7.1.37]$$

The parameter j is the revolution index starting at 1 and N are the number of encoder segments per revolution.

Assuming that the shaft speed is constant over a single revolution, the percentage of time that each encoder segment 'n' occupies for each revolution 'j' can be determined (Resor et al., 2005):

$$r_j(n) = \frac{t((j - 1) \cdot N + n + 1) - t((j - 1) \cdot N + n)}{T_j}, \quad 1 \leq n \leq N. \quad [7.1.38]$$

By averaging over all revolutions, the average percentage of time that each encoder segment occupies can be resolved. The effects of shaft torsional vibration are averaged out by this process because it is assumed that the torsional vibration is independent of encoder passage times (i.e. torsional shaft vibration is asynchronous to shaft rotation) (Resor et al., 2005).

$$r(n) = \frac{1}{M} \cdot \sum_{j=1}^M r_j(n), \quad 1 \leq n \leq N \quad [7.1.39]$$

The parameter M refers to the number of revolutions considered.

The average segment ratios can then be used to correct for variations in the encoder geometry (Resor et al., 2005).

A time difference vector is created using the true encoder zero crossing times and a reference signal assuming an ideal uniform encoder geometry (Resor et al., 2005).

$$\Delta t(n) = t_{encoder}(n) - \frac{n}{N \cdot f_{shaft}}, \quad 1 \leq n \leq N \cdot B \quad [7.1.40]$$

The shaft speed is assumed constant over each individual revolution. A vector containing the shaft speeds for each revolution, in hertz, is presented below (Resor et al., 2005).

$$f_{shaft}(j) = \frac{1}{t(N \cdot j + 1) - t(N \cdot j)} \quad [7.1.41]$$

The average shaft speed can be determined by taking the mean of the shaft speeds over all revolutions 'B' (Resor et al., 2005).

$$f_{shaft\ average} = \frac{1}{B} \cdot \sum_{j=1}^B f_{shaft}(j) \quad [7.1.42]$$

This average shaft speed can be substituted into Equation [7.1.40] (Resor et al., 2005).



$$\Delta t(n) = t_{encoder}(n) - \frac{n}{N \cdot f_{shaft\ average}}, \quad 1 \leq n \leq N \cdot B \quad [7.1.43]$$

Equation [7.1.43] assumes equal encoder segment widths. The previously computed ratios can now be used to correct the time difference vector (Resor et al., 2005).

$$\Delta t_{corrected}(n) = \Delta t(n) \cdot \frac{1/N}{r(n)} \quad [7.1.44]$$

Finally the time corrected vector can be used to calculate the shaft vibration (Resor et al., 2005).

$$\theta(n) = \Delta t_{corrected}(n) \cdot f_{shaft} \cdot 360 \text{ (deg)} \quad [7.1.45]$$

7.2. Appendix B – Additional BTT Literature

7.2.1. B1 – General BTT Theory

7.2.1.1. Synchronous vs Asynchronous BTT

BTT techniques originate from the 1960s where asynchronous vibration of rotor blades was investigated (Heath and Imregun, 1996). Asynchronous response occurs at frequencies which are not integer multiples of rotational speed; it generally occurs due to aerodynamic instabilities such as flutter, rotating stall and acoustic resonance (Zielinski and Ziller, 1997). Due to the fact that the response resonant frequency and phase of an asynchronously vibrating blade is arbitrary with respect to the angular velocity, a single measurement point can be utilised with classic sampling and sub-sampling techniques to illicit response information (Heath and Imregun, 1996). This is because the single measurement point is exposed to the full range of response amplitudes given a long enough measurement period.

The question of synchronous response measurement is a more complex issue to solve. The synchronous (also known as engine-ordered or integral order) response phenomenon is characterised by vibration at frequencies which are at integer multiples of the engine rotation speed. The response vibration can be due to mechanical effects (residual unbalance of rotors and non-concentric casings) or aerodynamic effects (irregular pressure distributions due to engine intake geometry or upstream stator blades) (Zielinski and Ziller, 1997).

The problem with synchronous response is that the phase remains constant with respect to an arbitrarily fixed datum (Heath and Imregun, 1996); this means that a single stationary measurement point will always encounter the same response instant along the dynamic behaviour response cycle of the vibrating blade. A single parameter technique was introduced to handle this problem in 1970 and became the standard method up until a more advanced two parameter plot method was introduced in 1996 (Heath and Imregun, 1996). An example of four BTT probes capturing synchronous data points for a non-accelerating or decelerating response is illustrated in Figure 7.2-1, it is clear that each probe captures the same response amplitude each time the true signal is sampled.

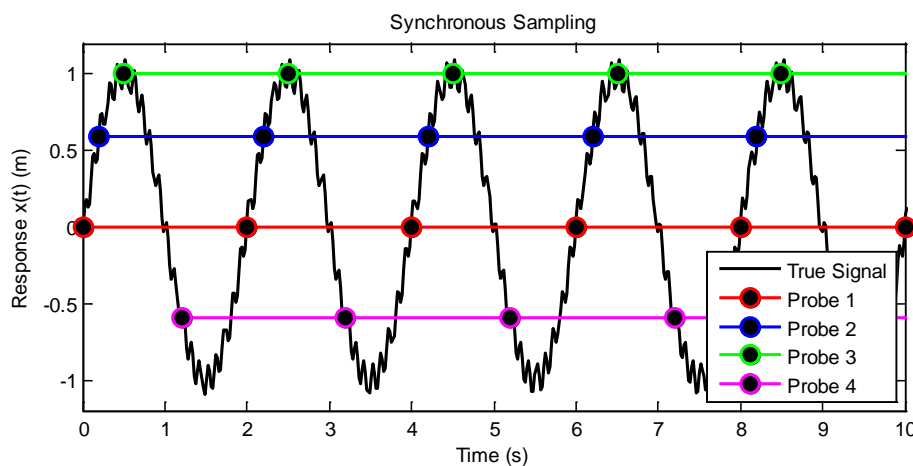


Figure 7.2-1 Synchronous BTT sampling

7.2.1.2. Direct vs Indirect BTT

The early single parameter and two parameter plot methods required that data be collected across the entire resonance region of the blades; this is done by sweeping the rotational speed of the rotor across all natural frequencies of interest (Carrington et al., 2001). This procedure is followed such that

the measurement points are exposed to a full range of excitation amplitudes at varying frequencies; this is similar to the exposure of a sensor to an asynchronous response. These methods have been termed indirect approaches and are capable of supplying both the response amplitude of a blade and the response vibrational frequency. A typical single parameter BTT system is presented in Figure 7.2-2.

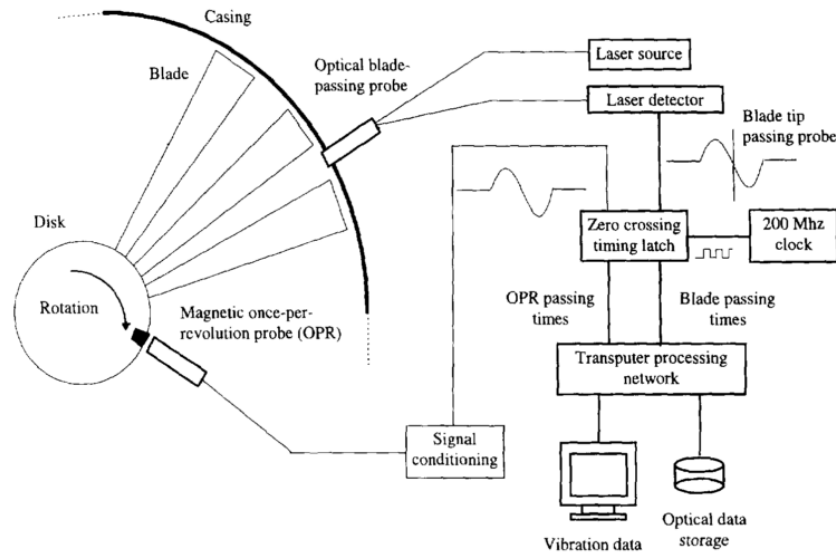


Figure 7.2-2 Indirect single parameter BTT experimental setup (Heath and Imregun, 1996)

Integral to the direct methods is the probe spacing on the resonance (PSR) concept. It is a measure of the percentage of the response waveform measured during one oscillatory cycle measured by the probes (Gallego-Garrido et al., 2007b). If the PSR is low then the response measurements become undersampled which results in a loss of accuracy. The PSR is directly influenced by the turbine's angular velocity; it was found that the AR methods perform increasingly poorly as the angular velocity increases as this causes the PSR to decrease (Grant, 2004). The PSR concept is presented in Figure 7.2-3; the true response is sinusoidal and two data sets with differing PSR values are used to fit the data.

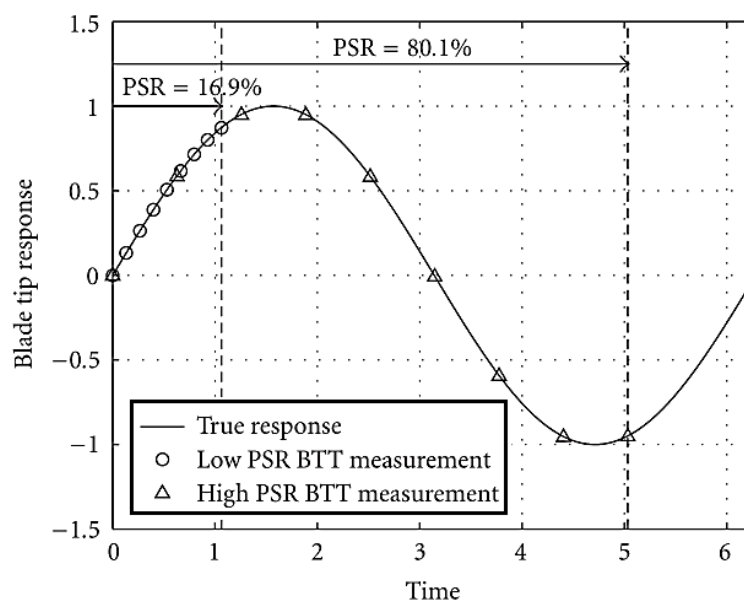


Figure 7.2-3 Probe spacing on resonance (Gallego-Garrido et al., 2007b)

In light of the synchronous sampling example, presented in Figure 7.2-1 it becomes clear how useful a high PSR can be for curve fitting a model to the actual response (in this case fitting a sinusoid).

The direct measurement approaches are more suitable for online condition monitoring schemes when compared to the indirect methods. Indirect methods can only be applied when a rotor is being swept through a range of angular speeds and so does not lend itself to monitoring a rotor operating at steady state conditions. This however does not completely disqualify the indirect methods from any form of usefulness; they may be applied during run up or shut down of a rotor using the same experimental equipment as an online direct system; they can provide crucial vibration information during these critical transient events.

7.2.2. B2 – Autoregressive Methods

7.2.2.1. General Theory

One of the simplest of the curve fitting techniques applied to the direct BTT approach is the autoregressive (AR) method. Due to its popularity, and the fact that it forms the basis for some of the most advanced current BTT methods, the basis theory will be presented here.

The physics of the problem is assumed to adhere to the following equation of motion (EOM) in the form of an ordinary differential equation (ODE) (Carrington et al., 2001):

$$\ddot{x} + \omega_n^2 \cdot x = 0 \quad [7.2.1]$$

The assumed blade tip response solution is a single degree of freedom (SDOF) sinusoidal response where the forcing frequency is assumed to be the tuned synchronous response at resonance ($\omega_f = \omega_n$) (Carrington et al., 2001).

$$x = A_n \cos(\omega_n t + \phi_n) + D \quad [7.2.2]$$

An alternative, yet equivalent form, of the previous equation is presented here (Carrington et al., 2001):

$$x_j = \hat{A} \cdot \cos(\omega_n \cdot t_j) + \hat{B} \cdot \sin(\omega_n \cdot t_j) + D \quad [7.2.3]$$

Where the index j denotes the specific probe from which a measurement is taken.

Let the ODE be discretised about time t_j (two possibilities exist, namely $\pm\Delta t$) using a second order Taylor expansions of the tip response x (Carrington et al., 2001):

$$\begin{aligned} x(t_j + \Delta t) &= x(t_j) + (\Delta t \cdot \dot{x})_{t_j} + \left(\frac{\Delta t^2}{2} \cdot \ddot{x}\right)_{t_j} \\ x(t_j - \Delta t) &= x(t_j) - (\Delta t \cdot \dot{x})_{t_j} + \left(\frac{\Delta t^2}{2} \cdot \ddot{x}\right)_{t_j} \end{aligned} \quad [7.2.4]$$

If the expressions in Equation [7.2.4] are summed and the acceleration term made the subject of the formula we obtain (Carrington et al., 2001):

$$\ddot{x} = \frac{x(t_j + \Delta t) - 2x(t_j) + x(t_j - \Delta t)}{\Delta t^2} = \frac{x_{j+1} - 2x_j + x_{j-1}}{\Delta t^2} \quad [7.2.5]$$



The time steps, Δt , between the three measurement points (x_{t+1} , x_t and x_{t-1}) must be constant in order for the expression in Equation [7.2.5] to hold (Carrington et al., 2001). This is important to note as it puts a physical constraint on the actual BTT physical setup; for the AR methods to work the probes have to be placed equidistant apart such that Δt remains constant.

It is now possible to substitute the Taylor approximations back into the ODE and rearrange the problem into the standard AR format (Carrington et al., 2001):

$$\ddot{x} + \omega_n^2 \cdot x = 0 \quad [7.2.6]$$

$$\frac{x_{j+1} - 2x_j + x_{j-1}}{\Delta t^2} + \omega_n^2 \cdot x_j = 0 \quad [7.2.7]$$

$$x_{j+1} - 2x_j + x_{j-1} + \omega_n^2 \cdot x_j \cdot \Delta t^2 = 0 \quad [7.2.8]$$

$$x_{j+1} + x_j(\omega_n^2 \cdot \Delta t^2 - 2) + x_{j-1} = 0 \quad [7.2.9]$$

$$\text{Let } a_1 = \omega_n^2 \cdot \Delta t^2 - 2, a_2 = 1, \quad [7.2.10]$$

*Introduce DC offset with substitution of $x_j = \bar{x}_j + D$
and rollback time by $(j - 1)$ in each term*

$$(\bar{x}_j + D) + a_1 \cdot (\bar{x}_{j-1} + D) + a_2 \cdot (\bar{x}_{j-2} + D) = 0 \quad [7.2.11]$$

$$\text{Let } \bar{x}_j = x_j \quad [7.2.12]$$

$$x_j + a_1 \cdot x_{j-1} + a_2 \cdot x_{j-2} = D(1 + a_1 + a_2) \quad [7.2.13]$$

$$x_j + a_1 \cdot x_{j-1} + 1 \cdot x_{j-2} = D(2 + a_1) \quad [7.2.14]$$

Equation [7.2.13] is in the standard AR problem format. Consider the form of the equation with $j = 3$:

$$x_3 + a_1 \cdot x_2 + 1 \cdot x_1 = D(2 + a_1) \quad [7.2.15]$$

$$[x_3 + x_1] = [x_2 \ 1] \cdot \begin{bmatrix} -a_1 \\ D(2 + a_1) \end{bmatrix} \quad [7.2.16]$$

If Equation [7.2.16] is expanded with a dataset of N terms and we solve using the least squares approach we obtain:

$$\begin{bmatrix} x_3 + x_1 \\ x_4 + x_2 \\ \vdots \\ x_N + x_{N-2} \end{bmatrix} = \begin{bmatrix} x_2 & 1 \\ x_3 & 1 \\ \vdots & \vdots \\ x_N & 1 \end{bmatrix} \cdot \begin{bmatrix} -a_1 \\ D(2 + a_1) \end{bmatrix} \quad [7.2.17]$$

$$\mathbf{b} = \mathbf{Xa} \quad [7.2.18]$$

$$\therefore \mathbf{a} = (\mathbf{X}^T \mathbf{X})^{-1} \mathbf{X}^T \mathbf{b} \quad [7.2.19]$$

Therefore for a single revolution with N probes the AR parameter a_1 and the offset D can be determined. From the AR parameter a_1 the natural frequency of vibration can be directly calculated

($a_1 = \omega_n^2$); the amplitude and phase of the solution form can then be determined by solving a simultaneous set of equations by making use of any two measured points of amplitude and time.

$$\begin{aligned} x_1 &= A \cdot \cos(\omega_n \cdot t_1) + B \cdot \sin(\omega_n \cdot t_1) + D \\ x_2 &= A \cdot \cos(\omega_n \cdot t_2) + B \cdot \sin(\omega_n \cdot t_2) + D \end{aligned} \quad [7.2.20]$$

There is unfortunately an inherent problem with this simple least squares approach; the issue is with severe biasing of the model to the noise in the experimental data (sometimes termed over-tuning). Noise in the system is inherently correlated in the $X^T X$ term in the solution of \mathbf{a} .

Various improvements to the simple AR method have been suggested and investigated. Consider the two degree of freedom system response and BTT sampling of that response is presented in Figure 7.2-4.

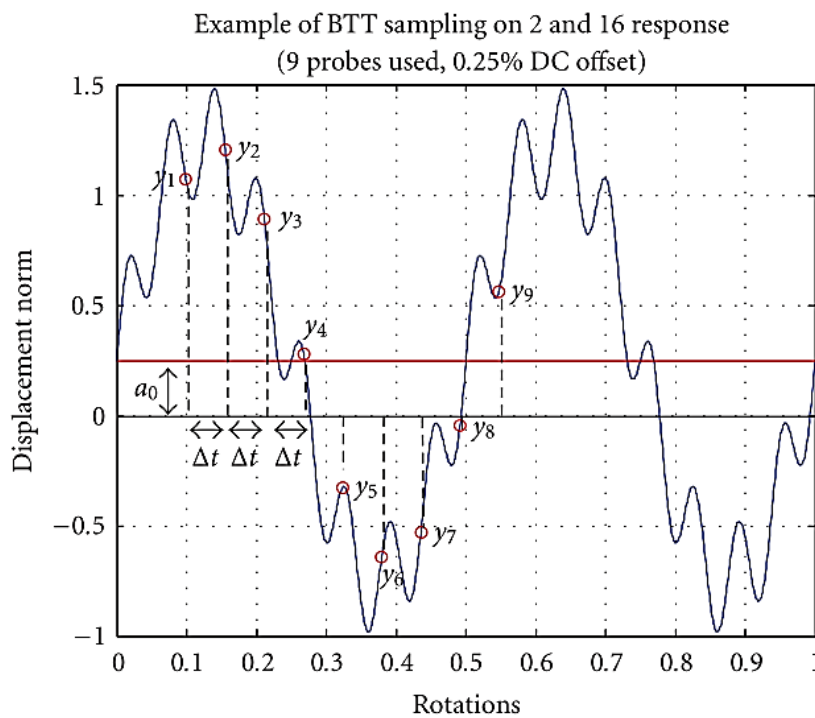


Figure 7.2-4 Example of a two DOF system (Gallego-Garrido et al., 2007b)

The improvements to the simple AR formulation were designed to overcome two limitation of AR. The first limitation is the poor fit that a SDOF model will provide to a response which may clearly require a higher order approach (as is the case seen in Figure 7.2-4). This improvement is provided by expanding the SDOF solution model to a multiple degree of freedom (MDOF) domain. This allows the model to better capture the true underlying physics of the response but requires the determination of more AR parameters (depending on the number of DOFs that the model is expanded to).

Gallego-Garrido et al. outlines two MDOF approaches; the first is termed the Prony methods and works on the assumption that the sample of data can be represented as the sum of damped exponentials; all of the AR parameters a_i are therefore assumed to be unknown (Gallego-Garrido et al., 2007a). The second MDOF family of methods is termed the exact methods; a solution form of sinusoidal motion with two harmonic components is assumed which then requires the determination of two unknown frequencies (and thus two unknown autoregressive parameters) (Gallego-Garrido et al., 2007a).

The second limitation to the AR methods is the inherent over tuning to noise in the measurements. The first improvement proposed to tackle this problem was termed global auto-regression (GAR); GAR works by solving for all blades response over all of the revolutions simultaneously and thus provides an average over the entire data set (Carrington et al., 2001). This improvement is limited by the computing power as it may become excessively expensive to solve over the entire data set of all blades simultaneously.

The second improvement suggested pre- and post-multiplying the observations matrix \mathbf{X} (see Eq. 21) with matrices which contain delayed observations. These matrices, \mathbf{X}_i , are termed instrumented variable (IV) matrices. The solution is therefore of the form:

$$\therefore \mathbf{a} = (\mathbf{X}_i^T \mathbf{X})^{-1} \mathbf{X}_i^T \mathbf{b} \quad [7.2.21]$$

The use of IV matrices avoids the inherent noise correlation with the $\mathbf{X}^T \mathbf{X}$ term in the original solution formulation.

The MDOF AR methods were compared by Gallego-Garrido et al. in a study in 2007 (Gallego-Garrido et al., 2007b). The methods were compared for a range of EOs with increasing levels of noise with simulated data. In order to simulate blade tip response data Gallego-Garrido et al. made use of a simple mathematical model where blades were simulated as cantilever beams with two bending modes of vibration; blades are coupled with springs and dampers. A four bladed example model is presented in Figure 7.2-5.

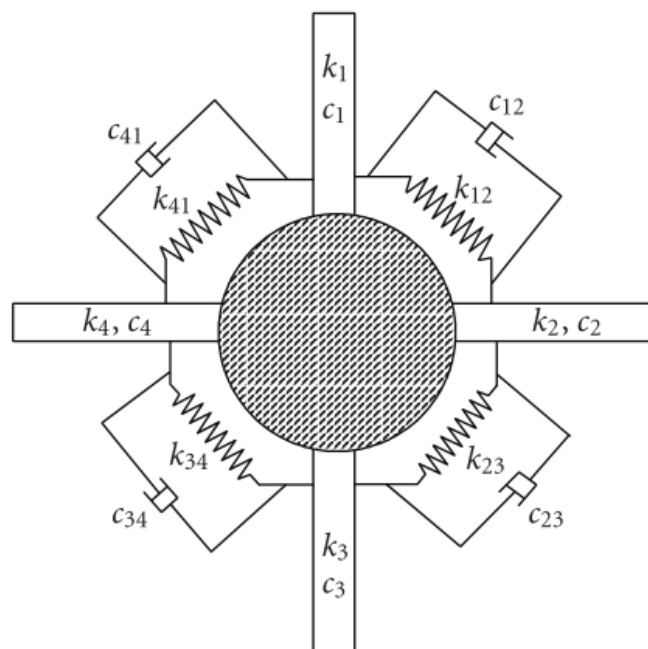


Figure 7.2-5 Four bladed disk model (Gallego-Garrido et al., 2007b)

The case of an actual EO of 6 is presented in Figure 7.2-6. The exact methods can be seen to perform very well up to extremely high noise levels. For this particular case the MDOF global AR method with instrumented variables (MGARIV) method performs the best out of all of the Prony based methods. A 95% confidence interval (CI) about the actual EO of 6, represented in grey, is also plotted. Response amplitudes were not reported in the study.

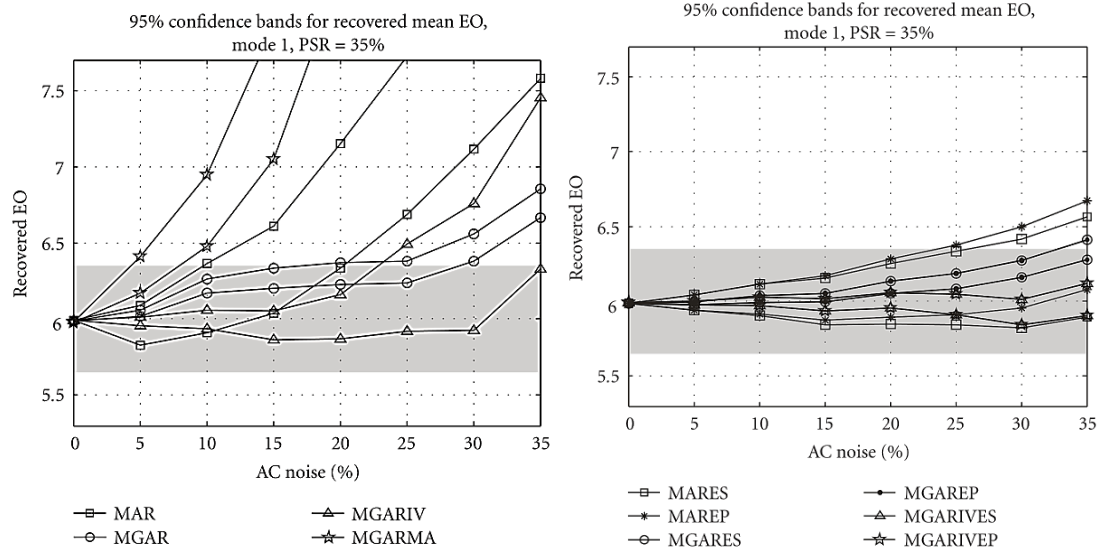


Figure 7.2-6 Comparison of MDOF AR methods for the determination of EO (Gallego-Garrido et al., 2007b)

The AR methods as a whole are very well documented with many publications investigating the accuracy and performance of the AR variants (Diamond et al., 2014b). Carrington et al. investigated the relative performance of the determinant method (DET), the SDOF global autoregressive method (GAR) and the SDOF global autoregressive method with instrument variables (GARIV); a numerical lumped spring mass damper model was used to simulate the blades response and interblade coupling effects (Carrington et al., 2001). Coupling effects refer to the situation where a blade no longer operates in isolation and must be viewed from an assembly level.

As was already stated the MDOF AR methods were compared by Gallego-Garrido et al. with a similar numerical model approach. Later Gallego-Garrido et al. experimentally compared two Prony based MDOF methods and two exact MDOF methods (Gallego-Garrido et al., 2007a). Grant experimentally compared the AR method with an indirect method developed by Heath (the two parameter plot method) (Grant, 2004; Heath, 2000). The overall results from these investigations found that the AR family of techniques were able to accurately infer the amplitude, frequency and phase of vibration (Diamond et al., 2014b).

7.2.2.2. Outline of Autoregressive Methods

A short summary of the AR improvement schemes from the first SDOF methods through to the more advanced MDOF methods is outlined below (Carrington et al., 2001; Gallego-Garrido et al., 2007b):

- SDOF methods:
 - GAR: Global AR
 - Solve for all blades and all revolutions simultaneously for a single a_1 and D parameter
 - Provides an average over the entire data set
 - GARIV: GAR with instrumental variables (IV)
 - Premultiply with IV matrix which contain delayed observations
 - $X_i \mathbf{b} = X_i \mathbf{X} \mathbf{a}$
 - $\therefore \mathbf{a} = (X_i^T X)^{-1} X_i^T \mathbf{b}$
 - Avoids inherent noise correlation within $X^T X$ term



- MDOF methods:
 - Prony based methods: Assumption that the sample of data can be represented as the sum of damped exponentials. All of the AR parameters a_i are therefore assumed to be unknown.
 - MAR: Multiple-frequency AR
 - Expand AR for a multiple-degree of freedom system with a chosen number of modes
 - An additional autoregressive parameter a_i is added for each additional mode
 - MGAR: Multiple-frequency GAR
 - Solve all revolutions simultaneously for all autoregressive parameters
 - MGARIV: Multiple-frequency GAR with IV
 - Decrease level of bias by avoiding inherent noise correlations
 - MGARMA: MGAR with Moving Average
 - Assume that white noise is an input into the system
 - White noise treated as random entries with a zero mean normal distribution and unit variance
 - Exact methods: Assume a solution form of sinusoidal motion with two harmonic components. There are therefore only two unknown frequencies (a_1 =unknown, $a_3=a_1$ and a_4 =unknown)
 - ES: Exact (E) with purely sinusoidal (S) assumption
 - MARES
 - MGARES
 - MGARIVES
 - EP: Exact solution (E) using Prony's method (P)
 - MAREP
 - MGAREP
 - MGARIVEP

7.2.3. B3 – Circumferential Fourier Fit

The circumferential Fourier fit (CFF) method assumes a SDOF blade response solution; it uses an order tracking approach to estimate the amplitude, phase and DC offset of vibration (Diamond et al., 2014b; Joung et al., 2006). The method is limited in that it requires the frequency of vibration to be provided (Diamond et al., 2014b).

In order to perform the CFF a minimum of three sensors are required to obtain the three unknowns of amplitude, phase and DC offset. For the case of synchronous excitation of a weakly coupled system individual blades oscillate with harmonics of EO (Joung et al., 2006). It is important to note that the CFF algorithm does not calculate the response frequency (EO); it must be supplied with it. A least squares approach is then used to determine the unknown parameters. The CFF equation to be solved is presented below.

$$\begin{pmatrix} \delta_1 \\ \delta_2 \\ \delta_3 \\ \delta_4 \end{pmatrix} = \begin{bmatrix} 1 & \sin(EO \cdot \theta_1) & \cos(EO \cdot \theta_1) \\ 1 & \sin(EO \cdot \theta_2) & \cos(EO \cdot \theta_2) \\ 1 & \sin(EO \cdot \theta_3) & \cos(EO \cdot \theta_3) \\ 1 & \sin(EO \cdot \theta_4) & \cos(EO \cdot \theta_4) \end{bmatrix} \begin{pmatrix} DC \\ A \cdot \cos(EO \cdot \phi) \\ A \cdot \sin(EO \cdot \phi) \end{pmatrix} \quad [7.2.22]$$

$$(\delta) = [M](p) \quad [7.2.23]$$

The parameters DC, A and ϕ represent the dc offset, amplitude of the response and the phase angle respectively. The parameter θ is the same as above, namely the circumferential angle of each sensor. An example of a CFF is shown in Figure 7.2-7 for the case of four data points from four sensors.

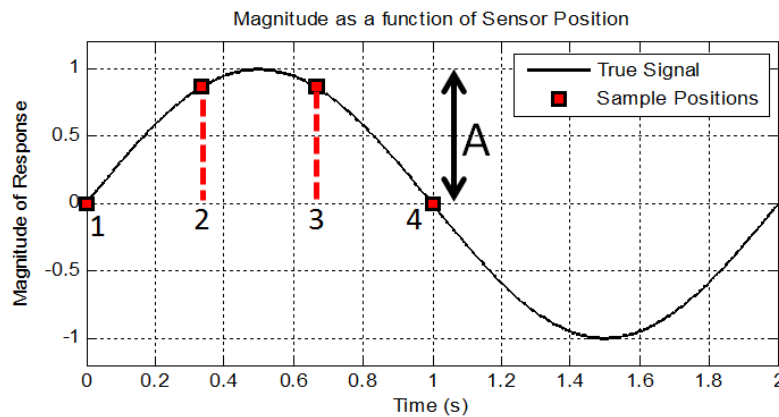


Figure 7.2-7 Magnitude as a function of sensor position (adapted from (Joung et al., 2006))

The positions of the sensors can be optimised if the EO of the vibrating system is known. A good circumferential spacing of sensors results in a large condition number for the matrix \mathbf{M} (Joung et al., 2006). Large spacing of sensors however causes the measured data to be sensitive to whole rotor whirl and unbalance and so a trade-off must be found (Joung et al., 2006).

7.2.4. B4 – Bayesian Curve Fitting

In order to overcome the curve fitting issues associated with AR, Diamond proposed using a different curve fitting technique altogether; he suggested use of a Bayesian linear regression methodology (Diamond et al., 2014a). Similar to the basic AR approaches the Diamond method first assumes a SDOF model for the blade vibration (Diamond et al., 2014a):

$$x_i(t) = A \cdot \cos(\omega \cdot t_i) + B \cdot \sin(\omega \cdot t_i) + C \quad [7.2.24]$$

The index 'i' refers to a specific blade displacement and TOA measurement within a set of N measurements. The model parameters A, B and C are then calculated from a standard Bayesian linear regression formulation.

Before Bayesian linear regression can be defined for fitting the sinusoid, consider the general form of linear regression where the model is a linear combination of non-linear functions of the input variables (Bishop, 2009):

$$y(\mathbf{x}, \mathbf{w}) = w_0 + \sum_{j=1}^{M-1} w_j \cdot \phi_j(\mathbf{x}) \quad [7.2.25]$$



Adjustable target parameters \mathbf{w} , or design variables, are the target outputs of a regression optimisation. These are the parameters which are to be fitted with observations (sometimes called training variables). The non-linear functions ϕ_j are termed basis functions. The total number of parameters to be fitted are M where the parameter w_0 provides a fixed offset and is sometimes called the bias parameter (Bishop, 2009). By allowing ϕ_0 to be unity ($\phi_0(\mathbf{x}) = 1$) equation 25 can be rewritten into a more convenient form.

$$y(\mathbf{x}, \mathbf{w}) = \sum_{j=0}^{M-1} w_j \cdot \phi_j(\mathbf{x}) = \mathbf{w}^T \Phi(\mathbf{x}) \quad [7.2.26]$$

The matrix Φ is termed the design matrix and forces the linear combination of non-linear functions of the observations \mathbf{x} . A commonly used linear regression model is the polynomial; consider the cubic polynomial regression model below.

$$y(\mathbf{x}, \mathbf{w}) = w_0 \cdot 1 + w_1 \cdot x^1 + w_2 \cdot x^2 + w_3 \cdot x^3 \quad [7.2.27]$$

$$\mathbf{w} = [w_0 \ w_1 \ w_2 \ w_3]^T \quad [7.2.28]$$

$$\Phi = \begin{bmatrix} \phi_0(\mathbf{x}_1) & \phi_1(\mathbf{x}_1) & \cdots & \phi_{M-1}(\mathbf{x}_1) \\ \phi_0(\mathbf{x}_2) & \phi_1(\mathbf{x}_2) & \cdots & \phi_{M-1}(\mathbf{x}_2) \\ \vdots & \vdots & \ddots & \vdots \\ \phi_0(\mathbf{x}_N) & \phi_1(\mathbf{x}_N) & \cdots & \phi_{M-1}(\mathbf{x}_N) \end{bmatrix} \quad [7.2.29]$$

$$\therefore \Phi = \begin{bmatrix} 1 & (\mathbf{x}_1)^1 & (\mathbf{x}_1)^2 & (\mathbf{x}_1)^3 \\ 1 & (\mathbf{x}_2)^1 & (\mathbf{x}_2)^2 & (\mathbf{x}_2)^3 \\ \vdots & \vdots & \vdots & \vdots \\ 1 & (\mathbf{x}_N)^1 & (\mathbf{x}_N)^2 & (\mathbf{x}_N)^3 \end{bmatrix} \quad [7.2.30]$$

Since there is a presupposition of the solution form being a linear combination of sinusoids the same process can be performed for the SDOF sinusoidal model.

$$x_i(t, \mathbf{w}) = A \cdot \cos(\omega \cdot t_i) + B \cdot \sin(\omega \cdot t_i) + C \quad [7.2.31]$$

$$\mathbf{w} = [A \ B \ C]^T \quad [7.2.32]$$

$$\therefore \Phi = \begin{bmatrix} \cos(\omega t_1) & \sin(\omega t_1) & 1 \\ \vdots & \vdots & \vdots \\ \cos(\omega t_N) & \sin(\omega t_N) & 1 \end{bmatrix} \quad [7.2.33]$$

Now that the regression model has been defined it would be useful to take a closer look at the mechanics behind Bayesian linear regression, namely Bayes' theorem (Bishop, 2009).

$$p(\mathbf{w}|D) = \frac{p(D|\mathbf{w}) \cdot p(\mathbf{w})}{p(D)} \quad [7.2.34]$$

Where \mathbf{w} are design variables and D is observed data

Bayes theorem states that the posterior distribution $p(\mathbf{w}|D)$, or the likelihood of the design variables \mathbf{w} given the observed data D , is proportional to the likelihood of the observed data D given the design

variables \mathbf{w} multiplied by a prior assumption of the form of \mathbf{w} (Bishop, 2009). The denominator $p(D)$ is a normalisation constant which ensures that the posterior distribution is valid and integrates to unity (the area under a distribution must integrate to one in order to be valid) (Bishop, 2009). In simple terms, Bayes' theorem states:

$$posterior \propto likelihood \cdot prior \quad [7.2.35]$$

Bayes theorem allows prior assumptions of the solution form to have an influence on the solution. Next it is important to define the Gaussian, or normal, distribution with mean μ and variance σ^2 . The underlying probability density functions are assumed to be Gaussian in nature.

$$\mathcal{N}(x|\mu, \sigma^2) = \frac{1}{(2\pi\sigma^2)^{0.5}} \cdot \exp\left(-\frac{1}{2\sigma^2}(x - \mu)^2\right) \quad [7.2.36]$$

In order to get an expression for the posterior distribution we first define the prior distribution of the weights having a mean of \mathbf{m}_0 and a covariance of \mathbf{S}_0 .

$$p(\mathbf{w}) = \mathcal{N}(\mathbf{w}|\mathbf{m}_0, \mathbf{S}_0) \quad [7.2.37]$$

The likelihood function, or the probability of the observations \mathbf{t} given inputs \mathbf{X} , adjustable weights \mathbf{w} and precision β (inverse of the variance) is given by (Bishop, 2009):

$$p(\mathbf{t}|\mathbf{X}, \mathbf{w}, \beta) = \prod_{n=1}^N \mathcal{N}(t_n|\mathbf{w}^T \boldsymbol{\phi}(x_n), \beta^{-1}) \quad [7.2.38]$$

Due to the choice of Gaussian prior and likelihood the posterior distribution will also be Gaussian (Bishop, 2009). The posterior distribution is therefore:

$$p(\mathbf{w}|\mathbf{t}) = \mathcal{N}(\mathbf{w}|\mathbf{m}_N, \mathbf{S}_N) \quad [7.2.39]$$

$$\mathbf{m}_N = \mathbf{S}_N(\mathbf{S}_0^{-1}\mathbf{m}_0 + \beta\boldsymbol{\Phi}^T\mathbf{t}) \quad [7.2.40]$$

$$\mathbf{S}_N^{-1} = \mathbf{S}_0^{-1} + \beta\boldsymbol{\Phi}^T\boldsymbol{\Phi} \quad [7.2.41]$$

No prior information is assumed to be known about the design parameters. Therefore a zero mean non-informative prior is chosen. The prior covariance and mean are therefore:

$$\mathbf{m}_0 = \mathbf{0} \quad [7.2.42]$$

$$\mathbf{S}_0 = \alpha^{-1}\mathbf{I} \quad [7.2.43]$$

The parameter α is also termed a precision parameter; it controls the confidence in the prior guess of \mathbf{w} . After substituting the prior mean and covariance into equations 40 and 41 the results of the problem formulation becomes (Diamond et al., 2014a):

$$\mathbf{w} = \mathbf{m}_N = \beta\mathbf{S}_N\boldsymbol{\Phi}^T\mathbf{t} \quad [7.2.44]$$

$$\mathbf{w} = [A \ B \ C]^T \quad [7.2.45]$$

$$S_N^{-1} = \alpha I + \beta \Phi^T \Phi \quad [7.2.46]$$

$$\Phi = \begin{bmatrix} \cos(\omega t_1) & \sin(\omega t_1) & 1 \\ \vdots & \vdots & \vdots \\ \cos(\omega t_N) & \sin(\omega t_N) & 1 \end{bmatrix} \quad [7.2.47]$$

In this specific implementation of Bayesian linear regression the prior guess has been chosen to be uninformative. The parameter α is therefore chosen to be very small as little confidence is placed in the prior knowledge. Conversely the parameter β assumes a large value as little tolerance to noise will be allowed.

It is clear from the formulation of the problem that no constraints are placed on the positioning of the BTT probes; this is the case with the AR formulation which requires probes to be spaced equidistant apart. It was reported that the Diamond algorithm performs best when the probes are placed at arbitrary irregular intervals from one another (Diamond et al., 2014a). No explanation for this phenomenon was however offered.

It is in the author’s opinion that by forcing the probes to be equidistant apart translates to allowing the angular positions of the probes to be integer multiples of one another. Therefore probe three may measure a TOA that is $2 \cdot \Delta t$ away from probe one. The vibration is synchronous so therefore it is conceivable that the second measurement will capture an amplitude value which is close to another measurement and thus provides little additional information to the problem. The situation is illustrated in Figure 7.2-8.

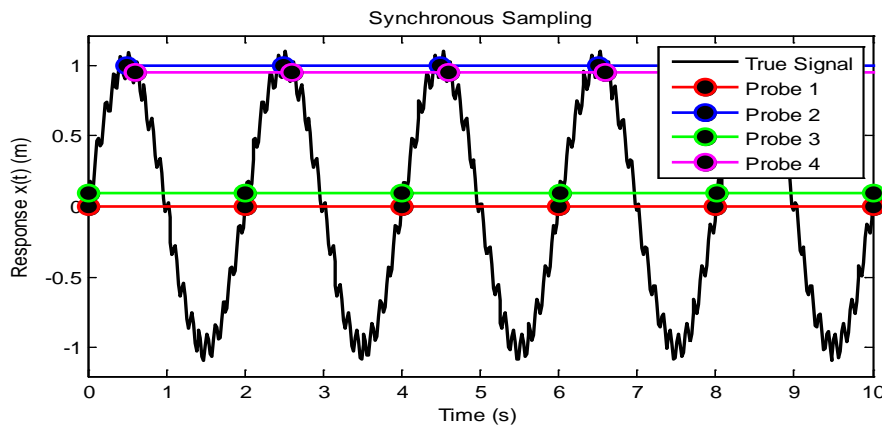


Figure 7.2-8 Synchronous sampling with limited informative sampling

The fundamental difference between the Diamond method and the AR methods is found in the next step of Diamond’s formulation (Diamond et al., 2014a). Instead of calculating the vibration frequencies from the measurements, a range of EOs (and thus vibration frequencies) are supplied to the algorithm. For each EO supplied the probability that it fits the measurements is then determined (along with variance about the probability). The most probable EO is then chosen from the set of EOs supplied to the algorithm.

The probability and standard deviation for each choice of EO are given by (Diamond et al., 2014a):

$$p(w) \propto \Pi N(\mu, \sigma^2) = \Pi_{i=1}^N N(t_i | x(t_i), \sigma^2(t_i)) \quad [7.2.48]$$

$$\sigma^2(t_i) = \frac{1}{\beta} + [\cos(\omega t_i) \quad \sin(\omega t_i) \quad 1] \mathbf{S}_N \begin{bmatrix} \cos(\omega t_i) \\ \sin(\omega t_i) \\ 1 \end{bmatrix} \quad [7.2.49]$$

An example of the Diamond implementation is presented in Figure 7.2-9. The underlying frequency of vibration was chosen to have an actual EO of 24. A signal to noise ratio (SNR) was set to 10%. EO integers ranging from 0 to 50 were evaluated; the EO with the highest probability of occurring was determined to be the true EO of 24. Other EOs of high probability were 18, 22, 19 and 3; Diamond prescribes their high probabilities to the sub-sampled nature of the measured TOAs (Diamond et al., 2014a).

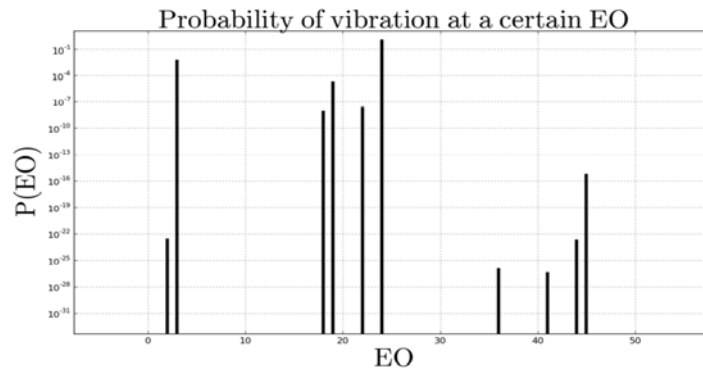


Figure 7.2-9 Example of Diamond method (Diamond et al., 2014a)

During his investigation Diamond compared his new method to the simplest of the AR methods; his method was found to be far superior in determining both the EO and the amplitude of vibration. The method used to generate the tip response was however not discussed.

In a later study Diamond compared his method's ability to infer the correct amplitude of vibration to both AR and CFF. The tip response, as a function of time, was generated with the use of a one fifth FE model of a bladed disk (generally referred to as a blisk). The blade was excited using periodic impulse forces in order to simulate the effects of stator vanes (Diamond et al., 2014b). The FE model and response of the blade, both in the time domain and the frequency domain, is presented in Figure 7.2-10.

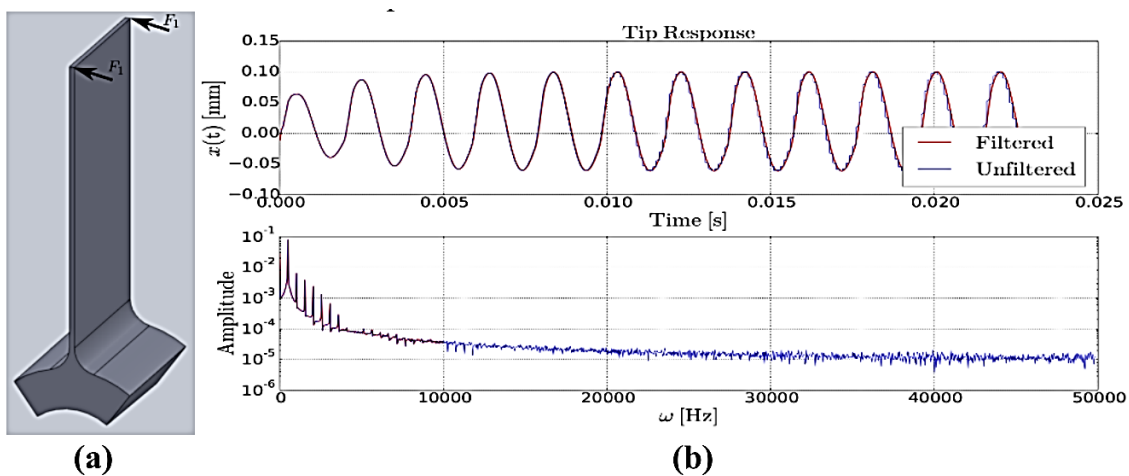


Figure 7.2-10 One fifth FE model with tip time and frequency response. (a) CAD drawing of one fifth model. (b) Simulated time and frequency responses. (Diamond et al., 2014b)

It is important to note that the response elicited is that of a SDOF system; only a single blade was modelled and so no inter-blade coupling effects could be generated. Secondly only the first bending mode of the blade was excited which supplies a near perfect sinusoid. One of the result sets from the study is presented in Figure 7.2-11.

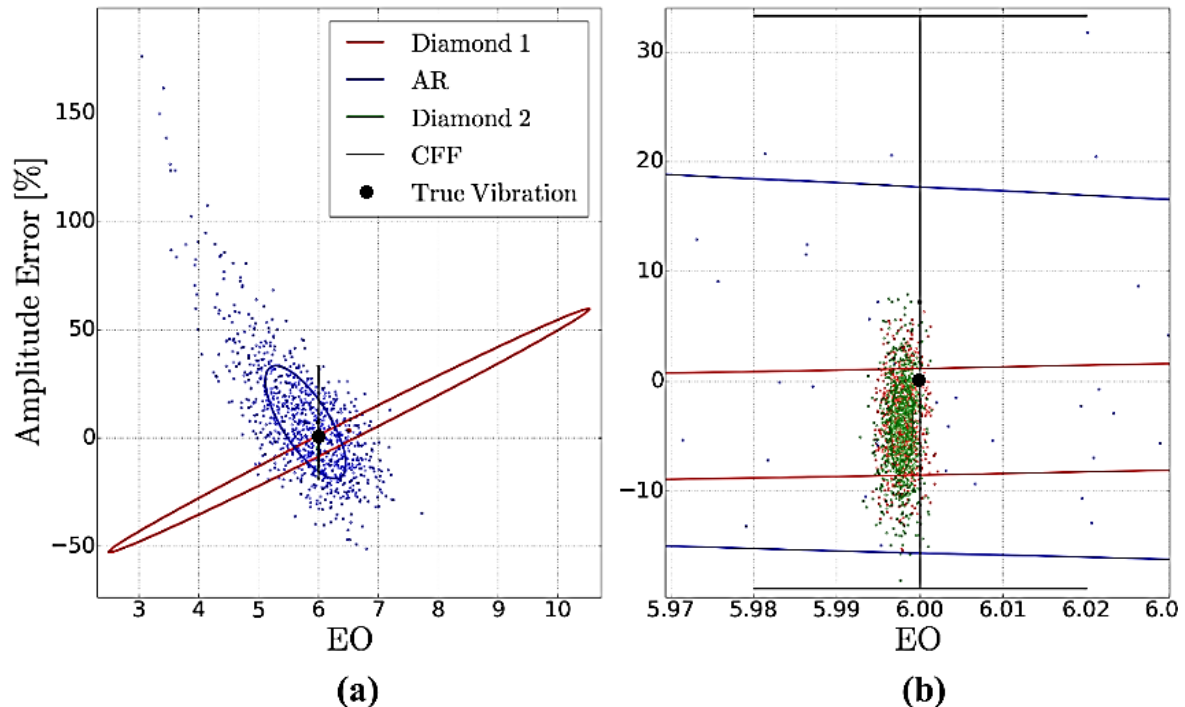


Figure 7.2-11 Amplitude errors for various BTT methods. *Figure (b) is an enlarged version of Figure (a).* (Diamond et al., 2014b)

The Diamond method was able to very closely infer the actual response amplitude (along with the frequency of vibration reported as an EO); the standard deviation of the amplitude error for the Diamond 2 method ranged between -2% and -8%. The CFF method was able to infer the correct amplitude of vibration within a standard deviation of -20% to 30% (Diamond et al., 2014b). This is highly significant as the Diamond method inferred both the response amplitude and frequency from the BTT measurements whereas the CFF was supplied with the correct frequency of vibration and was still unable to achieve the same level of accuracy of the Diamond method.

7.3. Appendix C – Example Application of CPS Method

The experimental setup, developed by Forbes for the purpose of investigating internal pressure signals containing blade vibration information, is given in Figure 7.3-1. Approximation of stator vane excitation of the turbine blades was achieved by high pressure air nozzles directed towards the turbine blades. A nozzle as well as the sensor mounting point are indicated in the figure.

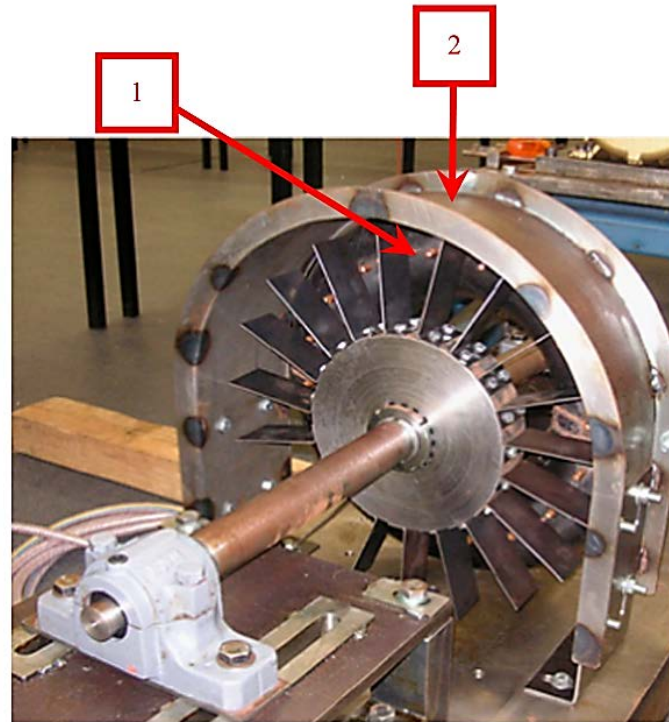


Figure 7.3-1 CPS experimental setup. (1) Air jets. (2) Accelerometer and microphone mounting position. (Forbes and Randall, 2013)

The test rig comprises of a 19 flat blade arrangement contained within the casing (Forbes and Randall, 2013). A total of 6 high pressure air jets were used to excite the blades during operation (Forbes and Randall, 2013). The configuration was such that air excitation could be turned on and off at will.

The casing vibration and the internal pressure signal were measured by means of an accelerometer and sound pressure transducer respectively (Forbes and Randall, 2013).

Two test rig configurations were considered. Configuration 1 consisted of 19 identical blades and configuration 2 consisted of 18 identical blades and one 'flawed' blade. The dimensions of the 19 identical 'healthy' blades were 100mm x 50mm x 1.2mm (length by width by thickness). The faulty blade had a reduced thickness of 0.9 mm (Forbes and Randall, 2013).

The natural frequencies of the blades were determined using a stationary test bench and are given in Table 7.3-1 (Forbes and Randall, 2013).

Table 7.3-1 First two bending natural frequencies from stationary bench test (Forbes and Randall, 2013)

Nominal Blade Thickness →	1.2 mm	0.9 mm
Mode excited ↓		
1 st Bending mode natural frequency (Hz)	117.4	69
2 nd Bending mode natural frequency (Hz)	726	432

The natural frequencies for the ‘healthy’ blades was determined by averaging the stationary test bench results over all blades. The analytically and experimentally derived ensemble averages for operation at 1200 RPM (for the ‘healthy’ blade arrangement) is presented in Figure 7.3-2. It is important to note that the experimentally obtained results are for operation with air excitation present.

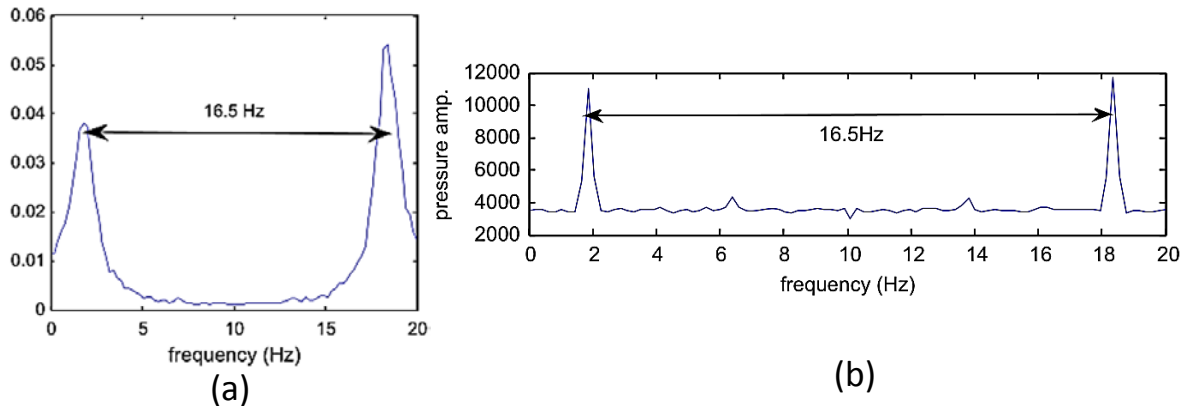


Figure 7.3-2 Narrow band peak spacing for operating at 1200 RPM. (a) Analytically derived NBPS. (b) Experimentally derived NBPS. (Forbes and Randall, 2013)

The blades’ natural frequencies can be estimated by measuring the NBPS. The difference frequency is given by Equation [7.3.1] (Forbes and Randall, 2013).

$$NBPS = (k \cdot \Omega + f_{blade}) - (m \cdot \Omega - f_{blade}) \quad [7.3.1]$$

The equation can be rearranged to make the natural frequency the subject of the formula.

$$f_{blade} = \frac{NBPS + (m - k) \cdot \Omega}{2} = \frac{NBPS + q \cdot \Omega}{2} \quad [7.3.2]$$

The parameters k , m and q are positive integers, k is less than m and the $NBPS$ and Ω are given in hertz.

In order to estimate the natural frequency of a blade in a turbine operating at 1200 RPM (20 Hz) (with the measured NBPS from the analytical model of 16.5 Hz) the value for the integer ‘ q ’ must first be determined. In order to estimate ‘ q ’ the blade’s natural frequency must be known within ± 0.5 the rotor operating frequency. The statically determined second bending natural frequency of 726 Hz is used for this purpose (Forbes and Randall, 2013).

$$q = \text{ceil}\left(\frac{2 \cdot f_{blade} - NBPS}{\Omega}\right) = \text{ceil}\left(\frac{2 \cdot 726 - 16.5}{20}\right) = \text{ceil}(71.775) = 72 \quad [7.3.3]$$

In the expression the ceil function rounds up to the nearest integer.

The value for q is rounded upward with the ‘ceil’ function because the expected natural frequency of the rotating system is higher than that of a non-rotating system due to centrifugal stiffening (Forbes and Randall, 2013). Thus the estimated natural frequency of the rotating blade is:

$$f_{blade} = \frac{16.5 + 72 \cdot 20}{2} = 725.25 \text{ Hz} \quad [7.3.4]$$

The motive behind using the second bending natural frequency for analysis (as opposed to the fundamental frequency) is not provided in the source material (Forbes and Randall, 2013).

Tests were performed to investigate if narrow band peaks would form under the condition of no air excitation. The ensemble averaged derived for operation of the healthy configuration at 2000 RPM with no air excitation is provided in Figure 7.3-3.

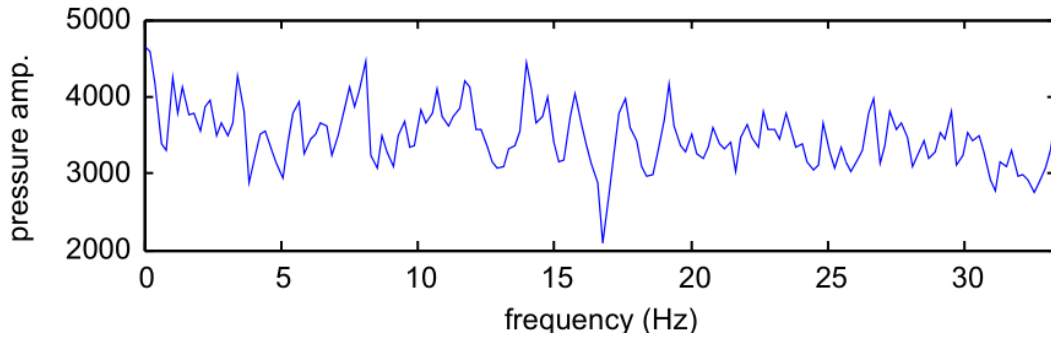


Figure 7.3-3 Experimentally obtained ensemble average for operation at 2000 ROM with no air excitation (Forbes and Randall, 2013)

It is clear from the figure that there is no significant appearance of narrow band peaks. The experimentally obtained ensemble average results for operation at 2000 RPM for the ‘healthy’ and ‘unhealthy’ configurations are illustrated in and.

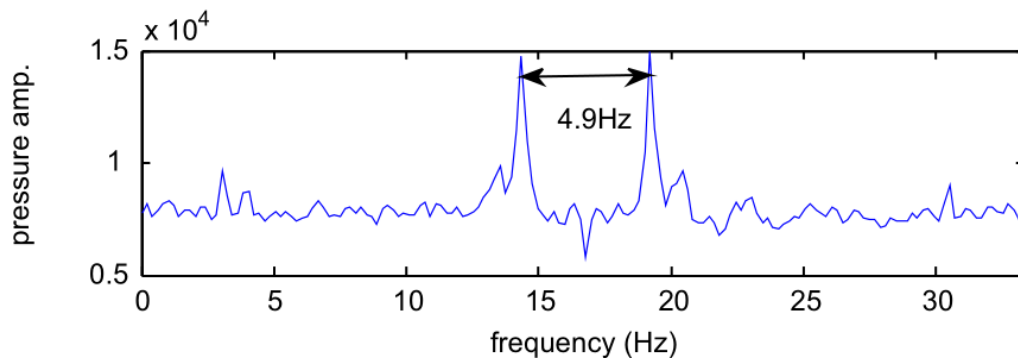


Figure 7.3-4 Experimentally obtained ensemble average for healthy configuration operating at 2000 ROM with air excitation(Forbes and Randall, 2013)

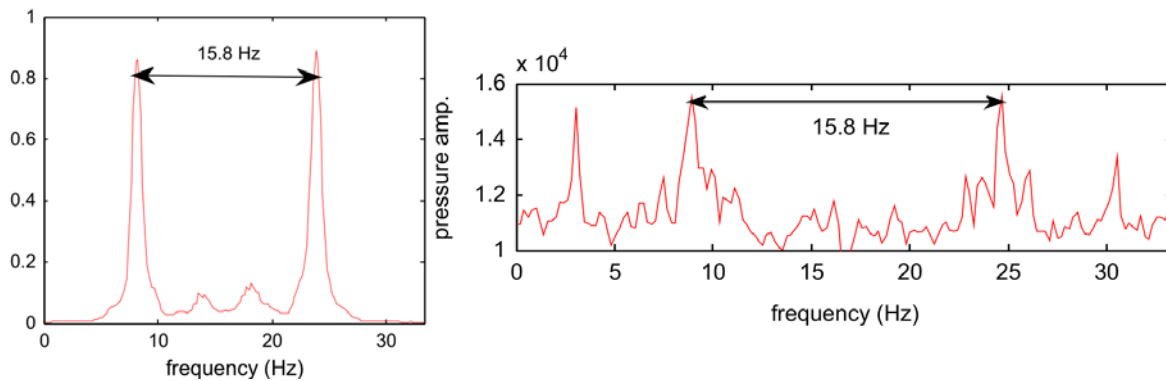


Figure 7.3-5 Analytically (a) and experimentally (b) obtained ensemble average for unhealthy configuration operating at 2000 ROM with air excitation (Forbes and Randall, 2013)

A portion of the experimental measurement recordings were made available online for further analysis. Specifically the set obtained at the 2000 RPM operating speed for both the healthy and unhealthy configurations as well as for the presence and absence air excitation. The signal processing and ensemble averaging procedures outlined in the literature review were followed independently in order to confirm the above results. An overlay of a portion of the time domain results for the case of no air excitation, divided into the stochastic and deterministic parts, is provided in Figure 7.3-6.

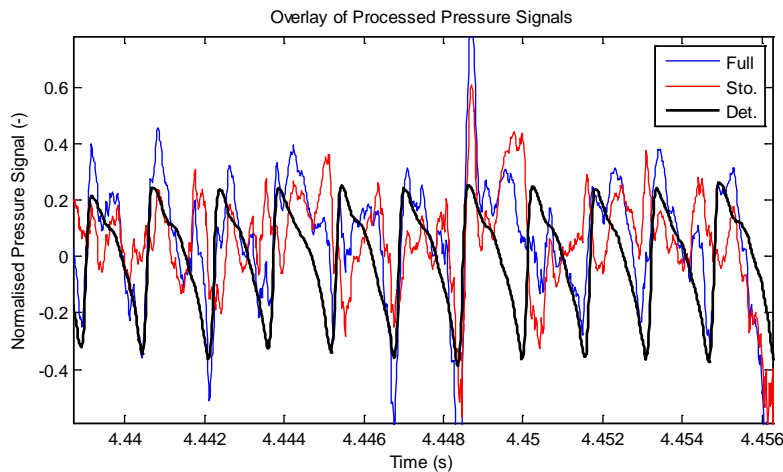


Figure 7.3-6 Portion of time domain signal processed pressure data for healthy configuration without air excitation

The ensemble average determined for the case of no air excitation can be seen in Figure 7.3-7.

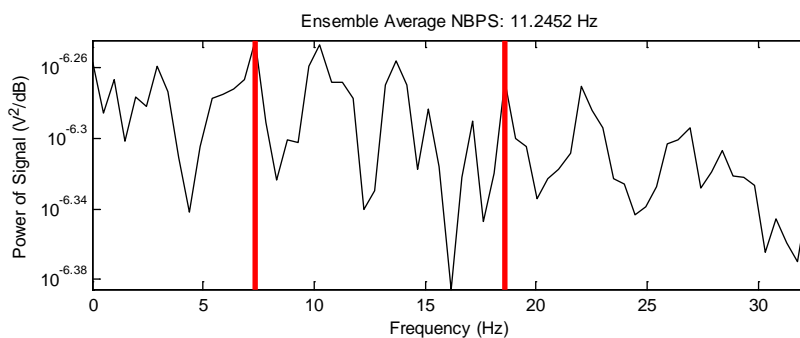


Figure 7.3-7 Independently obtained ensemble average for healthy configuration without air excitation

Similarly the results obtained for the healthy and unhealthy configurations, operating at 2000 RPM, are provided in Figure 7.3-8 and Figure 7.3-9 respectively.

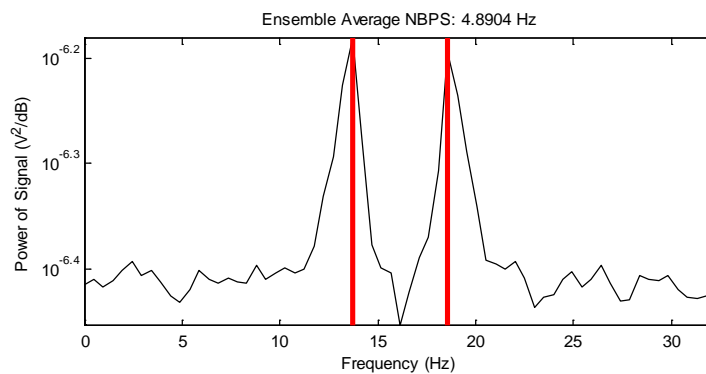


Figure 7.3-8 Independently obtained ensemble average for healthy system with air excitation

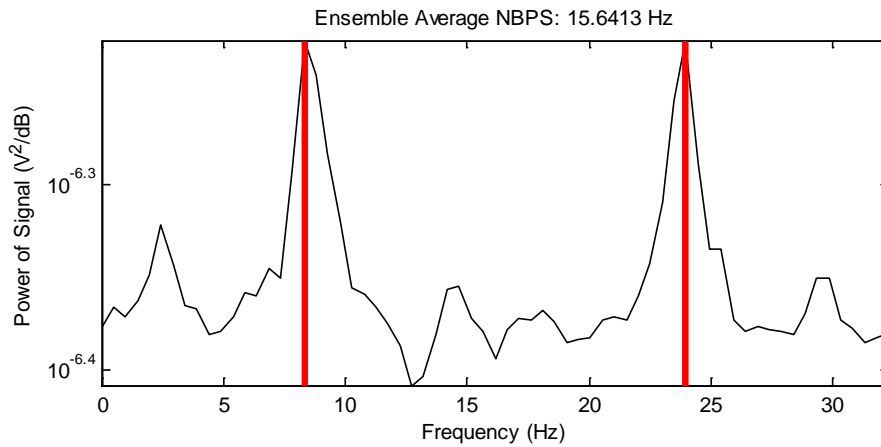


Figure 7.3-9 Independently obtained ensemble average for unhealthy system with air excitation

A summary of the ensemble average results is provided in Table 7.3-2.

Table 7.3-2 Summary of ensemble average results

Simulation	Analytical NBPS (Hz)	Experimentally derived NBPS (Hz)	Independently Derived NBPS (Hz)
2000 RPM no air no fault	N/A	None	None
2000 RPM air no fault	4.9	4.9	4.89
2000 RPM air fault	15.8	15.8	15.64

The blade natural frequency estimation method outlined above was independently performed on all of the ensemble average results; a summary is provided in Table 7.3-3.

Table 7.3-3 Summary of estimated blade natural frequencies

Simulation	Analytical Blade Natural Frequency (Hz)	Experimental Blade Natural Frequency (Hz)	Independently Derived Blade Natural Frequency (Hz)
2000 RPM no air no fault	N/A	None	None
2000 RPM air no fault	733	733	735.0463
2000 RPM air fault	441.5	441.5	457.3714

A counting scheme was employed to determine the average number of time based deterministic peaks occur per revolution. The results are summarised in Table 7.3-4.

Table 7.3-4 Average number of deterministic peaks per revolution

Recording	Average peaks per revolution
2000 RPM no air no fault	19.000
2000 RPM air no fault	19.003
2000 RPM air fault	18.000

The counting scheme was implemented to ascertain whether or not the deterministic part of the pressure signal could be used for BTT. An example of a section of the deterministic pressure signal over one revolution is given in Figure 7.2-10. The once per revolution (OPR) counter is also shown.

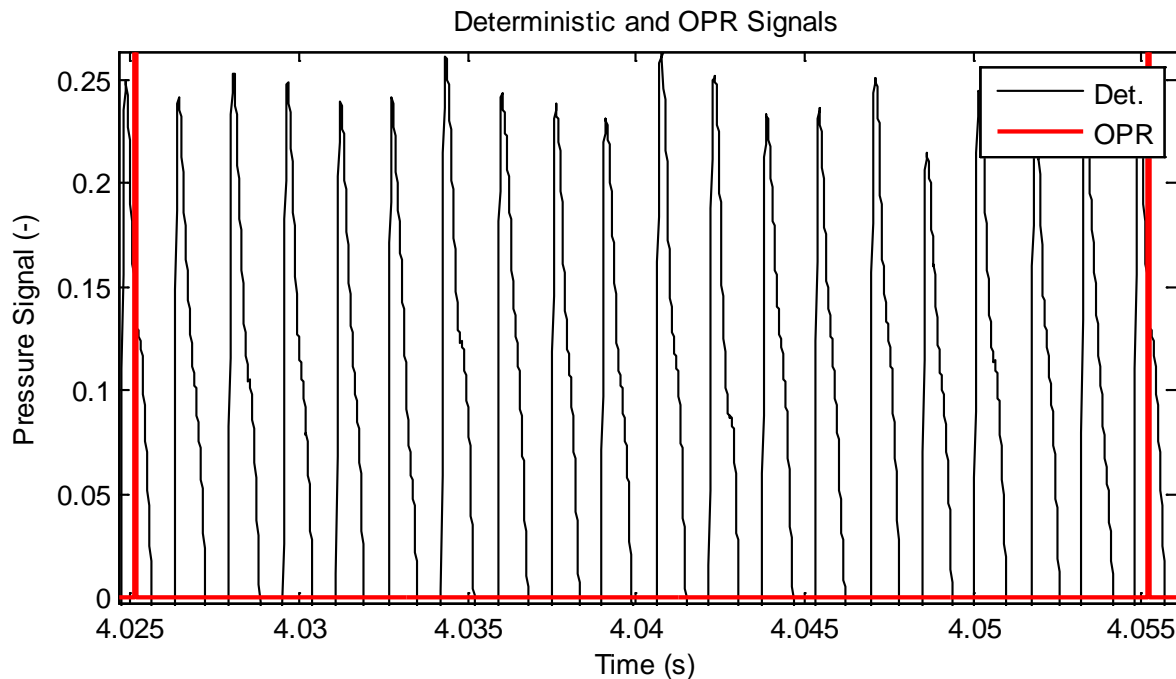


Figure 7.3-10 Deterministic pressure signal for healthy configuration with air excitation

It is interesting to note that the counting scheme 'misses' one blade every revolution for the unhealthy configuration (where one 'healthy' blade is replaced with a thinner 'faulty' blade). For the case where no high pressure air excitation existed as well as for the healthy blade configuration 19 blades were counted per revolution. For the faulty configuration only 18 blades were counted.

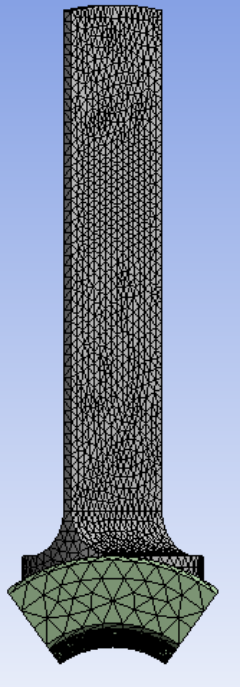
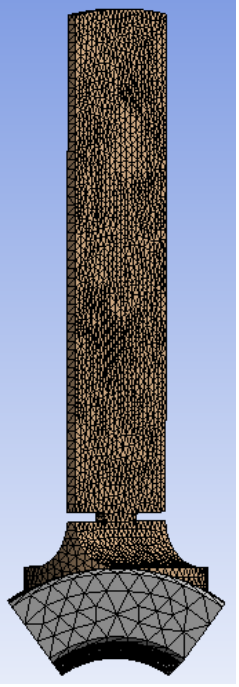
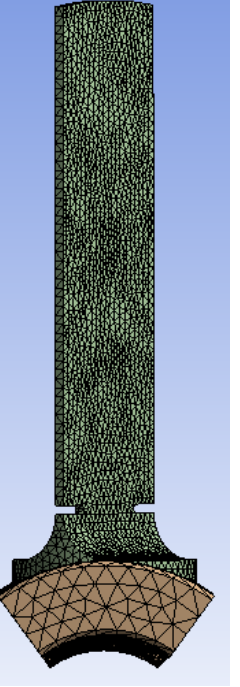
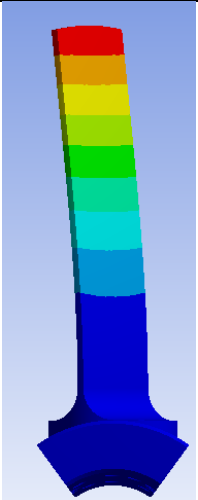
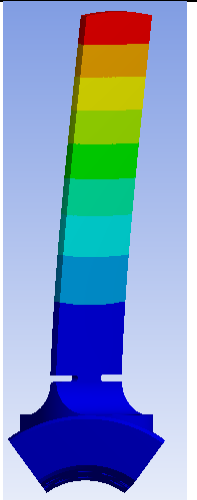
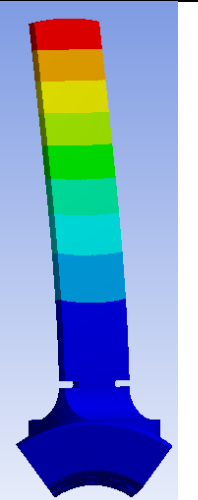
Through independent signal processing of the basis measurements similar NBPS values were obtained. This resulted in similar estimations of the blade natural frequencies to the source findings. It is interesting to note that once the deterministic portion of the signal was separated from the combined full signal the same number of peaks as blades form. Therefore it may be possible to collect blade tip times of arrival using the internal pressure signal given the experimental methodology and equipment used in the source investigation.

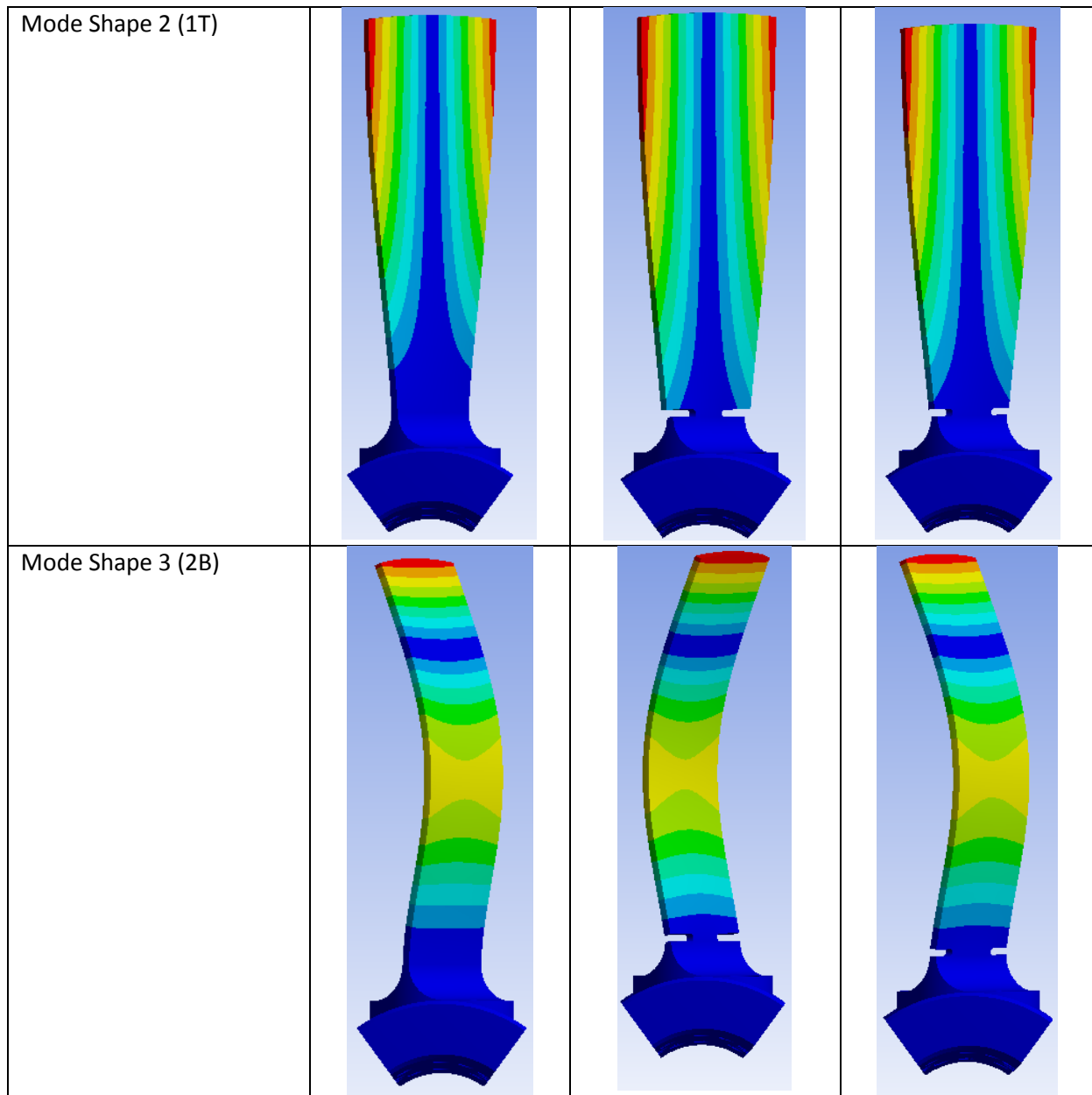
7.4. Appendix D – FE Analyses

7.4.1. D1 – FE Analysis Configuration

7.4.1.1. Fifth Model

A fifth cyclic symmetric model was created for the various blade geometries in order to analytically determine mode shapes and natural frequencies. Element sizes were reduced until a negligible change in the fundamental frequency was found.

Category		Healthy Blade	Damaged Blade 1	Damaged Blade 2
Geometry and Mesh				
Model statistics	Bodies	4	4	4
	Nodes	28622	49406	47366
	Elements	16033	29344	27965
Natural frequencies (Hz)	Mode 1	127.08	105.22	116.40
	Mode 2	733.55	620.08	676.96
	Mode 3	791.15	707.18	744.43
Mode Shape 1 (1B)				



Bonded contact was chosen between all of the bodies in each investigation (portion of hub, 2 screws and the blade). A fixed support was applied to the inner surface of the hub that would have been in contact with the rotating shaft. A cyclic symmetry condition was applied to all of the fifth models. No harmonic modes were reported on.

A generic aluminium alloy linear elastic material model was chosen for the investigation. The material properties used are presented in Table 7.4-1.

Table 7.4-1 FE analysis material properties

Property	Value
Density	2770 kg/m ³
Young's modulus	70 GPa
Poisson's ratio	0.33

7.4.2. D2 - Analytical Investigation for Strain Gauge Position Choice

Table 7.4-2 provides the results of a FE investigation to determine improved SG application loci for the 'healthy blade'. The same model considerations as the preceding section were maintained.

Table 7.4-2 Mode shapes and strain distributions for strain gauge choice on healthy blade

Mode	Strain and scale (m/m)	X-Y Strain	Y-Z Strain	Vector Principal
1 (1B)	Maximum Principal 			
2 (1T)	Elastic Shear 			
3 (2B)	Maximum Principal 			

7.4.3. D3 – Strain Gauge Positioning for Healthy Blade

A modal finite element (FE) analysis was performed in order to better position the SG application loci. Improved sensitivity to modes 1 through 3 were sought for the healthy blade. Modes 1 through 3 refer to flap bending mode 1, torsional mode 1 and flap bending mode 2 respectively. The results of this FE analysis are presented in '7.4.2 D2 - Analytical Investigation for Strain Gauge Position Choice'.

Figure 7.4-1 illustrates the strain gauge position choices for the healthy blade geometry derived from the FE analysis and the SG relative sizes. All SGs used were coupled as full bridges, therefore the strain gauge positions are mirrored on both sides of the blade.

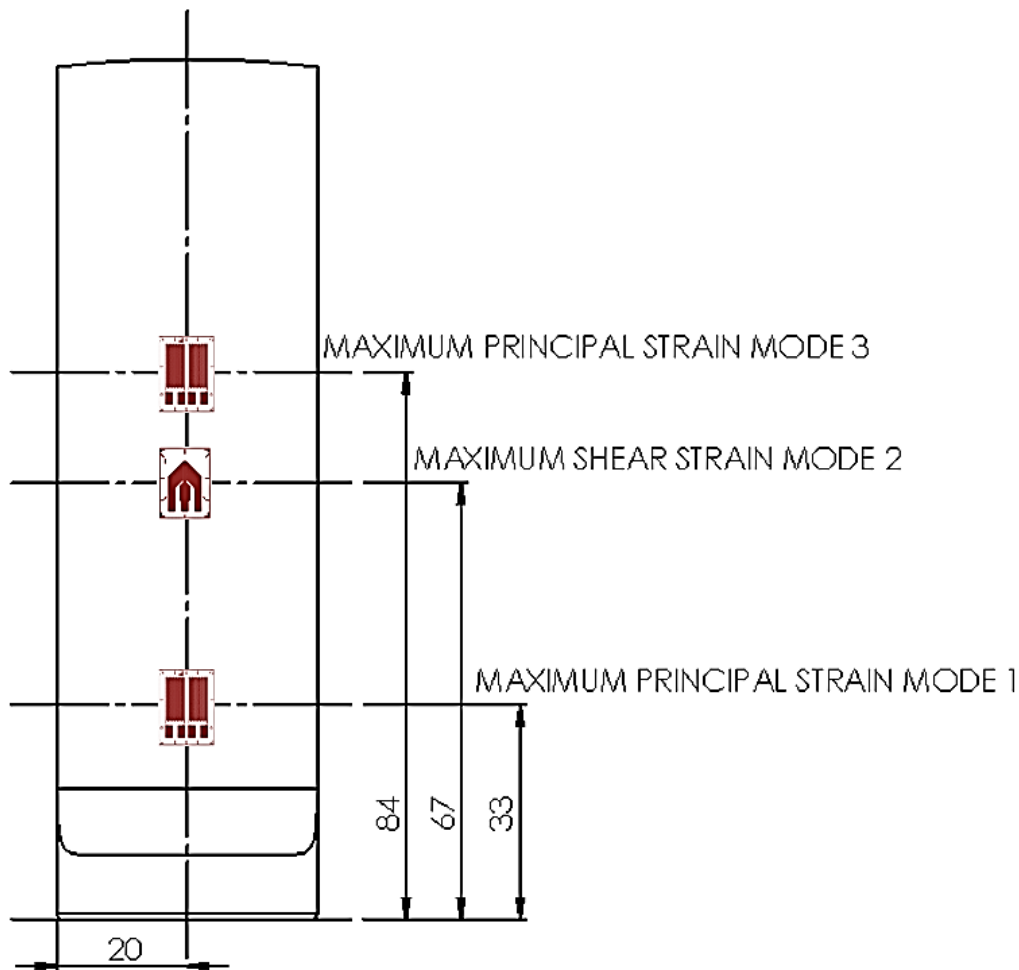


Figure 7.4-1 Strain Gauge Positions

The SG positions were chosen such that the sensors would be exposed to maximum strain conditions given the mode under investigation. At the same time the gauges were placed away from stress raisers to reduce their impact on the measured values. This was particularly important with the placing of the bending strain gauges on the damaged blade geometries due to the slots cut just above the radius on the blade.

The application loci for the damaged blades was inferred from this analysis. Only one set of full bridges per damaged blade was installed and investigated; the gauge was placed with sensitivity to mode 1 flap bending. Only one instrumentation setup per blade geometry was installed and investigated.

7.4.4. D4 – Analytical Campbell Diagrams for Damaged Blades

The Campbell diagrams generated for the two damaged blade geometries are presented in Figure 7.4-2 and Figure 7.4-3. EOs 1 to 100 are provided on the plots.

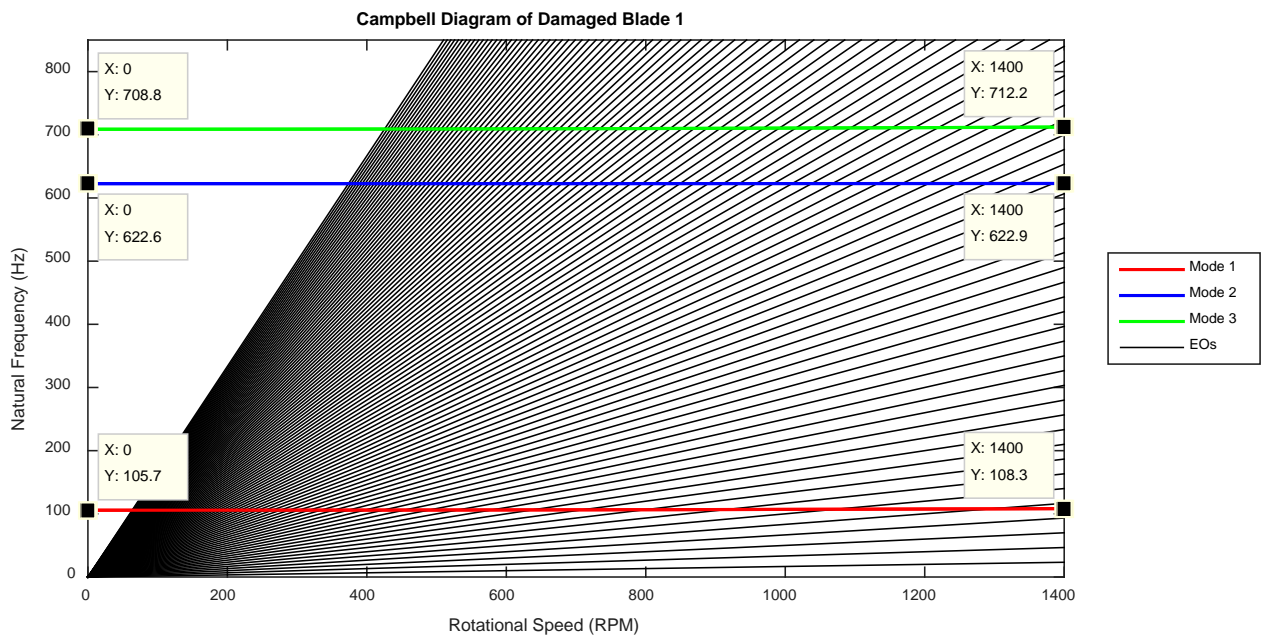


Figure 7.4-2 Campbell diagram of damaged blade 1

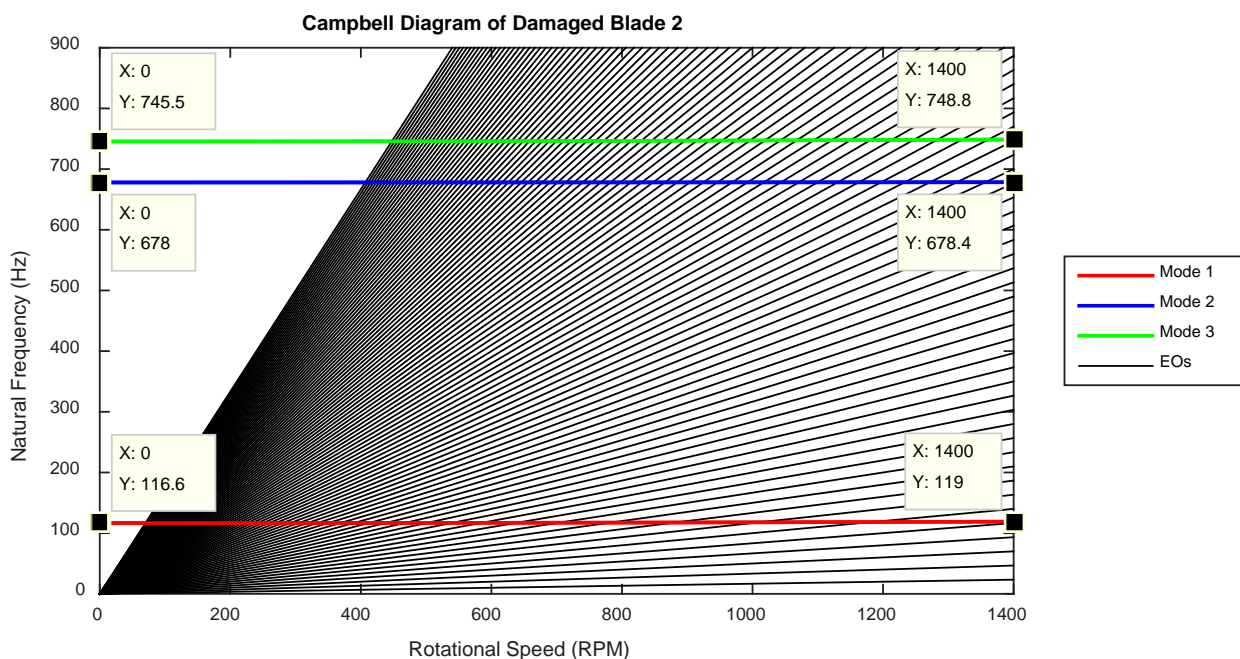


Figure 7.4-3 Campbell diagram of damaged blade 2

The change in natural frequency value due to centrifugal stiffening, for the first three modes and for both blade geometries, is estimated to change minimally across the operating range of interest. The torsional modes (mode 2) is the least sensitive to an increase in rotational speed.

7.5. Appendix E – Experimental Setup, Characterisation and Methodology

7.5.1. E1 – Instrumentation List

Instrumentation utilised during testing and experimental setup validation are listed in Table 7.5-1.

Table 7.5-1 Instrumentation list

#	Name	Sensitivity/ GF/ Calibration	Make & Model/ Serial	Notes
1	Impulse force hammer	2.15 mV/N	PCB Modal 086C03 (SN 8133)	Modal hammer with nylon tip
2	Microphone*	2.00 mV/Pa	PCB 378C01	0.25" free-field pre-polarised microphone and preamplifier
3	Dual uniaxial strain gauges	2.07	HBM 1-DY13-3/350	Utilised in full bridge configuration for bending measurements
4	Dual torsion gauges	2.04	HBM K-XY4-3-25-350-3-05	Utilised in full bridge configuration for torsion measurements
5	Data acquisition module	N/A	OROS OR35 901056	DAQ operated with NVGate 9.10.008 software
6	Strain gauge amplifier 1	0.547 $\mu\epsilon$ /mV (variable linear output)	Vishay P-3500	Experimentally obtained output sensitivity (divide measured strain by number of active SGs in full bridge)
7	Strain gauge amplifier 2	0.515 $\mu\epsilon$ /mV (variable linear output)	Vishay P-3500	Experimentally obtained output sensitivity (divide measured strain by number of active SGs in full bridge)
8	Strain gauge amplifier 3	0.535 $\mu\epsilon$ /mV (variable linear output)	Vishay P-3500	Experimentally obtained output sensitivity (divide measured strain by number of active SGs in full bridge)
9	Optical fibre switch	N/A	Optel Thevon 152 G8	Tachometer used with 79 PPR zebra tape
10	Proximity transducer	8.000 mV/ μ m (range of 2 mm)	Meggitt TQ401	Eddy current probe used with IQS450 signal conditioner
11	Scanning laser Doppler vibrometer	N/A	Polytec PSV-400	PSV-400 scanning head, PSV-400 Junction Box, OFV-500 Controller with PSV 8.8 acquisition software

*The calibration report for the microphone is provided in the succeeding section.



7.5.2. E2 – Sound Pressure Transducer Calibration Report

The calibration report for the sound pressure transducer is provided in Figure 7.5-1.

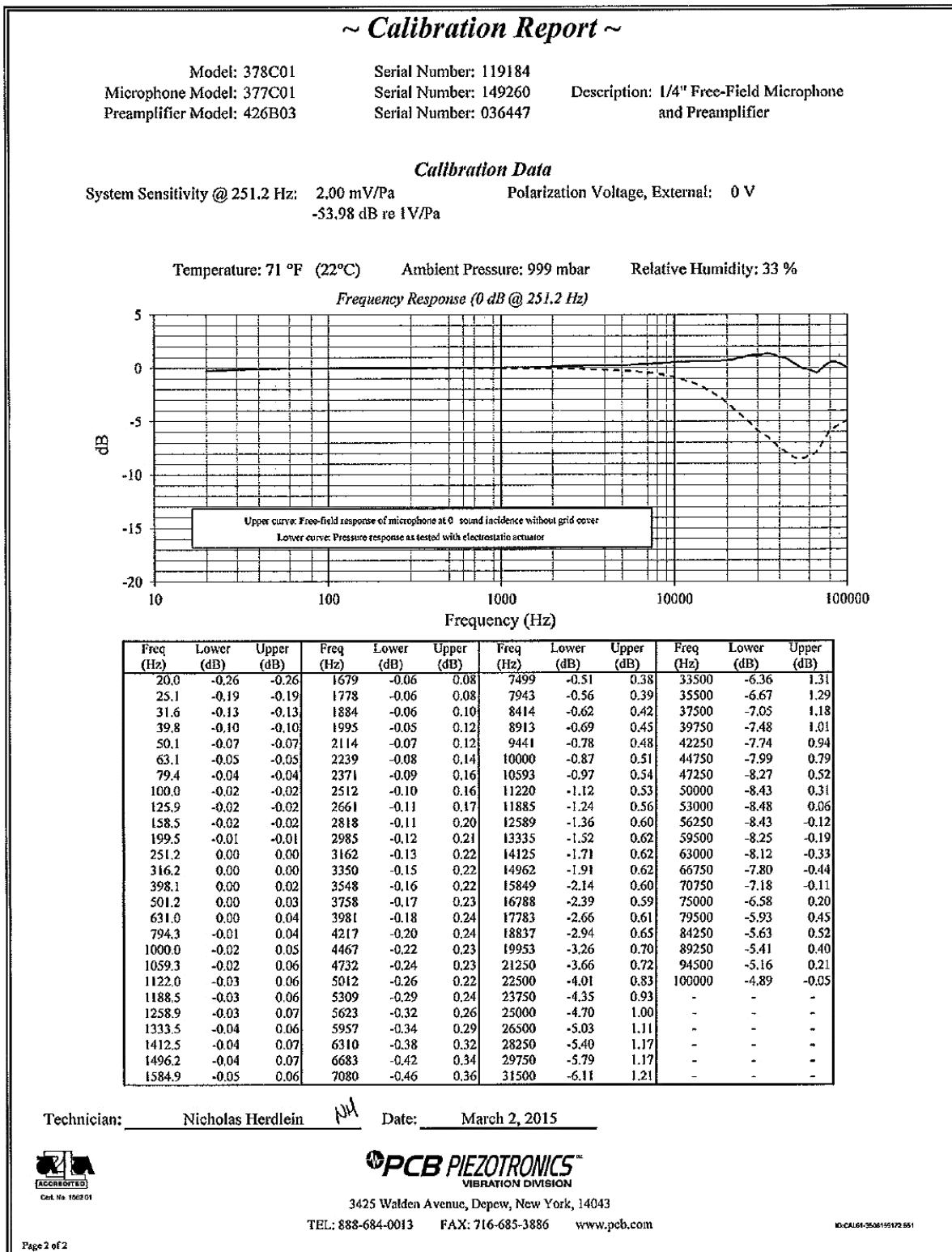


Figure 7.5-1 PCB 378C01 calibration report

7.5.3. E3 – Images of Experimental Setup

7.5.3.1. Test Bench



Figure 7.5-2 Experimental test bench

7.5.3.2. Drum

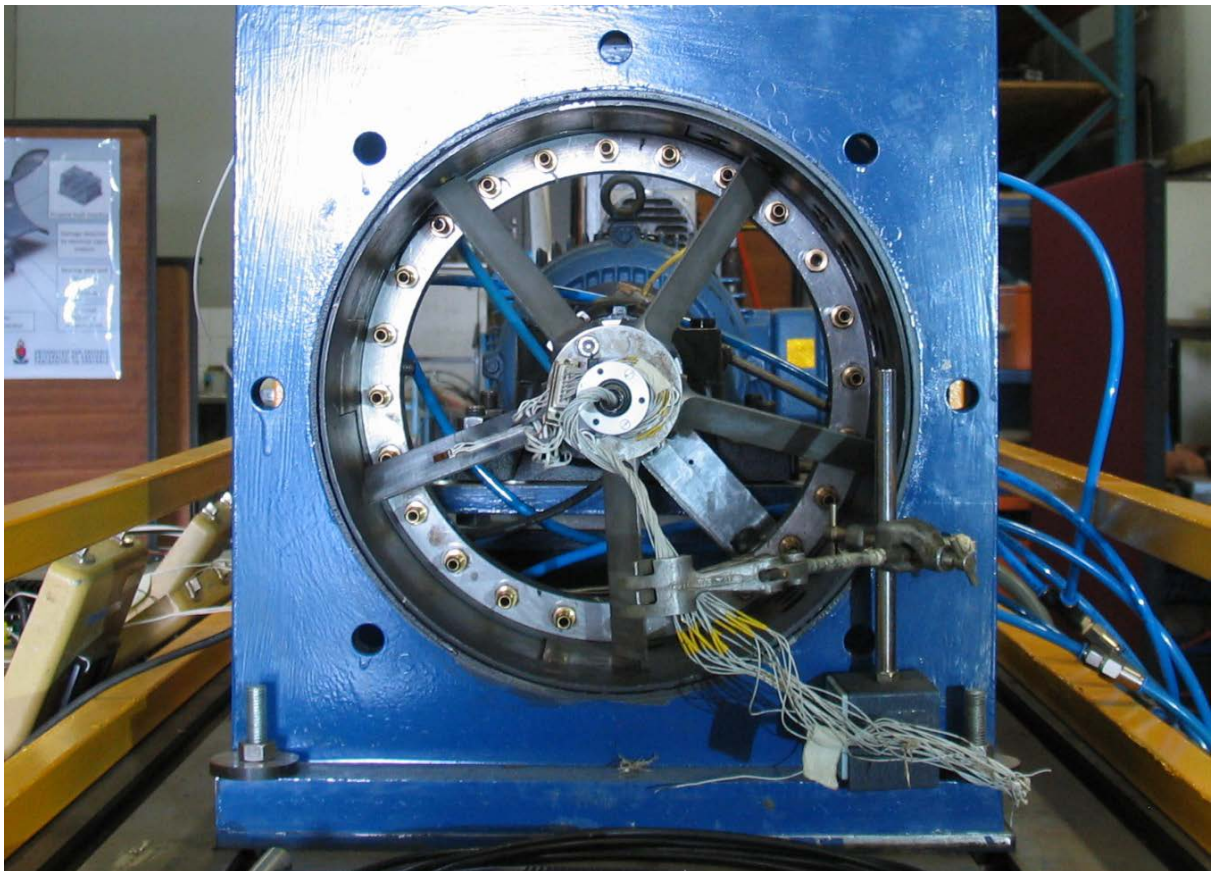


Figure 7.5-3 Front view of drum with air nozzles, hub and blade assembly and slip ring

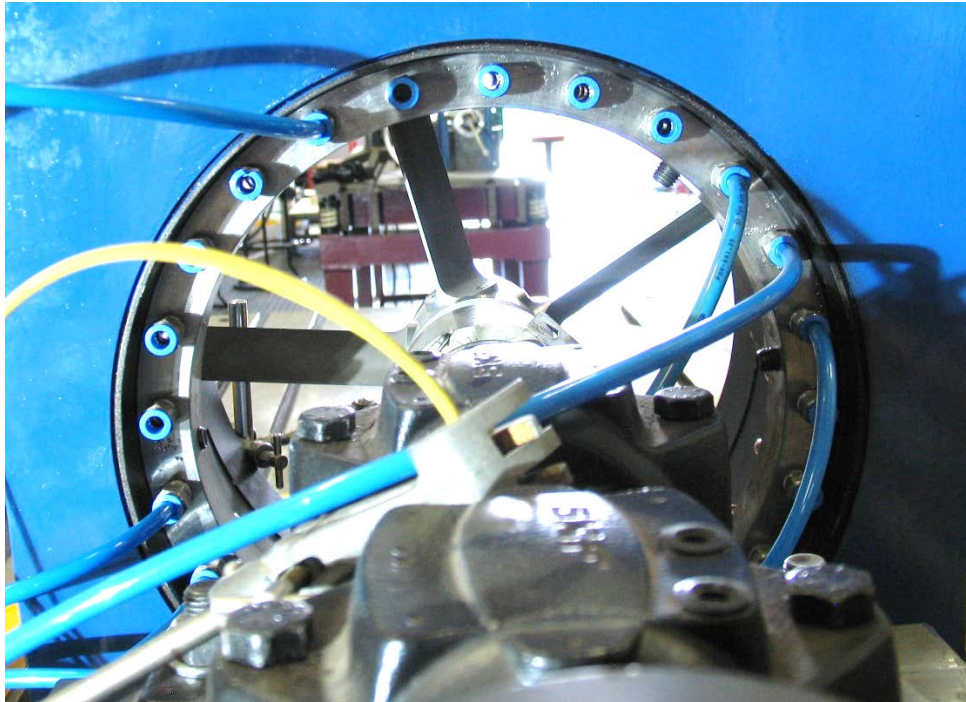


Figure 7.5-4 Rear view of drum with excitation nozzle attachment points

7.5.3.3. Blade and Hub Assembly Components



Figure 7.5-5 Blade and hub assembly with set of healthy blades



Figure 7.5-6 Hub with blade attachment holes and locating recess

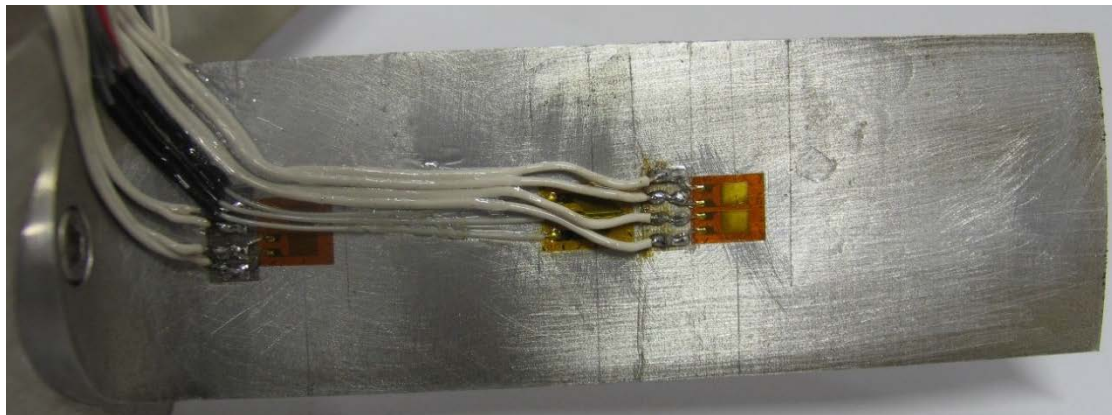


Figure 7.5-7 Instrumented healthy blade

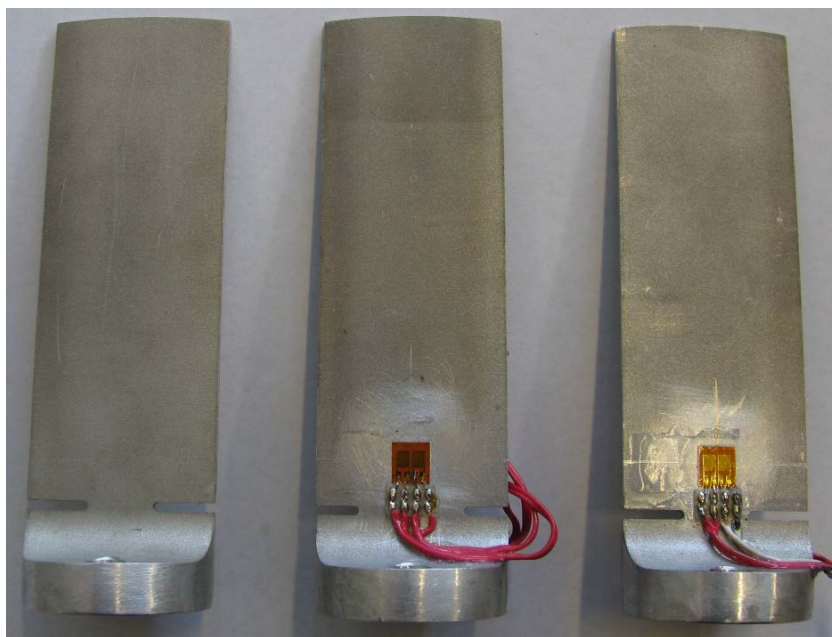


Figure 7.5-8 Set of damaged blades

7.5.3.4. Sensor Plate and Attachments



Figure 7.5-9 Sensor plate with attached microphone mount, microphone and proximity probes



Figure 7.5-10 Inside view of drum with sensor plate, microphone and proximity transducers

7.5.3.5. Instrumentation and Sensors



Figure 7.5-11 OROS OR35 data acquisition system

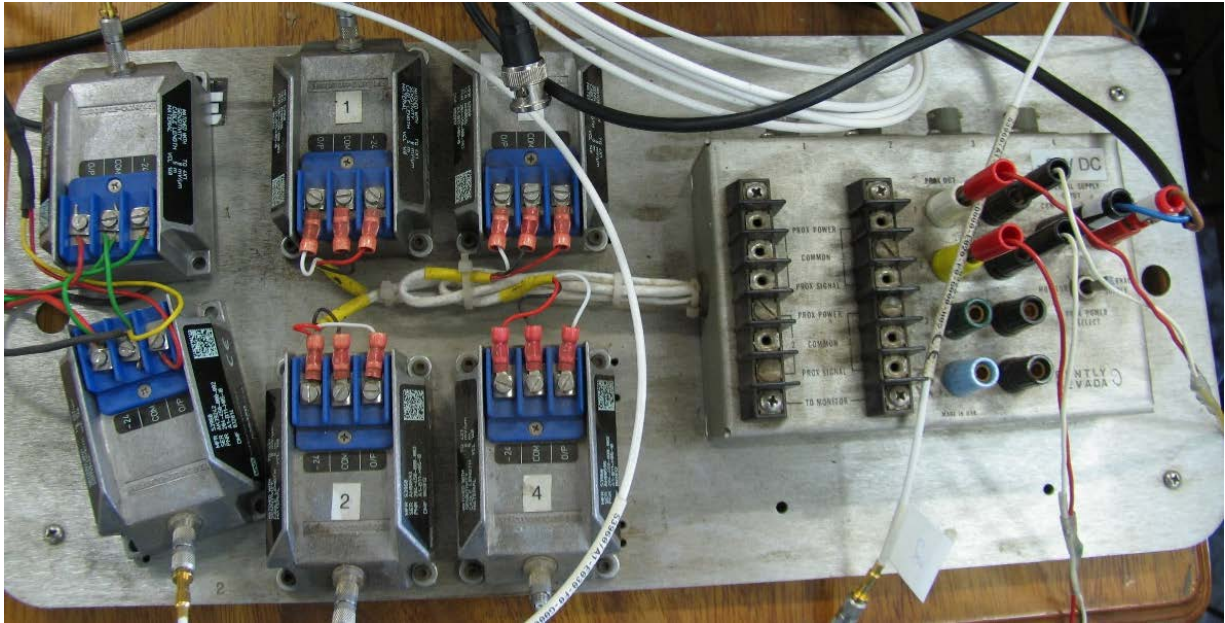


Figure 7.5-12 Eddy current probe signal conditioner and amplifier



Figure 7.5-13 Shaft tachometer with 79 PPR zebra tape

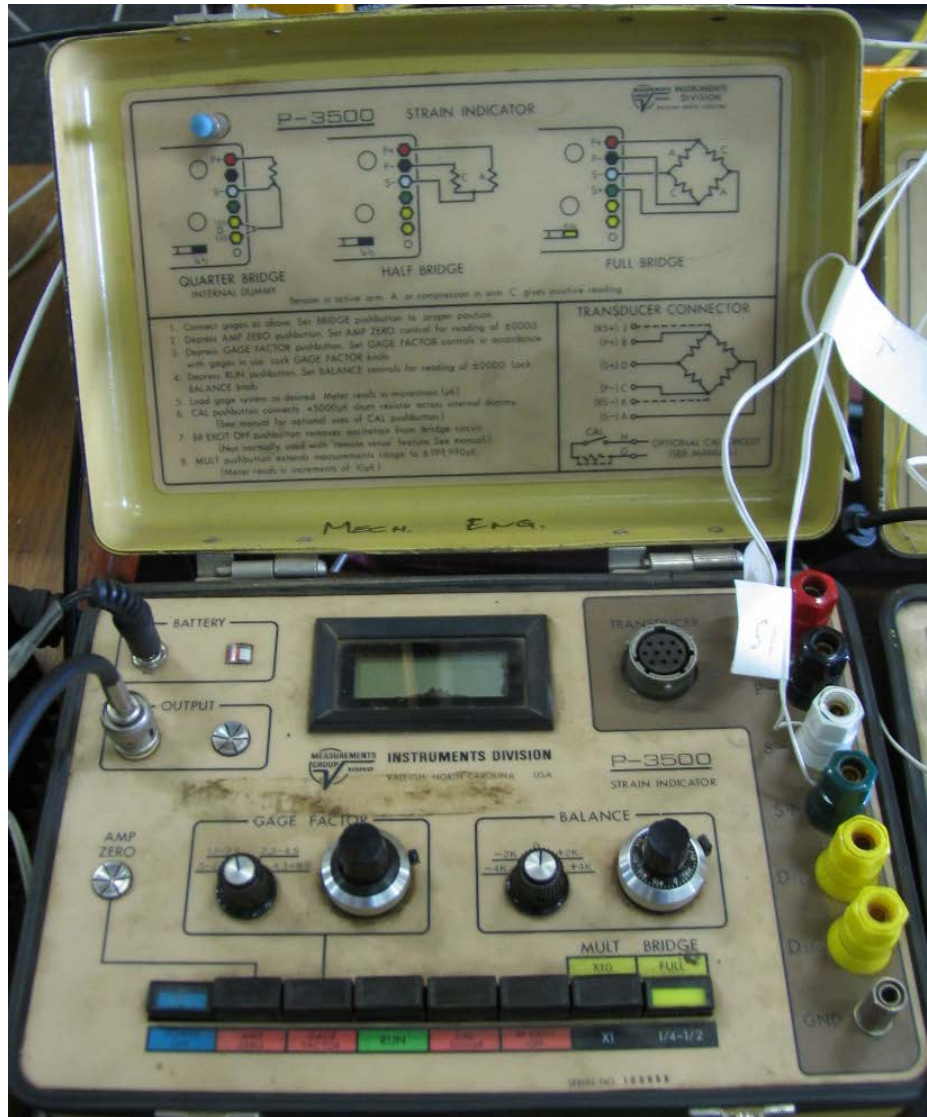


Figure 7.5-14 Analog strain gauge amplifier



Figure 7.5-15 Modal hammer

7.5.3.6. Scanning Laser Vibrometer



Figure 7.5-16 Scanning laser vibrometer set-up

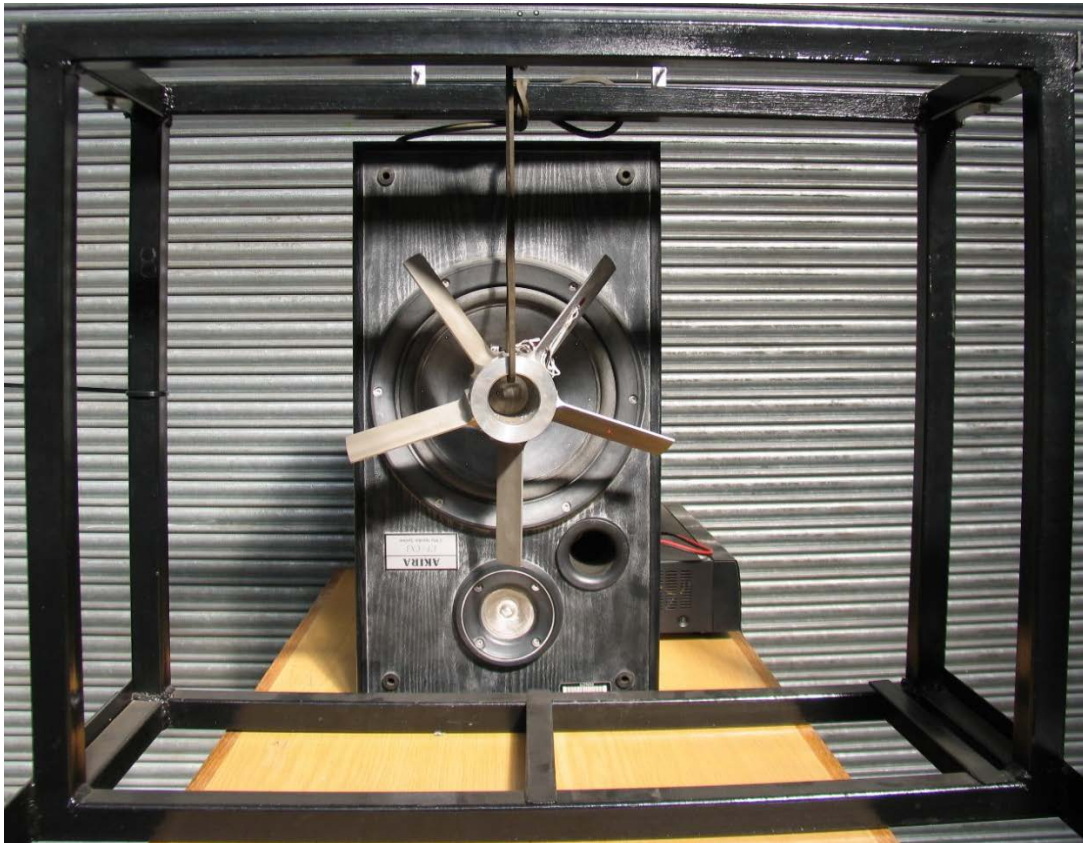


Figure 7.5-17 Hub and blade assembly positioned in scanning laser vibrometer setup



7.5.4. E4 – Relative Tip Distances

Tip distances were measured, in terms of voltages, using eddy current proximity probes on the leading and lagging edges of the turbine blades' tips. The higher the voltage the closer the tip was to the sensor. 'ED 1' refers to the leading edge and 'ED 2' refers to the lagging edge of tip. The unique pattern of tip distances, in terms of voltage, is used to identify individual blades passing the microphone.

7.5.4.1. Configuration 1

Table 7.5-2 Tip distances configuration 1

Blade	ED 1 (V) (order)	ED2 (V) (order)	Attached Sensors	Sensor designation	Notes (Nat. Freq. (Hz))
1	1.75 (3)	1.45 (3)	Mode 1, Mode 2, Mode 3	B1, T1, B2	Healthy (128.1)
2	1.15 (4)	1.34 (4)	None	N/A	Healthy (125.0)
3	1.10 (5)	0.759 (5)	None	N/A	Healthy (126.3)
4	2.32 (2)	2.48 (2)	None	N/A	Healthy (125.6)
5	2.41 (1)	2.50 (1)	None	N/A	Healthy (125.6)

7.5.4.2. Configuration 2

Table 7.5-3 Tip distances configuration 2

Blade	ED 1 (V) (order)	ED2 (V) (order)	Attached Sensors	Sensor designation	Notes (Nat. Freq. (Hz))
1	1.24 (4)	1.38 (3)	Mode 1	B1	Healthy (128.1)
2	1.26 (3)	1.09 (5)	None	N/A	Healthy (125.0)
3	1.07 (5)	1.20 (4)	None	N/A	Healthy (126.3)
4	2.31 (1)	2.23 (1)	None	N/A	Healthy (125.6)
5	1.57 (2)	1.50 (2)	Mode 1	B2	Damaged 1 (101.9)

7.5.4.3. Configuration 3

Table 7.5-4 Tip distances configuration 3

Blade	ED 1 (V) (order)	ED2 (V) (order)	Attached Sensors	Sensor designation	Notes (Nat. Freq. (Hz))
1	1.79 (2)	1.83 (2)	Mode 1	N/A	Healthy (128.1)
2	0.2 (5)	0.5 (5)	Mode 1	B3	Damaged 2 (112.5)
3	1.2 (4)	1.3 (4)	None	N/A	Healthy (126.3)
4	2.3 (1)	2.23 (1)	None	N/A	Healthy (125.6)
5	1.4 (3)	1.38 (5)	Mode 1	B2	Damaged 1 (101.9)

7.5.4.4. Configuration 4

Table 7.5-5 Tip distances configuration 4

Blade	ED 1 (V) (order)	ED2 (V) (order)	Attached Sensors	Sensor designation	Notes (Nat. Freq. (Hz))
1	1.65 (2)	1.81 (2)	Mode 1	N/A	Healthy (128.1)
2	0.3 (5)	0.5 (5)	Mode 1	B3	Damaged 2 (112.5)
3	0.75 (4)	1.07 (4)	None	N/A	Damaged 1 (100.0)
4	2.3 (1)	2.4 (1)	None	N/A	Healthy (125.6)
5	1.48 (3)	1.45 (3)	Mode 1	B2	Damaged 1 (101.9)

7.5.5. E5 - Unconstrained System Response

All observed mode shapes have blade 1 at the 12 o'clock position counting clockwise to blade 5.

7.5.5.1. Configuration 1

Figures 8.10-1 to 3 show the average unconstrained response spectrum of the assembly.

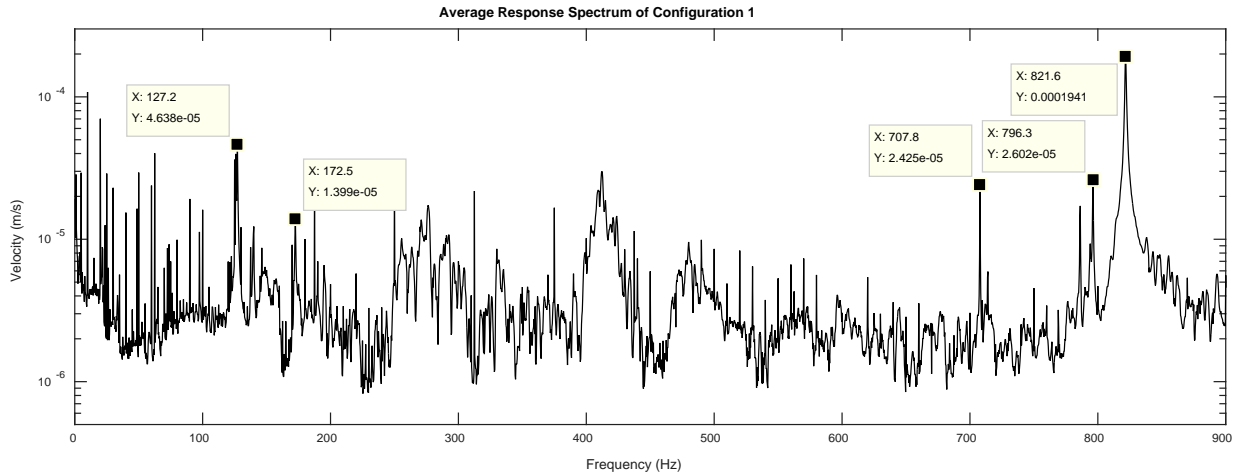


Figure 7.5-18 Average response spectrum of unconstrained hub and blade assembly in config. 1

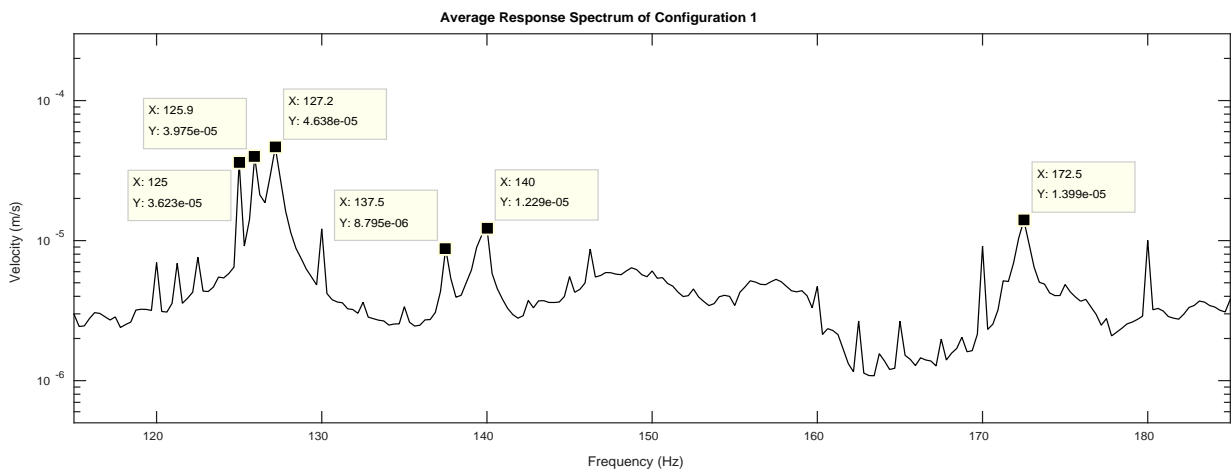


Figure 7.5-19 Average response spectrum of unconstrained config. 1 in vicinity of mode 1

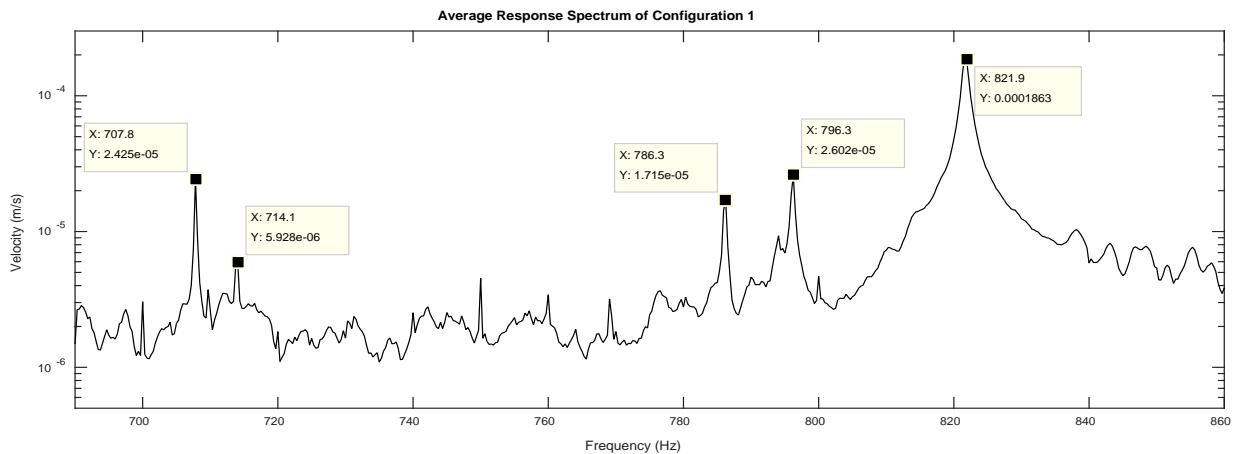
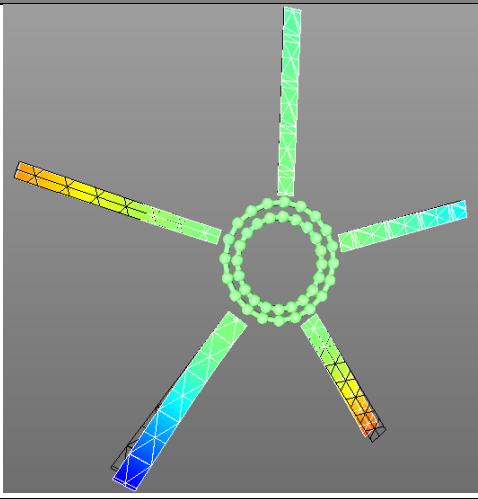
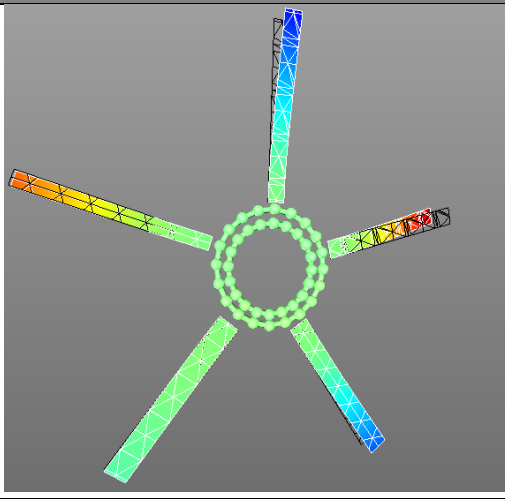
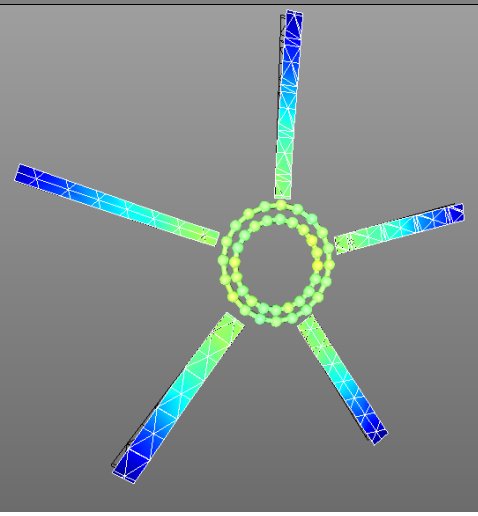
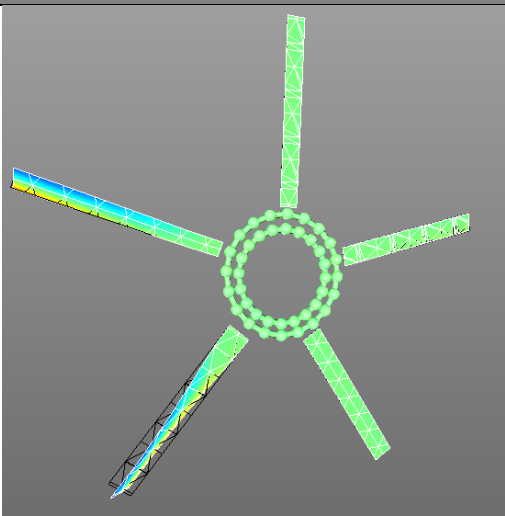
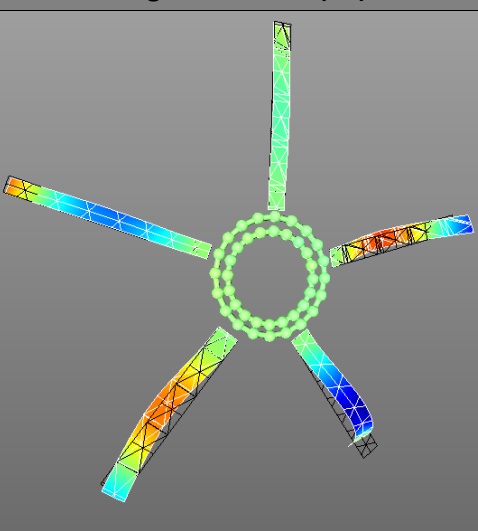
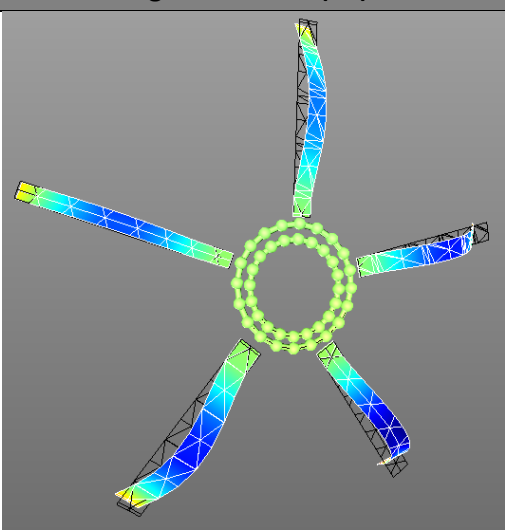


Figure 7.5-20 Average response spectrum of unconstrained config. 1 in vicinity of modes 2 and 3

Table 7.5-6 illustrates selected operational mode shapes obtained for unconstrained configuration 1.

Table 7.5-6 Unconstrained hub & blade assembly operational mode shapes for configuration 1

Mode 1 Bending at 125.94 Hz (1B)	Mode 1 Bending at 127.19 Hz (1B)
	
Mode 1 Bending at 172.5 Hz (1B)	Mode 2 Twisting at 707.81 Hz (1T)
	
Mode 3 Bending at 786.25 Hz (2B)	Mode 3 Bending at 821.56 Hz (2B)
	

7.5.5.2. Configuration 2

The average velocity response spectrum for configuration 2 is provided in Figure 7.5-21, Figure 7.5-22 and Figure 7.5-23.

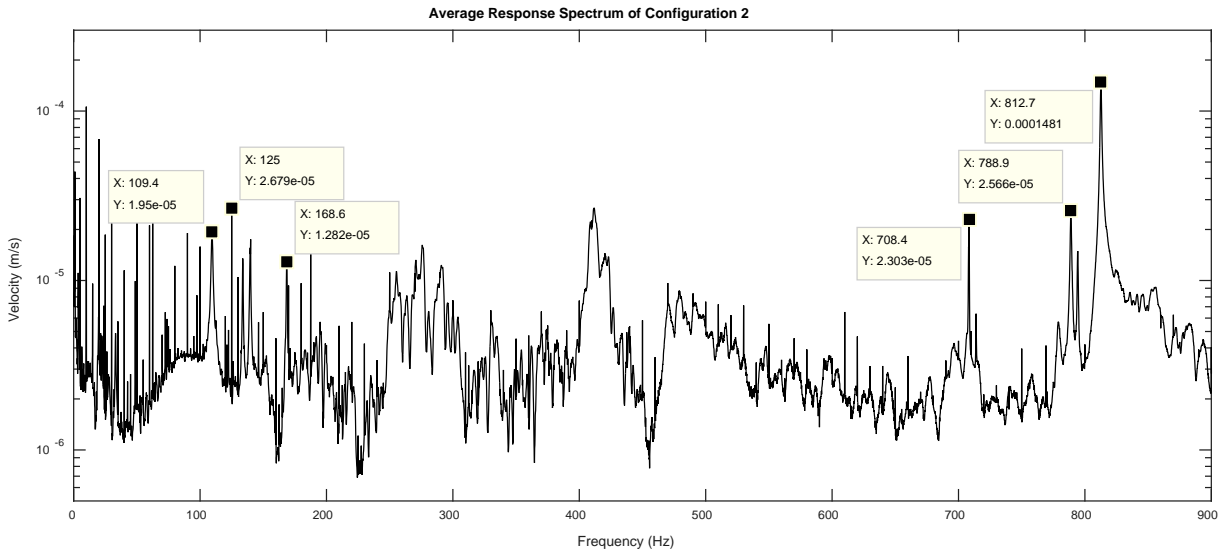


Figure 7.5-21 Average response spectrum of unconstrained hub and blade assembly in config. 2

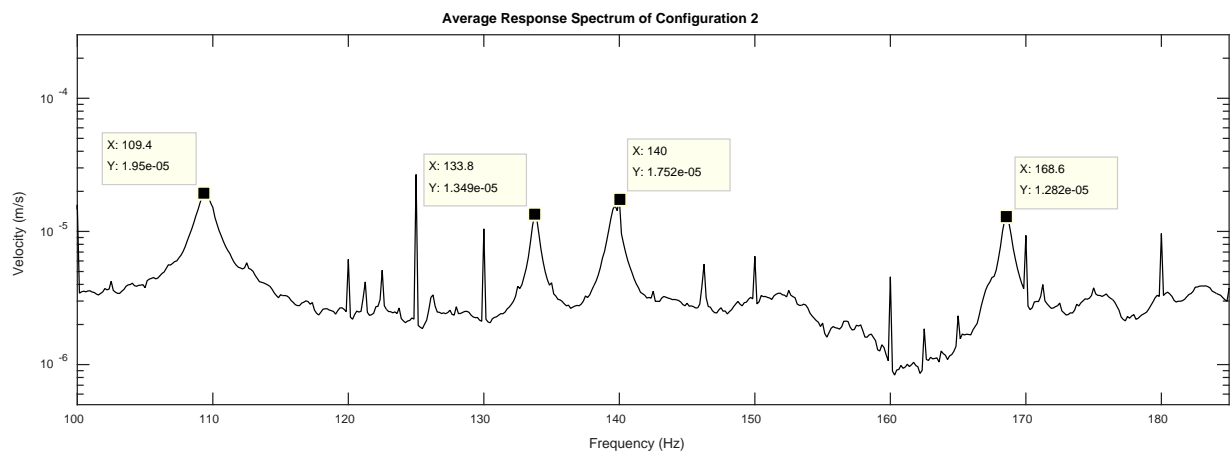


Figure 7.5-22 Average response spectrum of unconstrained config. 2 in vicinity of mode 1

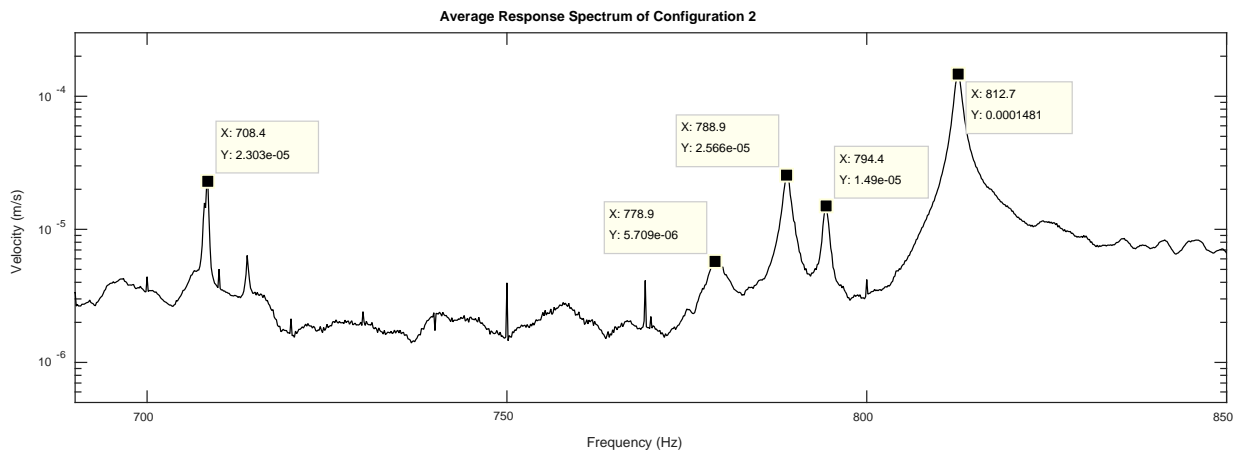
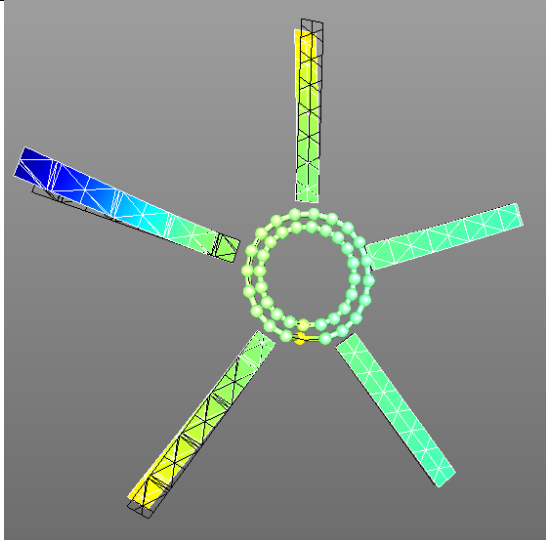
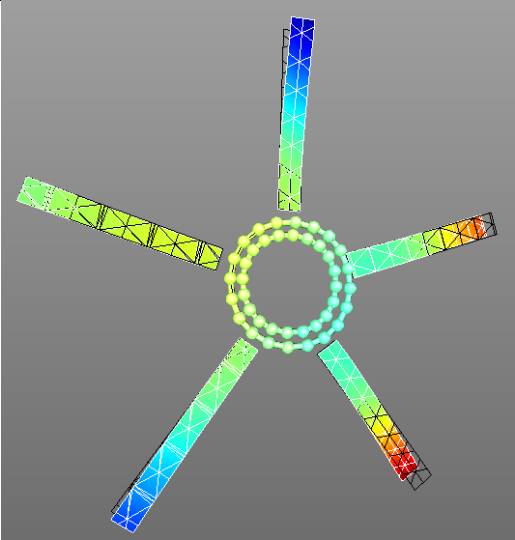
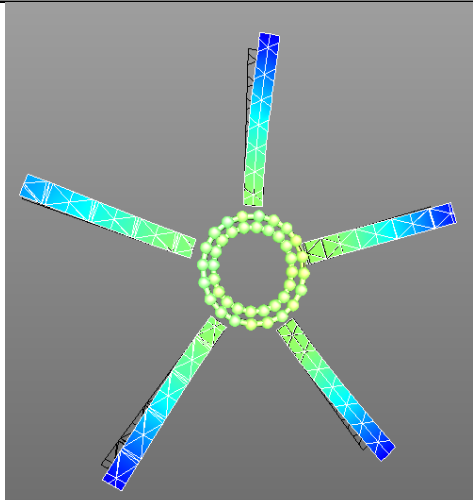
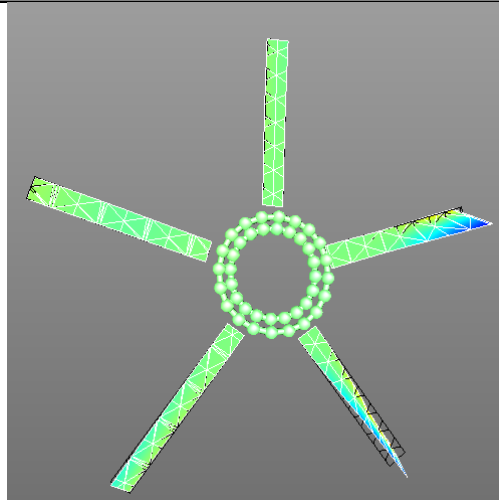
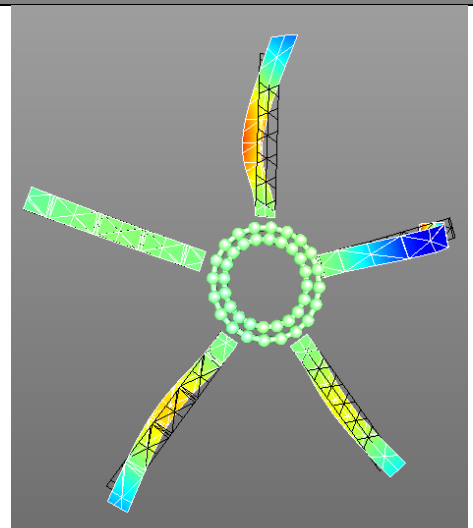
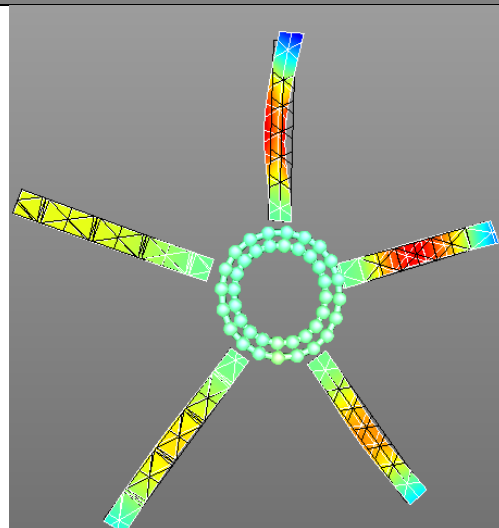


Figure 7.5-23 Average response spectrum of unconstrained config. 2 in vicinity of modes 2 and 3

Table 7.5-7 contains a selection of the operational mode shapes for configuration 2.

Table 7.5-7 Unconstrained hub & blade assembly operational mode shapes for configuration 2

<p>Mode 1 Bending at 109.53 Hz (1B)</p>  A 3D visualization of a five-bladed wind turbine hub and blade assembly in its first bending mode. The blades are shown in a curved shape, with a color gradient from blue (low displacement) to red (high displacement). The hub is a circular ring of green spheres.	<p>Mode 1 Bending at 133.75 Hz (1B)</p>  A 3D visualization of a five-bladed wind turbine hub and blade assembly in its first bending mode. The blades are shown in a curved shape, with a color gradient from blue to red. The hub is a circular ring of green spheres.
<p>Mode 1 Bending at 168.59 Hz (1B)</p>  A 3D visualization of a five-bladed wind turbine hub and blade assembly in its first bending mode. The blades are shown in a curved shape, with a color gradient from blue to red. The hub is a circular ring of green spheres.	<p>Mode 2 Twisting at 708.44 Hz (1T)</p>  A 3D visualization of a five-bladed wind turbine hub and blade assembly in its second mode, which is twisting. The blades are shown in a twisted shape, with a color gradient from blue to red. The hub is a circular ring of green spheres.
<p>Mode 3 Bending at 788.91 Hz (2B)</p>  A 3D visualization of a five-bladed wind turbine hub and blade assembly in its third mode, which is bending. The blades are shown in a curved shape, with a color gradient from blue to red. The hub is a circular ring of green spheres.	<p>Mode 3 Bending at 812.66 Hz (2B)</p>  A 3D visualization of a five-bladed wind turbine hub and blade assembly in its third mode, which is bending. The blades are shown in a curved shape, with a color gradient from blue to red. The hub is a circular ring of green spheres.

7.5.5.3. Configuration 3

The average response spectra for configuration 3 is presented in Figure 7.5-24, Figure 7.5-25 and Figure 7.5-26.

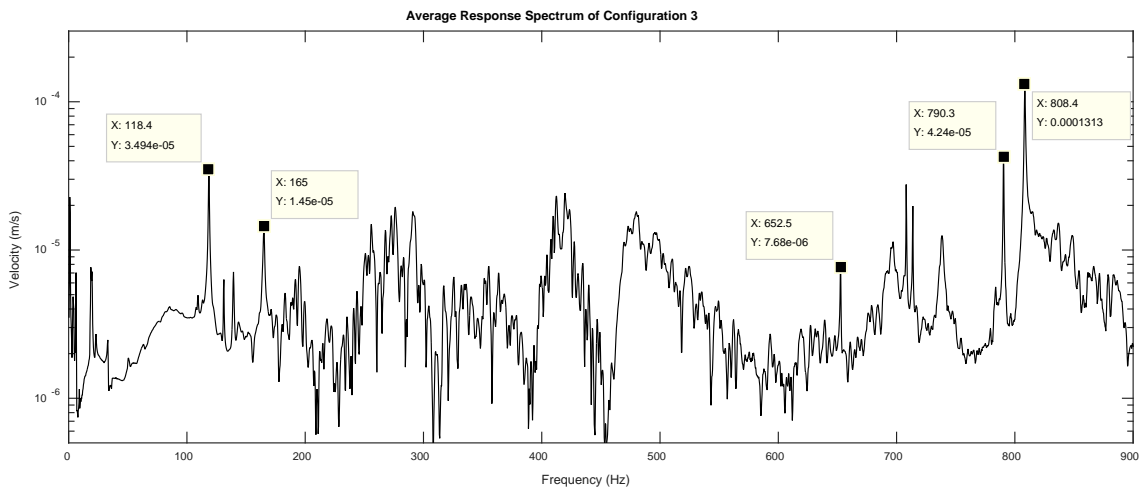


Figure 7.5-24 Average response spectrum of unconstrained hub and blade assembly in config. 3

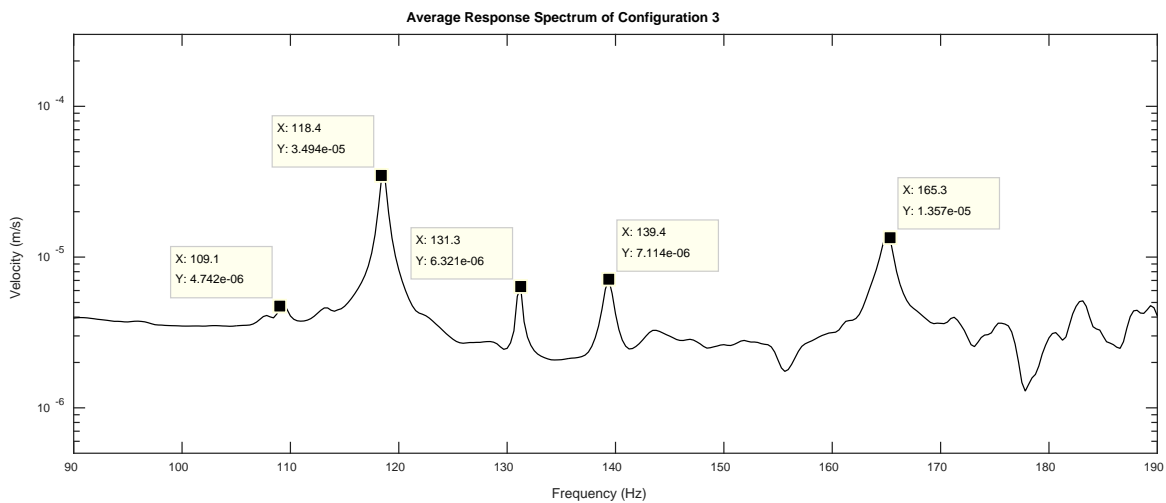


Figure 7.5-25 Average response spectrum of unconstrained config. 3 in vicinity of mode 1

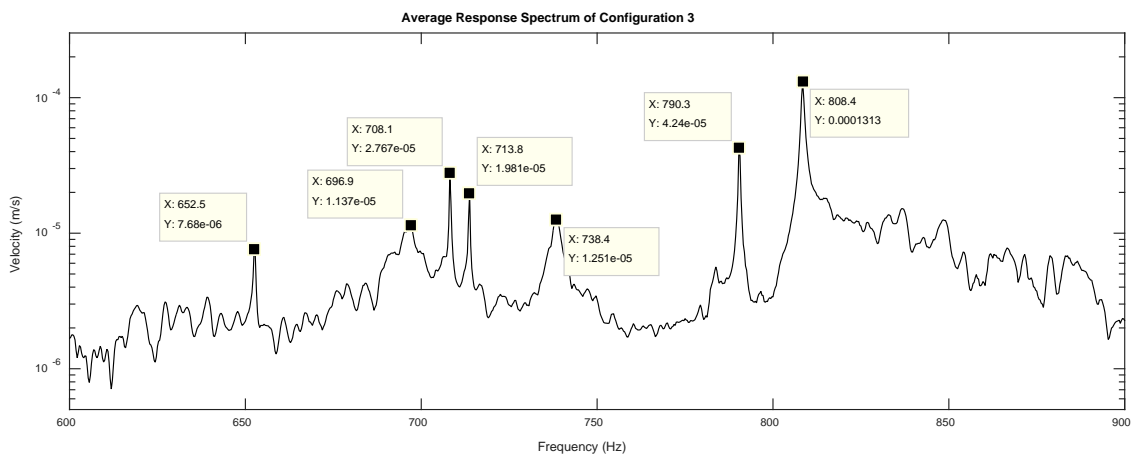
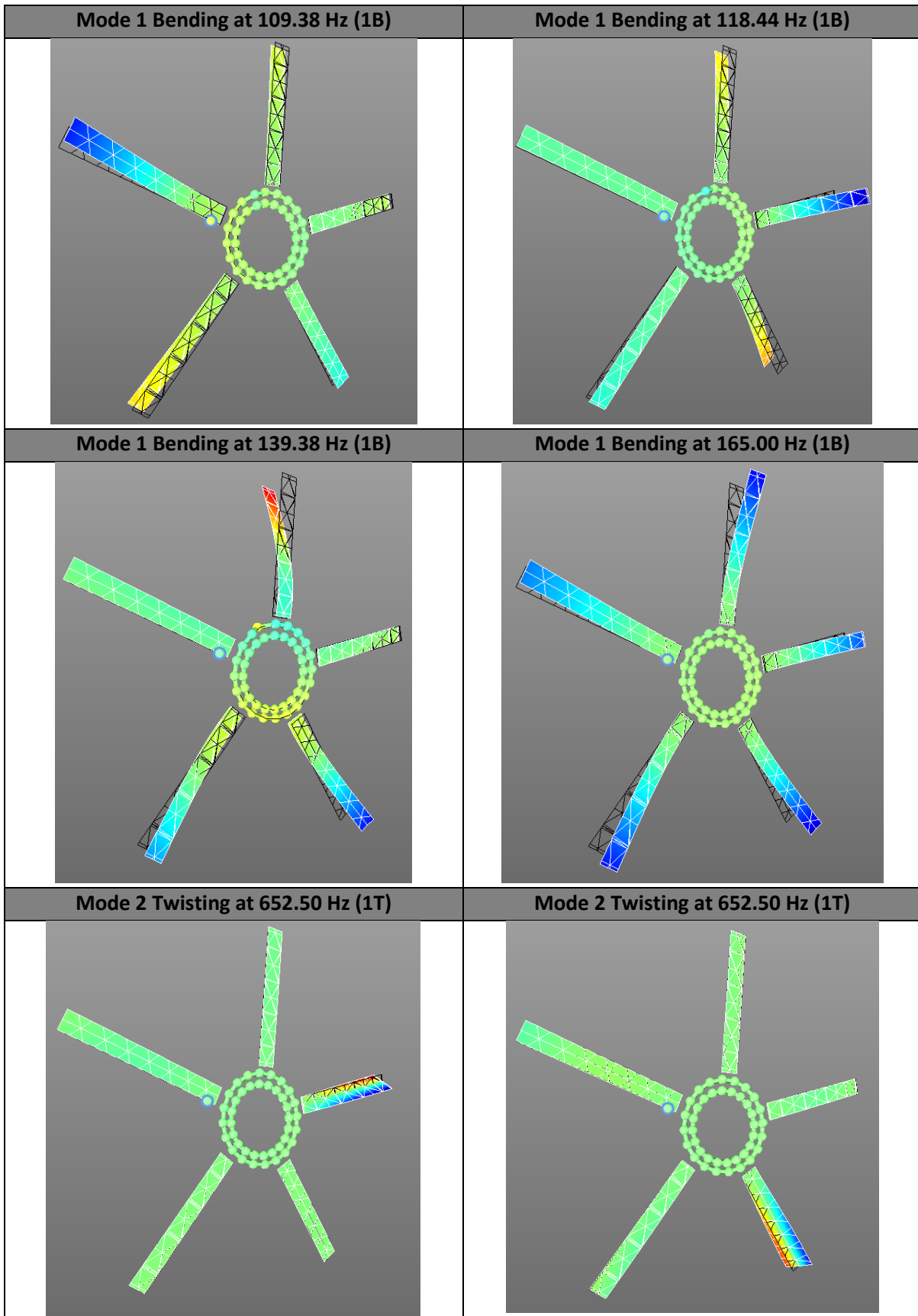
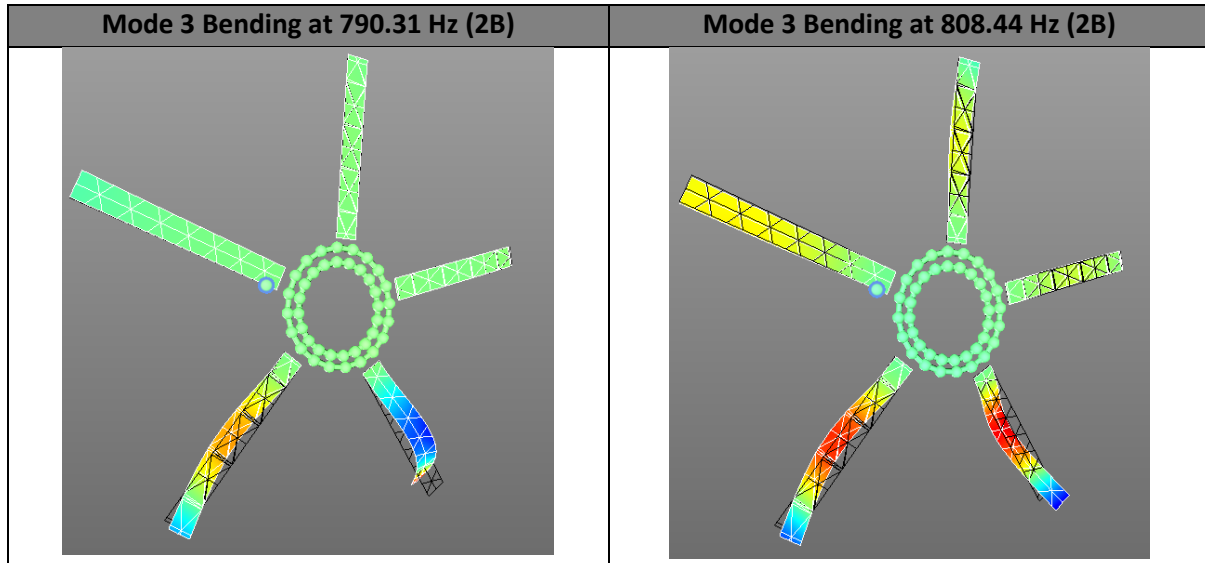


Figure 7.5-26 Average response spectrum of unconstrained config. 3 in vicinity of modes 2 and 3

Table 7.5-8 illustrates a selection of the operational mode shapes obtained for configuration 3.

Table 7.5-8 Unconstrained hub & blade assembly operational mode shapes for configuration 3





7.5.5.4. Configuration 4

The average response spectra for configuration 4 is presented in the following figures.

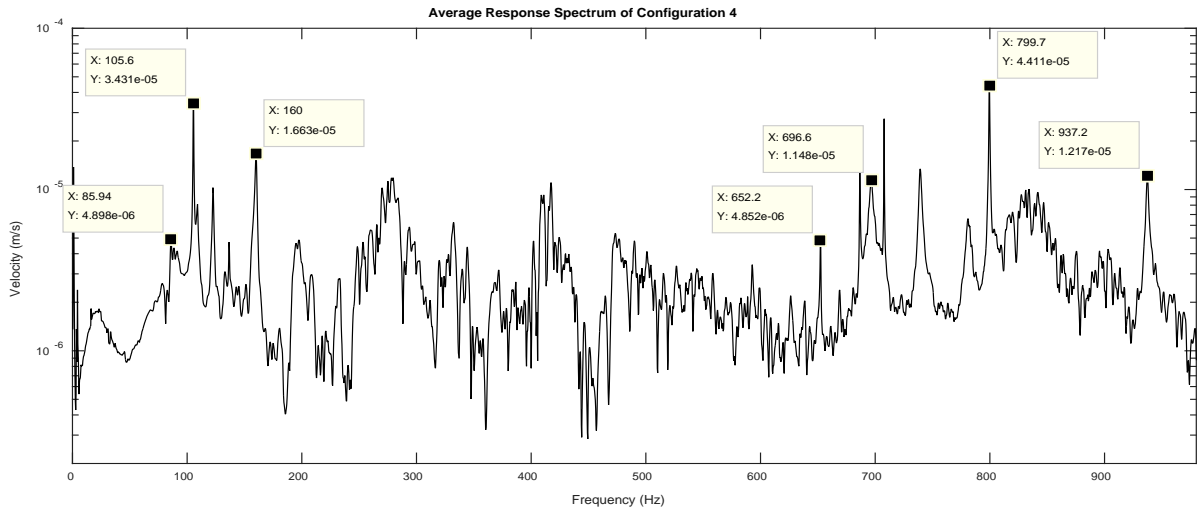


Figure 7.5-27 Average response spectrum of unconstrained hub and blade assembly in config. 4

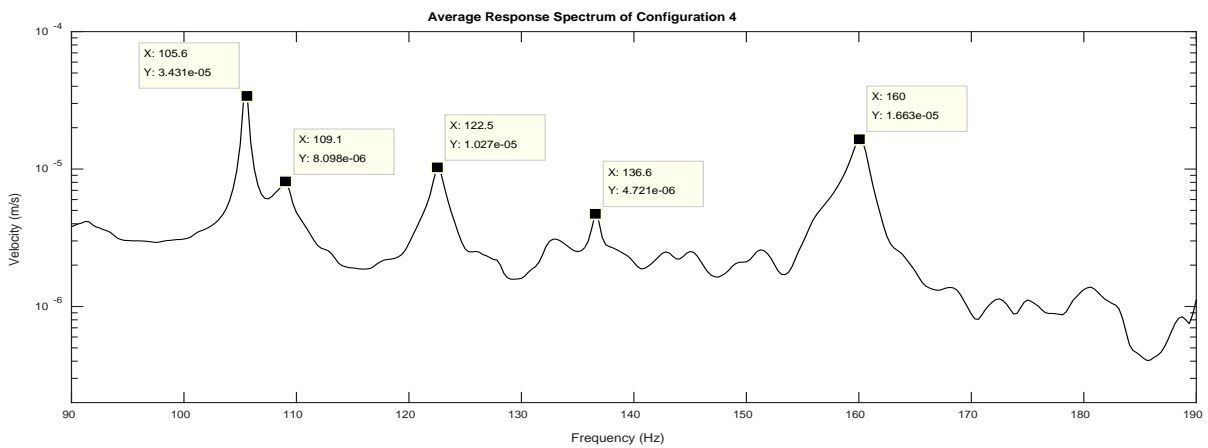


Figure 7.5-28 Average response spectrum of unconstrained config. 4 in vicinity of mode 1

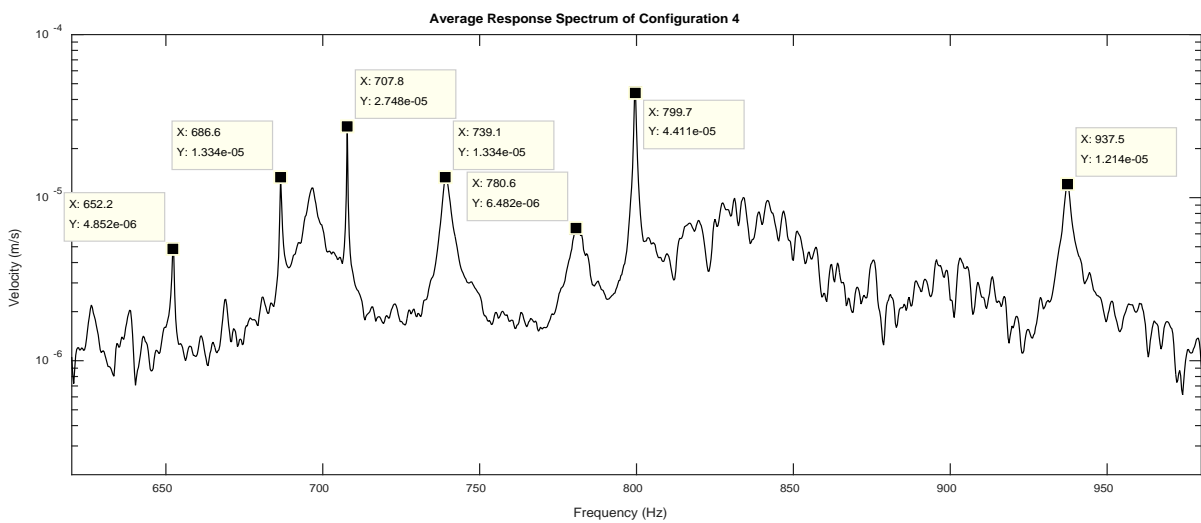
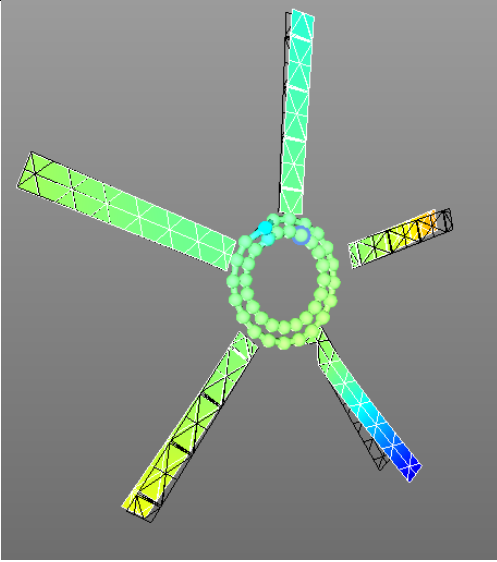
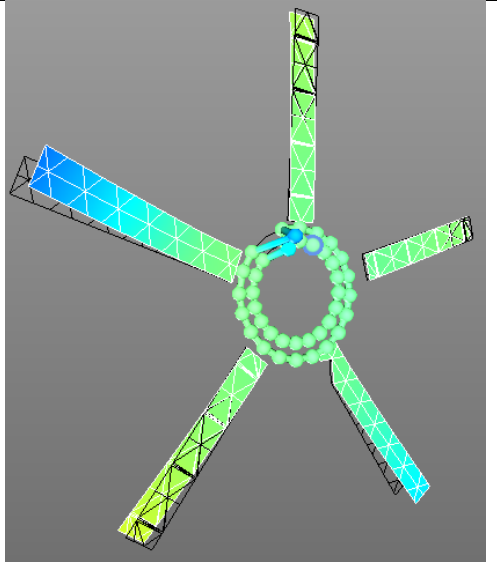
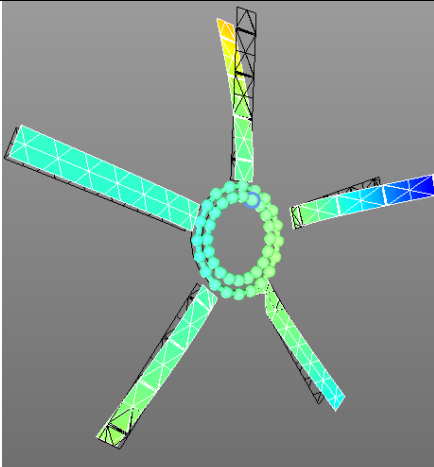
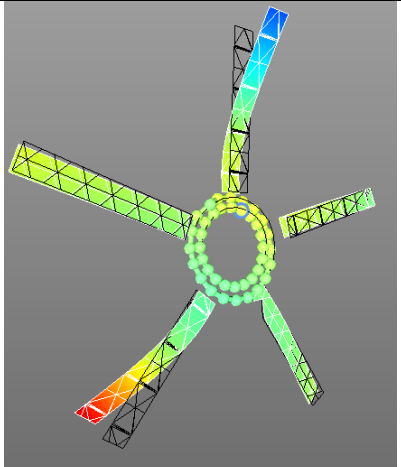
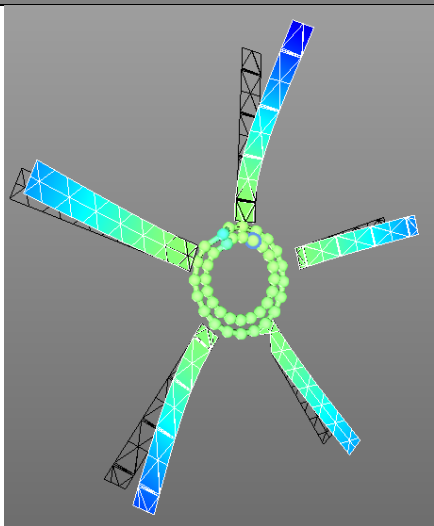
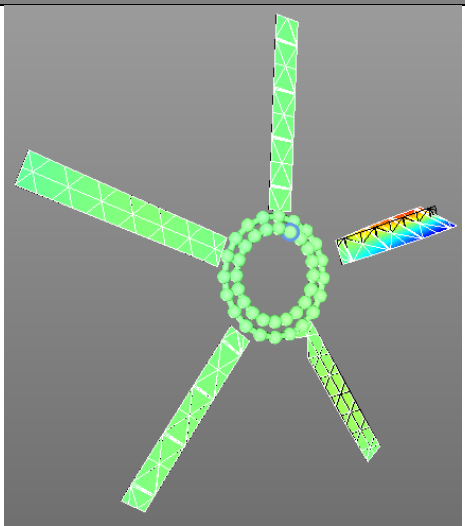
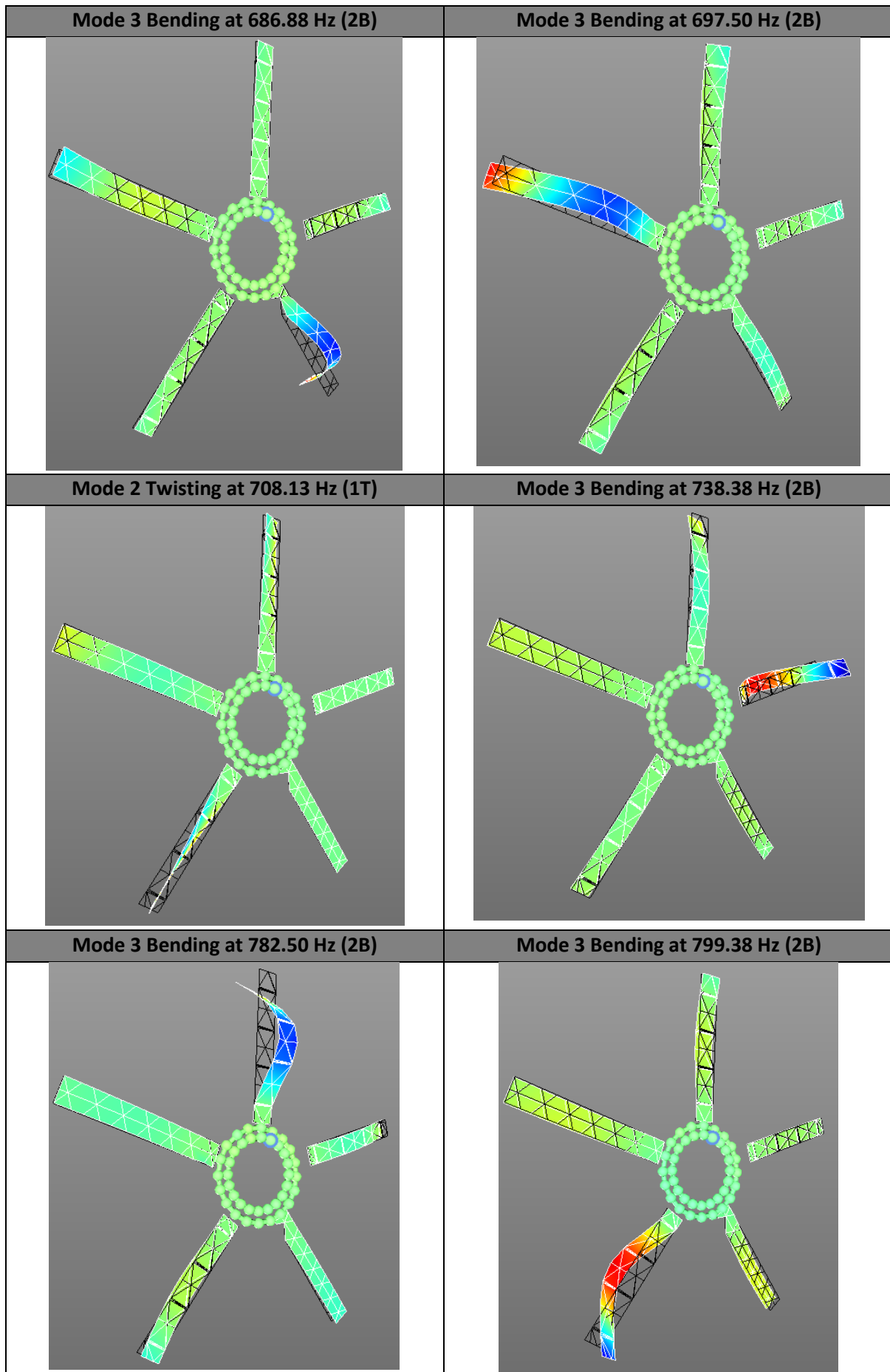


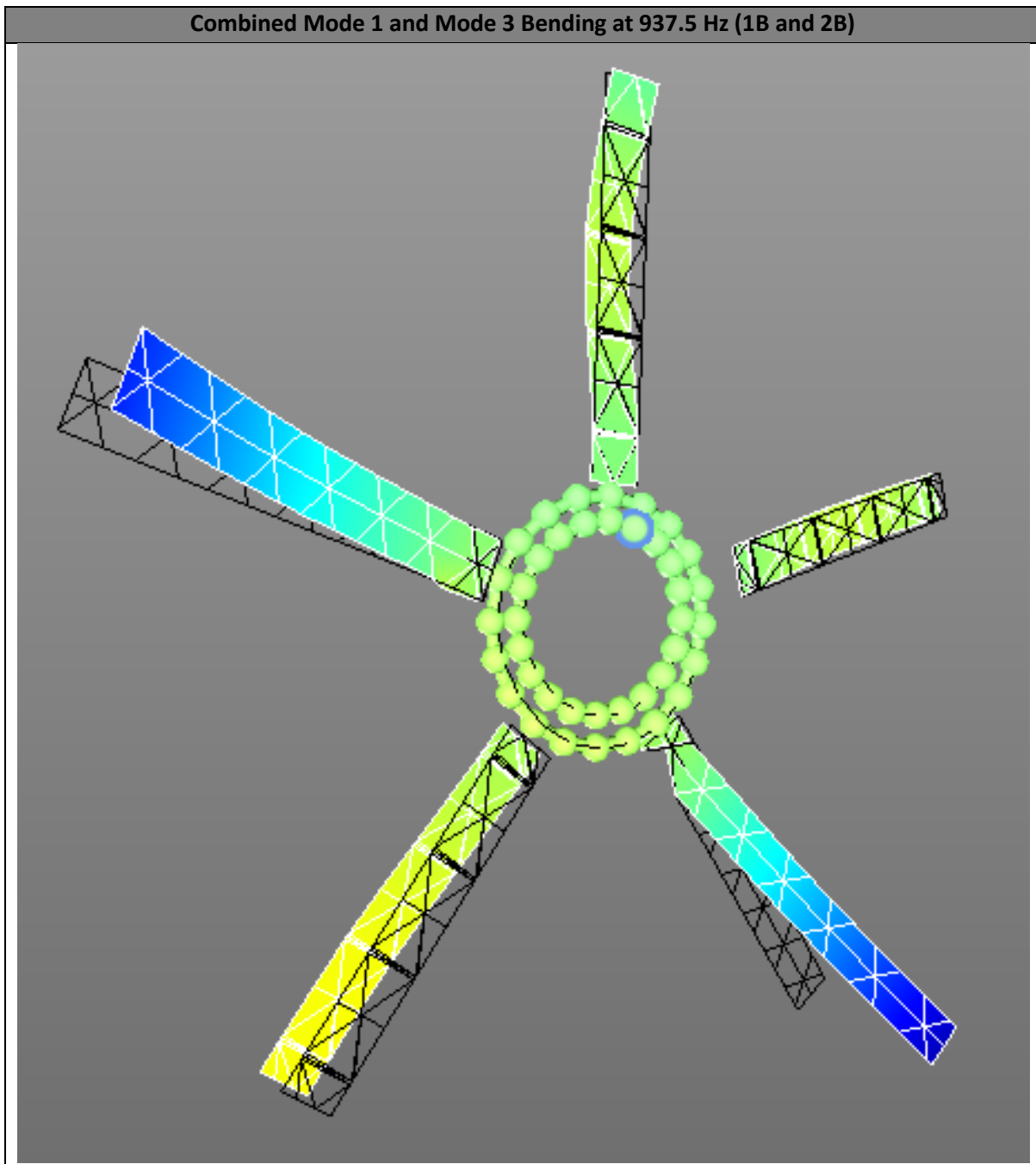
Figure 7.5-29 Average response spectrum of unconstrained config. 4 in vicinity of modes 2 & 3

Table 7.5-9 illustrates a selection of the operational mode shapes obtained for configuration 4.

Table 7.5-9 Unconstrained hub & blade assembly operational mode shapes for configuration 4

Mode 1 Bending at 105.63Hz (1B)	Mode 1 Bending at 109.38 Hz (1B)
	
Mode 1 Bending at 122.50 Hz (1B)	Mode 1 Bending at 136.88 Hz (1B)
	
Mode 1 Bending at 160.00 Hz (1B)	Mode 2 Twisting at 652.50 Hz (1T)
	





7.5.6. E6 – Response Spectra of Individual Blades

The response spectra of the individual blades to a hammer impact are presented in this section. Investigations were performed for all experimental configurations.

The individual blades were positioned such that the leading edge of their tip were in line with the microphone during the hammer impact.

Depending on the configuration certain blades were instrumented with SGs on the surface. The SG responses to the impacts on the individual blades were recorded (for all cases whether the SGs were present on the blade under investigation or not).

The SGs were found to be sensitive to hammer impacts on adjacent non-instrumented blades.

7.5.6.1. Configuration 1

The response of three SGs, all present on blade 1, was measured during the investigation of configuration 1.

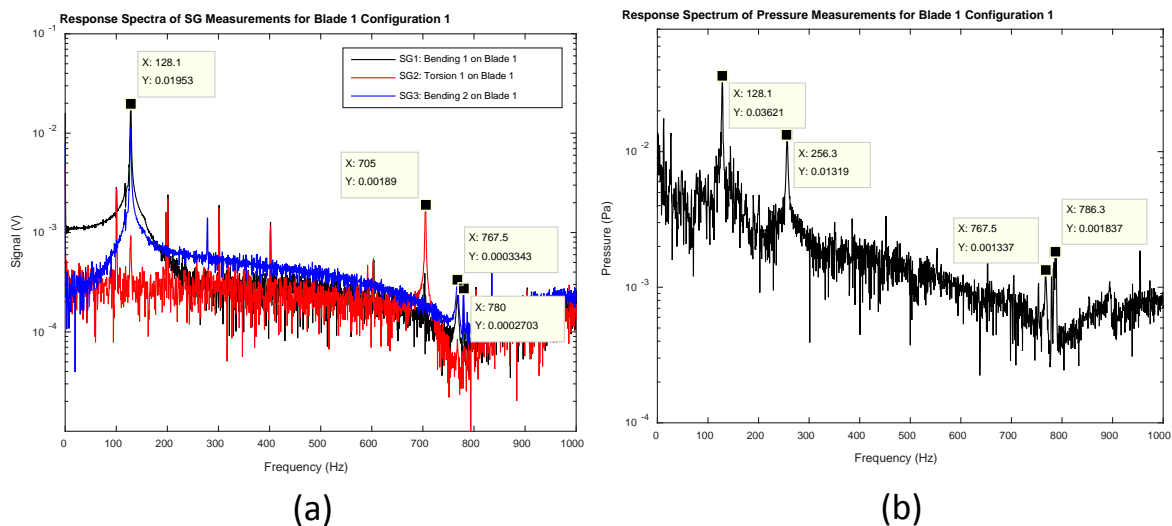


Figure 7.5-30 Response spectra for blade 1 config. 1. (a) SG Spectra. (b) Pressure spectrum.

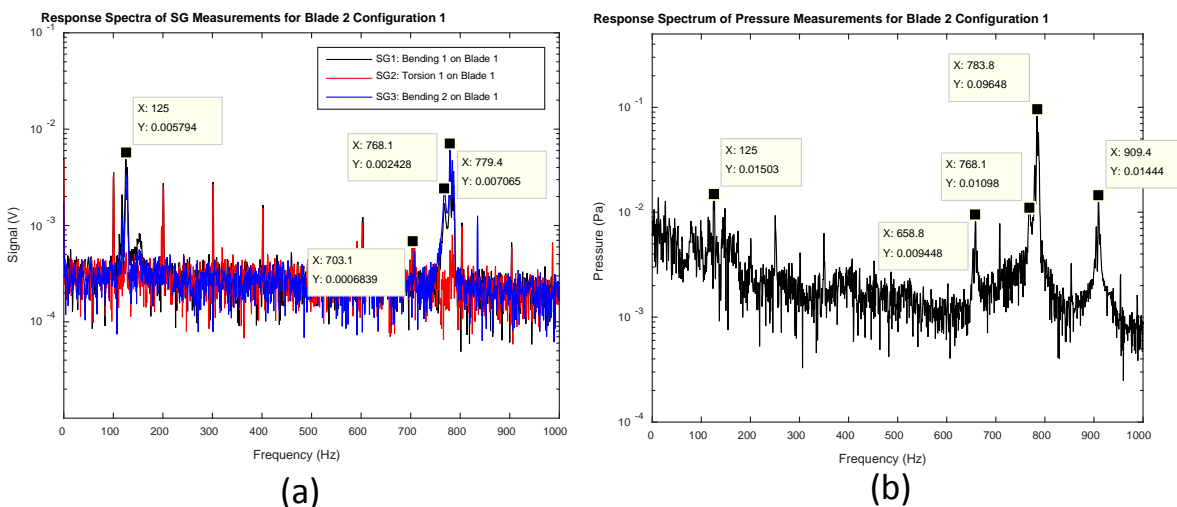
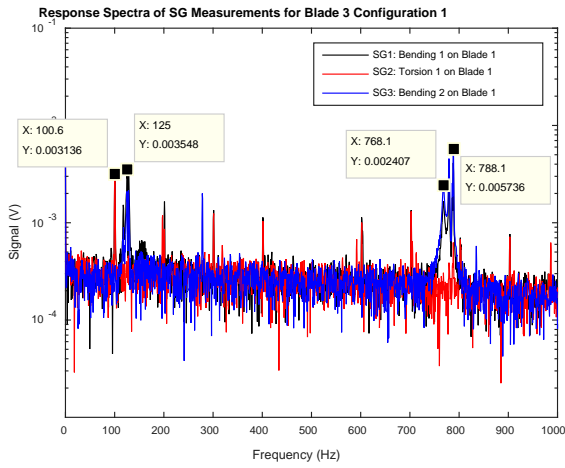
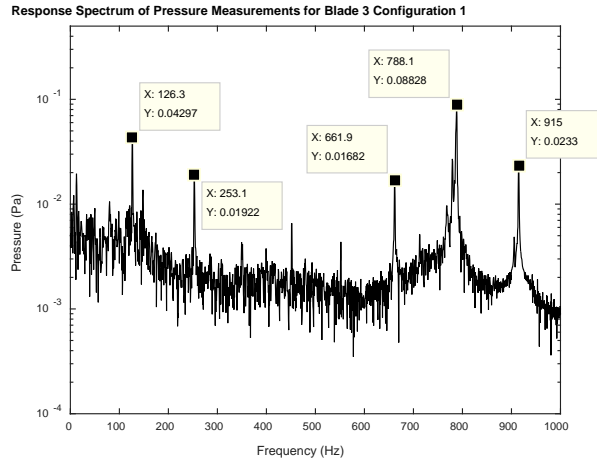


Figure 7.5-31 Response spectra for blade 2 config. 1. (a) SG Spectra. (b) Pressure spectrum.

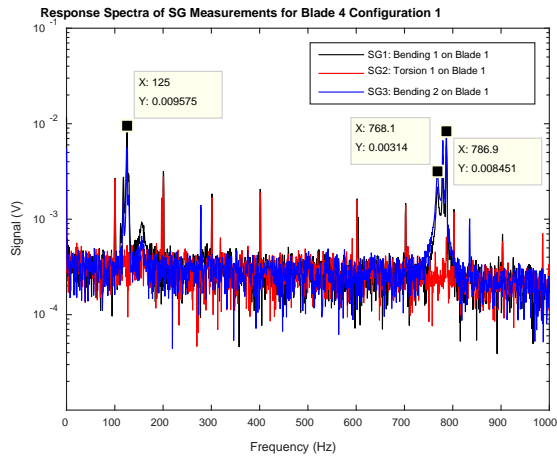


(a)

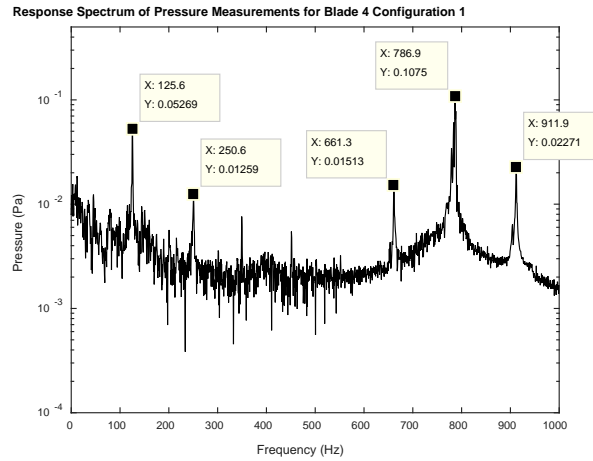


(b)

Figure 7.5-32 Response spectra for blade 3 config. 1. (a) SG Spectra. (b) Pressure spectrum.

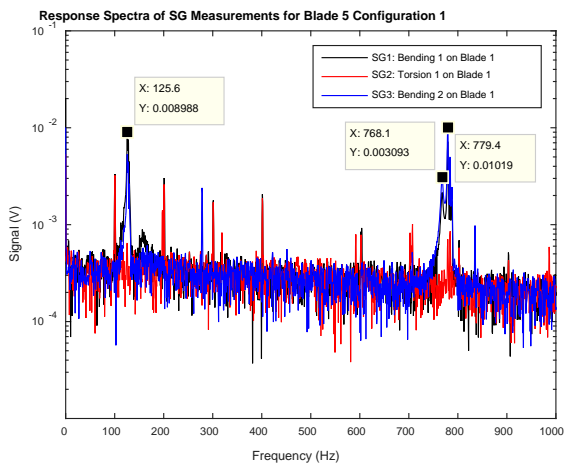


(a)

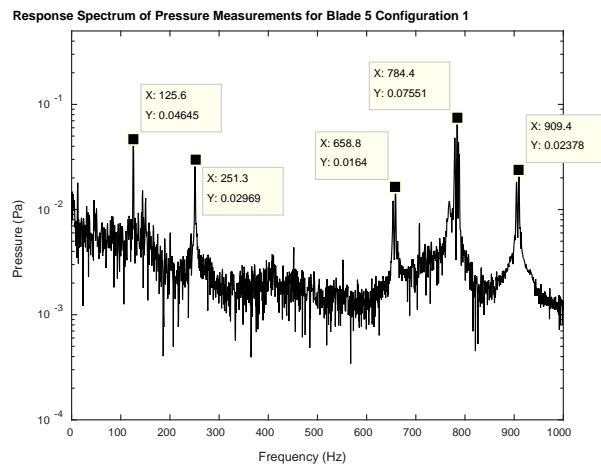


(b)

Figure 7.5-33 Response spectra for blade 4 config. 1. (a) SG Spectra. (b) Pressure spectrum.



(a)

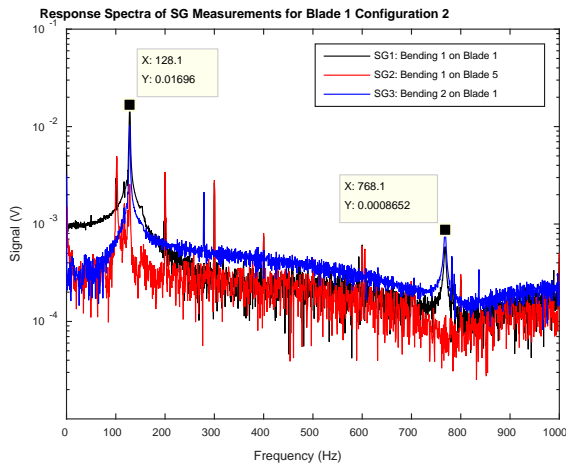


(b)

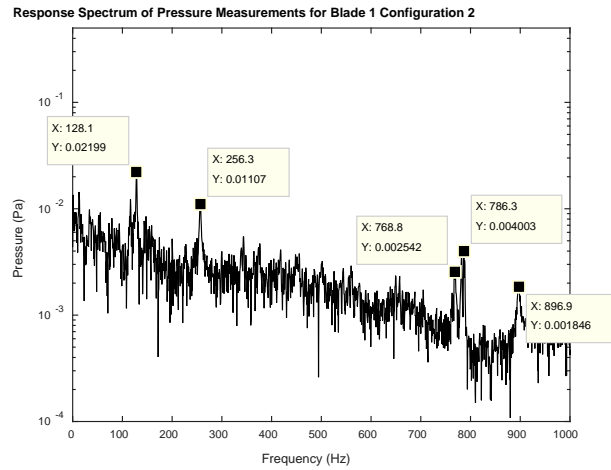
Figure 7.5-34 Response spectra for blade 5 config. 1. (a) SG Spectra. (b) Pressure spectrum.

7.5.6.2. Configuration 2

Three SGs were instrumented during hammer impact modal analysis of blade and hub configuration 2. Two SGs sensitive to mode 1 and 3 (bending modes 1 and 2) were recorded on blade 1. A SG present on blade 5 (sensitive to mode 1) was also recorded.

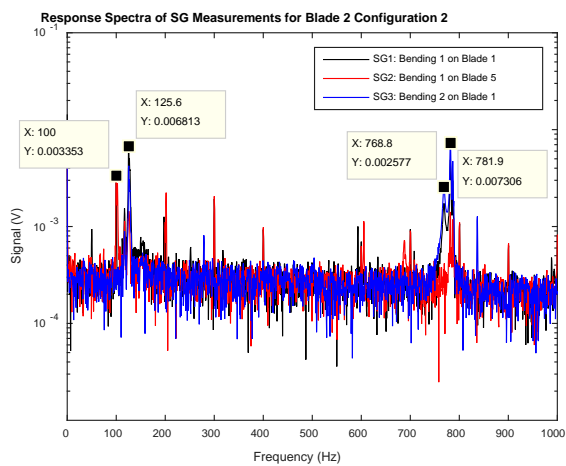


(a)

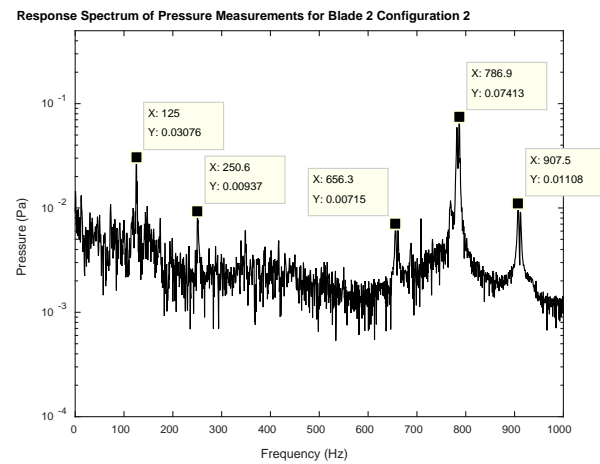


(b)

Figure 7.5-35 Response spectra for blade 1 config. 2. (a) SG Spectra. (b) Pressure spectrum.

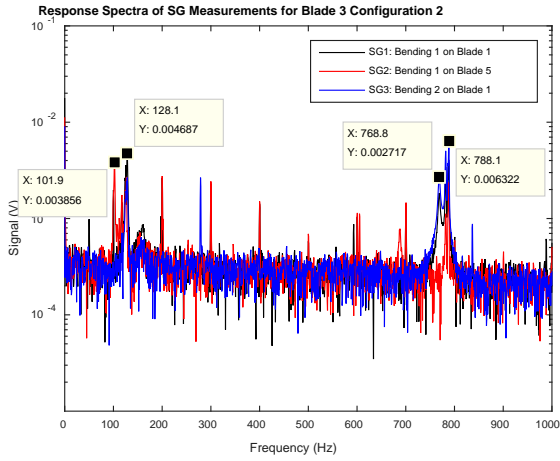


(a)

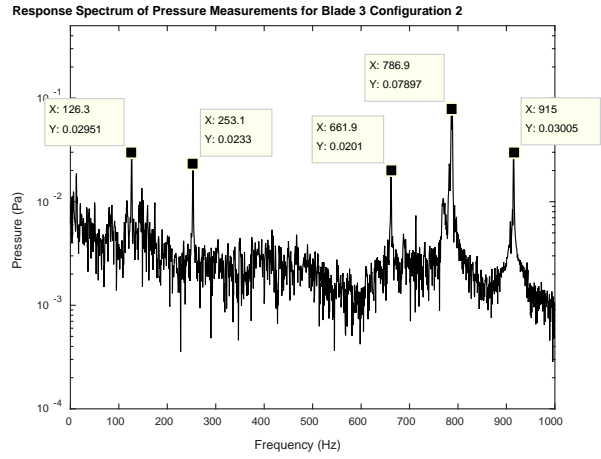


(b)

Figure 7.5-36 Response spectra for blade 2 config. 2. (a) SG Spectra. (b) Pressure spectrum.

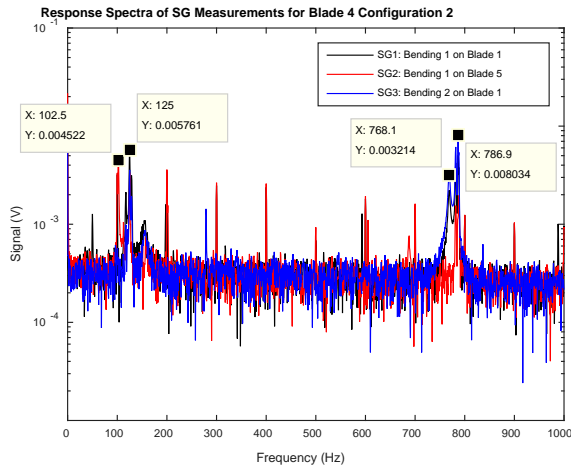


(a)

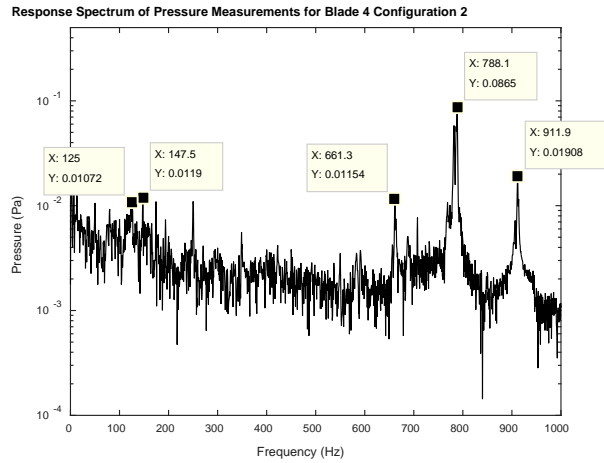


(b)

Figure 7.5-37 Response spectra for blade 3 config. 2. (a) SG Spectra. (b) Pressure spectrum.

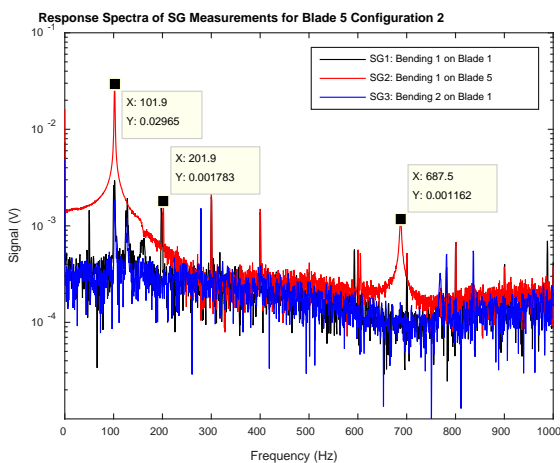


(a)

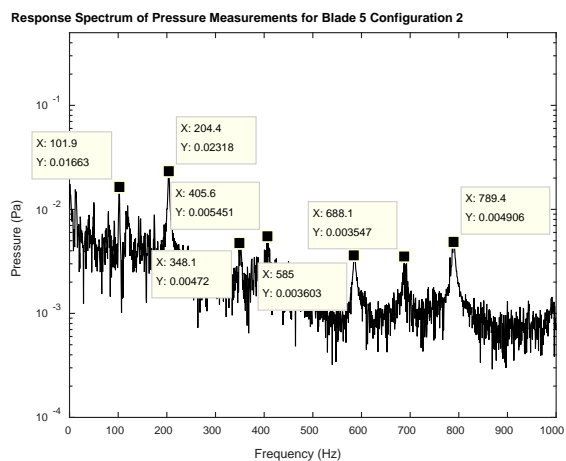


(b)

Figure 7.5-38 Response spectra for blade 4 config. 2. (a) SG Spectra. (b) Pressure spectrum.



(a)

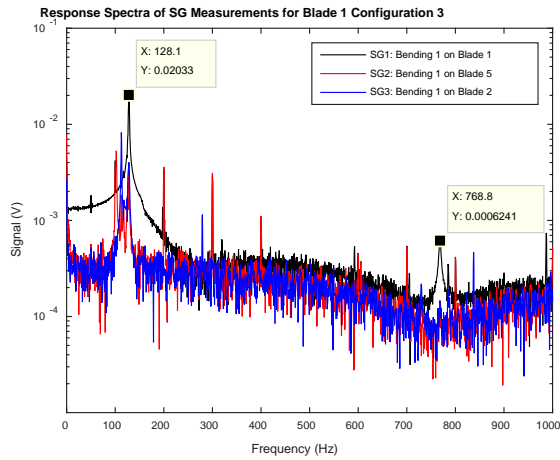


(b)

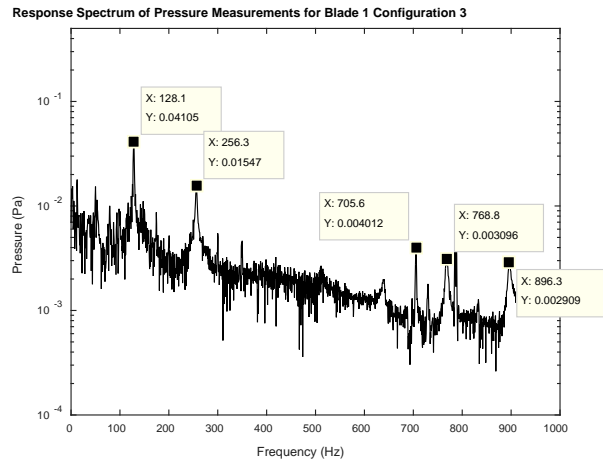
Figure 7.5-39 Response spectra for blade 5 config. 2. (a) SG Spectra. (b) Pressure spectrum.

7.5.6.3. Configuration 3

Three SG responses were used to generate response spectra during the investigation of configuration 3. The SGs were positioned on blades 1, 2 and 5.

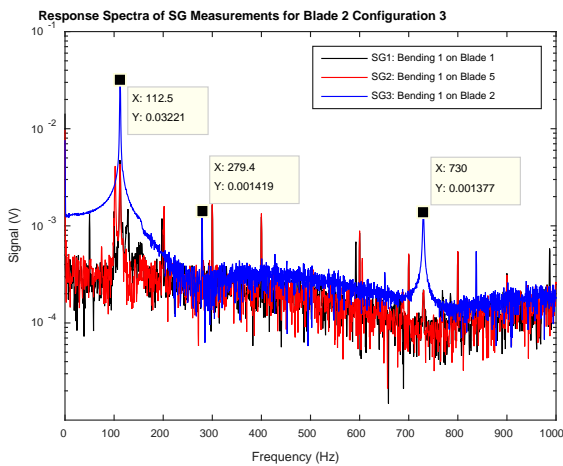


(a)

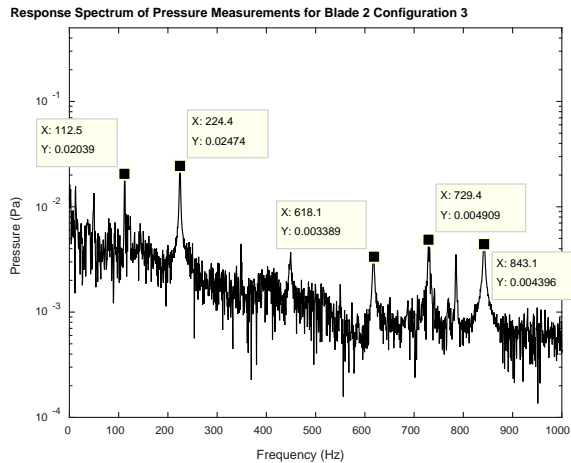


(b)

Figure 7.5-40 Response spectra for blade 1 config. 3. (a) SG Spectra. (b) Pressure spectrum.

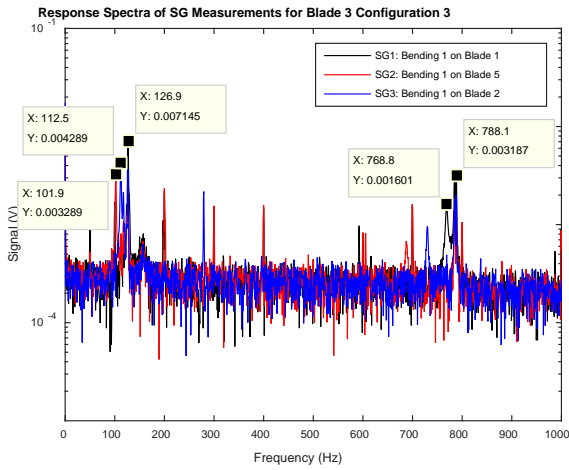


(a)

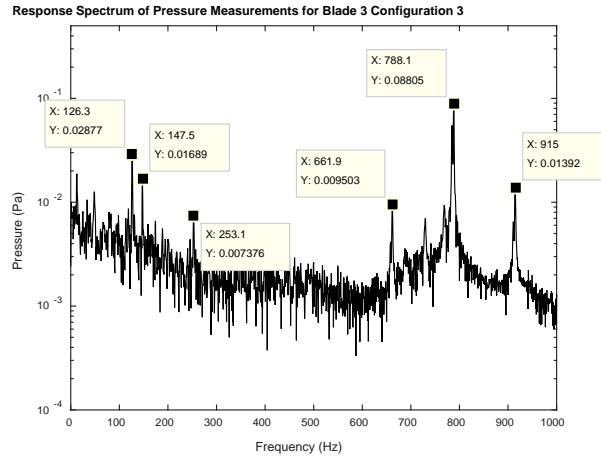


(b)

Figure 7.5-41 Response spectra for blade 2 config. 3. (a) SG Spectra. (b) Pressure spectrum.

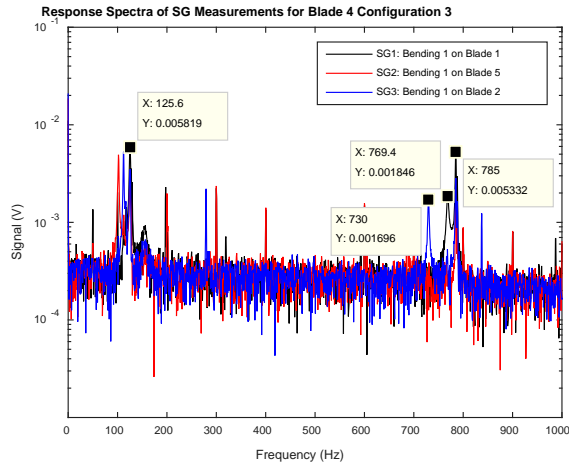


(a)

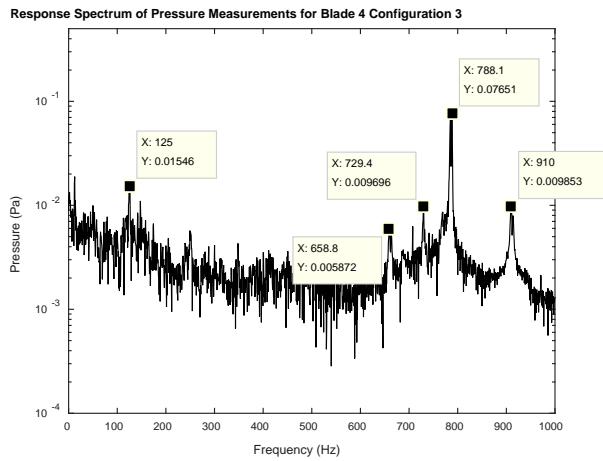


(b)

Figure 7.5-42 Response spectra for blade 3 config. 3. (a) SG Spectra. (b) Pressure spectrum.

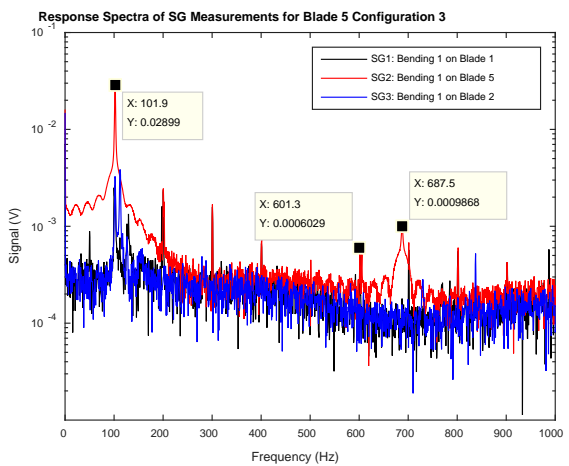


(a)

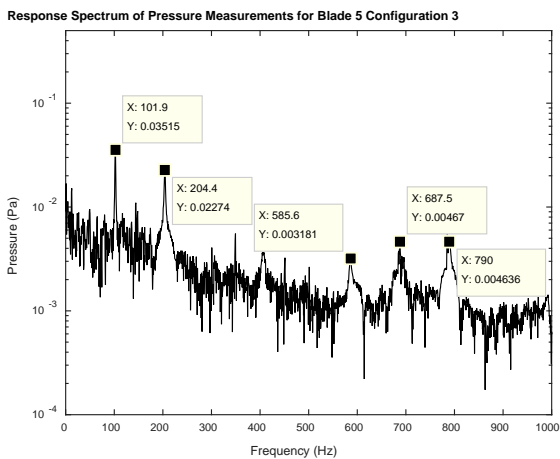


(b)

Figure 7.5-43 Response spectra for blade 4 config. 3. (a) SG Spectra. (b) Pressure spectrum.



(a)



(b)

Figure 7.5-44 Response spectra for blade 5 config. 3. (a) SG Spectra. (b) Pressure spectrum.

7.5.6.4. Configuration 4

Three SG responses were recorded during the investigation of configuration 4. A SG was present on blades 1, 2 and 5.

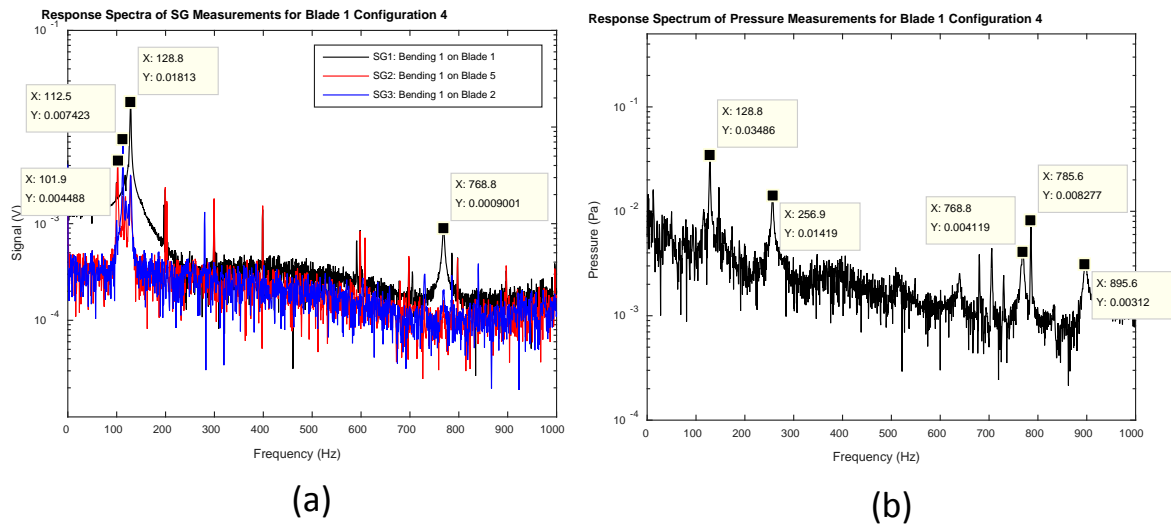


Figure 7.5-45 Response spectra for blade 1 config. 4. (a) SG Spectra. (b) Pressure spectrum.

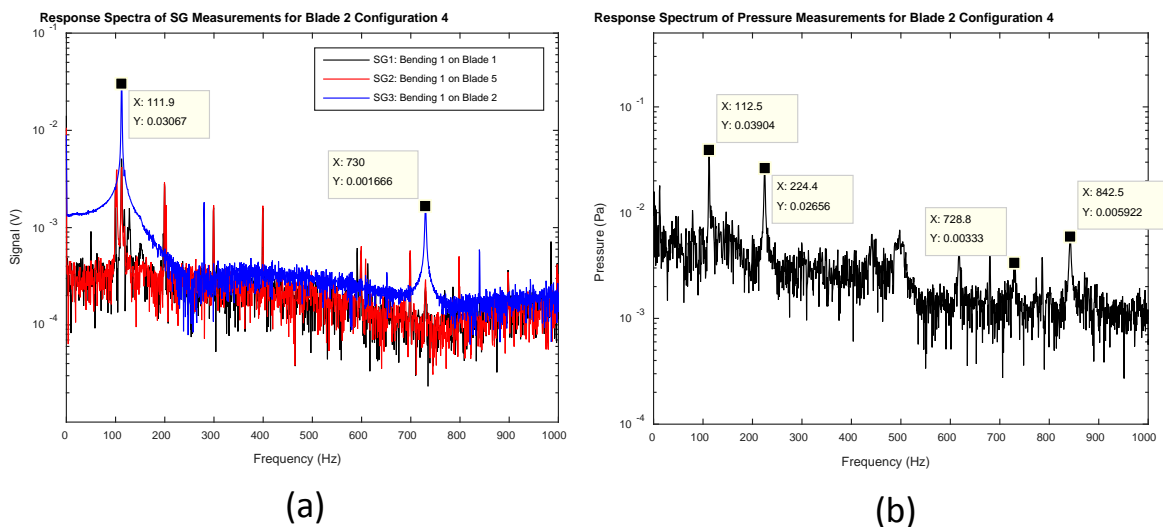
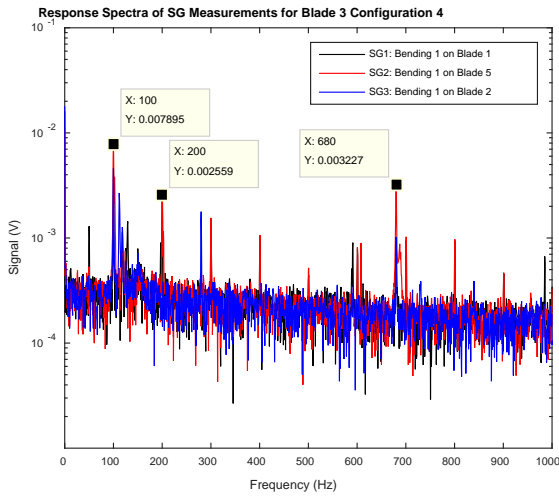
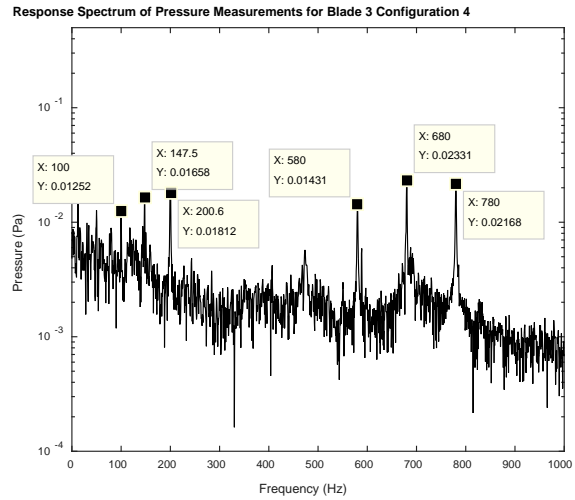


Figure 7.5-46 Response spectra for blade 2 config. 4. (a) SG Spectra. (b) Pressure spectrum.

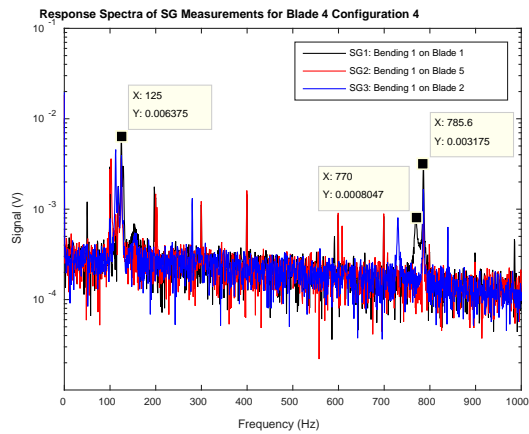


(a)

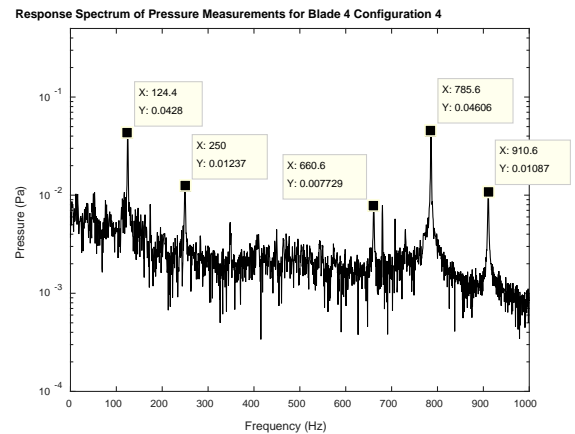


(b)

Figure 7.5-47 Response spectra for blade 3 config. 4. (a) SG Spectra. (b) Pressure spectrum.

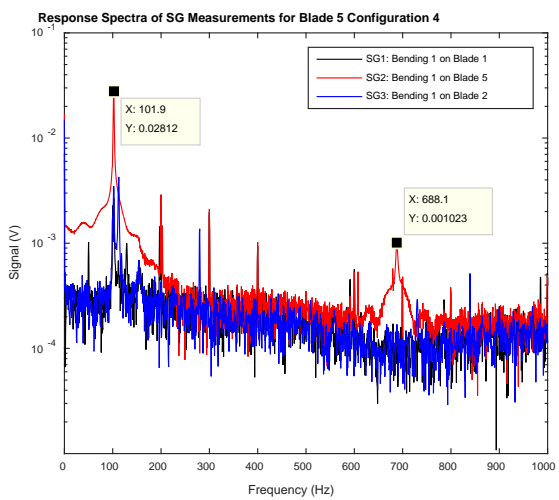


(a)

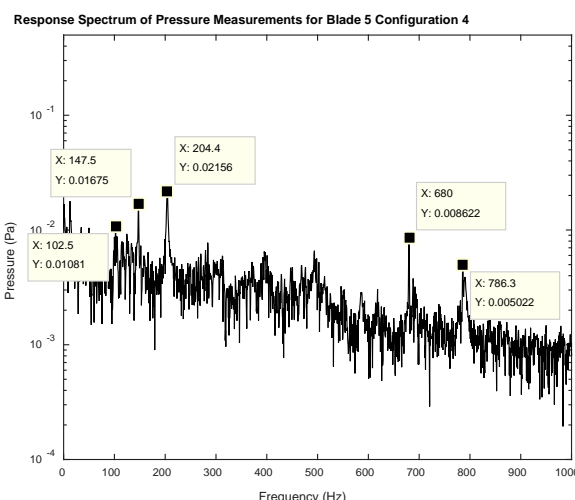


(b)

Figure 7.5-48 Response spectra for blade 4 config. 4. (a) SG Spectra. (b) Pressure spectrum.



(a)



(b)

Figure 7.5-49 Response spectra for blade 5 config. 4. (a) SG Spectra. (b) Pressure spectrum.

7.5.7. E7 – Run-Up Resonance Detection

Run-up investigations were only performed on the first three experimental configurations.

7.5.7.1. Configuration 1

SGs were applied to the surface of blade 1 in order to capture the response of the first three modes. The position of SG ‘Bending 1’ was optimised to capture blade 1’s first mode; the position of SG ‘Bending 2’ was optimised to capture blade 1’s third mode and finally SG ‘Torsional 1’ was optimised to capture blade 1’s second mode.

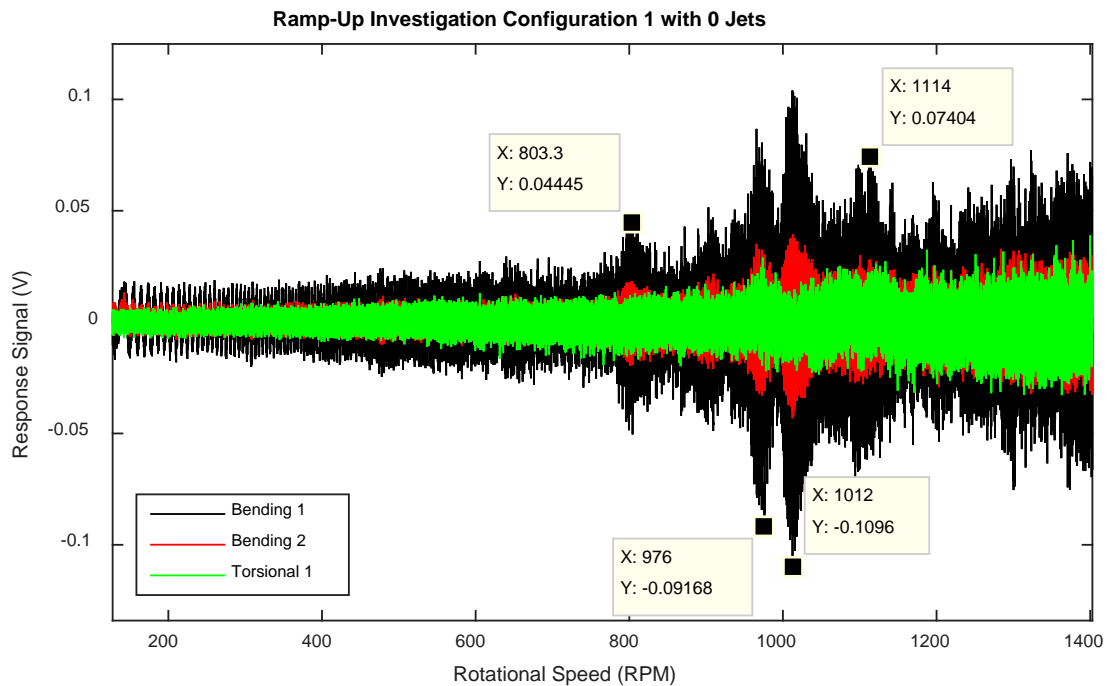


Figure 7.5-50 Ramp-up configuration 1 with 0 jets

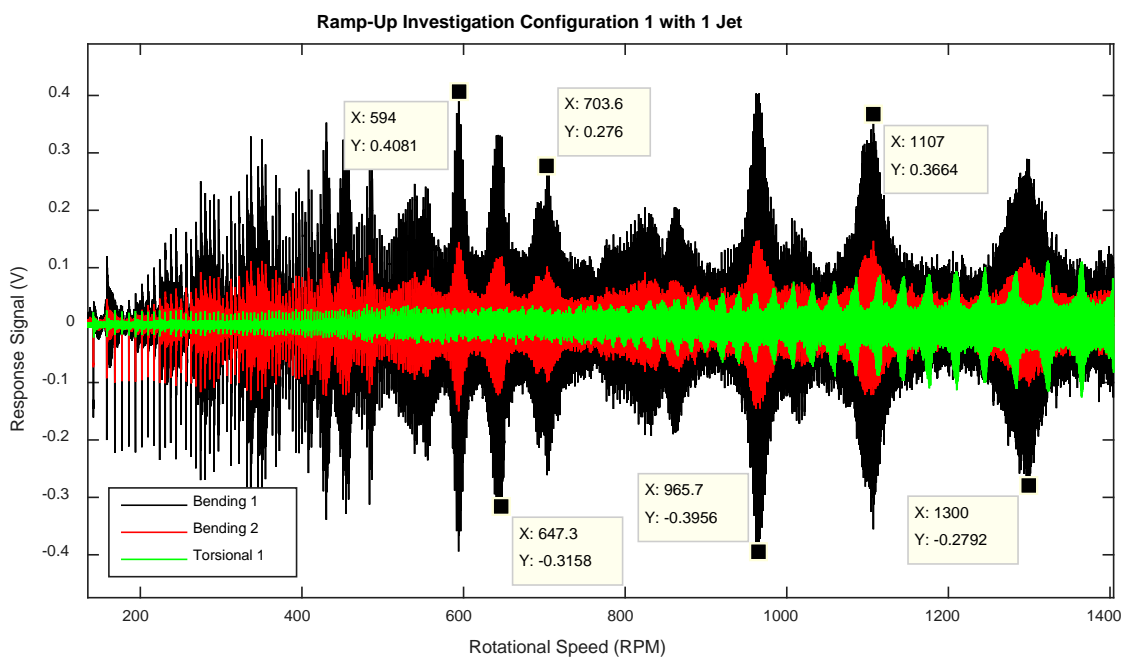


Figure 7.5-51 Ramp-up configuration 1 with 1 jet

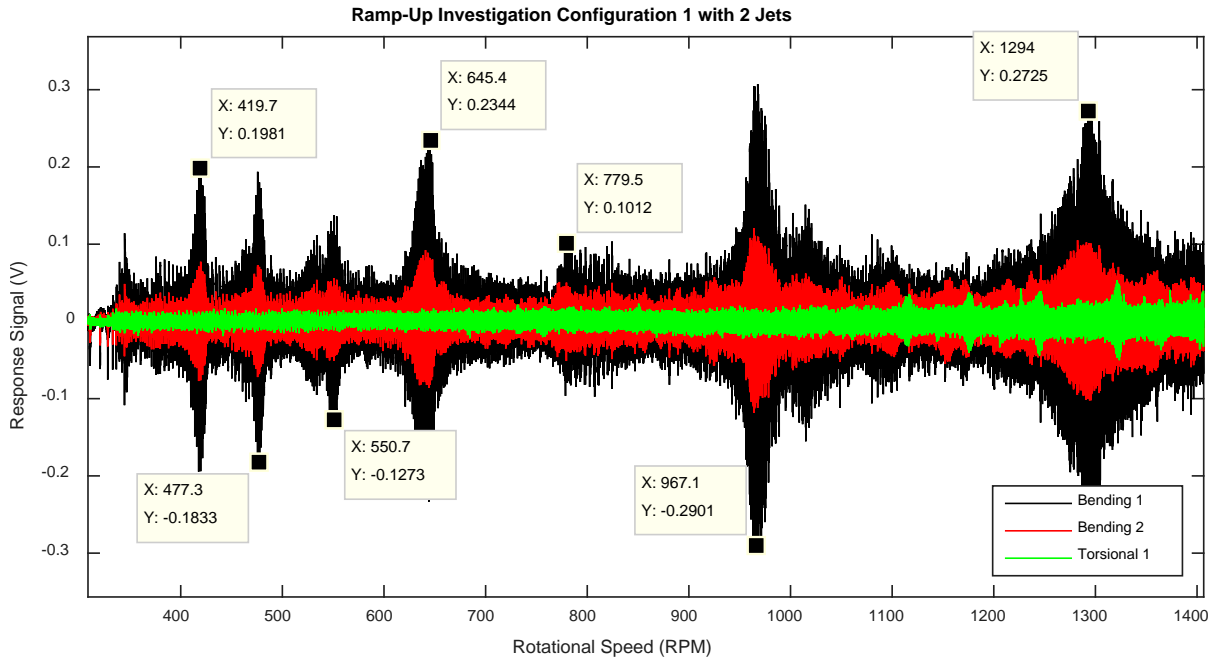


Figure 7.5-52 Ramp-up configuration 1 with 2 jets

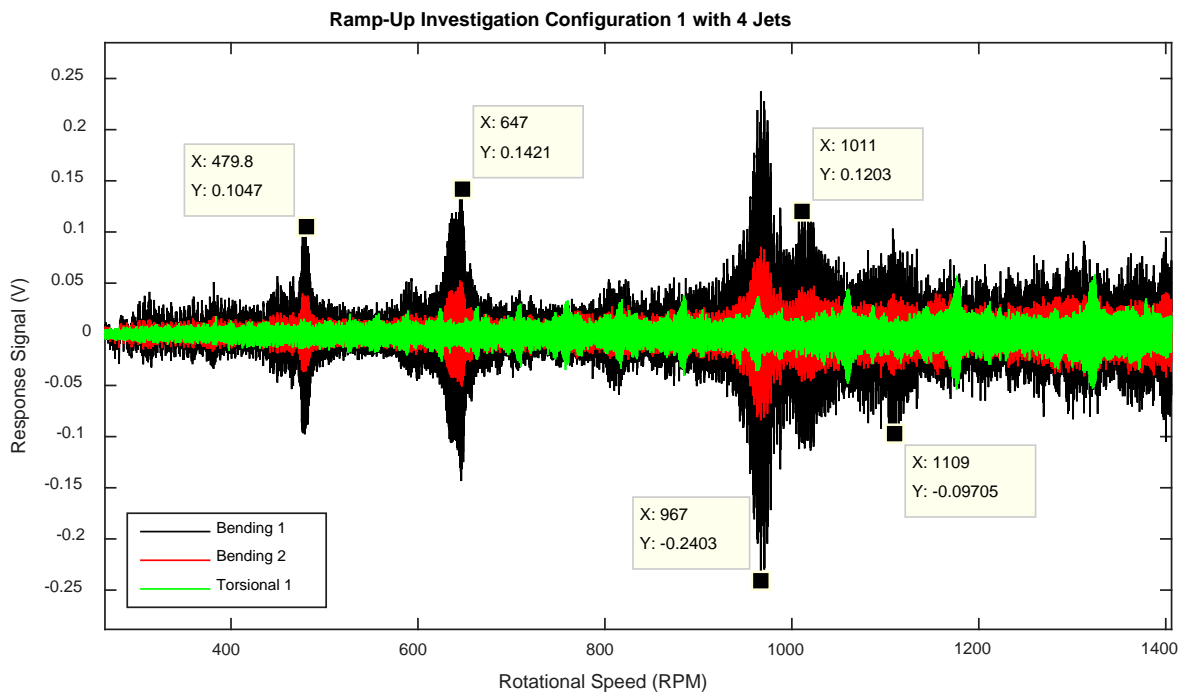


Figure 7.5-53 Ramp-up configuration 1 with 4 jets

7.5.7.2. Configuration 2

Two SGs were measured during the second run-up investigation. SG 'Blade 1' was optimised to capture the first mode of blade 1; similarly SG 'Blade 5' was optimised to capture the first mode of blade 5. Blade 5 is changed to 'damaged blade 1' in configuration 2.

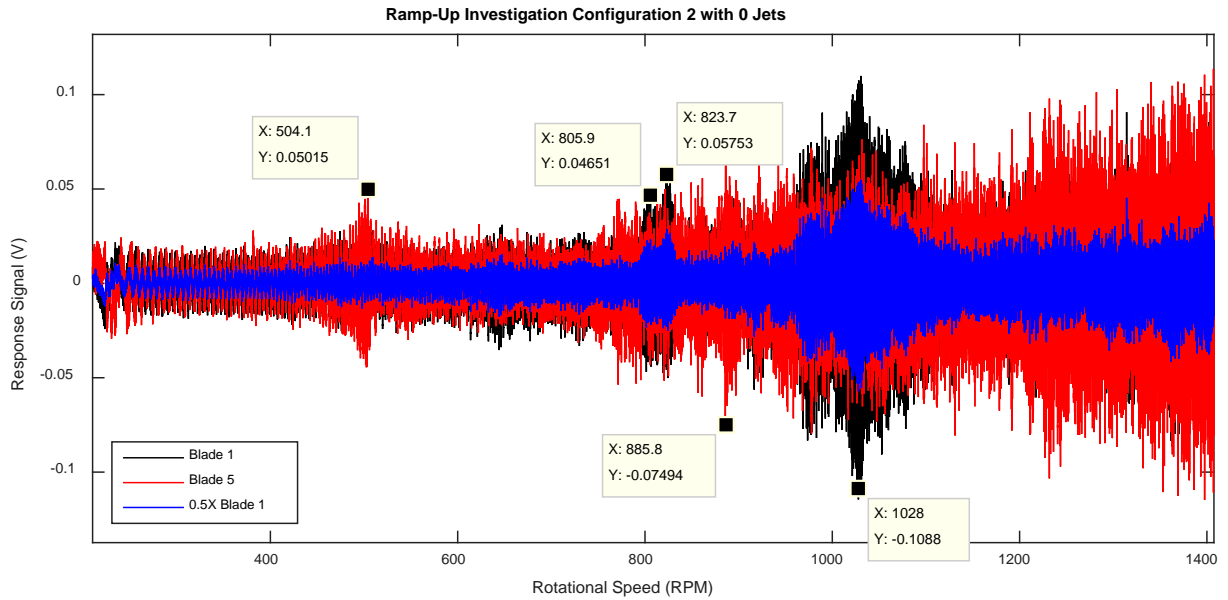


Figure 7.5-54 Ramp-up configuration 2 with 0 jets

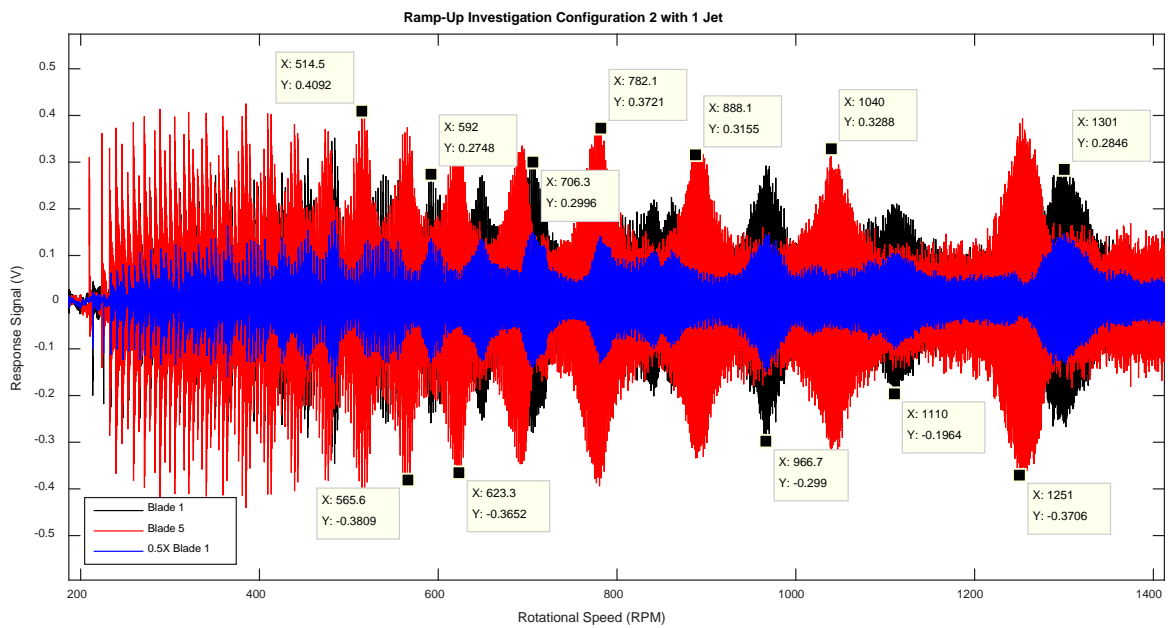


Figure 7.5-55 Ramp-up configuration 2 with 1 jet

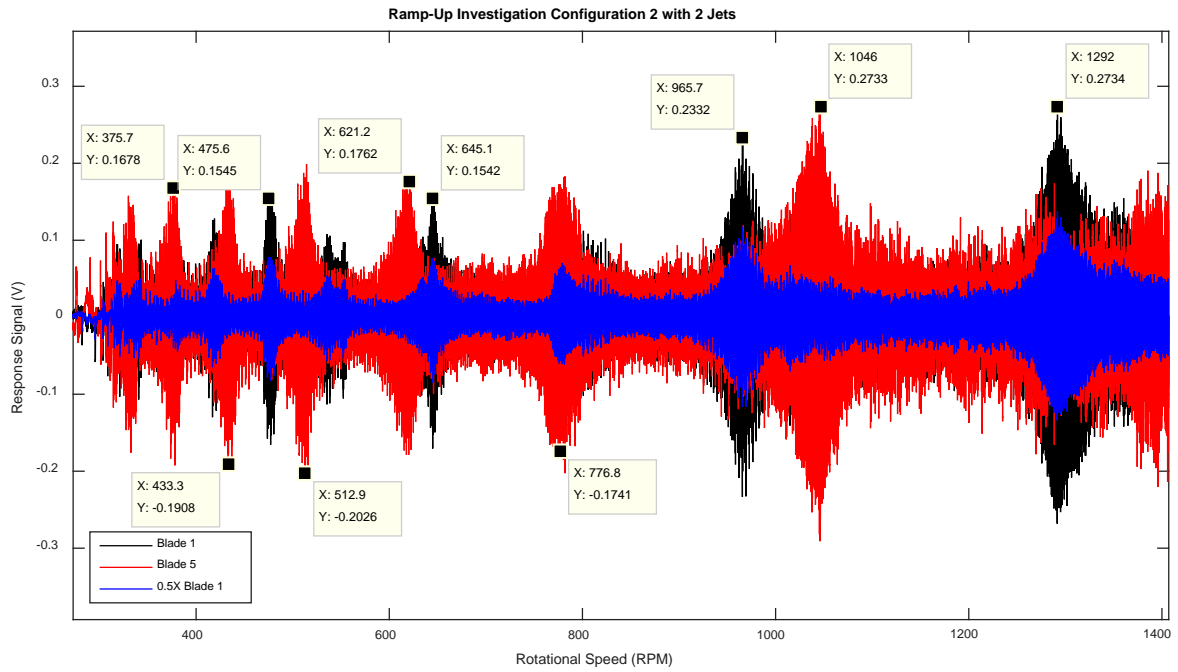


Figure 7.5-56 Ramp-up configuration 2 with 2 jets

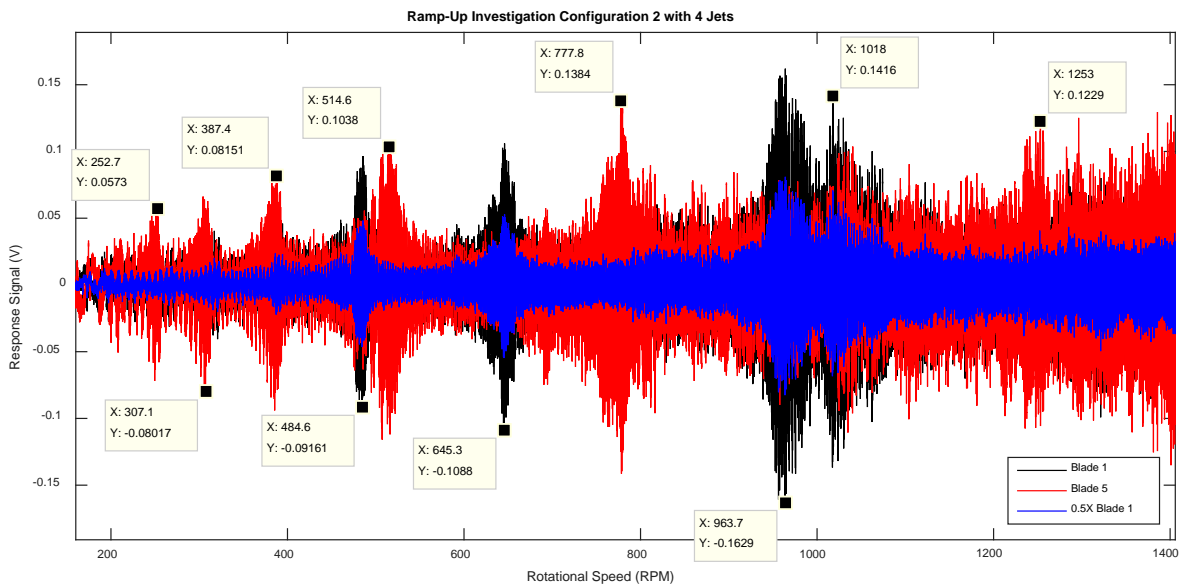


Figure 7.5-57 Ramp-up configuration 2 with 4 jets

7.5.7.3. Configuration 3

Three SG responses were measured during the third run-up investigation. SG 'Blade 1' was positioned to capture mode 1 on blade 1 (healthy blade); SG 'Blade 5' was positioned to capture mode 1 on blade 5 (damaged blade 1); and finally SG 'Blade 2' was positioned to capture mode 1 on blade 2 (damaged blade 2).

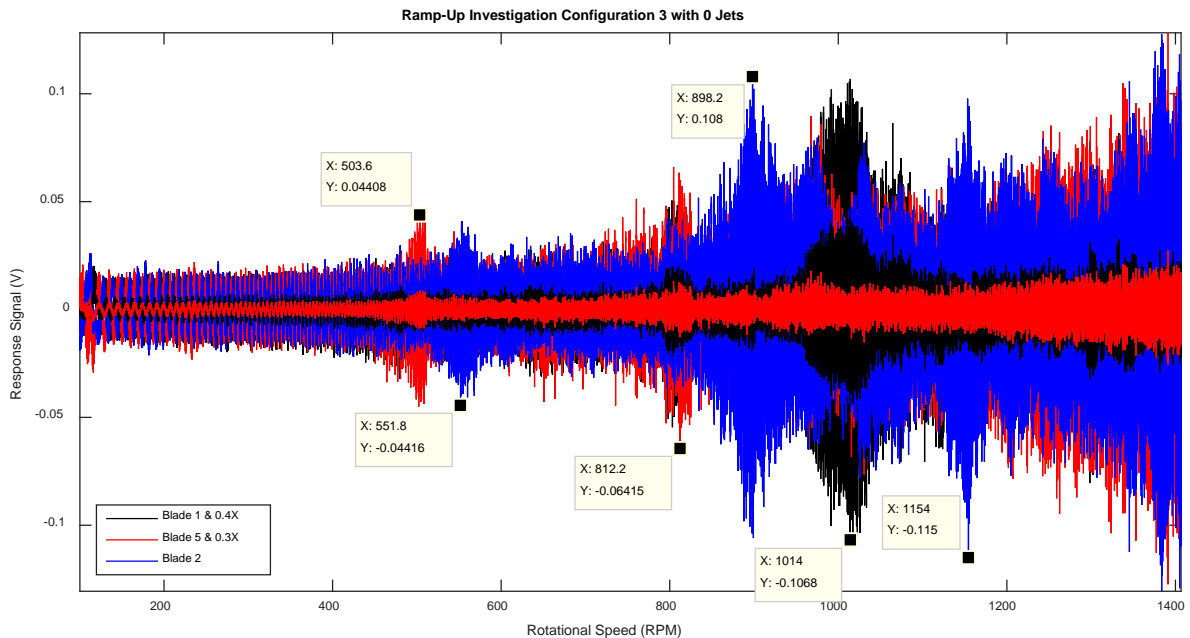


Figure 7.5-58 Ramp-up configuration 3 with 0 jets

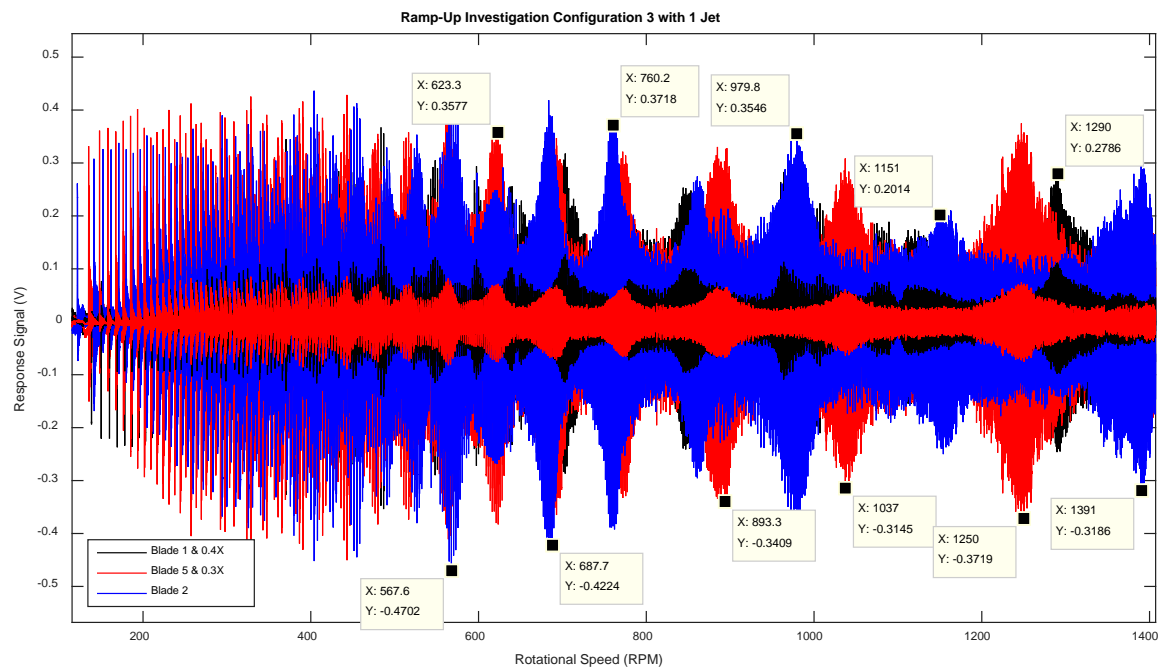


Figure 7.5-59 Ramp-up configuration 3 with 1 jet

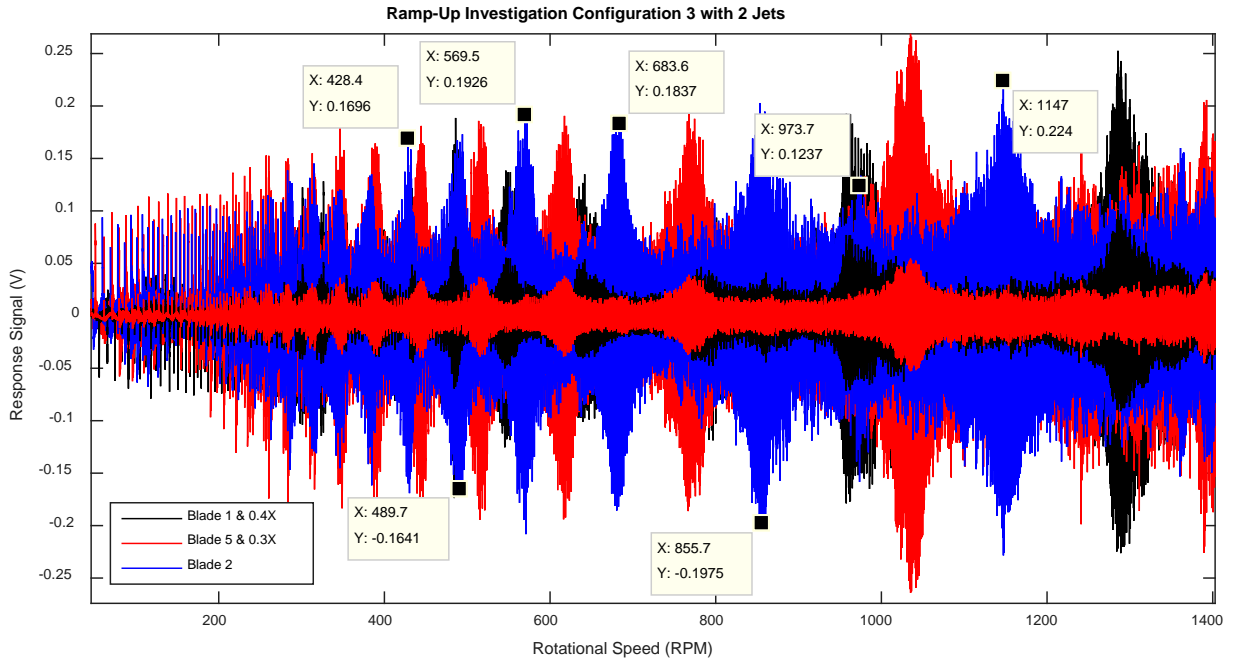


Figure 7.5-60 Ramp-up configuration 3 with 2 jets

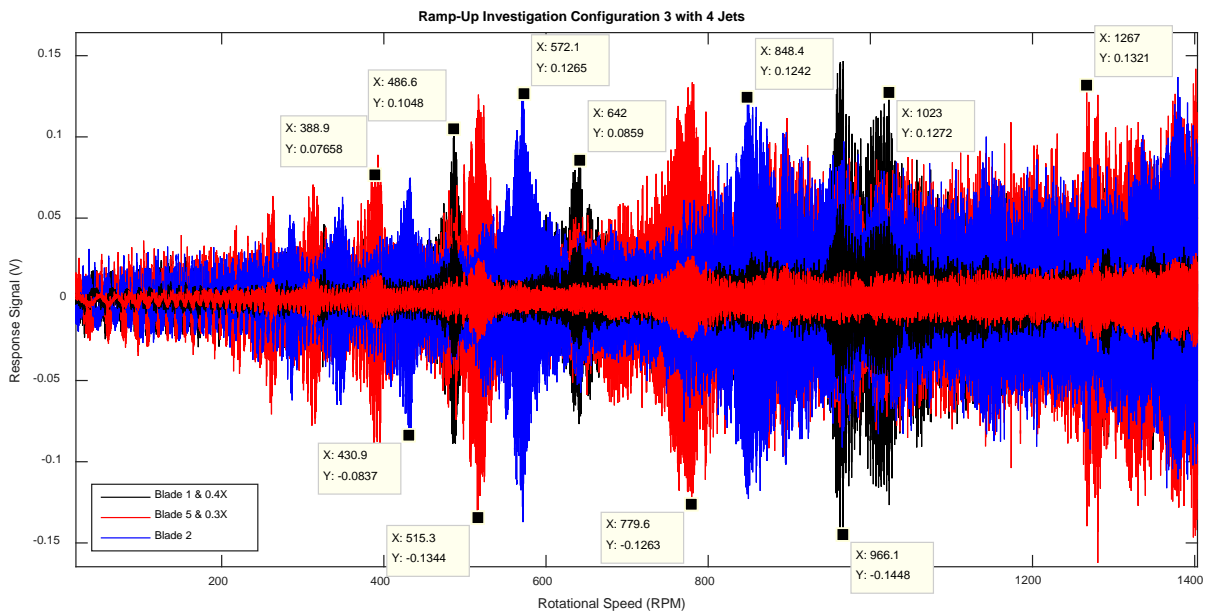


Figure 7.5-61 Ramp-up configuration 3 with 4 jets

7.5.8. E8 – Signal Processing Methodology

Various signal processing (SP) techniques were used to transform the measured data into different forms for later analysis. The first signal processing steps are outlined in Figure 7.5-62.

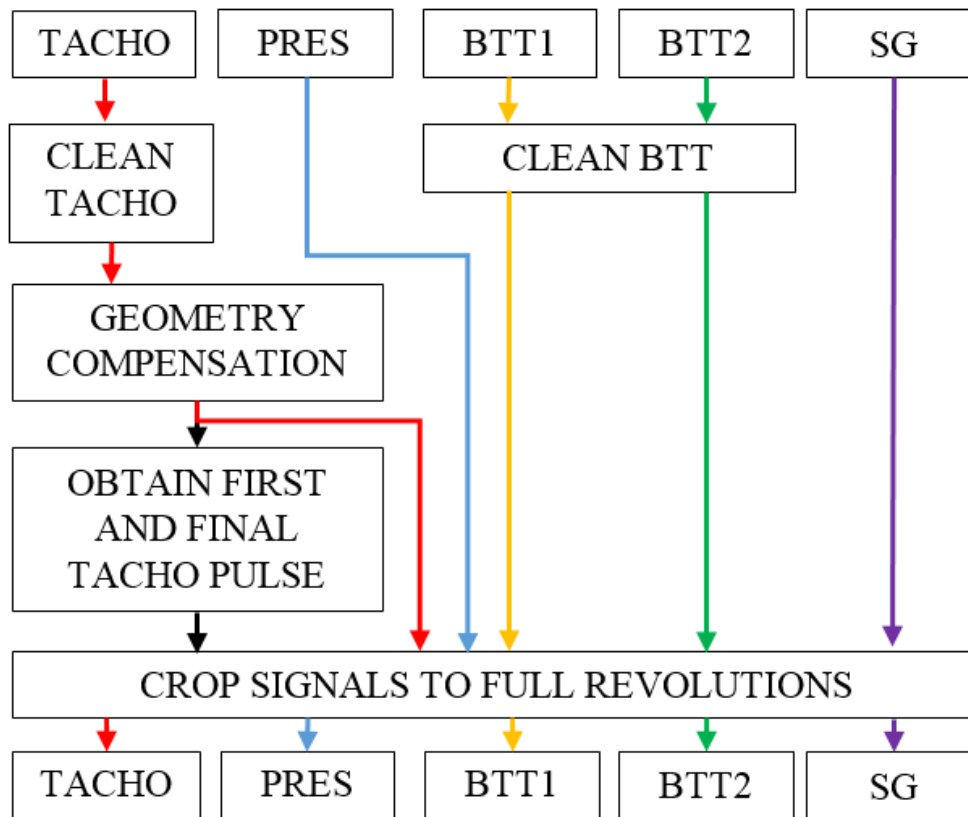


Figure 7.5-62 Tachometer compensation and signal cropping

The signals TACHO, PRES, BTT 1, BTT2 and SG refer to the measured tachometer, pressure, eddy current proximity probes 1 and 2, and the strain gauge (SG) signals respectively. All signals undergo an analogue to digital conversion during measurement by the data acquisition (DAQ) system.

The tachometer and eddy current probe measurements were for reference and SP purposes. They required pre-processing in order to convert them from noisy voltage recordings to individual tachometer and blade passing times. These processes are designated 'CLEAN' in the flow chart.

The tachometer signal required geometry compensation because it was captured using an optical sensor and zebra tape arrangement. Compensation was achieved by using the algorithm developed by Resor et al. (Resor et al., 2005). The compensation algorithm is provided in section '7.1.4 A4 – Shaft Encoder Geometry Compensation Algorithm'.

Finally all of the time domain signals were then be cropped to full revolutions using the tachometer pulse times and number of pulses per revolution (PPR). Everything before the first pulse and after the final once per revolution (OPR) pulse was deleted from each signal. The sampling frequency and cropped signal length could then be used to generate a time signal.

No further SP was required on the SG signal, therefore the SG and time signals were then passed through a fast Fourier transform (FFT) algorithm in order to obtain the SG frequency response spectrum.

The following SP steps are outlined in Figure 7.5-63.

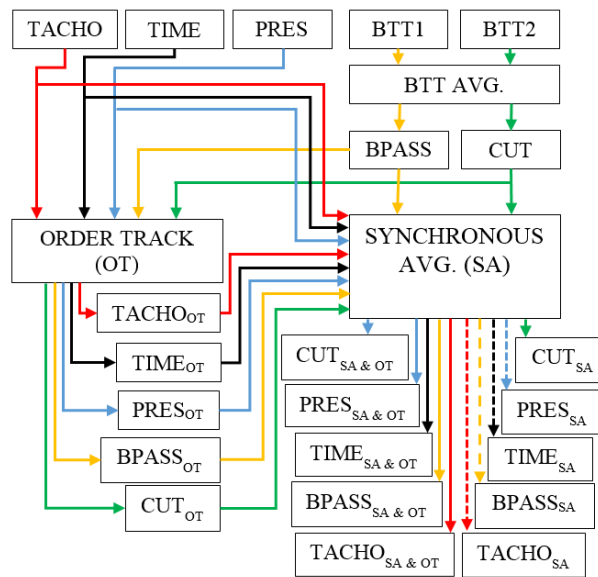


Figure 7.5-63 BTT averaging, order tracking and synchronous averaging processes

The first SP step shown in the diagram was to estimate the times at which the blades pass the microphone (BPASS) and the times centered between the blades passing times (CUT). Assuming that the leading edge of the blade tip was captured by sensor BTT 1 and the lagging edge was captured by sensor BTT 2, the blade passing estimates and cut estimates could be obtained by using Equations [7.5.1] and [7.5.2] respectively. In the equations BTT_1 is a vector which contains the times at which the blades pass sensor BTT 1 and similarly BTT_2 is a vector containing the times at which the blades pass sensor BTT 2. These times are obtained in the SP step labelled 'BTT AVG'.

$$BPASS = \frac{BTT_1 + BTT_2}{2} \quad [7.5.1]$$

$$CUT_n = \frac{BPASS_{n+1} + BPASS_n}{2} \quad [7.5.2]$$

The vector lengths were the same as the signals were cropped to full revolutions only using the common tachometer signal. Further, for each revolution the individual blades passed sensors BTT 1 and BTT 2 only once.

The tachometer signal was used to order track (OT) the pressure, blade passing and cut signals. The OT process supplies linearly resampled signals (with a certain number of chosen samples per revolution). Similarly the tachometer signal was used to synchronously average (SA) the pressure, blade passing and cut signals.

The synchronous averaging process supplies the average signal form for a single revolution, averaged over all revolutions. The OT signals were also synchronously averaged. Due to the OT process there were a specific number of sample points per revolution making the synchronous averaging process simple to implement. The results of this step are two data sets, one set contains OT and synchronously averaged data (OT & SA) and the second which only contains synchronously averaged data (SA).

In a separate step the eddy current signals, BTT 1 and BTT 2, were compared with stationary eddy current measurements in order to identify the blade passing order (used to differentiate between the individual blades given a particular assembly configuration). This process is outlined in Figure 7.5-64.

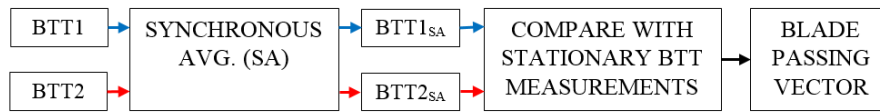


Figure 7.5-64 Blade passing order

The BTT signals obtained after the cropping process were used. There after the synchronous averaging process was used to obtain a robust estimate of the measured eddy current voltages over a single revolution. The voltage peaks were related to individual passing blades, the synchronous averaging process supplied average passing peaks which could be isolated. These peak measurements were then compared to the stationary eddy current measurements. The stationary eddy current measurements are available in section '7.5.4 E4 – Relative Tip Distances'. Finally the order in which the blades pass the microphone, for each individual measurement, could be inferred via the comparison.

The synchronously averaged pressure signals could then be used to obtain the stochastic signal, this process is outlined in Figure 7.5-65. This was done for both the order tracked and SA & OT data.

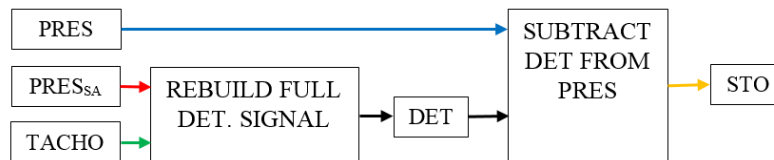


Figure 7.5-65 Process to obtain stochastic signal

First each tachometer signal was used to rebuild a full time length synchronously averaged signal. The tachometer signal provided the actual data lengths for each revolution and so the synchronously averaged data could simply be stretched according to the revolution data length by means of an interpolation algorithm. The full time length synchronously averaged signal was termed the deterministic signal (DET in the diagram). Obtaining the stochastic signal (STO in the diagram) was a simple subtraction of the deterministic signal from the full pressure signal. Once again this process is performed on both data sets, namely the OT & SA data set as well as the SA data set.

The blade passing (BPASS) and cut (CUT) times could then be used to split the data sets into signals about individual blades. It was also used to provide as signal sets isolated ahead of the moving blades (HP blade side) and behind the moving blades (LP blade side) (once again assuming that the turbomachine is operating as a compressor and not a turbine).

As the blade tips passed the microphone the pressure ahead of each blade tip was captured first followed by the pressure behind each individual blade tip. The splitting process utilised the sigmoidal windowing process outlined in the theoretical development in order to split the signal.

When viewed in the time domain there was a pressure drop associated with each blade passing the microphone because the system was operating as a compressor. With time running from left to right on the ordinate axis, and signal windowing boundaries located at the estimated blade passing times, the signal to the left (in the time domain) of the blade passing times were associated with the HP signal portion (for each passing blade). Similarly the signals to the right of the blade passing times were

associated with the LP signal portion (for each passing blade). Thus these halves of the individual blade passing waves were termed the left and right sides ('LEFT' and 'RIGHT' in the diagram). The splitting procedure is provided in Figure 7.5-66.

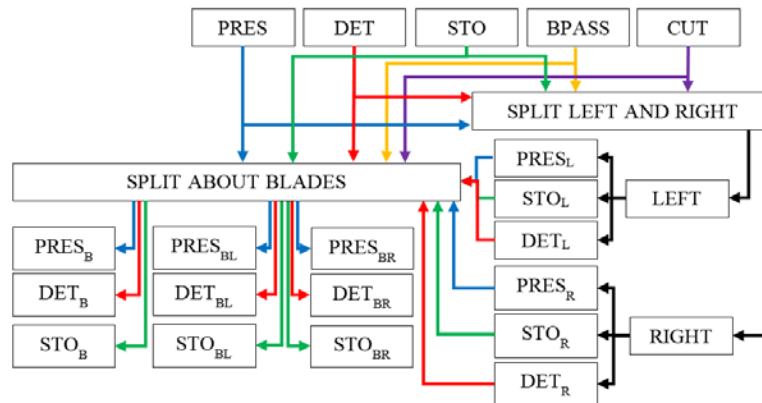


Figure 7.5-66 Splitting procedure

In the diagram the signals split about individual blades are differentiated with the subscript 'B'. Similarly signals split into the left and right halves have subscripts 'L' and 'R' respectively. The subscripts 'BL' and 'BR' refer to data sets obtained for individual blade passing waves which have been split into left and right halves about the blade passing times.

A total of 30 additional data sets were created using this process, 15 from the OT & SA data as well as 15 from the SA data. The splitting procedure was also performed on the synchronously averaged data (average waveform over an individual revolution) in order to find the average individual blade passing waveform. Once again the sigmoidal windowing function was used to perform this operation.

Given the order in which the blades pass the microphone, from a previous step, it was possible to reorder the data such that blade 1 always passes the microphone first in the data set. The first SP step ensure that only full revolutions of data were present in the signal from the cropping process. In this way datasets from different measurements could be directly compared, blade for blade, as the modal behaviour of each individual blades was known from the experimental characterisation. This reordering process has not been shown.

The final SP procedure is spectral analysis and ensemble averaging of the spectra. This process had to account for the effective frequency range given the measurement instrumentation (3 Hz to 51.2 kHz). This process is outlined in Figure 7.5-67.

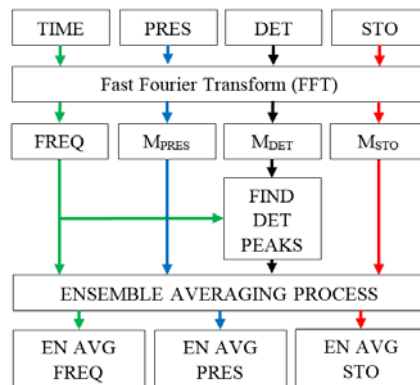


Figure 7.5-67 Fourier transform and ensemble averaging process



All signals, separated and not, were moved into the frequency domain via the fast Fourier transform (FFT). The locations of the deterministic peaks were then obtained in order to perform the ensemble averaging process on the different signals. It is about these deterministic peaks that the signals can be averaged in the frequency domain using the procedure developed by Forbes et al. (Forbes and Randall, 2013). This resulted in full pressure and stochastic pressure ensemble averages, from both OT and non-OT sets, which can be compared for different measurements.

A summary of the main signal processes performed on the measured signals is provided here:

1. Measure/Simulate casing pressure signal (CPS) along with associated tachometer, BTT signals and SG signals
2. Perform geometry compensation on the tachometer signal
3. Crop all time domain signals to full revolutions only
4. Perform FFT on SG signal
5. Determine blade passing and cut time locations
6. Find blade passing order
7. Order track all signals
8. Synchronously average all signals (both order tracked and not)
9. Build full length deterministic signals from synchronously averaged signals
10. Subtract deterministic signal from full pressure signal to obtain stochastic signals
11. Split CPS signals using the sigmoidal windowing function
 - a. Into left and right halves
 - b. About individual blades
 - c. About individual blades and into left and right halves for each blade
12. Perform FFT on pressure, deterministic and stochastic signals
13. Find deterministic peaks from deterministic frequency response spectra
14. Use deterministic peaks to ensemble average pressure and stochastic signals
15. Repeat steps 1 through 14 for all measurements
16. Generate ensemble average waterfall plots from all ensemble averages

Due to multiple measurements being taken at a range of operational speeds the spectra and ensemble averages from different speeds can be combined into waterfall plots. Trends in the data may be found using this technique. All the signal processes outlined provide a range of time and frequency domain information which can be evaluated and compared.

The SP also supplies various derived signals which can be used in the experimental evaluation of the inverse problem. It is important to note that not all of the SP results will be investigated or commented on, the procedure was simply followed in order to provide a library of different signals from raw measurements.



7.6. Appendix F – Steady Measurement Plan

The following tables contain the experimental measurement plans for configurations 1 through 4. Measurement speeds were chosen at and about resonance of interest. The resonance speeds were experimentally estimated using run-up investigations (see previous appendix). The resonance speeds, obtained from individual blades have been designated **H** for the healthy blade (blade 1 config. 1), **D1** for damaged blade type 1 (blade 5 config 2) and **D2** for damaged blade type 2 (blade 2 config 3).

Table 7.6-1 Steady measurement plan for blade and hub assembly configuration 1

Number of Jets	Observation Speed (RPM)	EO	Notes
0	200, 800	N/A	Reference
1	574, 584, 589, 594* , 599, 604, 614.	13	
1	623, 633, 638, 643* , 648, 653, 663.	12	
1	948, 955, 961, 966* , 971, 975, 976, 986.	8	
2	626, 635, 641, 646* , 651, 656, 666.	6	
2	948, 957, 963, 968* , 973, 978, 988.	4	
4	627, 637, 642, 647* , 652, 657, 667.	3	
4	947, 957, 962, 967* , 972, 977, 987.	2	

*Resonance speed of H.

Table 7.6-2 Steady measurement plan for blade and hub assembly configuration 2

Number of Jets	Observation Speed (RPM)	Notes
0	200, 800	Reference
1	593* , 608, 622# , 635, 648* , 670, 692# , 698, 704* , 742, 760, 780# , 800, 837, 893# , 929, 964* , 1003, 1042# , 1075, 1107* , 1181, 1255*# , 1278, 1301* .	
2	618# , 632, 645* , 712, 758, 778*# , 798, 872, 965* , 1006, 1046# , 1169, 1292* .	
4	387# , 436, 485* , 500, 515# , 580, 645* , 712, 778# , 870, 962* , 996, 1030.	

*Resonance speed of blade H. # Resonance speed for blade D1.

Table 7.6-3 Steady measurement plan for blade and hub assembly configuration 3

Number of Jets	Observation Speed (RPM)	Notes
0	200, 800	Reference
1	566# , 599, 622#~ , 643, 692# , 771, 861*~ , 962* , 980~ , 1037# , 1153~ , 1247, 1290*~ .	
2	572~ , 617# , 682~ , 769, 858~ , 961* , 1037, 1149~ , 1289* .	
4	486* , 519, 571~ , 638, 781# , 849~ , 897, 962* , 1014.	

*Resonance speed of blade H. # Resonance speed for blade D1. ~Resonance speed for blade D2.

Table 7.6-4 Steady measurement plan for blade and hub assembly configuration 4

Number of Jets	Observation Speed (RPM)	Notes
0	200, 800	Reference
1	454, 515, 568# , 594* , 621#~ , 641, 684~ , 761~ , 779# , 961* , 1103* ,	
2	512# , 570~ , 618# , 642* , 857~ , 965* , 1042# , 1148~ , 1295* .	
4	384# , 431~ , 479* , 516# , 572~ , 647* , 779# , 850~ , 968* .	

*Resonance speed of blade H. # Resonance speed for blade D1. ~Resonance speed for blade D2.

7.7. Appendix G – SG Response Results

7.7.1. G1 – Waterfall Plots of Full SG Responses

7.7.1.1. Configuration 1

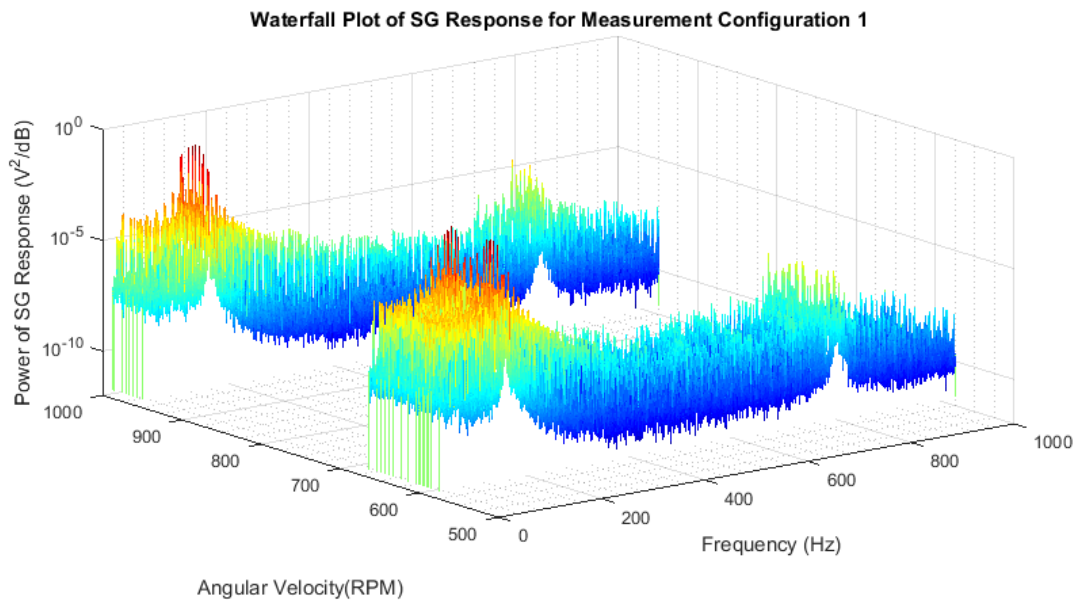


Figure 7.7-1 Waterfall plot of SG responses measured on blade 1 configuration 1 under 1 jet excitation conditions

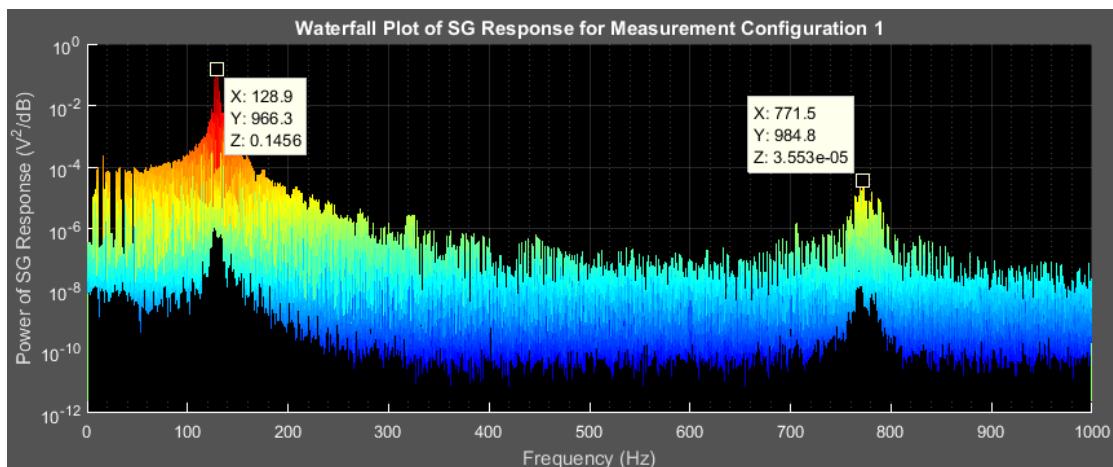


Figure 7.7-2 Frequency-Power view of SG waterfall plot for configuration 1 under 1 jet excitation

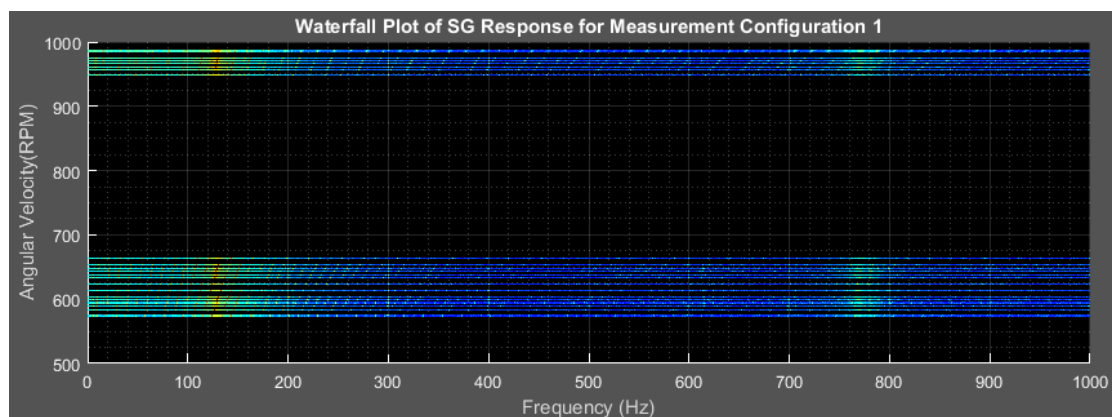


Figure 7.7-3 Frequency-Angular velocity view of SG waterfall plot for configuration 1 under 1 jet excitation

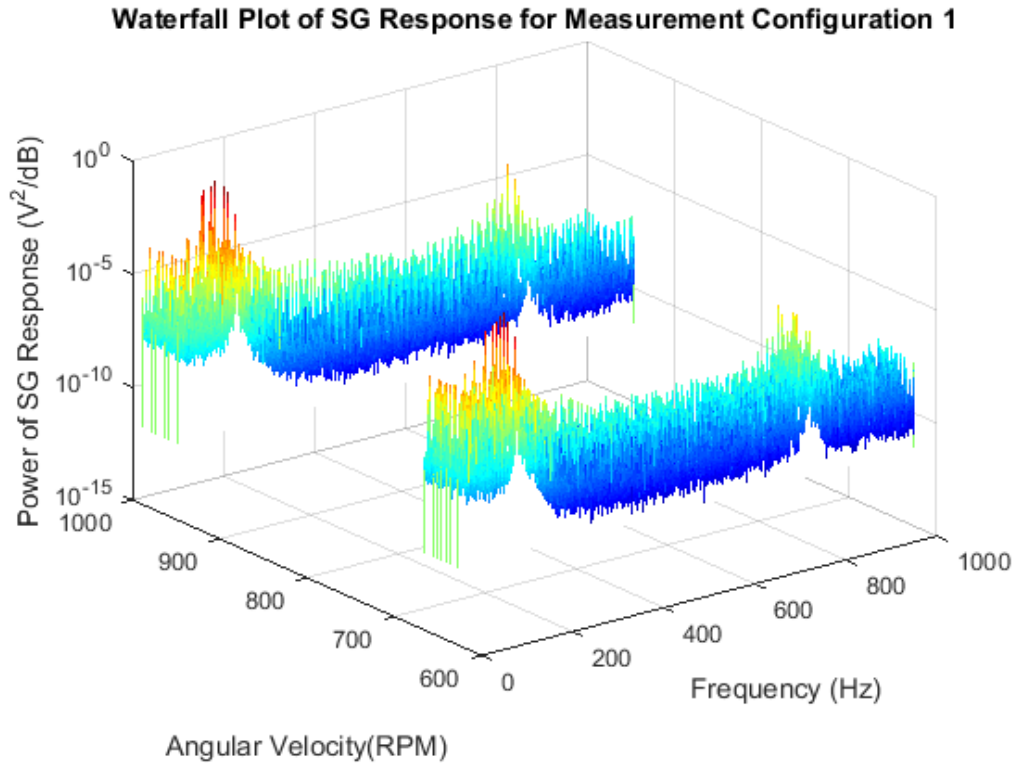


Figure 7.7-4 Waterfall plot of SG responses measured on blade 1 configuration 1 under 2 jet excitation conditions

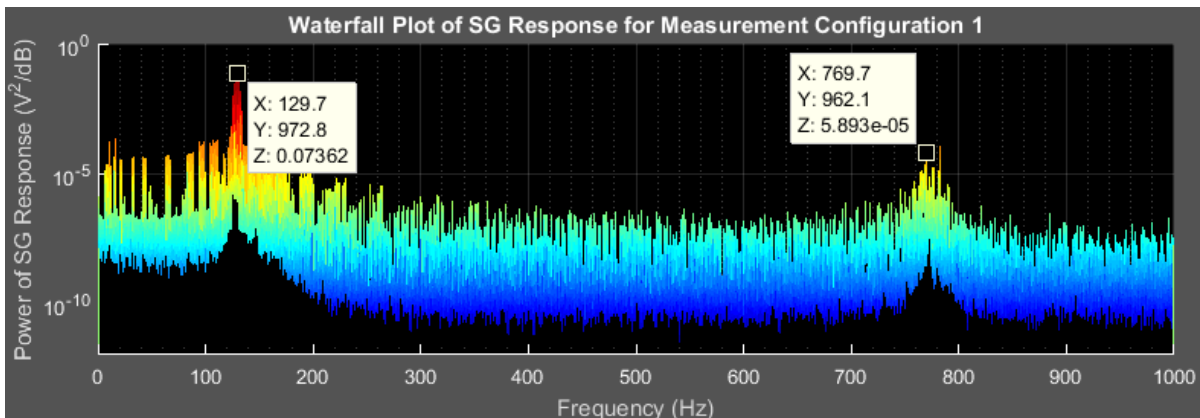


Figure 7.7-5 Frequency-Power view of SG waterfall plot for configuration 1 under 2 jet excitation

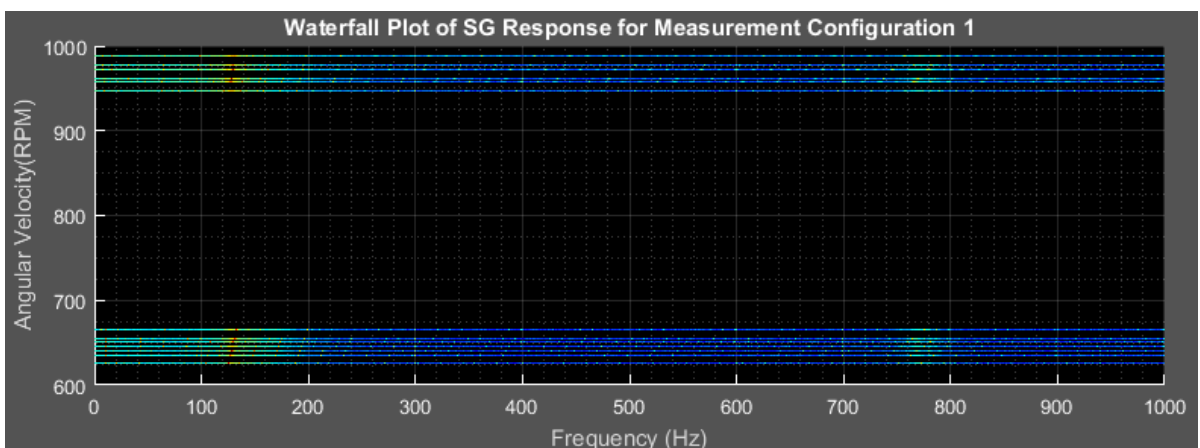


Figure 7.7-6 Frequency-Angular velocity view of SG waterfall plot for configuration 1 under 2 jet excitation

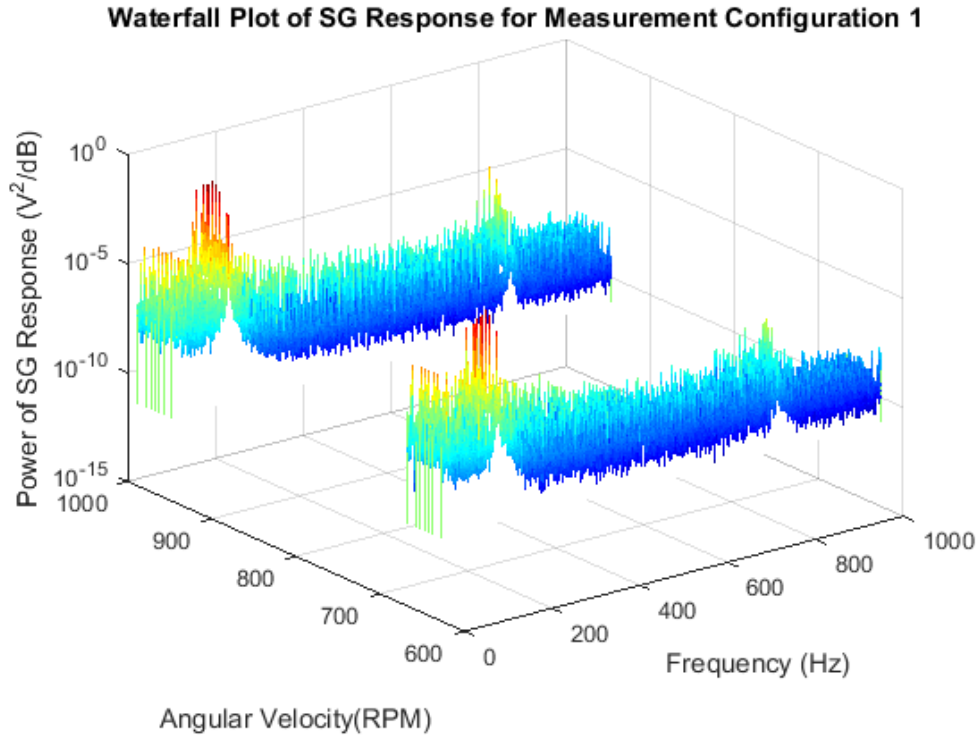


Figure 7.7-7 Waterfall plot of SG responses measured on blade 1 configuration 1 under 4 jet excitation conditions

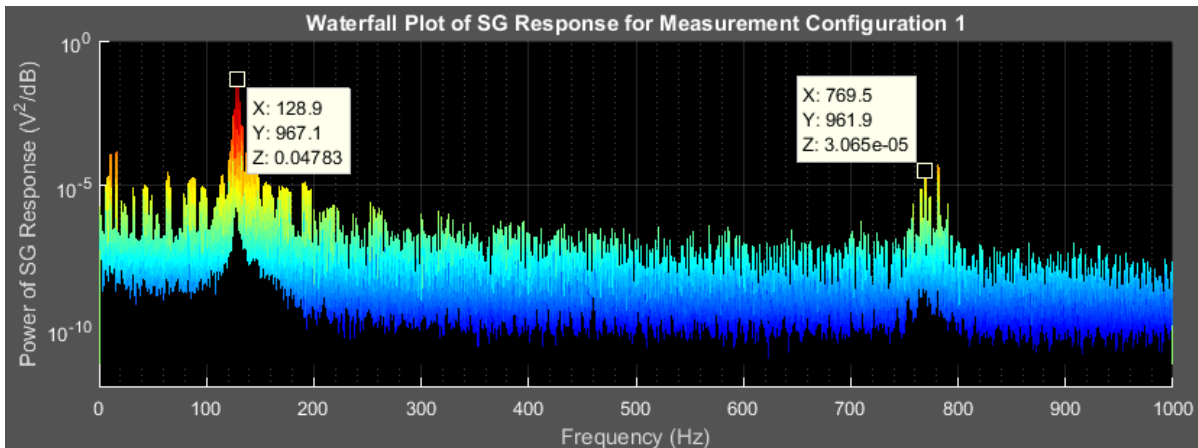


Figure 7.7-8 Frequency-Power view of SG waterfall plot for configuration 1 under 2 jet excitation

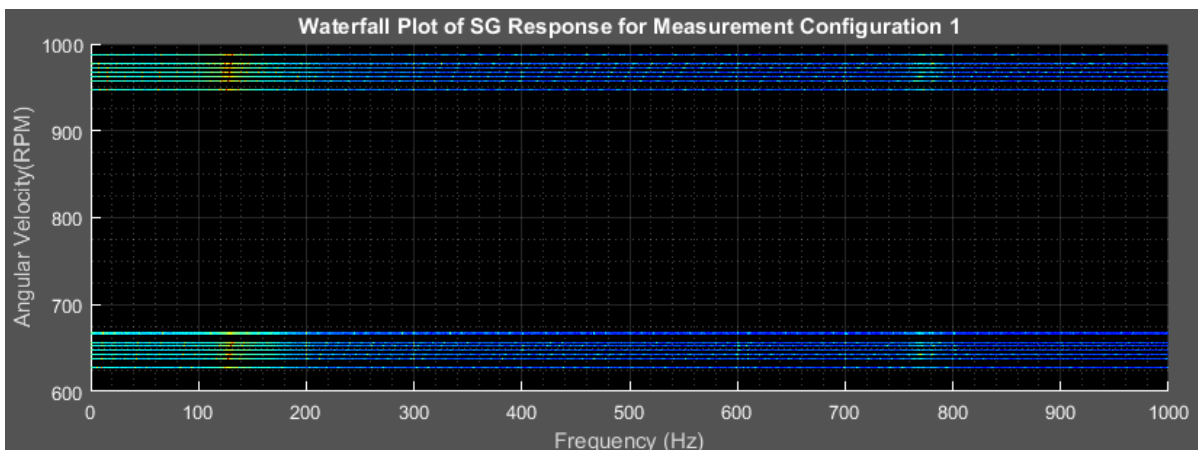


Figure 7.7-9 Frequency-Angular velocity view of SG waterfall plot for configuration 1 under 4 jet excitation

7.7.1.2. Configuration 2

Waterfall Plot of SG Response for Measurement Configuration 2

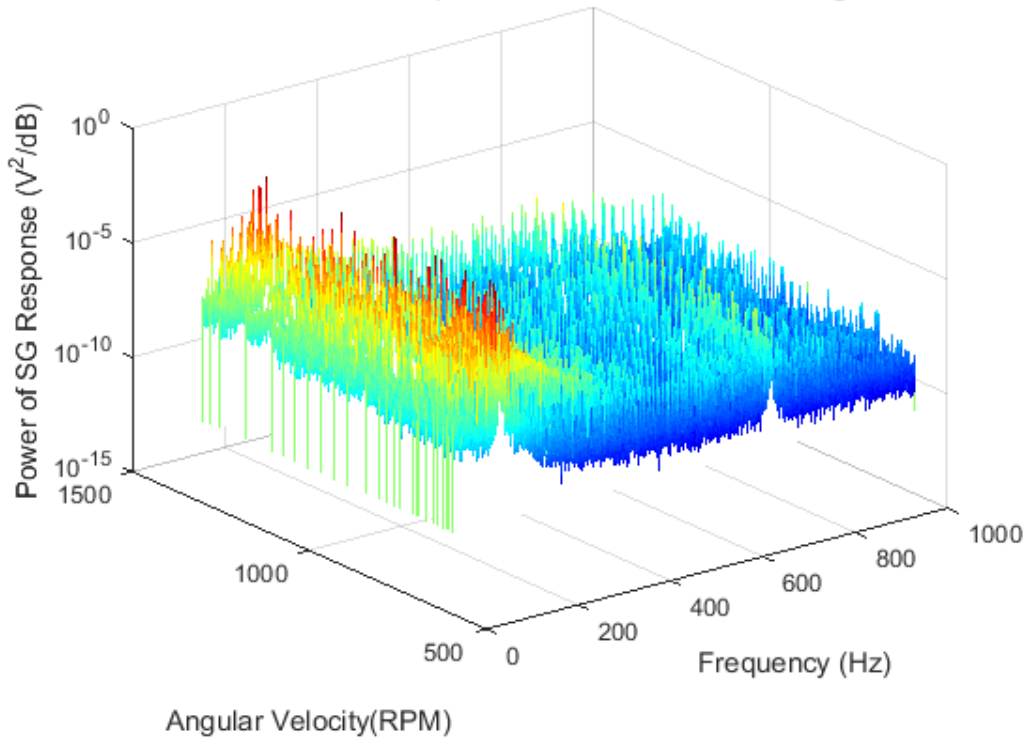


Figure 7.7-10 Waterfall plot of SG responses measured on blade 5 configuration 2 under 1 jet excitation conditions

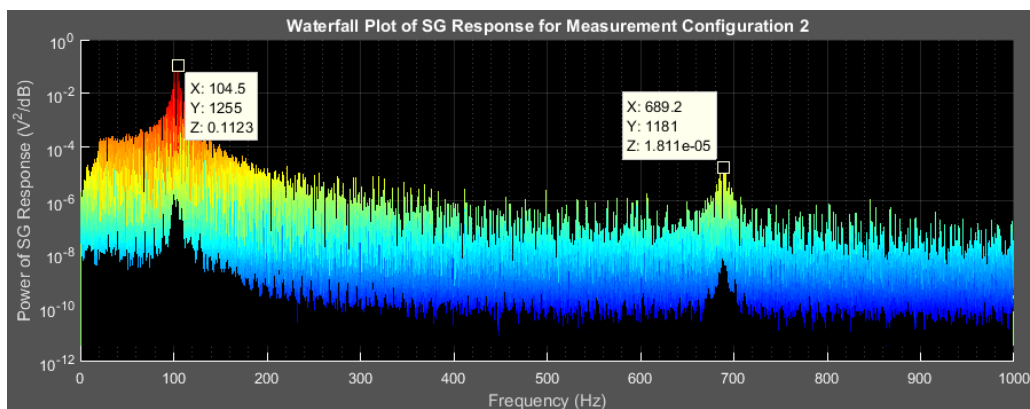


Figure 7.7-11 Frequency-Power view of SG waterfall plot for configuration 2 under 1 jet excitation

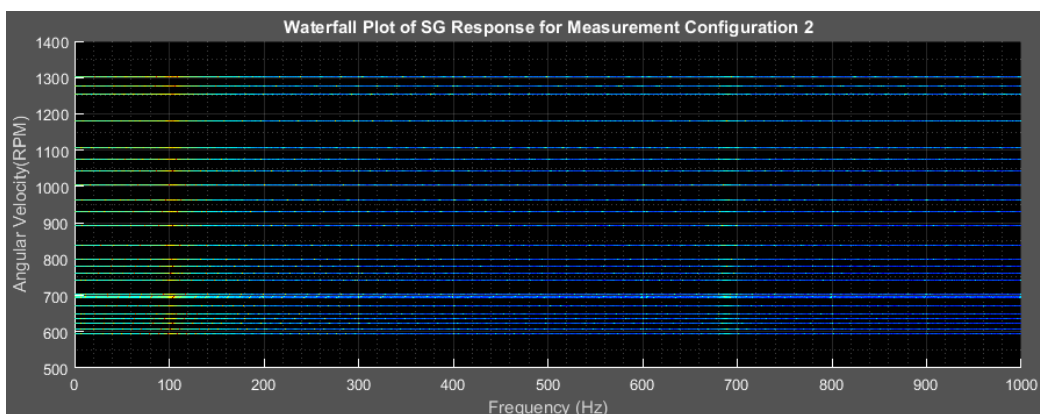


Figure 7.7-12 Frequency-Angular velocity view of SG waterfall plot for configuration 2 under 1 jet excitation

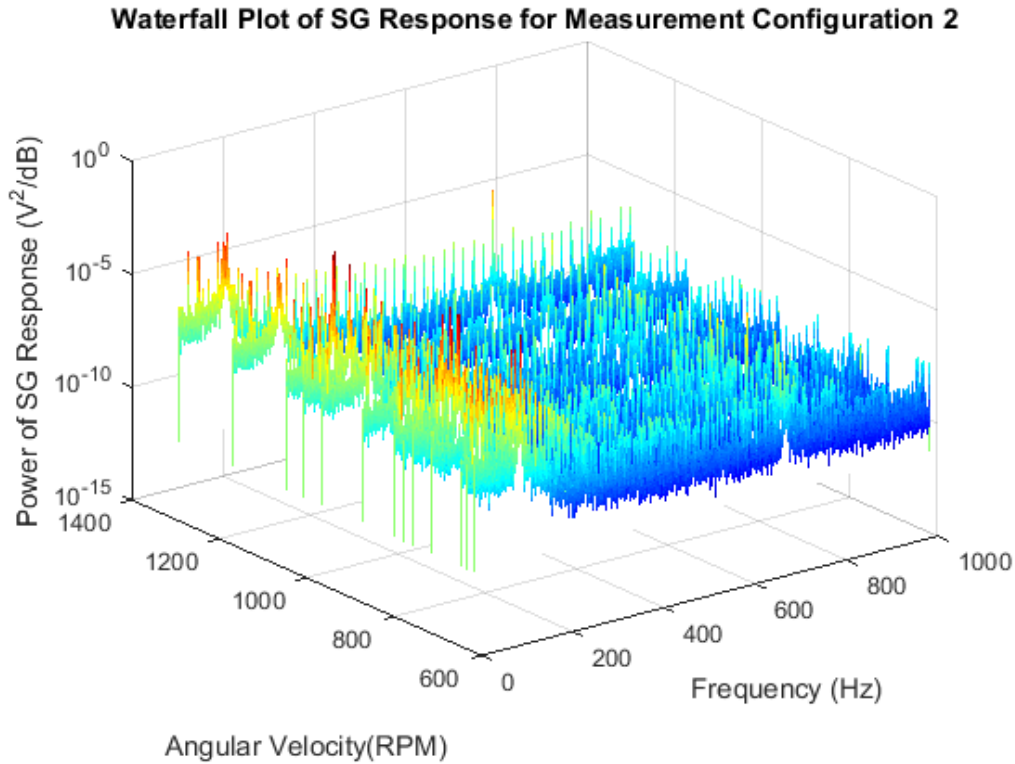


Figure 7.7-13 Waterfall plot of SG responses measured on blade 5 configuration 2 under 2 jet excitation conditions

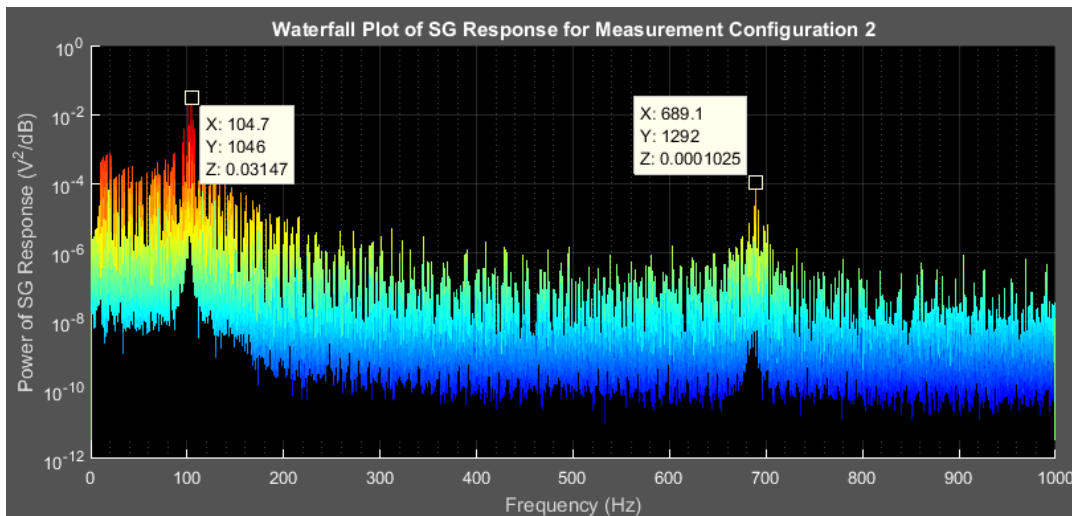


Figure 7.7-14 Frequency-Power view of SG waterfall plot for configuration 2 under 2 jet excitation

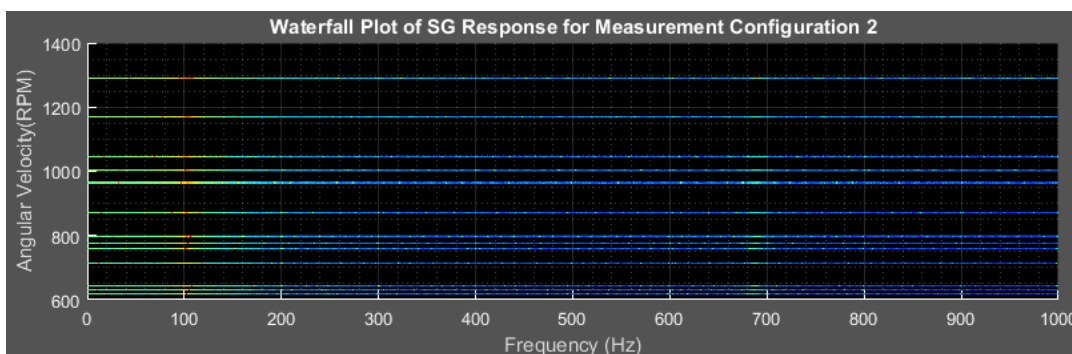


Figure 7.7-15 Frequency-Angular velocity view of SG waterfall plot for configuration 2 under 2 jet excitation

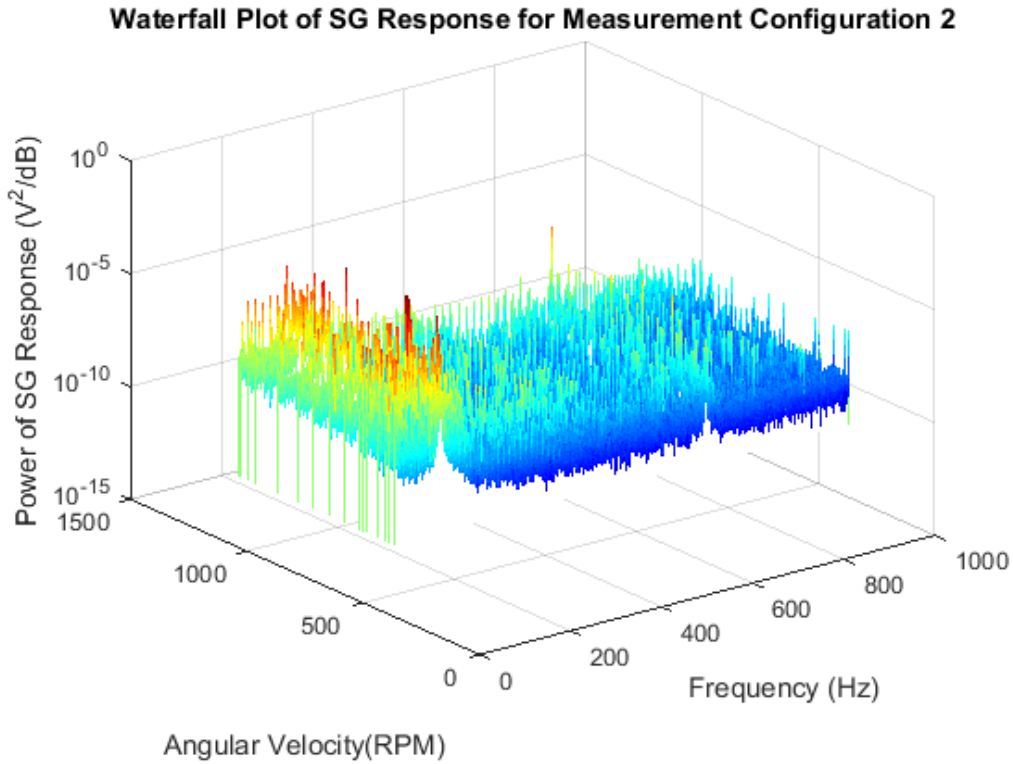


Figure 7.7-16 Waterfall plot of SG responses measured on blade 5 configuration 2 under 4 jet excitation conditions

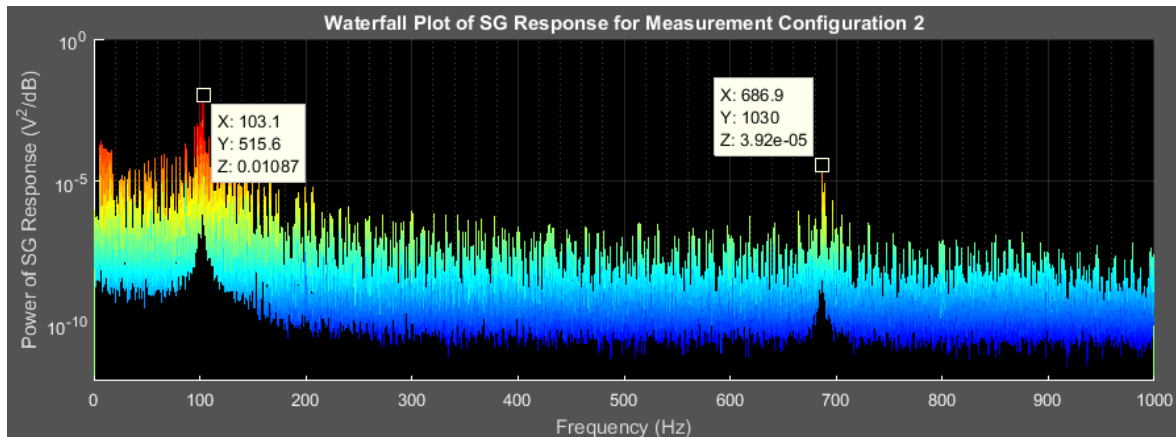


Figure 7.7-17 Frequency-Power view of SG waterfall plot for configuration 2 under 4 jet excitation

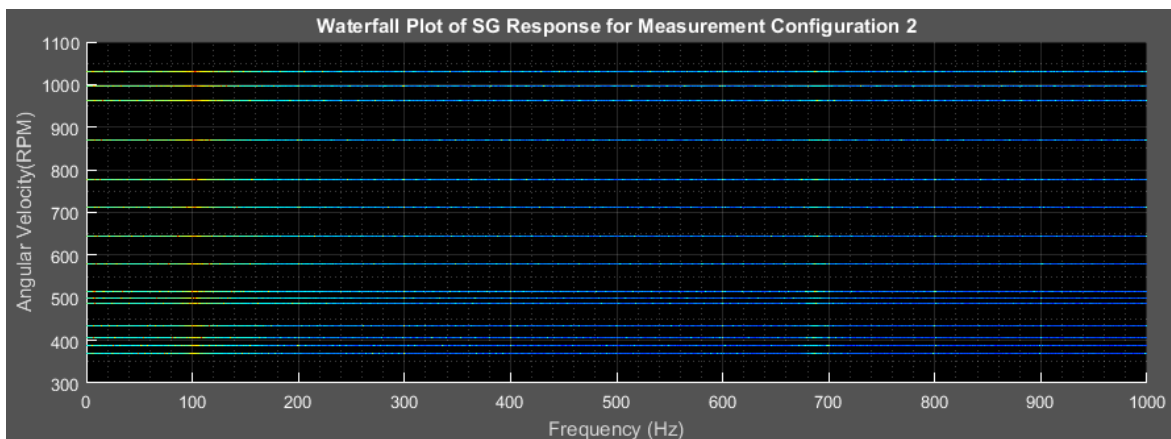


Figure 7.7-18 Frequency-Angular velocity view of SG waterfall plot for configuration 2 under 4 jet excitation

7.7.2. G2 – Waterfall Plots of SG Forcing Function Spectra

7.7.2.1. Configuration 1

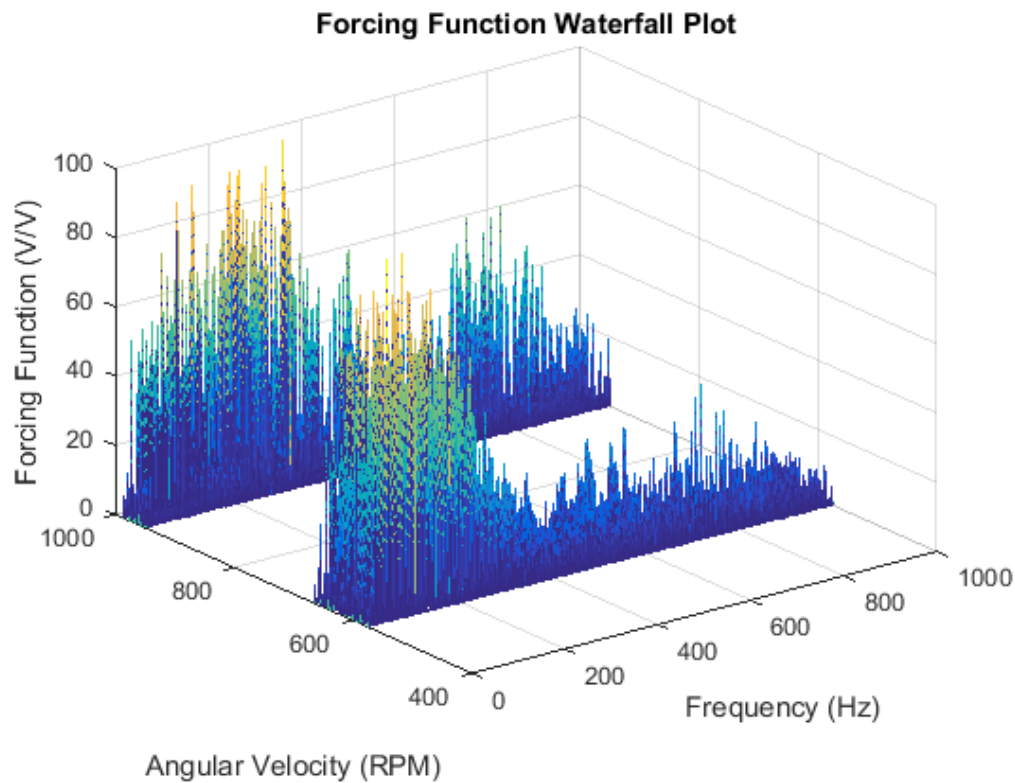


Figure 7.7-19 Forcing function waterfall plot for configuration 1 under 1 jet excitation conditions

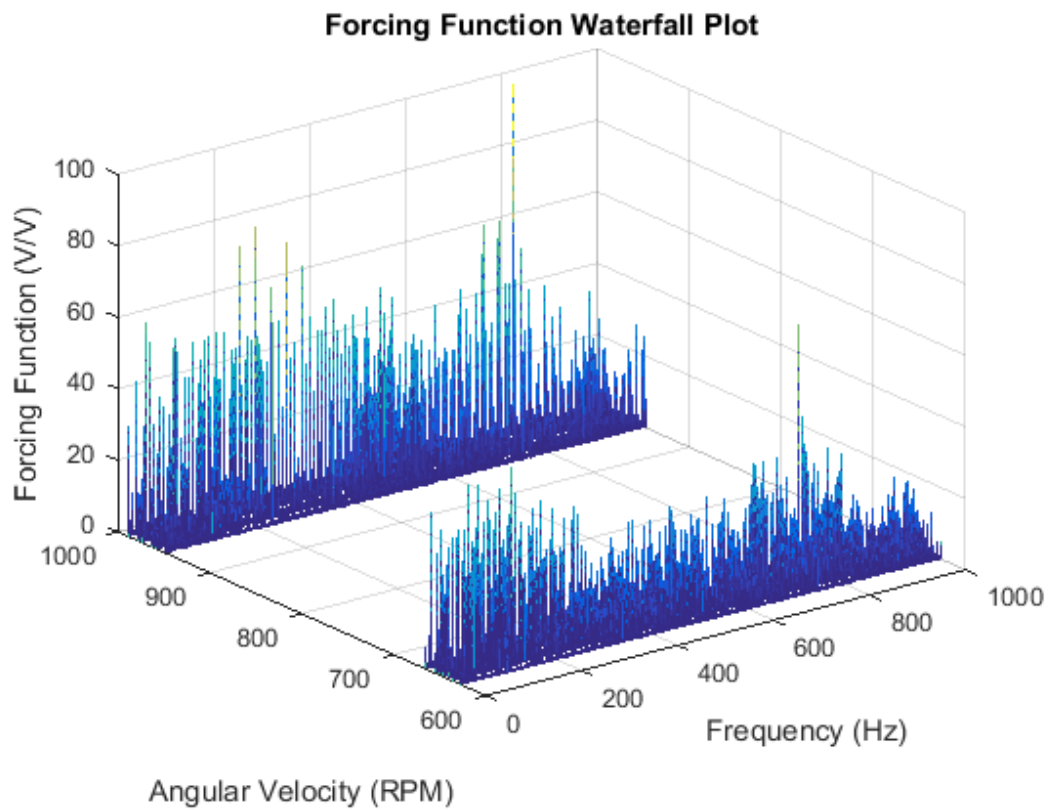


Figure 7.7-20 Forcing function waterfall plot for configuration 1 under 2 jet excitation conditions

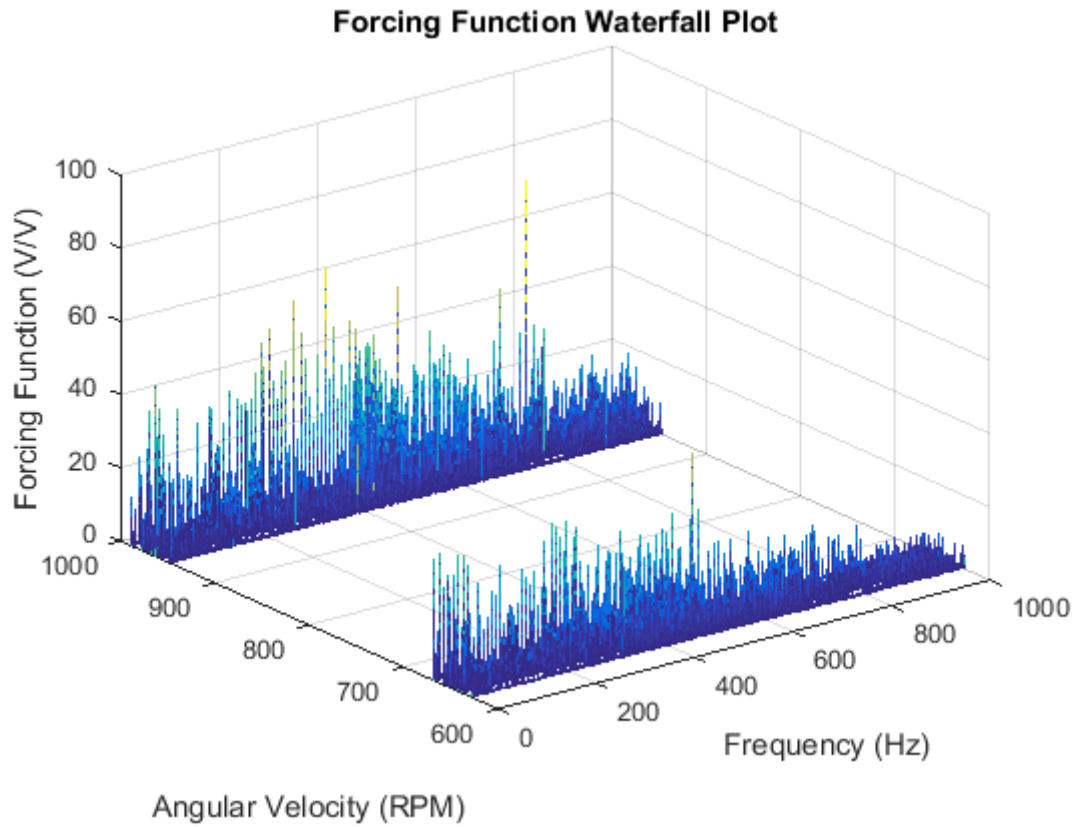


Figure 7.7-21 Forcing function waterfall plot for configuration 1 under 4 jet excitation conditions

7.7.2.2. Configuration 2

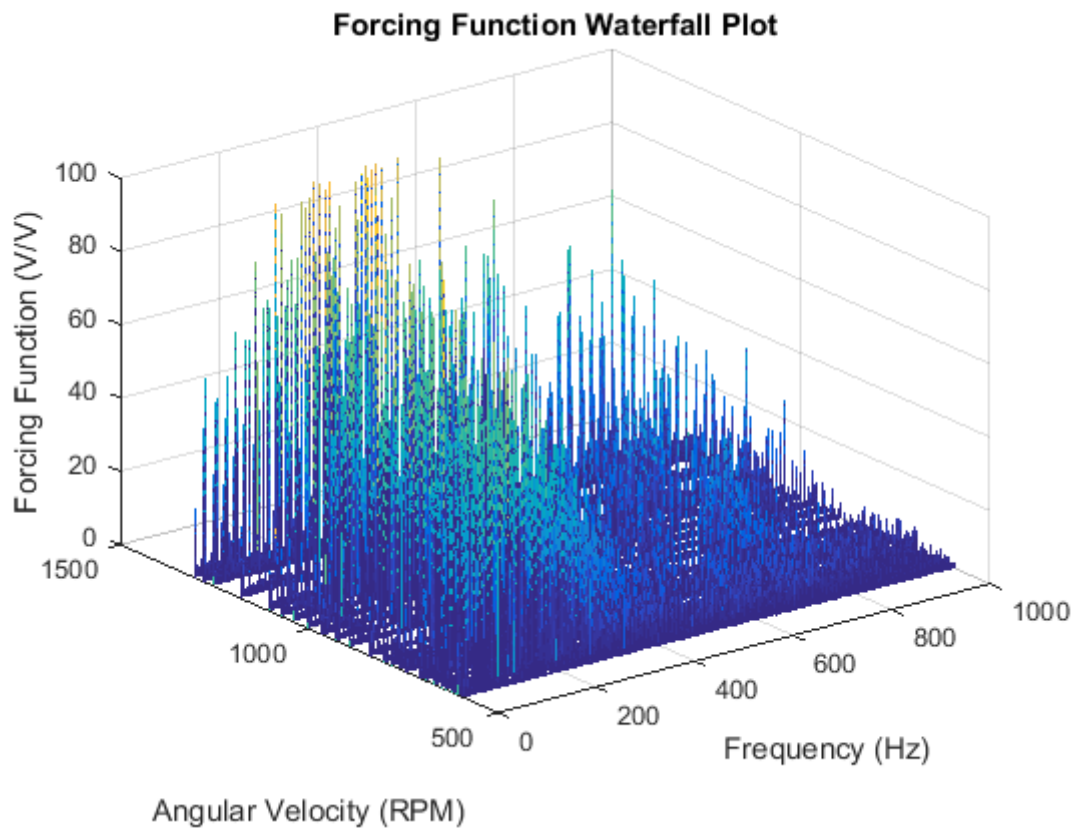


Figure 7.7-22 Forcing function waterfall plot for configuration 2 under 1 jet excitation conditions

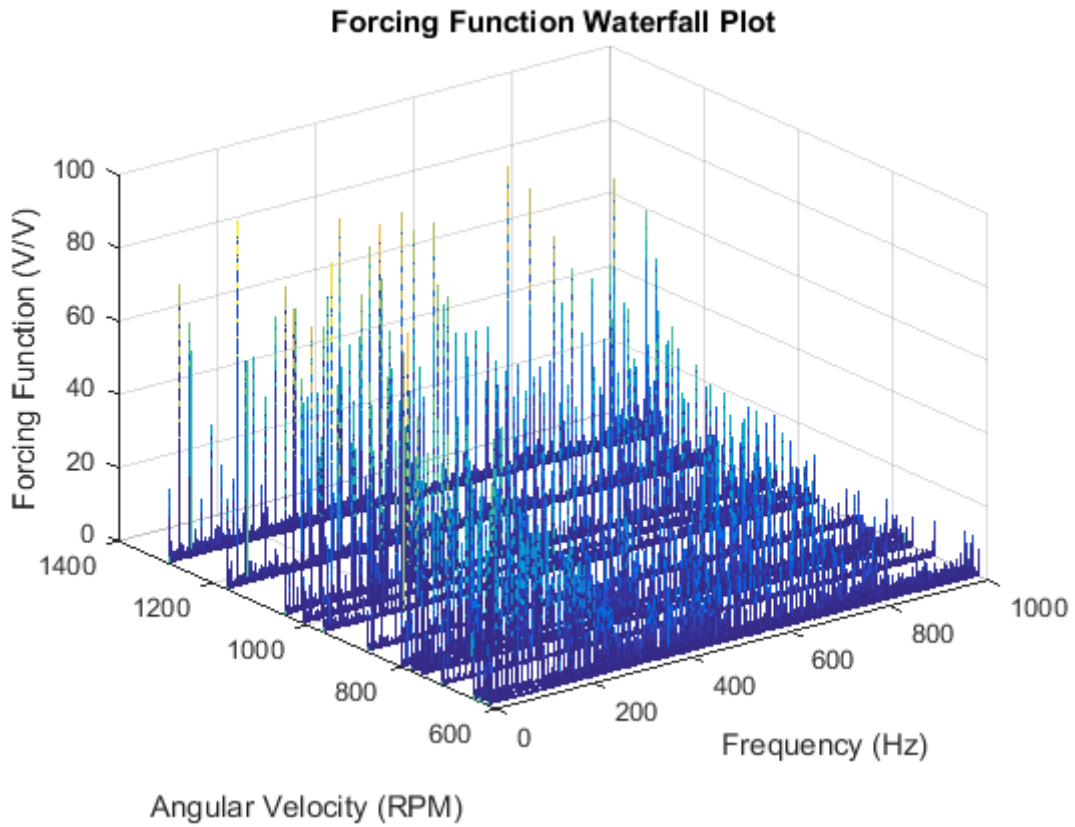


Figure 7.7-23 Forcing function waterfall plot for configuration 2 under 2 jet excitation conditions

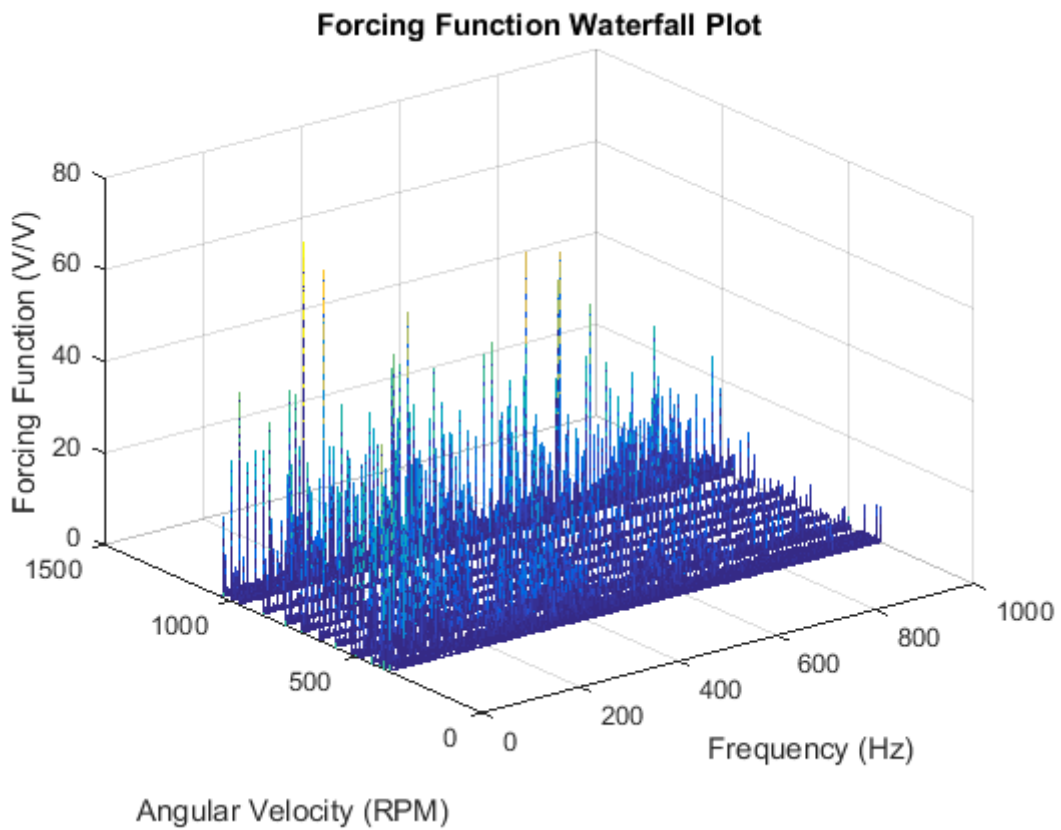


Figure 7.7-24 Forcing function waterfall plot for configuration 2 under 4 jet excitation conditions

7.7.3. G3 – SG Forcing Function Fitting Results

The following table contains the results obtained during the fitting of the SG derived forcing function results. A nonlinear constrained optimisation problem was set up to fit the forcing function model to the SG measurement derived forcing form. The mean square error (MSE) between the absolute of the model and the absolute of the measurement derived results was minimised over. The response magnitude of the different excitation schemes (number of jets) differed, therefore the MSE is not comparable between excitation schemes. The coefficient of determination, R^2 , provides a goodness of fit between the model and the experimentally derived results and so may be used to compare between excitation schemes.

Table 7.7-1 SG based forcing function fitting results

Data Set	Number of Items	Mean MSE	Std. Dev. MSE	Min MSE	Max MSE	Mean R^2	Std. Dev. R^2	Min R^2	Max R^2	Mean iterations	Mean Function Count
Whole	285	2.2004	1.668	0.3508	7.2315	0.3694	0.2574	0	0.7974	49.6877	500.4386
Config. 1	135	2.2226	0.7937	0.8114	4.0330	0.3756	0.2725	0	0.7974	50.8	517.5481
Config. 2	150	2.1804	1.4240	0.3508	7.2315	0.3637	0.2437	0	0.6985	48.6867	485.0400
Jets 1	133	2.8874	1.0451	1.6582	7.2315	0.6111	0.0767	0.2413	0.7974	22.0977	185.1880
Jets 2	67	2.0646	0.9446	1.1292	4.6042	0.2765	0.1174	0	0.4967	39.7164	391.2687
Jets 4	85	1.2324	0.6895	0.3508	2.6501	0.0642	0.1014	0	0.3519	100.7176	1079.80
Config. 1 Jets 1	62	2.7634	0.4415	1.6582	3.7201	0.6352	0.0479	0.5220	0.7974	21.3226	180.6935
Config. 1 Jets 2	31	1.9340	0.9329	1.1292	4.0330	0.3048	0.1456	0	0.4967	44.8065	451.9355
Config. 1 Jets 4	42	1.6373	0.5253	0.8114	2.6501	0.0447	0.0771	0	0.2605	98.7381	1063.20
Config. 2 Jets 1	71	2.9957	1.3654	1.8335	7.2315	0.5901	0.0902	0.2413	0.6985	22.7746	189.1127
Config. 2 Jets 2	36	2.1771	0.9532	1.1434	4.6042	0.2522	0.0807	0.0941	0.4374	35.3333	339.0278
Config. 2 Jets 4	43	0.8369	0.5979	0.3508	2.5726	0.0833	0.1183	0	0.3519	102.6512	1095.90

The best coefficient of determination was found for configuration 1 under 1 jet excitation operating at 593.95 RPM (value of 0.7974). Within the same set (configuration 1 under 1 jet excitation) the worst fit was found for the measurement taken at 961.12 RPM (with a coefficient of determination of 0.5220).

7.7.4. G4 – Multi-Start SG Blade Transfer Function Fitting Results

The results from fitting the blade transfer function model to the filtered and smoothed SG response spectra using 1000 initial guesses generated from a Latin hypercube is provided in Table 7.7-2.

Table 7.7-2 Multi-start SG blade transfer function fitting results

Blade 1 Configuration 1					Blade 5 Configuration 2				
Item	Mean	Std. Dev.	Max	Min	Item	Mean	Std. Dev.	Max	Min
A_1	58.7219	9.9258	107.5351	0.1	A_1	68.8764	12.5013	127.3938	0.1
A_2	26.1586	20.9280	211.6096	0.1	A_2	26.9515	20.9488	215.1739	0.1
A_3	163.9035	40.7130	207.6449	0.1	A_3	207.5299	91.2715	300.0000	0.1
f_{n1} (Hz)	128.6089	1.7033	134.8707	103.3669	f_{n1} (Hz)	103.0794	2.2972	1350	91.3985
f_{n2} (Hz)	755.9164	37.7755	780	650	f_{n2} (Hz)	694.7925	23.0866	780	650.0001
f_{n3} (Hz)	813.7635	78.8885	1343.50	785	f_{n3} (Hz)	825.0826	90.7880	1343.4	785.0000
η_1	0.0147	0.0040	0.350	0.0000	η_1	0.0350	0.0002	0.350	0.0294
η_2	0.0146	0.0089	0.350	0.0001	η_2	0.0230	0.0078	0.350	0.0024
η_3	0.7243	0.1392	0.9999	0.0117	η_3	0.8378	0.3308	0.9999	0.0173
MSE	6.2649e-09	1.1608e-08	1.2352e-07	2.9361e-09	MSE	1.1459e-08	2.4136e-08	1.8766e-07	5.3583e-09
R^2	0.9440	0.0934	0.9735	0	R^2	0.9238	0.1050	0.9429	0
Iter.	163.2440	18.6413	296	73	Iter.	144.2900	13.8475	238	71
Func. Evals.	1674.30	196.4343	3009	748	Func. Evals.	1471.20	143.7380	2424	724

7.7.5. G5 – Exemplar SG Response and Forcing Function Forms

7.7.5.1. Configuration 1: SG Derived Data Measured on Blade 1

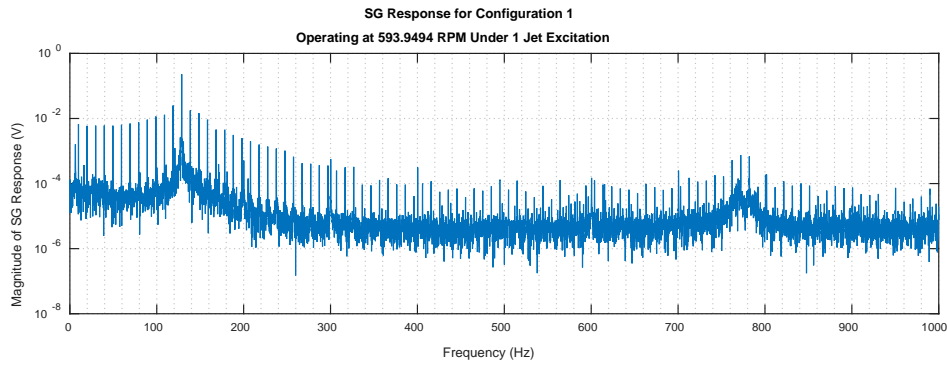


Figure 7.7-25 SG response obtained for operation at approximately EO 13 under 1 jet excitation

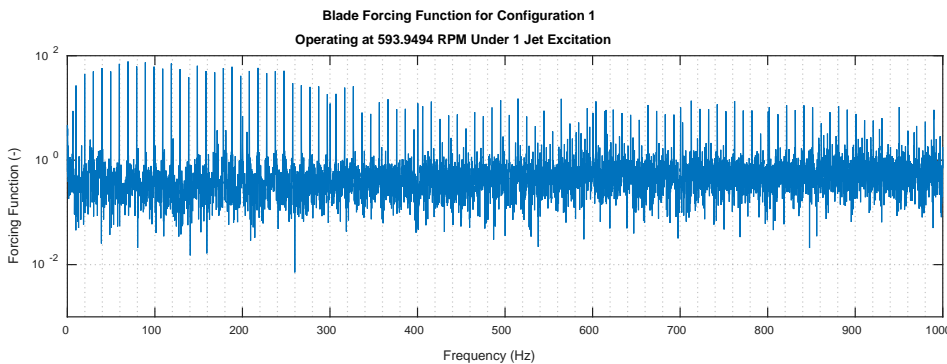


Figure 7.7-26 Extracted SG forced response form for operation at approximately EO 13 under 1 jet excitation

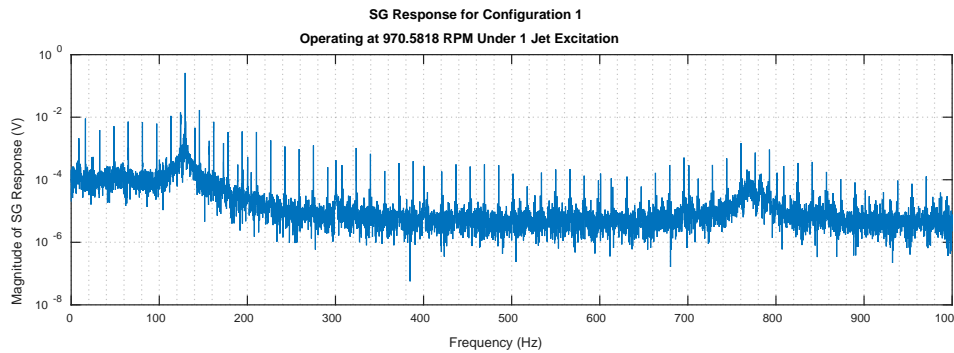


Figure 7.7-27 SG response for operation at approximately 5 RPM above EO 8 under 1 jet excitation

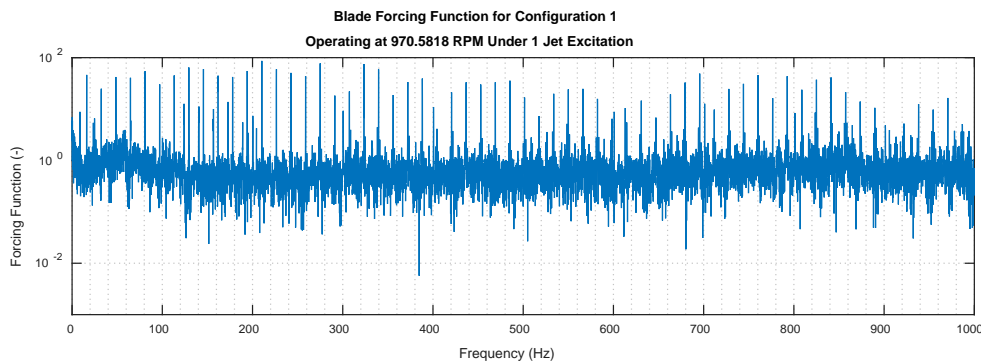


Figure 7.7-28 Extracted SG forced response form for operation at approximately 5 RPM above EO 8 under 1 jet excitation

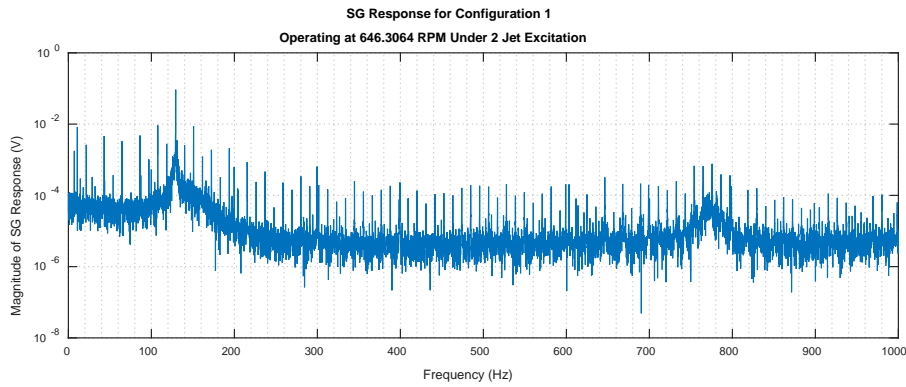


Figure 7.7-29 SG response for operation at approximately EO 6 under 2 jet excitation

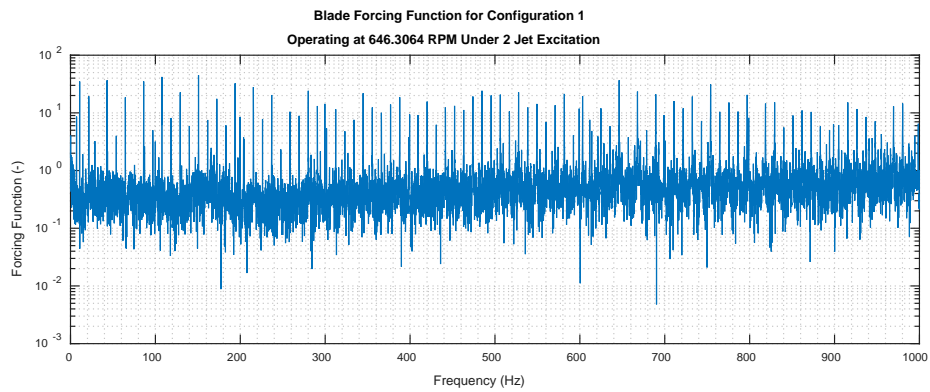


Figure 7.7-30 Extracted SG forced response form for operation at approximately EO 8 under 2 jet excitation

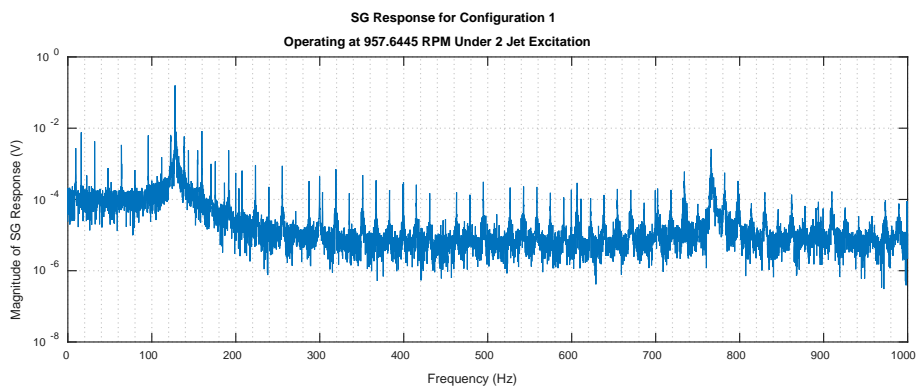


Figure 7.7-31 SG response for operation at approximately 10 RPM below EO 4 under 2 jet excitation

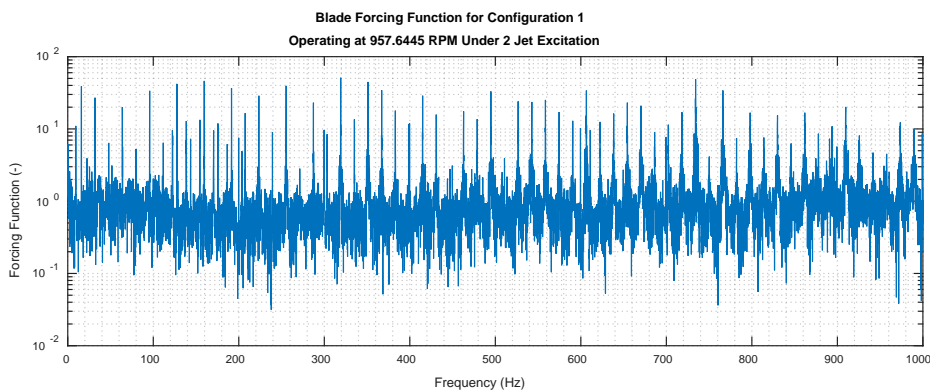


Figure 7.7-32 Extracted SG forced response form for operation at approx. 10 RPM below EO 4 under 2 jet excitation

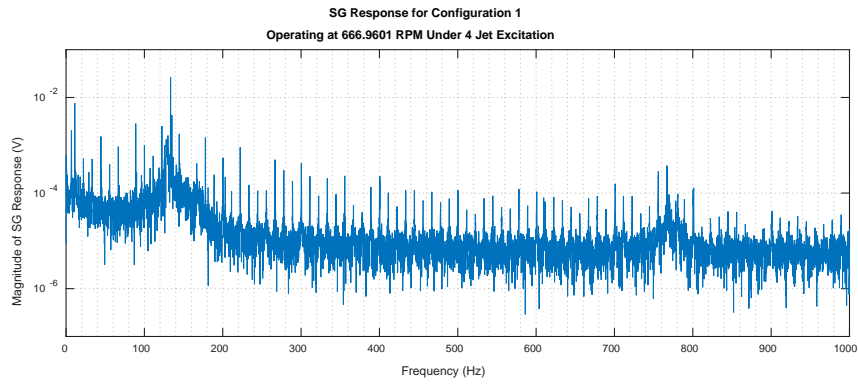


Figure 7.7-33 SG response for operation at approximately 20 RPM above EO 3 under 4 jet excitation

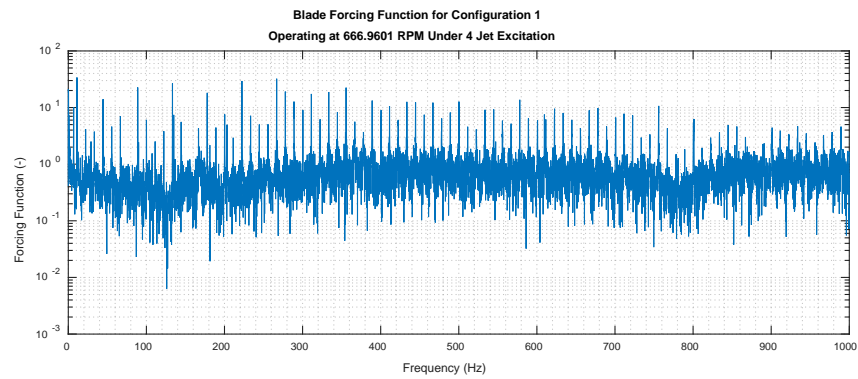


Figure 7.7-34 Extracted SG forced response form for operation at approx. 5 RPM above EO 8 under 4 jet excitation

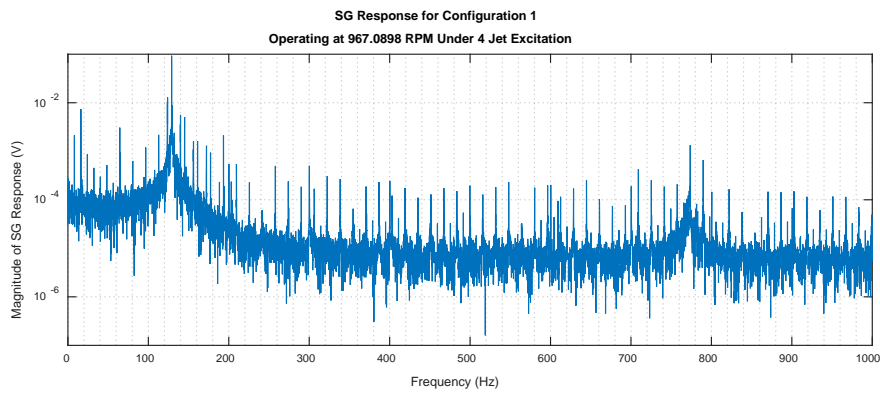


Figure 7.7-35 SG response for operation at approximately EO 2 under 4 jet excitation

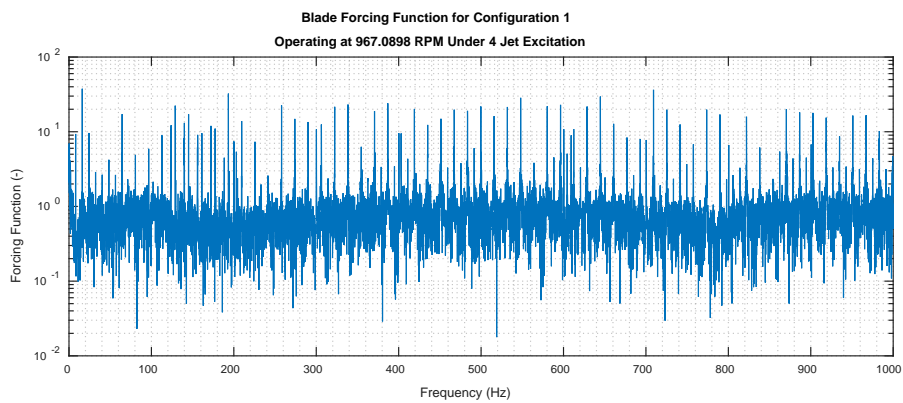


Figure 7.7-36 Extracted SG forced response form for operation at approx. EO 2 under 4 jet excitation

7.7.5.2. Configuration 2: SG Derived Data Measured on Blade 5

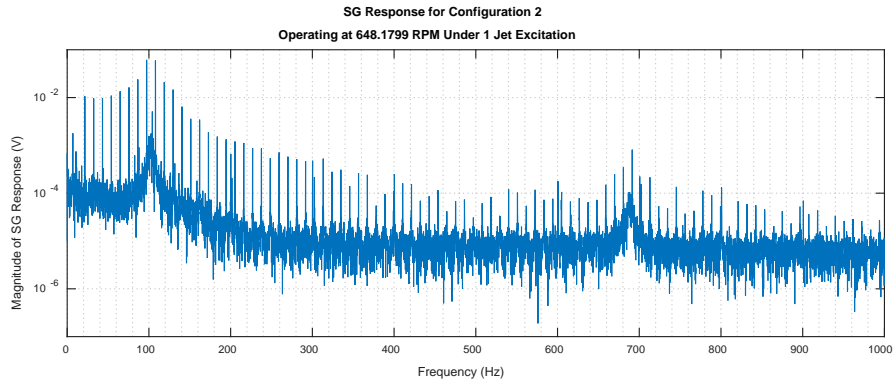


Figure 7.7-37 SG response of blade 5 at resonance of blade 1 at approximately 648 RPM under 1 jet excitation

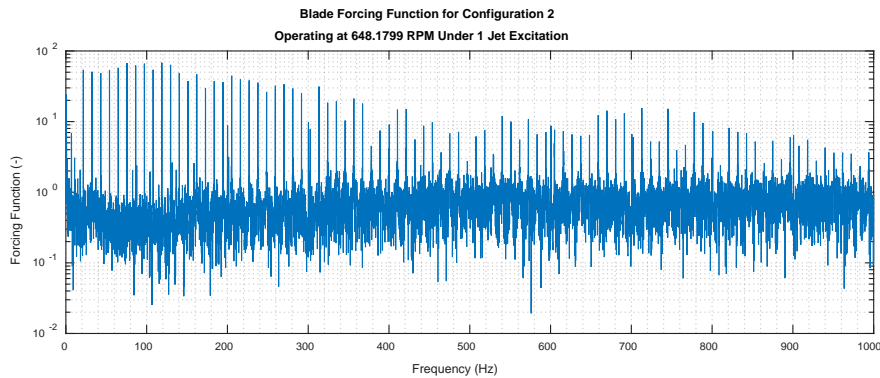


Figure 7.7-38 Extracted SG forced response form of blade 5 at approximately 648 RPM under 1 jet excitation

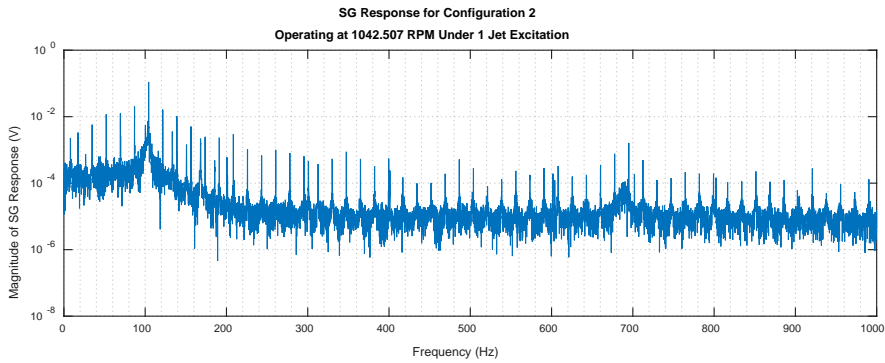


Figure 7.7-39 SG response of blade 5 at resonance of blade 5 at approximately 1042 RPM under 1 jet excitation

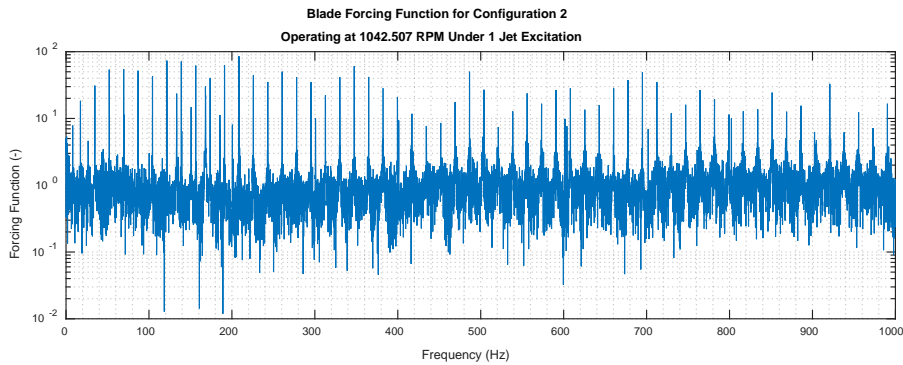


Figure 7.7-40 Extracted SG forced response form of blade 5 at approximately 1042 RPM under 1 jet excitation

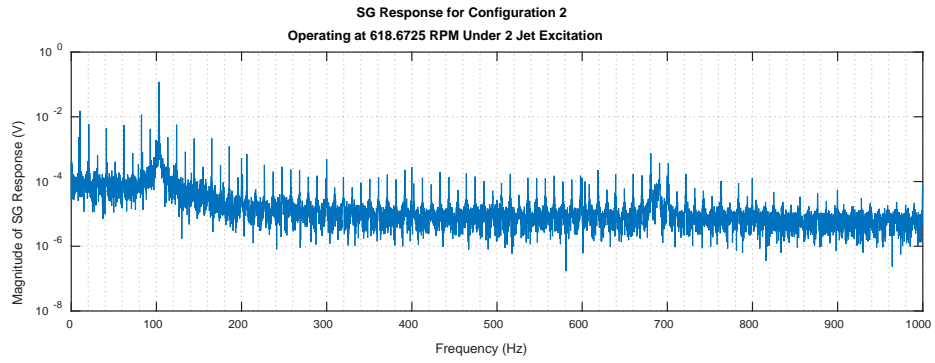


Figure 7.7-41 SG response of blade 5 at resonance of blade 5 at approximately 619 RPM under 2 jet excitation

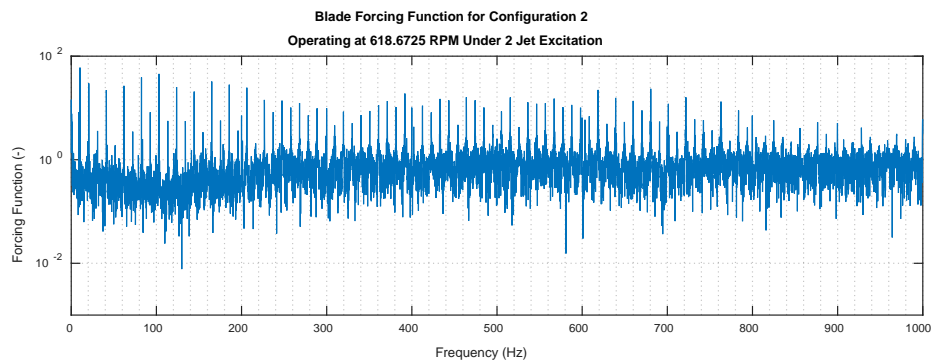


Figure 7.7-42 Extracted SG forced response form of blade 5 at approximately 619 RPM under 2 jet excitation

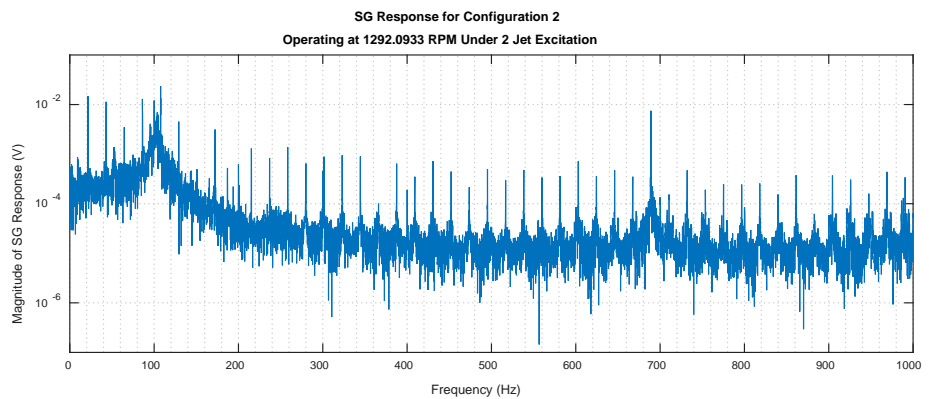


Figure 7.7-43 SG response of blade 5 at resonance of blade 1 at approximately 1292 RPM under 2 jet excitation

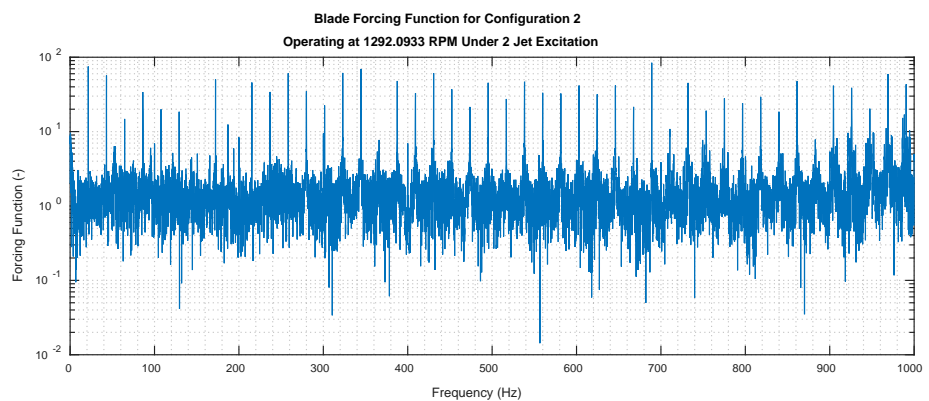


Figure 7.7-44 Extracted SG forced response form of blade 5 at approximately 1292 RPM under 2 jet excitation

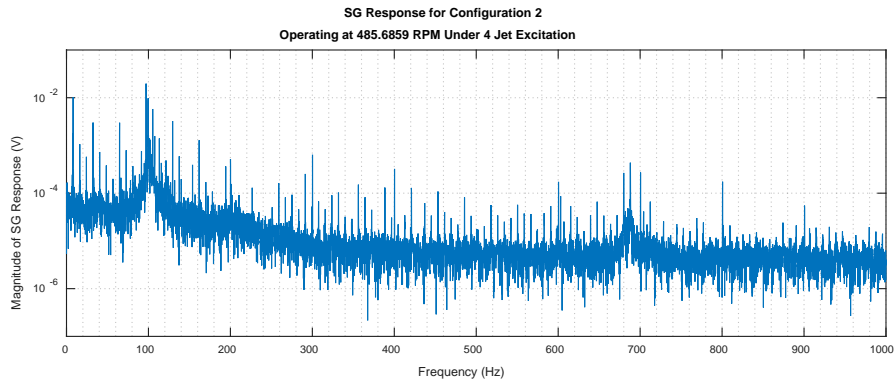


Figure 7.7-45 SG response of blade 5 at resonance of blade 1 at approximately 486 RPM under 4 jet excitation

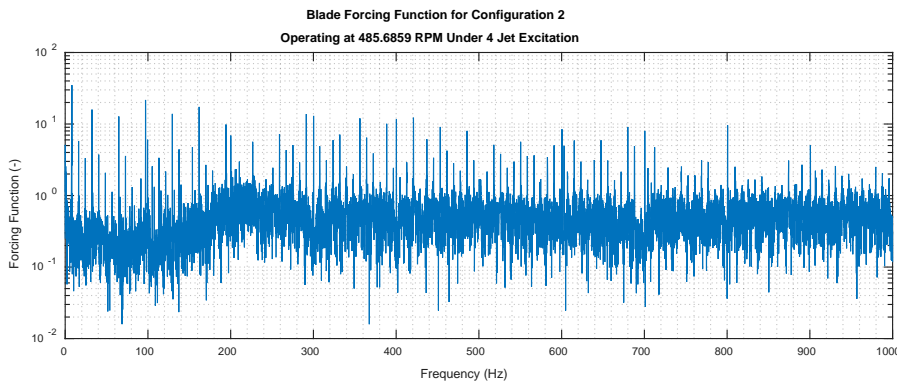


Figure 7.7-46 Extracted SG forced response form of blade 5 at approximately 486 RPM under 4 jet excitation

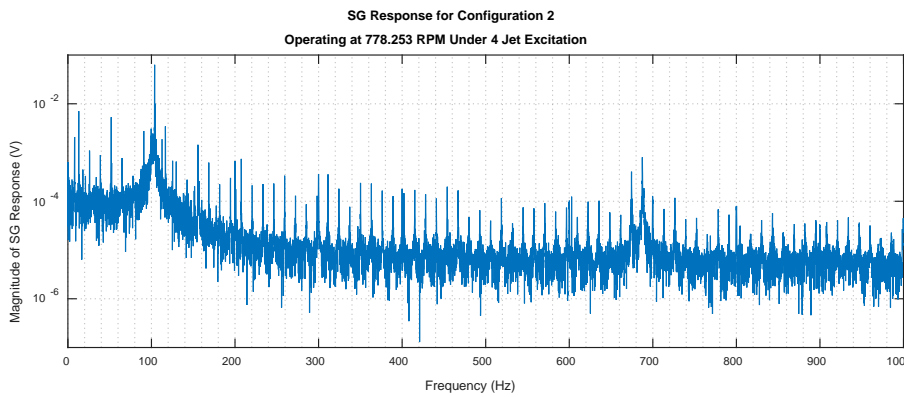


Figure 7.7-47 SG response of blade 5 at resonance of blade 5 at approximately 778 RPM under 4 jet excitation

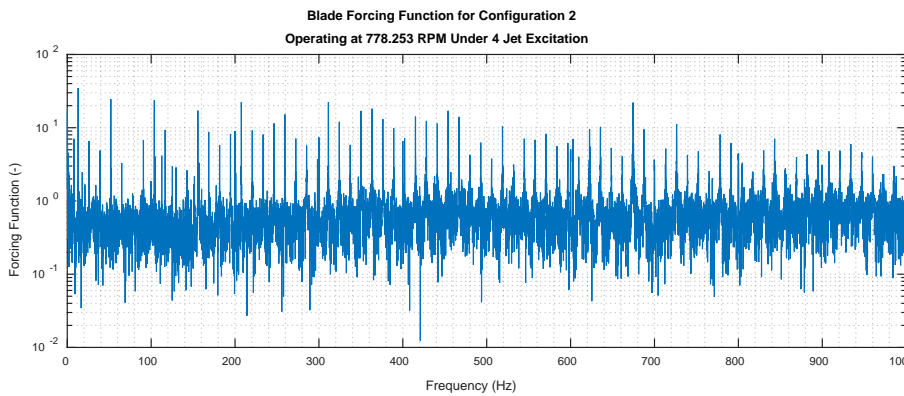


Figure 7.7-48 Extracted SG forced response form of blade 5 at approximately 778 RPM under 4 jet excitation



7.8. Appendix H – Pressure Results

7.8.1. H1 – Average Pressure Waveforms

7.8.1.1. Configuration 1



Figure 7.8-1 Average pressure waveform for configuration 1 under 1 jet excitation

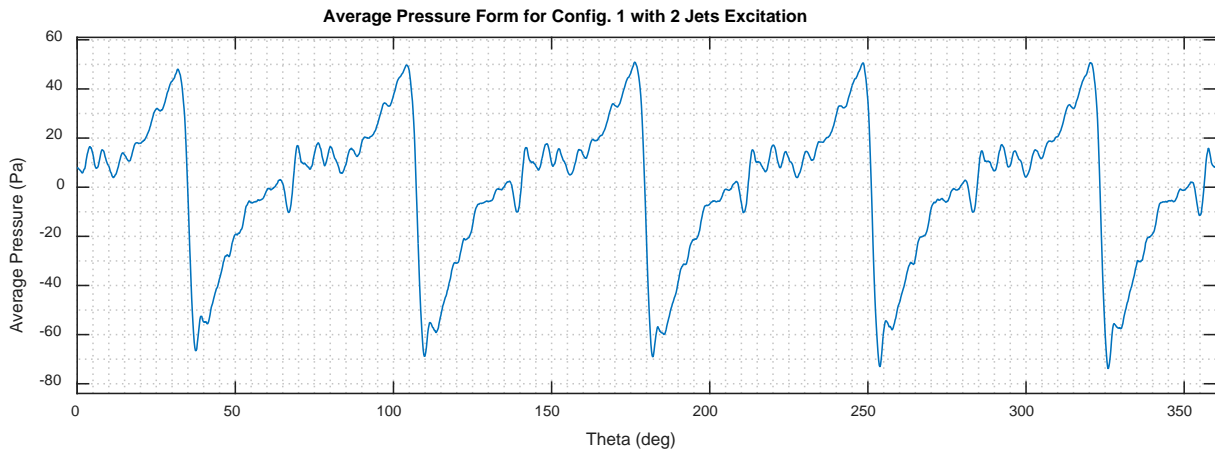


Figure 7.8-2 Average pressure waveform for configuration 1 under 2 jet excitation

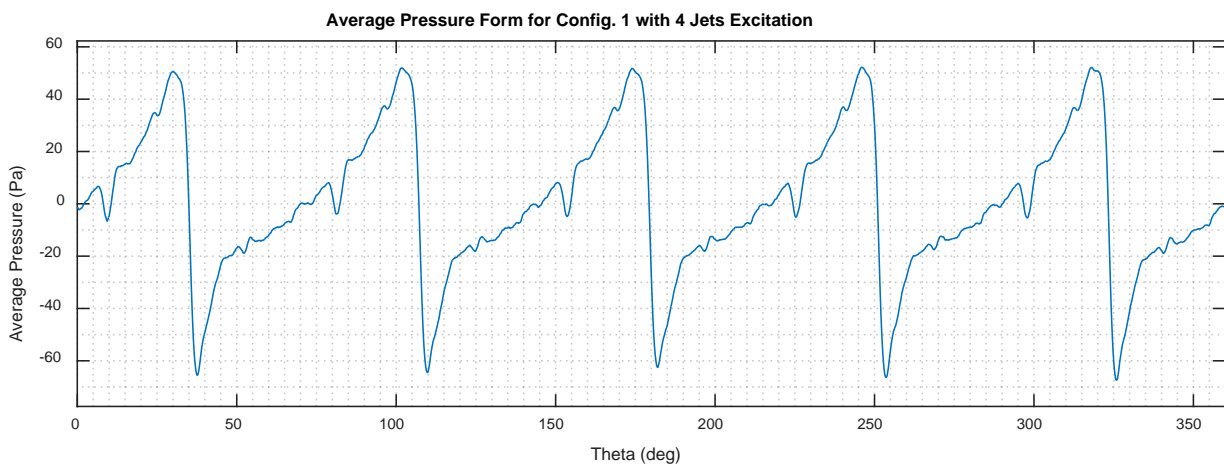


Figure 7.8-3 Average pressure waveform for configuration 1 under 4 jet excitation

7.8.1.2. Configuration 2

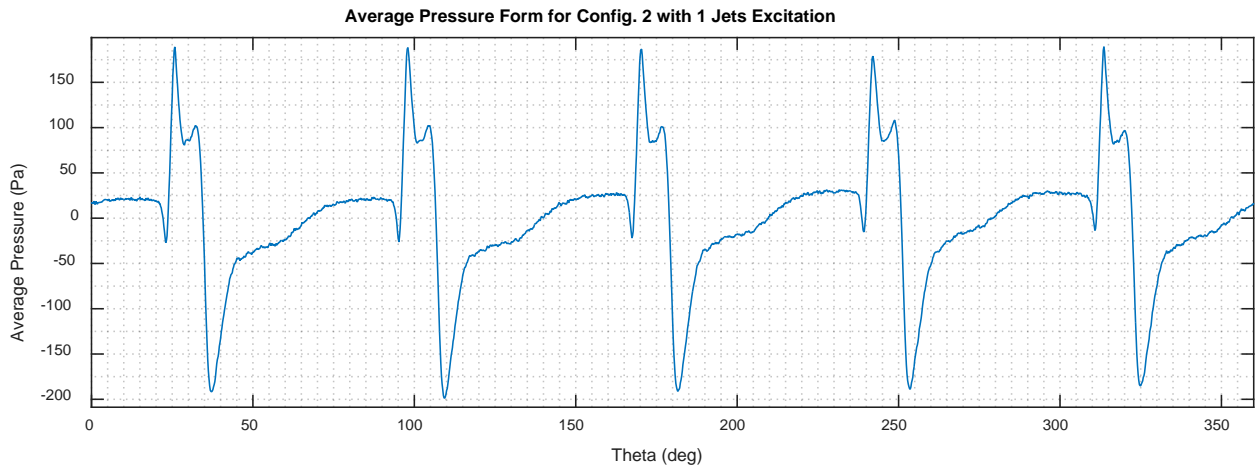


Figure 7.8-4 Average pressure waveform for configuration 2 under 1 jet excitation

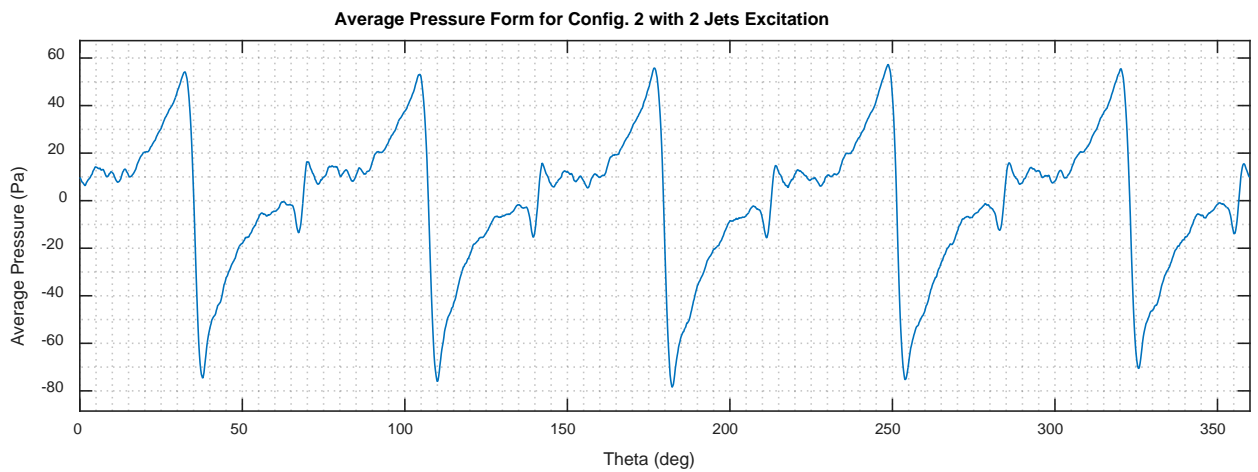


Figure 7.8-5 Average pressure waveform for configuration 2 under 2 jet excitation

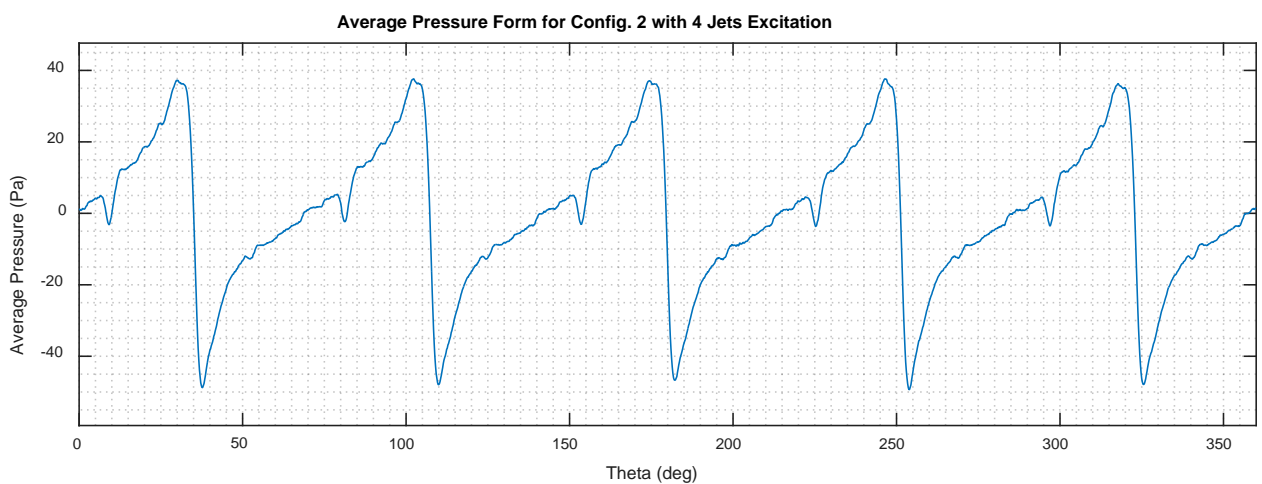


Figure 7.8-6 Average pressure waveform for configuration 2 under 4 jet excitation



7.8.1.3. Configuration 3

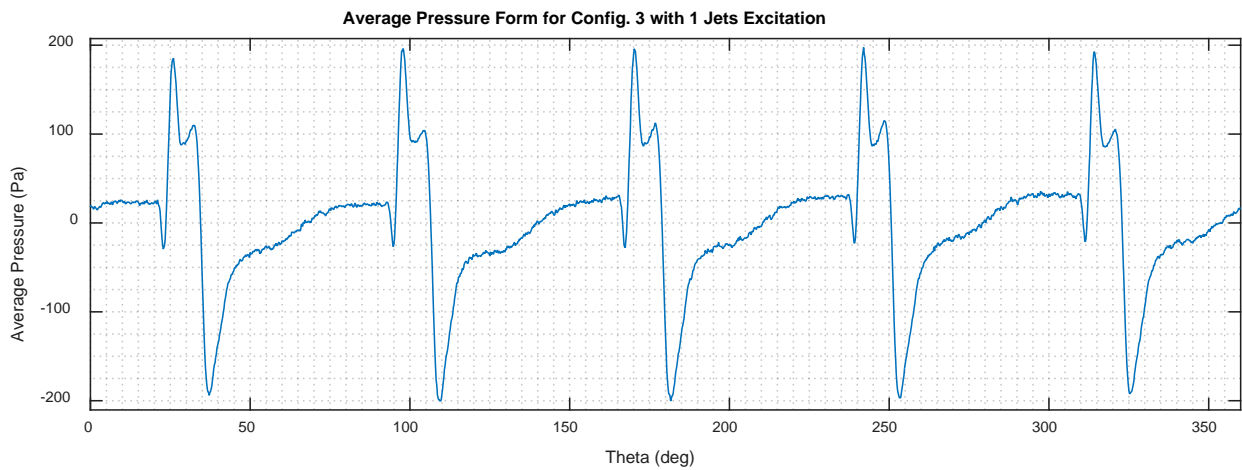


Figure 7.8-7 Average pressure waveform for configuration 3 under 1 jet excitation

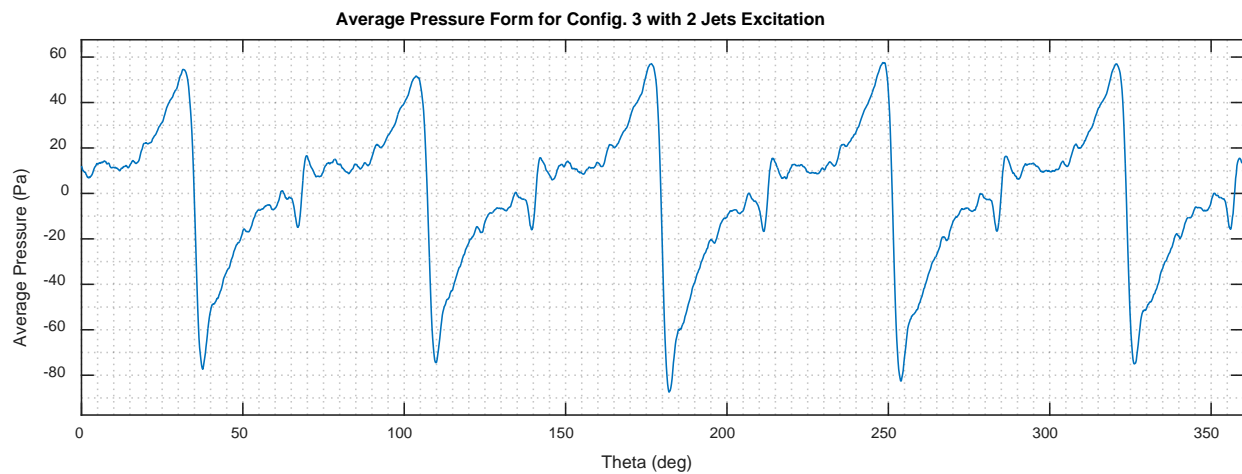


Figure 7.8-8 Average pressure waveform for configuration 3 under 2 jet excitation

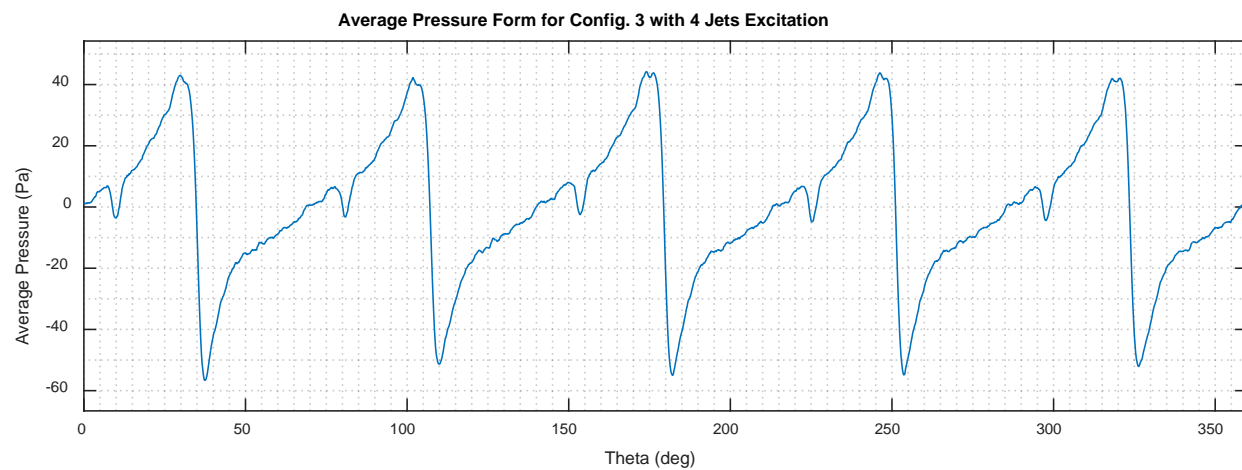


Figure 7.8-9 Average pressure waveform for configuration 3 under 4 jet excitation



7.8.1.4. Configuration 4

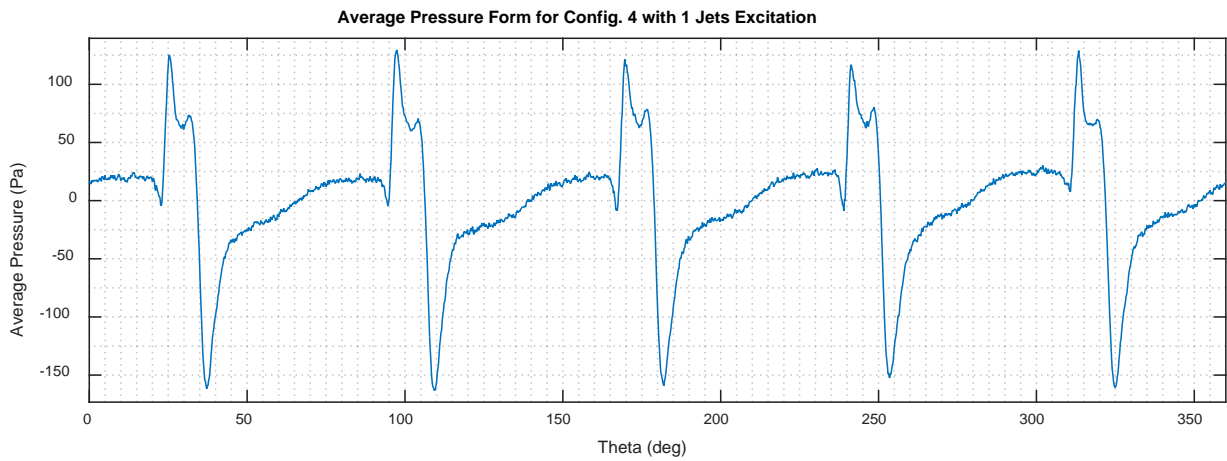


Figure 7.8-10 Average pressure waveform for configuration 4 under 1 jet excitation

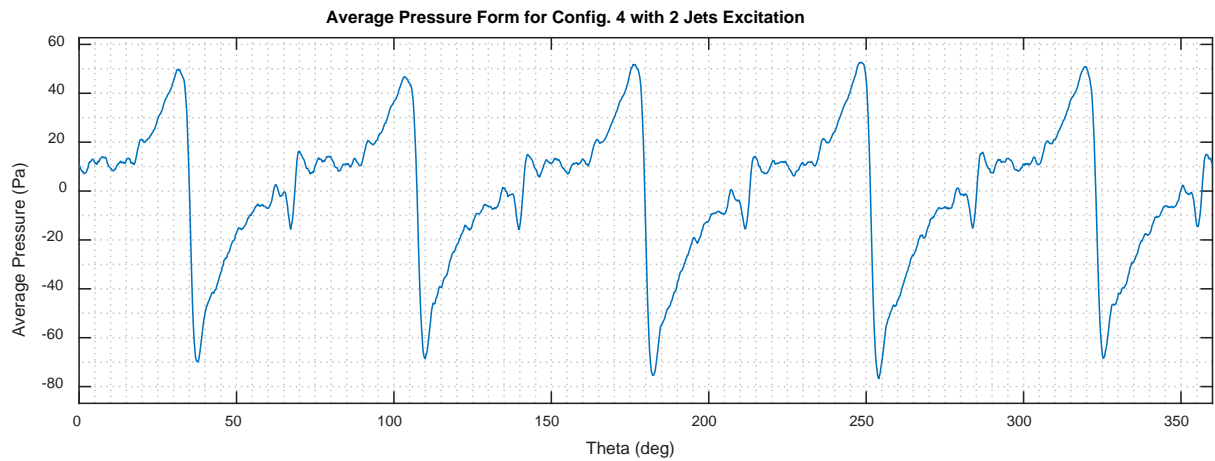


Figure 7.8-11 Average pressure waveform for configuration 4 under 2 jet excitation

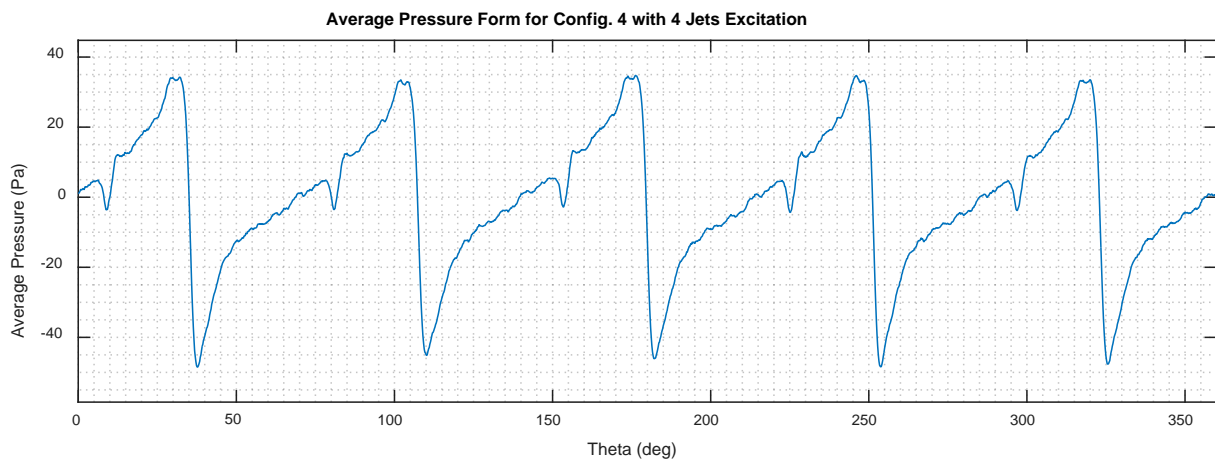


Figure 7.8-12 Average pressure waveform for configuration 4 under 4 jet excitation



7.8.1.5. Comparison of Average Pressure Distributions

7.8.1.5.1. 1 Jet Excitation

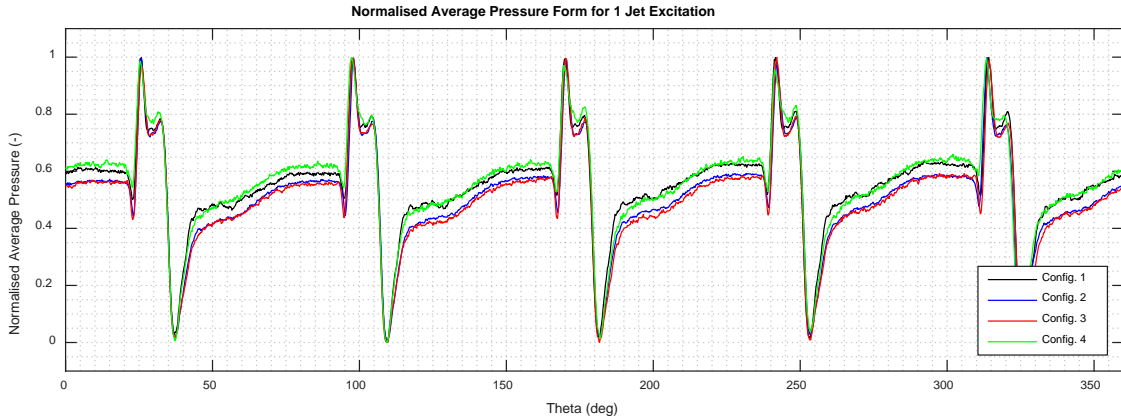


Figure 7.8-13 Normalised average pressure for 1 jet excitation

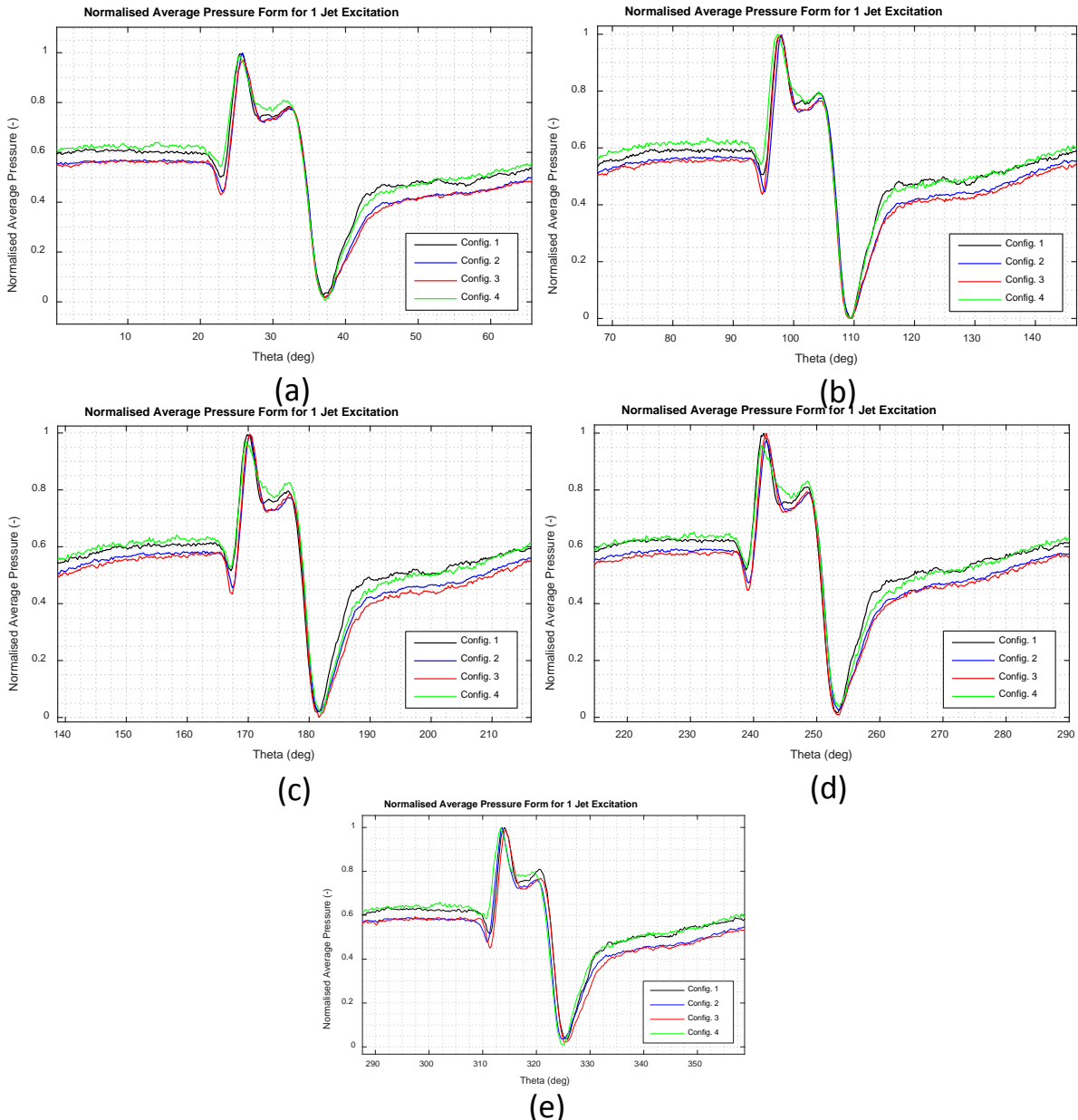


Figure 7.8-14 Individual normalised average pressures. (a) Blade 1. (b) Blade 2. (c) Blade 3. (d) Blade 4. (e) Blade 5.

7.8.1.5.2. 2 Jet Excitation

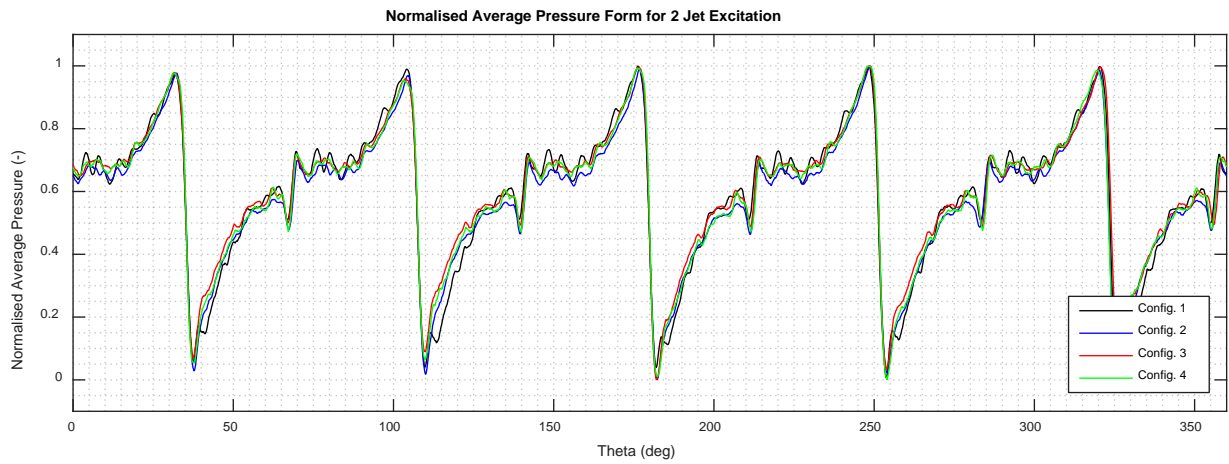


Figure 7.8-15 Normalised average pressure for 2 jet excitation

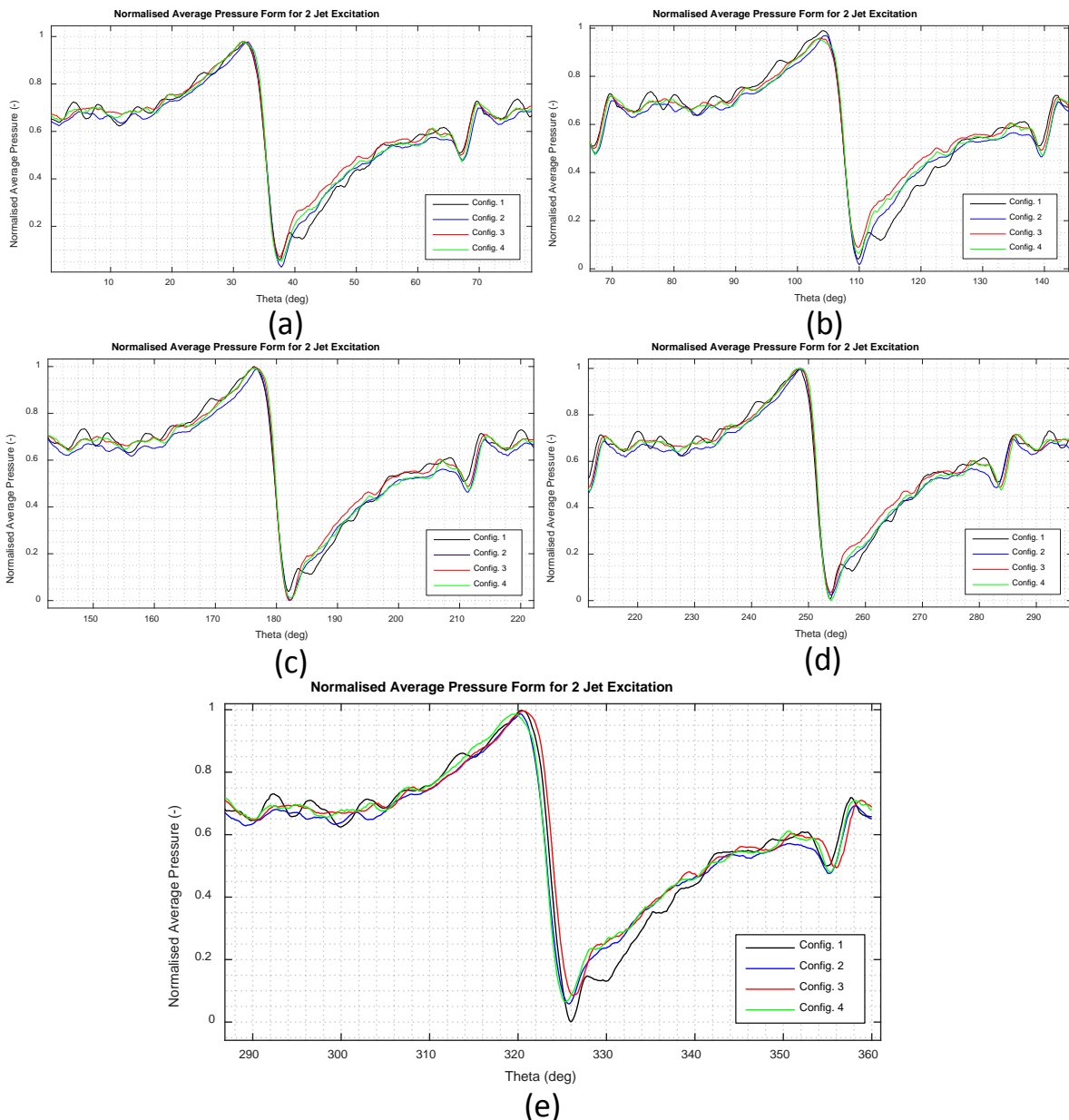


Figure 7.8-16 Individual normalised average pressures. (a) Blade 1. (b) Blade 2. (c) Blade 3. (d) Blade 4. (e) Blade 5.



7.8.1.5.3. 4 Jet Excitation

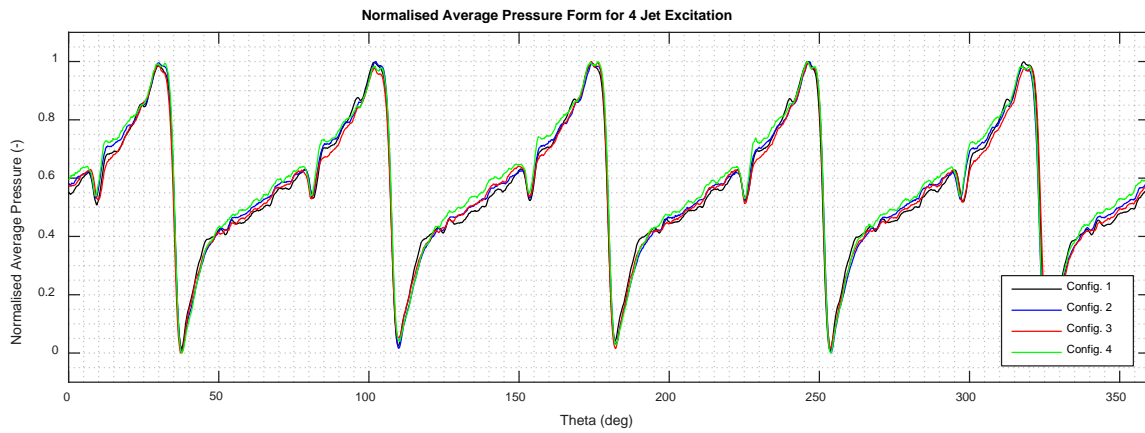


Figure 7.8-17 Normalised average pressure for 2 jet excitation

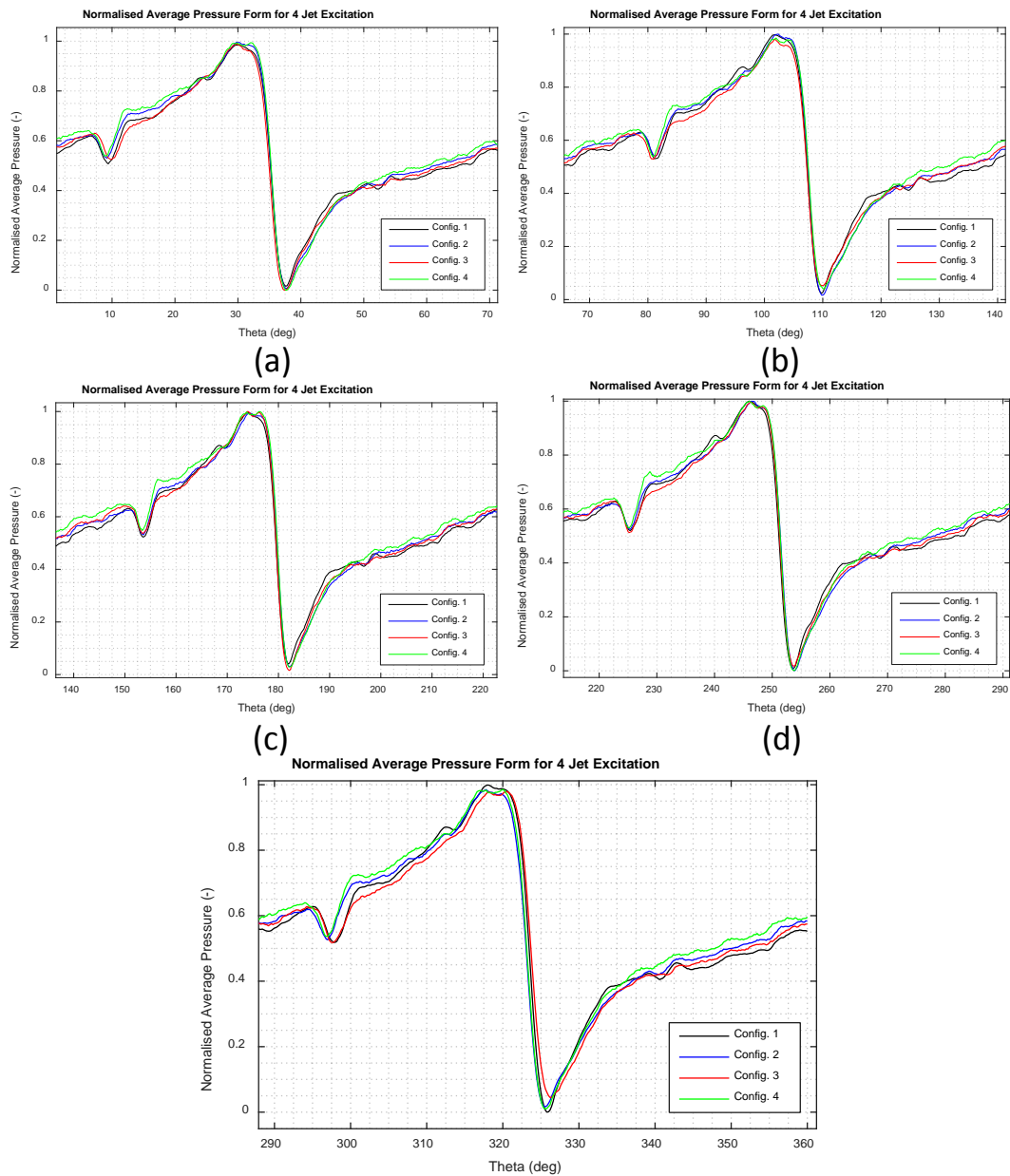


Figure 7.8-18 Individual normalised average pressures. (a) Blade 1. (b) Blade 2. (c) Blade 3. (d) Blade 4. (e) Blade 5.



7.8.2. H2 – Variance Heat Maps for Average Wave Forms

The variance heat maps between the individual average blade wave forms can be seen in Table 7.8-1, Table 7.8-2 and Table 7.8-3.

Table 7.8-1 Variance heat map in average wave form about blades given 1 Jet excitation

Config.	Blade 1	Blade 2	Blade 3	Blade 4	Blade 5
Config. 1/Config. 2	0.000601	0.000734	0.001022	0.001308	0.000872
Config. 1/Config. 3	0.000724	0.000517	0.001155	0.000912	0.000453
Config. 1/Config. 4	0.000469	0.000602	0.000861	0.000659	0.002598
Config. 2/Config. 3	8.65E-05	0.000378	0.000168	0.000217	0.001657
Config. 2/Config. 4	0.000803	0.001374	0.00049	0.000551	0.000886
Config. 3/Config. 4	0.000814	0.000699	0.000467	0.000523	0.004033

Table 7.8-2 Variance heat map in average wave form about blades given 2 Jet excitation

Config.	Blade 1	Blade 2	Blade 3	Blade 4	Blade 5
Config. 1/Config. 2	0.000838	0.001702	0.000968	0.000801	0.001681
Config. 1/Config. 3	0.003585	0.003461	0.003972	0.003752	0.003437
Config. 1/Config. 4	0.000868	0.00205	0.00121	0.001032	0.001989
Config. 2/Config. 3	0.002981	0.002475	0.003152	0.002873	0.00296
Config. 2/Config. 4	0.000194	0.000237	0.000318	0.000451	0.000225
Config. 3/Config. 4	0.002889	0.002789	0.003216	0.00317	0.003507

Table 7.8-3 Variance heat map in average wave form about blades given 4 Jet excitation

Config.	Blade 1	Blade 2	Blade 3	Blade 4	Blade 5
Config. 1/Config. 2	0.000429	0.000496	0.000587	0.000751	0.001134
Config. 1/Config. 3	0.000397	0.000486	0.000307	0.000349	0.000717
Config. 1/Config. 4	0.000813	0.001036	0.000941	0.000742	0.001244
Config. 2/Config. 3	0.000545	0.000431	0.000285	0.00024	0.001967
Config. 2/Config. 4	0.000121	0.000216	0.00014	0.000125	9.19E-05
Config. 3/Config. 4	0.000862	0.000509	0.000464	0.000362	0.001985

7.8.3. H3- Waterfall Plots of Synchronously Averaged Configuration 1 Pressure Signals

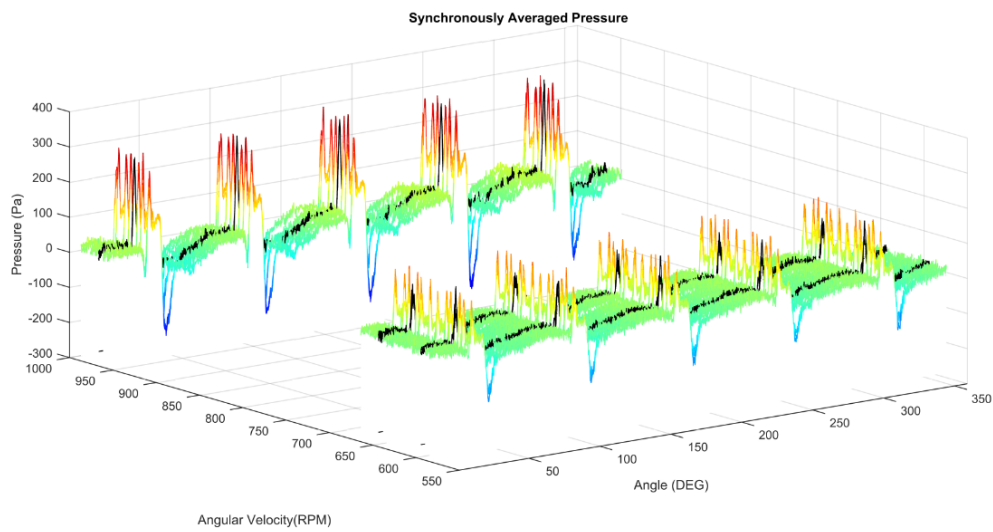


Figure 7.8-19 Waterfall plot of synchronously averaged pressure wave forms for configuration 1 under 1 jet excitation

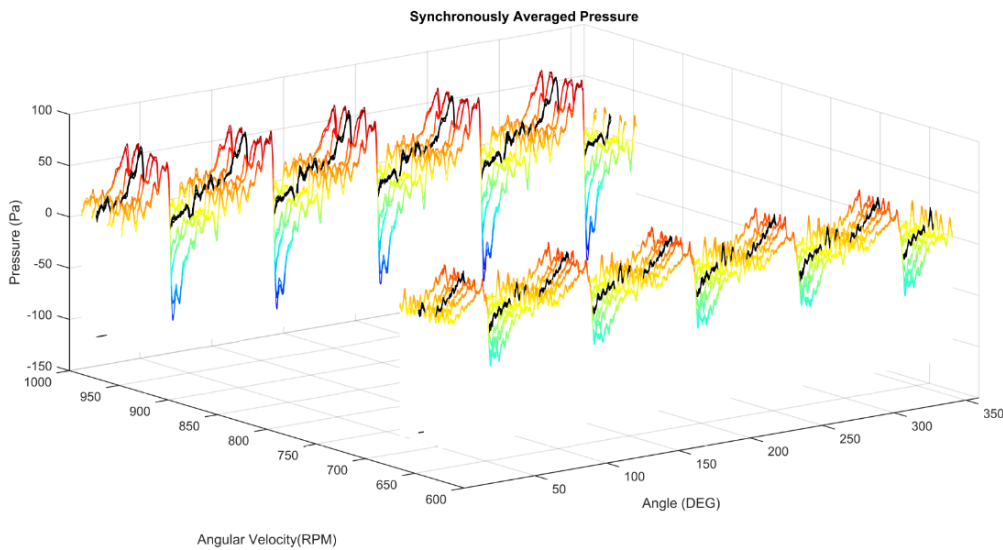


Figure 7.8-20 Waterfall plot of synchronously averaged pressure wave forms for configuration 1 under 2 jet excitation

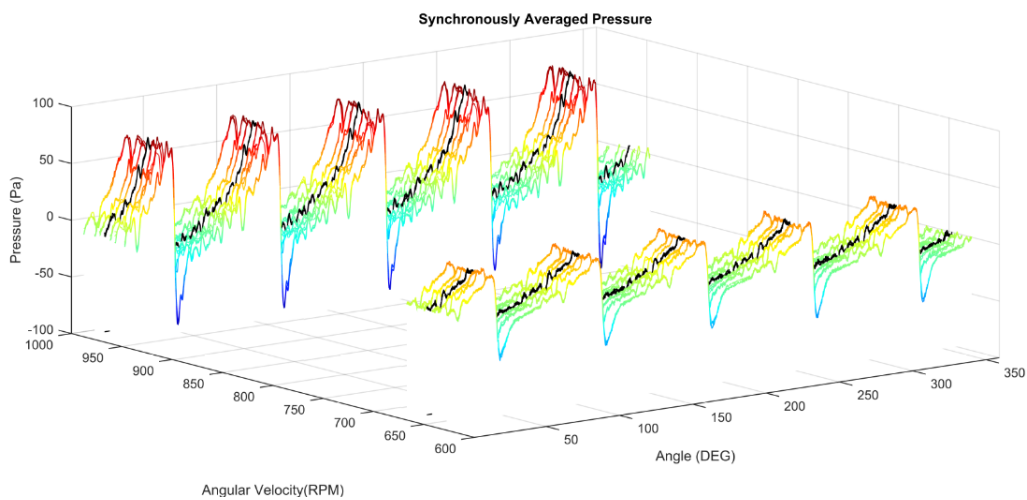


Figure 7.8-21 Waterfall plot of synchronously averaged pressure wave forms for configuration 1 under 4 jet excitation



7.8.4. H4 – Selected Pressure Range Plots and Linear Fit Table

The following plots contains pressure range fits. Best and worst case fits have been included.

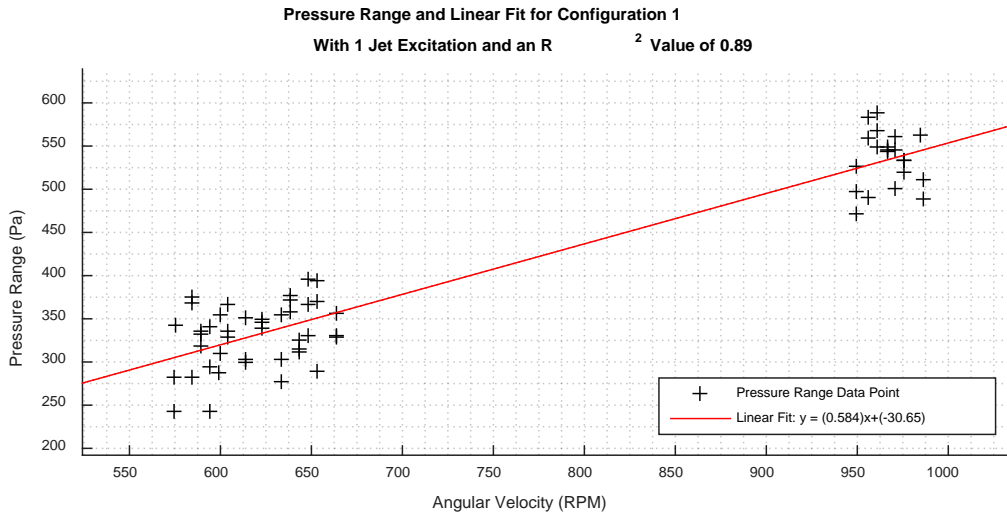


Figure 7.8-22 Pressure range and linear fit for configuration 1 under 1 jet excitation

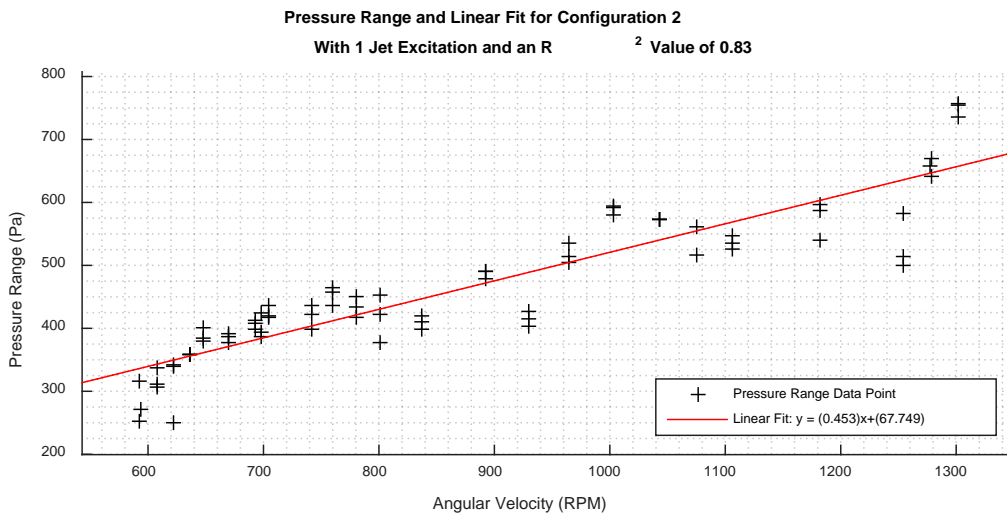


Figure 7.8-23 Pressure range and linear fit for configuration 2 under 1 jet excitation

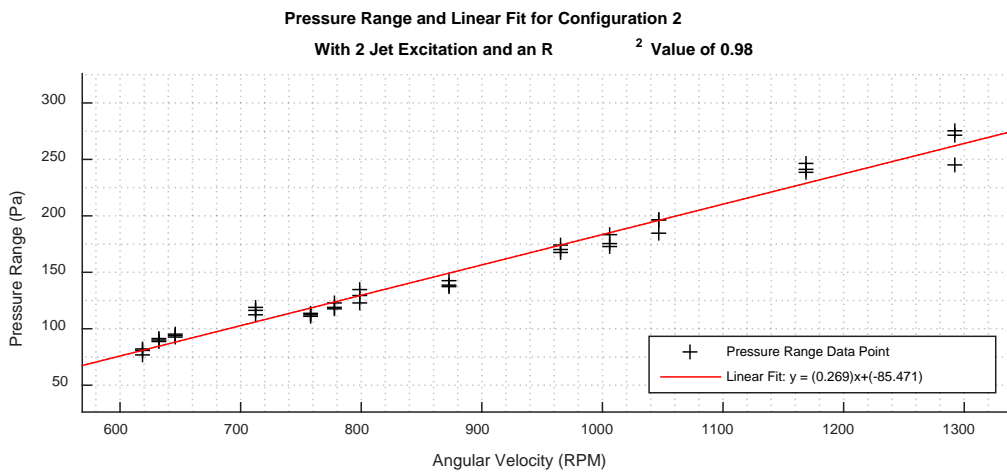


Figure 7.8-24 Pressure range and linear fit for configuration 2 under 1 jet excitation

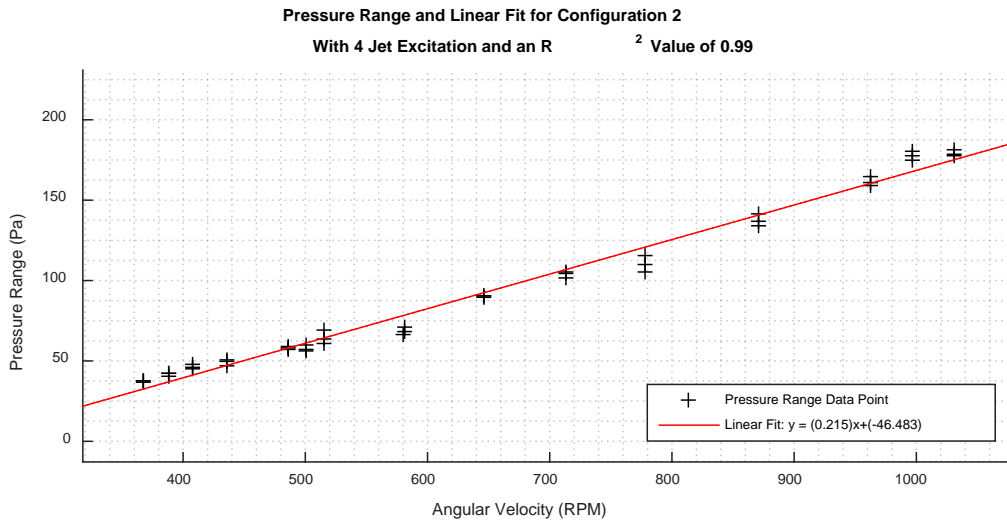


Figure 7.8-25 Pressure range and linear fit for configuration 2 under 1 jet excitation

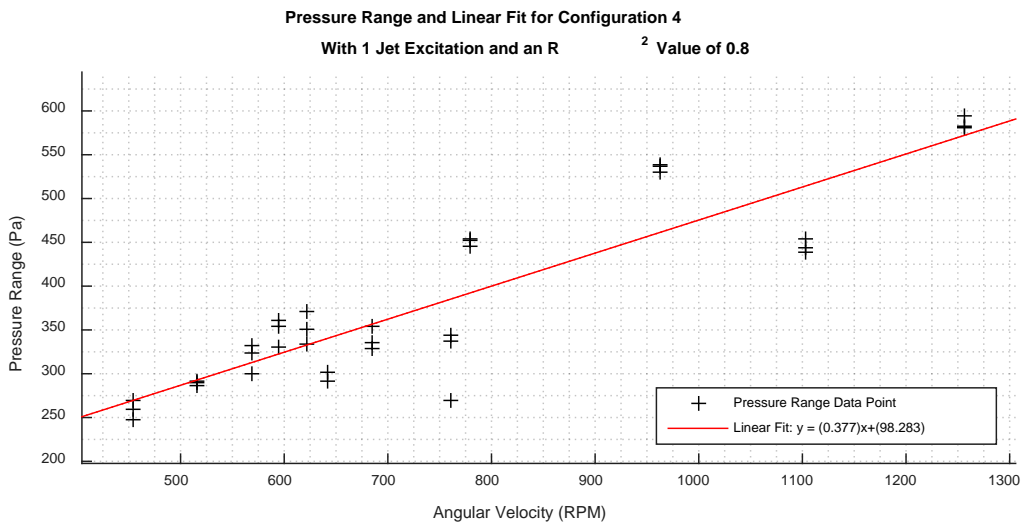


Figure 7.8-26 Pressure range and linear fit for configuration 4 under 1 jet excitation

Table 7.8-4 contains an evaluation of all of the linear fits for the various configurations and excitation schemes.

Table 7.8-4 Evaluation of linear fit to pressure range data

Jets ↓	Config. →	1	2	3	4	Mean	Std. Dev.
1		0.89	0.83	0.93	0.8	0.863	0.051
2		0.97	0.98	0.98	0.98	0.978	0.004
4		0.97	0.99	0.97	0.99	0.980	0.010
Mean		0.943	0.933	0.960	0.923	0.940	0.022
Std. Dev.		0.038	0.073	0.022	0.087	0.055	0.021



7.8.5. H5 – Selected Phase Modulation Due to Forced Response Plots

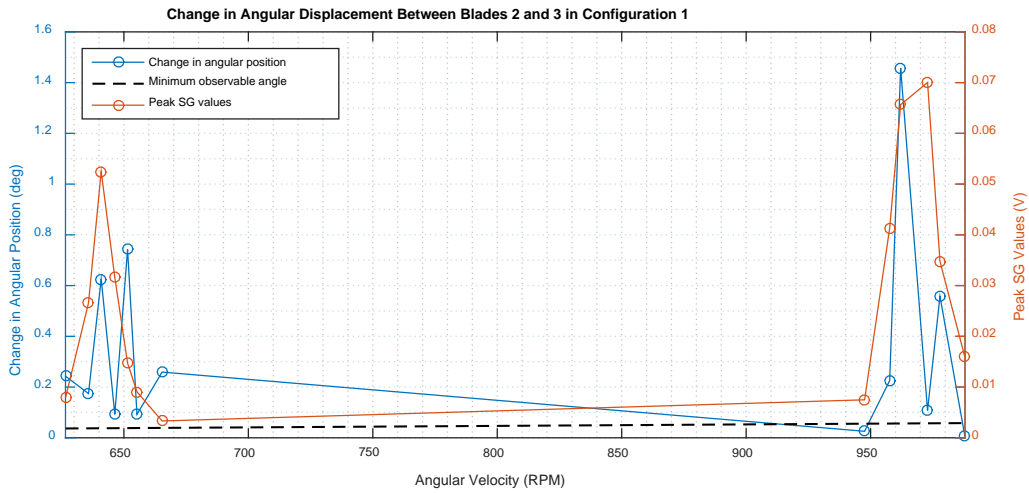


Figure 7.8-27 Change in angular displacement between blades 2 and 3 in configuration 1 with 1 jet excitation

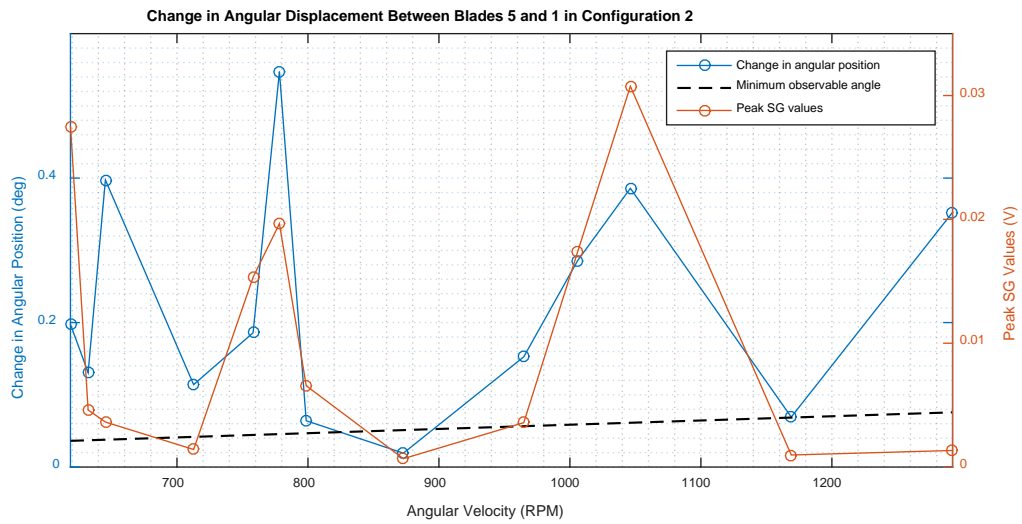


Figure 7.8-28 Change in angular displacement between blades 5 and 1 in configuration 2 with 2 jet excitation

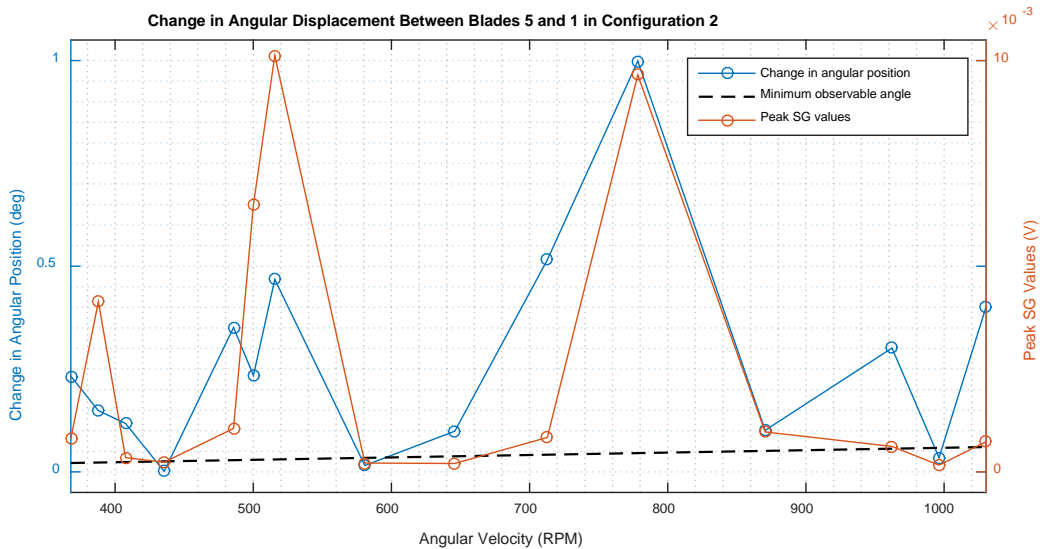


Figure 7.8-29 Change in angular displacement between blades 5 and 1 in configuration 2 with 4 jet excitation